

IMPERIAL COLLEGE LONDON

DEPARTMENT OF CHEMISTRY

**Electrocatalytic and catalytic oxygen  
reduction utilising transition metal and  
heteroatom doped carbon materials**

*by*

Daniel Malko

*Supervisor:*

Anthony R. J. Kucernak

*A thesis submitted in partial fulfilment of the requirements  
for the degree Doctor of Philosophy*

18 October 2016

# Declaration of Authorship

The present work was carried out in the period from 01.10.2013 to 31.08.2016 at the Department of Chemistry at Imperial College London and supervised by Prof. Anthony Kucernak. Results from research visits to the Department of Chemistry, Sao Carlos, Sao Paulo from 01.11.2016 to 07.12.2014 and from 03.07.2015 to 20.07.2015 also part of this work.

I declare that I have written this paper on my own and used no other than the named aids. Where results form collaborative experiments have been used it is clearly stated.

Signed:     Daniel Malko    

Date:     19/12/2016

# Copyright Declaration

The copyright of this thesis rests with the author and is made available under a Creative Commons Attribution Non-Commercial No Derivatives licence. Researchers are free to copy, distribute or transmit the thesis on the condition that they attribute it, that they do not use it for commercial purposes and that they do not alter, transform or build upon it. For any reuse or redistribution, researchers must make clear to others the licence terms of this work

*“An expert is a man who has made all the mistakes, which can be made,  
in a very narrow field.”*

Niels Henrik David Bohr (1885-1962)

# Abstract

## Electrocatalytic and catalytic oxygen reduction utilising transition metal and heteroatom doped carbon materials

by Daniel Malko

The commercialisation of polymer electrolyte fuel cells (PEFCs) is partly delayed due to the use of expensive and scarce precious metal catalysts for the oxygen reduction reaction (ORR). Transition metal and nitrogen containing carbon materials (M-N/C) could potentially replace Pt.

However, the activity and stability is still too low. This is due to a lack in the understanding of the active site, a difficulty in determining intrinsic catalyst parameters and the challenges posed by the higher catalyst loading in fuel cells.

A new precursor was identified. It can be doped with different metal centres and readily forms self-supporting ORR active carbon catalysts upon pyrolysis. Physicochemical characterisations of the Fe-N/C material suggests atomic metal centres as active sites. A proton coupled electron transfer is presumably the rate determining step.

The catalyst is exceptionally poison tolerant against a wide range of compounds that affect Pt based materials.

It was found that nitrite and nitric oxide interact with the active site(s). Fundamental insight was gained and it seems that two different types of metal centred active sites are present within Fe-N/C catalysts.

A methodology was developed to electrochemically count one type of those active sites by means of reductive nitrite stripping in a conventional rotating disk electrode (RDE) setup. It is possible to estimate the turnover frequency and active site density.

The material also catalyses the epoxidation of alkenes at room temperature and ambient pressure, suggesting a similar working principle as transition metal macrocycles.

A study of M-N/C catalysts in operating PEFCs has been conducted. The catalyst layer was investigated by means of impedance spectroscopy. The peculiar 45 degree feature and its deviation in the impedance spectrum can be used to determine the optimal ionomer content in the catalyst layer and therefore speed up the investigation in single cells.

# Acknowledgements

First and foremost I would like to thank Prof. Anthony Kucernak for taking me on and supervising my PhD studies. He always encouraged and supported me throughout. He always provided valuable insight no matter how busy he was and pushed me to question the obtained results. I learned many valuable things.

I would also like to thank Anthony and Dr Javier Rubio-Garcia for cofounding the company SweetGen Ltd during the last two years.

I would like to thank the EPSRC for sponsoring my PhD under project EP/J016454/1 and the Imperial College Global engagement scheme for funds that enabled a UK-Brasil collaborative project.

I would also like to thank Dr Thiago Lopes for introducing me to this topic, by supervising my masters project and then continuing with further fruitful collaborations throughout the course of my PhD. I would also like to thank him and Prof. Edson Ticianelli for hosting me in Sao Carlos under the Imperial College Global Engagement Scheme and for the amazing hospitality.

Gratitude also goes to all members of the "Kucernak group" that I had the privilege to get to know over the years and that made the lab such a great working environment. I would also like to thank all the technicians in the chemistry department for always being approachable and keeping the building running.

I would like to thank Pip Jones for great work on the epoxidation. I also would like to thank all other people mentioned in this work that helped me gather the results for this thesis, through support with various specialist equipment and discussions.

And last but not least, I thank my mother and sister for always supporting me through all difficulties and my girlfriend Tanja for support and also for letting me use her kitchen and eat her chocolate during all the late nights of writing.

# Contents

<b>Declaration of Authorship</b>	<b>2</b>
<b>Copyright Declaration</b>	<b>3</b>
<b>Abstract</b>	<b>5</b>
<b>Acknowledgements</b>	<b>6</b>
<b>List of Publications</b>	<b>12</b>
<b>List of Figures</b>	<b>14</b>
<b>List of Schemes</b>	<b>25</b>
<b>List of Tables</b>	<b>27</b>
<b>Abbreviations</b>	<b>28</b>
<b>Physical Constants</b>	<b>31</b>
<b>Symbols</b>	<b>32</b>
<b>1 Introduction</b>	<b>35</b>
1.1 Polymer electrolyte fuel cells (PEFCs) . . . . .	36
1.2 The Oxygen Reduction Reaction (ORR) . . . . .	40
1.3 Reason for electrocatalysts - PEMFC efficiency and losses . . . . .	43
1.4 Electrokinetics and electrocatalysis . . . . .	46
1.5 Cost, durability and activity requirements for fuel cell catalysts . . . . .	52
1.6 Types of ORR electrocatalysts . . . . .	53
1.7 M-N/C type non-precious metal catalysts (NPMCs) . . . . .	55
1.7.1 Reasons for research into non-precious metal catalysts . . . . .	55
1.7.2 Development of biologically inspired ORR catalysts . . . . .	58
1.7.3 Heat treatment and first applications in PEFCs . . . . .	62
1.7.4 The controversial role of the metal center. . . . .	67
1.7.5 Mechanistic proposals on and stability of Fe sites . . . . .	75
1.7.6 State of the art activities . . . . .	77
1.7.7 Major gaps in the understanding of NPMCs . . . . .	78
1.8 Proposal and structure of the thesis . . . . .	79

---

1.9	References . . . . .	81
<b>2</b>	<b>Experimental Techniques</b>	<b>110</b>
2.1	Electrochemical Techniques . . . . .	110
2.1.1	Rotating Ring Disk Electrode . . . . .	110
2.1.2	Electrochemical Impedance Spectroscopy . . . . .	117
2.1.3	Cyclic Voltammetry . . . . .	121
2.1.4	Chronocoulometry . . . . .	124
2.1.5	Membrane electrode assembly single cell testing . . . . .	125
2.2	Physical and analytical characterization methods . . . . .	126
2.2.1	Nitrogen adsorption analysis . . . . .	126
2.2.2	Total reflection x-ray fluorescence . . . . .	129
2.2.3	Scanning electron microscopy . . . . .	131
2.2.4	Transmission electron microscopy . . . . .	132
2.2.5	Scanning transmission electron microscopy . . . . .	133
2.2.6	Electron energy loss and energy dispersive spectroscopy . . . . .	134
2.2.7	X-ray photoelectron spectroscopy . . . . .	135
2.2.8	Temperature programmed desorption . . . . .	137
2.2.9	Electron paramagnetic resonance . . . . .	138
2.2.10	Ion Chromatography . . . . .	139
2.2.11	Gas Chromatography . . . . .	140
2.2.12	Mass spectrometry . . . . .	142
2.3	References . . . . .	142
<b>3</b>	<b>Synthesis and characterisation of M-N/C catalysts</b>	<b>147</b>
3.1	Introduction . . . . .	147
3.2	Results and Discussion . . . . .	148
3.2.1	A catalyst based on poly-1,5-Diaminonaphthalene and its ORR activity . . . . .	148
3.2.2	Effect of metal centre on ORR activity . . . . .	156
3.2.3	Elemental composition and surface element distribution of Fe-N/C and N/C material . . . . .	158
3.2.4	Effect of nano-MgO template and S doping on ORR activity . . . . .	161
3.2.5	Electronic structure (EPR) of selected catalysts . . . . .	163
3.2.6	Microstructure and element distribution (STEM and EELS) of the Fe-N/C and N/C catalysts . . . . .	166
3.2.7	MEA Single Cell testing . . . . .	171
3.3	Conclusions . . . . .	172
3.4	Experimental Part . . . . .	173
3.4.1	Catalyst Synthesis . . . . .	173
3.4.2	RRDE/RDE measurements . . . . .	176
3.4.3	SEM . . . . .	177
3.4.4	Nitrogen adsorption analysis . . . . .	178
3.4.5	TXRF . . . . .	178
3.4.6	XPS . . . . .	178
3.4.7	EPR . . . . .	179
3.4.8	TEM/STEM/EDX . . . . .	179
3.4.9	STEM and EELS . . . . .	180
3.4.10	MEA testing . . . . .	180
3.5	References . . . . .	181



---

<b>4</b>	<b>Experimental identification of the active site and mechanistic insight into its activity</b>	<b>186</b>
4.1	Introduction . . . . .	186
4.2	Results and Discussion . . . . .	187
4.2.1	Poison tolerance and implications for practical devices . . . . .	187
4.2.2	Nitrogen cycle molecules as possible active site probes . . . . .	191
4.2.3	Organic reactions to track the active site . . . . .	192
4.2.4	Gas sorption of oxygen on Fe-N/C catalyst . . . . .	194
4.2.5	Mechanistic investigation of Fe-N/C catalyst . . . . .	196
4.2.5.1	pH dependence of the ORR . . . . .	197
4.2.5.2	Kinetic isotope effect of the ORR in alkaline and acid . . . . .	199
4.2.5.3	Rate determining step proposal . . . . .	203
4.3	Conclusion . . . . .	204
4.4	Experimental Part . . . . .	205
4.4.1	RDE poisoning experiments . . . . .	205
4.4.2	MEA poisoning experiments . . . . .	205
4.4.3	Organic treatment of catalyst . . . . .	206
4.4.4	Gas sorption and TPD . . . . .	207
4.4.5	pH study . . . . .	207
4.4.6	H/D experiments . . . . .	208
4.5	References . . . . .	209
<b>5</b>	<b>Interaction of nitric oxide and nitrite with the Fe-N/C catalyst</b>	<b>213</b>
5.1	Introduction . . . . .	213
5.2	Results and Discussion . . . . .	216
5.2.1	The interaction of the Fe-N/C catalyst with nitrogen containing poisons . . . . .	216
5.2.2	The interaction of the Fe-N/C catalyst with nitrite . . . . .	217
5.2.3	The interaction of the Fe-N/C catalyst with nitric oxide . . . . .	220
5.2.4	The interaction of the Fe-N/C catalyst with hydroxylamine . . . . .	224
5.2.5	Effect of poisons on metal free N/C catalyst . . . . .	225
5.2.6	Effect of the poison on the cyclic voltammetry of the Fe-N/C catalyst	226
5.2.7	Nitrite electroreduction to ammonia . . . . .	228
5.2.8	Nitric oxide electroreduction . . . . .	231
5.2.9	Possible use of Fe-N/C catalysts as diagnostic sensor materials . . . . .	233
5.3	Conclusions . . . . .	234
5.4	Experimental Part . . . . .	234
5.4.1	Electrochemical Experiments . . . . .	234
5.4.2	Poisoning Protocols . . . . .	235
5.4.3	Ion Chromatography . . . . .	238
5.5	References . . . . .	239
<b>6</b>	<b><i>In situ</i> electrochemical quantification of active sites in Fe-N/C catalysts</b>	<b>247</b>
6.1	Introduction . . . . .	247
6.2	Results and Discussion . . . . .	249
6.2.1	Electrochemical stripping protocol . . . . .	249
6.2.2	Alternative coulometric stripping protocol . . . . .	252
6.2.3	Active site density and turnover frequency . . . . .	252
6.2.4	Comparison to Pt based catalysts . . . . .	254
6.2.5	Stripping charge on the metal free N/C catalyst and systematic error	255

---

6.2.6	Justification for using pH 5.2 . . . . .	257
6.2.7	Application of the stripping technique to other Fe-N/C catalysts . . . . .	260
6.2.8	Application of the stripping technique to a FeCo-N/C catalysts . . . . .	260
6.2.9	Concentration of nitrite - evidence for 2 types of Fe active sites . . . . .	262
6.3	Conclusions . . . . .	265
6.4	Experimental Part . . . . .	266
6.4.1	Electrochemical stripping experiments . . . . .	266
6.4.2	Electrochemical cleaning protocol . . . . .	266
6.4.3	Stripping protocol using cyclic voltammetry . . . . .	267
6.4.4	Stripping protocol using chronocoulometry . . . . .	268
6.4.5	Synthesis of FeCo catalyst: . . . . .	268
6.5	References . . . . .	269
<b>7</b>	<b>M-N/C materials as catalysts for alkene epoxidation</b>	<b>274</b>
7.1	Introduction . . . . .	274
7.1.1	Epoxidation reactions . . . . .	275
7.1.2	Epoxidations with transition metal macrocycles . . . . .	277
7.1.3	Information to be gained for the active site . . . . .	280
7.2	Results and Discussion . . . . .	280
7.2.1	M-N/C catalyst for ORR and epoxidation of cyclohexene . . . . .	280
7.2.2	Epoxidation of different substrates with the Fe-N/C catalyst . . . . .	283
7.2.3	Recyclability of Fe-N/C catalyst . . . . .	284
7.2.4	Oxygen uptake measurements - estimation of reaction rate . . . . .	285
7.2.5	Measuring the potential of the reaction mixture . . . . .	286
7.2.6	Correlating the potential with oxygen consumption . . . . .	287
7.2.7	Comparison of Fe-N/C catalyst to free Fe ions . . . . .	287
7.2.8	Mechanistic considerations . . . . .	289
7.2.9	Further possible experiments . . . . .	293
7.3	Conclusions . . . . .	293
7.4	Experimental Part . . . . .	294
7.4.1	Epoxidation reactions . . . . .	294
7.4.2	GC analysis of reaction mixture . . . . .	295
7.4.3	Oxygen uptake measurements . . . . .	295
7.4.4	Potential measurements . . . . .	295
7.5	References . . . . .	296
<b>8</b>	<b>M-N/C catalysts in PEM single cells - catalyst layer optimisation utilising impedance spectroscopy</b>	<b>299</b>
8.1	Introduction . . . . .	299
8.2	Electrochemical Impedance Spectroscopy for fuel cell analysis . . . . .	301
8.3	Information on catalyst layer structure . . . . .	303
8.4	Results and Discussions . . . . .	303
8.4.1	Microstructure and RDE performance of 3 different catalysts . . . . .	303
8.4.2	Structure and thickness of the catalyst layer . . . . .	305
8.4.3	Performance of catalysts with different ionomer loadings . . . . .	306
8.4.4	Impedance in the absence of a faradaic reaction . . . . .	308
8.4.5	Impedance under operation . . . . .	310
8.4.6	Effect of CL thickness, relative humidity and backpressure on the EIS spectrum . . . . .	312
8.4.7	Interpretation of observed results . . . . .	313

---

8.4.8	Optimisation protocol . . . . .	316
8.5	Conclusions . . . . .	317
8.6	Experimental Part . . . . .	317
8.6.1	Electrochemical testing . . . . .	317
8.6.2	AC Impedance Measurements . . . . .	317
8.6.3	SEM . . . . .	318
8.6.4	BET . . . . .	319
8.7	References . . . . .	319
<b>9</b>	<b>Concluding remarks</b>	<b>324</b>
9.1	Final Conclusions . . . . .	324
9.2	Future work . . . . .	328

# List of Publications

A number of manuscripts have been published, were submitted for publication or are in the process of being prepared from the material in this thesis. These and the chapters they cover are:

1. A paper covering the poison tolerance of the carbon based catalyst and also detailing the new method of producing this catalyst. The material in this paper is described in parts of Chapter 3 (3.2.1) and Chapter 4 (4.2.1): Malko, D., Lopes, T., Symianakis, E. & Kucernak, A. R. The intriguing poison tolerance of non-precious metal oxygen reduction reaction (ORR) catalysts. *J. Mater. Chem. A* 4, 142-152 (2015).
2. A communication, investigating the kinetic isotope effect, as detailed in a part of Chapter 4 (4.2.5.2): Malko, D. & Kucernak, A. R. Kinetic isotope effect in the oxygen reduction reaction (ORR) over Fe-N/C catalysts under acidic and alkaline conditions. *Manuscript submitted*.
3. A paper on the interaction of nitrogen cycle molecules with the Fe-N/C catalyst as described in Chapter 5: Malko, D., Kucernak, A. R. & Lopes, T. Performance of Fe-N/C oxygen reduction electrocatalysts towards  $\text{NO}_2^-$ , NO, and  $\text{NH}_2\text{OH}$  electroreduction - from fundamental insights into the active center to a new method for environmental nitrite destruction *Manuscript submitted*.
4. A paper on the determination of active sites within Fe-N/C catalysts as described in Chapter 6. Some characterisation and the pH dependence of the ORR as described in parts of Chapters 3 (3.2.6) and 4 (4.2.5.1) are also content of the thesis: Malko D., Lopes T. & Kucernak A. R. *In situ* electrochemical quantification of active sites in Fe-N/C non-precious metal catalysts. *Nat. Commun.* 7, 13285 (2016).

5. A paper on the epoxidation reaction catalysed by M-N/C catalysts as described in Chapter 7: Malko D., Jones P., Britovsek G., & Kucernak A. R. Crossover catalyst - from fuel-cell oxygen reduction to alkene epoxidation. *Manuscript in preparation.*
6. A paper on the impedance analysis of M-N/C catalysts in single cells as described in Chapter 8: Malko, D., Lopes, T., Ticianelli, E. A. & Kucernak, A. R. A catalyst layer optimisation approach using electrochemical impedance spectroscopy for PEM fuel cells operated with pyrolysed transition metal-N-C catalysts. *J. Power Sources* 323, 189-200 (2016).

# List of Figures

1.1	Operating principle of a PEFC. (left) Operated with a proton exchange membrane (PEM). (right) Operated with an anion exchange membrane (AEM). [8, 20]	37
1.2	(top) Structure of Nafion <sup>®</sup> , where n,m,l are integers and the ratio of those determines the type of Nafion <sup>®</sup> . (bottom) Example of a functionalized polysulfone as anion exchange membrane.	38
1.3	(a) schematic representation of the cross section of a classic membrane electrode assembly (MEA), consisting of a membrane, sandwiched between two sets of gas transport layer (GTL), mesoporous layer (MPL), and catalyst layer (CL). The membrane coated with the catalyst and without GTL and MPL is commonly referred to as catalyst coated membrane (CCM). (b) example of a flow field machined into a bipolar plate. The MEA is sandwiched between two such plates in order to supply reactants and conduct electrons. [8]	39
1.4	PEM Fuel Cell stack. [Reprinted with permission from Ref. [26]]	40
1.5	Molecular orbital (MO) diagram of oxygen.	40
1.6	Reaction scheme of the ORR to water after Woroblowa [28], showing the direct 4 electron ( $k_1$ ) and indirect 2 + 2 electron pathway ( $k_2, k_3$ ). The superscripts b, s and * denote the species in the bulk, close to the surface and adsorbed, respectively.	41
1.7	Representative fuel cell polarisation curve, showing the different parasitic losses and the typical potential region at which those dominate.	45
1.8	Diagram showing the free energy of different intermediates for the ORR along a reaction coordinate. The values for the activation barrier of a particular reaction step $\Delta G_n^\ddagger$ , the free energy of a particular reaction step $\Delta G_n$ , the free energy of the complete reaction $\Delta G_{rxn}^0$ and the energetic location of the respective transition state are indicated. In this case the first electron transfer is the RDS, as it has the highest activation barrier.	49
1.9	A plot of the electrochemical binding energy of O <sub>2</sub> on different metal surfaces and the respective ORR activity. [Reprinted with permission from Ref. [36]. Copyright 2004 American Chemical Society.]	51
1.10	Breakdown of costs for the components in a fuel cell stack at different production volumes. [Taken from [64]]	55
1.11	Abundance of the elements in the earth's crust [Taken from [68, 69]].	56
1.12	Distribution of known Pt reserves in the world. [71, 72]	57
1.13	Active site structure of cytochrome c oxidase (CcO) [77]	58

1.14	Different spatial configuration for dioxygen, when it interacts with metal active sites. a) End-on configuration with frontier orbital interactions. b) Side-on configuration with frontier orbital interactions. c) Further possible configurations, when the active centre consists of 2 sites. [83] M is a metal site and X can be either a metal site or a different atom that might interact with the substrate, <i>e.g.</i> nitrogen from the ligand. . . . .	60
1.15	General structure of a) metalloporphyrin and b) metallophthalocyanine. [85]	61
1.16	Plot of $\log k$ versus redox potentials of the metal for O <sub>2</sub> reduction in 0.1M NaOH on different metal macrocycles adsorbed on glassy carbon. [Taken with permission from Ref. [93]] . . . . .	62
1.17	Increase in (a) ORR activity and (b) stability of different metal-macrocy-cles adsorbed onto Norit carbon black after heat treatment [Taken with permis-sion from Ref. [107]] . . . . .	63
1.18	General structure of different precursors used for the incorporation of nitro-gen groups into M-N/C catalysts ( <b>top</b> ) small N-containing molecules (a) acetonitrile (b) cyanamide (c) aliphatic terminal diamines ( <b>middle</b> ) aro-matic N-containing compounds d) perylene-tetracarboxylic dianhydride in combination with gaseous NH <sub>3</sub> e) 1,10-phenanthroline ( <b>bottom</b> ) polymeric precursors f) polynitroaniline g) polyaniline . . . . .	64
1.19	(a) Polarization curves for MEAs comprising a cathode made with Fe-ZIF8-derived catalyst (blue stars) and Fe-N/C from Lefvre <i>et al.</i> [62] (red circles). For comparison, the polarization curve of an MEA made with a state-of-the-art Pt-based cathode with a loading of 0.3 mg <sub>Pt</sub> cm <sup>2</sup> (green squares). (b) Power density curves corresponding to polarization curves shown in a. For the two MEAs made with iron-based cathodes, the catalyst loading was 3.9 mg cm <sup>2</sup> . [Taken and adapted with permission from Ref. [119]] . .	65
1.20	Proposed reaction steps of a porphyrin with the carbon support upon heat treatment. [Reproduced after Ref. [113]] . . . . .	67
1.21	Different nitrogen functionalities found in heat treated nitrogen doped amorphous carbon. [130] . . . . .	68
1.22	Proposed structure of an active iron site coordinated with pyridinic nitrogen groups a) hosted in a micropore [211] and b) embedded in the carbon framework [152] . . . . .	69
1.23	a) Side view of the different proposed FeN <sub>4</sub> centres as extracted from Mössbauer spectroscopy b) electronic configuration of the respective species. [Reproduced after Ref. [140]] . . . . .	70
1.24	Proposed mode of deactivation of active nitrogen sites under acidic condi-tions after Ref. [168] . . . . .	72
1.25	a) synthetic route to a Fe-N/C catalyst rich in Fe <sub>3</sub> C nano-particulate phases, which are encapsulated with carbon. b) SEM micrograph of the material. c) - e) TEM images, showing the Fe <sub>3</sub> C particles as dark spots. e) identification of Fe <sub>3</sub> C and graphite through lattice spacing analysis [Reprinted with permission from Ref. [221]. Copyright 2015 American Chemical Society]. . . . .	74
2.1	(a) 3-compartment electrochemical cell with equipment. (b) Cross section of the RDDE. (c) Block diagram of the setup. . . . .	111
2.2	(a) Representation of electrolyte streamlines during disk rotation. (b) Bot-tom view of streamlines. (c) Radii of disk, inner ring and outer ring. [2] .	112

2.3	Representative ORR curves at different rotation rates for a non-precious metal catalyst in alkaline solution. . . . .	116
2.4	a) Equivalent <i>Randles-Ershler</i> circuit of a faradaic half reaction. b) <i>Nyquist</i> -plot of the impedance response expected for this circuit. c) <i>Bode</i> magnitude plot and d) <i>Bode</i> phase angle plot of the same circuit. Traces <b>1</b> , <b>2</b> and <b>3</b> in b) - d) represent the mass transport response for the blocking electrode case, the infinite linear diffusion and the semi-infinite linear diffusion, respectively. [12, 13] . . . . .	120
2.5	Representative voltammograms of a platinum catalyst deposited on carbon black (Pt/C) and a Fe-N/C catalyst (Fe/CN <sub>x</sub> ). . . . .	123
2.6	Representative reductive coulometric stripping of a species from the surface of an Fe-N/C catalyst as compared to the baseline trace. . . . .	124
2.7	(a) Schematic of an MEA. CL = catalyst layer, GTL = Gas Transport Layer, PEM = Polymer Electrolyte Membrane.(b) MEA embedded onto one half of the testing device (right) other half shows the graphite plate with the flow field. Both parts are sandwiched and screwed together, to obtain the complete device. . . . .	125
2.8	Representative BET isotherm of a carbon based high surface area FeCo-N/C catalyst with micropores. . . . .	128
2.9	a) Image of a quartz carrier with a deposited sample which is unsuitable for the measurement, due to being inhomogeneous (left) and a suitable homogeneous sample layer (right). b) Representative total reflection X-ray fluorescence (TXRF) spectrum of a Fe-N/C catalyst with Ga as internal standard. . . . .	130
2.10	SEM image of a pyrolyzed CN <sub>x</sub> catalyst. . . . .	132
2.11	TEM image of a pyrolyzed Fe/Co-N/C catalyst. . . . .	133
2.12	STEM image of a pyrolyzed Fe-N/C catalyst. . . . .	134
2.13	Representative EELS spectrum of Fe-N/C catalyst. . . . .	135
2.14	XPS wide scan spectrum of Fe-N/C catalyst. . . . .	136
2.15	TPD spectrum of water adsorbed onto Fe-N/C catalyst. . . . .	137
2.16	(a) Relationship between magnetic field and <i>Zeeman</i> splitting. (b) resulting radical EPR spectrum.[Taken from [36]] . . . . .	139
2.17	Representative ion chromatogram of an electrolyte, containing various ions. . . . .	140
2.18	Representative gas chromatogram of a crude reaction mixture used in this work. . . . .	141
3.1	(a) Schematic, depicting the synthesis procedure of the catalyst (b) Scanning Electron Microscopy image of polymerized 1,5-diaminonaphthalene as precursor for the ODAN catalyst (c) Scanning Electron Microscopy image of ODAN catalyst material after heat treatment at 1000 °C for 2 h. . . . .	149
3.2	(a) Steady-state RRDE measurements in 0.5 M H <sub>2</sub> SO <sub>4</sub> , rotating speed: 1600 rpm, 30 s hold, 30 mV step potential, catalyst loading: non-precious metal catalysts: 750 μg cm <sup>-2</sup> , Pt/C: 60 μg <sub>Pt</sub> cm <sup>-2</sup> , O <sub>2</sub> -saturated at 1 atm (bottom) ORR activity (top) peroxide yield (b) in 0.1 M NaOH. [Adapted with permission from Ref. [6]] . . . . .	150
3.3	<i>Tafel</i> -plots of selected catalysts in 0.5 M H <sub>2</sub> SO <sub>4</sub> and 0.1 M NaOH corresponding to the measurements in Figure 3.2. . . . .	152
3.4	Steady-state RRDE measurements in 0.5 M H <sub>2</sub> SO <sub>4</sub> at different catalyst loadings, rotating speed: 1600 rpm, 30 s hold, 30 mV step potential, O <sub>2</sub> -saturated at 1 atm. [Adapted with permission from Ref. [6]] . . . . .	154



3.5	Steady-state RDE measurements of Fe-N/C catalyst in 0.5 M H <sub>2</sub> SO <sub>4</sub> after first and second heat treatment, catalyst loading: 750 μg cm <sup>-2</sup> rotating speed: 1600 rpm, 30 s hold, 30 mV step potential, O <sub>2</sub> -saturated at 1 atm.	154
3.6	Steady-state RRDE measurements of M-N/C catalyst with different metals (M) in 0.5 M H <sub>2</sub> SO <sub>4</sub> , catalyst loading: 750 μg cm <sup>-2</sup> , rotating speed: 1600 rpm, 30 s hold, 30 mV step potential, O <sub>2</sub> -saturated at 1 atm. . . . .	157
3.7	Potential of M-N/C catalysts at a current density of 250 μA cm <sup>-2</sup> . In black 3d, green 4d and blue 5d transition metals. Black dashed line is not a fit but indicates a volcano shape in the 3d transition metals. . . . .	158
3.8	XPS wide scan of Fe-N/C catalyst. [Taken with permission from Ref. [6]]	159
3.9	High resolution N1s XPS spectrum of Fe-N/C catalyst with the peaks deconvoluted into pyridinic, pyrrolic, quarternary and oxidised nitrogen species. [Taken with permission from Ref. [6]] . . . . .	160
3.10	High resolution S2p XPS spectrum of Fe-N/C catalyst.[taken with permission from Ref. [6]] . . . . .	160
3.11	(a) Steady-state RDE measurements of M-N/C catalyst with and without nano-MgO template in 0.5 M H <sub>2</sub> SO <sub>4</sub> , catalyst loading: non-precious metal catalysts 750 μg cm <sup>-2</sup> , Pt/C 60 μg <sub>Pt</sub> cm <sup>-2</sup> , rotating speed: 1600 rpm, 30 s hold, 30 mV step potential, O <sub>2</sub> -saturated at 1 atm. (b) Normalised RDE measurements in 0.5 M H <sub>2</sub> SO <sub>4</sub> of different nano-MgO templated catalysts, 5 mV s <sup>-1</sup> , background corrected cathodic cycle, catalyst loading: 750 μg cm <sup>-2</sup> , O <sub>2</sub> -saturated at 1 atm . . . . .	162
3.12	(a) X-band EPR spectra of (M)-N/C catalysts with and without metal centre, recorded at room temperature. (b) X-band EPR spectrum of N/C catalysts with and without post-synthetic addition of iron species, recorded at room temperature. . . . .	164
3.13	X-band EPR spectrum of Mn-N/C catalyst, recorded at room temperature.	165
3.14	X-band EPR spectra of Fe-N/C catalyst under varying conditions, recorded at 77 K. . . . .	165
3.15	(a), (b) Representative high resolution TEM images of the Fe-N/C catalyst, showing the absence of solid inclusions or nanoparticles and the amorphous structure. inset (a) high resolution EDX of region corresponding to image (a) clearly showing the presence of iron. (c) and (d) high resolution STEM images of Fe-N/C catalyst. [Taken with permission from Ref. [25]] . . . .	167
3.16	(a) TEM image of Fe-N/C material. (b) Representative analysis of the lattice spacing of some ordered domains within the material. [Taken with permission from Ref. [25]] . . . . .	168
3.17	(a) HAADF STEM image of Fe-N/C material. (b) Representative EELS spectrum of the respective pixels in image (c). (c) <i>left</i> : pixel area over which EELS spectra were collected, <i>right</i> : EELS map of the Fe L <sub>2/3</sub> peak, corresponding to area shown on the <i>left</i> . . . . .	168
3.18	(a) HAADF STEM image of Fe-N/C material. (b) Fe L <sub>2/3</sub> EELS map of the highlighted region. <i>left</i> : representative EELS spectra of 2 distinct regions, showing the presence ( <i>blue</i> spectrum) and absence ( <i>black</i> spectrum) of iron in the respective region. (c) and (d) HAADF STEM images of a particularly thin region in the Fe-N/C sample. . . . .	169

3.19	(a) HAADF STEM image of Fe-N/C material showing the possible existence of iron clusters. (b) Magnified HAADF STEM image of region over which two EELS spectra were recorded, highlighted in <i>blue</i> and <i>black</i> , <i>red</i> circles indicate possible iron clusters. (c) EELS spectra <i>blue</i> and <i>black</i> , corresponding to the respective areas in (b). . . . .	170
3.20	(a) HAADF STEM image of N/C material. (b) EELS spectrum of region shown in (a). (c) Intensity of C, Si and N EELS peaks over line scan, indicated in (a). (d) Intensity of Fe $L_{2/3}$ peak. No iron detected in the sample. . . . .	170
3.21	H <sub>2</sub> /O <sub>2</sub> steady-state polarization plot for MEAs comparing a brush painted cathode of Fe-ODAN-1% (4 mg cm <sup>-2</sup> ) to a commercial Pt cathode (0.4 mg <sub>Pt</sub> cm <sup>-2</sup> ). 80 °C cell temperature. 100% RH and 2 bar back-pressure (gauge) for both gases. . . . .	171
4.1	Bar plots showing the performance at the respective half wave potential of the RDE measurement, comparing a Pt/C catalyst to ODAN at a rotating speed of 1600 rpm, 30 s hold, 30 mV step potential, catalyst loading: ODAN: 750 μg cm <sup>-2</sup> , Pt/C: 30 mg <sub>Pt</sub> cm <sup>-2</sup> , O <sub>2</sub> -saturated at 1 atm before and after adding (a) Cl <sup>-</sup> to 0.5 M H <sub>2</sub> SO <sub>4</sub> , (b) urea to 0.5 M H <sub>2</sub> SO <sub>4</sub> and (c) methanol to 0.1 M NaOH to obtain the respective concentrations. (d) RDE measurements, comparing the ORR activity of ODAN to Pt/C in ( <i>left</i> ) 0.5 M HCl and ( <i>right</i> ) Ringers solution (same conditions and parameters as (a) - (c)). [Taken with permission from Ref. [7]] . . . . .	188
4.2	Cell voltage of MEA running on Pt or ODAN as cathode catalyst, before and after adding (b) 83 ppm H <sub>2</sub> S (c) 77 ppm toluene and (d) 163 ppm benzene into the cathode gas stream. [Adapted with permission from Ref. [7]]	190
4.3	(a) Steady-state RDE measurements of Fe-N/C catalyst in 0.5 M H <sub>2</sub> SO <sub>4</sub> , before and after exposure to NO <sup>+</sup> BF <sub>4</sub> <sup>-</sup> , catalyst loading: 750 μg cm <sup>-2</sup> , rotating speed: 1600 rpm, 30 s hold, 30 mV step potential, O <sub>2</sub> -saturated at 1 atm. (b) RDE measurement of Fe-N/C catalyst in 0.5 M H <sub>2</sub> SO <sub>4</sub> , before and after exposure to NO gas, catalyst loading: 750 μg cm <sup>-2</sup> , 5 mV s <sup>-1</sup> , rotating speed: 1600 rpm, O <sub>2</sub> -saturated at 1 atm. . . . .	192
4.4	Steady-state RDE measurements of Fe-N/C catalyst in 0.5 M H <sub>2</sub> SO <sub>4</sub> , catalyst loading: 750 μg cm <sup>-2</sup> , rotating speed: 1600 rpm, 30 s hold, 30 mV step potential, O <sub>2</sub> -saturated at 1 atm. Before and after (a) exposing to <i>Friedel-Crafts</i> conditions and (b) acylpyridinium, acyl chloride and recovery.	193
4.5	Scheme showing the possible reactions of the acylpyridinium species with the Fe-N/C catalyst. . . . .	193
4.6	Gas desorption measurements, when heating the Fe-N/C catalyst at 10 °min <sup>-1</sup> , after exposure to O <sub>2</sub> or Ar for 1h at room temperature. Species detected in the mass spectrometer (a) m/z=32, oxygen (b) m/z=17, water and (c) m/z=44, carbon dioxide. . . . .	194
4.7	Temperature programmed desorption measurements at different heating rates, after exposing the Fe-N/C catalyst to O <sub>2</sub> for 1h at room temperature. Detection of species with a mass spectrometer (a) m/z=32, oxygen (b) m/z=17, water. (c) and (d) linearisation of T <sub>max</sub> and β relationship of measurements (a) and (b), respectively. . . . .	196

4.8	(a) Rotating disk electrode measurements of Fe-N/C catalyst at different pH values in O <sub>2</sub> -saturated 0.5 M electrolytes, 1600 rpm, 5 mV s <sup>-1</sup> ; Loading 270 μg cm <sup>-2</sup> . Corrected for solution resistance, capacitive background and different oxygen solubility and diffusivity. b) Plot of the potential at a current density of 0.1 mA cm <sup>-2</sup> (iR-free) versus pH. (bottom) versus SCE; linear fit shows a slope of 57±2 mV pH <sup>-1</sup> in the pH range 0 - 9 (top) corrected to RHE scale. All values become the same within the error margin in the pH range 0 - 9. . . . .	197
4.9	(a) Tafel-plots corresponding to measurements in Figure 4.8 (a) versus SCE scale, (b) versus RHE scale. . . . .	198
4.10	Rotating disk electrode (RDE) measurements of Fe-N/C catalyst in N <sub>2</sub> -saturated electrolyte at 1 atm and 25°C. 1600 rpm, 5 mV s <sup>-1</sup> ; Loading: 270 μg cm <sup>-2</sup> . . . . .	199
4.11	Rotating disk electrode (RDE) measurements of Fe-N/C catalyst, 1600 rpm, loading 270 μg cm <sup>-2</sup> . (a) 50mV s <sup>-1</sup> , N <sub>2</sub> -saturated electrolyte, (b) background corrected, 5 mV s <sup>-1</sup> O <sub>2</sub> -saturated electrolyte, at 1 atm and 25 °C. . . . .	200
4.12	Tafel-plots, where the potentials have been converted to overpotential, corresponding to the measurements in Figure 4.11 . . . . .	201
4.13	Rotating disk electrode (RDE) measurements of Fe-N/C catalyst, 1600 rpm, loading 270 μg cm <sup>-2</sup> . (a) 50mV s <sup>-1</sup> , N <sub>2</sub> -saturated electrolyte, (b) background corrected, 5 mV s <sup>-1</sup> O <sub>2</sub> -saturated electrolyte, at 1 atm and 25 °C. . . . .	202
4.14	Tafel-plots, where the potentials have been converted to overpotential, corresponding to the measurements in Figure 4.13 . . . . .	202
4.15	Proposed proton coupled electron transfer as rate determining step under acidic conditions. . . . .	203
4.16	Possible outer sphere electron transfer in highly alkaline conditions. . . . .	203
5.1	Rotating disk electrode (RDE) measurements of the ORR activity in acid (a,c) or base (b,d) of a Fe-N/C catalyst before (untreated) and after subjecting it to poisoning by a 0.125 M NaNO <sub>2</sub> solution at pH 7 (a,b); or nitric oxide saturated 0.5 M PO <sub>4</sub> -buffer at pH 7. RDE at 1600 rpm, catalyst loading at 270 μg cm <sup>-2</sup> , scan rate at 5 mV s <sup>-1</sup> and O <sub>2</sub> -saturated electrolytes. Electrodes washed with DI water before retuning to the electrolyte solutions, 0.5 M H <sub>2</sub> SO <sub>4</sub> or 1.0 M NaOH for the poisoned measurement. . . . .	216
5.2	(a) Scheme showing the sequence of catalyst layer treatments, with the crucial difference is the washing step that was either performed in 0.5 M H <sub>2</sub> SO <sub>4</sub> ( <b>Pathway A</b> ) or DI water ( <b>Pathway B</b> ). The corresponding measurements are shown in (b) and (c): Rotating disk electrode (RDE) measurements in O <sub>2</sub> -saturated 0.5 M H <sub>2</sub> SO <sub>4</sub> of the ORR activity of a Fe-N/C catalyst before (untreated) and after poisoning by a 0.125 M NaNO <sub>2</sub> solution at pH 7. (b) Performance towards the ORR after acid wash following nitrite treatment and then cycling in 1 M NaOH alkaline solution before returning to acid solution to perform the ORR. Inset: Effect of shifting cathodic endpoint to -0.3 V;(c) Performance towards the ORR after DI water wash following the poisoning protocol and then cycling in 1 M NaOH alkaline solution before returning to acid solution to perform the ORR. 1600 rpm, catalyst loading at 270 μg cm <sup>-2</sup> , scan rate at 5 mV s <sup>-1</sup> . . . . .	218

- 5.3 Rotating disk electrode (RDE) measurements in O<sub>2</sub>-saturated 0.5 M H<sub>2</sub>SO<sub>4</sub> of the ORR activity of a Fe-N/C catalyst before (untreated) and after poisoning in a NO-saturated 0.5 M PO<sub>4</sub>-buffer solution at pH 7. Performance towards the ORR after (a) acid wash following NO treatment and then cycling in 1 M NaOH alkaline solution before returning to acid solution to perform the ORR or (b) DI water wash following NO treatment and then cycling in 1 M NaOH alkaline solution before returning to acid solution to perform the ORR. In both cases the effect of extending the potential sweep to -0.3 V is also displayed. 1600 rpm, loading: 270 μg cm<sup>-2</sup>, 5 mV s<sup>-1</sup>, electrolyte: 0.5 M H<sub>2</sub>SO<sub>4</sub>, O<sub>2</sub>-saturated electrolyte. . . . . 221
- 5.4 Rotating disk electrode (RDE) measurements in O<sub>2</sub>-saturated 0.5 M H<sub>2</sub>SO<sub>4</sub> of the ORR activity of a Fe-N/C catalyst before (untreated) and after poisoning in a saturated nitric oxide 0.5 M H<sub>2</sub>SO<sub>4</sub> solution. (a) effect of poisoning the electrode at OCV; (b) effect of poisoning the electrode by performing cyclic voltammetry (1.05 V to -0.3 V) in the NO-saturated 0.5 M H<sub>2</sub>SO<sub>4</sub> solution. Inset: ORR response of electrode in 1 M NaOH. In both cases the effect of extending the potential sweep to -0.3 V is also displayed. 1600 rpm, loading: 270 μg cm<sup>-2</sup>, 5 mV s<sup>-1</sup>, electrolyte: 0.5 M H<sub>2</sub>SO<sub>4</sub>, O<sub>2</sub>-saturated electrolyte. . . . . 222
- 5.5 ORR performance before and after treatment in a 0.125 M hydroxylamine solution at pH 7. 1600 rpm, loading: 270 μg cm<sup>-2</sup>, 5 mV s<sup>-1</sup>, electrolyte: 0.5 M pH 7 PO<sub>4</sub>-buffer, O<sub>2</sub>-saturated. . . . . 224
- 5.6 Rotating disk electrode measurements of the metal free N/C catalyst before and after subjecting it to nitrite, hydroxylamine and nitric oxide, 1600 rpm, loading: 270 μg cm<sup>-2</sup>, 5 mV s<sup>-1</sup>, 0.5M H<sub>2</sub>SO<sub>4</sub>, O<sub>2</sub>-saturated electrolyte. . . 226
- 5.7 Cyclic voltammetry of the Fe-N/C catalyst in nitrogen saturated electrolyte, comparing the unpoisoned state to the strongly poisoned state. It can be seen that the redox peak at ~0.6 V *vs* RHE is not significantly affected by the poison. (a) 10 mV s<sup>-1</sup> in pH 5.2 acetate buffer without and with 3 mM NaNO<sub>2</sub>. The N/C catalyst does not show this redox peak. Inset: measurement in O<sub>2</sub>-saturated electrolyte with and without 3 mM NaNO<sub>2</sub>, 5 mV s<sup>-1</sup> (b) 100 mV s<sup>-1</sup> in 0.5 M H<sub>2</sub>SO<sub>4</sub> before and after subjecting it to cycling in NO saturated electrolyte. 1600 rpm, loading: 270 μg cm<sup>-2</sup>, N<sub>2</sub>-saturated electrolyte. . . . . 227
- 5.8 Rotating disk electrode measurements of a metal free catalyst N/C and an iron containing catalyst Fe-N/C towards nitrite reduction as a function of pH. 3 mM NaNO<sub>2</sub> containing N<sub>2</sub>-saturated electrolyte (a) pH 5.2 acetate buffer, (b) pH 7 phosphate buffer (c) pH 9 borate buffer. (d) pH dependence of the corrected potential at 0.1 mA cm<sup>-2</sup> towards nitrite reduction on the Fe-N/C catalyst Inset: corresponding *Tafel*-plots. . . . . 228

- 5.9 (a) and (b) Rotating disk electrode (RDE) *Koutecky-Levich* (K-L) analysis of the Fe-N/C towards nitrite reduction in (a) 0.5 M pH 5.2 acetate buffer, (b) 0.5 M pH 7 PO<sub>4</sub>-buffer. Insets: K-L plots to extract electron transfer number (c) and (d) Rotating ring disk electrode (RRDE) measurements, to determine the amount of hydroxylamine formed. (bottom) disk current (top) ring current in % disk current, when taking the collection efficiency of the ring into account. (c) Electrolyte: 0.5 M pH 5.2 acetate buffer; Ring potential: 0.45 V *vs* SCE (b) Electrolyte: 0.5 M pH 7 PO<sub>4</sub>-buffer; Ring potential: 0.3 V *vs* SCE. 1600 rpm, 270 μg cm<sup>-2</sup> catalyst loading, 5 mV s<sup>-1</sup>. (inset) chronoamperometry of the ring at the respective ring potential before and after adding 1 μM hydroxylamine to the solution. Current spike occurs when the solution is added. . . . . 230
- 5.10 Ion chromatographic ammonia yield and nitrite consumed *versus* charge. . 230
- 5.11 Rotating disk electrode (RDE) measurements in O<sub>2</sub>-saturated 0.5M H<sub>2</sub>SO<sub>4</sub> of the ORR activity of a Fe-N/C catalyst before (untreated) and after poisoning by a 0.125 M NaNO<sub>3</sub> solution at pH 7. a) Performance towards the ORR after acid wash following nitrite treatment and then cycling in 1M alkaline solution before returning to acid solution to perform the ORR. Inset: Effect of shifting cathodic endpoint to -0.3V; b) Performance towards the ORR after DI water wash following the poisoning protocol and then cycling in 1M alkaline solution before returning to acid solution to perform the ORR. RDE at 1600 rpm, catalyst loading at 270 μg cm<sup>-2</sup>, scan rate at 5 mV s<sup>-1</sup>. . . . . 231
- 6.1 (a) flow diagram showing steps required to assess the performance of a catalyst and determine the catalyst site density; (b) Measurement protocol used to measure the electrochemical performance of the ORR and assess the charge associated with reductive stripping of the adsorbed nitrite; (c) protocol used to poison the electrode using a nitrite containing solution. (d) ORR performance of catalyst layer before, during and after nitrite adsorption; (e) wide range baseline scan (avoiding nitrite reduction area) for the catalyst layer before, during and after nitrite adsorption; (f) Narrow baseline scan in the nitrite reductive stripping region before, during and after nitrite adsorption (g) expansion of the region associated with nitrite stripping. All experiments were performed in a 0.5 M acetate buffer at pH 5.2 for Fe-N/C catalyst using a rotating disk electrode (RDE) setup, loading 270 μmg cm<sup>-2</sup>. [Taken with permission from Ref. [18]] . . . . . 250
- 6.2 (a) comparison between homogeneous reduction of aqueous nitrite (3 mM NaNO<sub>2</sub> in acetate buffer), and excess current associated with reductive stripping of intermediate on Fe-N/C or N/C catalyst. The reductive stripping curve is produced by subtracting the unpoisoned from poisoned curve in Figure 3(g) (b) Kinetic current density of Fe-N/C catalyst before and after the poisoning step. O<sub>2</sub>-saturated electrolyte, 5 mV s<sup>-1</sup> background and iR-corrected RDE experiments at 1600 rpm, electrolyte: 0.5 M acetate buffer, loading: 0.27 mg cm<sup>-2</sup>. [Adapted with permission from Ref. [18]] . . 252
- 6.3 (a) Potential time protocol for the choronocoulometric stripping protocol (analogous to Figure 6.1) (b) Chronoamperometric transients for determination of the reductive stripping charge for the Fe-N/C catalyst. [Adapted with permission from Ref. [18]] . . . . . 252

- 6.4 *Tafel*-plots of the **N/C** and **Fe-N/C** catalyst in the unpoisoned and poisoned state. Corresponding to measurements on the respective catalysts shown in Figure 6.1 . . . . . 256
- 6.5 RDE measurement of Fe-N/C catalyst before and after poisoning with 0.125 M nitrite. Comparing 0.5 M acetate buffer (pH 5.2) to 0.5 M H<sub>2</sub>SO<sub>4</sub>. Loading: 0.27 mg cm<sup>-2</sup>, 1600 rpm, 5 mV s<sup>-1</sup>, background corrected, normalised to the same limiting current and iR-corrected. Note that there are different limiting current densities in the two electrolytes due to the difference in solubility and diffusion coefficient of oxygen in the two electrolytes, and (to a much lesser extent) the difference of viscosity of the two electrolytes. [Taken with permission from Ref. [18]] . . . . . 257
- 6.6 RDE measurement of Fe-N/C catalyst before and after poisoning and recovery. Loading: 0.27 mg cm<sup>-2</sup>, 1600 rpm (a and c) O<sub>2</sub>-saturated electrolyte, 5 mV s<sup>-1</sup>. (b and d) Stripping voltammetry, N<sub>2</sub>-saturated electrolyte, 10 mV s<sup>-1</sup>. Comparing the behaviour in 0.5 M H<sub>2</sub>SO<sub>4</sub> when 0.125 M nitrite was used as poison (top) to 0.5 M acetate buffer when 12.2 M nitrite was used as poison (bottom). [Taken with permission from Ref. [18]] . . . . . 258
- 6.7 Difference between capacitive traces as measured for the respective wide scan at pH 0.3 (a and b) and pH 5.2 (c and d) in the stripping region. The charge difference between the poisoned and unpoisoned trace has been used to extract the stripping charge (a and c), while the difference between unpoisoned and recovered trace has been used to estimate the uncertainty due to varying capacitance. [Taken with permission from Ref. [18]] . . . . . 259
- 6.8 (a) RDE measurement of standard Fe-N/C catalyst, 5 mV s<sup>-1</sup>, O<sub>2</sub>-saturated electrolyte. (b) *Tafel*-plot. (c) Stripping voltammetry 10 mV s<sup>-1</sup>, N<sub>2</sub>-saturated electrolyte. Loading: 0.27 mg cm<sup>-2</sup>, 1600 rpm, , 0.5 M acetate-buffer, pH 5.2 . . . . . 260
- 6.9 (a) RDE measurement of bimetallic FeCo catalyst, 5 mV s<sup>-1</sup>, O<sub>2</sub>-saturated electrolyte. (b) *Tafel*-plot. (c) Stripping voltammetry 10 mV s<sup>-1</sup>, N<sub>2</sub>-saturated electrolyte. Loading: 0.27 mg cm<sup>-2</sup>, 1600 rpm, , 0.5 M acetate-buffer, pH 5.2. [Adapted with permission from Ref. [18]] . . . . . 261
- 6.10 (a) RDE measurements of the Fe-N/C catalyst under different conditions compared to the N/C catalyst. (b) kinetic currents. Loading: 0.27 mg cm<sup>-2</sup>, 1600 rpm, O<sub>2</sub>-saturated electrolyte, 0.5 M acetate-buffer, pH 5.2, 5 mV s<sup>-1</sup>. [taken with permission from Ref. [18]] . . . . . 262
- 6.11 (a) RDE measurements of the Fe-N/C catalyst after subjecting it to the poisoning/stripping protocol at different concentrations of nitrite solution. (b) Kinetic currents. Loading: 0.27 mg cm<sup>-2</sup>, 1600 rpm, O<sub>2</sub>-saturated electrolyte, 0.5 M acetate-buffer, pH 5.2, 5 mV s<sup>-1</sup>. (c) effect of nitrite concentration on the magnitude of activity decrease (d) effect of nitrite concentration on the magnitude of stripping charge. The included blue dotted lines shall aid interpretation and do not represent a mathematical fit. [taken with permission from Ref. [18]] . . . . . 263
- 6.12 (a) Correlation of stripping charge to decrease in activity. (b) - (d) scheme to aid interpretation of the observed correlations of poison concentration, charge and activity decrease. 2 general metal based active sites are proposed. Strongly with nitrite interacting type A (red) and weakly interacting type B (green). [taken with permission from Ref. [18]] . . . . . 264

7.1	(a) Steady-state RDE measurements in 0.5 M H <sub>2</sub> SO <sub>4</sub> , rotating speed: 1600 rpm, 30 s hold, 30 mV step potential, catalyst loading: 750 μg cm <sup>-2</sup> , O <sub>2</sub> -saturated at 1 atm. (b) Conversion of cyclohexene in epoxidation reaction with different M-N/C catalyst over time, as determined by GC. 2 eq of isobutyraldehyde and 0.2 wt% catalyst to cyclohexene, 1 atm O <sub>2</sub> . . . . .	281
7.2	(a) Conversion, yield and selectivity of the Fe-N/C catalyst towards cyclohexene epoxidation, when reusing the catalyst multiple times. (b) TEM image of unused Fe-N/C catalyst and after 5 repeats. . . . .	284
7.3	(a) Set-up used to measure oxygen uptake. (b) oxygen uptake measurement for the Fe-N/C catalyst and (c) without catalyst during the epoxidation reaction. Stirring rate: 1400 rpm, 30 mg catalyst, 1 mL cyclohexene and 1 mL isobutyraldehyde in 25 mL acetonitrile. . . . .	285
7.4	Potential of reaction mixture measured over time before and after addition of reactants cyclohexene and isobutyraldehyde to the solvent containing either the <b>Fe-N/C</b> catalyst or no catalyst.(a) Starting period. (b) Full time scale. Solvent: Acetonitrile + 0.1 mM (t-Bu) <sub>4</sub> NBF <sub>4</sub> . . . . .	286
7.5	Set-up used to study the rate of oxygen uptake at the same time as the electrochemical potential. [Taken from Ref. [22]] . . . . .	288
7.6	Correlation of oxygen flow rate to the electrochemical potential during the epoxidation reaction. Addition of cyclohexene at 6 minutes and isobutyraldehyde at 14 minutes. [Taken from Ref. [22]] . . . . .	288
8.1	(a) Transmission line equivalent circuit of the catalyst layer (grey) between the membrane (ionic) and electronic resistive elements in the absence of a faradaic reaction, with the protonic resistance R <sub>p</sub> and the double layer capacitance C <sub>DL</sub> . (b) Transmission line equivalent circuit in the presence of a faradaic reaction represented by the addition of the charge transfer resistance R <sub>CT</sub> . [Adapted from Ref. [21]] . . . . .	302
8.2	Pore size distribution, as determined by the BJH method from the desorption branch of the respective isotherm for (a) FeCo-N/C catalyst (b) Fe-N/C catalyst and (c) MgO_APS_2 catalyst. [Adapted from Ref. [21]] .	304
8.3	Steady-state Rotating Disk Electrode (RDE) measurements of utilised catalysts. Catalyst loading: 750 μg cm <sup>-2</sup> , rotation rate: 1600 rpm, O <sub>2</sub> -saturated 0.5 M H <sub>2</sub> SO <sub>4</sub> , 30 s hold 30 mV step potential. [Adapted from Ref. [21]] .	304
8.4	Representative scanning electron micrograph showing the freeze fractured cross section of a membrane electrode assembly, with the anode catalyst layer/membrane/cathode catalyst layer from left to right. [Adapted from Ref. [21]] . . . . .	305
8.5	High resolution SEM images at low magnification ( <b>left</b> ) and high magnification ( <b>right</b> ) of catalyst layer cross section for the cathode with catalyst FeCo-N/C (a) I/C 0.5 (b) I/C 1 (c) I/C 2. [Taken with permission from Ref. [21]] . . . . .	306

- 8.6 **Left:** Galvanostatic polarisation curves for single cells with different ionomer loadings at the cathode, Anode: H<sub>2</sub>, 160 sccm, 2 bar back pressure (gauge), 100% RH, Johnson Matthey Hydrogen reformate electrode 0.4 mg<sub>Pt</sub> cm<sup>-2</sup>, Cathode: O<sub>2</sub>, 550 sccm, 2 bar back pressure (gauge), 100% RH, 4mg<sub>catalyst</sub> cm<sup>-2</sup>; Cell Temperature: 80 °C. **Right:** Bar plot depicting the respective current density at 2 different cell potentials. a) FeCo-N/C b) Fe-N/C c) MgO\_APS\_2. Cell voltages are iR-corrected using the resistance determined from the high frequency intercept with the real axis in the *Nyquist*-plot. [Taken with permission from Ref. [21]] . . . . . 307
- 8.7 **Left:** *Nyquist*-plots, **centre:** *Bode* phase angle plots, **right:** Magnified *Nyquist*-plots, recorded for the cells operating on (a) FeCo-N/C (b) Fe-N/C (c) MgO\_APS\_2 at the cathode at 0.1 V cell potential, anode: 20 sccm hydrogen, cathode: 550 sccm argon. Dashed red line corresponds to 45° in *Nyquist*-plot. Dashed black line corresponds to 30°. [Taken with permission from Ref. [21]] . . . . . 308
- 8.8 **Left:** *Nyquist*-plots, *inset:* magnification of high frequency region, **right:** *Bode* phase angle plots, recorded for the cells operating on (a) FeCo-N/C (b) Fe-N/C (c) MgO\_APS\_2 at the cathode at 0.6 V cell potential, Anode: 160 sccm hydrogen, Cathode: 550 sccm oxygen. Dashed red line corresponds to 45° in *Nyquist*-plot. [Taken with permission from Ref. [21]] 310
- 8.9 **Left:** *Nyquist*-plots, **right:** *Bode* phase angle plots, recorded for the cells operating on (a) FeCo-N/C (b) Fe-N/C (c) MgO\_APS\_2 at the cathode at 0.6 V cell potential, Anode: 160 sccm hydrogen, Cathode: 550 sccm oxygen. Dashed red line corresponds to 45° in *Nyquist*-plot. [Taken with permission from Ref. [21]] . . . . . 311
- 8.10 Galvanostatic polarisation curves for single cells with different catalyst loadings at the cathode, anode: H<sub>2</sub>, 160 sccm, 2 bar back pressure (gauge), 100% RH, Johnson Matthey Hydrogen reformate electrode 0.4 mg<sub>Pt</sub> cm<sup>-2</sup>, cathode: O<sub>2</sub>, 550 sccm, 2 bar back pressure (gauge), 100% RH, 4mg<sub>catalyst</sub> cm<sup>-2</sup>; Cell temperature: 80 °C. [Taken with permission from Ref. [21]] . . 312
- 8.11 *Nyquist*-plots (**left**) and *Bode* phase plot (**right**) for the cells operating on catalyst FeCo-N/C at the cathode at 0.1 V cell potential with different loadings, anode: 160 sccm hydrogen, cathode: 550 sccm argon. Dashed red line corresponds to 45° angle. [Taken with permission from Ref. [21]] . . . 313
- 8.12 H<sub>2</sub>/Ar *Nyquist*-plots for catalyst FeCo-N/C with and without backpressure at I/C ratio (a) 0.5 (b) 1.0 (c) 2.0. [Taken with permission from Ref. [21]] 313
- 8.13 *Nyquist*-plots for the cell operating on catalyst Fe-N/C for an optimum I/C ratio (a), and a non-ideal ratio (b). 0.1 V cell potential at different relative humidity levels, anode: 160 sccm Hydrogen, cathode: 550 sccm Argon. Dashed red line corresponds to 45° angle and dashed black line to 30°. [Taken with permission from Ref. [21]] . . . . . 314
- 8.14 (a) Schematic describing porous carbon covered with a layer of ionomer (b) - (d) showing how the ionomer coverage corresponds to electrolyte filled pores. (b) incomplete coverage (c) homogeneous coverage (d) high loading with inhomogeneously filled pore. On the right hand side are representative *Nyquist* plots associated with the characteristic pore shapes as described in Ref. [30]. [Taken with permission from Ref. [21]] . . . . . 315
- 8.15 Flow chart illustrating the optimisation strategy to obtain the best performing catalyst layer. [Taken with permission from Ref. [21]] . . . . . 316



# List of Schemes

1.1	Proposed mechanism for the activation of dioxygen by cytochrome P450. . . . .	59
5.1	Typical compounds of the different nitrogen oxidation states present in an acidic aqueous solution in descending order of oxidation state. The major pathways for nitrite and nitric oxide electroreduction are highlighted. Green and blue pathway: possible products and intermediates upon subsequent cleavage of N-O bonds without N-N bond formation. Red and yellow pathway: likely products and intermediates upon N-O cleavage with N-N bond formation. Grey dash-dot pathway: kinetically hindered route. . . . .	215
5.2	Proposed reaction steps of the Fe-N/C active site after treatment with a nitrite containing solution and subsequent treatment under different pH conditions. . . . .	219
5.3	Proposed reaction steps of the Fe-N/C active site after treatment with nitric oxide at pH 7 and subsequent treatment under different pH conditions.	221
5.4	Proposed reaction steps and active site species formed when subjecting the catalyst to an acidic NO solution, without electrochemical cycling ( <b>Pathway E</b> ) and with electrochemical cycling ( <b>Pathway F</b> ). . . . .	223
5.5	Proposed reaction steps of the active site upon contact with hydroxylamine and subsequent electrochemical recovery. . . . .	225
6.1	Formation of a nitrosyl complex. . . . .	253
6.2	Reduction of nitrosyl complex to ammonia. . . . .	253
7.1	Accepted mechanism for <i>Prilezhaev</i> reaction to form an epoxide. . . . .	276
7.2	General reactions in the chlorohydrin process. . . . .	276
7.3	Scheme showing steps in oxygen activation by P450 involving electron and proton uptake, where Fe represents the heme iron atom. . . . .	277
7.4	Mechanisms of olefin epoxidation (A) by oxenoid-iron involving a charge-transfer complex and leading to epimerization, (B) by oxenoid-iron leading to a concerted insertion of oxygen, and (C) by hydroperoxo-iron in a concerted reaction. . . . .	278
7.5	(a) Oxidation based on the model of monooxygenase. (b) Free radical oxidation. (c) Oxidation of a coordinated substrate by a metal ion. (d) Oxidation mimicking dioxygenase. . . . .	278
7.6	Reaction of alkene with oxygen to give an epoxide with concomitant oxidation of isobutyraldehyde as coreductant. A transition metal complex is added as catalyst. . . . .	279
7.7	Epoxidation of cyclohexene to cyclohexene-oxide. . . . .	281
7.8	Iron-catalyzed epoxidation of stilbene with air. . . . .	289
7.9	Mechanism proposed in Ref. [14] for the epoxidation of alkene with O <sub>2</sub> and aldehyde, catalysed by metal complexes. . . . .	289

---

7.10 Mechanism proposed for the epoxidation of alkene with O <sub>2</sub> and aldehyde, catalysed by metal salts. . . . .	291
7.11 Possible mechanism for the epoxidation of alkene with O <sub>2</sub> and aldehyde, catalysed by Fe-N/C catalyst. . . . .	292

# List of Tables

1.1	Metrics of a selection of high performing M-N/C catalysts from literature.	77
3.1	External, microporous and total surface area (SA) of the respective catalysts, as determined by nitrogen adsorption analysis.	150
3.2	Mass activities and volumetric current densities of selected catalysts. Values taken at the respective potential <i>versus</i> RHE in the RDE setup at room temperature and are not mass transport corrected.	152
3.3	External, microporous and total surface area (SA) of the Fe-N/C catalyst after first and second heat treatment, as determined by nitrogen adsorption analysis.	155
3.4	External, microporous and total surface area (SA) of the catalysts with different metal centres, as determined by nitrogen adsorption analysis.	156
3.5	Surface element content as detected by XPS.	159
3.6	External, microporous and total surface area (SA) of templated catalysts, as determined by nitrogen adsorption analysis.	161
3.7	g-values for radical signal of different catalysts at room temperature.	164
3.8	g-values of Fe-N/C radical signal under different conditions at 77 K.	166
4.1	Mean values and standard deviation for pH, apparent Tafel slopes and potentials at the respective pH, corresponding to measurements shown in Figure 4.8, from 3 independent runs for each data point. Independent here means that for each run a new catalyst layer from a different newly prepared ink was measured.	198
7.1	Epoxidation of cyclohexene with different metal centres and metal free catalyst. 2 eq of isobutyraldehyde and 0.2 wt% catalyst to cyclohexene, 1 atm O <sub>2</sub> . Values after 6 h at room temperature as determined by GC.	282
7.2	Epoxidation of different alkenes with Fe-N/C catalyst. Substrate:Fe molar ratio 3000:1, assuming 1 wt% active Fe in the Fe-N/C catalyst. 2 eq of isobutyraldehyde to alkene, 1atm O <sub>2</sub> , room temperature. Values as determined by GC.	283
7.3	Epoxidation of cyclohexene comparing Fe-N/C catalyst to FeCl <sub>3</sub> ·6H <sub>2</sub> O. 2 eq of isobutyraldehyde and 5 mol% Fe to cyclohexene, 1 atm air. Values after 24 h at room temperature as determined by GC. [data taken from Ref. [22]]	289

# Abbreviations

<b>AAEMFC</b>	<b>Alkaline Anion Exchange Membrane Fuel Cell</b>
<b>AC</b>	<b>Alternating Current</b>
<b>ACN</b>	<b>Acetonitrile</b>
<b>AFC</b>	<b>Alkaline Fuel Cell</b>
<b>BET</b>	<b>Brunauer Emmet Teller</b>
<b>BJH</b>	<b>Barret Joyner Halenda</b>
<b>CCM</b>	<b>Catalyst Coated Membrane</b>
<b>CcO</b>	<b>Cytochrome-c Oxidase</b>
<b>CL</b>	<b>Catalyst Layer</b>
<b>CNT</b>	<b>Carbon Nanotube</b>
<b>CV</b>	<b>Cyclic Voltammetry</b>
<b>DC</b>	<b>Direct Current</b>
<b>DEMS</b>	<b>Differential Electrochemical Mass Spectrometry</b>
<b>DFT</b>	<b>Density Functional Theory</b>
<b>DMFC</b>	<b>Direct Methanol Fuel Cell</b>
<b>ECSA</b>	<b>Electrochemical Surface Area</b>
<b>EDS</b>	<b>Energy Dispersive Spectroscopy</b>
<b>EELS</b>	<b>Electron Energy Loss Spectroscopy</b>
<b>EI</b>	<b>Electron Ionisation</b>
<b>EIS</b>	<b>Electrochemical Impedance Spectroscopy</b>
<b>EPR</b>	<b>Electron Paramagnetic Resonance</b>
<b>ESI</b>	<b>Electron Spray Ionisation</b>
<b>EXAFS</b>	<b>Extended X-ray Absorption Fine Structure</b>
<b>FC</b>	<b>Fuel Cell</b>
<b>FID</b>	<b>Flame Ionisation Detector</b>

---

<b>GC</b>	<b>Gas Chromatography</b>
<b>GTL</b>	<b>Gas Transport Layer</b>
<b>HOPG</b>	<b>Highly Ordered Pyrolytic Graphite</b>
<b>HOR</b>	<b>Hydrogen Oxidation Reaction</b>
<b>IC</b>	<b>Ion Chromatography</b>
<b>ICE</b>	<b>Internal Combustion Engine</b>
<b>ICP-AES</b>	<b>Inductively Coupled Plasma Atomic Emission Spectroscopy</b>
<b>KIE</b>	<b>Kinetic Isotope Effect</b>
<b>MCFC</b>	<b>Molten Carbonate Fuel Cell</b>
<b>MEA</b>	<b>Membrane Electrode Assembly</b>
<b>MFC</b>	<b>Mass Flow Controller</b>
<b>MPL</b>	<b>Mesoporous Layer</b>
<b>MS</b>	<b>Mass Spectrometry</b>
<b>MSD</b>	<b>Mass Site Density</b>
<b>OCV</b>	<b>Open Circuit Potential</b>
<b>ORR</b>	<b>Oxygen Reduction Reaction</b>
<b>PAFC</b>	<b>Phosphoric Acid Fuel Cell</b>
<b>PCET</b>	<b>Proton Coupled Electron Transfer</b>
<b>PEFC</b>	<b>Polymer Electrolyte Fuel Cell</b>
<b>PEMFC</b>	<b>Proton Exchange Membrane Fuel Cell</b>
<b>PES</b>	<b>Polyethersulphone</b>
<b>PGM</b>	<b>Platinum Group Metals</b>
<b>PM</b>	<b>Particulate Matter</b>
<b>ppb</b>	<b>parts per billion</b>
<b>ppm</b>	<b>parts per million</b>
<b>PSD</b>	<b>Pore Size Distribution</b>
<b>PTFE</b>	<b>Polytetrafluoroethylene</b>
<b>RDE</b>	<b>Rotating Disk Electrode</b>
<b>RDS</b>	<b>Rate Determining Step</b>
<b>RH</b>	<b>Relative Humidity</b>
<b>RHE</b>	<b>Reversible Hydrogen Electrode</b>
<b>rms</b>	<b>root mean square</b>
<b>rpm</b>	<b>revolutions per minute</b>

---

<b>RRDE</b>	<b>R</b> otating <b>R</b> ing <b>D</b> isk <b>E</b> lectrode
<b>RRF</b>	<b>R</b> elative <b>R</b> esponse <b>F</b> actor
<b>SA</b>	<b>S</b> urface <b>A</b> rea
<b>SCE</b>	<b>S</b> aturated <b>C</b> alomel <b>E</b> lectrode
<b>SDD</b>	<b>S</b> ilicon <b>D</b> rift <b>D</b> etector
<b>SEM</b>	<b>S</b> canning <b>E</b> lectron <b>M</b> icroscopy
<b>SOFC</b>	<b>S</b> olid <b>O</b> xide <b>F</b> uel <b>C</b> ell
<b>STEM</b>	<b>S</b> canning <b>T</b> ransmission <b>E</b> lectron <b>M</b> icroscopy
<b>TCD</b>	<b>T</b> hermal <b>C</b> onductivity <b>D</b> etector
<b>TEM</b>	<b>T</b> ransmission <b>E</b> lectron <b>M</b> icroscopy
<b>TOF</b>	<b>T</b> urnover <b>F</b> requency
<b>ToF-SIMS</b>	<b>T</b> ime of <b>F</b> light <b>S</b> econdary <b>I</b> on <b>M</b> ass <b>S</b> pectrometry
<b>TON</b>	<b>T</b> urnover <b>N</b> umber
<b>TPD</b>	<b>T</b> emperature <b>P</b> rogrammed <b>D</b> esorption
<b>TXRF</b>	<b>T</b> otal reflection <b>X</b> - <b>R</b> ay <b>F</b> luorescence
<b>UHV</b>	<b>U</b> ltra <b>H</b> igh <b>V</b> acuum
<b>XANES</b>	<b>X</b> -ray <b>A</b> bsorption <b>N</b> ear <b>E</b> dge <b>S</b> tructure
<b>XPS</b>	<b>X</b> -ray <b>P</b> hotoelectron <b>S</b> pectroscopy
<b>XRD</b>	<b>X</b> - <b>R</b> ay <b>D</b> iffraction
<b>XRF</b>	<b>X</b> - <b>R</b> ay <b>F</b> luorescence

# Physical Constants

$$\textit{Avogadro constant } N_A = 6.022\,140\,857 \times 10^{23} \text{ mol}^{-1}$$

$$\textit{Bohr magneton } \mu = 9.274\,009\,68 \times 10^{-24} \text{ J T}^{-1} \text{ mol}^{-1}$$

$$\textit{Ideal gas constant } R = 8.314\,4598 \text{ J K}^{-1} \text{ mol}^{-1}$$

$$\textit{Faraday constant } F = 96\,485.3329 \text{ s A mol}^{-1}$$

# Symbols

$a$	adsorbent mass	kg
$A$	area	$\text{m}^2$ <i>or</i> $\text{cm}^2$
	<i>or</i> pre-exponential factor	dimensionless
$B$	magnetic field strength	G
$c$	BET constant	dimensionless
$C_R$	reactant concentration	$\text{mol dm}^{-3}$ <i>or</i> $\text{mol cm}^{-3}$
$C_R^*$	bulk reactant concentration	$\text{mol dm}^{-3}$ <i>or</i> $\text{mol cm}^{-3}$
$C_{dl}$	double layer capacitance	F
$C$	capacitance	F
	<i>or</i> concentration	$\text{mol cm}^{-3}$
$D$	diffusion coefficient; subscript indicates type	$\text{cm}^2 \text{s}^{-1}$
$E$	potential; subscript indicates type	V
	<i>or</i> energy; subscript indicates type	J <i>or</i> kJ <i>or</i> eV
$f$	frequency	Hz
$\Delta G^0$	free energy of formation	$\text{kJ mol}^{-1}$
$\Delta G^\ddagger$	activation energy; subscript indicates type	$\text{kJ mol}^{-1}$
$G$	free energy; sub and superscript indicate type	$\text{kJ mol}^{-1}$
$\Delta H_f^0$	free enthalpy of formation	$\text{kJ mol}^{-1}$
$H$	enthalpy; sub and superscript indicate type	$\text{kJ mol}^{-1}$
$i_L$	diffusion limited current	$\text{mA cm}^{-2}$
$i_k$	kinetic current	$\text{mA cm}^{-2}$
$I$	current	A
$I_R$	ring current	A
$I_D$	disk current	A
$j$ <i>or</i> $i$	geometric current density	$\text{A m}^{-2}$ <i>or</i> $\text{mA cm}^{-2}$



$j_0$	exchange current density	$\text{A cm}^{-2}$ or $\text{mA cm}^{-2}$
$j_{kin}$	kinetic current density	$\text{A g}^{-1}$ or $\text{mA cm}^{-2}$
$j_{lim}$	limiting current density	$\text{A cm}^{-2}$ or $\text{mA cm}^{-2}$
$k$	rate constant; subscript indicates type	depends on mechanism
$L$	inductance	H
$m$	mass; subscript indicates type	kg
$n$	electron transfer number	dimensionless
$N$	collection efficiency	dimensionless
	or count rate; subscript indicates type	counts $\text{s}^{-1}$
$p$	pressure	Pa
$p_0$	saturation pressure	Pa
$P$	power or power density	W or $\text{W cm}^{-2}$
$Q^0$	capacitive element	F
$Q$	charge	C
$Q_{step}$	charge associated with potential step	C
$R$	resistance; subscript indicates type	$\Omega$
$R_{ct}$	charge transfer resistance	$\Omega$
$S_{tot}$	total surface area	$\text{m}^2$
$S_{spec}$	specific surface area	$\text{m}^2$
$S$	sensitivity factor; subscript indicates type	dimensionless
$s$	cross sectional surface area	$\text{m}^2$
$t$	time	s
$t_{int}$	interval time	s
$T$	temperature	K or $^{\circ}\text{C}$
$\vec{V}$	scan rate	$\text{V s}^{-1}$
$V$	volume	$\text{m}^3$ or $\text{dm}^3$
$v_y$	velocity of fluid in y direction	$\text{cm s}^{-1}$
$v$	adsorbed gas quantity	L
$v_m$	monolayer adsorbed gas quantity	L
$Z$	impedance; subscript indicates source	$\Omega$ or $\Omega \text{ cm}^2$
$\alpha$	transfer coefficient	dimensionless
$\beta$	heating rate	$\text{K s}^{-1}$

---

$\delta$	diffusion layer thickness	m
$\Delta$	difference	dimensionless
$\eta$	overpotential	V
	<i>or</i> polarisation; subscript indicates type	V
	<i>or</i> efficiency; subscript indicates type	dimensionless
$\lambda$	reorganisation energy	kJ mol <sup>-1</sup>
$\nu$	kinematic viscosity	cm <sup>2</sup> s <sup>-1</sup>
$\phi$	phase angle	deg
	<i>or</i> work function	eV
$\rho$	constant phase exponent	dimensionless
$\tau$	time constant	s
$\omega$	angular frequency	rad s <sup>-1</sup>

# Chapter 1

## Introduction

Anthropogenic climate change, which is now undoubtedly happening, is one of the biggest challenges mankind is facing at the beginning of the 21st century. [1] This makes the development of carbon neutral technologies a pressing issue. The change from the current fossil fuel based to a sustainable renewable energy economy requires not only green energy generation methods, such as solar or wind energy, but also renewable energy conversion methods. This is because the generated energy needs to be stored and distributed to its point of use. [2]

Urban areas are facing increasing amounts of particulate matter (PM), which is largely generated by the combustion of fossil fuels in combustion engines or power plants. [3, 4] The health effects of PM are severe, ranging from cardiovascular disease to lung cancer. [5] The progress in developing countries comes with an increased combustion of fossil fuels which leads to catastrophic air pollution with PM and the associated detrimental health effects. [6] This makes a zero emission technology for transportation desirable.

Fuel cells (FCs) are a promising technology that can generate electricity for use in stationary and transportation applications, from a variety of fuels, with no emission of hazardous combustion by-products such as  $\text{NO}_x$ ,  $\text{SO}_x$ , PM and  $\text{CO}_2$ . [7, 8] Hence they are considered a zero emission energy conversion technology. Due to the fact that fuel cells utilise an electrochemical rather than a thermal reaction, they are not limited by the *Carnot* cycle and can theoretically reach higher efficiencies. [7, 8] Unlike batteries which need to be recharged and have a limited operating time, FCs will run as long as fuel is provided, making these devices particularly suitable for transportation where a long range is necessary. [9, 10] Therefore FCs and batteries can be complementary technologies, where the

former serves long distance high weight vehicles and the latter short range small vehicle for urban transport. [9, 10] Different types of FCs have been described. [7, 8] The most common ones that also find commercial use are alkaline fuel cells (AFCs), molten carbonate fuel cells (MCFCs), phosphoric acid fuel cells (PAFCs), solid oxide fuel cells (SOFCs), direct methanol fuel cells (DMFCs) and polymer electrolyte fuel cells (PEFCs), where DMFCs are mostly a PEFCs, operated with methanol as fuel instead of hydrogen. [7, 8] Fuels proposed as energy carrier are methanol, ethanol, formic acid, methane and hydrogen. [7, 8] While FCs operated with hydrocarbons still emit carbon dioxide, one can envision a scenario where these fuels are derived from biological sources and hence the net carbon emission is zero. [11] The benefit of hydrocarbon fuels is their ease of storage and transport, while offering a high energy density. [12] However, besides the efficient renewable synthesis the difficulty lies in the efficient utilisation in the fuel cell, due to poor oxidation kinetics and the associated need for large amounts of expensive precious metal based catalysts. [13] The hypothetically ideal energy vector is hydrogen which combines with oxygen in the FC to yield water and electricity. [8, 12] Hydrogen can either be generated by steam reforming of methane with high efficiency, from bacterial metabolisation of biowaste or by electrolysis of water with electricity from renewable sources. [12] When electrolysis is used a sustainable energy cycle based on water with no carbon emissions is the result. [12] Although this scenario still faces significant challenges, including hydrogen storage, transport and distribution [12], efficient and durable electrolysis [14], low cost fuel cell components [15] and low cost and durable electro-catalysts for oxygen evolution as well as oxygen reduction [16], progress is being made in all respective areas.

The oxygen reactions are particularly challenging as they involve a complex 4 electron, 4 proton mechanism. [13] This work is mainly concerned with the development and understanding of low cost oxygen reduction reaction (ORR) catalysts to reduce the prohibitive price of low temperature PEFCs with a foray into the use of these materials as efficient heterogeneous epoxidation catalysts utilising molecular oxygen.

## 1.1 Polymer electrolyte fuel cells (PEFCs)

Among the various types of fuel cells, PEFCs are considered the most suitable ones for transportation applications, but can also be used for residential stationary combined heat and power applications. [8] Examples of commercial fuel cell cars based on PEFCs to date

are the Hyundai Tucson iX 35 and the Toyota Mirai. [17, 18] A commercial residential PEFC unit is the Panasonic Enefarm.[19] The benefit of PEFCs are the low operating temperature (60 - 120 °C), a solid non-volatile electrolyte and the compact design which offers high power densities. [8]

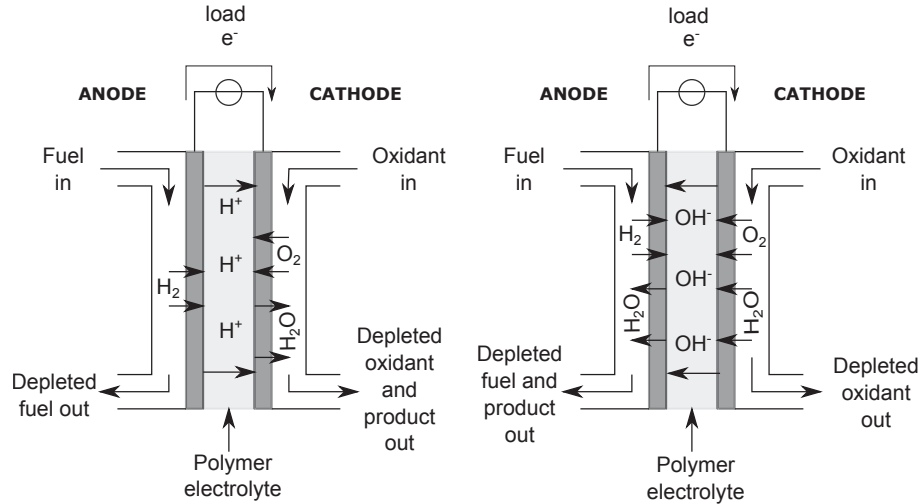
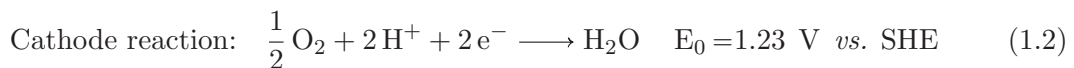
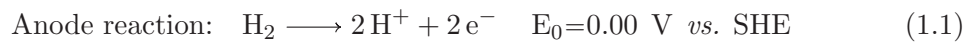


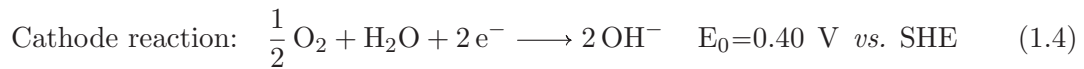
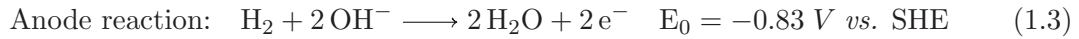
FIGURE 1.1: Operating principle of a PEFC. (left) Operated with a proton exchange membrane (PEM). (right) Operated with an anion exchange membrane (AEM). [8, 20]

Figure 1.1 shows the operating principle of a PEFC. Left, the operation with an acidic cation exchange membrane, termed a proton exchange membrane fuel cell (PEMFC) and right the operation with an alkaline anion exchange membrane, termed alkaline anion exchange membrane fuel cell (AAEMFC). [8, 20] On the anode side the fuel, in this case hydrogen is oxidised, while at the cathode oxygen is reduced. The released electrons on the anode side travel through an external circuit to the cathode side and provide work in the form of an electrical load, while the protons in case of a PEMFC travel through the membrane from anode to cathode to combine with the reduced oxygen species to form water. [8] The associated electrochemical reactions are as follows [8]:



In an AAEMFC the difference is that instead of protons moving from anode to cathode, hydroxide ions move from the cathode to the anode to combine with the protons there and form water. [8] AAEMFCs would offer some advantages as compared to a PEMFC. These include faster ORR kinetics, allowing for a lower precious metal catalyst loading,

and a less corrosive environment, allowing the use of a wider variety of materials and reducing degradation issues present in PEMFCs. [20] However, the hydrogen oxidation reaction (HOR) would be significantly slower at high pH values ( $\approx 100$  times on Pt), shifting the precious metal problem from anode to cathode. [21] The reactions occurring in an AAEMFC are given by the following equations [8]:



However, alkaline fuel cells have not been successfully commercialised to date, this is mainly due to the unstable membrane. [20]

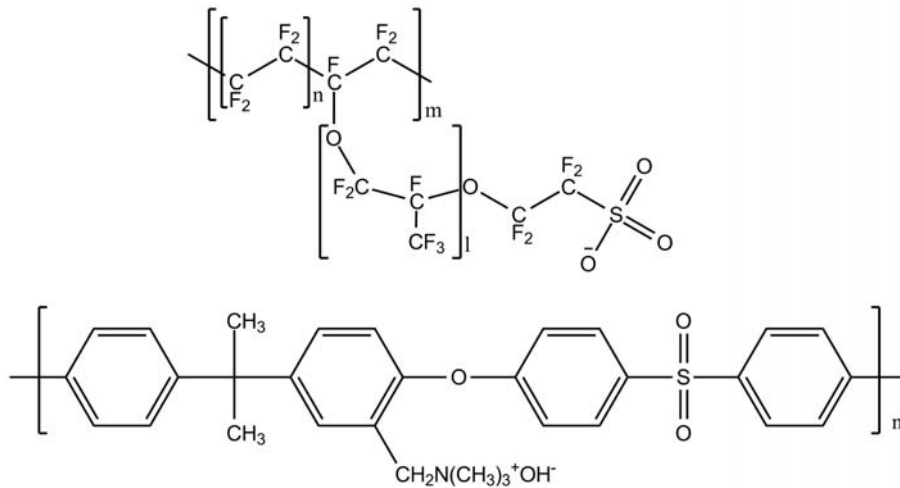


FIGURE 1.2: (top) Structure of Nafion<sup>®</sup>, where  $n, m, l$  are integers and the ratio of those determines the type of Nafion<sup>®</sup>. (bottom) Example of a functionalized polysulfone as anion exchange membrane.

In PEMFCs the most established types of membranes are based on a polymer with a perfluorinated backbone that contains side chains with sulphonic acid groups for the proton conduction, as shown in Figure 1.2 (top), *i.e.* Nafion<sup>®</sup>. [8] This allows the formation of channels through which protons can be conducted. [22] On the other hand one type of anion exchange membranes is based on polymers with a polyethersulfone (PES) backbone and side chains with quaternary ammonium groups for anion conduction, as shown in Figure 1.2 (bottom). [20]

The fuel cell electrodes, anode and cathode, typically consist of a porous carbon substrate which acts as a gas transport layer (GTL), with a mesoporous layer (MPL) and the

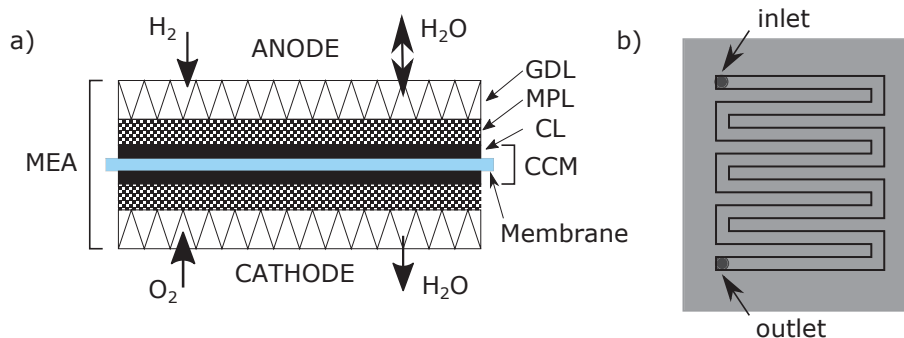


FIGURE 1.3: (a) schematic representation of the cross section of a classic membrane electrode assembly (MEA), consisting of a membrane, sandwiched between two sets of gas transport layer (GTL), mesoporous layer (MPL), and catalyst layer (CL). The membrane coated with the catalyst and without GTL and MPL is commonly referred to as catalyst coated membrane (CCM). (b) example of a flow field machined into a bipolar plate. The MEA is sandwiched between two such plates in order to supply reactants and conduct electrons. [8]

catalyst layer (CL) between which the membrane is sandwiched. Bonding is usually achieved by hot pressing above the glass transition temperature  $T_g$  of the membrane. This unit is called a membrane electrode assembly (MEA) and is depicted in Figure 1.3 (a). [8] The GTL is usually treated with 5 - 35 wt% of a hydrophobic Polytetrafluoroethylene (PTFE) agent. [23] This increases the ability of the electrode assembly to conduct water away from the catalyst layer and prevent flooding. [8] The MPL is employed to increase gas dispersion and helps to maximise mass transport, while offering an intermediate pore size between GTL and CL, which helps to produce a more uniform CL and helps to prevent loss of catalyst through the large pores of the GTL. It usually consists of high surface area carbon bonded to the GTL. [8] The catalyst layer is where the respective reaction takes place. The active catalyst is usually finely dispersed on a high surface area carbon support, *e.g.* VulcanXC72, in order to further increase the accessible surface of the catalyst. The catalyst layer is further impregnated with an ionomer at approximately 50 wt%, typically Nafion<sup>®</sup>, to facilitate good ion transport and bond the catalyst to electrode and membrane. [8] This complex set-up is necessary to maximise reactant transport to the catalyst while ensuring optimal catalyst utilisation and at the cathode facilitating product water transport away from the catalyst. [8] The catalysts used to date are, on the anode and the cathode, Pt based. While on the anode the amount of precious metal is acceptable, the 8 to 10 times higher loading is necessary at the cathode, due to the sluggish ORR kinetics can be problematic in terms of economic viability. [24] This MEA is then sandwiched between bipolar plates (Figure 1.4) that supply the gases through a flow field and collect the electrons. The bipolar plates usually consists of graphitised

and hardened carbon. [8] Recently novel concepts that move away from this classical configuration have been used. For example combined metal flow field and gas diffusion electrodes.[25]

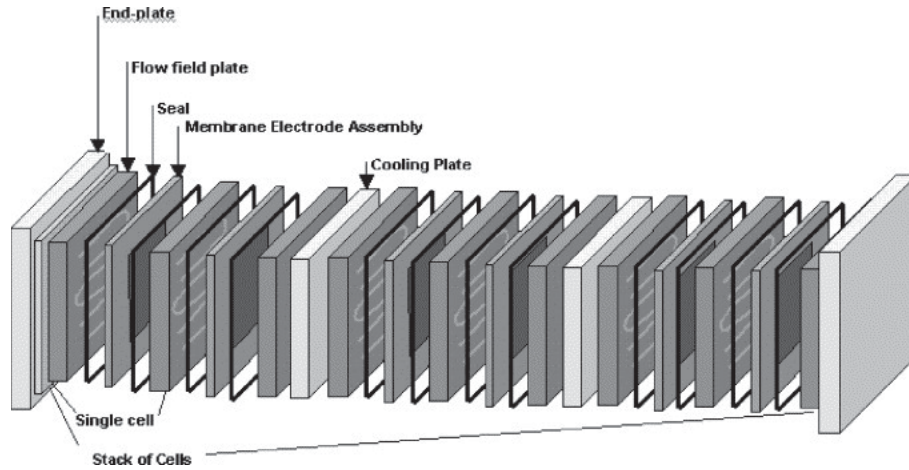


FIGURE 1.4: PEM Fuel Cell stack. [Reprinted with permission from Ref. [26]]

A large number of these units is then connected in series to form a stack and provide the necessary power for the respective application, as depicted in Figure 1.4.[26]

## 1.2 The Oxygen Reduction Reaction (ORR)

The oxygen reduction reaction is essential to life as we know it. With 21% in the atmosphere, oxygen is the preferred oxidant for most living organisms. [27] Therefore it is the best choice for fuel cells and recently metal-air batteries. [10] Oxygen occurs as diatomic molecule with a bond order of 2. In the ground state it is a diradical with 2 unpaired electrons in the antibonding orbital as shown in Figure 1.5. [27]

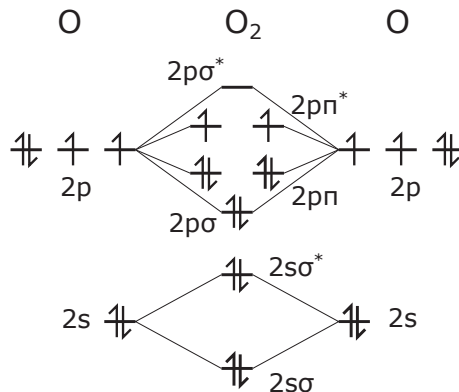


FIGURE 1.5: Molecular orbital (MO) diagram of oxygen.



The reduction of one oxygen molecule to give two molecules of water involves four electrons and four protons, the breakage of a double bond and the formation of four hydrogen oxygen bonds. [8] This makes the ORR significantly more complex and also sluggish than the two electron hydrogen oxidation reaction (HOR) to protons. [8] The ORR can proceed through various pathways with hydrogen peroxide as an intermediate. [28]

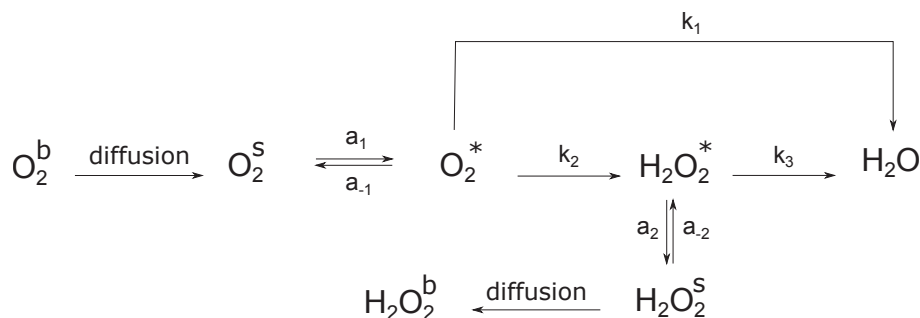
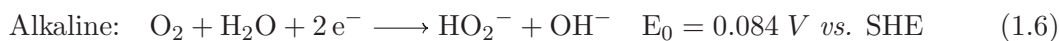
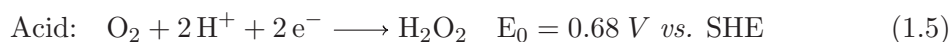


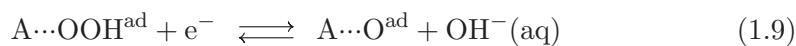
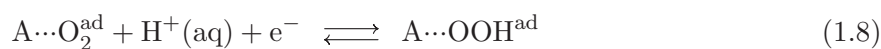
FIGURE 1.6: Reaction scheme of the ORR to water after Woroblowa [28], showing the direct 4 electron ( $k_1$ ) and indirect 2 + 2 electron pathway ( $k_2, k_3$ ). The superscripts b, s and \* denote the species in the bulk, close to the surface and adsorbed, respectively.

Figure 1.6 depicts the main pathways. The direct 4 electron pathway ( $k_1$ ) converts oxygen directly to water without the formation of peroxide. The 2+2 pathway leads to intermediate hydrogen peroxide ( $\text{H}_2\text{O}_2$ ) formation before reduction to  $\text{H}_2\text{O}$ . If the rate constant for the formation of peroxide ( $k_2$ ) is larger than the one for the consumption of peroxide to produce water ( $k_3$ ), the intermediate peroxide species can desorb from the catalyst surface. A rate constant for the desorption of  $\text{H}_2\text{O}_2$  ( $a_2$ ) which is large enough leads to the 2 electron pathway with peroxide as a product. [28] The standard potentials for peroxide formation are as follows [29]:

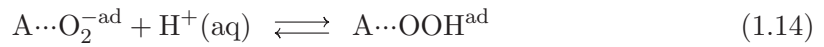
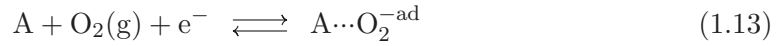


The free peroxide species will degrade fuel cell components and is therefore undesirable. [8] The 1 electron reduction of oxygen to superoxide ( $\text{O}_2^-$ ) can be observed in aprotic or highly alkaline electrolytes. [30, 31] The pathway will depend on the utilised catalyst and the applied potential, which affects the stabilisation imparted by the adsorption of the intermediate on the catalyst. [32] In order to facilitate the direct 4 electron pathway, the relatively strong O-O bond (498 kJ/mol) would need to be broken before or during the second electron transfer. [8] This so called dissociative mechanism would require a strong

interaction of oxygen with the catalyst surface. However, recent results suggest that even for Pt, one of the best ORR electrocatalysts, the reaction might proceed predominantly via the 2+2 pathway. For some catalysts a strong pH dependence is observed. This might occur when the superoxo/peroxo pathway is present, where the first electron transfer to produce  $O_2^-$  is the rate determining step (RDS). [31, 32] This strong pH behaviour is observed for metal surfaces, *e.g.* Ag or Au, and for carbon or heteroatom doped carbon surfaces. [13, 32] In general the ORR becomes more facile under more alkaline conditions. [8] It was argued based on a modified *Pourbaix* diagram, that the pH change shifts the reversible potential of the pH independent first electron transfer relative to the reversible hydrogen electrode (RHE) thus providing a larger driving force for this reaction. [32] On carbon surfaces doped with heteroatoms an associative mechanism is suggested by density functional theory (DFT) calculations. [33, 34] A general pathway for the associative mechanism on a single active site is as follows [8] :



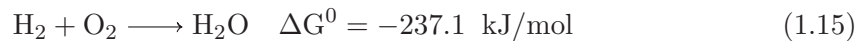
Where A is the active site and Equations 1.9 and 1.10 are competing reactions and 1.10 leads to the 2 electron pathway. It has to be mentioned that DFT calculations have to be taken with care, as most procedures do not take the double layer or the solvation of the reactants into account. These parameters play important roles in determining the stability of activated complexes and intermediates. [35] Alternatively a reductive adsorption with a superoxide species might precede the first proton transfer. Instead of a proton coupled electron transfer (PCET) (Equation 1.8), the first electron transfer and the first proton transfer are then not concerted, but occur successively, as shown in the following equations [36]:



The pH dependence of the activity on these carbon based catalysts, with a significantly higher activity in alkaline solutions might arise due to protonation/deprotonation of the active site or sites associated with the catalytic activity or due to the superoxide formation (Equation 1.13) being the RDS and being more favoured in alkaline electrolyte. [8, 32] In order for the complex ORR to proceed with a suitable rate and selectivity electrocatalysts are necessary. [8]

### 1.3 Reason for electrocatalysts - PEMFC efficiency and losses

When operating an electrochemical device it is crucial to minimise parasitic losses and maximise current or fuel efficiency in order to make this device economically feasible. The theoretical energy efficiency of a device is generally defined by the ratio of useful work that can be extracted to the amount of chemical energy stored in the respective fuel. [8] In an electrochemical device the maximum amount of work that can be extracted is given by the *Gibbs* free energy of the reaction. In the case of a hydrogen fuel cell [8]:



The standard enthalpy of formation of liquid water from  $\text{H}_2$  and  $\text{O}_2$  under standard conditions, which can be considered as the chemical energy stored in hydrogen, is  $\Delta H_f^0 = -285.8 \text{ kJ/mol}$ . The efficiency is then calculated by [8]:

$$\eta = \frac{\Delta G^0}{\Delta H_f^0} = \frac{-237.1}{-285.8} = 0.83 \quad (1.16)$$

Therefore the maximum theoretical efficiency is 83 %.<sup>1</sup> The reversible cell voltage  $E$  (V) of an electrochemical system is linked to the free energy  $\Delta G$  (kJ mol<sup>-1</sup>) by the following relationship [8, 37]:

$$\Delta G = -nFE \quad (1.17)$$

where  $n$  is the number of electrons and  $F$  (C mol<sup>-1</sup>) the *Faraday* constant. At standard conditions ( $\Delta G^0 = -237.1$  kJ/mol) one arrives at 1.23 V. This is the theoretical open circuit potential (OCP) of a hydrogen/oxygen fuel cell.<sup>2</sup> [30] When work in the form of electricity is extracted from a fuel cell, the cell needs to be polarized to provide current ( $I$  in A). This decreases the potential of the cell, while providing power ( $P = E \times I$  in W) to perform work. The Voltage efficiency is defined as [30]:

$$\eta_e = \eta \times \frac{E_{cell}}{E_{OCV}} = 0.83 \times \frac{E_{cell}}{1.23V} \quad (1.18)$$

From the above relationship it is clear that the cell needs to run at as high potential as possible to obtain a high efficiency while providing as much current as possible to provide a high power density. Commercial fuel cells need to run at cell potentials between 0.65 and 1.0 V to achieve efficiencies between 40% to 67%, while delivering a sufficient power density for the required application.<sup>3</sup> [38]

In a fuel cell there are three major losses upon polarisation. (i) the activation polarisation  $\eta_{act}$ , (ii) ohmic drop  $\eta_{ohm}$  and (iii) concentration polarisation  $\eta_{conc}$  in V.[8] Figure 1.7 shows a typical PEMFC polarisation curve where the typical region of the respective losses are indicated. The activation polarisation arises due to the kinetic limitations of the reactions involved and for each reaction can be approximated by [8]:

$$\eta_{act} = \frac{RT}{\alpha nF} \ln \left( \frac{j}{j_0} \right) \quad (1.19)$$

<sup>1</sup>in this example the higher heating value (HHV) is used. This assumes the formation of liquid water rather than water vapour.

<sup>2</sup>varying the conditions such as partial pressure of reactant or temperature will alter the values. The respective values can be obtained by the relevant thermodynamic relationships and are omitted in this discussion for clarity.

<sup>3</sup>this consideration does not take into account the efficiency losses due to production, storage and transport of the fuel (well to wheel efficiency).

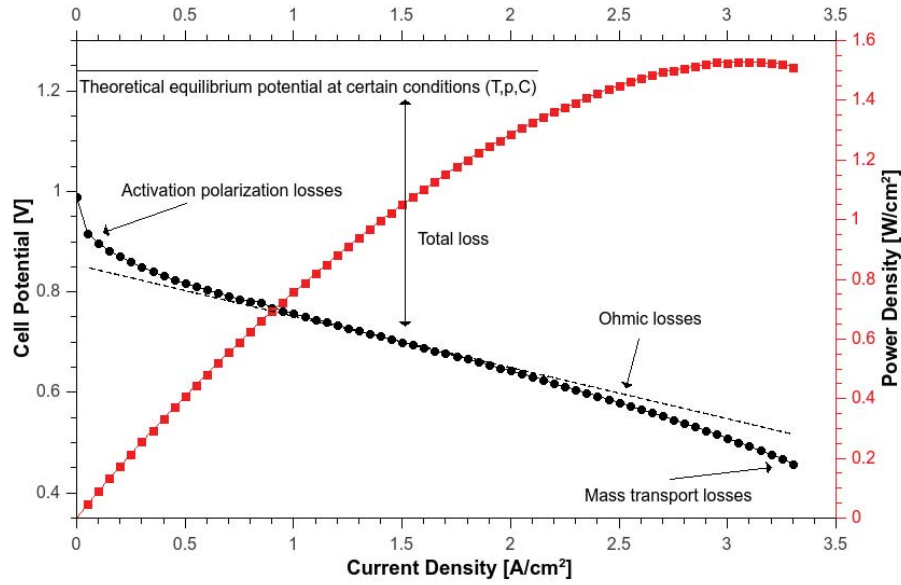


FIGURE 1.7: Representative fuel cell polarisation curve, showing the different parasitic losses an the typical potential region at which those dominate.

Where  $R$  ( $\text{J mol}^{-1} \text{K}^{-1}$ ) is the gas constant,  $T$  (K) the temperature,  $\alpha$  the transfer coefficient of the reaction,  $F$  ( $\text{C mol}^{-1}$ ) the *Faraday* constant,  $j$  ( $\text{A cm}^{-2}$ ) the respective current density and  $j_0$  ( $\text{A cm}^{-2}$ ) the exchange current density of the reaction under consideration.  $j_0$  is only well described for an elementary reaction step and for a complex reaction such a the ORR it can be crudely considered a measure on how facile the reaction is. [37] The ohmic drop is given by [30]:

$$\eta_{ohm} = jR_{cell} \quad (1.20)$$

where  $R_{cell}$  ( $\Omega$ ) is the combined cell resistance, consisting of electrolyte resistance and all the electrical resistances including contact resistance between components and lead resistances. The concentration polarisation is given by [30]:

$$\eta_{conc} = \frac{RT}{nF} \left( 1 - \frac{j}{j_{lim}} \right) \quad (1.21)$$

where  $j_{lim}$  is the limiting current density. The cell potential at a given current density  $j$  is then given by [30]:

$$E(j) = E_{OCV} - \eta_{act}^{anode}(j) - \eta_{act}^{cathode}(j) - \eta_{ohm}(j) - \eta_{conc}(j) \quad (1.22)$$

where  $\eta_{act}^{anode}(j)$  is the activation polarisation associated with the anode reaction, *i.e.* the hydrogen oxidation reaction (HOR) and  $\eta_{act}^{cathode}(j)$  the activation polarisation associated with the ORR respectively. It is clear that the polarisation losses have to be minimised in order to obtain the maximum potential and hence efficiency and power density. [30] The ohmic drop can be minimised by using high performance ultra-thin membranes which are as thin as 10  $\mu\text{m}$ , such as in the recently released Toyota Mirai [18, 25], by minimising the contact resistance between and the electrical conductivity of the stack components. [8] The concentration polarisation can be minimised by clever engineering of gas distribution, gas diffusion media and catalyst layer. [18, 25] This leaves the activation polarisation, which is defined by the electrokinetics of the respective reaction and can only be decreased by suitable catalysts. This makes the development of high performing electrocatalysts crucial for the operation of electrochemical devices. In hydrogen fuel cells, the HOR is usually considered facile enough on the utilised Pt catalysts. [16] The ORR however is especially challenging and contributes to the major part of  $\eta_{act}$  as it involves this complex mechanism with a detrimental  $\text{H}_2\text{O}_2$  intermediate that needs to be avoided. The selectivity towards water is therefore another performance metric for ORR electrocatalysts. [28]

## 1.4 Electrokinetics and electrocatalysis

In general for an elementary chemical reaction step to occur an activation barrier has to be overcome. [37]



The rate of this reaction step is then correlated with this activation barrier and is given by following relationship which was first introduced by Arrhenius and then extended in the transition state theory [37]:

$$k = Ae^{-\Delta G^\ddagger/RT} \quad (1.24)$$

where  $k$  is the respective rate constant for the forward ( $k_f$ ) and backward ( $k_b$ ) reaction respectively. When at equilibrium,  $k_f = k_b$  and is called  $k_0$ .  $\Delta G^\ddagger$  ( $\text{kJ mol}^{-1}$ ) is the free energy of activation that needs to be overcome in order to reach the transition state.  $R$  is the gas constant,  $T$  the temperature and  $A$  a pre-exponential factor which includes the statistical probability of collisions that lead to a reaction. [37] Thus, if the activation barrier is lowered,  $k$  is increased and the reaction proceeds more facile. This is the task of every catalyst. Generally it is achieved by a favourable catalyst-reactant interaction that stabilises the activated complex or transition state. [37] An electrochemical reaction is given by [37]:



when at equilibrium, the reaction will have the reversible potential according to the *Nernst* equation [37]:

$$E = E_0^* + \frac{RT}{nF} \ln \left( \frac{C_{ox}^*}{C_{red}^*} \right) \quad (1.26)$$

where  $E$  (V) is the equilibrium potential,  $E_0^*$  (V) is the formal standard potential,  $C_{ox}^*$  and  $C_{red}^*$  (in  $\text{mol cm}^{-3}$ ) the bulk concentrations of the oxidised and reduced species and  $n$  the number of electrons transferred. The potential current relationship was first empirically found by *Tafel* to be [37]:

$$\eta = a + b \log j \quad (1.27)$$

where  $a$  and  $b$  are constants.  $\eta$  (V) is the so called overpotential and describes the deviation from the respective equilibrium potential ( $E_{system} - E_{OCV}$ ). For anodic processes, *i.e.* oxidations,  $\eta$  is positive and for cathodic processes, *i.e.* reductions,  $\eta$  is negative. Based on this observation the *Butler-Volmer* model of electrode kinetics was developed [37]. It depends upon the relative modulation of the energies and thus activation barrier upon change of potential. If the potential is increased relative to the OCP, the reduced species becomes less stable, which increases its relative free energy and hence the activation barrier towards oxidation becomes smaller as compared to the opposite process and vice versa. The imbalance in activation energies results in a net reaction which means a current. [37]

The following expression results from the derivation and describes the current-potential characteristic of a one electron elementary electrochemical reaction [37]:

$$j = j_0 \left\{ \exp \left[ \frac{\alpha n F \eta}{RT} \right] - \exp \left[ -\frac{(1 - \alpha) n F \eta}{RT} \right] \right\} \quad (1.28)$$

where  $j_0$  is the exchange current density and  $\alpha$  is the transfer coefficient. The *Tafel* relationship is a limiting case of the *Butler-Volmer* model, where the overpotential is sufficiently large, so the reverse reactions contribute less than 1% and can be neglected. [37] For a simple electrochemical step kinetic parameters can be extracted from a *Tafel* plot, as the constants  $a$  and  $b$  are then [37]:

$$a = \frac{2.3RT}{\alpha F} \log j_0 \quad \text{and} \quad b = \frac{-2.3RT}{\alpha F} \quad (1.29)$$

Thus the exchange current density and the transfer coefficient can be extracted. [37] The exchange current density is correlated with the rate constant of an electrochemical step by the following relation [37]:

$$j_0 = n F k_0 C_{\text{ox}}^\alpha C_{\text{red}}^{(1-\alpha)} \quad (1.30)$$

where  $C_{\text{ox}}$  and  $C_{\text{red}}$  (in mol cm<sup>-3</sup>) are the concentrations of oxidised and reduced species at the surface, respectively. This means ultimately  $j_0$ , so  $k_0$  need to be increased and therefore the principle of an electrocatalyst is similar to the catalyst; it has to favourably interact with the substrate and lower the activation barrier  $\Delta G^\ddagger$  for the reaction to be kinetically more facile. The additional requirement for an electrocatalyst as compared to a catalyst is that it has to be electrically conductive in order to minimise ohmic losses. Most technologically important reactions, including the ORR, are not simple elementary charge transfer steps as shown in equation 1.25. These usually involve a complex series of steps, including (i) diffusion of species to the catalyst surface (ii) adsorption and desorption of the unreacted substrate (iii) a series of electron and/or proton transfer steps (iv) desorption of intermediates (v) competitive blocking of sites (vi) desorption of the product and (vii) diffusion of the product away from the catalyst surface. [37] These steps can either occur successively or in parallel, so competitively. Every step has a rate associated with it and the complex interplay of these rate constants then defines the exact current potential



behaviour. [37, 39] These steps can be modelled and give mathematical expressions which can support proposed reaction mechanisms upon fitting with experimental data. [39]

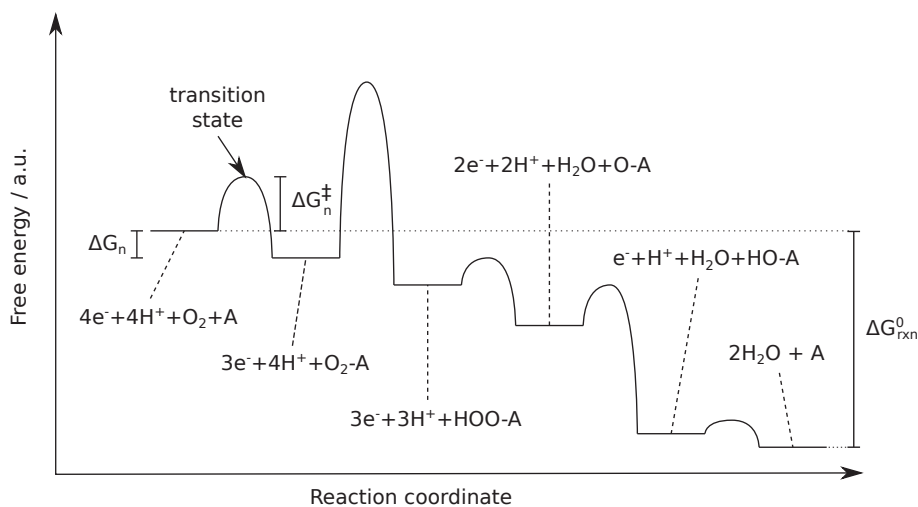


FIGURE 1.8: Diagram showing the free energy of different intermediates for the ORR along a reaction coordinate. The values for the activation barrier of a particular reaction step  $\Delta G_n^\ddagger$ , the free energy of a particular reaction step  $\Delta G_n$ , the free energy of the complete reaction  $\Delta G_{rxn}^0$  and the energetic location of the respective transition state are indicated. In this case the first electron transfer is the RDS, as it has the highest activation barrier.<sup>4</sup>

For many reactions it is assumed that one step is significantly slower, i.e. has a significantly higher activation barrier  $\Delta G^\ddagger$ , than all other steps and is the RDS. [37] Figure 1.8 shows the reaction pathway described in Equations 1.7 to 1.12 (without 1.10).<sup>4</sup> [36, 40] Even complex reactions can show some sort of *Tafel* behaviour. However, extracting the kinetic parameters as is done for the elemental step is not possible. [37] This is because the contributions from the other reaction steps cannot be neglected. [37] Nevertheless, *Tafel* slopes and apparent exchange current densities can be used to compare the kinetic facility of a reaction on similar materials to each other and get some insight.

The nature and energetic shape of the activation barrier can be explained with microscopic theories of charge transfer, among which the *Marcus* theory is the most prominent one. [37] It holds for electrochemical charge transfer as well chemical charge transfer. [37] An extensive treatment is outside the scope of this work and the interested reader is referred to the respective literature. [37, 41–43] A summary will be given for completeness. The theory distinguishes between outer sphere and inner sphere electron transfer. While in the outer sphere electron transfer the solvation shell of the reactant stays intact during the reaction step and the molecule does not interact with the electrode material directly,

<sup>4</sup>the relative energies have been chosen arbitrarily and vary for each catalyst.

the inner sphere mechanism involves a strong direct interaction of the substrate with the electrode, *i.e.* chemisorption. Almost all electrocatalytic reactions are inner sphere mechanisms, as this very catalyst-substrate interaction defines the role of most catalysts. The basis of the theory is the assumption that the electron transfer is a radiationless isoenergetic process. This means the electron has to move from the donating state, *i.e.* electrode or reduced reactant, to the same energy level of the receiving species, *i.e.* reduced reactant or electrode, respectively. [37, 41–43] Expressed in a very simplified way, the theory considers the reaction coordinate in terms of bond lengths of initial and final state with contributions from solvent molecules and terms associated with the movement of charged species through an electrical field. An electron transfer can then only occur when the physical state of the initial and the final state are the same. This is then the transition state. [37, 41–43] The following relationship was derived for an electrochemical system [37]:

$$\Delta G_f^\ddagger = \frac{\lambda}{4} \left( 1 + \frac{F(E - E^0)}{\lambda} \right)^2 \quad (1.31)$$

where  $\Delta G_f^\ddagger$  (kJ mol<sup>-1</sup>) is the activation energy of the forward step and  $\lambda$  (kJ mol<sup>-1</sup>) is the reorganisation energy that results from the derivation as the amount of work necessary to bring the configuration in terms parameters such as bond length, bond angle, solvation shell and spatial orientation of the initial state to that in the final state. At equilibrium  $\Delta G^\ddagger \approx \frac{\lambda}{4}$ . This means the reorganisation energy is smaller when the reduced and oxidised state are more similar to each other and  $k_0$  becomes larger hence the reaction more facile. [37] It has to be mentioned that this relationship was derived for an outer sphere electron transfer and expressions for inner sphere electron transfers are more complex and subject to ongoing research. [35, 37]

From this consideration one can in a simplified way understand the principle of a catalyst to lower  $\Delta G^\ddagger$ . This can be done by inducing a transition state which leads to a configuration in which the two states are arranged to be similar, *e.g.* in terms of bond length. For the first step of the ORR, the electron transfer to form  $\text{O}_2^-$ , a favourable interaction with a catalyst could be the donation of electron density from the catalyst into the antibonding orbital of the oxygen molecule, creating a state where this intermediate is similar to the initial as well as the final state, by increasing the O-O bond length. If the catalyst facilitates this with the RDS, the reaction is enhanced significantly. An ideal catalyst

however would facilitate this for every step of a multi step mechanism. To achieve this, the active site would have to be highly complex and be able to change during the course of the reaction. To date only enzymes might behave in such a way.

In catalyst development it is useful to find descriptors, *e.g.* material properties, which govern catalyst activity. [36, 40, 44] This potentially enables a more rational catalyst design and minimises the trial and error approach. The most basic activity descriptor for catalysts as well as electrocatalysts is the energy of adsorption  $E_{ads}$  of a substrate with the catalyst surface. [36] The *Sabatier* principle states that the most active catalyst should bind the substrate strong enough to facilitate a good interaction. If it binds too strongly however the desorption is hindered and the catalyst becomes poisoned. [36] Plotting  $E_{ads}$  or any other activity descriptor *versus* the activity for different materials usually results in an ascending branch and a descending branch, with the most active material on the top.

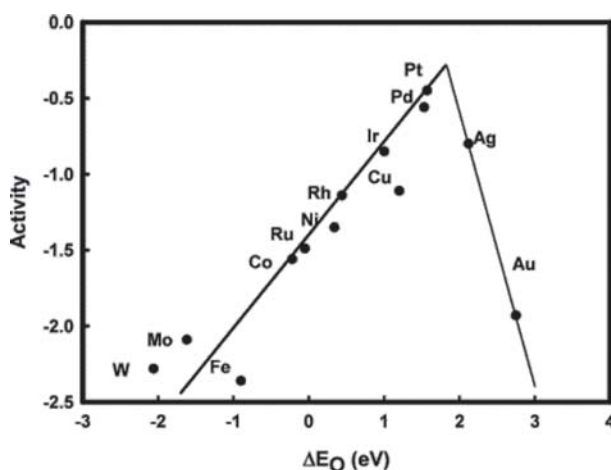


FIGURE 1.9: A plot of the electrochemical binding energy of  $O_2$  on different metal surfaces and the respective ORR activity. [Reprinted with permission from Ref. [36]. Copyright 2004 American Chemical Society.]

An example of such a plot for the ORR is shown in Figure 1.9, it is called a *Volcano* curve, owing to its shape. The activity is given as the logarithm of current density. It can be seen that Pt is the by far the most active pure metal for the ORR. [36] The same applies for the HOR. [8] In complex mechanisms as for the ORR, different descriptors have been used for metal surfaces, such as binding constants of certain intermediates or the d-band center of the metal. [40, 45]

## 1.5 Cost, durability and activity requirements for fuel cell catalysts

The biggest challenges in commercial fuel cell development remain the cost and the durability. [38, 46] Other challenges, such as system power density (W/L), stack specific power (W/kg) or cold start-up are acceptable for transportation applications. [38, 46] Therefore the US Drive partnership, a consortium that gives feedback to the US Department of Energy (DoE), set the following development targets for commercial fuel cells. [38, 46] The requirements are based on the necessity of a FC stack to compete with an internal combustion engine (ICE). Therefore the durability target was set to  $\geq 5000$  hours operation with a voltage loss of  $\leq 10\%$  under realistic operating conditions such as load cycling and start/stop operation. This is equivalent to 150 000 miles ( $\sim 241\,000$  km) of driving. [46] 2530h have already been projected for current fuel cell technology. [47] The cost of a stack should be competitive and was set to \$40/kW by 2020. [46] From these requirements the desired metrics of fuel cell catalysts arise. The main reasons that make the development of fuel cell catalysts challenging are (i) the corrosive conditions within a PEMFC, i.e high potentials and low pH (ii) the fact that Pt is by far the most active electrocatalyst for both the ORR and the HOR and (iii) the need for a high power density at a potential of  $\geq 0.65$  V in order to ensure adequate fuel utilisation and provide the necessary volumetric power density for transportation or small stationary applications. [38] To date only Pt based catalysts can perform this task with a reasonably low loading. [25, 38] Currently, state of the art fuel cells use a Pt based catalyst at the anode and cathode. The loading at the anode could be reduced to  $0.05 \text{ mg}_{\text{Pt}}/\text{cm}^2$  without significant performance loss. [38] This is 1/8 of current state-of the art cathodes which use a loading of  $0.4 \text{ mg}_{\text{Pt}}/\text{cm}^2$ . [16] Based on the DoE cost projections a target value for precious group metals (PGM) of  $0.125 \text{ mg}/\text{cm}^2_{\text{MEA}}$  (or  $0.125 \text{ g}_{\text{Pt}}/\text{kW}_{\text{stack}}$ ) without performance loss is set for 2020. [46] The mass activity target is  $0.44 \text{ A}/\text{mg}_{\text{PGM}}$  @900 mV<sub>ir-free</sub> cell potential. [46] To achieve this, either ORR catalysts without the use of PGMs need to be developed or the utilisation and/or specific activity of existing PGM catalysts needs to be increased. [13] A new group of non-precious metal catalysts, based on carbon doped with transition metals, Fe or Co and nitrogen (M-N/C) is considered a promising non-PGM type replacement material. [13] Although the specific activity is significantly lower, it is argued that due to

the negligible cost, the loading can be increased to reach the necessary activity. [38] However, this increase in loading is not unrestricted, as a higher loading would impose mass transport and water management issues with detrimental effects on fuel utilisation. [38] Moreover for transportation application the space requirements need to be considered in order to maintain the required volumetric power density. Based on these considerations a target of  $300 \text{ A/cm}^3$  @  $800 \text{ mV}_{\text{iR-free}}$  cell potential was suggested for non-PGM catalysts. The performance is normalised to the volume, as the electrode volume is considered to be the limiting factor. [38]

## 1.6 Types of ORR electrocatalysts

Different approaches are investigated to reach the required targets, all of which have their justification. The main approaches will be summarized here. [45]

**For pure Pt** it is known from single crystal studies that different surface facets exhibit different activities, *e.g.*  $\text{Pt}(110) \approx \text{Pt}(111) \ll \text{Pt}(100)$  in  $\text{HClO}_4$  electrolyte, and that terraces and steps also modulate the activity. [48, 49] The possibility of an ideal surface with the maximum activity can be hypothesised. However, restructuring effects make this elusive. Another approach is to increase the effective exposed surface of the utilised Pt. [45] This can be done by either preparing smaller nanoparticles or nanostructured thin films of atomic thickness on a support. A particle size and shape effect on the specific activity of Pt is topic of ongoing debate. [45] The difficulty in reducing the Pt content with this approach is that as the loading is decreased, the sensitivity of the catalyst to even trace amounts of poisons increases, which is problematic under real operating conditions. [45, 50] Periodic electrochemical or chemical cleaning of the catalyst surface would be an option. [50]

**Alloying of Pt** with inexpensive late transition metals has shown to increase the specific activity towards the ORR. In fact the catalyst used by Toyota in the Mirai is a PtCo alloy. [18, 25] Fe, Ni and Co show the most promising stability and activity characteristics. [45] The agreement is that upon post-synthetic annealing a Pt skin forms around the alloy particle and the enhancement is attributed to lattice strain effects. [40, 45] Recently

it also has been shown that alloys with early transition metals and rare earth elements can be a promising option. Pt<sub>5</sub>Gd or Pt<sub>3</sub>Y show an enhancement in specific activity of 5. [44] Porous structures can also be produced by selective leaching of the non-noble elements. This can leave hollow Pt polyhedra which have shown significantly increased activities of up to 36-fold in model studies. [51] The most promising alloys show problems with respect to operational stability and scalability of the synthesis. [45] Another concern is how to translate the enhancements seen in model studies into the operating device. [45, 52]

**The core-shell approach** tries to deposit a monolayer of Pt onto nanoparticles of less expensive other metals, such as lower cost PGMs or transition metals. [53] The increase of Pt utilisation comes about, because the ~70% Pt in the bulk of pure particles is not utilised. [45] It has been shown that the core can even be used to influence the properties of the Pt skin beneficially by modulating the d-band center. [45] Higher specific activities have been demonstrated for Pt–AuNi<sub>10</sub>, Pt–Cu and Pt–Pd core-shell nanoparticles. [45, 53, 54] The major problem with this approach is the scalable synthesis and for non-noble cores, the stability. [45]

**Metal Oxides and related structures:** For reasons outlined in 1.7.1 it is desirable to eliminate the precious metal content altogether. One group of materials that show appreciable ORR activity are transition metal oxides, nitrides, oxynitrides and carbides. [45] Due to the oxidised state, these materials are stable in acid. Various combinations of materials have been synthesised and assessed, including ZrO<sub>2-x</sub>, Co<sub>3</sub>O<sub>4-x</sub> and TaO<sub>x</sub>. [45] It is believed that oxygen vacancies might be the source of the catalytic activity. [45] Some of these nanoparticles show encouraging onset potentials of as high as 0.94V *vs* RHE. [55–58] However, the synthesis and poor conductivity are major challenges to be overcome for these materials. [45] Approaches which are studied include the doping with nitrogen to reduce the band-gap and produce oxynitrides, deposition on supports such as carbon nanotubes (CNTs) or reduction of size for better dispersion. [45] Metal nitrides, such as TiN on CNTs have also been developed and tested. However, with a low activity. Metal carbonitrides such as TaC<sub>x</sub>N<sub>y</sub> have shown promising activities, especially after partial oxidation. [45] These materials could be promising, if they show the required stability, 4 electron selectivity and if their synthesis can be scalable. At the moment most materials

are prepared by sputtering and annealing on a small scale. [45]

**Metal chalcogenides**, such as transition metal compounds with S, Se or Te show appreciable ORR activity. [45] One of the most promising materials,  $\text{Ru}_2\text{Mo}_4\text{Se}_8$ , has shown an only 100 - 150 mV lower half-wave potential than Pt in  $\text{H}_2\text{SO}_4$ . [59] It was found that the chalcogenide can lower the otherwise strong oxygen binding energy and thus increase the catalytic activity of Ru, Rh and Co. [45] The main concern with these materials is the cycle stability and the toxic selenium. [45]

**Carbon based metal containing (M-N/C) and metal free (N/C) catalysts:** Biological systems utilise transition metal macrocycles for oxygen activation. [60] Inspired by the impressive capabilities of living systems to use oxygen efficiently, this approach has been translated to electrocatalysis. [61] A promising material emerged after successive improvement. [62] It has been found that carbon materials which are doped with nitrogen and some transition metal after a high temperature heat treatment show appreciable activity and stability towards the ORR. [45] These materials are the topic of this thesis and are introduced in the following section.

## 1.7 M-N/C type non-precious metal catalysts (NPMCs)

### 1.7.1 Reasons for research into non-precious metal catalysts

Price and availability are the main incentives to substitute Pt or other PGMs. [63, 64]

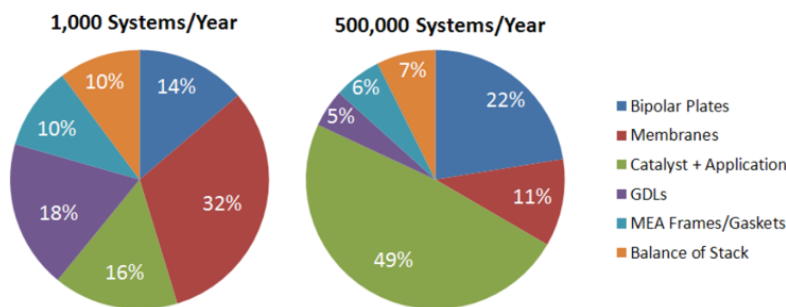


FIGURE 1.10: Breakdown of costs for the components in a fuel cell stack at different production volumes. [Taken from [64]]

It can be seen in Figure 1.10 that the catalyst alone contributes a significant fraction to the production cost of a fuel cell stack. While economies of scale decrease the price of all other components, the contribution of the catalyst cannot be further decreased and will be the major expenditure in the stack.[64] As an example, the Toyota Mirai uses approximately 40g of Pt with a raw material cost of  $\sim 1500$  USD. [65, 66] This cost might be deemed acceptable for an expensive luxury car, where the price of the catalyst would only contribute to a fraction of the sales price. However, for a combustion engine equivalent mid range passenger car comparable to the Mirai that sells in the range of 30000\$ this would constitute  $\sim 5\%$  of the sales price and would make the vehicle commercially challenging.[67]

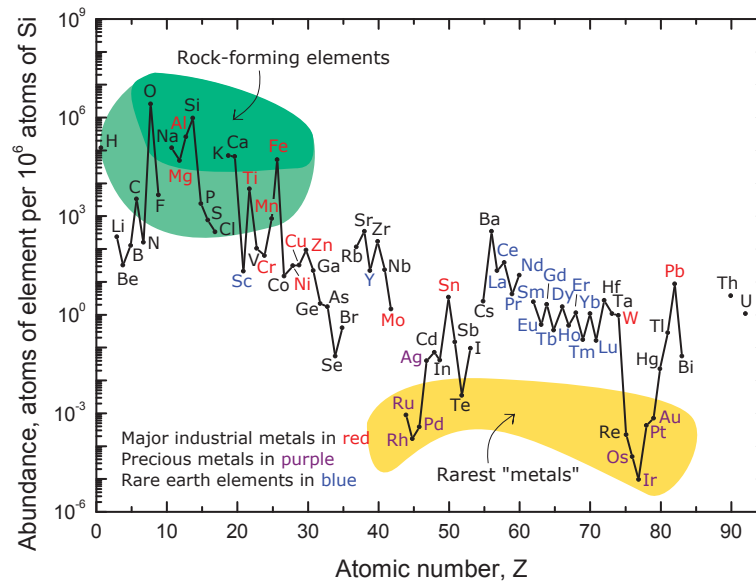


FIGURE 1.11: Abundance of the elements in the earth's crust [Taken from [68, 69]].

It is clear from Figure 1.11 platinum and other platinum group metals that are active for fuel cell reactions are among the scarcest elements in the earth's crust.[68] This leads to constraints in the total amount of Pt available, its geolocation and the volatility of the price.[63]

Due to the scarcity, the already high price of Pt is subject to strong fluctuations in times of economic uncertainty. For instance, during the oil crisis in the 1980s and the financial crisis 2008 the price of Pt increased by a factor of 2 - 3 on short time-scales of 1 - 2 months. [70] This will be a problem if Pt is a critical raw material for vehicle manufacturing.



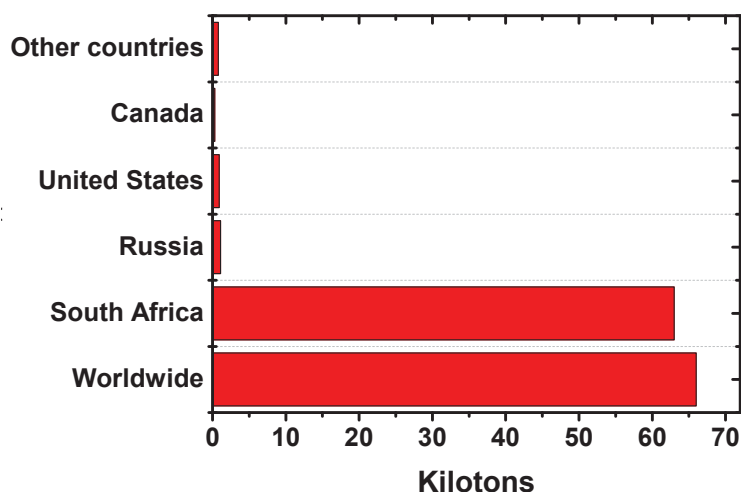


FIGURE 1.12: Distribution of known Pt reserves in the world. [71, 72]

An increased supply risk for Pt is additionally present, as the major amount of known reserves are located in South Africa, as shown in Figure 1.12. [71, 72] Another drawback of Pt base catalysts is their sensitivity to poisons. While they show a high activity on a mass basis, the performance of the catalyst is strongly affected by trace amounts of contaminants which can be present in the atmosphere, *e.g.* sulfur dioxide, volatile organic compounds or ammonia to name only a few. [50, 73, 74] This will be an issue, as fuel cells will consume oxygen from the air, which can be contaminated with detrimental compounds from pollution in urban areas and agriculture in rural areas. This issue will be discussed in more detail in the relevant section. Finally,  $\sim 90$  million vehicles are produced per year. [75] If only 20% of the fleet was replaced with fuel cell cars that use a comparable amount of Pt as the Mirai, a supply of  $\sim 720$  tons of Pt per year would be necessary. Currently the annual global production of Pt is  $\sim 300$  tons, including recycled material. [71] Therefore, such a scenario would not be possible with the currently used Pt loading and Pt production. It is questionable whether it would be possible to increase the production to the necessary degree, without significant price pressure. Therefore alternatives for Pt based materials are crucial for the mass commercialisation of fuel cell vehicles. The materials subject to this work consist mainly of carbon, which is doped with nitrogen and different transition metals, such as Fe, Mn, Co or Cr. As can be seen in Figure 1.11, all these elements are highly abundant in the earth's crust and therefore the raw material cost for the production of such catalysts is significantly lower than for Pt.

### 1.7.2 Development of biologically inspired ORR catalysts

All aerobic organisms utilise oxygen as the final oxidant. [76] Therefore nature has devised highly efficient ways of oxygen reduction. [76] Living organisms require the ORR to be conducted in a highly controlled manner and the avoidance of damaging intermediates, such as  $O_2^-$  and  $H_2O_2$ . [76] Therefore biomimetic catalysts with a high activity would be interesting for electrochemical applications. The reaction in the respiratory chain is carried out by complex enzymes and the most prominent is cytochrome c oxidase CcO. [76] Within this complex oxygen is reduced to water. [76]

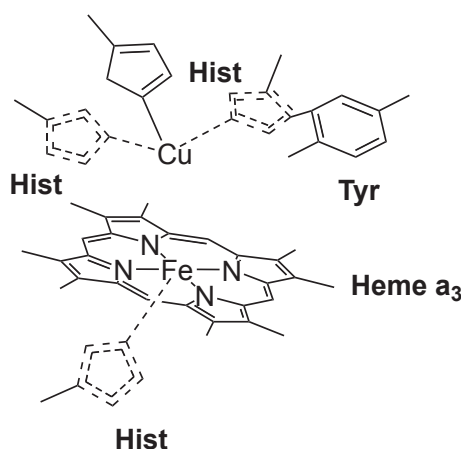
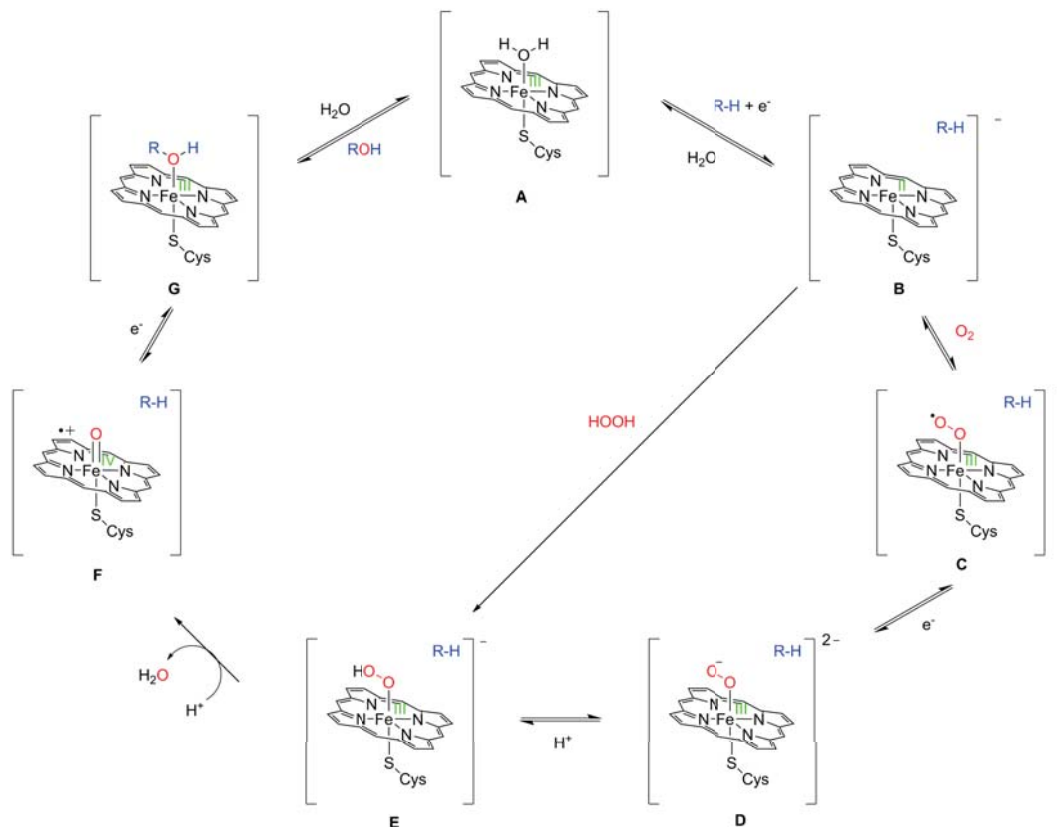


FIGURE 1.13: Active site structure of cytochrome c oxidase (CcO) [77]

Although enzymes are too complex and delicate to be used as fuel cell catalysts, the study of the active site might offer the possibility to reproduce it in a simpler, more robust system. Figure 1.13 depicts the active center of CcO. [77] It consists of an iron atom, coordinated with a porphyrin derivative and is surrounded with amino acid residues and a Cu atom in the vicinity of the iron center. [77] It is believed the surrounding structure is required in order to facilitate fast electron and proton transport for the reaction. [77] The active site is the iron center, where oxygen coordinates and is successively reduced. [77] The iron center coordinated with porphyrin is also termed heme, and a prominent group of heme containing enzymes is cytochrome P450. [78] This structure is a ubiquitous moiety that is found across organisms and enzymes which interact with various small molecules. [78] It takes part in most metabolic cycles. [78] CcO itself contains two cytochrome centers and two copper centres. [79, 80] The additional metal centres facilitate efficient electron transport.



SCHEME 1.1: Proposed mechanism for the activation of dioxygen by cytochrome P450. [Reproduced after Ref. [81]]

The catalytic cycle of oxygen activation on cytochromes is well studied, as it interacts with various molecules and is also an efficient hydroxylation catalyst (Chapter 7 will be devoted to this topic). [82] Figure 1.1 shows a widely accepted proposed cycle for the reduction of dioxygen, to generate a iron-oxo species (**F**), which then hydroxylates an aliphatic hydrocarbon to regenerate the original state. [81, 82] The capability to cleave the strong O-O bond is the striking feature of this type of moiety, with the resulting Fe<sup>IV</sup>=O being a strong oxidant or in other words easy to reduce, thus overcoming the kinetic limitation of O-O bond cleavage. [81, 82] In case of CcO, the final product is a second water molecule after species (**F**). [77, 80] It is proposed that after the O-O bond cleavage, the active center of CcO is an oxidised state of Tyr<sup>•</sup>/Cu<sup>II</sup>/Fe<sup>IV</sup>=O which then easily reacts with 4 electrons and 2 protons to give water and the original state of Tyr/Cu<sup>I</sup>/Fe<sup>II</sup>. [77, 80]

It is known that O<sub>2</sub> interacts with most late transition metals. [84] The reason for this interaction is the ability of oxygen to act as a ligand and can be explained with molecular orbital (MO) theory. [84] On a single metal site 2 different modes of adsorption are

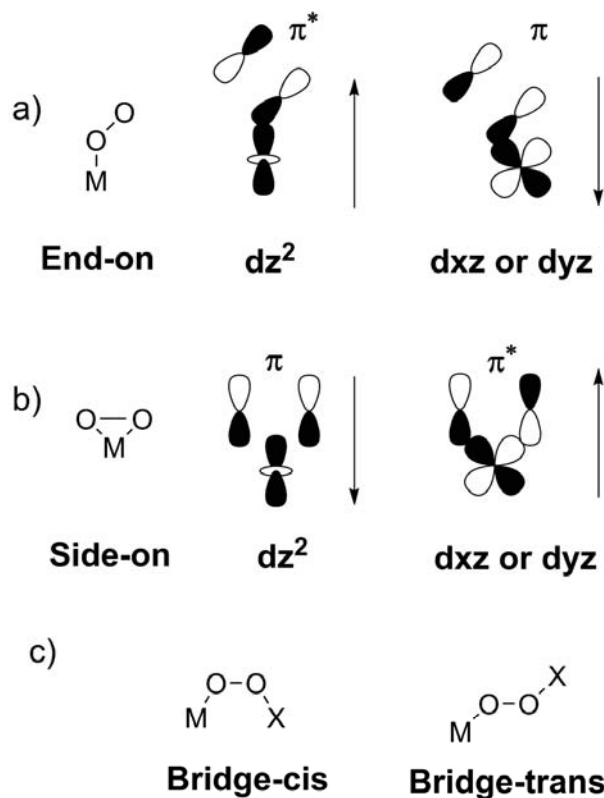


FIGURE 1.14: Different spatial configuration for dioxygen, when it interacts with metal active sites. a) End-on configuration with frontier orbital interactions. b) Side-on configuration with frontier orbital interactions. c) Further possible configurations, when the active centre consists of 2 sites. [83] M is a metal site and X can be either a metal site or a different atom that might interact with the substrate, *e.g.* nitrogen from the ligand.

possible. [83] Figure 1.14 (a) shows the end-on configuration, where the metal  $dz^2$  orbital donates electron density into the oxygen  $\pi^*$  antibonding orbital thus decreasing the bond order. Additionally, the metal  $d_{xz}$  or  $d_{yz}$  orbitals interact with the oxygen  $\pi$  orbital and receive electron density through backbonding. [83] For the side on configuration the interactions are slightly different, due to the orbital symmetry (Figure 1.14 (b)). [83] Scenarios of 2 metal sites, as shown in Figure 1.14 (c) are also known. [85] This has been reported for Co cofacial porphyrins or Cu complexes. [85] The filling and energy levels of the d orbitals are therefore crucial parameters that determine the interaction with oxygen and hence the catalytic activity. The chemical environment and the type of metal center are the main descriptors to influence these parameters. [86]

Transition metal porphyrins and phthalocyanines, shown in Figure 1.15, are two model compounds which resemble the most fundamental part of the enzymatic systems. [78, 82] The first report of using this type of molecules for the electrochemical ORR was made by Jasinski in 1964 and started this research field. [87, 88] Co-phthalocyanine was used and

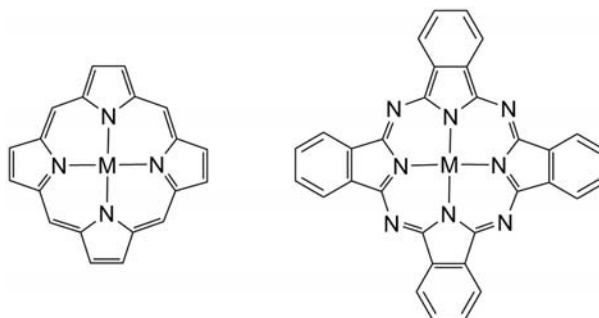


FIGURE 1.15: General structure of a) metalloporphyrin and b) metallophthalocyanine. [85]

showed reasonable ORR activity. [87, 88] Subsequently it was found that the catalytic activity has a strong dependence on the metal centre.[89–93] The molecules were either prepared into composite electrodes [88] or adsorbed onto high surface area carbon. [89] Early on however it was also found that the porphyrins lack the necessary selectivity, stability and activity to operate under fuel cell conditions, *e.g.* under elevated temperature and highly acidic conditions. [89, 94, 95] The catalytic activity and selectivity to water rather than peroxide also depends on the pH. While the iron based macrocycles have been shown to favour the 4 electron pathway in alkaline and the 2 electron pathway under acidic condition, the reverse trend was found for Co based complexes. [85] The stability of these complexes is compromised by dissolution of the central metal species or the degradation of the macrocycle.[96, 97] Nevertheless, studies on these complexes are useful to gain fundamental insight into activity trends. [85] The advantage of molecular complexes is that the d orbital configuration can easily be controlled and the molecules can be well characterised in order to develop structure property relationships. [98–100] It is furthermore much easier to run DFT calculations on well defined molecules rather than complex structures. [99, 101] The results suggest that on cobalt catalysts only the end-on coordination is observed, while for iron side-on is also possible. [101]

The most notable result that emerged from studies is the apparent correlation between the formal  $M(\text{III})/M(\text{II})$  redox potential and activity. [85] The electro-negativity of the porphyrin (P) and phthalocyanine (Pc) ligand, which can be influenced by attaching either electron withdrawing or donating side groups to the ligand modulates this potential. [85] Zagal *et al.* studied the redox potential relationship of different Fe and Co complexes with different redox potential *versus* the observed activity at a fixed potential. [93] It was found that electron withdrawing groups can increase the activity of the catalyst. [93] This is correlated with the shift of the metal redox potential to higher values. [93] Other studies

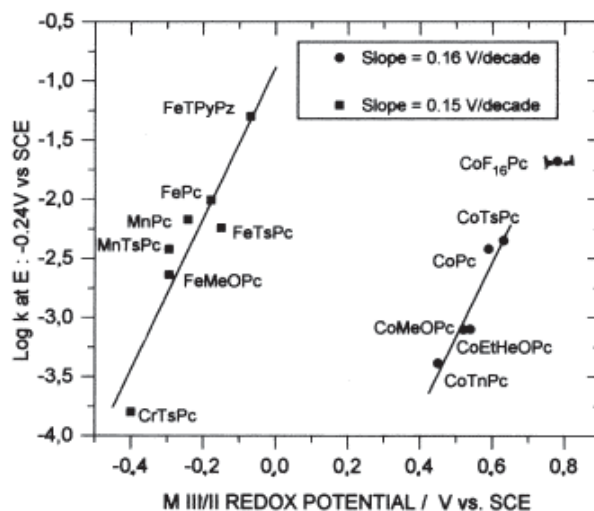


FIGURE 1.16: Plot of  $\log k$  versus redox potentials of the metal for  $\text{O}_2$  reduction in 0.1M NaOH on different metal macrocycles adsorbed on glassy carbon. [Taken with permission from Ref. [93]]

found similar relationships under various conditions and also for other reactions, such as oxidation of hydrazine.[102, 103] Figure 1.16 shows that an almost linear relationship is present, resembling the ascending part of a volcano curve (Figure 1.9). [85, 93] This implies that there is room for significant improvement on the activity. [85] The correlation of  $\text{O}_2$  onset potential and Fe(III)/Fe(II) redox potential has also been observed with Fe K-edge XANES (X-ray Absorption Near Edge Structure), in situ in 0.5M  $\text{H}_2\text{SO}_4$ . [104] A volcano like relationship was found for the filling of the d-orbitals and the catalytic activity under alkaline conditions. [105] Due to the found correlations, it is the consensus in the community that the active ORR site in these compounds is the central metal ion. [85, 96] Although the research into molecularly well defined complexes for the ORR is ongoing, due to the vast body of literature, the survey in this section is by no means exhaustive. It is limited to the most important findings and trends that might have implications for the heat treated materials.

### 1.7.3 Heat treatment and first applications in PEFCs

Shortly after Jasinski's report it was discovered that a heat treatment step under inert atmosphere increases the stability and activity of metal macrocycles. [92] Fundamental work of Jahnke, Bagotsky, Wiesener and Fuhrmann and later van Veen established activity trends, focusing on the pyrolysis of transition metal porphyrins and phthalocyanines adsorbed onto carbon blacks. [92, 94, 95, 106–111] The heat treatment was conducted

under an inert atmosphere of N<sub>2</sub>, He or Ar or under vacuum at temperatures between 300 °C and 1000 °C. An optimum temperature range of 600 °C to 800 °C was established for these precursors. [96, 106]

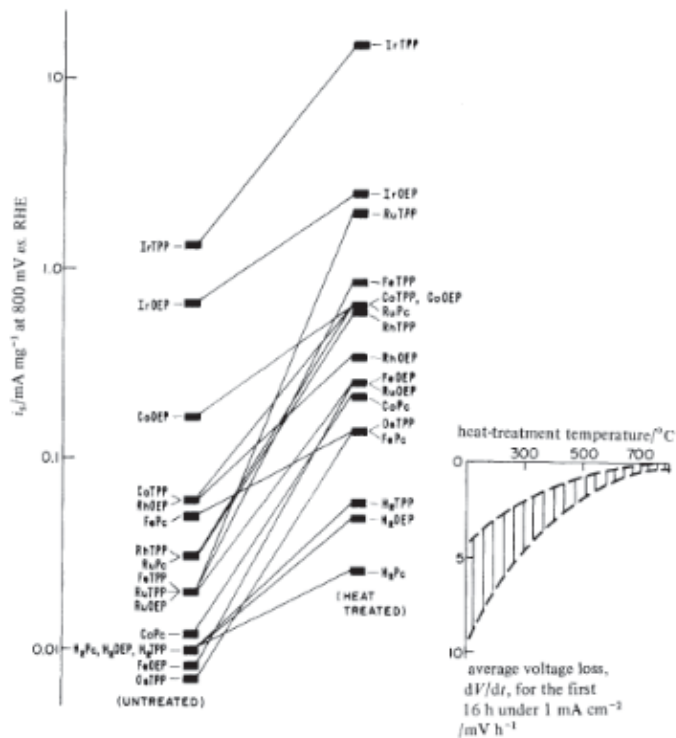


FIGURE 1.17: Increase in (a) ORR activity and (b) stability of different metal-macrocycles adsorbed onto Norit carbon black after heat treatment [Taken with permission from Ref. [107]]

Figure 1.17 (a) shows the general trend of increasing the activity of differently substituted metallo-porphyrins and -phthalocyanins adsorbed onto carbon black upon heat treatment. It can also be seen in Figure 1.17 (b) that a higher temperature yields a material with higher stability. [96] It was established that the order of activity for the 3d metal centres is: Fe > Co > Ni  $\cong$  Mn. [96] Although the activity could be increased, it was still insufficient to be considered a viable alternative to Pt in fuel cells. An additional major problem was the complex synthesis of these macrocycles, offsetting the price benefit over Pt due to the low cost of the precursors. [112] It is proposed that the macrocycle might retain its nitrogen coordination to the metal centre and therefore the activity stems from the metal center as it does for the non-heat treated material. [113–115] Gupta *et al.* reported the first synthesis of heat treated M-N/C catalysts with a non-macro-cyclic precursor, utilising a simple metal salt of Fe(II) or Co(II) and poly-acrylonitrile on carbon black. [116] This showed that a macrocycle was not necessary in order to form highly active materials upon

heat treatment and opened the way for the development of heat treated M-N/C catalysts prepared with a wide range of different nitrogen and metal precursors. [96, 117] Therefore the synthesis of ORR catalysts at a significantly lower cost as compared to the macrocycles is possible. Further research established that virtually any mixture of nitrogen precursor and metal salt will yield a material with some ORR activity. [96, 117] However, the final activity and stability strongly depends on the choice of precursors and synthesis conditions, *e.g.* temperature, duration, heating rate and gas atmosphere. [117] Generally the synthesis of highly active M-N/C materials is divided into 3 major groups [96, 117]: (1) catalysts from precursors based on transition metal macrocycles; (2) catalysts derived from high surface area carbon in the presence of a metal salt and a gaseous nitrogen precursor, *e.g.*  $\text{NH}_3$ ; (3) catalysts prepared from a metal salt and nitrogen containing molecules, either in the presence of carbon black or a leachable template, such as  $\text{SiO}_2$  nanoparticles. Although an  $\text{N}_4$ -containing precursor is not crucial to obtain highly active catalysts, a nitrogen source is. [96, 117] A wide variety of nitrogen precursors have been used to prepare NPMCs. [96, 117]

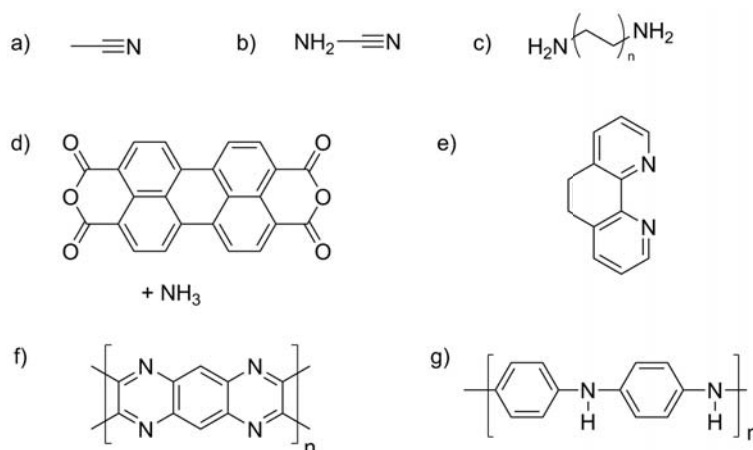


FIGURE 1.18: General structure of different precursors used for the incorporation of nitrogen groups into M-N/C catalysts (**top**) small N-containing molecules (a) acetonitrile (b) cyanamide (c) aliphatic terminal diamines (**middle**) aromatic N-containing compounds d) perylene-tetracarboxylic dianhydride in combination with gaseous  $\text{NH}_3$  e) 1,10-phenanthroline (**bottom**) polymeric precursors f) polynitroaniline g) polyaniline

Figure 1.18 shows some typical examples of nitrogen containing molecules used as nitrogen source to prepare M-N/C catalysts. [96, 117] They can be subdivided into i) small molecules ((a) - (c)) ii) aromatic compounds ((d) and (e)) and iii) polymerised compounds ((f) and (g)). [96, 117] The right combination of precursors and heat treatment regimen can lead to a high surface area material with high conductivity, chemical resistance and high ORR activity. [96, 117] Most publication focus on Fe and Co as the metal source,



as these have shown to yield the most active materials. [96, 117] Although early applications in working PEMFC single cells showed a low activity as compared to Pt [118], successive optimisation resulted in materials with promising potential. [62, 117, 119–121] Notably the work of the Dodelet and the Los Alamos National Laboratory (LANL) groups pioneered the development of these materials. [62, 117–121] Examples of highly active catalysts with promising performance in PEMFCs were prepared by i) the polymerisation of aniline over carbon black, in the presence of a mixture of an Fe and/or Co salt and successive heat treatment at 900 °C under Ar (LANL) [120] ii) the ball milling of carbon black with a mixture of 1,10-phenanthroline and iron-acetate, heat treated under an atmosphere of Ar and/or NH<sub>3</sub> (Dodelet) and lately [62] iii) the pyrolysis of iron-acetate and 1,10-phenanthroline and a microporous metal organic framework as template, *e.g.* ZIF-8 (Dodelet). [119] Usually the catalysts are refluxed in a solution of acid after heat treatment, *e.g.* 0.5M H<sub>2</sub>SO<sub>4</sub>, in order to remove unreacted metal residues. A second heat treatment after this acid leaching step has shown to improve the activity. [117]

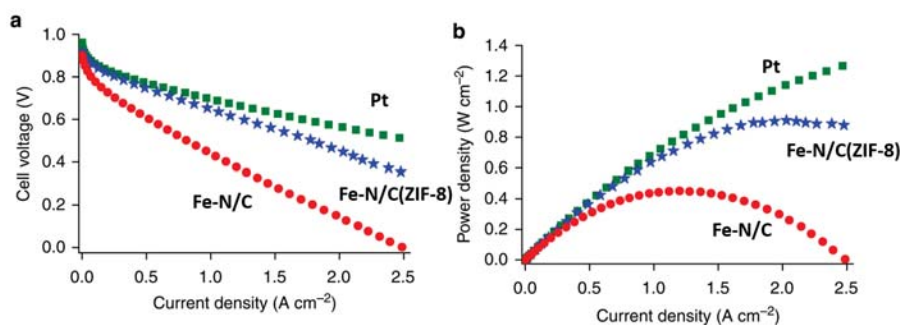


FIGURE 1.19: (a) Polarization curves for MEAs comprising a cathode made with Fe-ZIF8-derived catalyst (blue stars) and Fe-N/C from Lefvre *et al.* [62] (red circles). For comparison, the polarization curve of an MEA made with a state-of-the-art Pt-based cathode with a loading of 0.3 mg<sub>Pt</sub> cm<sup>2</sup> (green squares). (b) Power density curves corresponding to polarization curves shown in a. For the two MEAs made with iron-based cathodes, the catalyst loading was 3.9 mg cm<sup>2</sup>. [Taken and adapted with permission from Ref. [119]]

Figure 1.19 shows the single fuel cell performance, comparing a state of the art Pt/C catalyst to a newly developed Fe-N/C catalyst which was prepared via the decomposition of iron-acetate and 1,10-phenanthroline over ZIF-8 and to an older Fe-N/C variant of the Dodelet group, which was prepared with the same metal and nitrogen source, but with carbon black as a support. [119] The increased activity is attributed to the higher surface area which then leads to a larger amount of active sites accessible. [119] Although the performance looks promising, the loading of the M-N/C catalyst in this study is 10 times higher than typically used for Pt (4 mg cm<sup>-2</sup> *versus* 0.4 mg cm<sup>-2</sup>). The argument

is the negligible price, which in theory allows a much higher loading. [38] However, as discussed in 1.5, considerations of electrode volume need to be taken into account, as mass transport effects will be detrimental at a certain electrode thickness, especially as lower concentrations of oxygen are used, such as the 23% present in air. The use of a significantly higher loading in M-N/C material results in a significantly higher thickness as compared to Pt based materials of 100  $\mu\text{m}$  to 10  $\mu\text{m}$ , respectively. The implementation of this material in single cells and associated challenges will be discussed in Chapter 8. To establish structure-property relationships on this type of material is challenging, as the parameters that influence the activity are multidimensional and varying a parameter such as the precursor ratio might change several properties such as surface area, degree of graphitization, accessible surface active sites etc. [117] Some general trends that emerged from studies vary certain properties while trying to keep other conditions constant are as follows [117]:

- the activity increases with an increase in heat treatment temperature for the same precursor up to 900 - 1000  $^{\circ}\text{C}$  and decreases thereafter. [120]
- the peroxide yield decreases with a higher BET surface area. [120]
- a transition metal ion, even in trace amounts increases the activity significantly. [122, 123]
- increasing the metal content in the precursors increases the activity to a certain level of  $\sim 0.5$  wt%, levelling at higher concentrations and then dropping at very high concentrations  $\sim 10$  wt%. [114, 124]
- a higher proportion of micropores in the same material leads to a higher activity. [125]
- a higher BET surface area in the same material leads to a higher activity. [117]
- acid leaching and subsequent second heat treatment increases the activity and stability. [117]
- there is a trade-off between stability and high activity, as a second heat treatment step in  $\text{NH}_3$  increases the activity. However, this increased activity has a lower stability. [117]

- there seems to be a correlation with the content of certain nitrogen functionalities, such as pyridinic and quarternary, and the catalytic activity. [126]
- the activity increases with the duration, the material is held at the optimal temperature until it levels off after around 40 - 60 min. This is presumably when the activity forming reactions is completed. [127]
- Fe seems to produce the most active catalysts among the 3d metals. [45, 117]

#### 1.7.4 The controversial role of the metal center.

The following discussion is restricted to Fe and Co containing materials, as those are the most active species of this type and the subject of most studies. [45] In order to further improve M-N/C materials, information on the origin of the catalytic activity is crucial. While in model compounds such as non-heat-treated metal macrocycles, it is likely that the active site is the metal centre, the picture is more ambiguous in the heat treated material. [63] Early hypotheses proposed that the active site is also the metal centre which becomes more active and stable due to improved interactions with the carbon support. [107, 113]

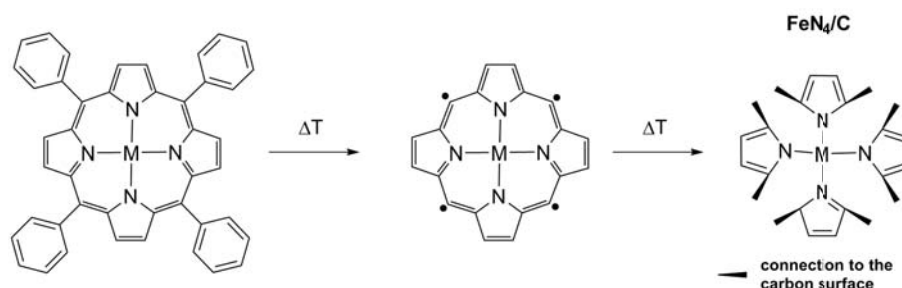


FIGURE 1.20: Proposed reaction steps of a porphyrin with the carbon support upon heat treatment. [Reproduced after Ref. [113]]

It has been suggested that the heat treatment cleaves certain bonds in the macrocycle, which is then incorporated into the carbon framework, while the metal coordination and mode of activity is retained (Figure 1.20). [107, 113] However, when other nitrogen precursors are used, it is not clear as to how the nitrogen atoms directly coordinate to the metal centre and form a similar structure after heat treatment. The pyrolysis of organic material in an inert atmosphere results in the loss of water, dehydrogenation due to bond scission, the formation of radicals and at higher temperature carbonisation. [128–130] When nitrogen atoms are present in the precursor, those will be incorporated into

the carbon lattice. [130] Pels *et al.* performed an in depth analysis of this process and showed that X-ray photoelectron spectroscopy (XPS) can be used to identify different nitrogen functionalities in heat treated carbon samples. [130] The nitrogen 1s peak can be deconvoluted to estimate the relative content of these different species. [130]

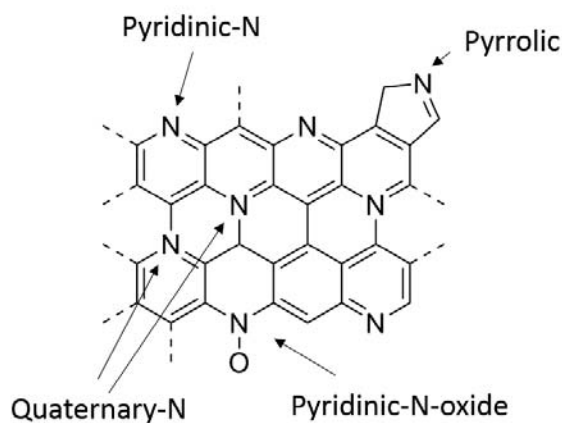


FIGURE 1.21: Different nitrogen functionalities found in heat treated nitrogen doped amorphous carbon. [130]

Figure 1.21 shows the most abundant nitrogen groups present in heat treated nitrogen containing carbon. [130] While the nitrogen of quaternary and pyridinic-N-oxide do not have free lone pairs to coordinate to metal centres, the pyridinic and pyrrolic do. [130] Different models for the active site emerged; 1) the metal centre in materials which have non-macrocyclic N-precursors is the active site  $C-N_x-Me$  and forms a similar structure to the one observed for the macrocycles [118, 122, 123, 125, 127, 131–152] 2) the metal centre is not the active centre, but might catalyse the formation of catalytically active nitrogen moieties  $CN_x$ . Therefore the active site is devoid of a metal. [124, 126, 153–197] 3) Nanoparticles or nanoclusters of a metal, metaloxide, metalcarbide or metalnitride form, which are encapsulated with few layers of carbon and these are active surfaces. [198–208]

**The hypothesis of a metal centre** as active site has been proposed when the first materials were prepared. Yeager *et al.* speculated that the metal will form particles upon heat treatment, which then dissolve when contacted with the acidic electrolyte. The metal ions will then redeposit and are coordinated by nitrogen atoms in the carbon lattice to serve as active sites. [209] However, this model has been refuted, as a material that is only doped with nitrogen and exposed to iron ions in order to emulate this coordination is significantly less active. [127] After a heat treatment however the activity matches the

sample with the metal in the initial precursor. [127] This shows that the active site needs a high temperature step in order to form. Dodelet and coworkers were proponents of a metal centred active site. [125, 127, 134–136, 140, 141] Time-of-flight secondary ion mass spectrometry (ToF-SIMS) on these materials showed that 2 fragments were abundant. The  $\text{FeN}_2\text{C}_4^+$  ion which was assigned to a  $\text{FeN}_2/\text{C}$  site was by far the most abundant fragment detected ( $\sim 80\%$  relative abundance). [141, 210] The studies concluded that the nitrogen atoms in this type of site were of pyridinic character. [141, 210] A second set of ions were assigned to a  $\text{FeN}_4/\text{C}$  site ( $\sim 20\%$  relative abundance), where the nitrogen atoms, according to the study are of pyrrolic character. The catalytic activity seems to be correlated with the amount of those species. [141, 210] From these studies and the observation that a higher microporosity leads to a higher activity, a model has been proposed that suggests at least 2 types of active sites which are simultaneously present. [141, 210]

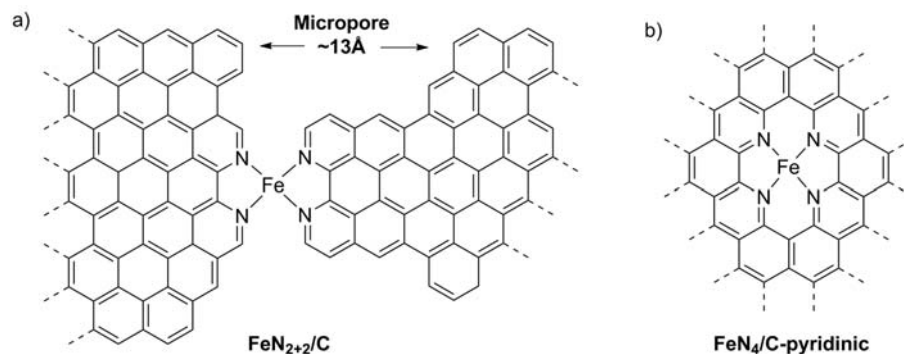


FIGURE 1.22: Proposed structure of an active iron site coordinated with pyridinic nitrogen groups a) hosted in a micropore [211] and b) embedded in the carbon framework [152]

i) an iron centre which is coordinated with 4 pyrrolic nitrogen atoms assigned to the  $\text{FeN}_4/\text{C}$  site, as shown in Figure 1.20 ii) an iron centre which is hosted in the micropore of the amorphous carbon lattice. The proposed site is formed in the slit of a micropore and coordinated by pyridinic nitrogen atoms in phenantrolic like arrangement and labelled  $\text{FeN}_{2+2}/\text{C}$  (Figure 1.22 (a)). [141, 210, 211] Additionally, active sites were proposed which are coordinated by pyridinic nitrogen and completely embedded into the carbon lattice (Figure 1.22). [152]

Utilising Mössbauer spectroscopy, the work of Kramm et. al revealed the possible existence of several electronically different  $\text{FeN}_4$  sites. [131, 139, 140] This has been achieved by deconvolution of the iron signal into the respective multipletts, which are observed for the different spin-states on well defined metal complexes and pure materials such as iron particles. [131, 139, 140] Six signal were detected and assigned to 5 species. [140] Figure 1.23

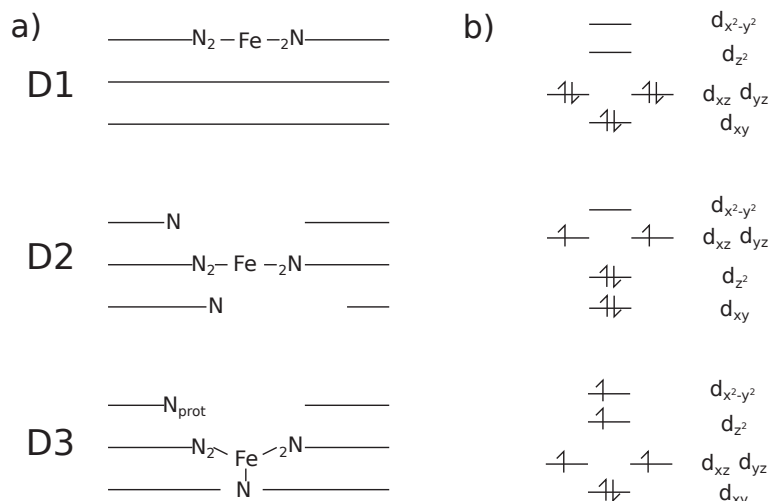


FIGURE 1.23: a) Side view of the different proposed FeN<sub>4</sub> centres as extracted from Mössbauer spectroscopy b) electronic configuration of the respective species. [Reproduced after Ref. [140]]

shows the species assigned to atomic iron signals (a) and the corresponding electronic configuration (b). [140] i) doublet D1 was assigned to a low spin ( $S=0$ ) Fe<sup>II</sup>N<sub>4</sub>/C species and suggested to be the site coordinated by the pyrrolic nitrogen groups (Figure 1.20), ii) doublet D2, to an intermediate spin ( $S=1$ ) FeN<sub>2+2</sub>/C species which is proposed to be one species to be hosted in the micropores, and iii) D3, the high spin state ( $S=2$ ) is also assigned to the FeN<sub>2+2</sub>/C species in the micropore. The difference however is that it is coordinated by a fifth nitrogen species from a graphene sheet below and has another nitrogen group in its vicinity, which can be protonated. (see Figure 1.23). [140] It has been speculated that species D1 and D3 are ORR active, with D3 having a significantly higher turnover frequency (TOF) that depends upon protonation of the proximal nitrogen group. [140] D2 is assumed to be ORR inactive, due to the filled d<sub>z<sup>2</sup></sub> orbital and the resulting inability to interact with the oxygen  $\pi^*$  orbital (see Figure 1.14). [140] It seems that the catalytic activity correlates well with the amount of D1 and D3 centres. The higher the content, the higher the activity. [140] Further evidence for atomic iron centres, coordinated with nitrogen, has been provided with X-ray absorption spectroscopies, such as Extended X-Ray Absorption Fine Structure (EXAFS) and XANES. [212] High resolution microscopy such as high resolution scanning tunnelling electron microscopy (STEM) in combination with electron energy loss spectroscopy (EELS) found iron sites in some materials. [142] Poisoning experiments that have been conducted, mostly in alkaline, are discussed in the relevant section 4.2.1. Some poisons that would interact with iron such as cyanide do indeed decrease the activity of heat treated Fe-N/C catalysts. [147] Further

evidence for the presences of catalytically active metallic sites is the  $\text{H}_2\text{O}_2$  decomposition behaviour. [136] Jaouen *et al.* and later Masa *et al.* showed that 3 d transition metals that significantly enhance the catalytic activity in acid are Cr, Mn, Co and Fe. [122, 123, 136]

**The metal free  $\text{CN}_x$  model** was proposed by Wiesener *et al.* [90, 213] and then further developed by Ozkan, Popov and others. [124, 126, 153–197] The main reasons that cast doubt on the role of the metal are i) non-precious metals are not thermodynamically stable under the acidic and oxidising conditions these materials are subjected to and should dissolve, [214] ii) typical poisons that usually strongly interact with iron centres, such as CO and  $\text{H}_2\text{S}$ , leave these catalysts completely unaffected, [158, 191] iii) completely metal free  $\text{CN}_x$  materials exhibit a significant ORR activity above the carbon baseline in acid and an excellent ORR activity in alkaline. [171, 215] It is without any doubt that even trace amounts of Fe or Co significantly increase the activity of (M)-N/C materials under acidic conditions. [122] Therefore it was argued that these metals catalyse the incorporation of active nitrogen groups into the carbon framework. [90, 178] An intriguing study by Birry *et al.* showed with pyrolysed iron macrocycles on carbon as Fe-N/C catalysts that when saturating the solution with carbon monoxide after running the ORR in  $\text{O}_2$  saturated solution and then resaturating the solution with  $\text{O}_2$  again, the activity is instantly recovered. [158] However, a poisoning effect would be expected if an iron centre similar to heme-like complexes was present. Interestingly the authors line of argument is still in favour of a metal centred active site, as the same experiment repeated with unpyrolysed samples (where the metal centre is most likely the active site) according to the authors also does not result in poisoning. [158] This leads to the conclusion, that although the metal is not poisoned, it would not be affected, as shown with the intact metal complex. [158] However, the data provided in the manuscript clearly show an effect of CO on the unpyrolysed samples (see Figure 2 in Ref. [158]). Before the poisoning step a current of 4 and 5  $\text{mA cm}^{-2}$  for the tested samples is achieved, after the poisoning, the current density is decreased by almost half. Given that the potential at which the current is measured during this poisoning regimen, which lies in the mass transport limiting region, this indicates that the macrocycles are significantly poisoned. [158] A full polarisation curve would yield more information. This study should therefore be evidence against a metal centred active site. [158] Nevertheless, it is well known from enzymes, that the chemical environment strongly affects the affinity of the metal centre to certain substrates. [216]

The pyrolysed sample might simply have a higher affinity to O<sub>2</sub> rather than CO.

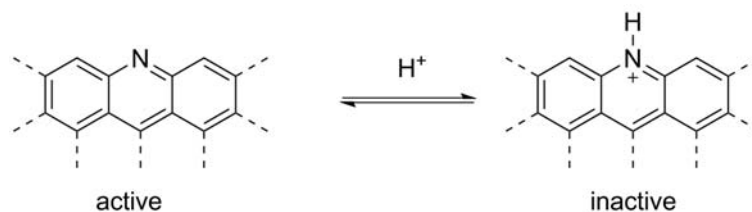


FIGURE 1.24: Proposed mode of deactivation of active nitrogen sites under acidic conditions after Ref. [168]

The lower activity of CN<sub>x</sub> material in acid as compared to alkaline conditions has been ascribed to the protonation of catalytically active nitrogen species, as shown in Figure 1.24. [168] However, comparing ORR activities in alkaline and acid should be taken with care, as the ORR is kinetically more facile under alkaline conditions. [145] It is highly likely that different mechanisms are present under acidic *versus* alkaline conditions. [145] This means, that even if metal free materials can show a significantly higher activity under alkaline conditions, this is not necessarily indicative of the active site present in alkaline. Dodelet compared the activity of metal free C/N material under acidic conditions reported in literature and concluded that the most active materials showed an onset potential<sup>5</sup> of  $\sim 0.75\text{V vs RHE}$ . [63] When it is claimed that a metal free catalyst has been synthesised, it has to be analysed for trace metal contamination, as it has been shown by Masa *et al.* that even low amounts of metal impurities can enhance the catalytic activity. [122, 123] Therefore in order to study the metal free active site under acidic conditions, the choice of precursors and reaction conditions has to be chosen in order to avoid any metal contamination. A recent publication, where utmost care was taken to avoid any contamination with trace metals arrives at an onset potential of  $\sim 0.85\text{ V vs RHE}$ . [217] However, the activity of this catalyst is significantly below metal containing materials and to date, there is no report in literature where a material has been prepared and analysed to ensure no metal contamination, which achieves an appreciable current at  $>0.75\text{ V vs RHE}$  in acidic electrolyte. The authors conclude that although metal centred active sites are more active under high potentials, the metal free sites can contribute significantly to the activity at lower potentials. [217] The active site in acid on nitrogen doped carbon has recently been studied in depth with model surfaces prepared by N<sup>+</sup> ion beam etching of

<sup>5</sup>The definition of onset potential has been taken from Ref. [63]. It is the extrapolation to zero current at the first inflection point during a cathodic scan.



highly oriented pyrolytic graphite (HOPG). [163] A combination of x-ray photoelectron spectroscopy (XPS), atomic force microscopy (AFM) and electrochemical characterisation led to the conclusion that carbon atoms next to the pyridinic N were the active sites, where O<sub>2</sub> would adsorb. [163] This is in line with computational studies, which suggest a similar active site. [218, 219] A change in charge and spin distribution of the electronic structure upon N doping has been suggested as source of the catalytic activity. [218] At the time of preparing this work it may be concluded that with the presently available synthesis techniques, a metal is required in order to achieve a significant activity at high potentials. Typical onset potentials for Fe-N/C materials range in the order of 0.9 to 1.0 V *vs* RHE. [45, 63] Nevertheless, it is striking that even in acid, heteroatom doping increases the activity and 4 electron selectivity of the material. [63] For fuel cell applications, a highly active and metal free material would be more desirable than a transition metal containing one, as metal ions such as Fe induce the decomposition of trace amounts of peroxide to form highly aggressive hydroxyl radicals, which are detrimental for the durability of the system. [220]

**Metal containing nanoparticulate phases** have also been found in heat treated materials. Under certain conditions a significant amount of nanoparticulate phases can form. [198–208] It has been proposed that these phases, which are encapsulated with carbon and therefore stable under oxidising and acidic conditions, serve as active surfaces. [198–208] If present in the material, these phases can typically be easily identified through high resolution transmission electron microscopy (TEM) or powder x-ray diffraction (XRD). [198–208]

Figure 1.25 (a) shows a synthetic route to a material which contains a significant amount of particulate phases. The particulate phases are visible as dark spots in the TEM images in Figure 1.25 (c) - (e). [221] The lattice spacing can be used to determine the identity of the respective phase (Figure 1.25). [221] Recently a study by Strickland *et al.* claimed to have produced a material which exclusively contains iron sites that are **not** coordinated with nitrogen and have a high activity. [205] The study claims to have removed the nitrogen coordination by tweaking the synthesis conditions. This interesting result is concluded from Mössbauer, EXAFS and XANES measurements. [205] The source of the activity is ascribed to iron clusters, encapsulated or coordinated with nitrogen doped carbon. [205] It is suggested that the encapsulated iron particle exhibits synergistic effects on the nitrogen doped carbon and hence enhanced the catalytic activity. This is therefore

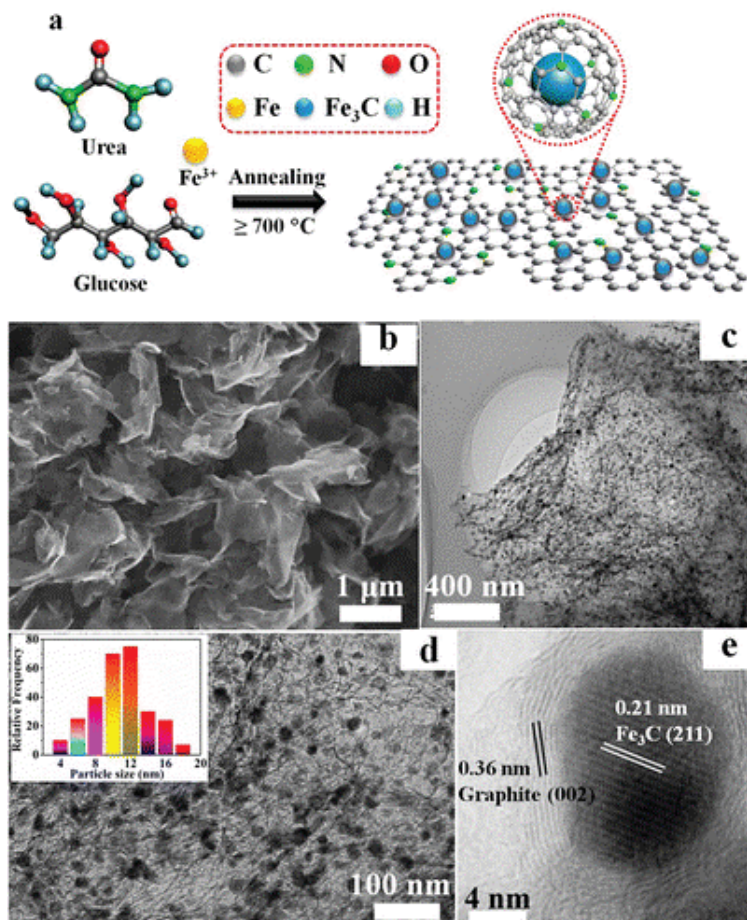


FIGURE 1.25: a) synthetic route to a Fe-N/C catalyst rich in  $\text{Fe}_3\text{C}$  nano-particulate phases, which are encapsulated with carbon. b) SEM micrograph of the material. c) - e) TEM images, showing the  $\text{Fe}_3\text{C}$  particles as dark spots. e) identification of  $\text{Fe}_3\text{C}$  and graphite through lattice spacing analysis [Reprinted with permission from Ref. [221]. Copyright 2015 American Chemical Society.].

in support of a metal free active site, where the metal influences the activity through remote interactions. [205] The selective removal of  $\text{Fe-N}_4$  by  $\text{Cl}_2$  has been reported by Varnell *et al.* [222] The study concludes that heat treatment under  $\text{Cl}_2$  and then under  $\text{H}_2$  results in a material exclusively with iron particulate phases, which are encapsulated with carbon. [222] Chlorine treatment first decreases the activity significantly and the hydrogen treatment step recovers the activity to the initial state. The authors claim the complete removal of  $\text{Fe-N}_4$  species and the selective formation of encapsulated nanoparticles after the treatment regimen. [222] They suggest that the donation of electron density into the surrounding carbon surface by the metal is the source of the increased activity. [222] However, the effect of nitrogen on this type of activity remains unexplained, as a material without nitrogen but with similar iron species, but present as significantly larger particles, is significantly less active. [222] It is interesting to note that in contrast to this study,

Kramm *et al.* claimed to have produced a material which contains exclusively Fe–N<sub>4</sub> sites. [223] The material shows an increased activity as compared to a similar material which contains both phases. [223] The conclusions in both publications are mainly based on Mössbauer spectroscopy results. [222, 223]

It is likely that the activity in a heat treated material contains various different types of the above described active sites. It is desirable to identify the most active, stable and selective site and aim the synthesis at preferably forming these with a high density or even derive a bottom up synthesis. Synergistic effects of the different moieties have been suggested which would complicate the isolation of specific active sites. [224]

### 1.7.5 Mechanistic proposals on and stability of Fe sites

**Mechanistic investigations** focused mainly on Fe–N/C materials as those seem to be the most active among the 3d transition metal variants. [45] A notable result was the observation of Herranz *et al.*, that the activity of an Fe–N/C material is decreased when cycling in an electrolyte which contains coordinating anions (*i.e.* SO<sub>4</sub><sup>2-</sup>). [225] The activity can be regenerated when the catalyst is heated at mild temperatures ( $\sim 300^\circ\text{C}$ ) and reversibly decreases when cycled in the presence of the anions again. [225] The activity could also be regenerated by treatment with OH<sup>-</sup>. [225] The authors attribute the effect to the binding of anions (*e.g.* SO<sub>4</sub><sup>2-</sup>) to a protonated nitrogen group in the vicinity of the active site, thus decreasing the turnover frequency of the respective site. [225] This implies that a proton transfer is either directly or indirectly involved in the rate determining step. Some in-situ XANES studies have been performed. [212, 226, 227] Based on these results, it was suggested that the activity is linked to the Fe<sup>2+</sup>/Fe<sup>3+</sup> redox transition. [144, 212, 226, 227] It was furthermore claimed that upon potential cycling an out-of plane switching behaviour can be observed, where the out-of plane species can bind oxygen and will become ORR active. [226, 227] Ramaswamy *et al.* investigated the influence of the carbon support on the activity of the hypothesised Fe–N<sub>4</sub> sites. [144] It was found that a higher basicity of the support leads to increased activity. [144] The results were correlated with a redox peak in the material, which was attributed to the Fe<sup>2+</sup>/Fe<sup>3+</sup> transition. [144] The same peak has been attributed to this transition earlier by Chlistunoff. [228] Mechanistic suggestions based on similar studies proposed the existence of different sites, where *site A* catalyses the reduction of O<sub>2</sub> to H<sub>2</sub>O<sub>2</sub> and a second *site B* the reduction of H<sub>2</sub>O<sub>2</sub> to H<sub>2</sub>O. [212, 229]

A 2+2 mechanism is supported by the observation that a thinner catalyst layer of these materials usually increases the amount of peroxide detected with the rotating ring disk electrode method (RRDE) (see 2.1.1). [229] The conclusion is that the 2+2 pathway is the predominant pathway on Fe-N/C sites in acid, with the possibility of the involvement of 2 distinctly different sites. [212, 229] On the other hand it was concluded that in alkaline the direct 4 electron pathway is occurring. [145] However, studies in alkaline are challenging, due to the increased kinetic facility of the ORR under these conditions. [145] Different surfaces and even carbon exhibit a significant catalytic activity, making the isolation of different contributions to the mechanism difficult. [145] Some studies attribute the higher activity of the ORR in alkaline to the thermodynamically higher stability of the superoxide ( $\text{O}_2^-$ ) intermediate, claiming the possibility of an outer sphere first electron transfer as part of the mechanism. [145]

**The operational stability** of Fe-N/C materials is a major concern for the application in PEMFCs. [45] Some materials show an impressive initial activity which decays rapidly upon continuous operation. [45] Additionally to degradation, this has been attributed to flooding of the porous structure, thus hampering mass transport. [45] Seemingly there are active sites which are more prone to degradation than others. A second heat treatment in ammonia for instance has been shown to improve the activity of the catalyst. This improvement however seems to be less stable than the activity which was achieved before. [63] In situ investigations of the stability have recently been conducted by Choi *et al.*, utilising a combination of differential electrochemical mass spectrometry (DEMS) for detection of CO and CO<sub>2</sub> decomposition products and inductively coupled plasma optical emission spectrometry (ICP-OEP) for metal detection. [230] The conclusion is that the catalyst can operate stable in the potential range between 0.6 and 0.9 V *vs* RHE. Above this potential carbon corrosion will occur, eventually degrading the activity. Below this potential iron demetallation as  $\text{Fe}^{2+}$  will occur, which is detrimental in various ways i) it will react with peroxide to form highly aggressive hydroxyl species (Fenton reaction) ii) it will bind to the anionic sulphonic acid groups in the Nafion<sup>®</sup> membrane, thus blocking efficient proton transport iii) it will be lost from the active sites of the catalyst thus decreasing the overall activity. [230] In a follow-up study Choi *et al.* found that some demetallation can be prevented by reductively removing inactive iron species. [227]

The majority of literature released between 2013 - 2016 supports the hypothesis of a metal centred active site or takes this hypothesis as the premise for the interpretation of the

observations.[212, 226, 227, 229–234]

### 1.7.6 State of the art activities

The highest performing M-N/C materials developed to date can achieve activities, which are close to Pt based cells, where the Pt loading is significantly lower ( $\sim 10$  times) and only under certain conditions, *i.e.* high partial pressure of (pure) oxygen, balanced water vapour and with lower stability. [119, 121] Typical cathode loadings for M-N/C catalysts are between 2 and 4 mg cm<sup>-2</sup>. [119, 121]

TABLE 1.1: Metrics of a selection of high performing M-N/C catalysts from literature.

$P_{\max}$ [W cm <sup>-2</sup> ]	Reactants	Bp.* [kPa <sub>gauge</sub> ]	$j(@0.8V)^\dagger$ [mA cm <sup>-2</sup> ]	Type <sup>‡</sup>	Ref.
0.64	H <sub>2</sub> /O <sub>2</sub>	100	$\sim 100$	Fe-MOF	[235]
0.56	H <sub>2</sub> /O <sub>2</sub>	170	120	Fe-Si	[236]
0.62	H <sub>2</sub> /O <sub>2</sub>	150	$\sim 100$	Fe-MOF	[237]
0.60	H <sub>2</sub> /O <sub>2</sub>	100	221	Fe-MOF	[238]
0.53	H <sub>2</sub> /O <sub>2</sub>	200	n/a	FeCo-C	[179]
0.55	H <sub>2</sub> /O <sub>2</sub>	180	$\sim 100$	FeCo-N/C	[120]
0.91	H <sub>2</sub> /O <sub>2</sub>	50	n/a	Fe-MOF	[119]
0.60	H <sub>2</sub> /O <sub>2</sub>	n/a	n/a	Fe-N/C	[239]
0.90	H <sub>2</sub> /O <sub>2</sub>	100	$\sim 220$	Fe-MOF	[121]
0.94	H <sub>2</sub> /O <sub>2</sub>	100	n/a	Fe-N/C	[240]
1.03	H <sub>2</sub> /O <sub>2</sub>	200	n/a	Fe-N/C	[240]
0.25	H <sub>2</sub> /Air	n/a	n/a	Fe-N/C	[241]
0.30	H <sub>2</sub> /Air	0	n/a	Fe-MOF	[242]
0.32	H <sub>2</sub> /Air	0	n/a	Fe-N/C	[239]
0.41	H <sub>2</sub> /Air	n/a	n/a	Fe-N/C	[243]

\* Bp. = backpressure

<sup>†</sup> Some publications report iR-free values and some uncorrected. Where  $j$  is approximated ( $\sim$ ), it has been visually extracted from the *Tafel*-plots. n/a (not available) means that no value was given and no *Tafel*-plot was provided to extract it.

<sup>‡</sup> The type is classified as follows: M-Support, where M is the metal used in the synthesis and support can either be a metal organic framework (MOF), carbon black (N/C) or a silica template (Si)

Table 1.1 shows a selection of some high performing M-N/C catalysts when tested in PEMFCs. Due to the large amount of publications only peak power densities above 0.5 W cm<sup>-2</sup> for H<sub>2</sub>/O<sub>2</sub> operation and 0.25 W cm<sup>-2</sup> for H<sub>2</sub>/Air operation were considered. Comparison of single cell results are difficult, as various factors other than the kinetic activity influence the performance. These can be ionomer content in the catalyst layer, deposition technique of the catalyst layer, operating conditions, internal cell resistances and mass transport losses. From the values presented in Table 1.1, it can be seen that

some materials which are based on MOFs show a significantly higher peak power. Especially the reports by Priozetti *et al.* [119], Shui *et al.* [121] and Wang *et al.* [240] show activities which come close to  $1 \text{ W cm}^{-2}$  under the utilised conditions. The first 2 studies report volumetric power densities of  $230 \text{ A cm}^{-3}$  [119],  $450 \text{ A cm}^{-3}$  [121], respectively. This impressive performance comes close and even surpasses the DoE target of  $300 \text{ A cm}^{-3}$ . However, the values are not truly measured under the recommended condition, but i) converted from measurements at high oxygen partial pressure and ii) extrapolated from the iR corrected linear region in the *Tafel* plots, assuming that the *Tafel* slope stays constant. These assumptions do not necessarily hold true and an activity which was actually measured under the correct conditions and reaches the target has not been reported yet. An additional problem is that this high activity quickly degrades to moderate values after few cycles.

### 1.7.7 Major gaps in the understanding of NPMCs

Although tremendous effort has been dedicated, the true nature of the active site(s) remains elusive. This is for instance, if the metal was the active site, the active site density in the carbon matrix is relatively low. Therefore the application of spectroscopic techniques to gain information on the active site is limited. Furthermore are most experiments with techniques such as Mössbauer, EXAFS or XANES are performed ex-situ and hence no true correlation to the activity is possible. The high complexity of the material make the identification of trends challenging.

Mechanistic insight into this material is limited. Many studies are concerned with the structure of the active site, but few studies offer mechanistic insight. [244, 245] Computational studies exist. [244, 245] However, modelling electrochemical reactions solely by ab initio methods is challenging, as the complex double layer structure can only be approximated to date, and the role of water is typically ignored. [244–246] Although progress has been made recently and with the development of more powerful computers, it is expected that calculations will get more accurate, experimental verification is still necessary. [246, 247]

A further difficulty in developing a rational structure-property relationship is the lack of a method to determine the intrinsic activity of this type of material. For Pt based catalyst, this can be achieved by normalising to the electrochemically active surface area

(ECSA), which is determined either via the hydrogen adsorption/desorption features or CO stripping. The featureless cyclic voltammetry, large capacitive background and the lack of an active site probe make this impossible for NPMCs (but see Chapter 6). This makes it difficult to assess what effect a change in synthesis conditions has on the active site density and/or turnover frequency. Therefore it is also challenging to compare materials developed in different laboratories.

It is proposed that due to the low price a higher loading at the cathode can be used to overcome this. With the typically reported loading for M-N/C catalysts, the cathode catalyst layer is up to 100  $\mu\text{m}$  thick, *versus* the currently used 10  $\mu\text{m}$  thick layer for Pt/C catalysts. This introduces mass transport and water management issues. The influence of certain parameters of the catalyst layers on the performance is not well understood and it is not clear whether losses are due to the poor kinetics or other parameters related to ion conductivity, water management and/or mass transport of reactants.

The stability of this materials is insufficient at the moment and no clear strategy on how to increase the stability has been reported, additionally to the one mentioned above.

Finally if the different types of active sites were unambiguously identified, the question would be how to synthesise them with the necessary degree of stability and density, in order to meet the performance targets.

## 1.8 Proposal and structure of the thesis

This work aims to provide new insight into the behaviour of the active site, and factors that govern the activity of M-N/C materials, both for fundamental studies in a 3-electrode aqueous electrochemical cell under defined mass transport and in an operating single cell.

In order to achieve this a number of sub-goals are required:

**Synthesis of a model system:** In order to draw far reaching conclusions, it is necessary to find a material which resembles the key features of a wide range of M-N/C materials reported in literature, such as highly dispersed metal in a conductive nitrogen doped carbon framework. A simpler synthesis where complexity is removed might enable the establishment of trends. This can be achieved by removing the carbon support from the synthesis, selecting a suitable precursor. Utilising various characterisation techniques,

such as XPS, nitrogen adsorption analysis, TEM, STEM, EDX, XRF and EPR will verify that the material produced is representative of other Fe-N/C materials reported and new insight is expected.

Once such a material is found it can be assessed, in a controlled manner, under a variation of external conditions, to generate fundamental insight into the active site:

One key question to answer is on the role of the metal centre; if the metal centre is the active site, does this site, in terms of affinity, reactivity and reaction mechanism, behave similarly to known model complexes, such as metal porphyrins?

To answer this question, experiments will be conducted, where the catalyst is subjected to various chemical environments. Molecules that usually act as poisons on transition metals, *e.g.*  $\text{Cl}^-$  and  $\text{NO}_x$ , will be used to probe eventual interactions with the active site. The affinity of oxygen to the catalyst will be investigated via temperature programmed desorption (TPD). Variation of pH and the hydrogen/deuterium effect will be investigated in order to gain further mechanistic insight.

Once a suitable probe is found, can the reactivity with this probe provide further insight?

This can be achieved by conducting a series of experiments in the rotating disk electrode (RDE) setup, where the catalyst and probe, *i.e.* nitrite and nitric oxide, is subjected to treatment regimes, *e.g.* acid and alkaline, and the outcome in terms of performance is assessed. This might allow to draw analogies to known model systems.

How can the intrinsic activity be determined?

A stripping technique will be developed, analogous to CO stripping on Pt, in order to determine the activity and density of active sites. This will allow the cross comparison of catalysts developed in different labs.

What other evidence can be found to verify the existence of chemically active atomic iron sites?

In order to find evidence for a metal centred active site, the catalyst will be used to catalyse the epoxidation reaction, which is also catalysed by metal macrocyclic complexes. Reaction conditions will be varied and implications for the active site will be sought.

How are ion conductivity, mass transport and activity translated to MEA level?



Impedance spectroscopy will be used to uncover information about the catalyst behaviour within a single cell. Insights are expected which highlight the challenges of thick catalyst layers.

The thesis is structured such that the following chapter will provide a short overview on the background of the experimental techniques used during the study, with sufficient depth so that the educated reader can follow the work without referring to additional literature. Following that, the results of the above proposed parts will be presented and discussed. It is the aim that each chapter constitutes a concluded body of work. Where experimental techniques were used specific to a chapter they will be explained therein. Finally the results will be concluded as a whole in a separate chapter and suggestions for future investigations will be given.

## 1.9 References

- [1] Rosenzweig C., Karoly D., Vicarelli M., Neofotis P., Wu Q., et al. Attributing physical and biological impacts to anthropogenic climate change. *Nature*, 453(7193), 353–357, May 2008. doi:10.1038/nature06937.
- [2] Johansson T.B. *Renewable Energy: Sources for Fuels and Electricity*. Island Press, 1993. ISBN 978-1-55963-138-9.
- [3] He K., Yang F., Ma Y., Zhang Q., Yao X., et al. The characteristics of PM<sub>2.5</sub> in Beijing, China. *Atmospheric Environment*, 35(29), 4959–4970, October 2001. doi:10.1016/S1352-2310(01)00301-6.
- [4] Harrison R.M., Deacon A.R., Jones M.R., Appleby R.S. Sources and processes affecting concentrations of PM<sub>10</sub> and PM<sub>2.5</sub> particulate matter in Birmingham (U.K.). *Atmospheric Environment*, 31(24), 4103–4117, December 1997. doi:10.1016/S1352-2310(97)00296-3.
- [5] Raaschou-Nielsen O., Andersen Z.J., Beelen R., Samoli E., Stafoggia M., et al. Air pollution and lung cancer incidence in 17 European cohorts: prospective analyses from the European Study of Cohorts for Air Pollution Effects (ESCAPE). *The Lancet Oncology*, 14(9), 813–822, August 2013. doi:10.1016/S1470-2045(13)70279-1.

- [6] BBC News. Beijing air pollution soars to hazard level. <http://www.bbc.co.uk/news/world-asia-china-20998147>. Accessed: 2016-06-02.
- [7] Vielstich W., Lamm A., Gasteiger H.A., editors. *Handbook of Fuel Cells: Vol. 2: Fundamentals, Technology, Applications*. Wiley-Blackwell, Chichester, England ; Hoboken, N.J, March 2003. ISBN 978-0-471-49926-8.
- [8] Zhang J. *PEM Fuel Cell Electrocatalysts and Catalyst Layers: Fundamentals and Applications*. Springer Science & Business Media, August 2008. ISBN 978-1-84800-936-3.
- [9] Winter M., Brodd R.J. What Are Batteries, Fuel Cells, and Supercapacitors? *Chemical Reviews*, 104(10), 4245–4270, October 2004. doi:10.1021/cr020730k.
- [10] Gröger O., Gasteiger H.A., Suchsland J.P. Review—Electromobility: Batteries or Fuel Cells? *Journal of The Electrochemical Society*, 162(14), A2605–A2622, January 2015. doi:10.1149/2.0211514jes.
- [11] Demirbas A. Biomethanol Production from Organic Waste Materials. *Energy Sources, Part A: Recovery, Utilization, and Environmental Effects*, 30(6), 565–572, January 2008. doi:10.1080/15567030600817167.
- [12] Christopher K., Dimitrios R. A review on exergy comparison of hydrogen production methods from renewable energy sources. *Energy & Environmental Science*, 5(5), 6640–6651, April 2012. doi:10.1039/C2EE01098D.
- [13] Shao M., editor. *Electrocatalysis in Fuel Cells*, volume 9 of *Lecture Notes in Energy*. Springer London, London, 2013. ISBN 978-1-4471-4910-1 978-1-4471-4911-8.
- [14] Carmo M., Fritz D.L., Mergel J., Stolten D. A comprehensive review on PEM water electrolysis. *International Journal of Hydrogen Energy*, 38(12), 4901–4934, April 2013. doi:10.1016/j.ijhydene.2013.01.151.
- [15] Vielstich W., Gasteiger H.A., Yokogawa H., editors. *Handbook of Fuel Cells: v. 5 & 6: Advances in Electrocatalysis, Materials, Diagnostics and Durability*. Wiley-Blackwell, May 2009.
- [16] Markovic N.M. Electrocatalysis: Interfacing electrochemistry. *Nature Materials*, 12(2), 101–102, February 2013. doi:10.1038/nmat3554.

- [17] Hyundai UK. Hydrogen Fuel Cell Powered Cars. <http://www.hyundai.co.uk/about-us/environment/hydrogen-fuel-cell>. Accessed: 2016-06-02.
- [18] Toyota. Toyota Mirai – The Turning Point. <https://ssl.toyota.com/mirai/fcv.html>. Accessed: 2016-06-02.
- [19] Panasonic Corporation. Specifications of a Residential fuel cell unit for a detached house. [http://panasonic.co.jp/ap/FC/en\\_about\\_01.html](http://panasonic.co.jp/ap/FC/en_about_01.html). Accessed: 2016-06-02.
- [20] Varcoe J.R., Atanassov P., Dekel D.R., Herring A.M., Hickner M.A., et al. Anion-exchange membranes in electrochemical energy systems. *Energy & Environmental Science*, 7(10), 3135–3191, September 2014. doi:10.1039/C4EE01303D.
- [21] Durst J., Siebel A., Simon C., Hasché F., Herranz J., et al. New insights into the electrochemical hydrogen oxidation and evolution reaction mechanism. *Energy & Environmental Science*, 7(7), 2255–2260, June 2014. doi:10.1039/C4EE00440J.
- [22] Mauritz K.A., Moore R.B. State of Understanding of Nafion. *Chemical Reviews*, 104(10), 4535–4586, October 2004. doi:10.1021/cr0207123.
- [23] SGL Group. Fuel cell components | SGL CARBON. [http://www.sglgroup.com/cms/international/products/product-groups/su/fuel-cell-components/index.html?\\_\\_locale=en](http://www.sglgroup.com/cms/international/products/product-groups/su/fuel-cell-components/index.html?__locale=en). Accessed: 2016-06-03.
- [24] Debe M.K. Electrocatalyst approaches and challenges for automotive fuel cells. *Nature*, 486(7401), 43–51, June 2012. doi:10.1038/nature11115.
- [25] Yoshida T., Kojima K. Toyota MIRAI Fuel Cell Vehicle and Progress Toward a Future Hydrogen Society. *The Electrochemical Society Interface*, 24(2), 45–49, January 2015. doi:10.1149/2.F03152if.
- [26] Mehta V., Cooper J.S. Review and analysis of PEM fuel cell design and manufacturing. *Journal of Power Sources*, 114(1), 32–53, February 2003. doi:10.1016/S0378-7753(02)00542-6.
- [27] Wiberg N., Holleman A.F., Wiberg E., editors. *Inorganic Chemistry*. Academic Press, San Diego:Berlin:New York, 1st edition, November 2001. ISBN 978-0-12-352651-9.

- [28] Wroblowa H.S., Yen-Chi-Pan, Razumney G. Electroreduction of oxygen. *Journal of Electroanalytical Chemistry and Interfacial Electrochemistry*, 69(2), 195–201, April 1976. doi:10.1016/S0022-0728(76)80250-1.
- [29] Bard A.J., Parsons R., Jordan J. *Standard Potentials in Aqueous Solution*. CRC Press, August 1985. ISBN 978-0-8247-7291-8.
- [30] Zhang C., Fan F.R.F., Bard A.J. Electrochemistry of Oxygen in Concentrated NaOH Solutions: Solubility, Diffusion Coefficients, and Superoxide Formation. *Journal of the American Chemical Society*, 131(1), 177–181, January 2009. doi:10.1021/ja8064254.
- [31] Shao M.h., Liu P., Adzic R.R. Superoxide Anion is the Intermediate in the Oxygen Reduction Reaction on Platinum Electrodes. *Journal of the American Chemical Society*, 128(23), 7408–7409, June 2006. doi:10.1021/ja061246s.
- [32] Blizanac B.B., Ross P.N., Markovic N.M. Oxygen electroreduction on Ag(111): The pH effect. *Electrochimica Acta*, 52(6), 2264–2271, January 2007. doi:10.1016/j.electacta.2006.06.047.
- [33] Kim H., Lee K., Woo S.I., Jung Y. On the mechanism of enhanced oxygen reduction reaction in nitrogen-doped graphene nanoribbons. *Physical Chemistry Chemical Physics*, 13(39), 17,505–17,510, September 2011. doi:10.1039/C1CP21665A.
- [34] Lai L., Potts J.R., Zhan D., Wang L., Poh C.K., et al. Exploration of the active center structure of nitrogen-doped graphene-based catalysts for oxygen reduction reaction. *Energy & Environmental Science*, 5(7), 7936–7942, June 2012. doi:10.1039/C2EE21802J.
- [35] Koper M.T.M. Theory of multiple proton–electron transfer reactions and its implications for electrocatalysis. *Chemical Science*, 4(7), 2710–2723, June 2013. doi:10.1039/C3SC50205H.
- [36] Nørskov J.K., Rossmeisl J., Logadottir A., Lindqvist L., Kitchin J.R., et al. Origin of the Overpotential for Oxygen Reduction at a Fuel-Cell Cathode. *The Journal of Physical Chemistry B*, 108(46), 17,886–17,892, November 2004. doi:10.1021/jp047349j.

- [37] Bard A.J., Faulkner L. *Electrochemical Methods: Fundamentals and Applications*. John Wiley & Sons, New York, 2nd edition, January 2001. ISBN 978-0-471-04372-0.
- [38] Gasteiger H.A., Kocha S.S., Sompalli B., Wagner F.T. Activity benchmarks and requirements for Pt, Pt-alloy, and non-Pt oxygen reduction catalysts for PEMFCs. *Applied Catalysis B: Environmental*, 56(1–2), 9–35, March 2005. doi:10.1016/j.apcatb.2004.06.021.
- [39] Markiewicz M., Zalitis C., Kucernak A. Performance measurements and modelling of the ORR on fuel cell electrocatalysts – the modified double trap model. *Electrochimica Acta*, 179, 126–136, October 2015. doi:10.1016/j.electacta.2015.04.066.
- [40] Stephens I.E.L., Bondarenko A.S., Grønbjerg U., Rossmeisl J., Chorkendorff I. Understanding the electrocatalysis of oxygen reduction on platinum and its alloys. *Energy & Environmental Science*, 5(5), 6744–6762, April 2012. doi:10.1039/C2EE03590A.
- [41] Koper M., Wieckowski A., editors. *Fuel Cell Catalysis: A Surface Science Approach*. Wiley-Blackwell, Hoboken, N.J., 1st edition, April 2009. ISBN 978-0-470-13116-9.
- [42] Marcus R.A. On the Theory of Oxidation-Reduction Reactions Involving Electron Transfer. I. *The Journal of Chemical Physics*, 24(5), 966–978, May 1956. doi:10.1063/1.1742723.
- [43] Marcus R.A. Electrostatic Free Energy and Other Properties of States Having Nonequilibrium Polarization. I. *The Journal of Chemical Physics*, 24(5), 979–989, May 1956. doi:10.1063/1.1742724.
- [44] Escudero-Escribano M., Malacrida P., Hansen M.H., Vej-Hansen U.G., Velázquez-Palenzuela A., et al. Tuning the activity of Pt alloy electrocatalysts by means of the lanthanide contraction. *Science*, 352(6281), 73–76, April 2016. doi:10.1126/science.aad8892.
- [45] Shao M., Chang Q., Dodelet J.P., Chenitz R. Recent Advances in Electrocatalysts for Oxygen Reduction Reaction. *Chemical Reviews*, 116(6), 3594–3657, March 2016. doi:10.1021/acs.chemrev.5b00462.

- [46] US Department of Energy. US DRIVE Fuel Cell Technical Team Roadmap. <http://energy.gov/eere/vehicles/downloads/us-drive-fuel-cell-technical-team-roadmap>. Accessed: 2016-06-03.
- [47] Stolten D., Samsun R.C., Garland N. *Fuel Cells: Data, Facts, and Figures*. John Wiley & Sons, January 2016. ISBN 978-3-527-69391-7.
- [48] Gómez-Marín A.M., Rizo R., Feliu J.M. Some reflections on the understanding of the oxygen reduction reaction at Pt(111). *Beilstein Journal of Nanotechnology*, 4, 956–967, December 2013. doi:10.3762/bjnano.4.108.
- [49] Adzic R.R. Platinum Monolayer Electrocatalysts: Tunable Activity, Stability, and Self-Healing Properties. *Electrocatalysis*, 3(3-4), 163–169, September 2012. doi:10.1007/s12678-012-0112-3.
- [50] Kakati B.K., Kucernak A.R.J. Gas phase recovery of hydrogen sulfide contaminated polymer electrolyte membrane fuel cells. *Journal of Power Sources*, 252, 317–326, April 2014. doi:10.1016/j.jpowsour.2013.11.077.
- [51] Chen C., Kang Y., Huo Z., Zhu Z., Huang W., et al. Highly Crystalline Multimetallic Nanoframes with Three-Dimensional Electrocatalytic Surfaces. *Science*, 343(6177), 1339–1343, March 2014. doi:10.1126/science.1249061.
- [52] Malacrida P., Casalongue H.G.S., Masini F., Kaya S., Hernández-Fernández P., et al. Direct observation of the dealloying process of a platinum–yttrium nanoparticle fuel cell cathode and its oxygenated species during the oxygen reduction reaction. *Physical Chemistry Chemical Physics*, 17(42), 28,121–28,128, October 2015. doi:10.1039/C5CP00283D.
- [53] Zhang J., Lima F.H.B., Shao M.H., Sasaki K., Wang J.X., et al. Platinum Monolayer on Nonnoble Metal-Noble Metal Core-Shell Nanoparticle Electrocatalysts for O<sub>2</sub> Reduction. *The Journal of Physical Chemistry B*, 109(48), 22,701–22,704, December 2005. doi:10.1021/jp055634c.
- [54] Mani P., Srivastava R., Strasser P. Dealloyed Pt-Cu Core-Shell Nanoparticle Electrocatalysts for Use in PEM Fuel Cell Cathodes. *The Journal of Physical Chemistry C*, 112(7), 2770–2778, February 2008. doi:10.1021/jp0776412.

- [55] Chisaka M., Ishihara A., Uehara N., Matsumoto M., Imai H., et al. Nano-TaOxNy particles synthesized from oxy-tantalum phthalocyanine: how to prepare precursors to enhance the oxygen reduction reaction activity after ammonia pyrolysis? *Journal of Materials Chemistry A*, 3(32), 16,414–16,418, August 2015. doi:10.1039/C5TA03860J.
- [56] Ishihara A., Chisaka M., Ohgi Y., Matsuzawa K., Mitsushima S., et al. Synthesis of nano-TaOx oxygen reduction reaction catalysts on multi-walled carbon nanotubes connected via a decomposition of oxy-tantalum phthalocyanine. *Physical Chemistry Chemical Physics*, 17(12), 7643–7647, March 2015. doi:10.1039/C5CP00317B.
- [57] Seo J., Cha D., Takanabe K., Kubota J., Domen K. Particle size dependence on oxygen reduction reaction activity of electrodeposited TaOx catalysts in acidic media. *Physical Chemistry Chemical Physics*, 16(3), 895–898, December 2013. doi:10.1039/C3CP54036G.
- [58] Seo J., Zhao L., Cha D., Takanabe K., Katayama M., et al. Highly Dispersed TaOx Nanoparticles Prepared by Electrodeposition as Oxygen Reduction Electrocatalysts for Polymer Electrolyte Fuel Cells. *The Journal of Physical Chemistry C*, 117(22), 11,635–11,646, June 2013. doi:10.1021/jp4013703.
- [59] Vante N.A., Tributsch H. Energy conversion catalysis using semiconducting transition metal cluster compounds. *Nature*, 323(6087), 431–432, October 1986. doi:10.1038/323431a0.
- [60] Zagal J.H., Bedioui F., Dodelet J.P. *N<sub>4</sub>-Macrocyclic Metal Complexes*. Springer Science & Business Media, July 2007. ISBN 978-0-387-28430-9.
- [61] Jasinski R. A New Fuel Cell Cathode Catalyst. *Nature*, 201(4925), 1212–1213, March 1964. doi:10.1038/2011212a0.
- [62] Lefèvre M., Proietti E., Jaouen F., Dodelet J.P. Iron-Based Catalysts with Improved Oxygen Reduction Activity in Polymer Electrolyte Fuel Cells. *Science*, 324(5923), 71–74, April 2009. doi:10.1126/science.1170051.
- [63] Dodelet J.P. The Controversial Role of the Metal in Fe- or Co-Based Electrocatalysts for the Oxygen Reduction Reaction in Acid Medium. In M. Shao, editor, *Electrocatalysis in Fuel Cells*, number 9 in Lecture Notes in Energy, pages

- 271–338. Springer London, 2013. ISBN 978-1-4471-4910-1 978-1-4471-4911-8. doi:10.1007/978-1-4471-4911-8\_10.
- [64] DoE Fuel Cell Technologies Office Record 14012: Fuel Cell System Cost. [https://www.hydrogen.energy.gov/pdfs/14012\\_fuel\\_cell\\_system\\_cost\\_2013.pdf](https://www.hydrogen.energy.gov/pdfs/14012_fuel_cell_system_cost_2013.pdf). Accessed: 2016-06-16.
- [65] John Cobb. First drive review - 2016 Toyota Mirai - Video(s). <http://gm-volt.com/2014/11/28/first-drive-review-2016-toyota-mirai-videos/>. Accessed: 2016-10-15.
- [66] Johnson Matthey. Price charts - PMM. <http://www.platinum.matthey.com/prices/price-charts>. Accessed: 2016-06-04.
- [67] Toyota UK. Toyota Prius - A Hybrid Icon. Again. <https://www.toyota.co.uk/new-cars/prius/index.json>. Accessed: 2016-10-15.
- [68] USGS. Rare Earth Elements—Critical Resources for High Technology | USGS Fact Sheet 087-02. <http://pubs.usgs.gov/fs/2002/fs087-02/>. Accessed: 2016-10-15.
- [69] Wikipedia. Abundance of the chemical elements. [https://en.wikipedia.org/w/index.php?title=Abundance\\_of\\_the\\_chemical\\_elements&oldid=732725221](https://en.wikipedia.org/w/index.php?title=Abundance_of_the_chemical_elements&oldid=732725221), August 2016. Accessed: 2016-08-09.
- [70] Kitco. Kitco Commentary. <http://www.kitco.com/ind/Saville/20120612.html>. Accessed: 2016-08-10.
- [71] USGS. Minerals Information: Platinum-Group Metals. <http://minerals.usgs.gov/minerals/pubs/commodity/platinum/>. Accessed: 2016-06-04.
- [72] Statista. Platinum metal reserves worldwide by country 2015 — Statistic. <http://www.statista.com/statistics/273624/platinum-metal-reserves-by-country/>. Accessed: 2016-06-04.
- [73] Garzon F., Lopes T., Rockward T., Sansiñena J.M., Kienitz B., et al. The Impact of Impurities on Long-Term PEMFC Performance. *ECS Transactions*, 25(1), 1575–1583, September 2009. doi:10.1149/1.3210713.



- [74] Malko D., Lopes T., Symianakis E., Kucernak A.R. The intriguing poison tolerance of non-precious metal oxygen reduction reaction (ORR) catalysts. *Journal of Materials Chemistry A*, 4(1), 142–152, December 2015. doi:10.1039/C5TA05794A.
- [75] OICA. Production Statistics. <http://www.oica.net/category/production-statistics/>. Accessed: 2016-08-10.
- [76] Murray R.K., Granner D.K., Mayes P.A., Rodwell V.W. *Harper's Illustrated Biochemistry*. McGraw-Hill, March 2003. ISBN 978-0-07-138901-3.
- [77] Collman J.P., Ghosh S. Recent Applications of a Synthetic Model of Cytochrome *c* Oxidase: Beyond Functional Modeling. *Inorganic Chemistry*, 49(13), 5798–5810, July 2010. doi:10.1021/ic100472p.
- [78] Sigel A., Sigel H., Sigel R.K.O., editors. *The Ubiquitous Roles of Cytochrome P450 Proteins*, volume 47. Wiley-Blackwell, 3rd edition, March 2007. ISBN 978-0-470-01672-5.
- [79] Tsukihara T., Aoyama H., Yamashita E., Tomizaki T., Yamaguchi H., et al. Structures of metal sites of oxidized bovine heart cytochrome *c* oxidase at 2.8 Å. *Science*, 269(5227), 1069–1074, August 1995. doi:10.1126/science.7652554.
- [80] Yoshikawa S., Shimada A. Reaction Mechanism of Cytochrome *c* Oxidase. *Chemical Reviews*, 115(4), 1936–1989, February 2015. doi:10.1021/cr500266a.
- [81] Grau M. *Coordination chemistry of manganese, iron, cobalt and zinc complexes bearing pentadentate ligands and their application in oxidation catalysis*. Ph.D. Thesis, Imperial College London, 2013.
- [82] Meunier B., de Visser S.P., Shaik S. Mechanism of Oxidation Reactions Catalyzed by Cytochrome P450 Enzymes. *Chemical Reviews*, 104(9), 3947–3980, September 2004. doi:10.1021/cr020443g.
- [83] Bytheway I., Hall M.B. Theoretical Calculations of Metal-Dioxygen Complexes. *Chemical Reviews*, 94(3), 639–658, May 1994. doi:10.1021/cr00027a005.
- [84] Savitskii A.V., Nelyubin V.I. Activation of Molecular Oxygen on Interaction with Transition Metal Complexes. *Russian Chemical Reviews*, 44(2), 110–121, February 1975. doi:10.1070/RC1975v044n02ABEH002250.

- [85] Masa J., Ozoemena K.I., Schuhmann W., Zagal J.H. Fundamental Studies on the Electrocatalytic Properties of Metal Macrocyclics and Other Complexes for the Electroreduction of O<sub>2</sub>. In M. Shao, editor, *Electrocatalysis in Fuel Cells*, number 9 in Lecture Notes in Energy, pages 157–212. Springer London, 2013. ISBN 978-1-4471-4910-1 978-1-4471-4911-8. doi:10.1007/978-1-4471-4911-8\_7.
- [86] Wiberg N. *Lehrbuch der Anorganischen Chemie*. De Gruyter, Berlin;Boston, 2008. ISBN 978-3-11-020684-5.
- [87] Jasinski R. Cobalt Phthalocyanine as a Fuel Cell Cathode. *Journal of The Electrochemical Society*, 112(5), 526–528, January 1965. doi:10.1149/1.2423590.
- [88] Jasinski R. A New Fuel Cell Cathode Catalyst. *Nature*, 201(4925), 1212–1213, March 1964. doi:10.1038/2011212a0.
- [89] Wiesener K., Ohms D., Neumann V., Franke R. N<sub>4</sub> macrocycles as electrocatalysts for the cathodic reduction of oxygen. *Materials Chemistry and Physics*, 22(3), 457–475, July 1989. doi:10.1016/0254-0584(89)90010-2.
- [90] Wiesener K. N<sub>4</sub>-chelates as electrocatalyst for cathodic oxygen reduction. *Electrochimica Acta*, 31(8), 1073–1078, August 1986. doi:10.1016/0013-4686(86)80022-6.
- [91] Bagotzky V.S., Tarasevich M.R., Radyushkina K.A., Levina O.A., Andrusyova S.I. Electrocatalysis of the oxygen reduction process on metal chelates in acid electrolyte. *Journal of Power Sources*, 2(3), 233–240, February 1978. doi:10.1016/0378-7753(78)85014-9.
- [92] Jahnke D.H., Schönborn D.M., Zimmermann D.G. Organic dyestuffs as catalysts for fuel cells. In F.P. Schäfer, H. Gerischer, F. Willig, H. Meier, H. Jahnke, M. Schönborn, G. Zimmermann, editors, *Physical and Chemical Applications of Dyestuffs*, number 61 in Topics in Current Chemistry, pages 133–181. Springer Berlin Heidelberg, 1976. ISBN 978-3-540-07559-2 978-3-540-38098-6. doi:10.1007/BFb0046059.
- [93] Zagal J.H., Gulppi M., Isaacs M., Cárdenas-Jirón G., Aguirre M.J.s. Linear versus volcano correlations between electrocatalytic activity and redox and electronic properties of metallophthalocyanines. *Electrochimica Acta*, 44(8–9), 1349–1357, December 1998. doi:10.1016/S0013-4686(98)00257-6.

- [94] van Veen J.A., van Baar J.F., Kroese C.J., Coolegem J.G.F., De Wit N., et al. Oxygen Reduction on Transition-Metal Porphyrins in Acid Electrolyte I. Activity. *Berichte der Bunsengesellschaft für physikalische Chemie*, 85(9), 693–700, September 1981. doi:10.1002/bbpc.19810850917.
- [95] van Veen J.a.R., Colijn H.A. Oxygen Reduction on Transition-Metal Porphyrins in Acid Electrolyte II. Stability. *Berichte der Bunsengesellschaft für physikalische Chemie*, 85(9), 700–704, September 1981. doi:10.1002/bbpc.19810850918.
- [96] Elbaz L., Wu G., Zelenay P. Heat-Treated Non-precious-Metal-Based Catalysts for Oxygen Reduction. In M. Shao, editor, *Electrocatalysis in Fuel Cells*, number 9 in Lecture Notes in Energy, pages 213–246. Springer London, 2013. ISBN 978-1-4471-4910-1 978-1-4471-4911-8. doi:10.1007/978-1-4471-4911-8.8.
- [97] Tarasevich M.R., Radiyschkina K.A., Androuseva S.I. Electrocatalysis of oxygen reduction on organic metallic complexes. *Bioelectrochemistry and Bioenergetics*, 4(1), 18–29, January 1977. doi:10.1016/0302-4598(77)80002-0.
- [98] Cárdenas-Jirón G.I., Zagal J.H. Donor–acceptor intermolecular hardness on charge transfer reactions of substituted cobalt phthalocyanines. *Journal of Electroanalytical Chemistry*, 497(1–2), 55–60, February 2001. doi:10.1016/S0022-0728(00)00434-4.
- [99] Zagal J.H., Gulppi M.A., Cárdenas-Jirón G. Metal-centered redox chemistry of substituted cobalt phthalocyanines adsorbed on graphite and correlations with MO calculations and Hammett parameters. Electrocatalytic reduction of a disulfide. *Polyhedron*, 19(22–23), 2255–2260, November 2000. doi:10.1016/S0277-5387(00)00486-1.
- [100] Zagal J.H., Cárdenas-Jirón G.I. Reactivity of immobilized cobalt phthalocyanines for the electroreduction of molecular oxygen in terms of molecular hardness. *Journal of Electroanalytical Chemistry*, 489(1–2), 96–100, July 2000. doi:10.1016/S0022-0728(00)00209-6.
- [101] Wang G., Ramesh N., Hsu A., Chu D., Chen R. Density functional theory study of the adsorption of oxygen molecule on iron phthalocyanine and cobalt phthalocyanine. *Molecular Simulation*, 34(10-15), 1051–1056, September 2008. doi:10.1080/08927020802258690.

- [102] Sehlotho N., Nyokong T. Effects of ring substituents on electrocatalytic activity of manganese phthalocyanines towards the reduction of molecular oxygen. *Journal of Electroanalytical Chemistry*, 595(2), 161–167, October 2006. doi:10.1016/j.jelechem.2006.07.011.
- [103] Zagal J.H., Griveau S., Silva J.F., Nyokong T., Bedioui F. Metallophthalocyanine-based molecular materials as catalysts for electrochemical reactions. *Coordination Chemistry Reviews*, 254(23–24), 2755–2791, December 2010. doi:10.1016/j.ccr.2010.05.001.
- [104] Stefan I.C., Mo Y., Ha S.Y., Kim S., Scherson D.A. In Situ Fe K-Edge X-ray Absorption Fine Structure of a Nitrosyl Adduct of Iron Phthalocyanine Irreversibly Adsorbed on a High Area Carbon Electrode in an Acidic Electrolyte. *Inorganic Chemistry*, 42(14), 4316–4321, July 2003. doi:10.1021/ic026053u.
- [105] Vasudevan P., Santosh, Mann N., Tyagi S. Transition metal complexes of porphyrins and phthalocyanines as electrocatalysts for dioxygen reduction. *Transition Metal Chemistry*, 15(2), 81–90, April 1990. doi:10.1007/BF01023892.
- [106] Wiesener K., Ohms D., Neumann V., Franke R. N<sub>4</sub> macrocycles as electrocatalysts for the cathodic reduction of oxygen. *Materials Chemistry and Physics*, 22(3), 457–475, July 1989. doi:10.1016/0254-0584(89)90010-2.
- [107] van Veen J.A.R., van Baar J.F., Kroese K.J. Effect of heat treatment on the performance of carbon-supported transition-metal chelates in the electrochemical reduction of oxygen. *Journal of the Chemical Society, Faraday Transactions 1: Physical Chemistry in Condensed Phases*, 77(11), 2827–2843, January 1981. doi:10.1039/F19817702827.
- [108] Tarasevich M.R., Radyuskina K.A. Pyropolymers of N<sub>4</sub>-complexes: Structure and electrocatalytic properties. *Materials Chemistry and Physics*, 22(3), 477–502, July 1989. doi:10.1016/0254-0584(89)90011-4.
- [109] Fuhrmann A., Wiesener K., Iliev I., Gamburgzev S., Kaisheva A. A contribution to the characterization of heat-treated electrocatalytically active tetramethoxyphenylporphyrinato-cobalt-II. *Journal of Power Sources*, 6(1), 69–81, January 1981. doi:10.1016/0378-7753(81)80007-9.

- [110] Bagotzky V.S., Tarasevich M.R., Radyushkina K.A., Levina O.A., Andrusyova S.I. Electrocatalysis of the oxygen reduction process on metal chelates in acid electrolyte. *Journal of Power Sources*, 2(3), 233–240, February 1978. doi:10.1016/0378-7753(78)85014-9.
- [111] van Veen J.A.R., Colijn H.A., van Baar J.F. On the effect of a heat treatment on the structure of carbon-supported metalloporphyrins and phthalocyanines. *Electrochimica Acta*, 33(6), 801–804, June 1988. doi:10.1016/S0013-4686(98)80010-8.
- [112] Kadish K.M., Smith K.M., Guillard R. *The Porphyrin Handbook: Synthesis and organic chemistry*. Elsevier, 2000. ISBN 978-0-12-393201-3.
- [113] Bouwkamp-Wijnoltz A.L., Visscher W., van Veen J.A.R., Boellaard E., van der Kraan A.M., et al. On Active-Site Heterogeneity in Pyrolyzed Carbon-Supported Iron Porphyrin Catalysts for the Electrochemical Reduction of Oxygen: An In Situ Mössbauer Study. *The Journal of Physical Chemistry B*, 106(50), 12,993–13,001, December 2002. doi:10.1021/jp0266087.
- [114] Dodelet J.P. The Controversial Role of the Metal in Fe- or Co-Based Electrocatalysts for the Oxygen Reduction Reaction in Acid Medium. In M. Shao, editor, *Electrocatalysis in Fuel Cells*, number 9 in Lecture Notes in Energy, pages 271–338. Springer London, 2013. ISBN 978-1-4471-4910-1 978-1-4471-4911-8. doi:10.1007/978-1-4471-4911-8\_10.
- [115] Schulenburg H., Stankov S., Schünemann V., Radnik J., Dorbandt I., et al. Catalysts for the Oxygen Reduction from Heat-Treated Iron(III) Tetramethoxyphenylporphyrin Chloride: Structure and Stability of Active Sites. *The Journal of Physical Chemistry B*, 107(34), 9034–9041, August 2003. doi:10.1021/jp030349j.
- [116] Gupta S., Tryk D., Bae I., Aldred W., Yeager E. Heat-treated polyacrylonitrile-based catalysts for oxygen electroreduction. *Journal of Applied Electrochemistry*, 19(1), 19–27, January 1989. doi:10.1007/BF01039385.
- [117] Jaouen F., Proietti E., Lefèvre M., Chenitz R., Dodelet J.P., et al. Recent advances in non-precious metal catalysis for oxygen-reduction reaction in polymer electrolyte fuel cells. *Energy & Environmental Science*, 4(1), 114–130, December 2010. doi:10.1039/C0EE00011F.

- [118] Bashyam R., Zelenay P. A class of non-precious metal composite catalysts for fuel cells. *Nature*, 443(7107), 63–66, September 2006. doi:10.1038/nature05118.
- [119] Proietti E., Jaouen F., Lefèvre M., Larouche N., Tian J., et al. Iron-based cathode catalyst with enhanced power density in polymer electrolyte membrane fuel cells. *Nature Communications*, 2, 416, August 2011. doi:10.1038/ncomms1427.
- [120] Wu G., More K.L., Johnston C.M., Zelenay P. High-Performance Electrocatalysts for Oxygen Reduction Derived from Polyaniline, Iron, and Cobalt. *Science*, 332(6028), 443–447, April 2011. doi:10.1126/science.1200832.
- [121] Shui J., Chen C., Grabstanowicz L., Zhao D., Liu D.J. Highly efficient nonprecious metal catalyst prepared with metal–organic framework in a continuous carbon nanofibrous network. *Proceedings of the National Academy of Sciences*, 112(34), 10,629–10,634, August 2015. doi:10.1073/pnas.1507159112.
- [122] Masa J., Xia W., Muhler M., Schuhmann W. On the Role of Metals in Nitrogen-Doped Carbon Electrocatalysts for Oxygen Reduction. *Angewandte Chemie International Edition*, 54(35), 10,102–10,120, August 2015. doi:10.1002/anie.201500569.
- [123] Masa J., Zhao A., Xia W., Sun Z., Mei B., et al. Trace metal residues promote the activity of supposedly metal-free nitrogen-modified carbon catalysts for the oxygen reduction reaction. *Electrochemistry Communications*, 34, 113–116, September 2013. doi:10.1016/j.elecom.2013.05.032.
- [124] Oh H.S., Kim H. The role of transition metals in non-precious nitrogen-modified carbon-based electrocatalysts for oxygen reduction reaction. *Journal of Power Sources*, 212, 220–225, August 2012. doi:10.1016/j.jpowsour.2012.03.098.
- [125] Jaouen F., Lefèvre M., Dodelet J.P., Cai M. Heat-Treated Fe/N/C Catalysts for O<sub>2</sub> Electroreduction: Are Active Sites Hosted in Micropores? *The Journal of Physical Chemistry B*, 110(11), 5553–5558, March 2006. doi:10.1021/jp057135h.
- [126] Matter P.H., Ozkan U.S. Non-metal Catalysts for Dioxygen Reduction in an Acidic Electrolyte. *Catalysis Letters*, 109(3-4), 115–123, July 2006. doi:10.1007/s10562-006-0067-1.

- [127] Herranz J., Lefèvre M., Larouche N., Stansfield B., Dodelet J.P. Step-by-Step Synthesis of Non-Noble Metal Electrocatalysts for O<sub>2</sub> Reduction under Proton Exchange Membrane Fuel Cell Conditions. *The Journal of Physical Chemistry C*, 111(51), 19,033–19,042, December 2007. doi:10.1021/jp0764438.
- [128] Mohan D., Pittman, C.U., Steele P.H. Pyrolysis of Wood/Biomass for Bio-oil: A Critical Review. *Energy & Fuels*, 20(3), 848–889, May 2006. doi:10.1021/ef0502397.
- [129] Richter H., Howard J.B. Formation of polycyclic aromatic hydrocarbons and their growth to soot—a review of chemical reaction pathways. *Progress in Energy and Combustion Science*, 26(4–6), 565–608, August 2000. doi:10.1016/S0360-1285(00)00009-5.
- [130] Pels J.R., Kapteijn F., Moulijn J.A., Zhu Q., Thomas K.M. Evolution of nitrogen functionalities in carbonaceous materials during pyrolysis. *Carbon*, 33(11), 1641–1653, January 1995. doi:10.1016/0008-6223(95)00154-6.
- [131] Ferrandon M., Kropf A.J., Myers D.J., Artyushkova K., Kramm U., et al. Multi-technique Characterization of a Polyaniline–Iron–Carbon Oxygen Reduction Catalyst. *The Journal of Physical Chemistry C*, 116(30), 16,001–16,013, August 2012. doi:10.1021/jp302396g.
- [132] Gupta S., Fierro C., Yeager E. The effects of cyanide on the electrochemical properties of transition metal macrocycles for oxygen reduction in alkaline solutions. *Journal of Electroanalytical Chemistry and Interfacial Electrochemistry*, 306(1), 239–250, May 1991. doi:10.1016/0022-0728(91)85233-F.
- [133] Herranz J., Jaouen F., Lefèvre M., Kramm U.I., Proietti E., et al. Unveiling N-Protonation and Anion-Binding Effects on Fe/N/C Catalysts for O<sub>2</sub> Reduction in Proton-Exchange-Membrane Fuel Cells. *The Journal of Physical Chemistry C*, 115(32), 16,087–16,097, August 2011. doi:10.1021/jp2042526.
- [134] Jaouen F., Dodelet J.P. Average turn-over frequency of O<sub>2</sub> electro-reduction for Fe/N/C and Co/N/C catalysts in PEFCs. *Electrochimica Acta*, 52(19), 5975–5984, May 2007. doi:10.1016/j.electacta.2007.03.045.
- [135] Jaouen F., Serventi A.M., Lefèvre M., Dodelet J.P., Bertrand P. Non-Noble Electrocatalysts for O<sub>2</sub> Reduction: How Does Heat Treatment Affect Their Activity and

- Structure? Part II. Structural Changes Observed by Electron Microscopy, Raman, and Mass Spectroscopy. *The Journal of Physical Chemistry C*, 111(16), 5971–5976, April 2007. doi:10.1021/jp068274h.
- [136] Jaouen F., Dodelet J.P. O<sub>2</sub> Reduction Mechanism on Non-Noble Metal Catalysts for PEM Fuel Cells. Part I: Experimental Rates of O<sub>2</sub> Electroreduction, H<sub>2</sub>O<sub>2</sub> Electroreduction, and H<sub>2</sub>O<sub>2</sub> Disproportionation. *The Journal of Physical Chemistry C*, 113(34), 15,422–15,432, August 2009. doi:10.1021/jp900837e.
- [137] Koslowski U.I., Abs-Wurmbach I., Fiechter S., Bogdanoff P. Nature of the Catalytic Centers of Porphyrin-Based Electrocatalysts for the ORR: A Correlation of Kinetic Current Density with the Site Density of Fe-N<sub>4</sub> Centers. *The Journal of Physical Chemistry C*, 112(39), 15,356–15,366, October 2008. doi:10.1021/jp802456e.
- [138] Kramm U.I., Herrmann-Geppert I., Behrends J., Lips K., Fiechter S., et al. On an Easy Way To Prepare Metal–Nitrogen Doped Carbon with Exclusive Presence of MeN<sub>4</sub> -type Sites Active for the ORR. *Journal of the American Chemical Society*, 138(2), 635–640, January 2016. doi:10.1021/jacs.5b11015.
- [139] Kramm U.I., Abs-Wurmbach I., Herrmann-Geppert I., Radnik J., Fiechter S., et al. Influence of the Electron-Density of FeN<sub>4</sub>-Centers Towards the Catalytic Activity of Pyrolyzed FeTMPPCl-Based ORR-Electrocatalysts. *Journal of The Electrochemical Society*, 158(1), B69–B78, January 2011. doi:10.1149/1.3499621.
- [140] Kramm U.I., Herranz J., Larouche N., Arruda T.M., Lefèvre M., et al. Structure of the catalytic sites in Fe/N/C-catalysts for O<sub>2</sub>-reduction in PEM fuel cells. *Physical Chemistry Chemical Physics*, 14(33), 11,673–11,688, August 2012. doi:10.1039/C2CP41957B.
- [141] Lefèvre M., Dodelet J.P., Bertrand P. Molecular Oxygen Reduction in PEM Fuel Cells: Evidence for the Simultaneous Presence of Two Active Sites in Fe-Based Catalysts. *The Journal of Physical Chemistry B*, 106(34), 8705–8713, August 2002. doi:10.1021/jp020267f.
- [142] Li Y., Zhou W., Wang H., Xie L., Liang Y., et al. An oxygen reduction electrocatalyst based on carbon nanotube-graphene complexes. *Nature Nanotechnology*, 7(6), 394–400, June 2012. doi:10.1038/nnano.2012.72.



- [143] Li J., Ghoshal S., Liang W., Sougrati M.T., Jaouen F., et al. Structural and mechanistic basis for the high activity of Fe–N–C catalysts toward oxygen reduction. *Energy & Environmental Science*, 9(7), 2418–2432, July 2016. doi:10.1039/C6EE01160H.
- [144] Ramaswamy N., Tylus U., Jia Q., Mukerjee S. Activity Descriptor Identification for Oxygen Reduction on Nonprecious Electrocatalysts: Linking Surface Science to Coordination Chemistry. *Journal of the American Chemical Society*, 135(41), 15,443–15,449, October 2013. doi:10.1021/ja405149m.
- [145] Ramaswamy N., Mukerjee S. Influence of Inner- and Outer-Sphere Electron Transfer Mechanisms during Electrocatalysis of Oxygen Reduction in Alkaline Media. *The Journal of Physical Chemistry C*, 115(36), 18,015–18,026, September 2011. doi:10.1021/jp204680p.
- [146] Sahraie N.R., Kramm U.I., Steinberg J., Zhang Y., Thomas A., et al. Quantifying the density and utilization of active sites in non-precious metal oxygen electroreduction catalysts. *Nature Communications*, 6, 8618, October 2015. doi:10.1038/ncomms9618.
- [147] Thorum M.S., Hankett J.M., Gewirth A.A. Poisoning the Oxygen Reduction Reaction on Carbon-Supported Fe and Cu Electrocatalysts: Evidence for Metal-Centered Activity. *The Journal of Physical Chemistry Letters*, 2(4), 295–298, February 2011. doi:10.1021/jz1016284.
- [148] Wang L., Ambrosi A., Pumera M. “Metal-Free” Catalytic Oxygen Reduction Reaction on Heteroatom-Doped Graphene is Caused by Trace Metal Impurities. *Angewandte Chemie International Edition*, 52(51), 13,818–13,821, December 2013. doi:10.1002/anie.201309171.
- [149] Wu G., Zelenay P. Nanostructured Nonprecious Metal Catalysts for Oxygen Reduction Reaction. *Accounts of Chemical Research*, 46(8), 1878–1889, August 2013. doi:10.1021/ar400011z.
- [150] Wu G., Johnston C.M., Mack N.H., Artyushkova K., Ferrandon M., et al. Synthesis–structure–performance correlation for polyaniline–Me–C non-precious metal cathode catalysts for oxygen reduction in fuel cells. *Journal of Materials Chemistry*, 21(30), 11,392–11,405, July 2011. doi:10.1039/C0JM03613G.

- [151] Ziegelbauer J.M., Olson T.S., Pylypenko S., Alamgir F., Jaye C., et al. Direct Spectroscopic Observation of the Structural Origin of Peroxide Generation from Co-Based Pyrolyzed Porphyrins for ORR Applications. *The Journal of Physical Chemistry C*, 112(24), 8839–8849, June 2008. doi:10.1021/jp8001564.
- [152] Zitolo A., Goellner V., Armel V., Sougrati M.T., Mineva T., et al. Identification of catalytic sites for oxygen reduction in iron- and nitrogen-doped graphene materials. *Nature Materials*, 14(9), 937–942, September 2015. doi:10.1038/nmat4367.
- [153] Bao X., von Deak D., Biddinger E.J., Ozkan U.S., Hadad C.M. A computational exploration of the oxygen reduction reaction over a carbon catalyst containing a phosphinate functional group. *Chemical Communications*, 46(45), 8621–8623, November 2010. doi:10.1039/C0CC03190A.
- [154] Biddinger E.J., Knapke D.S., von Deak D., Ozkan U.S. Effect of sulfur as a growth promoter for CN<sub>x</sub> nanostructures as PEM and DMFC ORR catalysts. *Applied Catalysis B: Environmental*, 96(1–2), 72–82, April 2010. doi:10.1016/j.apcatb.2010.02.003.
- [155] Biddinger E.J., von Deak D., Singh D., Marsh H., Tan B., et al. Examination of Catalyst Loading Effects on the Selectivity of CN<sub>x</sub> and Pt/VC ORR Catalysts Using RRDE. *Journal of The Electrochemical Society*, 158(4), B402–B409, January 2011. doi:10.1149/1.3552944.
- [156] Biddinger E.J., Ozkan U.S. Methanol Tolerance of CN<sub>x</sub> Oxygen Reduction Catalysts. *Topics in Catalysis*, 46(3-4), 339–348, November 2007. doi:10.1007/s11244-007-9014-7.
- [157] Biddinger E.J., Ozkan U.S. Role of Graphitic Edge Plane Exposure in Carbon Nanostructures for Oxygen Reduction Reaction. *The Journal of Physical Chemistry C*, 114(36), 15,306–15,314, September 2010. doi:10.1021/jp104074t.
- [158] Birry L., Zagal J.H., Dodelet J.P. Does CO poison Fe-based catalysts for ORR? *Electrochemistry Communications*, 12(5), 628–631, May 2010. doi:10.1016/j.elecom.2010.02.016.

- [159] Chokai M., Taniguchi M., Moriya S., Matsubayashi K., Shinoda T., et al. Preparation of carbon alloy catalysts for polymer electrolyte fuel cells from nitrogen-containing rigid-rod polymers. *Journal of Power Sources*, 195(18), 5947–5951, September 2010. doi:10.1016/j.jpowsour.2010.01.012.
- [160] Dai L., Xue Y., Qu L., Choi H.J., Baek J.B. Metal-Free Catalysts for Oxygen Reduction Reaction. *Chemical Reviews*, 115(11), 4823–4892, June 2015. doi:10.1021/cr5003563.
- [161] Franke R., Ohms D., Wiesener K. Investigation of the influence of thermal treatment on the properties of carbon materials modified by N4-chelates for the reduction of oxygen in acidic media. *Journal of Electroanalytical Chemistry and Interfacial Electrochemistry*, 260(1), 63–73, February 1989. doi:10.1016/0022-0728(89)87099-8.
- [162] Gouérec P., Biloul A., Contamin O., Scarbeck G., Savy M., et al. Oxygen reduction in acid media catalyzed by heat treated cobalt tetraazaannulene supported on an active charcoal: correlations between the performances after longevity tests and the active site configuration as seen by XPS and ToF-SIMS. *Journal of Electroanalytical Chemistry*, 422(1), 61–75, February 1997. doi:10.1016/S0022-0728(96)04895-4.
- [163] Guo D., Shibuya R., Akiba C., Saji S., Kondo T., et al. Active sites of nitrogen-doped carbon materials for oxygen reduction reaction clarified using model catalysts. *Science*, 351(6271), 361–365, January 2016. doi:10.1126/science.aad0832.
- [164] Jin H., Zhang H., Zhong H., Zhang J. Nitrogen-doped carbon xerogel: A novel carbon-based electrocatalyst for oxygen reduction reaction in proton exchange membrane (PEM) fuel cells. *Energy & Environmental Science*, 4(9), 3389–3394, August 2011. doi:10.1039/C1EE01437D.
- [165] Li X., Liu G., Popov B.N. Activity and stability of non-precious metal catalysts for oxygen reduction in acid and alkaline electrolytes. *Journal of Power Sources*, 195(19), 6373–6378, October 2010. doi:10.1016/j.jpowsour.2010.04.019.
- [166] Li X., Liu L., Lee J.W., Popov B.N. Development of tellurium-modified carbon catalysts for oxygen reduction reaction in PEM fuel cells. *Journal of Power Sources*, 182(1), 18–23, July 2008. doi:10.1016/j.jpowsour.2008.04.017.

- [167] Liu G., Li X., Lee J.W., Popov B.N. A review of the development of nitrogen-modified carbon-based catalysts for oxygen reduction at USC. *Catalysis Science & Technology*, 1(2), 207–217, April 2011. doi:10.1039/C0CY00053A.
- [168] Liu G., Li X., Ganesan P., Popov B.N. Studies of oxygen reduction reaction active sites and stability of nitrogen-modified carbon composite catalysts for PEM fuel cells. *Electrochimica Acta*, 55(8), 2853–2858, March 2010. doi:10.1016/j.electacta.2009.12.055.
- [169] Lyon J.L., Stevenson K.J. Anomalous Electrochemical Dissolution and Passivation of Iron Growth Catalysts in Carbon Nanotubes. *Langmuir*, 23(22), 11,311–11,318, October 2007. doi:10.1021/la7019186.
- [170] Lyth S.M., Nabae Y., Moriya S., Kuroki S., Kakimoto M.a., et al. Carbon Nitride as a Nonprecious Catalyst for Electrochemical Oxygen Reduction. *The Journal of Physical Chemistry C*, 113(47), 20,148–20,151, November 2009. doi:10.1021/jp907928j.
- [171] Lyth S.M., Nabae Y., Islam N.M., Kuroki S., Kakimoto M., et al. Electrochemical Oxygen Reduction Activity of Carbon Nitride Supported on Carbon Black. *Journal of The Electrochemical Society*, 158(2), B194–B201, January 2011. doi:10.1149/1.3519365.
- [172] Maldonado S., Stevenson K.J. Direct Preparation of Carbon Nanofiber Electrodes via Pyrolysis of Iron(II) Phthalocyanine: Electrocatalytic Aspects for Oxygen Reduction. *The Journal of Physical Chemistry B*, 108(31), 11,375–11,383, August 2004. doi:10.1021/jp0496553.
- [173] Maldonado S., Stevenson K.J. Influence of Nitrogen Doping on Oxygen Reduction Electrocatalysis at Carbon Nanofiber Electrodes. *The Journal of Physical Chemistry B*, 109(10), 4707–4716, March 2005. doi:10.1021/jp044442z.
- [174] Matter P.H., Wang E., Millet J.M.M., Ozkan U.S. Characterization of the Iron Phase in  $CN_x$  -Based Oxygen Reduction Reaction Catalysts. *The Journal of Physical Chemistry C*, 111(3), 1444–1450, January 2007. doi:10.1021/jp0651236.
- [175] Matter P.H., Wang E., Arias M., Biddinger E.J., Ozkan U.S. Oxygen Reduction Reaction Catalysts Prepared from Acetonitrile Pyrolysis over Alumina-Supported

- Metal Particles. *The Journal of Physical Chemistry B*, 110(37), 18,374–18,384, September 2006. doi:10.1021/jp062206d.
- [176] Matter P.H., Wang E., Arias M., Biddinger E.J., Ozkan U.S. Oxygen reduction reaction activity and surface properties of nanostructured nitrogen-containing carbon. *Journal of Molecular Catalysis A: Chemical*, 264(1–2), 73–81, March 2007. doi:10.1016/j.molcata.2006.09.008.
- [177] Matter P.H., Wang E., Ozkan U.S. Preparation of nanostructured nitrogen-containing carbon catalysts for the oxygen reduction reaction from SiO<sub>2</sub>- and MgO-supported metal particles. *Journal of Catalysis*, 243(2), 395–403, October 2006. doi:10.1016/j.jcat.2006.07.029.
- [178] Matter P.H., Zhang L., Ozkan U.S. The role of nanostructure in nitrogen-containing carbon catalysts for the oxygen reduction reaction. *Journal of Catalysis*, 239(1), 83–96, April 2006. doi:10.1016/j.jcat.2006.01.022.
- [179] Nallathambi V., Lee J.W., Kumaraguru S.P., Wu G., Popov B.N. Development of high performance carbon composite catalyst for oxygen reduction reaction in PEM Proton Exchange Membrane fuel cells. *Journal of Power Sources*, 183(1), 34–42, August 2008. doi:10.1016/j.jpowsour.2008.05.020.
- [180] Niwa H., Horiba K., Harada Y., Oshima M., Ikeda T., et al. X-ray absorption analysis of nitrogen contribution to oxygen reduction reaction in carbon alloy cathode catalysts for polymer electrolyte fuel cells. *Journal of Power Sources*, 187(1), 93–97, February 2009. doi:10.1016/j.jpowsour.2008.10.064.
- [181] Niwa H., Kobayashi M., Horiba K., Harada Y., Oshima M., et al. X-ray photoemission spectroscopy analysis of N-containing carbon-based cathode catalysts for polymer electrolyte fuel cells. *Journal of Power Sources*, 196(3), 1006–1011, February 2011. doi:10.1016/j.jpowsour.2010.08.054.
- [182] Oh H.S., Oh J.G., Roh B., Hwang I., Kim H. Development of highly active and stable non-precious oxygen reduction catalysts for PEM fuel cells using polypyrrole and a chelating agent. *Electrochemistry Communications*, 13(8), 879–881, August 2011. doi:10.1016/j.elecom.2011.05.027.

- [183] Oh H.S., Oh J.G., Lee W.H., Kim H.J., Kim H. The influence of the structural properties of carbon on the oxygen reduction reaction of nitrogen modified carbon based catalysts. *International Journal of Hydrogen Energy*, 36(14), 8181–8186, July 2011. doi:10.1016/j.ijhydene.2011.04.139.
- [184] Ozaki J.i., Tanifuji S.i., Kimura N., Furuichi A., Oya A. Enhancement of oxygen reduction activity by carbonization of furan resin in the presence of phthalocyanines. *Carbon*, 44(7), 1324–1326, June 2006. doi:10.1016/j.carbon.2005.12.026.
- [185] Ozaki J.i., Tanifuji S.i., Furuichi A., Yabutsuka K. Enhancement of oxygen reduction activity of nanoshell carbons by introducing nitrogen atoms from metal phthalocyanines. *Electrochimica Acta*, 55(6), 1864–1871, February 2010. doi:10.1016/j.electacta.2009.10.037.
- [186] Ozaki J.i., Kimura N., Anahara T., Oya A. Preparation and oxygen reduction activity of BN-doped carbons. *Carbon*, 45(9), 1847–1853, August 2007. doi:10.1016/j.carbon.2007.04.031.
- [187] Rao C.V., Cabrera C.R., Ishikawa Y. In Search of the Active Site in Nitrogen-Doped Carbon Nanotube Electrodes for the Oxygen Reduction Reaction. *The Journal of Physical Chemistry Letters*, 1(18), 2622–2627, September 2010. doi:10.1021/jz100971v.
- [188] Subramanian N.P., Li X., Nallathambi V., Kumaraguru S.P., Colon-Mercado H., et al. Nitrogen-modified carbon-based catalysts for oxygen reduction reaction in polymer electrolyte membrane fuel cells. *Journal of Power Sources*, 188(1), 38–44, March 2009. doi:10.1016/j.jpowsour.2008.11.087.
- [189] von Deak D., Biddinger E.J., Ozkan U.S. Carbon corrosion characteristics of  $CN_x$  nanostructures in acidic media and implications for ORR performance. *Journal of Applied Electrochemistry*, 41(7), 757–763, July 2011. doi:10.1007/s10800-011-0292-1.
- [190] von Deak D., Biddinger E.J., Luthman K.A., Ozkan U.S. The effect of phosphorus in nitrogen-containing carbon nanostructures on oxygen reduction in PEM fuel cells. *Carbon*, 48(12), 3637–3639, October 2010. doi:10.1016/j.carbon.2010.05.022.

- [191] von Deak D., Singh D., Biddinger E.J., King J.C., Bayram B., et al. Investigation of sulfur poisoning of  $\text{CN}_x$  oxygen reduction catalysts for PEM fuel cells. *Journal of Catalysis*, 285(1), 145–151, January 2012. doi:10.1016/j.jcat.2011.09.027.
- [192] Wang X., Hou Z., Ikeda T., Huang S.F., Terakura K., et al. Selective nitrogen doping in graphene: Enhanced catalytic activity for the oxygen reduction reaction. *Physical Review B*, 84(24), 245,434, December 2011. doi:10.1103/PhysRevB.84.245434.
- [193] Wiesener K. N4-chelates as electrocatalyst for cathodic oxygen reduction. *Electrochimica Acta*, 31(8), 1073–1078, August 1986. doi:10.1016/0013-4686(86)80022-6.
- [194] Wiggins-Camacho J.D., Stevenson K.J. Effect of Nitrogen Concentration on Capacitance, Density of States, Electronic Conductivity, and Morphology of N-Doped Carbon Nanotube Electrodes. *The Journal of Physical Chemistry C*, 113(44), 19,082–19,090, November 2009. doi:10.1021/jp907160v.
- [195] Wiggins-Camacho J.D., Stevenson K.J. Indirect Electrocatalytic Degradation of Cyanide at Nitrogen-Doped Carbon Nanotube Electrodes. *Environmental Science & Technology*, 45(8), 3650–3656, April 2011. doi:10.1021/es104229m.
- [196] Woods M.P., Biddinger E.J., Matter P.H., Mirkelamoglu B., Ozkan U.S. Correlation Between Oxygen Reduction Reaction and Oxidative Dehydrogenation Activities Over Nanostructured Carbon Catalysts. *Catalysis Letters*, 136(1-2), 1–8, February 2010. doi:10.1007/s10562-010-0304-5.
- [197] Zhang L., Xia Z. Mechanisms of Oxygen Reduction Reaction on Nitrogen-Doped Graphene for Fuel Cells. *The Journal of Physical Chemistry C*, 115(22), 11,170–11,176, June 2011. doi:10.1021/jp201991j.
- [198] Chu W., Higgins D., Chen Z., Cai R. Non-precious Metal Oxides and Metal Carbides for ORR in Alkaline-Based Fuel Cells. In Z. Chen, J.P. Dodelet, J.Z. Dodelet, editors, *Non-Noble Metal Fuel Cell Catalysts*, pages 357–388. Wiley-VCH Verlag GmbH & Co. KGaA, 2014. ISBN 978-3-527-66490-0.
- [199] Dodelet J.P., Chenitz R., Yang L., Lefèvre M. A New Catalytic Site for the Electroreduction of Oxygen? *ChemCatChem*, 6(7), 1866–1867, July 2014. doi:10.1002/cctc.201402133.

- [200] Hu Y., Jensen J.O., Zhang W., Martin S., Chenitz R., et al. Fe<sub>3</sub>C-based oxygen reduction catalysts: Synthesis, hollow spherical structures and applications in fuel cells. *Journal of Materials Chemistry A*, 3(4), 1752–1760, December 2014. doi:10.1039/C4TA03986F.
- [201] Hu Y., Jensen J.O., Zhang W., Cleemann L.N., Xing W., et al. Hollow Spheres of Iron Carbide Nanoparticles Encased in Graphitic Layers as Oxygen Reduction Catalysts. *Angewandte Chemie International Edition*, 53(14), 3675–3679, April 2014. doi:10.1002/anie.201400358.
- [202] Li J.S., Li S.L., Tang Y.J., Han M., Dai Z.H., et al. Nitrogen-doped Fe/Fe<sub>3</sub>C@graphitic layer/carbon nanotube hybrids derived from MOFs: Efficient bifunctional electrocatalysts for ORR and OER. *Chemical Communications*, 51(13), 2710–2713, January 2015. doi:10.1039/C4CC09062D.
- [203] Park M.J., Lee J.H., Hembram K.P.S.S., Lee K.R., Han S.S., et al. Oxygen Reduction Electrocatalysts Based on Coupled Iron Nitride Nanoparticles with Nitrogen-Doped Carbon. *Catalysts*, 6(6), 86, June 2016. doi:10.3390/catal6060086.
- [204] Qian Y., Cavanaugh J., Khan I.A., Wang X., Peng Y., et al. Fe/Fe<sub>3</sub>C/N-Doped Carbon Materials from Metal–Organic Framework Composites as Highly Efficient Oxygen Reduction Reaction Electrocatalysts. *ChemPlusChem*, 81(8), 718–723, August 2016. doi:10.1002/cplu.201600174.
- [205] Strickland K., Miner E., Jia Q., Tylus U., Ramaswamy N., et al. Highly active oxygen reduction non-platinum group metal electrocatalyst without direct metal–nitrogen coordination. *Nature Communications*, 6, 7343, June 2015. doi:10.1038/ncomms8343.
- [206] Wu T., Zhang H., Zhang X., Zhang Y., Zhao H., et al. A low-cost cementite (Fe<sub>3</sub>C) nanocrystal@N-doped graphitic carbon electrocatalyst for efficient oxygen reduction. *Physical chemistry chemical physics*, 17(41), 27,527–27,533, November 2015. doi:10.1039/c5cp04252f.
- [207] Yang W., Yue X., Liu X., Chen L., Jia J., et al. Superior oxygen reduction electrocatalysis enabled by integrating hierarchical pores, Fe<sub>3</sub>C nanoparticles and bamboo-like carbon nanotubes. *Nanoscale*, 8(2), 959–964, December 2015. doi:10.1039/C5NR08008H.



- [208] Yin H., Zhang C., Liu F., Hou Y. Hybrid of Iron Nitride and Nitrogen-Doped Graphene Aerogel as Synergistic Catalyst for Oxygen Reduction Reaction. *Advanced Functional Materials*, 24(20), 2930–2937, May 2014. doi:10.1002/adfm.201303902.
- [209] Gupta S., Tryk D., Bae I., Aldred W., Yeager E. Heat-treated polyacrylonitrile-based catalysts for oxygen electroreduction. *Journal of Applied Electrochemistry*, 19(1), 19–27, January 1989. doi:10.1007/BF01039385.
- [210] Lefèvre M., Dodelet J.P., Bertrand P. O<sub>2</sub> Reduction in PEM Fuel Cells: Activity and Active Site Structural Information for Catalysts Obtained by the Pyrolysis at High Temperature of Fe Precursors. *The Journal of Physical Chemistry B*, 104(47), 11,238–11,247, November 2000. doi:10.1021/jp002444n.
- [211] Charretier F., Jaouen F., Ruggeri S., Dodelet J.P. Fe/N/C non-precious catalysts for PEM fuel cells: Influence of the structural parameters of pristine commercial carbon blacks on their activity for oxygen reduction. *Electrochimica Acta*, 53(6), 2925–2938, February 2008. doi:10.1016/j.electacta.2007.11.002.
- [212] Tylus U., Jia Q., Strickland K., Ramaswamy N., Serov A., et al. Elucidating Oxygen Reduction Active Sites in Pyrolyzed Metal–Nitrogen Coordinated Non-Precious-Metal Electrocatalyst Systems. *The Journal of Physical Chemistry C*, 118(17), 8999–9008, May 2014. doi:10.1021/jp500781v.
- [213] Franke R., Ohms D., Wiesener K. Investigation of the influence of thermal treatment on the properties of carbon materials modified by N<sub>4</sub>-chelates for the reduction of oxygen in acidic media. *Journal of Electroanalytical Chemistry and Interfacial Electrochemistry*, 260(1), 63–73, February 1989. doi:10.1016/0022-0728(89)87099-8.
- [214] Pourbaix M. *Atlas of Electrochemical Equilibria in Aqueous Solutions*. NACE International, 2nd edition, December 1974. ISBN 978-0-915567-98-0.
- [215] Zhang S., Cai Y., He H., Zhang Y., Liu R., et al. Heteroatom doped graphdiyne as efficient metal-free electrocatalyst for oxygen reduction reaction in alkaline medium. *Journal of Materials Chemistry A*, 4(13), 4738–4744, March 2016. doi:10.1039/C5TA10579J.

- [216] Miller M.A., Coletta M., Mauro J.M., Putnam L.D., Farnum M.F., et al. Carbon monoxide recombination in cytochrome c peroxidase: Effect of the local heme environment on carbon monoxide binding explored through site-directed mutagenesis. *Biochemistry*, 29(7), 1777–1791, February 1990. doi:10.1021/bi00459a017.
- [217] Liu J., Yu S., Daio T., Ismail M.S., Sasaki K., et al. Metal-Free Nitrogen-Doped Carbon Foam Electrocatalysts for the Oxygen Reduction Reaction in Acid Solution. *Journal of The Electrochemical Society*, 163(9), F1049–F1054, January 2016. doi:10.1149/2.0631609jes.
- [218] Zhang L., Xia Z. Mechanisms of Oxygen Reduction Reaction on Nitrogen-Doped Graphene for Fuel Cells. *The Journal of Physical Chemistry C*, 115(22), 11,170–11,176, June 2011. doi:10.1021/jp201991j.
- [219] Kim H., Lee K., Woo S.I., Jung Y. On the mechanism of enhanced oxygen reduction reaction in nitrogen-doped graphene nanoribbons. *Physical Chemistry Chemical Physics*, 13(39), 17,505–17,510, September 2011. doi:10.1039/C1CP21665A.
- [220] Goldstein S., Meyerstein D., Czapski G. The Fenton reagents. *Free Radical Biology and Medicine*, 15(4), 435–445, October 1993. doi:10.1016/0891-5849(93)90043-T.
- [221] Jiang H., Yao Y., Zhu Y., Liu Y., Su Y., et al. Iron Carbide Nanoparticles Encapsulated in Mesoporous Fe–N-Doped Graphene-Like Carbon Hybrids as Efficient Bifunctional Oxygen Electrocatalysts. *ACS Applied Materials & Interfaces*, 7(38), 21,511–21,520, September 2015. doi:10.1021/acsami.5b06708.
- [222] Varnell J.A., Tse E.C.M., Schulz C.E., Fister T.T., Haasch R.T., et al. Identification of carbon-encapsulated iron nanoparticles as active species in non-precious metal oxygen reduction catalysts. *Nature Communications*, 7, 12,582, August 2016. doi:10.1038/ncomms12582.
- [223] Kramm U.I., Herrmann-Geppert I., Behrends J., Lips K., Fiechter S., et al. On an Easy Way To Prepare Metal–Nitrogen Doped Carbon with Exclusive Presence of MeN<sub>4</sub>-type Sites Active for the ORR. *Journal of the American Chemical Society*, 138(2), 635–640, January 2016. doi:10.1021/jacs.5b11015.
- [224] Jiang W.J., Gu L., Li L., Zhang Y., Zhang X., et al. Understanding the High Activity of Fe–N–C Electrocatalysts in Oxygen Reduction: Fe/Fe<sub>3</sub>C Nanoparticles

- Boost the Activity of Fe–N<sub>x</sub>. *Journal of the American Chemical Society*, 138(10), 3570–3578, March 2016. doi:10.1021/jacs.6b00757.
- [225] Herranz J., Jaouen F., Lefèvre M., Kramm U.I., Proietti E., et al. Unveiling N-Protonation and Anion-Binding Effects on Fe/N/C Catalysts for O<sub>2</sub> Reduction in Proton-Exchange-Membrane Fuel Cells. *The Journal of Physical Chemistry C*, 115(32), 16,087–16,097, August 2011. doi:10.1021/jp2042526.
- [226] Jia Q., Ramaswamy N., Hafiz H., Tylus U., Strickland K., et al. Experimental Observation of Redox-Induced Fe–N Switching Behavior as a Determinant Role for Oxygen Reduction Activity. *ACS Nano*, 9(12), 12,496–12,505, December 2015. doi:10.1021/acsnano.5b05984.
- [227] Li J., Ghoshal S., Liang W., Sougrati M.T., Jaouen F., et al. Structural and mechanistic basis for the high activity of Fe–N–C catalysts toward oxygen reduction. *Energy & Environmental Science*, 9(7), 2418–2432, July 2016. doi:10.1039/C6EE01160H.
- [228] Chlistunoff J. RRDE and Voltammetric Study of ORR on Pyrolyzed Fe/Polyaniline Catalyst. On the Origins of Variable Tafel Slopes. *The Journal of Physical Chemistry C*, 115(14), 6496–6507, April 2011. doi:10.1021/jp108350t.
- [229] Muthukrishnan A., Nabae Y., Okajima T., Ohsaka T. Kinetic Approach to Investigate the Mechanistic Pathways of Oxygen Reduction Reaction on Fe-Containing N-Doped Carbon Catalysts. *ACS Catalysis*, 5(9), 5194–5202, September 2015. doi:10.1021/acscatal.5b00397.
- [230] Choi C.H., Baldizzone C., Grote J.P., Schuppert A.K., Jaouen F., et al. Stability of Fe-N-C Catalysts in Acidic Medium Studied by Operando Spectroscopy. *Angewandte Chemie International Edition*, 54(43), 12,753–12,757, October 2015. doi:10.1002/anie.201504903.
- [231] Goellner V., Baldizzone C., Schuppert A., Sougrati M.T., Mayrhofer K., et al. Degradation of Fe/N/C catalysts upon high polarization in acid medium. *Phys. Chem. Chem. Phys.*, 16(34), 18,454–18,462, July 2014. doi:10.1039/C4CP02882A.
- [232] Chlistunoff J., Sansiñena J.M. Effects of Axial Coordination of the Metal Center on the Activity of Iron Tetraphenylporphyrin as a Nonprecious Catalyst for Oxygen

- Reduction. *The Journal of Physical Chemistry C*, 118(33), 19,139–19,149, August 2014. doi:10.1021/jp5044249.
- [233] Tse E.C.M., Varnell J.A., Hoang T.T.H., Gewirth A.A. Elucidating Proton Involvement in the Rate-Determining Step for Pt/Pd-Based and Non-Precious-Metal Oxygen Reduction Reaction Catalysts Using the Kinetic Isotope Effect. *The Journal of Physical Chemistry Letters*, pages 3542–3547, August 2016. doi: 10.1021/acs.jpcllett.6b01235.
- [234] Choi C.H., Baldizzone C., Polymeros G., Pizzutilo E., Kasian O., et al. Minimizing Operando Demetallation of Fe-N-C Electrocatalysts in Acidic Medium. *ACS Catalysis*, 6(5), 3136–3146, May 2016. doi:10.1021/acscatal.6b00643.
- [235] Morozan A., Sougrati M.T., Goellner V., Jones D., Stievano L., et al. Effect of Furfuryl Alcohol on Metal Organic Framework-based Fe/N/C Electrocatalysts for Polymer Electrolyte Membrane Fuel Cells. *Electrochimica Acta*, 119, 192–205, February 2014. doi:10.1016/j.electacta.2013.12.022.
- [236] Serov A., Artyushkova K., Atanassov P. Fe-N-C Oxygen Reduction Fuel Cell Catalyst Derived from Carbendazim: Synthesis, Structure, and Reactivity. *Advanced Energy Materials*, 4(10), 2650–2676, July 2014. doi:10.1002/aenm.201301735.
- [237] Zhao D., Shui J.L., Grabstanowicz L.R., Chen C., Commet S.M., et al. Highly Efficient Non-Precious Metal Electrocatalysts Prepared from One-Pot Synthesized Zeolitic Imidazolate Frameworks. *Advanced Materials*, 26(7), 1093–1097, February 2014. doi:10.1002/adma.201304238.
- [238] Barkholtz H.M., Chong L., Kaiser Z.B., Xu T., Liu D.J. Highly Active Non-PGM Catalysts Prepared from Metal Organic Frameworks. *Catalysts*, 5(2), 955–965, June 2015. doi:10.3390/catal5020955.
- [239] Nabae Y., Kuang Y., Chokai M., Ichihara T., Isoda A., et al. High performance Pt-free cathode catalysts for polymer electrolyte membrane fuel cells prepared from widely available chemicals. *Journal of Materials Chemistry A*, 2(30), 11,561–11,564, July 2014. doi:10.1039/C4TA01828A.

- [240] Wang Y.C., Lai Y.J., Song L., Zhou Z.Y., Liu J.G., et al. S-Doping of an Fe/N/C ORR Catalyst for Polymer Electrolyte Membrane Fuel Cells with High Power Density. *Angewandte Chemie International Edition*, 54(34), 9907–9910, August 2015. doi:10.1002/anie.201503159.
- [241] Lei M., Li P.G., Li L.H., Tang W.H. A highly ordered Fe–N–C nanoarray as a non-precious oxygen-reduction catalyst for proton exchange membrane fuel cells. *Journal of Power Sources*, 196(7), 3548–3552, April 2011. doi:10.1016/j.jpowsour.2010.12.026.
- [242] Tian J., Morozan A., Sougrati M.T., Lefèvre M., Chenitz R., et al. Optimized Synthesis of Fe/N/C Cathode Catalysts for PEM Fuel Cells: A Matter of Iron–Ligand Coordination Strength. *Angewandte Chemie International Edition*, 52(27), 6867–6870, July 2013. doi:10.1002/anie.201303025.
- [243] Chokai M., Daidou T., Nabae Y. Development of Pt-Free Carbon-Based Catalyst for PEFC Cathode Prepared from Polyacrylonitrile. *ECS Transactions*, 64(3), 261–270, August 2014. doi:10.1149/06403.0261ecst.
- [244] Szakacs C.E., Lefèvre M., Kramm U.I., Dodelet J.P., Vidal F. A density functional theory study of catalytic sites for oxygen reduction in Fe/N/C catalysts used in H<sub>2</sub>/O<sub>2</sub> fuel cells. *Physical Chemistry Chemical Physics*, 16(27), 13,654–13,661, June 2014. doi:10.1039/C3CP55331K.
- [245] Liu K., Kattel S., Mao V., Wang G. Electrochemical and Computational Study of Oxygen Reduction Reaction on Nonprecious Transition Metal/Nitrogen Doped Carbon Nanofibers in Acid Medium. *The Journal of Physical Chemistry C*, 120(3), 1586–1596, January 2016. doi:10.1021/acs.jpcc.5b10334.
- [246] Steinmann S.N., Sautet P. Assessing a First-Principles Model of an Electrochemical Interface by Comparison with Experiment. *The Journal of Physical Chemistry C*, 120(10), 5619–5623, March 2016. doi:10.1021/acs.jpcc.6b01938.
- [247] Hansen M.H., Jin C., Thygesen K.S., Rossmeisl J. Finite Bias Calculations to Model Interface Dipoles in Electrochemical Cells at the Atomic Scale. *The Journal of Physical Chemistry C*, 120(25), 13,485–13,491, June 2016. doi:10.1021/acs.jpcc.6b00721.

*An overview on the background of the experimental techniques used is provided. It is by no means an extensive treatment and the reader is referred to the referenced literature instead. The detail of each section is based on the importance of the respective technique to this work. The chapter is included in order to allow the reader to follow the thesis without the need to refer to external resources.*

## Chapter 2

# Experimental Techniques

### 2.1 Electrochemical Techniques

#### 2.1.1 Rotating Ring Disk Electrode

The Rotating Disk Electrode (RDE) and its extension, the Rotating Ring Disk Electrode (RRDE) are widely used for evaluating the electrocatalytic activity and H<sub>2</sub>O selectivity of ORR catalysts for PEMFCs. It allows for the screening of catalysts under quasi fuel cell conditions *i.e.* constant reactant flux and steady state. Information that can be obtained include kinetic parameters such as the rate constant of the reaction, electron transfer number and symmetry factor [1–3]. It is the main tool of catalyst evaluation in this work.

The RDE is used in a conventional three electrode set-up, with a reference electrode, counter electrode and the disk of the RDE as working electrode. In case of RRDE the ring serves as second working electrode. It is therefore a four electrode setup. For all RDE/RRDE experiments in this work a three compartment electrochemical cell was used. Figure 2.1 (a) shows a schematic of the assembly. All compartments are filled with electrolyte. The main compartment is occupied by the RRDE in the centre. The reference electrode utilizes a separate compartment which is connected to the main compartment via

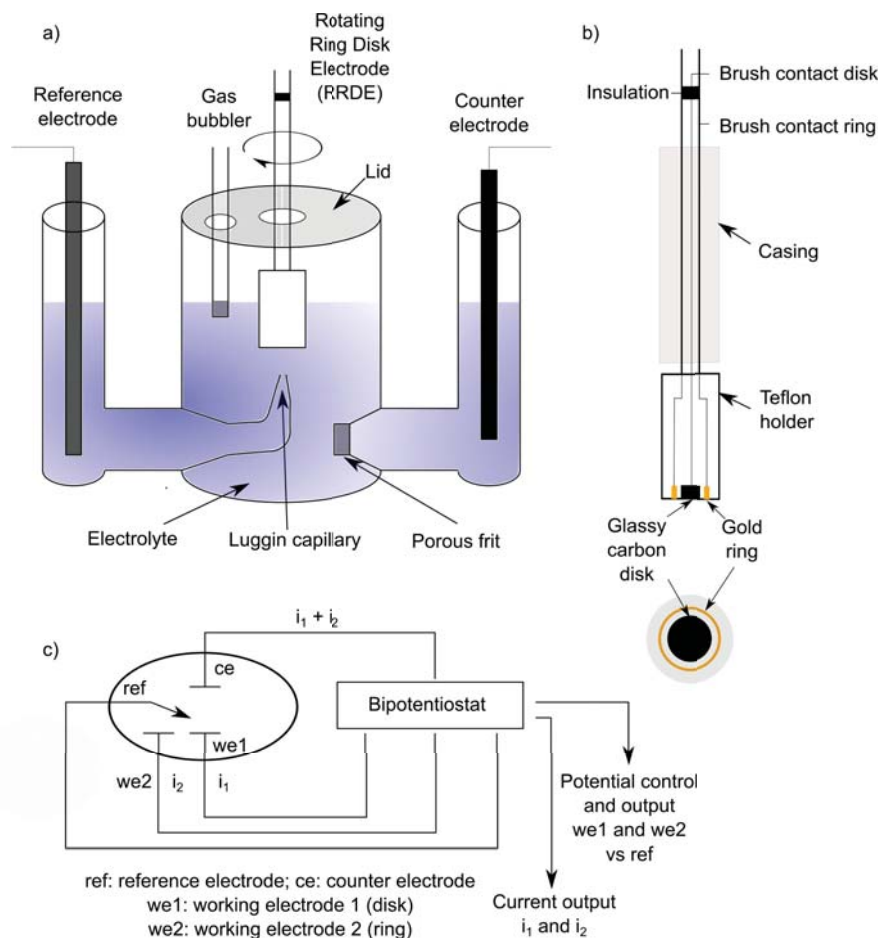


FIGURE 2.1: (a) 3-compartment electrochemical cell with equipment. (b) Cross section of the RRDE. (c) Block diagram of the setup.

a *Luggin-Haber*-capillary. This offers a distinct sensing point for the reference electrode [2]. It is important to maintain the capillary in close distance to the working electrode to minimize the uncompensated solution resistance  $R_u$ . However a minimal separation has to be kept in order to avoid significant current disturbance. A distance of 2.5 times the diameter of the capillary is considered appropriate. [2] The counter electrode (glassy carbon rod) is situated in another compartment and separated by a porous frit. This serves the purpose of preventing electrochemically active species formed at the counter electrode from contaminating the main compartment and interfering with the reactions at the working electrodes. Additionally the main compartment is equipped with a gas bubbler to purge the electrolyte, *i.e.* with nitrogen or oxygen. The lid ensures the saturation of the solution with the respective gas and prevents the diffusion of atmospheric gases into the cell.

The RRDE (Figure 2.1 (b)) consists of a glassy carbon disk and a gold ring embedded in a cylindrical polytetrafluorethylen (PTFE) holder. The holder is connected via a rod to

a rotator which can apply a defined rotating speed. Electrical connection to the working electrodes is established through brush contacts. Figure 2.1 (c) shows a block diagram of the setup. A bipotentiostat controls the potential of the working electrodes and collects the currents ( $i_1$  and  $i_2$ ).

Processes by which reactants are transported to the electrode surface are usually diffusion, convection and migration (for charged species). [2] In a stagnant electrolyte at thermal equilibrium and with a large background of unreacting ionic species present, the dominant mechanism of mass transport is diffusion. [2] This poses severe limitations in obtaining kinetic data because the current in the kinetic region is dominated by mass transport and at a planar electrode, the region of depleted and hence mass transport is increasing with time. [2] In order to enhance mass transport, forced convection can be introduced. In the RDE/RRDE technique this is achieved by spinning the electrode relative to the electrolyte at a certain frequency  $f$  (revolutions per second) or angular velocity  $\omega = 2\pi f$  ( $\text{s}^{-1}$ ). [2]

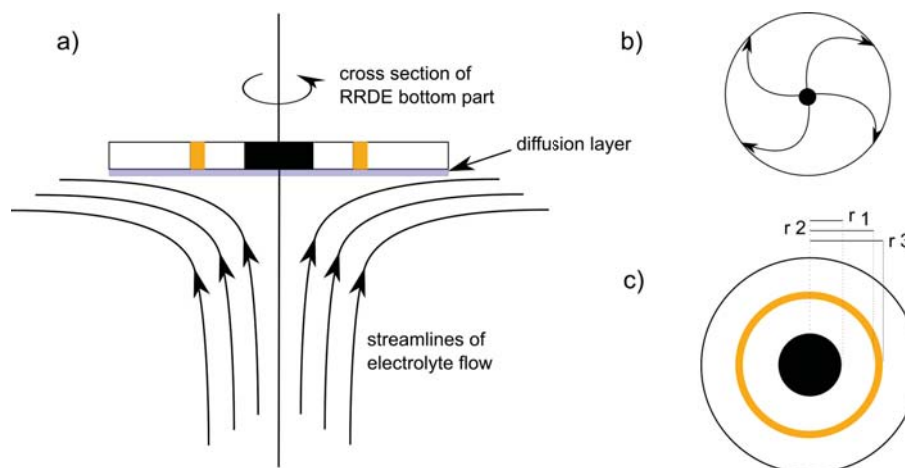


FIGURE 2.2: (a) Representation of electrolyte streamlines during disk rotation. (b) Bottom view of streamlines. (c) Radii of disk, inner ring and outer ring. [2]

This causes the electrolyte and reactants to be dragged towards the surface of the electrode and spun off laterally. [2] However the region adjacent to the electrode is still stagnant of reactants. The transport mechanism through this region is still diffusion. [2] It is therefore called the "diffusion layer" and the thickness of this layer  $\delta$  (m) is determined by the rotation rate,  $\omega$  ( $\text{s}^{-1}$ ), *i.e.* thinner for higher rotation speeds [2, 3]. It is important to maintain a laminar flow for the model to be valid. Rotation rates are thus chosen to be between 5 and 10,000 revolutions per minute (rpm). Figure 2.2 (a) depicts the streamlines of electrolyte and reactants during rotation and the diffusion layer. Figure



2.2 (b) shows the lateral movement of the solution. [2]

The net mass transport and thus the current is determined directly by the diffusion of the reacting species through the diffusion layer. Since the thickness of the diffusion layer is determined by the rotation speed, the current is also controlled by convection. [2] A scan is usually conducted from a potential with no reaction occurring to a potential where the complete reactant is consumed instantaneously at the electrode surface, leading to a maximum current and mass transport control. [3] The convective-diffusion equations at steady-state ( $\partial C_R/\partial t = 0$ ) after simplification for symmetry (*i.e.* flux is indifferent in disk radius and angle) can be expressed as the equilibrium between the flux normal to the disc ( $y$  direction) caused by convection and the one caused by diffusion [2]:

$$v_y \left( \frac{\partial C_R}{\partial y} \right) = D_R \left( \frac{\partial^2 C_R}{\partial y^2} \right) \quad (2.1)$$

where  $C_R$  (mol cm<sup>-3</sup>) is the reactant concentration,  $D_R$  (cm<sup>2</sup> s<sup>-1</sup>) is the reactant diffusion coefficient and  $v_y$  (cm s<sup>-1</sup>) is the velocity of the fluid in  $y$  direction. Solving for  $(\partial C_R/\partial y)_{y=0}$  under limiting current conditions:  $C_R = 0$  at  $y = 0$ ;  $\lim_{y \rightarrow \infty} C_R = C_R^*$  and considering that the current is given by, [2]

$$i = nFAD_R \left( \frac{\partial C_R}{\partial y} \right)_{y=0} \quad (2.2)$$

yields the *Levich equation* [2]:

$$i_l = 0.62nFAD_R^{2/3} \omega^{1/2} \nu^{-1/6} C_R^* \quad (2.3)$$

where  $C_R^*$  (mol cm<sup>-3</sup>) is the bulk concentration of the reactant,  $n$  is the number of electrons transferred,  $F$  (C mol<sup>-1</sup>) is *Faraday's* constant, and  $\nu$  (cm<sup>2</sup> s<sup>-1</sup>) is the kinematic viscosity of the electrolyte. For a certain rotation rate a specific limiting current is obtained. Before reaching mass transport control the current is also affected by the reaction kinetics. This simply involves changing the boundary conditions in the solution of the convective-diffusion equation towards having a non zero concentration  $C_R$  at  $y = 0$ . [2] Considering further the current for a totally irreversible one step one electron transfer [2]

$$i = F A k_f(E) C_R(y = 0) \quad (2.4)$$

defining

$$i_k = F A k_f(E) C_R^* \quad (2.5)$$

where  $k_f$  ( $s^{-1}$ ) is the rate constant for the forward reaction. Rearranging gives the *Koutecky-Levich equation* [2]:

$$\frac{1}{i} = \frac{1}{i_k} + \frac{1}{i_l} = \frac{1}{i_k} + \frac{1}{0.62nFAD_R^{2/3}\omega^{1/2}\nu^{-1/6}C_R^*} \quad (2.6)$$

A plot of  $i^{-1}$  versus  $\omega^{-1/2}$  thus gives a straight line. The slope can yield parameters like  $D$  or for the ORR the electron transfer number  $n$ , given all other variables are known. The intercept at  $\omega^{-1/2} = 0$  allows the determination of  $k_f$ . [2]

It has to be stressed that this equation assumes a simple first order reaction or a multi-step reaction in which the slow step at the potential and reactant concentrations remains the same. Although this might not be the given for the complex ORR it is the best practical approximation available to date. These relationships can be applied both to the RDE and the disk of the RRDE. Moreover, to the RRDE a ring electrode is coaxially added to the disk electrode. As the reactants and products are swept away laterally from the disk this allows the detection and quantification of products and byproducts, *i.e.*  $H_2O_2$  formation during the ORR. [1, 2] This is achieved by holding the ring potential at a certain value to ensure selective reaction of the desired compound and measuring the produced current. The ratio of disk current ( $I_d$  in A) to ring current ( $I_r$  in A) is the collection efficiency [1, 2]:

$$N = \frac{-I_r}{I_d} \quad (2.7)$$

The negative sign indicates opposite directions of the disk and ring reaction. In particular, for the ORR this means the ring is kept at a potential that ensures the oxidation of the peroxide formed. This is then an oxidative current opposite to the actual reductive one at the disk. [1, 2]

The collection efficiency is determined by the dimensions of the electrode ( $r_1$ ,  $r_2$ ,  $r_3$  in Figure 2.2 (c)) and can be calculated from these values. [2] Alternatively it can be determined experimentally using a redox reaction, *e.g.* the  $\text{Fe}(\text{CN})_6^{3-}/\text{Fe}(\text{CN})_6^{4-}$  couple. [3] As for an ORR catalyst to be applied in a fuel cell it should produce close to no  $\text{H}_2\text{O}_2$ , because the subsequently formed hydroxyl and peroxy radicals corrode ionomer and other components of the fuel cell and thus lead to a shorter lifetime. Since the formation of peroxide is a 2 electron process in contrast to the 4 electron ORR it can be derived that the percentage of peroxide produced during the ORR is given by [1]:

$$\% \text{H}_2\text{O}_2 = \left[ \frac{(2I_r/N)}{(I_d + I_r/N)} \right] * 100 \quad (2.8)$$

where  $N$  is the collection efficiency and  $I_d$  (A) and  $I_r$  (A) are the disk and ring currents respectively. Although RDE and RRDE have been employed for a long time and have been applied to study redox reactions, recent improvements to using the RDE as a standard method to test catalysts were made by Schmidt *et al.* [4], who established a procedure consistent to test ultra-thin Pt/C catalyst layers. In this procedure, the catalyst is dispersed in a solvent to obtain an ink, which is then deposited by drop coating onto the disk. A small amount of Nafion<sup>®</sup> acts as binder to attach the catalyst powder to the disk. In order to obtain reasonable results the catalyst layer should be thin and homogeneous. [4, 5] Later Paulus *et al.* [1] showed that also the RRDE technique can be applied to electrocatalysis in order to determine the 4 electron selectivity of the reaction. Numerous studies utilised this method to non precious metal catalysts as well, however at relatively high loadings (up to  $1 \text{ mg cm}^{-2}$ ). [5–8] The applicability of high loadings is questionable and is presumably strongly dependent on the catalyst morphology and the flatness of the resulting catalyst layer. [5, 9, 10] If the layer is either too thick and/or has a high macroscopic roughness it will lead to erroneous results. This results from the possibility of electrode roughness introducing a convective component adjacent to the electrode layer, and the fact that the electrode layer is now thick relative to the boundary layer. This can produce a higher than theoretical limiting current and the diffusion layer with constant thickness, which is the underlying assumption of this technique will not be present. [9, 10]

Figure 2.3 shows a representative RDE voltammogram of an oxygen saturated solution at a scan rate ( $1 \text{ mV s}^{-1}$ ) and step size ( $30 \text{ mV}$ ) to ensure steady-state conditions, *e.g.*

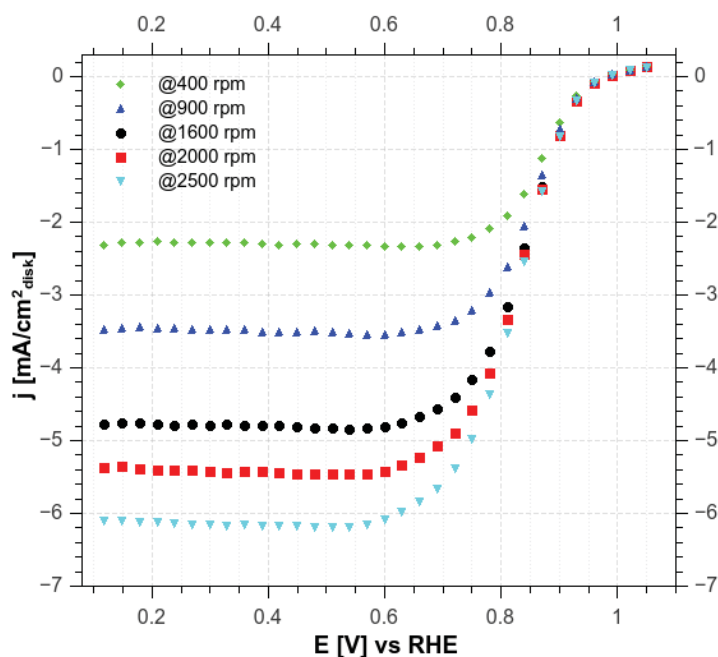


FIGURE 2.3: Representative ORR curves at different rotation rates for a non-precious metal catalyst in alkaline solution.

30 s per point, which eliminates contributions from capacitive currents. In contrast, Pt catalysts are usually evaluated at a higher scan rate of  $20 \text{ mV s}^{-1}$ . This is because of poisoning effects and growth of an oxide layer interfere with the analysis. [4] This is not the case for NPMCs and hence a lower scan rate can be used. It can be seen that a higher rotation rate provides a higher limiting current density. In general, for the ORR, a catalyst which shows a higher current at higher potential is better for fuel cell applications, given that  $\text{O}_2$  is reduced to  $\text{H}_2\text{O}$  rather than  $\text{H}_2\text{O}_2$ . The use of the RDE/RRDE to determine activities of NPMCs under acidic conditions is challenging, as these materials are generally significantly less active than PGM based materials and at low loading do not achieve limiting current densities. [11] Therefore either high loadings can be used as mentioned above or the loading can be reduced in order to better reflect the assumptions of the technique. [10, 11] This will however prevent the determination of the electron transfer number  $n$  from the limiting current. The peroxide yield monitored at the ring has also been shown to be dependent on the CL thickness. [5] A higher loading generally leads to the detection of less  $\text{H}_2\text{O}_2$ , as the species will have a longer residence time within the catalyst layer and will therefore be able to decompose or to be electrochemically reduced. [5] Hence it is necessary to determine the peroxide content at various catalyst loadings in order to be able to make statements on whether a 4 electron

reduction or a 2+2 process is present. [5]

### 2.1.2 Electrochemical Impedance Spectroscopy

Electrochemical impedance spectroscopy (EIS) is a technique where the electrochemical system is set to certain steady-state conditions, *i.e.* constant current or constant potential, and then subjected to a sinusoidal excitation signal of variable frequency, *i.e.* current or potential perturbation. [12] From the response, information such as solution resistance, capacitance, charge transfer resistance and mass transport phenomena can be extracted. [12] For most analysis it is important to ensure that the system behaves linear. This means that the magnitude of the perturbation should be chosen small enough in order to ensure no deviation from this linear behaviour and large enough to trigger a suitable response. [12, 13] A potential input signal of

$$E(t) = E_c + \Delta E \sin(\omega t) \quad (2.9)$$

will then produce a current output signal of

$$I(t) = I_c + \Delta I \sin(\omega t + \phi) \quad (2.10)$$

and *vice versa*. [12]  $E$  is the potential signal,  $E_c$  (V) is the constant steady-state potential,  $\Delta E$  (V) the amplitude of potential modulation,  $\omega$  ( $\text{s}^{-1}$ ) the angular frequency,  $I$  (A) the current signal output,  $I_c$  (A) the constant steady-state current,  $\Delta I$  (A) the amplitude of current modulation,  $t$  (s) the time and  $\phi$  (degree) the phase angle between the signals. It can be shown that input and output function are correlated with a transfer function. [12, 13] For an electrical circuit or an electrochemical system, the impedance is the transfer function between the potential (input) and the current (output) [12, 13]:

$$Z(\omega) = \frac{\Delta \bar{E}(\omega)}{\Delta \bar{I}(\omega)} \quad (2.11)$$

where  $\Delta \bar{E}(\omega)$  is the *Laplace* transform of the potential output function in the frequency domain and  $\Delta \bar{I}(\omega)$  the respective current input function.  $Z(\omega)$  is a complex function, with real part  $\text{Re}Z(\omega)$  and imaginary part  $\text{Im}Z(\omega)$ . The modulus is defined as [12, 13]:

$$|Z(\omega)| = \sqrt{\text{Re}Z(\omega)^2 + \text{Im}Z(\omega)^2} \quad (2.12)$$

and the phase angle between the signals is given by [12, 13]:

$$\phi = \arctan \left[ \frac{\text{Im}Z(\omega)}{\text{Re}Z(\omega)} \right] \quad (2.13)$$

Electrochemical phenomena in an ideal model system can be represented by basic electrical circuits consisting of resistive and capacitive elements with the addition of a term that represents mass transport effects. [12, 13] The impedance of a resistor is based on *Ohm's* law and given by [12, 13]:

$$Z(\omega) = R \quad (2.14)$$

and therefore the alternating part of the current response across a resistor is given by [12, 13]:

$$\Delta I(t) = \frac{\Delta E}{R} \sin(\omega t) \quad (2.15)$$

where R is the resistance in  $\Omega$ . This means a purely resistive element will not introduce de-phasing into the alternating part of the current and has only a real component. On the other hand, a capacitive element will have the following impedance [12, 13]:

$$Z(\omega) = -\frac{j}{\omega C} \quad (2.16)$$

and current response [12, 13]:

$$\Delta I(t) = \Delta E C \omega \sin(\omega t + \pi/2) \quad (2.17)$$

where  $j$  is the imaginary unit ( $j^2 = -1$ ) and C is the capacitance in F. A pure capacitor will therefore de-phase current and potential by  $\phi = 90^\circ$  and has only an imaginary component. [12, 13] From equations 2.14 and 2.16 it can be seen that, while the impedance

of a resistor is frequency independent, the impedance of the capacitor for very high frequencies ( $\omega \rightarrow \infty$ ) will become negligible while for very small frequencies ( $\omega \rightarrow 0$ ) will become infinite. [12, 13] The solution resistance can be represented by a resistive element  $R_s$ . [12, 13] Furthermore, it can be shown that the electrochemical charge transfer can also be represented by a resistive element  $R_{ct}$ . [12, 13] The double layer capacitance can be represented by a capacitive element  $C_{dl}$ . [12, 13] Deviation from the ideal behaviour can have multiple reasons, such as inhomogeneities on the surface, blocking species or a high porosity and can be approximated by introducing a so called constant phase element (CPE) [12, 13]:

$$Z_Q = \frac{1}{Q^0(j\omega)^\rho} \quad (2.18)$$

where  $\rho$  has a value between 0 and 1, with 1 representing an ideal capacitor.  $Q^0$  in F represents the capacitive element in the CPE. The mass transport impedance of a redox reaction, which is also called *Warburg* impedance, can be derived from the respective equations when taking concentration effects at the electrode into account and for a stagnant solution, *i.e.* no fixed diffusion layer, is given by [12, 13]:

$$Z_w = \frac{\sigma(1-j)}{\sqrt{\omega}} \quad (2.19)$$

where  $\sigma$  is a constant which is defined by the concentration and diffusion coefficients of the reactants.  $Z_W$  is frequency dependent, will grow with smaller frequencies at the same rate in the real as well as imaginary part and introduce a phase shift of  $45^\circ$ . [12, 13] For diffusion layers of fixed length, such as in a cell with forced convection, *e.g.* RDE/RRDE, or where the diffusion layer is bounded by a wall, *e.g.* thin layer electrochemical cell, the behaviour will deviate at low frequencies and will introduce a more complex dependency on the diffusion layer thickness  $\delta$ . [12, 13] The impedances of the various components can then be combined and behave according to Kirchoff's laws, *i.e.* a series configuration of  $Z_1$  and  $Z_2$  will produce a total impedance of  $Z_{tot} = Z_1 + Z_2$  and a parallel configuration a total impedance of  $1/Z_{tot} = 1/Z_1 + 1/Z_2$  etc. [12, 13]

A simple electrochemical redox reaction on an electrode can be described with the *Randles-Ershler* circuit, as shown in Figure 2.4 (a) and will yield the impedance response of the combination of the single components. This response can be represented in various ways.

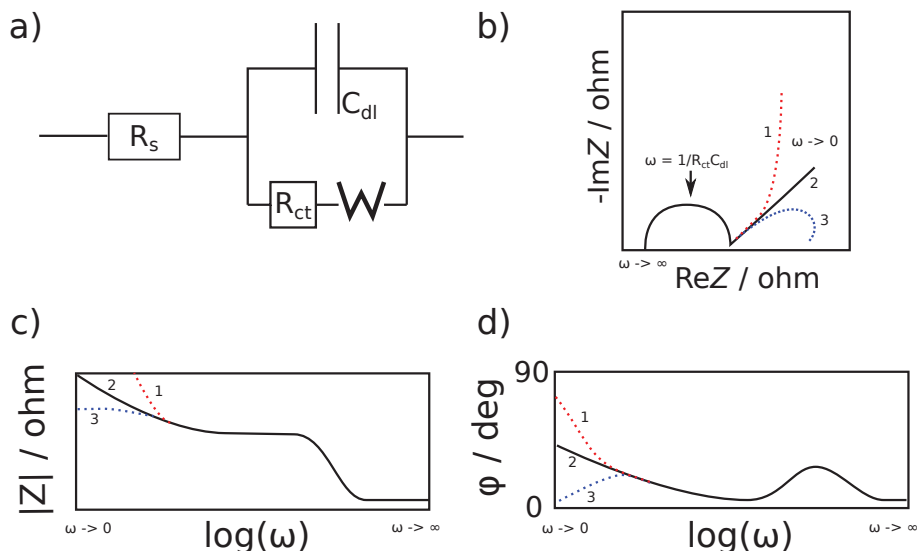


FIGURE 2.4: a) Equivalent *Randles-Ershler* circuit of a faradaic half reaction. b) *Nyquist*-plot of the impedance response expected for this circuit. c) *Bode* magnitude plot and d) *Bode* phase angle plot of the same circuit. Traces **1**, **2** and **3** in b) - d) represent the mass transport response for the blocking electrode case, the infinite linear diffusion and the semi-infinite linear diffusion, respectively. [12, 13]

A plot of  $\text{Re}Z(\omega)$  versus  $-\text{Im}Z(\omega)$  is called *Nyquist*-plot and allows the easy identification of resistive, capacitive and mass transport elements. [12, 13] It can be seen in Figure 2.4 (b) that the *Nyquist*-plot of the *Randles-Ershler* circuit will produce a semicircle, which is offset on the real axis. This first intercept is caused by the solution resistance  $R_s$ , which only has a real component. [12, 13] A faradaic charge transfer together with the double layer capacitance of the electrode are modelled with a resistor in parallel with a capacitor. This will produce a semicircle in the *Nyquist*-plot. [12, 13] In case of a deviation from the ideal behaviour a CPE can be used instead of a capacitor. The semicircle will then be depressed. [12, 13] The position of the maximum of the semicircle with respect to frequency is defined by the time constant  $\tau = R_{ct}C_{dl}$  of the system ( $\omega_{max} = 1/\tau$ ). [12, 13] The magnitude of the semicircle is defined by the magnitude of  $R_{ct}$  and  $C_{dl}$ . This means a more facile reaction will produce a smaller semicircle, observed at higher frequencies. [12, 13] Finally the mass transfer resistance  $W$  can be observed at low frequencies. [12, 13] In the circuit it is positioned in series with  $R_{ct}$ . In a reaction with growing diffusion layer, *i.e.* no forced convection, the response in the *Nyquist*-plot will be a straight line with an angle of  $45^\circ$  (trace **2** in Figure 2.4 (b) - (d)). [12, 13] If a fixed diffusion layer thickness is present, it will show a second semicircle (trace **3** in Figure 2.4 (b) - (d)). If the diffusion layer has a fixed thickness (trace **1** in Figure 2.4 (b) - (d)), with no reactant species outside the barrier, the mass transport impedance will curve towards a  $90^\circ$  line and the total



impedance will increase. [12, 13] The plots of  $\log(\omega)$  versus  $\phi$  and  $|Z(\omega)|$  are called *Bode* plots and allow to identify the associated phase shift and modulus of the impedance at a given modulation frequency. [12, 13] The respective *Bode* plots are shown in Figures 2.4 (c) and (d). If a suitable equivalent circuit can be identified for an electrochemical system, the response can be fit and the respective parameters can be determined.[12–14]

In this work EIS has been used to extract the solution resistance in the 3 electrode set-up shown in 2.1.1 above, in order to obtain the *iR*-free potential. This can be done by simply reading the real value at zero phase angle or the first intercept with the real axis in the *Nyquist*-plot. [14, 15] Moreover, EIS has been used to gain information on the catalyst layer in the membrane electrode assembly (MEA). [14] On porous electrodes such as used in fuel cells a more complex behaviour is present. [13] The impedance response of fuel cells will be introduced in the respective chapter ( 8). [13, 14]

In practice, a frequency response analyser (FRA) is used in order to generate input and extract the output signals. Typical frequencies range from 10 mHz to 0.1 MHz. At high frequencies the inductance of the utilised circuitry, *i.e.* cables, becomes a significant interference. [13, 14] This inductive impedance ( $Z_L = j\omega L$ , where  $L$  is the inductance in H) is visible as negative imaginary component in the *Nyquist*-plot. [13, 14] This contribution can be minimised by ensuring that the cell to be tested is connected through short wide cables and that no loops are present in the current carrying connections. [13, 14] Typical magnitudes of excitation range around 5% of the constant current or potential (root mean square (rms)). [13, 14] The linearity of input to output response can be verified by following the *Lissajous* curve of the signals. [13, 14] A linear response is ensured when the figure exhibits a strictly ellipsoid shape. The consistency of impedance data can further be verified with the *Kramers-Kronig* relationship. [13, 14, 16] This ensures correlation between the signals and whether the system maintains its steady-state throughout the measurement. [13, 14, 16] Schönleber *et al.* [16–18] developed and verified an improved algorithm which was used in this work to verify impedance data.

### 2.1.3 Cyclic Voltammetry

Cyclic voltammetry (CV) is the cycling of potential between 2 points at a fixed scan rate while recording the current. [2] The obtained current *versus* potential plot is the voltammogram. The sweep rate is constant for each voltammogram and lies between 1

and 500 mV/s in this work. [2] The measurement is taken with the same set-up as the RRDE experiments. CVs are applied to every catalyst before the activity is evaluated by RRDE, in order to condition the catalyst layer. The RRDE measurements are also taken as CVs with a slow scan rate (1 - 5 mV s<sup>-1</sup>), in order to reduce capacitive currents.

Traditionally, CV is conducted by linearly sweeping the potential. However, in contrast to analogue instrumentation, newer instruments which contain digital components apply a stair-case voltammogram. [19] The parameters defining the staircase scan are the scan rate  $\vec{V}$  (V s<sup>-1</sup>) and step potential  $E_{step}$  (V) and give the interval time  $t_{int}$  (s) [19]:

$$t_{int} = \frac{E_{step}}{\vec{V}} \quad (2.20)$$

Instead of linearly sweeping the potential and constantly sampling the current, the potential is stepped by  $E_{step}$  and the current is sampled at the end of the interval time. [19] For scan rates between 10 and 100 mV s<sup>-1</sup> and  $E_{step}$  of 1 - 2 mV, the interval times lie between 10  $\mu$ s and 20 ms. It has been shown that the error is negligible when investigating kinetic processes. [19] However, the current associated with fast surface adsorbate reactions and double layer contributions might be undetected. [19] This might be the case when performing stripping voltammetry. To mitigate this drawback of the digital instrumentation, a current integrator can be used. [19]

A current integrator is an analogue circuit element, which directly measures the total passed charge associated with the potential step,  $Q_{step}$ . At the end division by the duration of the step  $t_{step}$  yields the total current as opposed to the current at the end of the step during normal stair-case voltammetry. This allows us to also capture currents associated with faster processes. It has been shown that this method produces comparable results to the linear scan method. [19]

When background corrected currents are reported the measurements in the presence and absence of O<sub>2</sub> have been recorded under the same conditions and the capacitive trace (in absence of O<sub>2</sub> and in the presence of N<sub>2</sub>) subtracted from the measurement under O<sub>2</sub>. This leaves the current associated with the faradaic reaction, *i.e.* the ORR. In order to condition the catalyst layer, the potential is cycled at various scan rates in the presence and absence of O<sub>2</sub>. This is done until the voltammogram does not change anymore and takes between 20 and 100 cycles under different scan rates and varying between O<sub>2</sub> and

$N_2$  (see relevant Experimental Part). It ensures that the surface is electrochemically clean and the whole accessible catalyst surface area is wet properly with electrolyte.

The capacitive current measured in the absence of a faradaic reaction can give an estimation about the specific surface area of the catalyst. [2] This is due to the fact that the double layer capacitance is, in a first approximation, proportional to the electrochemically accessible surface area. [2]

CV can provide information on redox active species within the catalyst, which might be correlated to the catalytic activity and ultimately give information about the active site. [2] If a redox active species is present, a reduction and oxidation peak will be observed. If the position of the peaks does not change with scan rate, it is a reversible reaction. [2, 3]

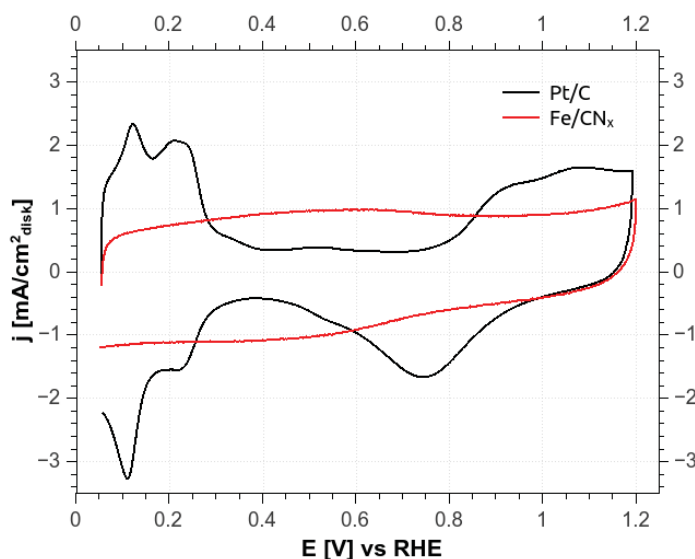


FIGURE 2.5: Representative voltammograms of a platinum catalyst deposited on carbon black (Pt/C) and a Fe-N/C catalyst (Fe/CN<sub>x</sub>).

As can be seen in Figure 2.5, NPMCs are mostly featureless as compared to Pt/C, which shows a rich behaviour in hydrogen adsorption/desorption and oxide formation. In some NPMC samples a reversible redox peak can be observed, which might either be associated with the transition of  $\text{Fe}^{2+}/\text{Fe}^{3+}$  in the material or the hydroquinone/quinone couple in the carbon. [8]

CV was mainly used in this study to measure the charge of a reductively stripped species from the catalyst surface. The charge passed in a CV is given by [2]:

$$Q = \frac{IE}{\vec{V}} \quad (2.21)$$

where  $Q$  is the charge in C,  $I$  the current in A,  $E$  the potential in V. Thus the magnitude of the peak-area is directly correlated to the charge associated with this peak. [2] As mentioned above a current integrator module should be used for these experiments. [19]

### 2.1.4 Chronocoulometry

Alternatively to CV, chronocoulometry can be used to measure the charge associated with an electrochemical process. [2] Chronocoulometry involves stepping the potential from a predefined value to another while measuring the charge associated with this potential step over time. [2] In this work chronocoulometry has been used complementary to stripping CV in order to verify the results.

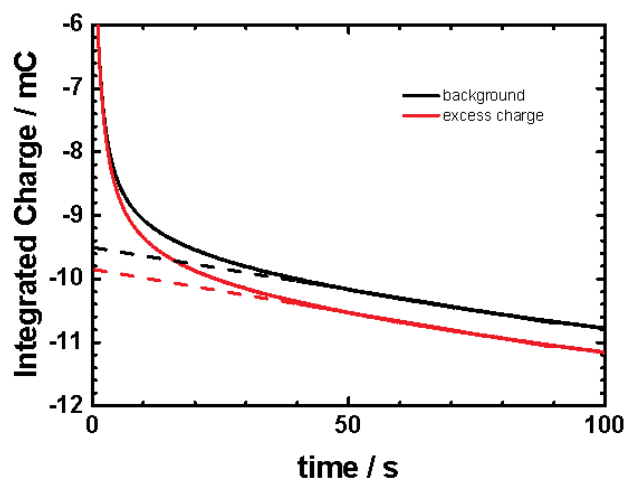


FIGURE 2.6: Representative reductive coulometric stripping of a species from the surface of an Fe-N/C catalyst as compared to the baseline trace.

Figure 2.6 shows a representative stripping measurement. The measurement has been recorded on a RDE, utilising the setup described in 2.1.1, at a rotation of 1600 rpm. The charge increase of the background measurement is associated with the capacitive current and the excess charge can be extracted by extrapolating the charge *versus* time curve at constant slope to zero time. The non-zero increases in charge after the capacitive and stripping charges have been passed is due to a small amount of faradaic reaction, *i.e.* the hydrogen evolution reaction, at the applied potential. [2] A potentiostat can be used to

generate the potential step and record the current. When a current integrator is used the passed charge is measured directly. Alternatively the current can be measured and integrated over the time. [2]

### 2.1.5 Membrane electrode assembly single cell testing

Ultimately the catalyst has to be tested under real operating conditions. This is done in a membrane electrode assembly (MEA). [20] However this method is usually reserved for the best catalysts, due to the time-consuming fabrication process. The MEA is the central part of the PEMFC. It is where the electrochemical reaction takes place and the power is created [20].

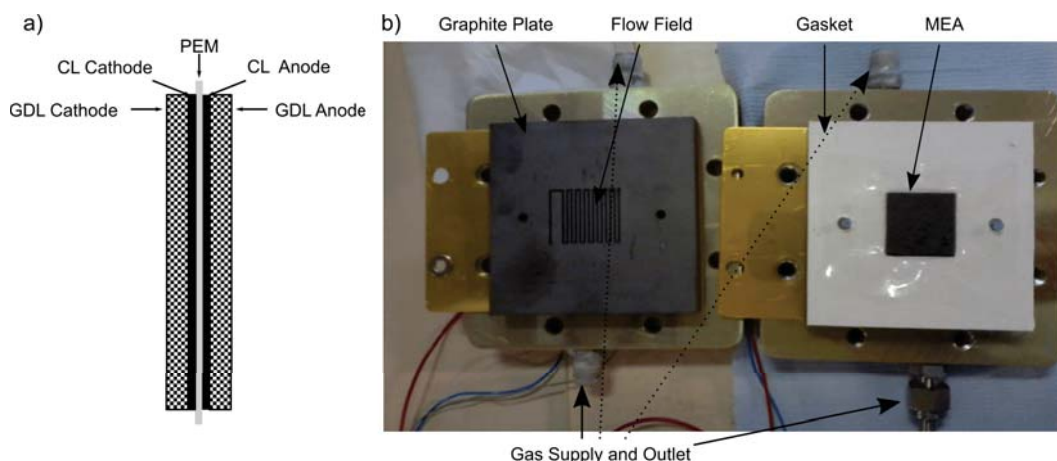


FIGURE 2.7: (a) Schematic of an MEA. CL = catalyst layer, GTL = Gas Transport Layer, PEM = Polymer Electrolyte Membrane. (b) MEA embedded onto one half of the testing device (right) other half shows the graphite plate with the flow field. Both parts are sandwiched and screwed together, to obtain the complete device.

The main components of the MEA are the proton exchange membrane (PEM) or anion exchange membrane (AEM) in case of the alkaline pendant, the catalyst layers (CL) and gas transport layers (GTL) of anode and cathode respectively (Figure 2.7 (a)). [20] The MEA can be prepared by different methods. The traditional method is that the CL is deposited onto the GDLs. Another method applies the CL to the membrane. There are several ways of applying the CL to either GDL or membrane. Spraying of a catalyst ink is suitable for the GDL, while for the membrane a catalyst layer is usually prepared onto a PTFE blank and then hot pressed onto the membrane (catalyst decal transfer) to form a catalyst coated membrane (CCM). [21] After applying the CLs to the respective component, those are hot pressed together to obtain the MEA shown in Figure 2.7 (a).

The MEA is then installed into the testing device which contains graphite plates with a flow field, gas inlet and outlet and heaters. The current can be collected from the graphite plates (Figure 2.7 (b)), which are in contact with gold plated current collectors. The testing device seen in Figure 2.7 is closed with a defined pressure, which can be achieved by using a defined torque on the screws that fix the device, and connected to a load cell and/or a potentiostat via the current collectors. Then the respective reactants  $H_2$  and  $O_2$  or air are supplied, which are usually humidified. Humidification is achieved by saturating the gases with water at the desired temperature to achieve a defined relative humidity (RH). [20] The gas flow is controlled with mass flow controllers (MFCs). A back-pressure unit can be used in order to increase the partial pressure of the reactants in the cell. The cell is usually heated to 60 - 80°C, when conducting the measurements. [20] In order to assess the performance of the cell, a steady state polarisation curve can be collected (Figure 1.7 in Chapter 1). EIS can be used to further analyse the cell. The features of the polarisation curve and the losses present in a single cell have been discussed in ( 1.3). EIS on single cell MEAs will be introduced in the relevant chapter ( 8).

## 2.2 Physical and analytical characterization methods

### 2.2.1 Nitrogen adsorption analysis

In order to assess the surface specific activity of a catalyst and compare different catalysts to each other it is important to know the specific surface area and the porosity of the material. This can be achieved by measuring the amount of adsorbed nitrogen with respect to pressure under isothermal conditions. The technique is named after Stephen Brunauer, Paul Hugh Emmett and Edward Teller, (BET), who described the theory in 1938. The BET theory is an extension of the Langmuir theory which describes the dependence of surface coverage on the gas pressure or the concentration of an adsorbent. While the Langmuir theory limits the surface coverage to a monolayer, the BET theory allows for the formation of infinite layers [22, 23]. Following assumptions are made [23]:

1. There is a fixed amount of surface sites onto which adsorbent molecules can adsorb (one molecule per site). The adsorbed molecules are considered to be spherical and has a specific cross sectional area on the surface.

2. A molecule can act as a single adsorption site for a molecule of the upper layer and the formed columns do not interact with each other.
3. The uppermost molecule layer is in equilibrium with the gas phase, *i.e.* equal rates of molecule adsorption and desorption.
4. The energy of adsorption for the first layer  $E_1$  is given by the molecule-surface interaction. The energy for all successive layers equals the adsorbate's heat of condensation.
5. At the saturation pressure, the number of layers approaches infinity (*i.e.* equivalent to the sample being surrounded by a liquid phase)

The following equation was derived [23]:

$$\frac{1}{v[(p_0/p) - 1]} = \frac{c - 1}{v_m c} \left( \frac{p}{p_0} \right) + \frac{1}{v_m c} \quad (2.22)$$

where  $p$  (Pa) and  $p_0$  (Pa) are the equilibrium and the saturation pressure of adsorbate at the temperature of adsorption,  $v$  is the adsorbed gas quantity (for instance, in volume units L), and  $v_m$  is the monolayer adsorbed gas quantity.  $c$  is the BET constant which is defined by the heat of adsorption for the first layer  $E_1$  and that of the second and higher layers  $E_L$ , [23]

$$c = \exp\left(\frac{E_1 - E_L}{RT}\right) \quad (2.23)$$

A plot of  $1/(v[(p_0/p) - 1])$  versus  $p/p_0$  gives a straight line in the range of  $0.05 < p/p_0 < 0.35$ . From the value of the slope  $A$  and the y-intercept  $I$  it is possible to calculate the monolayer adsorbed gas quantity  $v_m$  and the BET constant, [23]

$$v_m = \frac{1}{A + I} \quad (2.24)$$

$$c = 1 + \frac{A}{I} \quad (2.25)$$

this then allows the determination of the total surface area  $S_{tot}$  and the specific surface area  $S_{spec}$ ,

$$S_{tot} = \frac{(v_m N s)}{V} \quad (2.26)$$

$$S_{spec} = \frac{S_{tot}}{a} \quad (2.27)$$

where  $v_m$  is in units of volume which are also the units of the molar volume of the adsorbate gas,  $N$  is *Avogadro's* number,  $s$  the adsorption cross section of the adsorbing species,  $V$  the molar volume of the adsorbate gas, and  $a$  the mass of the adsorbent. [23, 24] Practically the equilibrium pressure and the amount of adsorbed gas is determined at a fixed temperature. [24] Different gases can be used with this technique. Nitrogen has been used in this work. [24] The obtained surface area can be taken to determine the specific current density.

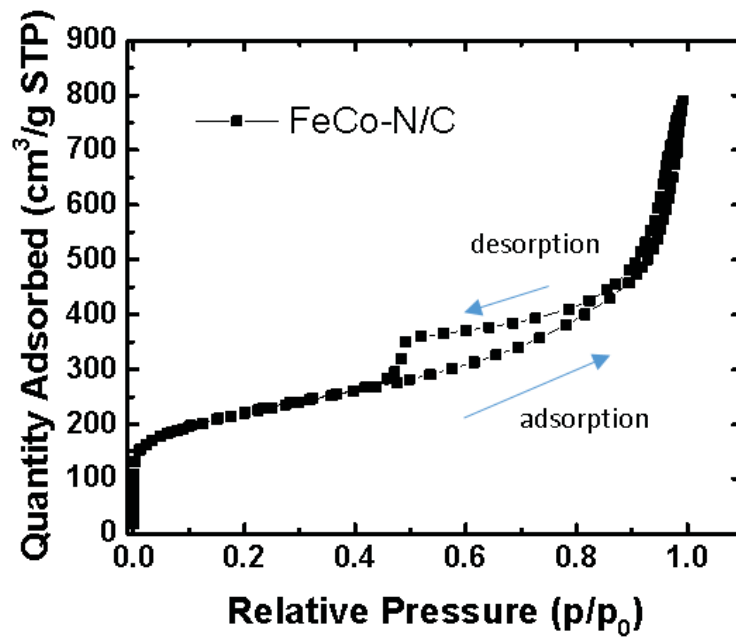


FIGURE 2.8: Representative BET isotherm of a carbon based high surface area FeCo-N/C catalyst with micropores.

Figure 2.8 shows a representative isotherm, from which the relevant data can be extracted by appropriate rearrangement of the plotting parameters. Rearranging the plot according to equation 2.22 will allow the determination of surface area. The BET isotherm can



furthermore yield information on the pore size distribution (PSD) of meso- and micropores. [24] The information can be extracted from the adsorption or desorption branch of the isotherm in the  $p/p_0$  range of 0.4 - 0.97. [24] Different underlying theories can be used to extract the PSD. In the Barret, Joyner, Halenda (BJH) method, the assumption is that all pores have a cylindrical shape and a modified *Kelvin* equation is used to relate the amount of adsorbate removed as  $p/p_0$  is decreased to the size of the pores. Usually a maximum pore size of 60 nm is accessible with this method. [24, 25] It has been shown that the BJH method can be used for carbon blacks. [24, 25] Further information to be gained is the determination of micropore *versus* external surface area, where the micropore area is defined as pores smaller than 2 nm. The Broekhoff-de Boer equation can be used in conjunction with the so called t-plot, to extract the micropore area versus external surface area of a material. [24] The BET in combination with the Broekhoff-de Boer and BJH methods have been used in this study to extract data from the isotherm. Although all methods use simplifications, it allows the establishment of general trends. In a typical measurement, the sample is usually filled into a specifically engineered glass tube and thoroughly dried before use, in order to clean the surface. The sample tube is then evacuated and then cooled down to the desired temperature by immersion into a liquid nitrogen vessel. The amount of gas and the relative partial pressure can then be adjusted with mass flow controllers (MFCs) and pressure transducers to collect the isotherm.

### 2.2.2 Total reflection x-ray fluorescence

Total reflection X-ray fluorescence (TXRF) can be used to determine the identity and quantity of elements present in a sample. [26] It is particularly useful for trace metal analysis with a detection limit in the low picogram (pg) range. [26] The working principle of X-ray fluorescence (XRF) is the ejection of electrons from the inner atomic orbitals by X-rays. The resulting hole is then filled by relaxation from an electron in a higher energy orbital. The released energy of this transition is emitted as fluorescence quanta. The energy of the photoemission light is distinct for each element, as it reflects the difference in the energy of the orbital transitions in this element. [26] For light elements the  $K_\alpha$  line and for heavy elements the  $L_\alpha$  line is used for identification and quantification. [26] A X-ray tube with either a Mo or W target is used to generate the X-rays and a silicon based detector, such as a silicon drift detector (SDD), detects and quantifies the emitted fluorescence light quanta. [26] The advantage of TXRF over other XRF methods is that

due to the shallow angle of the incident light beam, the penetration depth is restricted to few nanometers. This decreases the occurrence of interferences from the X-ray source and increases the signal-to-noise ratio significantly. [26] Suitable optical components such as monochromators and mirrors ensure the suitable processing of the incident X-rays from the source to the sample and the emitted light from the sample to the detector, while further minimising interferences. [26]

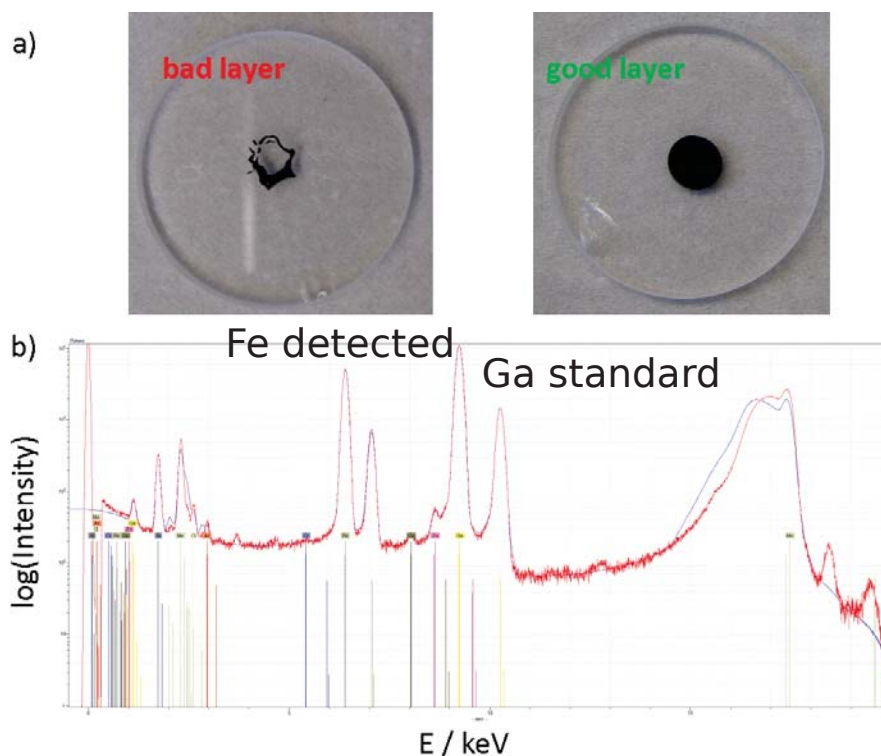


FIGURE 2.9: a) Image of a quartz carrier with a deposited sample which is unsuitable for the measurement, due to being inhomogeneous (left) and a suitable homogeneous sample layer (right). b) Representative total reflection X-ray fluorescence (TXRF) spectrum of a Fe-N/C catalyst with Ga as internal standard.

The analyte is deposited onto a carrier, which should be made of high purity material that only contains elements which do not interfere with the measurement. High purity quartz is an option if silicon is not the desired element to be detected. [26] If a material with a solid matrix, such as carbon, is measured, a homogeneous thin film has to be prepared. This is achieved by mixing and sonicating the sample with an aqueous surfactant solution in order to produce an ink. An internal standard is added for quantification. This is usually an element which does not interfere with the detection signal, such as Ga. [26] The ink is then deposited onto the sample carrier, dried in order to produce a homogeneous thin film, and subjected to analysis. [26] A homogeneous thin film is important to obtain the correct signal for quantification. Figure 2.9 (a) shows the preparation of a good

and a bad sample carrier. The identity of the detected elements can be obtained by comparing the energy of the emitted radiation with tabulated values. The instrument needs to be suitably calibrated with a standard in order to correct for a possible drift in the detector. [26] Due to the known ratio of sample weight to standard weight, from the relative intensities of the signal, the weigh percentage (wt%) of the desired element in the sample can be determined. [26] Figure 2.9 (b) shows a representative TXRF spectrum of a Fe-N/C catalyst with Ga as internal standard. It can be seen that various elements with different amounts are present in the sample. The formula used to determine the concentration of the desired element is as follows [26]:

$$C_i = \frac{C_{IS}N_iS_{IS}}{N_{IS}S_i} \quad (2.28)$$

where  $C_i$  is the concentration of the desired element,  $C_{IS}$  is the concentration of the standard,  $N_i$  and  $N_{IS}$  the count rates of the desired element and internal standard,  $S_{IS}$  and  $S_i$  the sensitivity factors of internal standard and desired element, respectively.

### 2.2.3 Scanning electron microscopy

Scanning Electron Microscopy (SEM) is used to get high resolution images of samples especially highlighting the topology. [27] This can give important information on the influence of synthesis conditions on morphology. The high resolution is due to the small wavelength of electrons used (0.12 Angstroms) and the magnification can range between 10 and 100000 with a excellent depth of field. [27] The electrons are usually generated in a tungsten-hairpin gun where a tungsten wire is heated and electrons are emitted. The electron beam is then focused onto the sample by applying an acceleration voltage and the interaction with the surface creates a variety of signals. This can include secondary electrons emitted from the substrate, backscattered electrons, X-rays, light, heat and transmitted electrons. [27] SEM's primary imaging method is the collection of secondary electrons and/or backscattered electrons. [27] The incident electron beam creates a splash of secondary electrons with significantly lower kinetic energies and low penetration depths. The detection of those with respect to the incident beam allows the construction of images with a high magnification and high resolution. [27] Secondary electrons are detected by

a scintillation material. [27] The material produces light upon interaction with electrons, which can be detected by a photomultiplier. [27]

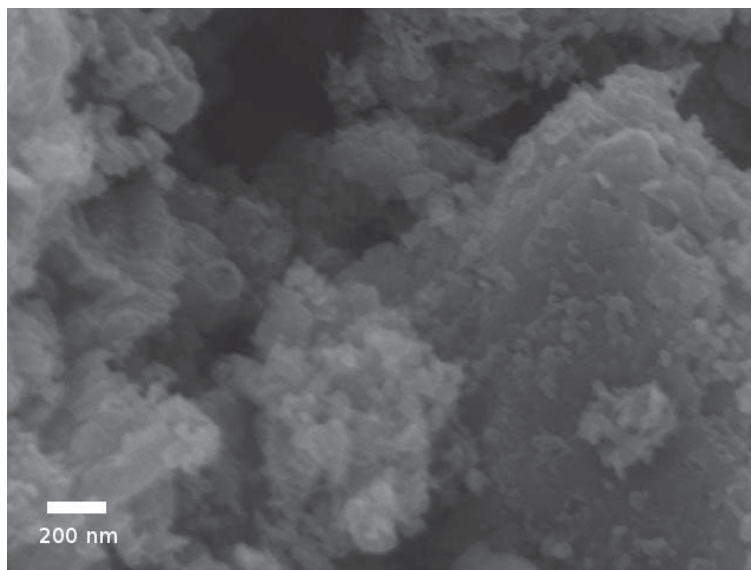


FIGURE 2.10: SEM image of a pyrolyzed  $\text{CN}_x$  catalyst.

An exemplary SEM micrograph of a pyrolyzed carbon material can be seen in Figure 2.10. Features of the particles can be identified or the morphology of the catalyst layer in an MEA can be investigated. If the sample is non-conductive, a thin layer (few nanometers) of a metal, such as chromium can be sputtered onto the specimen in order to avoid charging. [27] In a typical measurement, the samples are deposited onto metallic aluminium stubs and immobilised with carbon tape. Cross sectional samples are mounted into specifically designed sample holders. The measurement is conducted in the evacuated chamber of the instrument.

#### 2.2.4 Transmission electron microscopy

Transmission electron microscopy (TEM) is a microscopy technique capable of significantly higher resolution than optical microscopes. [28] The resolution of those is limited by the wavelength of visible light. Electrons however have a much smaller *DeBroglie*-wavelength. [28] Structures as small as some Angstroms can be resolved. TEM utilizes this fact by passing an accelerated electron beam through a thin sample. The image is created by way of differential contrast. [28] Some electrons surpass the sample, while others are stopped or deflected, thus creating a black and white image. [28] Unlike in light microscopes, the focusing of the beam is not achieved by traditional glass lenses, but

by electromagnetic fields. For very high magnifications complex wave interactions occur that contribute to the final image [28]. The resulting image is a 2D representation of the sample. These images can highlight microstructural features on the nanometer length scale. [28] The interpretation of TEM images can be challenging for amorphous materials, since the 3D sample will be reduced to a 2D image. On the other hand TEM can be useful for the investigation of crystalline domains with the possibility to identify those via the respective lattice spacing. [28]

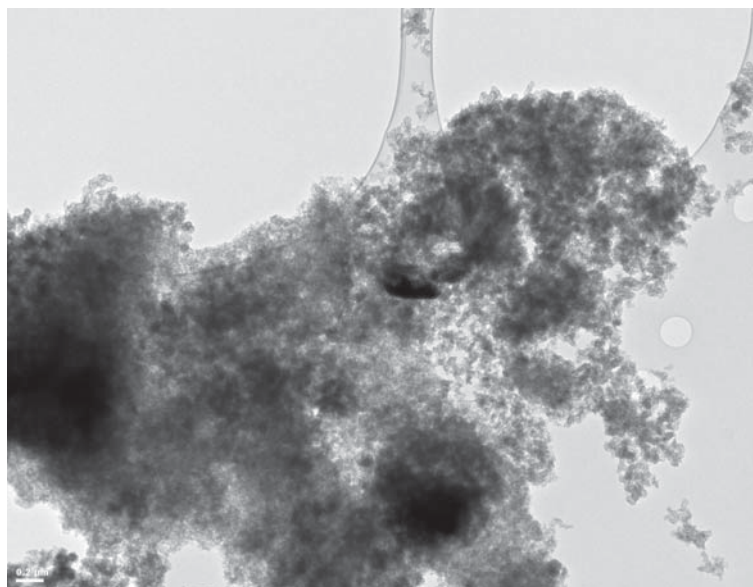


FIGURE 2.11: TEM image of a pyrolyzed Fe/Co-N/C catalyst.

Figure 2.11 shows a representative TEM image of a carbonaceous material. Usually, the samples can be deposited from a suspension onto a specific TEM grid, which consists of gold and copper and may be coated with an amorphous carbon matrix. The measurements are conducted in an evacuated chamber.

### 2.2.5 Scanning transmission electron microscopy

In contrast to TEM, scanning transmission electron microscopy (STEM) focuses the beam onto the sample and scans the sample in a raster. [29] Unlike TEM the contrast of the signal is directly proportional to the atomic number of the element. [29] A further advantage is that the beam can be used to perform electron energy loss spectroscopy (EELS) for element identification and to correlate the measurement with the observed image. [29, 30]

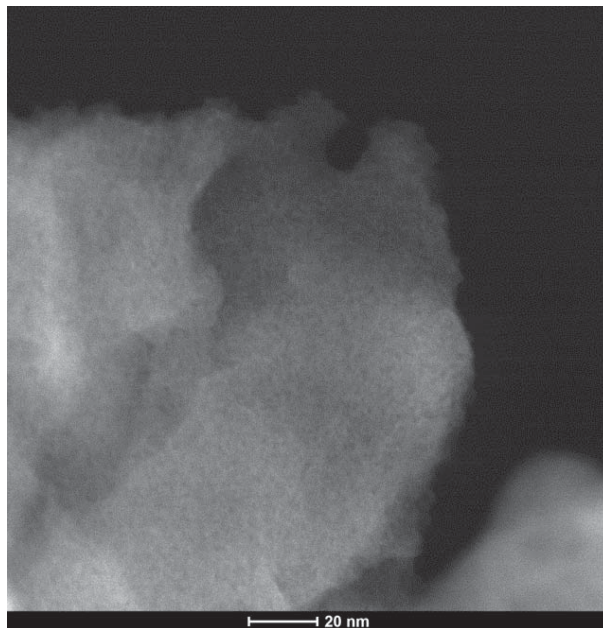


FIGURE 2.12: STEM image of a pyrolyzed Fe-N/C catalyst.

Figure 2.12 shows a STEM image of a Fe-N/C material. With the right instrumentation atomic resolution images are possible with the further possibility to identify the observed atoms with EELS. The samples can be prepared in the same way as for TEM by drop casting onto a sample carrier.

### 2.2.6 Electron energy loss and energy dispersive spectroscopy

Electron energy loss spectroscopy (EELS) is often used in combination with STEM in order to identify the observed elements and gain further information, such as on the local chemical environment. [30] When the electrons hit the sample, some will be inelastically scattered. The energy of the scattered electrons can be determined with a detector and forms a spectrum. Causes for the scattering include phonon excitations, plasmon excitations and inner shell ionisations amongst others. [30] The inner shell ionisations, which arise due to the energy loss associated with removing an electron from an atom, can be used to identify elements, since each element has specific energies of ionisation. If a certain element is present, which the incident electrons can ionize, a peak of electron energy will occur where this energy of ionisation is subtracted from the incident electron energy beam. The fine structure of the associated peak can give further information on the chemical environment. [30]

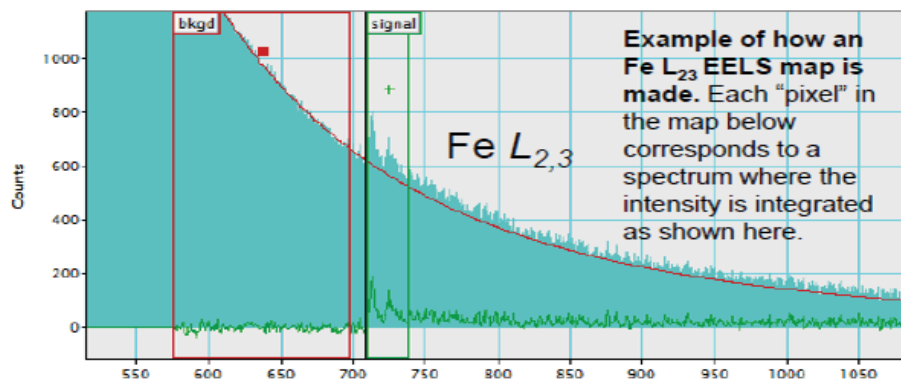


FIGURE 2.13: Representative EELS spectrum of Fe-N/C catalyst.

Figure 2.13 shows a representative EELS spectrum of a Fe-N/C catalyst, the visible peak is associated with the energy loss due to Fe ionisation. With the suitable equipment and sample, atomic spatial resolution is possible. In this study EELS has been used to verify the identity of atoms observed in STEM images and can be performed directly on the same sample in the chamber.

Energy dispersive X-ray spectroscopy (EDS) is another common technique used in conjunction with electron microscopy. [31] The principle is similar to XRF, with the difference that the mode of excitation is the removal of electrons from the atoms by the collision with incident electrons rather than X-rays. Like XRF it can be used for qualitative as well as quantitative elemental analysis, however with lower sensitivity. [31] It can be performed directly on the samples in the chamber of the electron microscope, if it is equipped with the suitable electron generator and detector. [31] EDS has been used for qualitative elemental analysis in this work.

### 2.2.7 X-ray photoelectron spectroscopy

X-ray photoelectron spectroscopy (XPS) can be used to determine the surface composition of a material. It can give information on the chemical as well as electronic state of the elements. [32] When a sample is irradiated with X-rays of well defined energy ( $E_{\text{photon}}$ ), *e.g.* from monochromatic Al  $K_{\alpha}$  rays, electrons will be ejected of which the kinetic energy  $E_{\text{kinetic}}$  can be precisely determined. [32] From the following relationship the binding energy  $E_{\text{binding}}$  can be determined [32]:

$$E_{\text{binding}} = E_{\text{photon}} - (E_{\text{kinetic}} + \phi) \quad (2.29)$$

where  $\phi$  is the work function of the material. Every element has specific binding energies for its electrons in the different orbitals. [32] Depending on the chemical environment, these energies can be shifted. Therefore it is possible to not only determine the identity of a surface species, but also its chemical state. [32] From the relative intensities, quantification is possible as well. XPS is usually conducted under ultra-high vacuum (UHV) conditions. XPS is surface specific in terms of the electrons released are from the uppermost 10 nm of the material. [32]

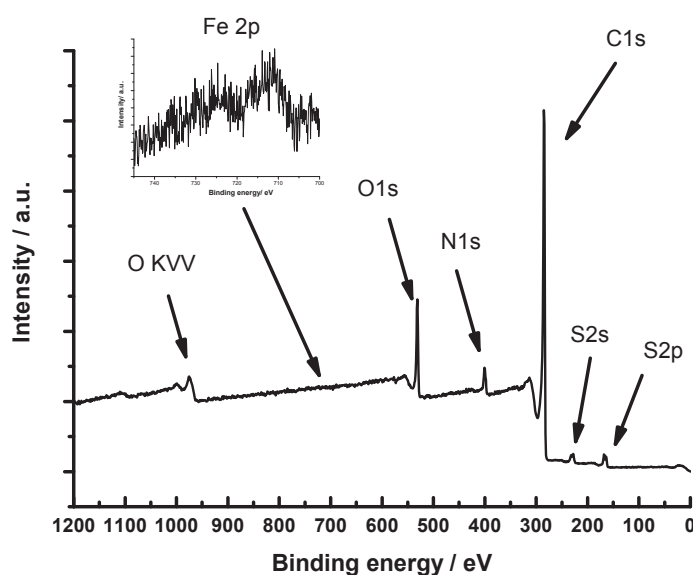


FIGURE 2.14: XPS wide scan spectrum of Fe-N/C catalyst.<sup>1</sup>

Figure 2.14 shows a representative XPS spectrum of a Fe-N/C material, where the electrons of the various elements are labelled. XPS has been used in this work in order to determine the type of nitrogen functionalities, *e.g.* pyridinic, pyrrolic etc., in the Fe-N/C material. This can be achieved by deconvolution of the nitrogen peak of the 1s electrons and comparison of the shift with tabulated literature values. [33] The determination of iron bonding properties was not possible due to the limited sensitivity. The sample has to expose a relatively flat surface to the X-ray source. A powdered sample can be prepared by pressing the powder to be analysed onto an indium substrate in order to obtain a flat pellet.

<sup>1</sup>The data analysis for this figure was performed by Dr. Emmanouil Symianakis



### 2.2.8 Temperature programmed desorption

Temperature programmed desorption (TPD) can be used to determine energies of desorption of different molecules which are adsorbed on surfaces. It is potentially possible to distinguish between physisorption and chemisorption, where latter is defined as a strong chemical interaction, typically with desorption energies exceeding 50 kJ/mol. [34] Firstly the sample surface needs to be cleaned by annealing at elevated temperature. [34] This can be done either in vacuum or under an inert atmosphere. Subsequently, the sample will be exposed to the adsorbent. Then the sample will be heated at a fixed heating rate. The amount of desorbed gas can be determined with a mass spectrometer. [34]

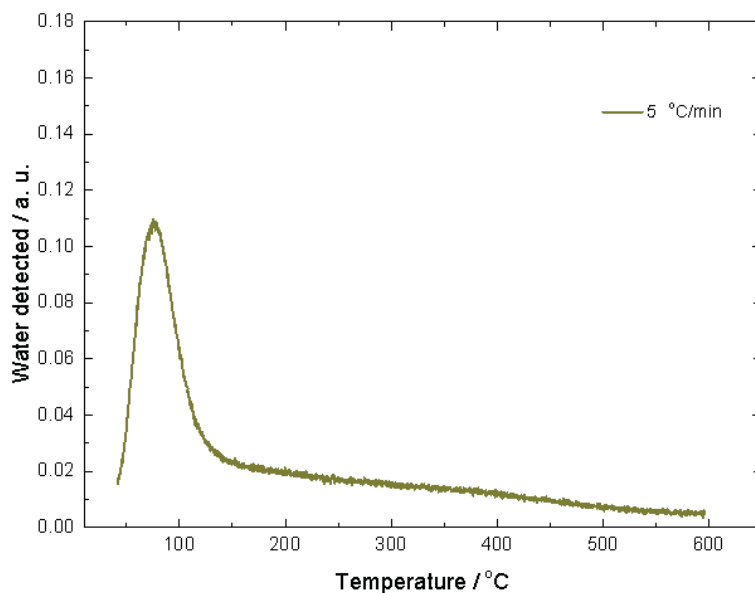


FIGURE 2.15: TPD spektrum of water adsorbed onto Fe-N/C catalyst.

Figure 2.15 shows a typical desorption measurement. Usually a peak will be observed. Varying the heating rate will shift the temperature-maximum of the observed peak and the following relationship has been derived [34]:

$$\ln \left( \frac{T_{\max}^2}{\beta} \right) = \frac{\Delta E_{\text{des}}}{RT_{\max}} + \ln \left( \frac{\Delta E_{\text{des}}}{\nu R} \right) \quad (2.30)$$

where  $T_{\max}$  is the temperature-maximum of the desorption peak,  $\beta = dT/dt$  is the heating rate,  $\Delta E_{\text{des}}$  the energy of desorption,  $R$  the universal gas constant and  $\nu$  a factor associated with the kinetics of the reaction. Thus a plot of  $\ln(T_{\max}^2/\beta)$  versus  $1/T_{\max}$  for different  $\beta$

will give a straight line with a slope of  $\Delta E_{\text{des}}/R$ . [34] TPD has been used in this study to determine the  $\text{O}_2$  energy of desorption on a Fe-N/C material. Ambient pressure under an inert Ar atmosphere have been used instead of UHV conditions. In a typical measurement, the sample is filled into a glass tube which allows the passage of carrier and adsorbent gas and can be heated. The gas flow is controlled with MFCs and the released gases are monitored with a mass spectrometer or a thermal conductivity cell (TCD).

### 2.2.9 Electron paramagnetic resonance

Electron paramagnetic resonance (EPR) gives information on unpaired electrons in a molecule or material. Due to their spin quantum number of  $s = 1/2$  and magnetic moment, electrons are subject to *Zeeman* splitting when exposed to a magnetic field. [35] They can either align with the magnetic spin component parallel ( $m_s = -\frac{1}{2}$ ) or anti-parallel ( $m_s = +\frac{1}{2}$ ) to the magnetic field. The energy difference between the two states is given by [35]:

$$\Delta E = g_e \mu_B B_0 \quad (2.31)$$

where  $g_e$  is the electron g-factor (2.0023 for the free electron),  $\mu_B$  the *Bohr* magneton and  $B_0$  the magnetic field strength. Due to the Maxwell-Boltzmann distribution the lower energy level has a higher population. [35] Absorption of a photon with the appropriate energy ( $h\nu$ ) that satisfies the resonance condition will excite the electron to the higher energy level. [35] Either the magnetic field can be varied and the sample irradiated with a fixed frequency electromagnetic wave which typically lies in the microwave region of the spectrum for electrons, or the radiation frequency can be varied while the magnetic field is kept constant. [35] In practice variation of the magnetic field is performed. [35]

Figure 2.16 (a) shows how varying the magnetic field can lead to the satisfaction of the resonance conditions. Figure 2.16 (b) shows the resulting spectrum. In EPR the derivative spectrum is plotted and the zero crossing is where the maximum of the absorption peak lies. [35] The electron  $g$ -value can be determined for all transitions in a material. Since the  $g$  factor of a free electron is a constant, the deviation from this value is caused by the interaction of the electron with local magnetic fields of the surrounding atoms. [35] EPR is particularly useful to characterise high spin transition metal complexed. If the electron

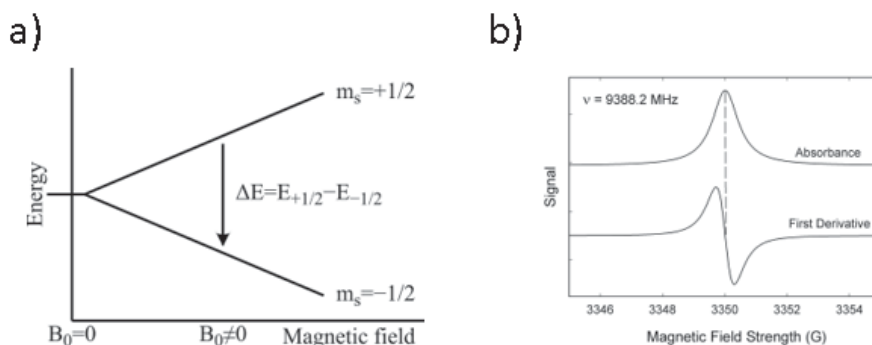


FIGURE 2.16: (a) Relationship between magnetic field and *Zeeman* splitting. (b) resulting radical EPR spectrum.[Taken from [36]]

is in the vicinity of a nucleus with a nuclear spin, it will exhibit hyperfine splitting. [35] This means that the energy levels will be split into  $2MI + 1$  lines, where  $M$  is the number of nuclei, the radical is interacting with and  $I$  the nuclear spin of those nuclei. [35] The material to be analysed was placed into a tube made of synthetic quartz in order to avoid contamination with paramagnetic impurities. The tube is inserted into a microwave cavity, which generates a standing wave at the desired frequency. Then the magnetic field strength is scanned and the response recorded. In this work EPR has been used to investigate the effect of metal doping on the radical character of the material.

### 2.2.10 Ion Chromatography

Ion Chromatography (IC) can be used for qualitative and quantitative analysis of water soluble ions in an aqueous solution. [37] An eluent is used as a mobile phase in order to flush the analyte through a column which contains the stationary phase. Based on their affinities to the stationary phase, the ions will exhibit different elution times and hence be separated. [37] After passing the column, the ions are fed through a detector. Detectors in use might be conductivity cells, UV-vis spectroscopes or mass spectrometers. [37] For anions, anion exchange materials are used as the stationary phase in the column and for cations, cation exchange materials, respectively. [37] Since each ion has a specific elution time and the magnitude of the response is proportional to the concentration in the analyte, by calibrating the instrument with the known pure ions, the technique is ideal for quantification of water soluble ions with a sensitivity in the parts per billion (ppb) range. [37]

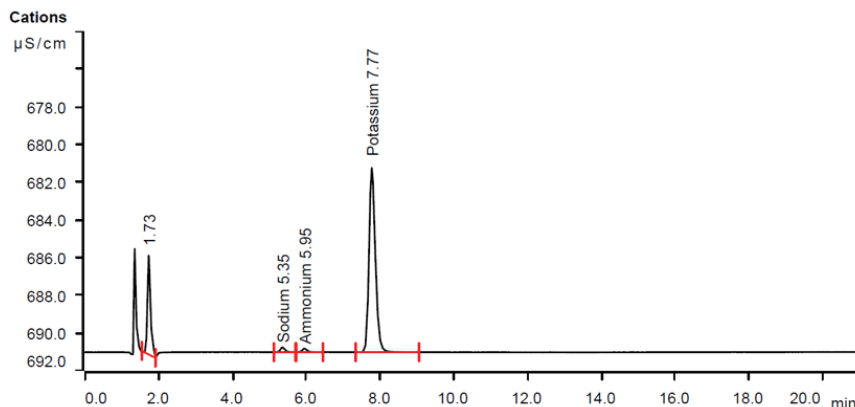


FIGURE 2.17: Representative ion chromatogram of an electrolyte, containing various ions.

Figure 2.17 shows a representative chromatogram. It can be seen that each ion will produce a peak, of which the area is correlated with its concentration. The analyte should be diluted with the eluent, to minimise fluctuation of the column environment upon injection of the sample. [37] A defined amount of sample is injected into the column by the instrument and then flushed at a defined pressure and flow rate with the eluent. A calibration curve with the pure ions at a minimum of 3 different concentrations needs to be recorded in order to correlate the measured peak area with the concentration.

### 2.2.11 Gas Chromatography

Gas chromatography (GC) can be used for qualitative and quantitative analysis of molecules that can be evaporated without decomposition, such as volatile organic compounds. [38] In GC the mobile phase is an inert carrier gas, *e.g.* He, and the stationary phase a polymer on an inert matrix. [38] Similar to IC, different compounds exhibit different elution times, based on their interaction with the column material. However, unlike IC, the analysis of uncharged molecules is possible. [38] After passing the column the organic compounds can be detected. Detectors in use include thermal conductivity detectors (TCD), flame ionisation detectors (FID) or mass spectrometers. [38]

Figure 2.18 shows a typical gas chromatogram, with cyclohexeneoxide eluting at 12.1 min and the standard mesitylene at 25.6 min. Identification is possible by determining the elution time of the pure substance under the same conditions, *e.g.* temperature of column, evaporation temperature, column type, flow rate of carrier gas etc. [38] In order to be able to quantify the components, an internal standard can be used. This is a molecule which

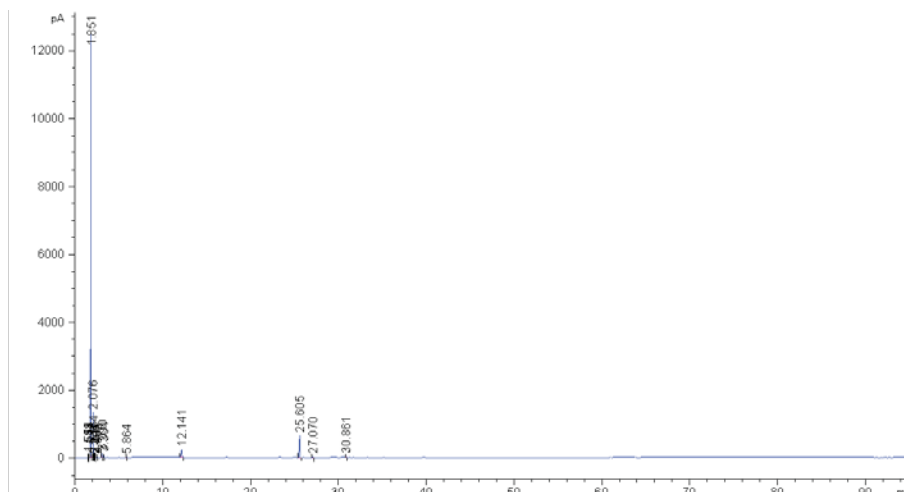


FIGURE 2.18: Representative gas chromatogram of a crude reaction mixture used in this work.

has a significantly different elution time than the other compounds of interest in the mixture and is chemically stable. [38] The response of the detector can then be calibrated with the relative response factor (RRF) method. [38] This means that a known quantity of both standard and pure compound to be quantified are measured in the same run and the peak heights are correlated. [38] For quantification, a known quantity standard is added to the crude analyte mixture. Due to the knowledge of the relative response factor, the relative heights of the peaks of the known standard can be correlated to the height of the compound to be quantified and hence the amount in the mixture determined [38]. The relationship to determine the RRF is as follows [38]:

$$RRF = \frac{Area_{\text{standard}} m_{\text{analyte}}}{Area_{\text{analyte}} m_{\text{standard}}} \quad (2.32)$$

And the amount of an unknown compound quantity in the mixture with a known standard quantity is then given by [38]:

$$m_{\text{analyte}} = RRF \frac{Area_{\text{analyte}} m_{\text{standard}}}{Area_{\text{standard}}} \quad (2.33)$$

where  $RRF$  is the relative response factor,  $Area_{\text{standard}}$ ,  $Area_{\text{analyte}}$  are the peak areas and  $m_{\text{standard}}$ ,  $m_{\text{analyte}}$  the masses in the sample solution of the standard and the compound to be analysed, respectively. In practice, a defined amount of crude sample is diluted into the sample vial with a common solvent such as acetonitrile (ACN) and the

standard is added. This sample is then injected into the GC instrument and analysed. GC has been used in this work to analyse the product mixture of an organic reaction, performed in presence of the investigated catalysts.

### 2.2.12 Mass spectrometry

Mass spectrometry (MS) performs the analysis of compounds by ionising them and separating the generated ions according to the mass to charge ratio. [39] It allows the qualitative and quantitative determination of molecules with a variety of molecular masses, from small molecules such as O<sub>2</sub> to large organic molecules or proteins. [39] Every molecule has a fragmentation pattern, which can be compared to a database and used as a fingerprint to identify unknown compounds. [39] In this work MS has been used to track the gases released upon TPD and to identify molecules in an organic mixture after separation by GC. The samples can be directly passed to the MS and ionised in an ionisation chamber. The resulting ions are then separated according to their mass to charge ratio by passage through a magnetic field, based on the *Lorentz* law and *Newton's* second law. [39] The separated ions can then be detected and quantified. [39] Various different methods of ionisation can be used. [39] Electron ionisation (EI) and electron spray ionisation (ESI) have been used in the utilised instruments.

## 2.3 References

- [1] Paulus U.A., Schmidt T.J., Gasteiger H.A., Behm R.J. Oxygen reduction on a high-surface area Pt/Vulcan carbon catalyst: a thin-film rotating ring-disk electrode study. *Journal of Electroanalytical Chemistry*, 495(2), 134–145, January 2001. doi:10.1016/S0022-0728(00)00407-1.
- [2] Bard A.J., Faulkner L.R. *Electrochemical Methods: Fundamentals and Applications*. Wiley, New York, 2nd edition, December 2000. ISBN 978-0-471-04372-0.
- [3] Qi Z. Electrochemical Methods for Catalyst Activity Evaluation. In J. Zhang, editor, *PEM Fuel Cell Electrocatalysts and Catalyst Layers*, pages 547–607. Springer London, 2008. ISBN 978-1-84800-935-6 978-1-84800-936-3. doi:10.1007/978-1-84800-936-3\_11.

- [4] Schmidt T.J., Gasteiger H.A., Stäb G.D., Urban P.M., Kolb D.M., et al. Characterization of High-Surface-Area Electrocatalysts Using a Rotating Disk Electrode Configuration. *Journal of The Electrochemical Society*, 145(7), 2354–2358, January 1998. doi:10.1149/1.1838642.
- [5] Biddinger E.J., von Deak D., Singh D., Marsh H., Tan B., et al. Examination of Catalyst Loading Effects on the Selectivity of CN<sub>x</sub> and Pt/VC ORR Catalysts Using RRDE. *Journal of The Electrochemical Society*, 158(4), B402–B409, January 2011. doi:10.1149/1.3552944.
- [6] Zhang L., Song C., Zhang J., Wang H., Wilkinson D.P. Temperature and pH Dependence of Oxygen Reduction Catalyzed by Iron Fluoroporphyrin Adsorbed on a Graphite Electrode. *Journal of The Electrochemical Society*, 152(12), A2421–A2426, January 2005. doi:10.1149/1.2109667.
- [7] Wu G., More K.L., Johnston C.M., Zelenay P. High-Performance Electrocatalysts for Oxygen Reduction Derived from Polyaniline, Iron, and Cobalt. *Science*, 332(6028), 443–447, April 2011. doi:10.1126/science.1200832.
- [8] Chlistunoff J. RRDE and Voltammetric Study of ORR on Pyrolyzed Fe/Polyaniline Catalyst. On the Origins of Variable Tafel Slopes. *The Journal of Physical Chemistry C*, 115(14), 6496–6507, April 2011. doi:10.1021/jp108350t.
- [9] Bonnacaze R.T., Mano N., Nam B., Heller A. On the Behavior of the Porous Rotating Disk Electrode. *Journal of The Electrochemical Society*, 154(2), F44–F47, January 2007. doi:10.1149/1.2403082.
- [10] Malko D. *The oxygen reduction reaction (ORR) catalyzed by non precious metal/nitrogen/carbon composites*. Master thesis, FAU Erlangen-Nürnberg/Imperial College London, 2013.
- [11] Shao M., editor. *Electrocatalysis in Fuel Cells*, volume 9 of *Lecture Notes in Energy*. Springer London, London, 2013. ISBN 978-1-4471-4910-1 978-1-4471-4911-8.
- [12] Girault H.H. *Analytical and Physical Electrochemistry*. EPFL Press, Lausanne:New York, 1st edition, October 2004. ISBN 978-0-8247-5357-3.
- [13] Lasia A. *Electrochemical Impedance Spectroscopy and its Applications*. Springer, New York, NY, June 2014. ISBN 978-1-4614-8932-0.

- [14] Barsoukov E., Macdonald J.R., editors. *Impedance Spectroscopy: Theory, Experiment, and Applications*. Wiley-Interscience, Hoboken, N.J, 2nd edition, March 2005. ISBN 978-0-471-64749-2.
- [15] van der Vliet D., Strmcnik D.S., Wang C., Stamenkovic V.R., Markovic N.M., et al. On the importance of correcting for the uncompensated Ohmic resistance in model experiments of the Oxygen Reduction Reaction. *Journal of Electroanalytical Chemistry*, 647(1), 29–34, August 2010. doi:10.1016/j.jelechem.2010.05.016.
- [16] Boukamp B.A. A Linear Kronig-Kramers Transform Test for Immittance Data Validation. *Journal of The Electrochemical Society*, 142(6), 1885–1894, January 1995. doi:10.1149/1.2044210.
- [17] Schönleber M., Ivers-Tiffée E. Approximability of impedance spectra by RC elements and implications for impedance analysis. *Electrochemistry Communications*, 58, 15–19, September 2015. doi:10.1016/j.elecom.2015.05.018.
- [18] Schönleber M., Klotz D., Ivers-Tiffée E. A Method for Improving the Robustness of linear Kramers-Kronig Validity Tests. *Electrochimica Acta*, 131, 20–27, June 2014. doi:10.1016/j.electacta.2014.01.034.
- [19] Ecochemie Metrohm. Autolab Application Note EC07. [http://www.ecochemie.nl/download/Applicationnotes/Autolab\\_Application\\_Note\\_EC07.pdf](http://www.ecochemie.nl/download/Applicationnotes/Autolab_Application_Note_EC07.pdf). Accessed: 2016-10-16.
- [20] Zhang J., editor. *PEM Fuel Cell Electrocatalysts and Catalyst Layers: Fundamentals and Applications*. Springer, London, November 2008. ISBN 978-1-84800-935-6.
- [21] Zhang H., Wang X., Zhang J., Zhang J. Conventional Catalyst Ink, Catalyst Layer and MEA Preparation. In J. Zhang, editor, *PEM Fuel Cell Electrocatalysts and Catalyst Layers*, pages 889–916. Springer London, 2008. ISBN 978-1-84800-935-6 978-1-84800-936-3. doi:10.1007/978-1-84800-936-3\_19.
- [22] Langmuir I. THE CONSTITUTION AND FUNDAMENTAL PROPERTIES OF SOLIDS AND LIQUIDS. PART I. SOLIDS. *Journal of the American Chemical Society*, 38(11), 2221–2295, November 1916. doi:10.1021/ja02268a002.



- [23] Brunauer S., Emmett P.H., Teller E. Adsorption of Gases in Multimolecular Layers. *Journal of the American Chemical Society*, 60(2), 309–319, February 1938. doi:10.1021/ja01269a023.
- [24] Lowell S., Shields J.E., Thomas M.A., Thommes M. *Characterization of Porous Solids and Powders: Surface Area, Pore Size and Density*. Springer Science & Business Media, April 2006. ISBN 978-1-4020-2302-6.
- [25] Barrett E.P., Joyner L.G., Halenda P.P. The Determination of Pore Volume and Area Distributions in Porous Substances. I. Computations from Nitrogen Isotherms. *Journal of the American Chemical Society*, 73(1), 373–380, January 1951. doi:10.1021/ja01145a126.
- [26] Klockenkämper R., von Bohlen A. *Total-Reflection X-Ray Fluorescence Analysis and Related Methods*. John Wiley & Sons, December 2014. ISBN 978-1-118-98587-8.
- [27] Reimer L. *Scanning Electron Microscopy: Physics of Image Formation and Microanalysis*. Springer Science & Business Media, September 1998. ISBN 978-3-540-63976-3.
- [28] Williams D.B., Carter C.B. *Transmission Electron Microscopy: A Textbook for Materials Science*. Springer, 2nd edition, August 2009. ISBN 978-0-387-76502-0.
- [29] Pennycook S.J., Nellist P.D., editors. *Scanning Transmission Electron Microscopy: Imaging and Analysis*. Springer, March 2011. ISBN 978-1-4419-7199-9.
- [30] Egerton R.F. *Electron Energy-Loss Spectroscopy in the Electron Microscope*. Springer Science & Business Media, 1996. ISBN 978-0-306-45223-9.
- [31] Bell D.C., Garratt-Reed A.J. *Energy Dispersive X-ray Analysis in the Electron Microscope*. Garland Science, July 2003. ISBN 978-0-203-48342-8.
- [32] van der Heide P. *X-ray Photoelectron Spectroscopy: An introduction to Principles and Practices*. Wiley, Hoboken, N.J, 1st edition, December 2011. ISBN 978-1-118-06253-1.
- [33] Pels J.R., Kapteijn F., Moulijn J.A., Zhu Q., Thomas K.M. Evolution of nitrogen functionalities in carbonaceous materials during pyrolysis. *Carbon*, 33(11), 1641–1653, January 1995. doi:10.1016/0008-6223(95)00154-6.

- [34] Rakić V., Damjanović L. Temperature-Programmed Desorption (TPD) Methods. In A. Auroux, editor, *Calorimetry and Thermal Methods in Catalysis*, number 154 in Springer Series in Materials Science, pages 131–174. Springer Berlin Heidelberg, 2013. ISBN 978-3-642-11953-8 978-3-642-11954-5. doi:10.1007/978-3-642-11954-5\_4.
- [35] Wertz J.E., Bolton J.R. *Electron spin resonance: elementary theory and practical applications*. Chapman and Hall, 1986. ISBN 978-0-412-01161-0.
- [36] Wikipedia. Electron paramagnetic resonance. [https://en.wikipedia.org/wiki/Electron\\_paramagnetic\\_resonance](https://en.wikipedia.org/wiki/Electron_paramagnetic_resonance). Accessed: 2016-09-14.
- [37] Fritz J.S., Gjerde D.T. *Ion Chromatography*. John Wiley & Sons, March 2009. ISBN 978-3-527-32052-3.
- [38] McNair H.M., Miller J.M. *Basic Gas Chromatography*. Wiley-Interscience, Hoboken, N.J, 2nd edition, July 2009. ISBN 978-0-470-43954-8.
- [39] de Hoffmann E., Stroobant V. *Mass Spectrometry: Principles and Applications*. Wiley-Interscience, 3rd edition, October 2007. ISBN 978-0-470-03311-1.

*A synthesis procedure for M-N/C catalysts is presented. The oxidative polymerisation of 1,5-diaminonaphthalene in the presence of a metal salt and subsequent pyrolysis is a facile way to synthesise active ORR catalysts. The resulting materials are characterised and it is found that the microporous area seems to be important for a high ORR activity. The metal centre has a profound effect on the ORR activity and the electronic properties of the material as determined by EPR. Electron microscopy reveals atomic iron centres in the Fe-N/C material. The analysis suggests that the catalyst shares the same set of highly active sites as other high performing catalysts described in literature. This catalyst is therefore used as a model in order to study the active site in subsequent chapters.*

## Chapter 3

# Synthesis and characterisation of M-N/C catalysts

### 3.1 Introduction

Typical routes to the synthesis of highly active non-precious metal catalysts are discussed in Chapter 1. In short, a carbon support or a template is mixed with a metal source (typically iron) and a nitrogen source. This precursor mixture is heated under inert atmosphere at 700 to 1000 °C. [1–3] The resulting material is then leached by heating in acid. When a template is used, such as SiO<sub>2</sub>, the catalyst has to be leached with HF in order to remove the template. [1–3] A second heat treatment has shown to increase the ORR activity. [1–3] If heated in ammonia gas the activity can be significantly increased, however at the expense of stability. [1–4] It has been speculated that this increase in

activity comes from the formation of axial ligands, improving electronic structure and proton transport capability of the active site. [1–4]

Although highly active catalysts have been synthesised, due to the complex composition in the precursor mixture, it has been challenging to establish structure property relationships. [1–4]

In this chapter a procedure is presented which allows the synthesis of a self-supporting catalyst. This means the need to include a carbon support or a templating agent is removed. The simplification of the synthesis allows identification of some structure property relationships. The material will be physically characterised by various techniques, with an emphasis on microstructure and the influence of a metal species on the properties of the material. It will be shown that this facile synthesis yields a catalyst which is similar and most likely contains the same types of active sites as other catalysts reported in the literature. Therefore, the study of the catalyst developed here in the subsequent chapters can be representative for most **M-N/C** catalysts, with a focus on atomic **Fe-N/C** sites.

The chapter builds on result obtained during a preceding masters project, where the study of different precursors led to the discovery that the use of polymerised 1,5-diaminonaphthalene in combination with a metal as precursor will yield a high surface area material which does not require addition of carbon black as additive. [5] A general trend has been found that addition of Fe and Co beyond 1 wt% led to an increase of graphitization, which was detrimental for the activity. [5] Based on these results, the synthesis has been optimised and conditions varied to obtain structure property relationship.

## 3.2 Results and Discussion

### 3.2.1 A catalyst based on poly-1,5-Diaminonaphthalene and its ORR activity<sup>1</sup>

The general procedure to obtain a high surface area catalyst from 1,5-diaminonaphthalene is shown in Figure 3.1 (a). Catalyst precursors were synthesized in a simple one pot process at room-temperature by dispersion of an appropriate diamine in ethanol with addition of ammonium persulfate to promote the formation of oligomers. The formation of oligomers

---

<sup>1</sup>This section is largely an excerpt of work published in Ref. [6]

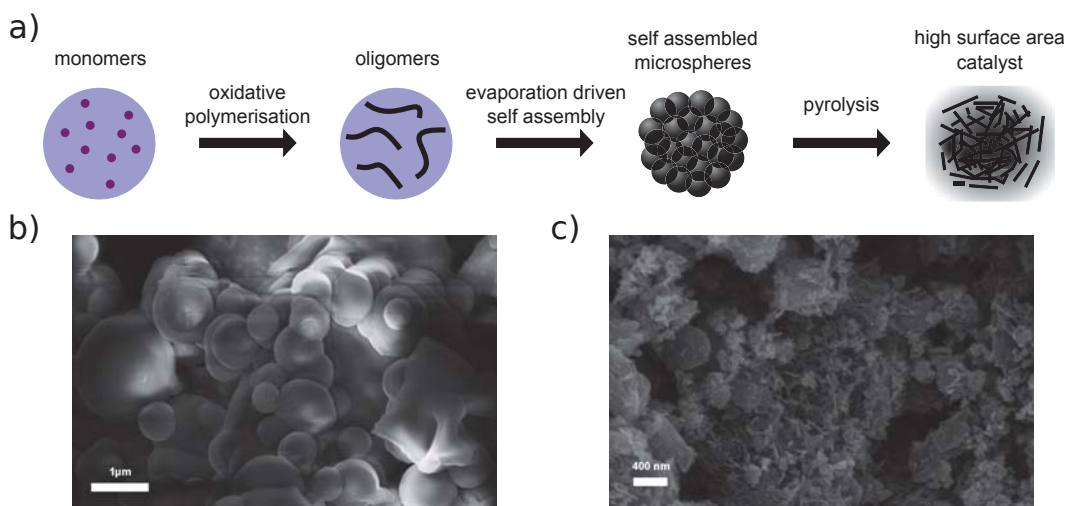


FIGURE 3.1: (a) Schematic, depicting the synthesis procedure of the catalyst (b) Scanning Electron Microscopy image of polymerized 1,5-diaminonaphthalene as precursor for the ODAN catalyst (c) Scanning Electron Microscopy image of ODAN catalyst material after heat treatment at 1000 °C for 2 h.

was confirmed in a previous study by UV-Vis spectroscopy and mass spectrometry. [5, 6] After 24h the temperature was raised to 80 °C, thereby removing the solvent. Upon polymerisation, the precursor formed self-assembled nanospheres, which was verified by scanning electron microscopy (Figure 3.1 (b)). The catalyst precursors were then subjected to heat treatment in a tube furnace at 1000 °C in an inert atmosphere for 2 h in order to obtain the final catalysts, with **ODAN** denoting a catalyst where no additional transition metal salt was added. The pyrolysis step promotes a number of chemical transformations towards achieving high electrically conductive and high surface area carbon materials, *e.g.* nitrogen and sulphur, which possess a desirable morphology (Figure 3.1) and a high electrocatalytic activity towards the ORR. The electrical conductivity of **ODAN** was determined as per modified literature method to be as high as  $100 \text{ S m}^{-1}$  under a compression of 2 MPa, a value that is comparable to that measured for highly conductive carbon blacks. [7] In this study, catalysts synthesized with addition of  $\text{FeCl}_2$  and  $\text{CoCl}_2$  to the ethanolic monomer solution and in the absence of an additional oxidant were also assessed. It was found in previous work that these metal cation species facilitate the oxidative polymerization. [5] Presumably, this occurs via the autoxidation to the metal +3 species by oxygen in this solution, a phenomenon already described for ferrous ions in water. [8] Co and Fe containing catalysts were synthesized with a high metal content of 2.2/0.9 molar ratio monomer/metal ion or 14 wt% monomer of Fe denoted as **Fe-ODAN-14%** and 16 wt% Co respectively denoted as **Co-ODAN-16%**. In an optimised procedure 1 wt% of Fe denoted as **Fe-ODAN-1%** in combination

with the oxidant  $(\text{NH}_4)_2\text{S}_2\text{O}_8$  was used. The surface area of the catalysts was determined by nitrogen adsorption analysis

TABLE 3.1: External, microporous and total surface area (SA) of the respective catalysts, as determined by nitrogen adsorption analysis.

Catalyst	External SA [ $\text{m}^2\text{g}^{-1}$ ]	Microporous SA [ $\text{m}^2\text{g}^{-1}$ ]	Total SA [ $\text{m}^2\text{g}^{-1}$ ]
ODAN	126	488	614
Fe-ODAN-1%	116	362	478
Fe-ODAN-14%	203	188	391
Co-ODAN-16%	38.5	26.5	65.0

The catalyst without any addition of metal salt (**ODAN**) has a BET surface area as high as  $614 \text{ m}^2 \text{ g}^{-1}$ , the catalyst **Fe-ODAN-14%**  $391 \text{ m}^2 \text{ g}^{-1}$ , the catalyst **Fe-ODAN-1%**  $493 \text{ m}^2 \text{ g}^{-1}$  and the catalyst **Co-ODAN-16%**  $64 \text{ m}^2 \text{ g}^{-1}$ . This suggests that metal ions promote carbon materials with lower surface areas. The analysis of the external *versus* microporous surface area is shown in Table 3.1. While for the catalyst **ODAN** and **Fe-ODAN-1%**, the contributions of microporous surface area is larger than that of external surface area, it is reversed for the catalysts **Fe-ODAN-14%** and **Co-ODAN-16%**. It seems that the addition of metal salts leads to the formation of a less microporous carbon framework.

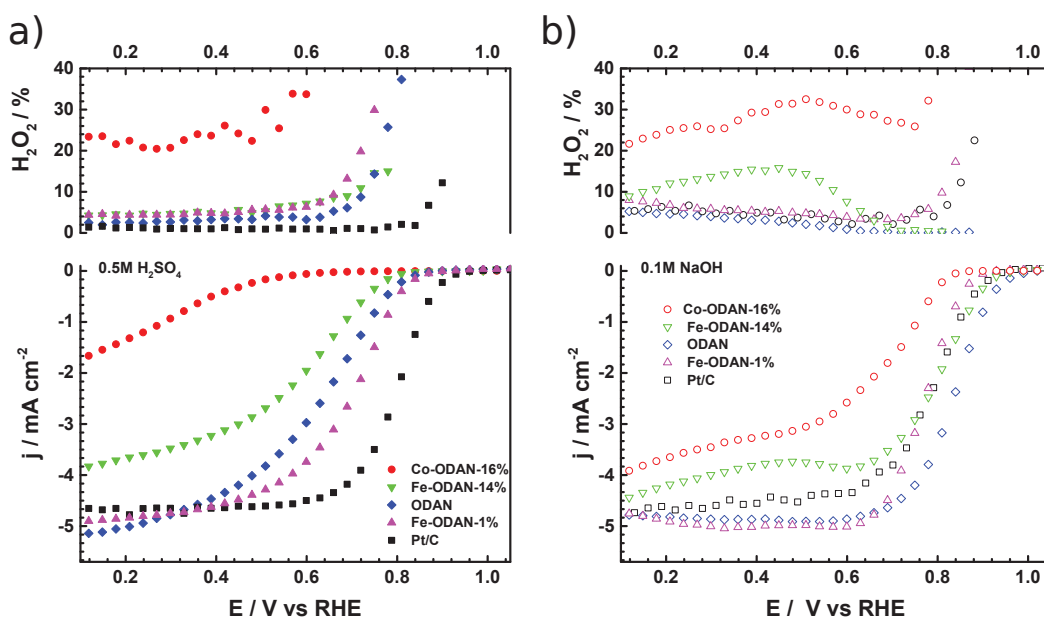


FIGURE 3.2: (a) Steady-state RRDE measurements in 0.5 M  $\text{H}_2\text{SO}_4$ , rotating speed: 1600 rpm, 30 s hold, 30 mV step potential, catalyst loading: non-precious metal catalysts:  $750 \mu\text{g cm}^{-2}$ , Pt/C:  $60 \mu\text{g}_{\text{Pt}} \text{ cm}^{-2}$ ,  $\text{O}_2$ -saturated at 1 atm (bottom) ORR activity (top) peroxide yield (b) in 0.1 M NaOH. [Adapted with permission from Ref. [6]]

The catalytic activity and 4 electron selectivity of the catalysts towards the ORR was assessed along with a reference Pt/C catalyst using the Rotating Ring Disc Electrode (RRDE) method, with cross-comparison at 1600 rpm (Figure 3.2). The mass activity of the Pt/C catalyst at 0.9 V *vs* RHE is 0.02 A mg<sup>-1</sup>. This is lower than the 0.07 - 0.18 A mg<sup>-1</sup>, which is reported as state of the art activities of similar catalysts. [9] This difference is attributed to the different measurement regime. Here, in order to allow for a suitable comparison, the RDE measurement was conducted at steady state, i.e. 30 s hold at the respective potential *versus* 20 mV s<sup>-1</sup> (see also 2.1.1). This leads to a lower activity due to the increasing oxygen coverage at this potential. [9] The adsorbing nature of the SO<sub>4</sub><sup>2-</sup> anion as compared to the typically used HClO<sub>4</sub> electrolyte further impacts the activity negatively. [9] However, these conditions were deemed more suitable for a cross comparison of the NPMCs than the typically employed advantageous conditions used for the investigation of Pt, as most experiments with NPMCs in literature are conducted in H<sub>2</sub>SO<sub>4</sub>. [18]

To ensure that no ORR active precious metal contamination was introduced into the electrochemical cell, a RRDE with a glassy carbon disc and gold ring together with a glassy carbon counter electrode was chosen. Among the various catalysts synthesized, the metal-free synthesized **ODAN** showed a remarkably high ORR activity under alkaline conditions, which surpasses the activity of the Pt catalyst used in this study (Figure 3.2 (b)). Although it has to be mentioned that a higher loading of NPMC was used. It shows a 40 mV reduction in overpotential ( $\sim 70$  mV at half-wave potential) *vs* Pt/C, determined by extrapolating the tangent at the half wave potential towards zero current. Additionally, the catalysts **ODAN** and **Fe-ODAN-1%** with only 1 wt% Fe perform also well in 0.5 M H<sub>2</sub>SO<sub>4</sub>, conditions that are not an unreasonable representation of the acidic environment in an operating fuel cell. **Fe-ODAN-1%** performs slightly better than **ODAN** and shows an only  $\sim 50$  mV increase in ORR overpotential ( $\sim 100$  mV at half-wave potential) *vs* Pt/C (Figure 3.2 (a)). The oxygen reduction pathway to the desirable water (4e<sup>-</sup>) *versus* the detrimental hydrogen peroxide (2e<sup>-</sup>) was assessed. For the **ODAN** catalyst, the electron transfer number was assessed indirectly with a *Koutecky-Levich* analysis to be  $\sim 4$  in 0.5 M H<sub>2</sub>SO<sub>4</sub> and  $\sim 3.6$  in 0.1 M NaOH.<sup>2</sup> The peroxide yield of the catalysts was determined via the oxidation at the ring (2.1.1). For the catalysts **Fe-ODAN-1%** and **ODAN** peroxide yield is below 4% measured in 0.5 M H<sub>2</sub>SO<sub>4</sub> and below 8% in 0.1 M NaOH, which is

<sup>2</sup>This is the net electron transfer number and might include the case where H<sub>2</sub>O<sub>2</sub> is produced but then autocatalytically decomposed within the catalyst layer

comparable to the Pt catalyst and shows that the reduction favours the formation of water. The catalysts with a higher metal content **Fe-ODAN-14%** and **Co-ODAN-16%** showed a significantly higher peroxide yield, especially in alkaline medium. Striking is the high peroxide yield of the Co containing catalyst of 20 - 30% in the potential region between 0.6 V and 0.2 V *vs* RHE. This selectivity might be exploited to create efficient hydrogen peroxide forming catalysts.

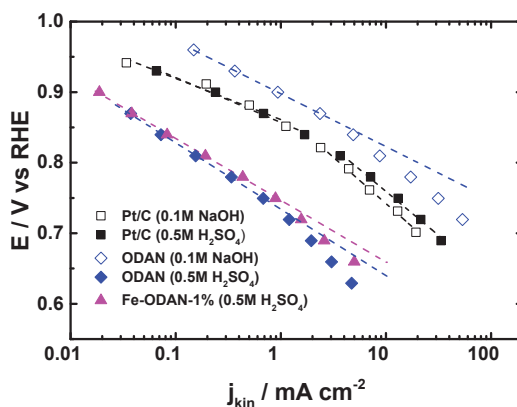


FIGURE 3.3: *Tafel*-plots<sup>3</sup> of selected catalysts in 0.5 M H<sub>2</sub>SO<sub>4</sub> and 0.1 M NaOH corresponding to the measurements in Figure 3.2. [Adapted with permission from Ref. [6]]

The *Tafel*-plot of the kinetic current density (Figure 3.3) shows the typical 2 slopes for Pt/C of  $\sim 60$  mV dec<sup>-1</sup> and  $\sim 120$  mV dec<sup>-1</sup>, both in 0.1 M NaOH and 0.5 M H<sub>2</sub>SO<sub>4</sub>. [10] The catalyst **ODAN** in 0.5 M H<sub>2</sub>SO<sub>4</sub> as well as in 0.1 M NaOH and the catalyst **Fe-ODAN-1%** in 0.5 M H<sub>2</sub>SO<sub>4</sub> are shown in the same plot as the Pt/C catalyst (Figure 3.3) with *Tafel* slopes of  $\sim 94$  mV dec<sup>-1</sup>,  $\sim 75$  mV dec<sup>-1</sup> and  $\sim 89$  mV dec<sup>-1</sup>, respectively.

TABLE 3.2: Mass activities and volumetric current densities of selected catalysts. Values taken at the respective potential *versus* RHE in the RDE setup at room temperature and are not mass transport corrected.

Catalyst	Electrolyte	Potential [V <i>vs.</i> RHE]	Mass activity [A g <sup>-1</sup> ]	Volumetric current* [A cm <sup>-3</sup> ]
ODAN	0.5M H <sub>2</sub> SO <sub>4</sub>	0.8	0.40	0.16
Fe-ODAN-1%	0.5M H <sub>2</sub> SO <sub>4</sub>	0.8	0.67	0.27
Fe-ODAN-14%	0.5M H <sub>2</sub> SO <sub>4</sub>	0.8	0.13	0.052
ODAN	0.1M NaOH	0.9	1.1	0.44
Fe-ODAN-1%	0.1M NaOH	0.9	0.065	0.026
Fe-ODAN-14%	0.1M NaOH	0.9	0.67	0.27

\* Assuming a catalyst layer density of 0.4 g cm<sup>-3</sup>

<sup>3</sup>The kinetic current density was obtained by correcting the RDE data with the well known mass transport correction as described in 4.4.5.



To enable comparison to other non-precious metal catalysts, Table 3.2 shows the mass activities and volumetric current densities of the best catalysts at 0.8 V *vs* RHE in acidic and 0.9 V *vs* RHE in alkaline electrolyte. Durability testing has been performed on the **ODAN** catalyst in previous work following a standard DoE protocol. [11] It has been found that the main degradation takes place during the first 100 cycles, approaching a low level of degradation thereafter. [5, 6] This is important for technological applications. The high activity of the metal free **ODAN** catalyst is striking. It is known in literature that even trace amounts of transition metal contamination can significantly increase the ORR activity. [12] Therefore, the catalyst was subjected to neutron activation analysis (NAA), a highly sensitive and reliable technique, suitable for trace metal analysis down to the low ppm level. [13] The NAA result of **ODAN** after being subjected to reflux in 0.5 M H<sub>2</sub>SO<sub>4</sub> for 8 h shows a concentration of 7 ppm, 10 ppm and 732 ppm by weight of Co, Fe and Mn, respectively. No other transition metals or precious metals were detected. Therefore, the higher activity than usually observed for metal free catalysts under acidic conditions might be due to Mn contamination. In the following section (3.2.2), a metal free catalyst will be synthesised, where meticulous care will be taken to avoid metal contamination. This catalyst will show a lower activity.

It is well known in literature that a higher catalyst loading can change the apparent peroxide yield detected on the ring. [14, 15] If a 2+2 mechanism is present, the thicker catalyst layer will allow the further reduction of peroxide before it can diffuse out of the layer, thereby reducing the observed yield and making it difficult to assess the true electron transfer number. [14, 15] Therefore, there might be different types of active sites, as suggested in literature. [16, 17] Firstly the desirable active sites that promote the true 4 electron pathway. Secondly active sites which predominantly promote a 2 electron pathway with or without the capability to further reduce peroxide and lastly a type of active site that predominantly reduces peroxide. [16, 17] All active sites might be present within the catalyst at the same time. [16, 17] If a high enough number of the 2 electron active sites is present, a lower loading of catalyst will show a higher measured peroxide yield at the ring. [16–18]

Therefore, the best performing acid catalyst **Fe-ODAN-1%** was tested at different loadings (Figure 3.4). It can be clearly seen that for this catalyst the peroxide yield seems to be independent of loading. This indicates a high proportion of 4 electron active sites.

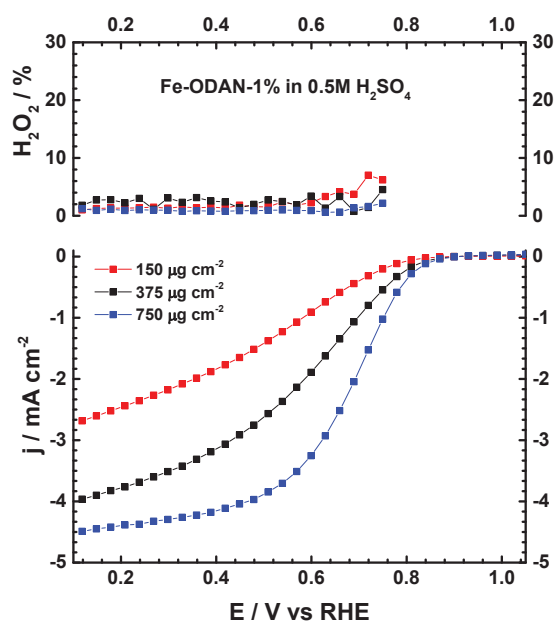


FIGURE 3.4: Steady-state RRDE measurements in 0.5 M  $H_2SO_4$  at different catalyst loadings, rotating speed: 1600 rpm, 30 s hold, 30 mV step potential,  $O_2$ -saturated at 1 atm. [Adapted with permission from Ref. [6]]

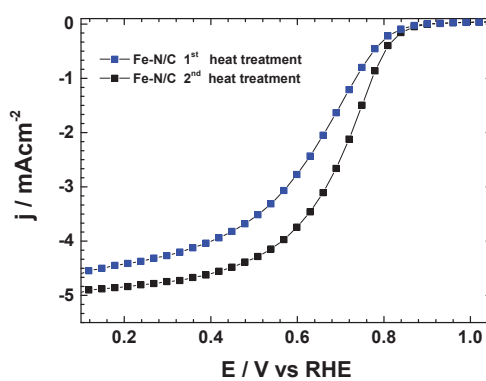


FIGURE 3.5: Steady-state RDE measurements of Fe-N/C catalyst in 0.5 M  $H_2SO_4$  after first and second heat treatment, catalyst loading:  $750 \mu g cm^{-2}$  rotating speed: 1600 rpm, 30 s hold, 30 mV step potential,  $O_2$ -saturated at 1 atm.

As it has been shown in literature, that the performance of the catalyst can be increased by subjecting it to a second heat treatment step [2], the best acid performing catalyst **Fe-ODAN-1%** was subjected to a second heat treatment under nitrogen, at 900 °C for 2 hours. Figure 3.5 shows the effect. A clear increase in activity can be seen. It can be seen that the catalyst reaches the mass transport limiting region at higher potentials and a shift in half-wave potential of  $\sim 70$  mV is present. The increase of activity has been attributed to i) the formation of new active sites, stemming from iron which has been leached from metallic residual particles and was coordinated by nitrogen functionalities on the surface. ii) the gasification of unstable carbon components which formed after the acid treatment, improving on the one hand mass transport properties and on the other hand exposing buried iron sites to the surface. Nitrogen adsorption has been used to examine the effect of the second heat treatment on the microstructure.

TABLE 3.3: External, microporous and total surface area (SA) of the Fe-N/C catalyst after first and second heat treatment, as determined by nitrogen adsorption analysis.

Catalyst	External SA [ $\text{m}^2\text{g}^{-1}$ ]	Microporous SA [ $\text{m}^2\text{g}^{-1}$ ]	Total SA [ $\text{m}^2\text{g}^{-1}$ ]
1 <sup>st</sup> heat	116	362	478
2 <sup>nd</sup> heat	38.0	418	457

As can be seen in Table 3.3, the second heat treatment does not significantly increase the total surface area, but significantly increases the microporous surface area. This would be consistent with the notion that the second heat treatment makes active sites accessible, if those were hosted in the micropores as suggested in literature. [4]

A further investigation into the effect of the second heat treatment is necessary in order to gain a better understanding. The catalyst **Fe-ODAN-1%** which was subjected to the second heat treatment is termed **Fe-N/C** henceforth throughout this thesis.

**To summarise:** Active non-precious metal catalysts can be synthesised by polymerising 1,5-diaminonaphthalene in the presence of a transition metal salt, such as  $\text{FeCl}_2$ , and pyrolysing this precursor under an inert atmosphere. The resulting material has a high surface area and resembles amorphous carbon in its physical properties. The synthesis has been described and optimised in this section. The catalyst showed a high activity in alkaline and acid, which is comparable to other high performing Fe-N/C catalyst reported in literature. A contamination with trace amounts of Mn is presumably the reason for the high acidic ORR activity of the catalyst without addition of a transition metal salt during

the synthesis (**ODAN**). The addition of 1 wt% Fe to the precursor resulted in a material which showed the highest activity under acidic conditions. A second heat treatment step improves the activity further.

### 3.2.2 Effect of metal centre on ORR activity

Due to the fact that the **ODAN** catalyst showed a significant amount of Mn contamination and it is reported in literature that even trace amounts can improve the activity, the effect of the transition metal centre on the ORR was probed for this catalyst. [12] The optimised **Fe-N/C** catalyst was used as a model, where Fe was substituted by other transition metals. In order to obtain a baseline catalyst, a metal free catalyst **N/C** was synthesised, where meticulous care was taken to prevent any transition metal contamination. The precursor 1,5-diaminonaphthalene was recrystallised twice and an oxidant with a high purity was used. Furthermore, the glassware was cleaned with concentrated and oxidising acids. Additionally, catalysts with various 3d, 4d and 5d transition metals were synthesised, by varying the metal salt, while keeping all other conditions constant.

TABLE 3.4: External, microporous and total surface area (SA) of the catalysts with different metal centres, as determined by nitrogen adsorption analysis.

Catalyst	External SA [ $\text{m}^2\text{g}^{-1}$ ]	Microporous SA [ $\text{m}^2\text{g}^{-1}$ ]	Total SA [ $\text{m}^2\text{g}^{-1}$ ]
Ir-N/C	106	448	554
Rh-N/C	106	427	533
Ru-N/C	102	258	360
Fe-N/C	38.0	418	457
Mn-N/C	42.0	55.0	98.0
Cr-N/C	65.0	314	379
Ni-N/C	75.0	330	405
Co-N/C	28.8	36.8	65.6
N/C	101	550	651

The resulting materials were all high surface area carbon materials and have been analysed by nitrogen adsorption. Table 3.4 shows the respective microporous, mesoporous and total surface area of the materials. It can be seen that while most materials have a comparable surface area, especially the Mn and Co variants have a significantly lower surface area than the other catalysts. For all materials the microporous surface area is significantly larger than the external surface area. This might be beneficial, if as proposed by Dodelet *et al.* the active sites are predominantly hosted in micropores. [4]

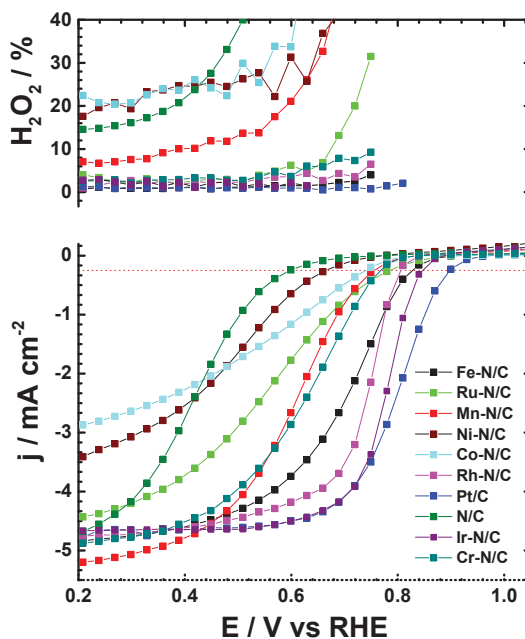


FIGURE 3.6: Steady-state RRDE measurements of M-N/C catalyst with different metals (M) in 0.5 M  $\text{H}_2\text{SO}_4$ , catalyst loading:  $750 \mu\text{g cm}^{-2}$ , rotating speed: 1600 rpm, 30 s hold, 30 mV step potential,  $\text{O}_2$ -saturated at 1 atm.

The ORR activity and 4 electron selectivity has been tested with the RRDE method under acidic conditions as shown in Figure 3.6. Interestingly, all tested metals improve in ORR activity compared to the metal free reference material. This indicates that the metals play an important role in promoting a high activity. It also suggests that the relatively high activity of the **ODAN** catalyst was caused by the Mn residues. A further interesting observation is that most materials promote the 4 electron reduction with a detected peroxide yield of less than 5%, while the catalysts **N/C**, **Ni-N/C**, **Co-N/C**, **Mn-N/C** promote a significantly higher peroxide yield of 22%, 24%, 24% and 10% at 0.4 V *vs* RHE, respectively.

Figure 3.7 shows the potential at a current density of  $250 \mu\text{A cm}^{-2}$ , while performing the ORR in acid *versus* the filling of the frontier 3d orbitals. This descriptor has been used for model macrocyclic complexes. [19] As the current density at which the potential is compared is  $<5\%$  of the theoretical mass transport limiting current under these conditions ( $\sim 5.2 \text{ mA cm}^{-2}$ )<sup>4</sup>, contributions from mass transport should be minimised and the current observed is close to the kinetic ORR current. [21] A higher potential at a given current

<sup>4</sup>As calculated from the Levich equation (Equation 2.3) for oxygen saturated 0.5 M  $\text{H}_2\text{SO}_4$  at ambient conditions and 1600 rpm.  $\text{CO}_2 = 1.13 \cdot 10^{-3} \text{ mol L}^{-1}$ ,  $\text{D}_{\text{O}_2} = 1.8 \cdot 10^{-5} \text{ cm}^2 \text{ s}^{-1}$ ,  $\nu = 0.01 \text{ cm}^2 \text{ s}^{-1}$ . [20]

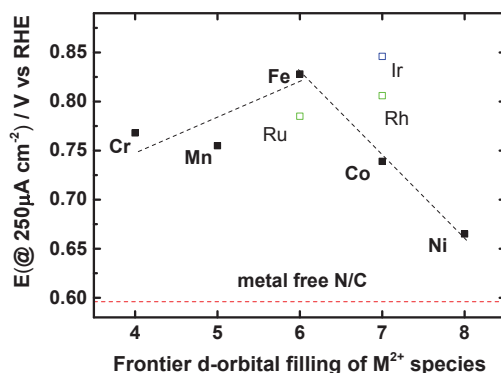


FIGURE 3.7: Potential of M-N/C catalysts at a current density of 250  $\mu\text{A cm}^{-2}$ . In black 3d, green 4d and blue 5d transition metals. Black dashed line is not a fit but indicates a volcano shape in the 3d transition metals.

density means a higher activity towards the ORR. It can be seen that the 3d metals follow a trend which might resemble a *Volcano* like shape, with iron at the top. The behaviour is more complex when the 4d and 5d metals are included. This might be an oversimplified view of the catalyst, as most likely different electronic configurations contribute to the overall d-orbital configuration. It is likely that this trend is merely a coincidence. Nevertheless a clear correlation with the addition of a metal centre and the ORR activity exists. It is without any doubt that the metal free catalyst has a significantly lower activity than all other investigated catalysts with metal addition.

**To summarise:** The optimised procedure with 1 wt% metal in the precursor, developed in 3.2.1, was used to incorporate different transition metal centres into the catalyst material. It was found that the catalyst without a metal is significantly less active than all other catalysts. For the transition metal containing materials, an activity trend similar to macrocyclic complexes was found. [19] Amongst the 3d metal centres, Fe showed the highest activity and 4 electron selectivity.

### 3.2.3 Elemental composition and surface element distribution of Fe-N/C and N/C material

In order to understand the influence of the metal centre on the material properties, the catalysts **Fe-N/C** and **N/C** were analysed by means of TXRF, in order to determine the trace metal content of these materials. The iron content was determined to be  $1.5 \pm 0.2$  wt% in the Fe-N/C catalyst and  $60 \pm 20$  ppm in the N/C catalyst. Other detected trace

elements (Zn and Cu) were below the 100 ppm threshold in the analysed catalysts, a value suggested to differentiate between metal free and metal containing catalysts. [12, 22]

Further insight on the surface element distribution can be gained via XPS.<sup>5</sup>

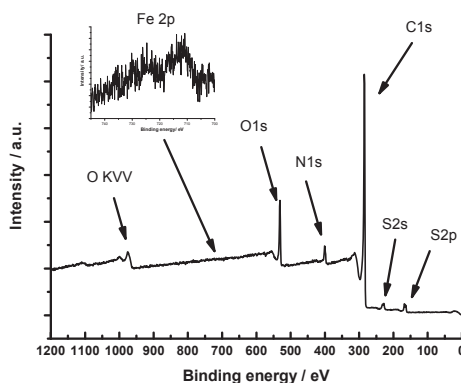


FIGURE 3.8: XPS wide scan of Fe-N/C catalyst. [Taken with permission from Ref. [6]]

Figure 3.8 shows the wide scan of **Fe-N/C**. The detected elements at the surface were C, N, O, S and a small amount of Fe.

TABLE 3.5: Surface element content as detected by XPS.

Catalyst	C [at%]	N [at%]	O [at%]	S [at%]	Fe [at%]
Fe-N/C	86.2	4.0	7.6	2.1	0.2
N/C	90.4	5.6	2.4	1.6	0.0

Table 3.5 shows a comparison of the elemental composition of the catalysts **Fe-N/C** and **N/C** within the topmost  $\sim 10$  nm from the surface. It can be seen that the composition of the non-metallic components is similar. A slightly higher amount of N is detected within the metal free catalyst, while the iron containing materials additionally shows  $\sim 0.2$  at% or  $\sim 0.9$  wt% (with respect to C) of Fe. This means that in the top most 10 nm of the material, the iron content is lower than in the bulk, as detected by TXRF (1.5%). This indicates that at the surface accessible to the reactants, the iron content might be even lower.

In order to understand, whether the material contains nitrogen species capable of coordinating Fe, in order to form the proposed  $\text{FeN}_4$  active sites, the N 1s peak is deconvoluted in Figure 3.9. The nitrogen species detected were 25% pyridinic, 11% pyrrolic, 45% quaternary, 14%  $\text{NO}_2^-$ , 5% NO. This shows that the **Fe-N/C** material has the necessary

<sup>5</sup>The XPS analysis is an excerpt from Ref. [6]. Experiments and data analysis were carried out by Dr. Emmanouil Symianakis. Interpretation and context was provided by the author.

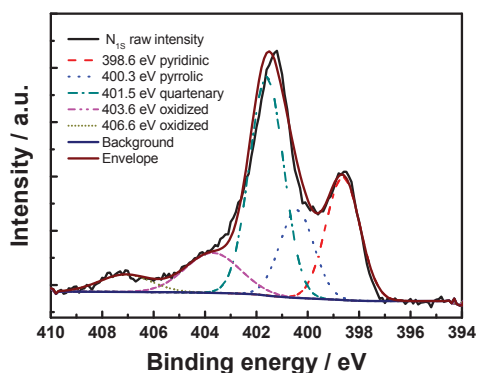


FIGURE 3.9: High resolution N<sub>1s</sub> XPS spectrum of Fe-N/C catalyst with the peaks deconvoluted into pyridinic, pyrrolic, quaternary and oxidised nitrogen species. [Taken with permission from Ref. [6]]

properties to form FeN<sub>4</sub> sites, namely surface Fe species, pyrrolic or pyridinic nitrogen species, a high content of micropores and a conductive amorphous carbon framework.

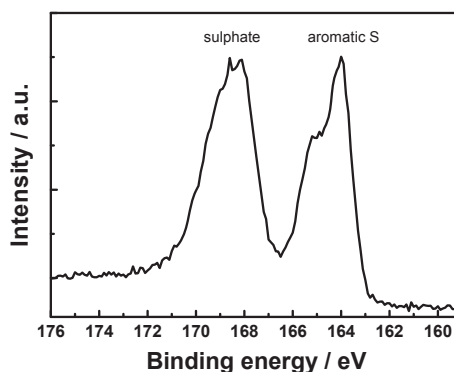


FIGURE 3.10: High resolution S<sub>2p</sub> XPS spectrum of Fe-N/C catalyst.[taken with permission from Ref. [6]]

Interestingly, examination of the sulphur 2p peak (Figure 3.10) reveals two main contributions of sulphur that can be assigned to aromatic sulphur or thiophene and sulfones or sulphates, respectively. [23] It is likely that all the sulphur introduced by the persulphate species used for oxidative polymerization is either decomposed or completely incorporated into the carbon framework as aromatic sulphur and the sulphate present on the surface is due to leaching with sulphuric acid. This is deduced because of the lack of a sulphate peak in a none acid-leached sample.

**To summarise:** The iron content of the **Fe-N/C** ( $1.5 \pm 0.2$  wt%) and **N/C** ( $60 \pm 40$  ppm) was determined by TXRF and their surface element distribution with XPS. It was found that the **Fe-N/C** catalyst has all necessary constituents to form a highly active catalyst



in terms of nitrogen functionalities, iron content and microstructure. Aromatic sulphur was found in both catalysts.

### 3.2.4 Effect of nano-MgO template and S doping on ORR activity

In order to probe possible effects of the microstructure on the catalytic activity of the material, the catalyst **Fe-N/C** was synthesised in the presence of MgO nanoparticles to obtain catalyst **MgO\_APS\_1**. The nanoparticles are believed to act a template and were added to the precursor mixture during the polymerisation step with ammonium persulfate (APS) (see 3.2.1). During the polymerisation, the naoparticles act as a template and upon pyrolysis can have beneficial influence on the microstructure. After the heat treatment step, the template was removed during the acid leaching step in 0.5 M H<sub>2</sub>SO<sub>4</sub>. A second heat treatment was performed on this catalyst to obtain **MgO\_APS\_2**. Additionally to probing the effect of the microstrucuture on the ORR activity, the influence of sulphur doping has been investigated. This has been done by changing the oxidant from sulphur containing APS to H<sub>2</sub>O<sub>2</sub>, to obtain **MgO\_H<sub>2</sub>O<sub>2</sub>\_1**. **MgO\_H<sub>2</sub>O<sub>2</sub>\_1** was then acid leached in 0.5 M H<sub>2</sub>SO<sub>4</sub> to remove the template. As second heat treatment of **MgO\_H<sub>2</sub>O<sub>2</sub>\_1** gave **MgO\_H<sub>2</sub>O<sub>2</sub>\_2**. A totally sulphur free catalyst **MgO\_H<sub>2</sub>O<sub>2</sub>\_2\_HCl** has been synthesised by swapping the acid in the leaching step from 0.5 M H<sub>2</sub>SO<sub>4</sub> to 0.5 M HCl.

TABLE 3.6: External, microporous and total surface area (SA) of templated catalysts, as determined by nitrogen adsorption analysis.

Catalyst	External SA [m <sup>2</sup> g <sup>-1</sup> ]	Microporous SA [m <sup>2</sup> g <sup>-1</sup> ]	Total SA [m <sup>2</sup> g <sup>-1</sup> ]
Fe-N/C	38.0	418	457
MgO_H <sub>2</sub> O <sub>2</sub> _1	505	450	955.0
MgO_H <sub>2</sub> O <sub>2</sub> _2	570	532	1102
MgO_APS_1	505	606	1113
MgO_APS_2	570	679	1249

Table 3.6 shows the surface area contribution for the templated and the untemplated material. Interestingly, although the total surface area more than doubles for the templated ( $\sim 1000 \text{ m}^2 \text{ g}^{-1}$ ) *versus* non-templated material ( $< 500 \text{ m}^2 \text{ g}^{-1}$ ), the increase in microporous surface area is moderate. All templated catalysts show a large external surface area of  $> 500 \text{ m}^2 \text{ g}^{-1}$ . It might be concluded that the addition of the template with nanoparticle sizes in the range of  $\sim 50 \text{ nm}$  facilitates a significant increase in total BET surface area with the majority of this increase as external surface area.

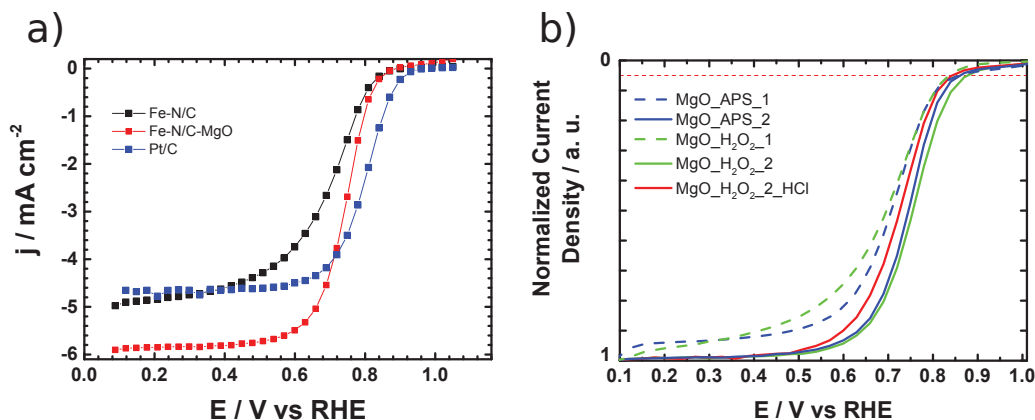


FIGURE 3.11: (a) Steady-state RDE measurements of M-N/C catalyst with and without nano-MgO template in 0.5 M  $\text{H}_2\text{SO}_4$ , catalyst loading: non-precious metal catalysts  $750 \mu\text{g cm}^{-2}$ , Pt/C  $60 \mu\text{g}_{\text{Pt}} \text{cm}^{-2}$ , rotating speed: 1600 rpm, 30 s hold, 30 mV step potential,  $\text{O}_2$ -saturated at 1 atm. (b) Normalised RDE measurements in 0.5 M  $\text{H}_2\text{SO}_4$  of different nano-MgO templated catalysts,  $5 \text{ mV s}^{-1}$ , background corrected cathodic cycle, catalyst loading:  $750 \mu\text{g cm}^{-2}$ ,  $\text{O}_2$ -saturated at 1 atm

The ORR activity of templated compared to non-templated catalyst and the reference Pt/C catalyst in 0.5 M  $\text{H}_2\text{SO}_4$  is shown in Figure 3.11 (a). It can be seen that there is no significant increase in activity in the kinetic region. Only at higher currents, the templated material seems to perform "better". Better in this sense means a higher current at higher potential. Moreover, it can be seen that the limiting current achieved by the templated material surpasses the theoretical limiting current under these conditions ( $\sim 5.2 \text{ mA cm}^{-2}$ )<sup>6</sup>. This phenomenon can be explained by inhomogeneities in the catalyst layer of the templated material. If the catalyst layer contains features which can penetrate the diffusion layer ( $\sim 10 \mu\text{m}$  under the utilised conditions), a higher apparent surface area will be accessible to the reaction and hence a higher limiting current is the result. Since the nanoparticles used to synthesise the templated catalysts are in the 50 nm range, it might be possible that the catalyst layer contains features of this length scale which might penetrate the diffusion layer and lead to the observed increase in limiting current. The absence of a higher activity in the templated catalyst, while showing a more than 2 fold increase in total BET surface area is striking. The fact that the microporous surface areas of the templated and non-templated catalyst are similar, supports the hypothesis of an active site which is hosted in the micropores.

The effect of sulphur doping on the ORR activity in 0.5 M  $\text{H}_2\text{SO}_4$  is presented in Figure 3.11 (b). The different limiting currents have been accounted for by rationing the

<sup>6</sup>As calculated from the Levich equation (Equation 2.3) for oxygen saturated 0.5 M  $\text{H}_2\text{SO}_4$  at ambient conditions and 1600 rpm.  $C_{\text{O}_2} = 1.13 \cdot 10^{-3} \text{ mol L}^{-1}$ ,  $D_{\text{O}_2} = 1.8 \cdot 10^{-5} \text{ cm}^2 \text{ s}^{-1}$ ,  $\nu = 0.01 \text{ cm}^2 \text{ s}^{-1}$ . [20]

measured currents to the respective limiting currents to obtain the "Normalised Current" for all measurements. It can be seen that there is no significant difference in the kinetic current (i. e. 5% of limiting current as indicated in Figure 3.11 (b)) in catalysts in the presence or absence of sulphur during the heat treatment. For both materials a second heat treatment improves the activity and increases the microporous surface area. The reason for the slightly lower activity of the catalyst treated with HCl instead of H<sub>2</sub>SO<sub>4</sub> might be that in the presence of chloride catalytically active Fe ions are leached more effectively from the material.

**To summarise:** The effect of surface area and microstructure was investigated by using MgO nanopowder as templating agent. It was found that the total surface area does not seem to correlate with the electrochemical activity. A correlation with the microporous surface area might be present, supporting the hypothesis of active sites hosted in micropores. [4] The effect of aromatic sulphur on the ORR activity in acid was investigated. No significant effect was found.

### 3.2.5 Electronic structure (EPR) of selected catalysts

In order to investigate the effect of a metal centre on the electronic properties of the material, selected catalysts were investigated using electron paramagnetic resonance.<sup>7</sup>

It can be seen in Figure 3.12 (a) that the metal free **N/C** catalyst exhibits a clear radical signal. It resembles the signal of a carbon centred radical typically found in amorphous carbon materials. Interestingly, the absence of a hyperfine splitting suggests that the radical does not occupy the vicinity of nitrogen atoms, which have a nuclear moment of  $I = 1$  and therefore a splitting in 3 lines would be observed. [24] Interestingly, the addition of metal ions Fe (**Fe-N/C**) and Mn (**Mn-N/C**) significantly broadens the radical signal. This indicates a profound effect of the transition metal on the electronic structure of the carbon. To exclude that this effect was due to an independent interaction of Fe<sup>2+</sup> or Fe<sup>3+</sup> ions, those were added to the metal free catalyst and an EPR scan was conducted. In Figure 3.12 it can be clearly seen that post-synthetic addition of metal ions does not alter the signal in the same profound way when the metal was added prior to heat treatment. This supports the notion that the metal ion indeed alters the properties of the free electrons in the structure.

<sup>7</sup>EPR was conducted at the national EPR facility in Manchester with the support of Daniel O Sells.

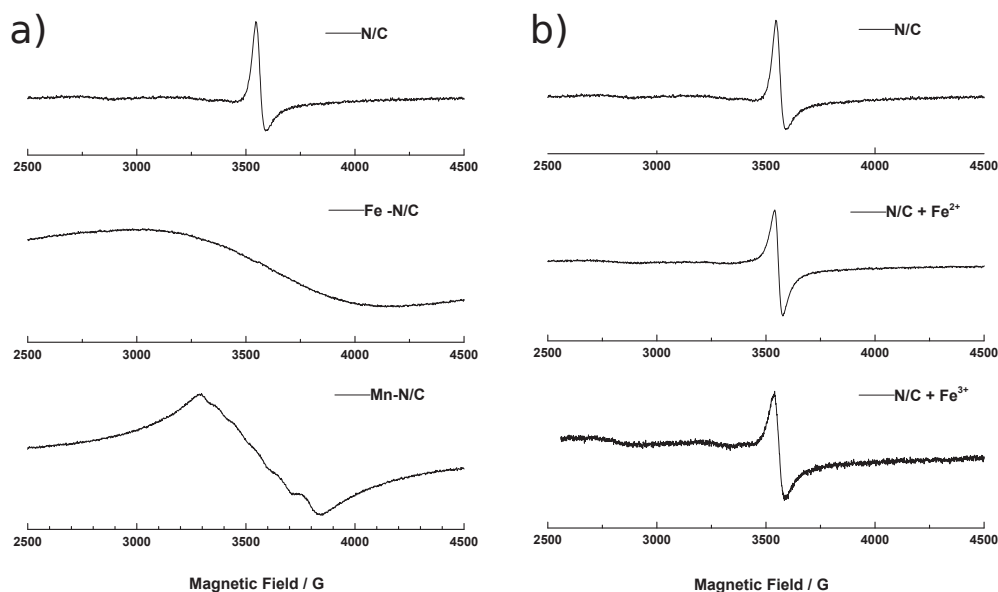


FIGURE 3.12: (a) X-band EPR spectra of (M)-N/C catalysts with and without metal centre, recorded at room temperature. (b) X-band EPR spectrum of N/C catalysts with and without post-synthetic addition of iron species, recorded at room temperature.

TABLE 3.7: g-values for radical signal of different catalysts at room temperature.

Sample	g-value
N/C	2.04
Fe-N/C	2.01
Mn-N/C	2.02

In Table 3.7 it can be seen that the g-values are close to that of the free electron (2.02). These values should be taken with care, as tuning of the microwave cavity was challenging and more repeat experiments would be necessary in order to confirm the results. However, the significant effect on the signal width is clear.

Taking a closer look at the Mn spectrum (Figure 3.13), it is discernible that a hyperfine splitting might be present in the spectrum. Mn has a nuclear magnetic moment of  $I = 5/2$ , which should split the signal into 6 lines. [24] These lines can be seen in the spectrum. A lower temperature measurement might reveal whether this is an artefact or a real signal. If it was true, this would be significant, as it would mean that the metal centre would interact with the radical signal and might give a clue on the source of the increased catalytic activity, when adding a metal. Further investigation is necessary.

A lower temperature measurement (77 K) was conducted for the **Fe-N/C** catalyst. It

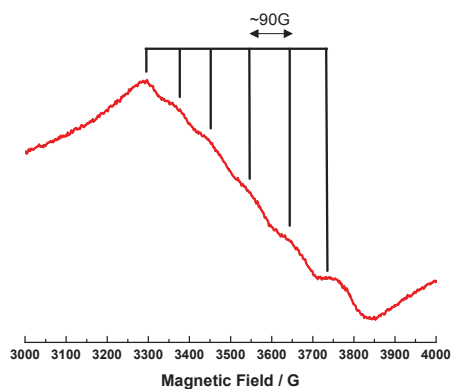


FIGURE 3.13: X-band EPR spectrum of Mn-N/C catalyst, recorded at room temperature.

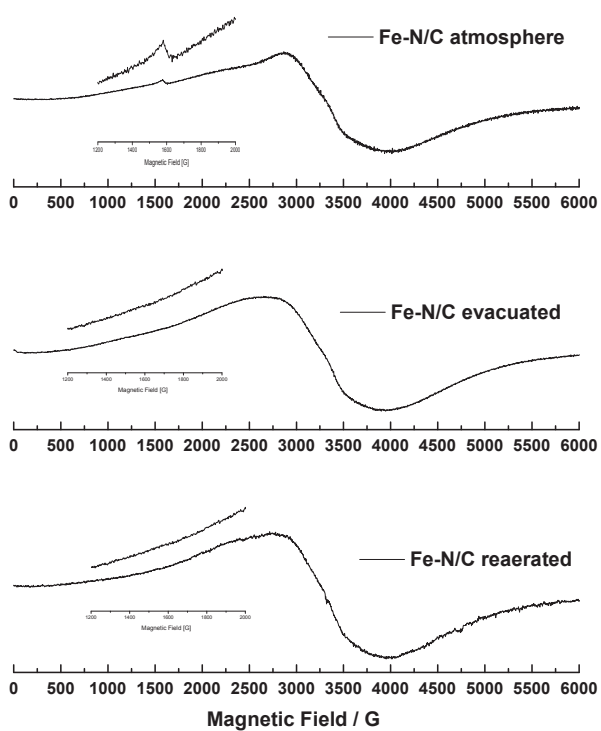


FIGURE 3.14: X-band EPR spectra of Fe-N/C catalyst under varying conditions, recorded at 77 K.

can be seen in Figure 3.14 that the signal width reduces upon lowering the temperature. An experiment was conducted where the catalyst was measured when exposed to the atmosphere (Figure 3.14 (top)), then when it was evacuated and heated to remove potentially adsorbed oxygen (Figure 3.14 (middle)), and finally when the catalyst was again subjected to the atmosphere (Figure 3.14 (bottom)).

TABLE 3.8: g-values of Fe-N/C radical signal under different conditions at 77 K.

Sample	g-value
Fe-N/C atmosphere	1.86
Fe-N/C evacuated	1.87
Fe-N/C reaerated	1.87

Table 3.8 shows the respective g-values. A significant shift can be observed, as compared to the room temperature measurement. Furthermore, the initial catalyst shows a second signal at  $g = \sim 4.18$ . These 2 g values  $\sim 1.9$  and  $\sim 4.2$  are typical for rhombohedral iron complexes. [24] However, the second signal disappears upon evacuation and does not reappear upon aeration. Therefore, this second signal was either an artefact or it takes a certain amount of time before the catalyst reorganises into its "rhombohedral" state when re-aerated. A follow up study would be necessary to confirm these findings.

**To summarise:** EPR has been used to study the effect of a metal centre on the electronic properties of the material. It was found that the incorporation of a metal centre profoundly changes the EPR signal, which suggests that the radical signal might play a role in the ORR activity of the signal. The incorporation of Mn shows some sort of hyperfine interaction, which indicates that the metal might directly interact with the radical signal. A study at 77 K reveals the possible existence of a rhombohedral iron species and further investigations might yield insight into crucial insight on the source of the catalytic activity.

### 3.2.6 Microstructure and element distribution (STEM and EELS) of the Fe-N/C and N/C catalysts

Further insight into the microstructure and element distribution within the materials was obtained with high resolution TEM and STEM in combination with EDS and EELS

spectroscopy.<sup>8</sup>

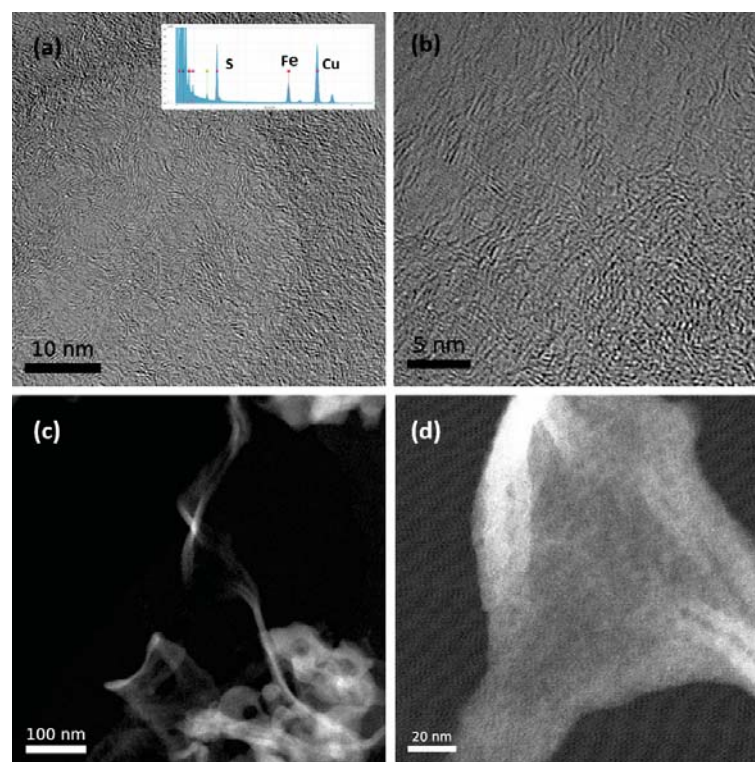


FIGURE 3.15: (a), (b) Representative high resolution TEM images of the Fe-N/C catalyst, showing the absence of solid inclusions or nanoparticles and the amorphous structure. inset (a) high resolution EDX of region corresponding to image (a) clearly showing the presence of iron. (c) and (d) high resolution STEM images of Fe-N/C catalyst. [Taken with permission from Ref. [25]]

Figure 3.15 shows representative TEM and STEM images of the Fe-N/C material. It can be seen that there are no significant encapsulated carbide phases visible, while iron is clearly present as confirmed by high resolution EDS (inset Figure 3.15 (a)). This indicates highly dispersed iron. If present in large quantities, nanoparticles should be visible in the images at this resolution, as observed for some types of Fe-N/C catalysts (see 1.7.4). [26–29] It is therefore inferred that these phases are not the predominant source of the activity and the iron sites in the Fe-N/C material are likely similar to those reported for the catalysts of the LANL and Dodelet groups [28, 30, 31], namely atomic FeN<sub>x</sub> sites. The presence of such sites is supported by the fact that it has been shown in various studies that different preparation methods lead to common sites. [32–34] The absence of ordered nanoparticulate phases such as Fe<sub>3</sub>C, FeN or Fe<sub>2</sub>O<sub>3</sub> is also supported

<sup>8</sup>Images and spectroscopy in Figures 3.15 and 3.16 were collected with the support of Dr. Catriona McGilvery and Dr. Mahmoud Arkadani (Imperial College London). Data in Figures 3.17 to 3.20 were collected at the national SuperSTEM facility in Daresbury. Data analysis and interpretation were provided by Dr. Fredrik Hage (SuperSTEM Daresbury).

by the fact that no crystallinity indicative of such nanophases was detected in various different TEM images from different regions within the same material. [28, 30, 31]

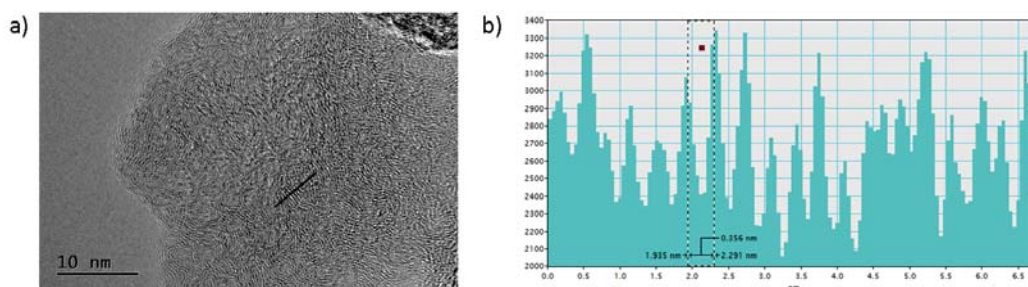


FIGURE 3.16: (a) TEM image of Fe-N/C material. (b) Representative analysis of the lattice spacing of some ordered domains within the material. [Taken with permission from Ref. [25]]

Where ordered domains have been identified by TEM, it has been validated that those resemble stacked graphene sheets, typically found in amorphous carbon, where some short range order is present. Figure 3.16 shows a representative TEM image which shows a region with short range ordering and the respective analysis of the lattice spacing. The determined distance of 0.356 nm is typical for values found in carbons and significantly larger than the values typically found for metallic nanoparticles in this type of material (<0.300 nm). [29, 35]

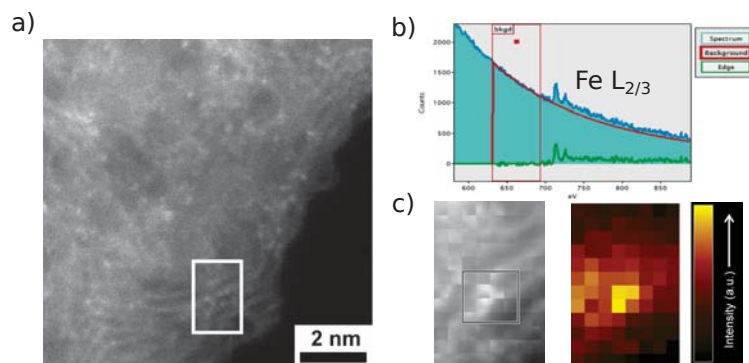


FIGURE 3.17: (a) HAADF STEM image of Fe-N/C material. (b) Representative EELS spectrum of the respective pixels in image (c). (c) *left*: pixel area over which EELS spectra were collected, *right*: EELS map of the Fe  $L_{2/3}$  peak, corresponding to area shown on the *left*.

In order to gain further insight and possible visualise atomic iron centres, high resolution HAADF STEM images of the **Fe-N/C** catalyst were collected. Figure 3.17 (a) shows the HAADF STEM image of a typical thin area within the material. It can be clearly seen that spots with higher contrast to the carbon background are visible. It was attempted to identify the bright spots. For this the highlighted area, in which such bright spots can be found, in Figure 3.17 (a) was mapped with EELS for the presence of Fe. Figure 3.17



(b) shows a typical EELS spectrum with an Fe  $L_{2/3}$  peak. The intensity of this peak was mapped over the highlighted area as shown in Figure 3.17 (c). It can be clearly seen that the bright spot coincides with a high Fe peak intensity. The diameter of the bright spot is  $\sim 0.3$  nm. This suggests that at least some of those bright spots are indeed atomic iron centres, as iron has an atomic radius of  $\sim 0.14$  nm. [36]

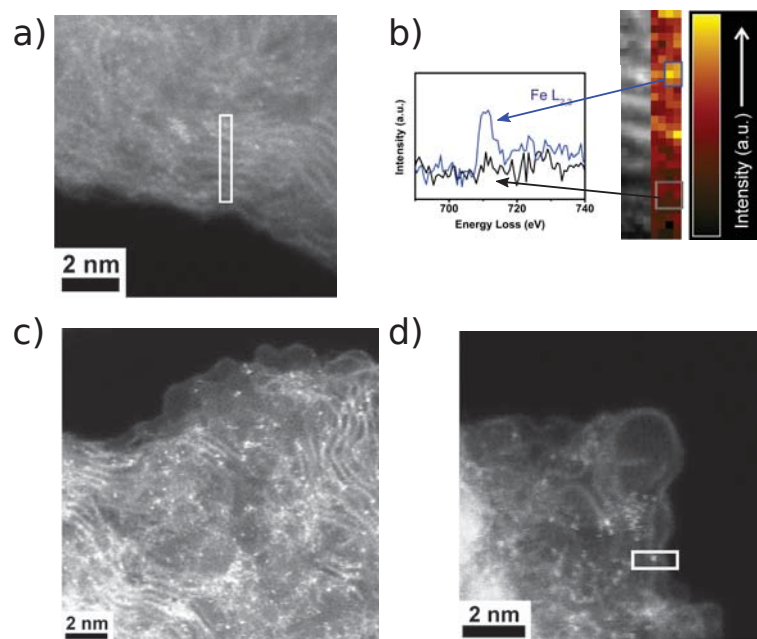


FIGURE 3.18: (a) HAADF STEM image of Fe-N/C material. (b) Fe  $L_{2/3}$  EELS map of the highlighted region. *left*: representative EELS spectra of 2 distinct regions, showing the presence (*blue* spectrum) and absence (*black* spectrum) of iron in the respective region. (c) and (d) HAADF STEM images of a particularly thin region in the Fe-N/C sample.

The HAADF STEM image of a second area is shown in Figure 3.18 (a). Again the presence of Fe in the bright spot was confirmed via EELS mapping analogous to the procedure described above. Figure 3.18 (b) shows a line scan over the fringes of what seems to be graphene layers, stacked in a short range ordering. It can clearly be seen that the bright spot shows an Fe EELS signal, while in a slightly different area no Fe is detected. This supports the presence of atomic iron, while also showing that on the nanoscale the distribution is not homogeneous. Figure 3.18 (c) and (d) shows the HAADF STEM images of a thinner region. Unfortunately, the identity of the bright spots could not be confirmed due to a drift in the sample. However, at least some of the bright spots seem to be contaminant Si atoms, as verified by EELS.

Figure 3.19 (a) shows another region within this material. This time 2 small bright clusters are visible, with a size of approaching 1 nm. It might be that these bright spots

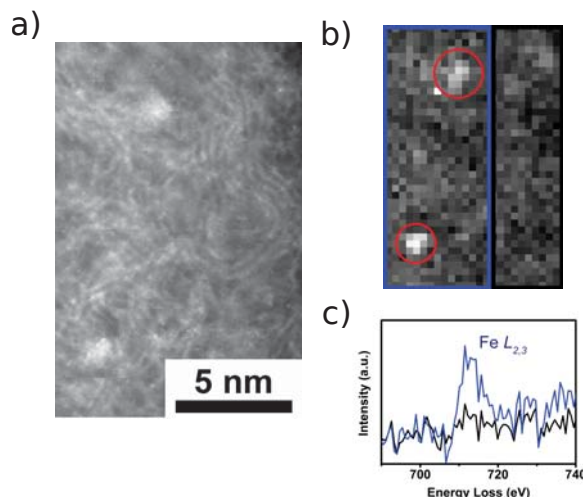


FIGURE 3.19: (a) HAADF STEM image of Fe-N/C material showing the possible existence of iron clusters. (b) Magnified HAADF STEM image of region over which two EELS spectra were recorded, highlighted in *blue* and *black*, *red* circles indicate possible iron clusters. (c) EELS spectra *blue* and *black*, corresponding to the respective areas in (b).

are clusters of few Fe atoms. EELS spectra averaging the area of the image with the clusters and without the clusters were taken (Figure 3.19 (b)). It can be seen that in the area where the spots are present (*blue*), a clear Fe signal is present, while in the area without the clusters (*black*), no signal is present. However, the *blue* area shows a higher proportion of bright spots that are smaller, and could be atomic centres, as well.

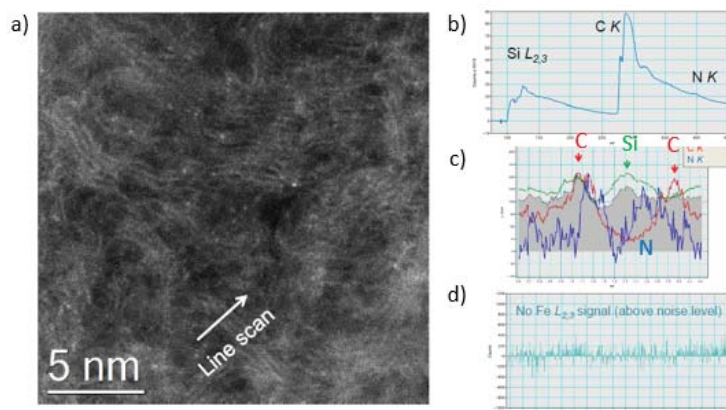


FIGURE 3.20: (a) HAADF STEM image of N/C material. (b) EELS spectrum of region shown in (a). (c) Intensity of C, Si and N EELS peaks over line scan, indicated in (a). (d) Intensity of Fe  $L_{2/3}$  peak. No iron detected in the sample.

For comparison HAADF STEM images were taken from the N/C catalyst as well (Figure 3.20 (a)). In general the microstructures of the two materials are comparable. However no iron was detected within the N/C material. Some bright spots were found to be Si contaminants.

**To summarise:** Extensive high resolution microscopy of the **Fe-N/C** material shows the clear absence of nanoparticulate crystalline iron phases, while finely dispersed iron was detected by EDS. HAADF STEM in combination with EELS verifies the presence of atomic iron centres. Clusters of few iron atoms might be present as well. The **N/C** catalyst has a similar carbonaceous microstructure, without the iron centres.

### 3.2.7 MEA Single Cell testing

Finally the **Fe-N/C** catalyst has been tested in a single cell in order to verify its applicability as fuel cell catalyst.

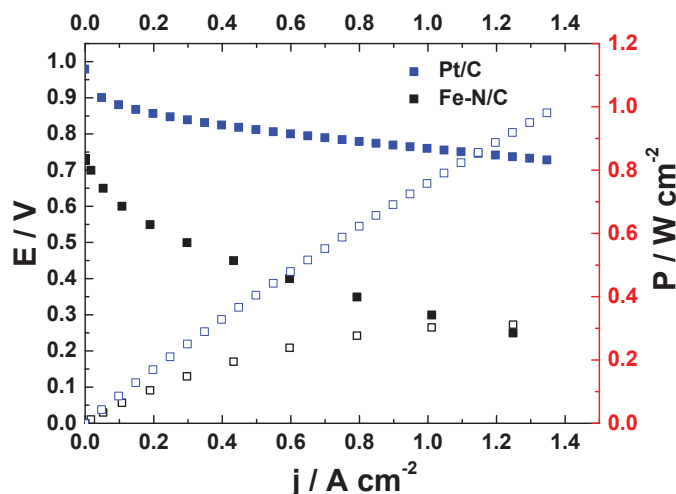


FIGURE 3.21:  $\text{H}_2/\text{O}_2$  steady-state polarization plot for MEAs comparing a brush painted cathode of Fe-ODAN-1% ( $4 \text{ mg cm}^{-2}$ ) to a commercial Pt cathode ( $0.4 \text{ mg}_{\text{Pt}} \text{ cm}^{-2}$ ).  $80^\circ\text{C}$  cell temperature. 100% RH and 2 bar back-pressure (gauge) for both gases.

Figure 3.21 shows a  $\text{H}_2/\text{O}_2$  polarisation curve of the **Fe-N/C** cathode catalyst in comparison to a state of the art Pt/C catalyst under the same conditions. The cathode was prepared by homogeneously brush painting the **Fe-N/C** catalyst onto a GDL/MPL at a loading of  $4 \text{ mg cm}^{-2}$ , while the commercial reference state of the art Pt cathode had loading of  $0.4 \text{ mg}_{\text{Pt}} \text{ cm}^{-2}$ . Both MEAs utilised a commercial Pt cathode as anode as well. The excessively high Pt anode loading ensured, that the measured kinetic losses were due to the cathode side. While the **Fe-N/C** catalyst is far away from the performance of a state of the art Pt cathode, it shows a significant activity. Although it does not match the activity of the best performing **Fe-N/C** catalysts in literature it reaches a reasonable activity within this group of materials. [1] An ionomer to carbon (I/C) ratio of 1:1 was

chosen for this MEA. A detailed electrochemical impedance study of MEAs operated with different non-precious metal catalysts is presented in Chapter 8.

**To summarise:** The **Fe-N/C** catalyst can be used in an MEA with reasonable activity for this type of material.

### 3.3 Conclusions

A methodology has been presented, where 1,5-diaminonaphthalene is oxidised in the presence of a metal salt with 1 wt% metal content in the precursor. The pyrolysis of this material with intermediate acid leaching and reheat treatment yields a conductive carbonaceous high surface area material. The microstructure resembles that of other carbon blacks. The material has a high microporosity.

The ORR activity has been determined and an optimised synthesis procedure was developed. Utilising this optimised procedure, different transition metal centres were incorporated into the material, and the ORR activity has been determined as a function of these metal centres. It has been found that among the 3d elements, Fe shows the highest activity.

The effect of microstructure has been investigated by producing a templated catalyst with a different surface area and porosity. It has been found that a higher surface area is not correlated with a higher activity, but the microporous surface area seems to play an important role.

The **Fe-N/C** catalyst was singled out for in depth investigation together with a metal free **N/C** catalyst for comparison.

Elemental analysis has been conducted for trace iron content (TXRF) and for surface element species (XPS). It has been found that the **Fe-N/C** catalyst contain all necessary requirements to form  $\text{FeN}_4$  sites as described in literature.

EPR has been performed and it was found that addition of a metal has a profound effect on the electronic properties of the catalyst. It seems that unpaired electrons are present in both metal containing and metal free samples. However, the signal is broadened in the presence of Fe or Mn. The unpaired electrons seem to reside close to the metal centre as suggested by hyperfine splitting.

Finally, electron microscopy (TEM and STEM) in combination with spectroscopy (EDS and EELS) has identified atomic iron centres within the **Fe-N/C** material. Furthermore, the material was free of nanoparticulate crystalline iron species, which was one type of active site suggested in literature. However, small ( $\leq 1$  nm) iron clusters seem to be present within the material.

In conclusion, the material synthesised here seems to be very similar to other M-N/C catalysts presented in literature, where the  $\text{FeN}_4$  centres have been identified. Therefore, further study of the active site within this material should be transferable to the majority of catalysts. Applicability of conclusions for this active site to other M-N/C materials will be confirmed in the relevant chapter (Chapter 6).

## 3.4 Experimental Part

Background information on the experimental techniques described herein and the equivalent sections in the other results chapters can be found in (Chapter 2).

The procedures described here are representative for the equivalent procedures used in other chapters of the thesis. Henceforth only specific differences for methods already described are mentioned in the respective experimental parts. As an example, for the RRDE/RDE this is the preparation of electrolytes, use of other reference electrodes, specific electrochemical cycling protocols etc..

### 3.4.1 Catalyst Synthesis

**ODAN:** 1,5-diaminonaphthalene (500 mg, 3.16 mmol) and  $(\text{NH}_4)_2\text{S}_2\text{O}_8$  (500 mg, 2.19 mmol, 98% Alfa Aesar) were dispersed in EtOH (50 mL, absolute VWR). The dispersion was stirred for 24 h at room temperature to obtain oligomers of 1,5-diaminonaphthalene. Then the mixture was heated to 80 °C in order to completely evaporate the solvent and drive the polymerization of the oligomers. When dry the resulting grey powder was heated in the tube furnace to 1000 °C at a heating rate of 20 °C  $\text{min}^{-1}$  and held there for 2 h. An alumina boat was used as crucible. The resulting black powder was refluxed for 8 h in 0.5 M  $\text{H}_2\text{SO}_4$  to remove any metal impurities. After filtering and drying in the oven at 60 °C overnight, the catalyst **ODAN** (143 mg) was ready to use.

**Fe-ODAN-14%:** 1,5-diaminonaphthalene (350 mg, 2.20 mmol, 98% Alfa Aesar) and FeCl<sub>2</sub> (114 mg, 0.900 mmol, anhydrous Sigma-Aldrich) were dispersed in EtOH (50 mL, absolute VWR). The dispersion was stirred for 24 h at room temperature to obtain oligomers of 1,5-diaminonaphthalene. Then the mixture was heated to 80 °C in order to completely evaporate the solvent and drive the polymerization of the oligomers. When dry the resulting dark violet residue was heated in the tube furnace to 1000 °C at a heating rate of 20 °C min<sup>-1</sup> and held there for 2 h while supplying a constant stream of inert nitrogen gas (BOC N6.0 grade). An alumina boat was used as crucible. The resulting black powder was refluxed for 8 h in 0.5 M H<sub>2</sub>SO<sub>4</sub> to remove residual metal. After filtering and drying in the oven at 60 °C overnight, the catalyst **Fe-ODAN-14%** (192 mg) was ready to use.

**Co-ODAN-16%:** The catalyst was synthesised in the same way as **Fe-ODAN-14%**, with the difference that FeCl<sub>2</sub> was replaced with CoCl<sub>2</sub> · 4 H<sub>2</sub>O (214 mg, 0.900 mmol, 99 % Sigma-Aldrich) to obtain **Co-ODAN-16%** (113 mg).

**Fe-ODAN-1%:** In a 250 mL round bottom flask, 1,5-diaminonaphthalene (1 g, 6.32 mmol, 98% Alfa Aesar) was dissolved in Ethanol (220 mL, absolute VWR). A solution of FeCl<sub>2</sub> · 4 H<sub>2</sub>O (35.6 mg, 0.200 mmol, 98 % Sigma-Aldrich) dissolved in ethanol (20 mL, absolute VWR) was added to the solution. After 10 Minutes NH<sub>4</sub>S<sub>2</sub>O<sub>8</sub> (1g, 4.38 mmol, 99.9 % Sigma-Aldrich) dissolved in H<sub>2</sub>O (10 mL, MilliQ 18.2 MΩ cm) was also added. The mixture was stirred for 22h. The solvent was removed under reduced pressure and the remaining black powder was subjected to heat treatment in a tube furnace to 950 °C at a heating rate of 20 °C min<sup>-1</sup> and held there for 2h while supplying a constant stream of inert nitrogen gas (BOC N6.0 grade). A quartz boat was used as crucible. The boat was thoroughly cleaned in aqua regia before use, in order to avoid cross contamination with transition metals. The resulting black powder was refluxed for 8 h in 0.5 M H<sub>2</sub>SO<sub>4</sub> to remove residual metal. After filtering and drying in the oven at 60 °C overnight, the catalyst **Fe-ODAN-1%** (660 mg) was ready to use.

**Fe-N/C:** The catalyst **Fe-ODAN-1%** was heat treated for a second time in the tube furnace with a heating rate of 20 °C min<sup>-1</sup> held at 900 °C for 2 h. After cooling down the catalyst **Fe-N/C** was ready to use.

**Co-N/C:** The catalyst was synthesised in the same was as **Fe-N/C**, with the difference that FeCl<sub>2</sub> · 4 H<sub>2</sub>O was replaced with CoCl<sub>2</sub> · 6 H<sub>2</sub>O (40 mg, 0.17 mmol, 98% Sigma-Aldrich) to obtain the **Co-N/C** catalyst (645 mg).

**Rh-N/C:** The catalyst was synthesised in the same way as **Fe-N/C**, with the difference that  $\text{FeCl}_2 \cdot 4\text{H}_2\text{O}$  was replaced with  $\text{RhCl}_3 \cdot x\text{H}_2\text{O}$  (26 mg, 99.8% Sigma-Aldrich 40 % Rh) to obtain the **Rh-N/C** catalyst (634 mg).

**Ru-N/C:** The catalyst was synthesised in the same way as **Fe-N/C**, with the difference that  $\text{FeCl}_2 \cdot 4\text{H}_2\text{O}$  was replaced with  $\text{RuCl}_3 \cdot x\text{H}_2\text{O}$  (23.5 mg, ReagentPlus<sup>®</sup> Sigma-Aldrich 38% Ru) to obtain the **Ru-N/C** catalyst (687 mg).

**Mn-N/C:** The catalyst was synthesised in the same way as **Fe-N/C**, with the difference that  $\text{FeCl}_2 \cdot 4\text{H}_2\text{O}$  was replaced with  $\text{MnCl}_2$  (23.0 mg, 0.18 mmol, purum anhydrous Sigma-Aldrich) to obtain the **Mn-N/C** catalyst (634 mg).

**Ni-N/C:** The catalyst was synthesised in the same way as **Fe-N/C**, with the difference that  $\text{NiCl}_2 \cdot 6\text{H}_2\text{O}$  (40.4 mg, 0.17 mmol, ReagentPlus<sup>®</sup> Sigma-Aldrich) to obtain the **Ni-N/C** catalyst (678 mg).

**Cr-N/C:** The catalyst was synthesised in the same way as **Fe-N/C**, with the difference that  $\text{CrCl}_3 \cdot 6\text{H}_2\text{O}$  (51.25 mg, 0.17 mmol, ReagentPlus<sup>®</sup> Sigma-Aldrich) to obtain the **Cr-N/C** catalyst (678 mg).

**Ir-N/C:** The catalyst was synthesised in the same way as **Fe-N/C**, with the difference that  $\text{IrCl}_3 \cdot x\text{H}_2\text{O}$  (23 mg, ReagentPlus<sup>®</sup> Sigma-Aldrich) to obtain the **Ir-N/C** catalyst (634 mg).

**N/C:** This catalyst was synthesised in the same way as **Fe-N/C**, with the difference that no metal salt was added to the reaction mixture. Additionally, in order to minimise trace metal contamination, the 1,5-diaminonaphthalene (98% Alfa Aesar) was recrystallized from ethanol (absolute, VWR) twice before use. Furthermore, the  $\text{NH}_4\text{S}_2\text{O}_8$  (BioXtra, >98.0% Sigma-Aldrich) utilised contained less than 5 ppm trace metal impurities. Moreover, all glassware was meticulously cleaned with aqua regia, a 1:1 solution of 2 M  $\text{H}_2\text{SO}_4/30 \text{ wt}\% \text{H}_2\text{O}_2$  and ultrapure water (MilliQ 18.2 M $\Omega$  cm) before use.

**MgO\_APS\_1:** In a 250 mL round bottom flask, MgO nanoparticles (1g, <60 nm Sigma-Aldrich) were dispersed in ethanol (250 mL, absolute VWR) and 1,5-diaminonaphthalene (1g, 6.3 mmol, 98% Alfa Aesar) was added. The mixture was stirred for 15 minutes in order to completely dissolve the diamine.  $\text{FeCl}_2 \cdot 4\text{H}_2\text{O}$  (40 mg, 0.17 mmol, 98% Sigma-Aldrich) was dissolved in ethanol (20 mL, absolute VWR). The solution was added to the diamine solution. It was stirred for 15 minutes in order to ensure a homogeneous dispersion

of the catalyst. 1 g (4.3 mmol) of  $(\text{NH}_4)_2\text{S}_2\text{O}_8$  (98% Sigma-Aldrich) was dissolved in 10 mL  $\text{H}_2\text{O}$  (MilliQ 18.2 M $\Omega$ cm) and added to the ethanolic solution. The mixture was stirred for 22h to allow polymerisation. The solvent was then removed under reduced pressure. The remaining black solid was heated at 20 °C min<sup>-1</sup> to 950 °C under a constant stream of inert nitrogen (BOC N6.0 Grade) in a tube furnace (Carbolite). The temperature was held for 2 h and the reaction was cooled to room temperature overnight. The black product was then refluxed in 0.5 M  $\text{H}_2\text{SO}_4$  for 8 h to remove any residual metal. After drying in the oven at 60 °C overnight, the catalyst (300 mg) was ready to use.

**MgO\_H<sub>2</sub>O<sub>2</sub>\_1:** 50 mg of **MgO\_ APS\_ 1** was heated at 20 °C min<sup>-1</sup> to 950 °C under a constant stream of inert nitrogen (BOC N6.0 grade) in a tube furnace (Carbolite). The temperature was held for 2 h and the reaction was cooled to room temperature overnight. The product 47 mg was ready to use.

**MgO\_H<sub>2</sub>O<sub>2</sub>\_2:** 50 mg of **MgO\_H<sub>2</sub>O<sub>2</sub>\_1** was heated at 20 °C min<sup>-1</sup> to 950 °C under a constant stream of inert nitrogen (BOC N6.0 grade) in a tube furnace (Carbolite). The temperature was held for 2 h and the reaction was cooled to room temperature overnight. The product (42 mg) was ready to use.

**MgO\_H<sub>2</sub>O<sub>2</sub>\_2\_HCl:** Was synthesised in the same way as **MgO\_H<sub>2</sub>O<sub>2</sub>\_2**, but 0.5 M HCl was used for the acid leaching step instead of 0.5 M  $\text{H}_2\text{SO}_4$

### 3.4.2 RRDE/RDE measurements

The electrochemical experiments were conducted with the Rotating Ring Disk Electrode (Pine Instruments, model AFE6R1AU with a mirror polished glassy carbon as disk and rotator model AFMSRCE) similar to literature procedures. [10, 37] The inks utilised consisted of 1 wt% catalyst in a 1:1 volume ratio mixture of IPA (VWR): $\text{H}_2\text{O}$  (MilliQ 18.2 M $\Omega$  cm) with a Nafion<sup>™</sup> (from 5 wt% in lower aliphatic alcohols, Sigma-Aldrich) to catalyst weight ratio of 1:1. This composition was found to give a uniform catalyst layer, which was characterised under an optical microscope. The respective amount of catalyst was deposited on the glassy carbon disk by drop casting the respective amount ink onto the electrode disk, which was mounted upside down. The catalyst layer was then dried under a rotation of 300 rpm. The reference platinum catalyst was 60 wt% Pt on high



surface area carbon from Johnson Matthey (HiSpec 9100, Alfa Aesar). A three compartment electrochemical glass cell was used. The electrolytes were prepared by diluting the concentrated reagent with ultra-pure water (MilliQ 18.2 M $\Omega$  cm) to the necessary degree; 0.5 M H<sub>2</sub>SO<sub>4</sub> (H<sub>2</sub>SO<sub>4</sub> 97% Aristar from VWR), 0.5 M HCl (HCl 37% from VWR), 0.1 M NaOH (NaOH 97% from Sigma-Aldrich), Ringers solution (Sigma Aldrich). The RHE reference electrode (GaskatelHydroFlex) was ionically connected to the main compartment of the electrochemical glass cell via a *Luggin-Haber*-Capillary. A glassy carbon rod was used as counter electrode and ionically connected to the main compartment of the glass cell through a porous frit. Glassy carbon was used instead of Pt in order to avoid contamination with catalytically active precious metals. A potentiostat (Autolab, model PGSTAT20) was used for potential or current control during the electrochemical measurements. Steady state oxygen reduction reaction polarization curves, performed in O<sub>2</sub>-saturated electrolyte solutions were obtained via step potentials of 30mV with waiting time of 30 seconds. Ultrapure gases, Nitrogen and Oxygen (BIP plus-X47S, Air products), were used to purge the electrolytes. It was found necessary that a cleaning protocol was performed for all electrochemical experiments in order to achieve a stable baseline. The procedure consisted of extensive cycling, alternating between N<sub>2</sub>-saturated electrolyte at 100 mV s<sup>-1</sup> (20 cycles) and 10 mV s<sup>-1</sup> (10 cycles) and O<sub>2</sub>-saturated electrolyte at 5 mV s<sup>-1</sup> (6 cycles), in the potential window 1.05 - -0.4 V *vs* RHE. This was repeated until stable non changing oxygen reduction performance and cyclic voltammograms under nitrogen were achieved (3 - 4 times). Where iR free potentials ( $E_{iR-free}$ ) are reported the potential (E) was corrected to be  $E_{iR-free} = E - I \cdot R$ , where I is the measured current and R the solution and lead resistance, as determined by electrochemical impedance spectroscopy (FRA module, Autolab, PGSTAT20) as described in literature. [38]

### 3.4.3 SEM

Samples were prepared by drop drying a suspension of the catalyst in acetone (AnalR NORMAPUR<sup>®</sup>, VWR) onto alumina stubs (AGG301, Agar Scientific). SEM was carried out on a high resolution field emission gun scanning electron microscope (LEO Gemini 1525 FEGSEM).

### 3.4.4 Nitrogen adsorption analysis

Nitrogen adsorption analysis was conducted on a Micromeritics Tristar II 3020. The analysis temperature was 77 K and the *Brunauer-Emmett-Teller* (BET) equation was used to extract the surface area. A molecular cross sectional area of 0.1620 nm<sup>2</sup> for nitrogen was used. The best region for the linear fit was determined by the *Rouquerol* method. Microporous and external surface area (SA) were determined from the t-plot using the Broekhoff-DeBoer thickness equation. Samples were thoroughly degassed and dried overnight at 300 °C under nitrogen prior to the measurement. Gases used were nitrogen (BIP plus-X47S) for drying and adsorption and He (BIP plus-X47S) for the free space measurement, which was necessary for compensation of the sample tube volume.

### 3.4.5 TXRF

TXRF was conducted on a Bruker S2 Picofox. Samples were prepared from a suspension of 10 mg catalyst in 1 mL H<sub>2</sub>O (MilliQ 18.2 MΩ cm), which contained 1 wt% Triton X-100 (Sigma Aldrich) as surfactant, 0.2 wt% polyvinylalcohol (Mowiol<sup>®</sup> 4-88, Sigma-Aldrich) as binder and 100 µg Ga (from 1 g/L Standard Solution, TraceCert<sup>®</sup>, Sigma-Aldrich) as internal standard. 10 µL were deposited onto a quartz glass sample carrier and dried at room temperature in a laminar flow hood to give a homogeneous thin film. 3 independent repeat measurements from different suspensions were conducted for each catalyst. For Fe, the characteristic 6.4 keV K<sub>α</sub>-1 emission line was used for calibration and quantification.

### 3.4.6 XPS

XPS analyses were performed using a Kratos Analytical AXIS UltraDLD spectrometer. Samples were prepared by pressing the catalyst powders into an indium substrate (pieces, Sigma-Aldrich 99.99%) to obtain a flat pellet (<1mm) with a diameter of ~1 cm. A monochromatic aluminium source (Al K<sub>α</sub> = 1486.6 eV) was used for excitation. The analyser was operated in constant pass energy of 40 eV using an analysis area of approximately 700 µm x 300 µm. Charge compensation was applied to minimise charging effects occurring during the analysis. The suitable C<sub>1s</sub> (285.0 eV) binding energy (BE) was used as internal reference. Pressure was in the 10<sup>-10</sup> mbar range during the experiments. Quantification and simulation of the experimental photopeaks were carried out using CasaXPS

and XPSPEAK41 software. Quantification was performed using the non-linear Shirley background subtraction.

### 3.4.7 EPR

The catalyst powders were manufactured into pellets ( $\sim 0.3$ cm diameter and  $\sim 0.5$ cm height) by homogenising a defined amount of catalyst with nonadecane (99%, Sigma-Aldrich) and compressing the mixture in a custom made dye. Although measurements could be conducted on the loose powders with the same result, the addition of dielectric nonadecane improved the reproducibility of the signals and alleviated the tuning of the microwave cavity. The pellets were inserted into EPR tubes equipped with *Young* taps in order to be able to evacuate the samples. For the samples with post-synthetic addition of Fe, the powder was impregnated with an aqueous solution of either  $\text{Fe}(\text{NO}_3)_3 \cdot 9\text{H}_2\text{O}$  (99.95%, Sigma-Aldrich) or  $\text{FeSO}_4 \cdot 7\text{H}_2\text{O}$  (99%, Sigma-Aldrich) and dried in a vacuum oven at 60 °C. The measurements on the Fe-N/C sample, which was evacuated at a temperature of 120 °C prior to the measurement, to remove eventually adsorbed oxygen, were performed on the loose powder. Measurements under atmosphere were conducted with the *Young* tap open and re-aeration was achieved by opening the *Young* tap of the evacuated sample. The measurements were conducted on a Bruker EMX Micro X-Band EPR spectrometer with a 1T magnet and the ability to measure at room temperature and at 77 K by cooling the cavity with liquid nitrogen. g-values were estimated from the utilised microwave frequency and the magnetic field at resonance condition according to equation ( 2.31).

### 3.4.8 TEM/STEM/EDX

Samples were prepared by drop drying a suspension of the catalyst in acetone (AnalR NORMAPUR<sup>®</sup>, VWR) onto copper TEM grids coated with holey carbon film (AGS147, Agar Scientific). Samples and TEM grids were dried under vacuum before use, to minimise contamination. TEM/STEM and EDX in Figure 3.15 were recorded on a FEI TITAN 80/300 equipped with a Quantax EDS system from Bruker. TEM for lattice spacing analysis in Figure 3.16 was carried out on a JEOL 2010.

### 3.4.9 STEM and EELS

Samples were prepared in the same way as for TEM. The machine was a Nion Ultra-STEM100 aberration corrected dedicated Scanning Transmission Electron Microscope, with a Gatan Enfina EEL Spectrometer attached. The microscope was operated at 60 kV, with an energy source spread of 0.35 eV and a spatial resolution of 1.1 Å.

### 3.4.10 MEA testing

Membrane Electrode Assemblies (MEA) were prepared according to a method developed by Paganin *et al.* [39]: Considering the targeted ionomer to carbon (I/C) ratio, the desired amount of carbon catalyst was mixed with Nafion™ ionomer solution (Sigma-Aldrich, 5 wt.%) and 1.5 mL of isopropanol (AnalR NORMAPUR®, VWR). This solution was homogenized in an ultrasound bath for 10 min, followed by complete evaporation of the solvents at room temperature. The dried solids were dispersed in isopropanol (AnalR NORMAPUR®, VWR) and quantitatively deposited on a gas transport medium (Toray paper TGP 60 with microporous layer, Alfa Aesar). As anode electrodes, commercial Johnson Matthey platinum electrodes, with a platinum loading of 0.4 mg<sub>Pt</sub> cm<sup>-2</sup> (Alfa Aesar, Johnson Matthey, Hydrogen Reformate/Cathode) were used. The MEAs were obtained by hot-pressing anode and cathode electrodes on both sides of a pre-treated Nafion™ 115 membrane (H<sup>+</sup>, DuPont) at 145 °C and 400 kg cm<sup>-2</sup>, for 3 min. Pretreatment of the Nafion™ membranes consisted of first boiling in 3 vol% H<sub>2</sub>O<sub>2</sub> (from 30wt% H<sub>2</sub>O<sub>2</sub> solution ACS grade, Sigma-Aldrich) in H<sub>2</sub>O (MilliQ 18.2 MΩ cm) for 1h, then boiling in 0.5M H<sub>2</sub>SO<sub>4</sub> (from H<sub>2</sub>SO<sub>4</sub> 97% Aristar from VWR) for 1h and finally boiling in H<sub>2</sub>O for 1h. The thicker Nafion™ 115 membranes was deliberately chosen over the thinner 221 membranes in order to avoid the possibility of any Pt crossover from the anode. Single PEFC tests refer to a 5 cm<sup>2</sup> electrode area and single serpentine flow fields (PEFC hardware from Fuel Cell Technologies, Inc.). During PEFC tests pure hydrogen (BIP plus-X47S, Air products) was used at a flow rate of 160 ccm and pure oxygen (BIP plus-X47S, Air products) at a flow rate of 550 ccm. Both anode and cathode compartments of the cell were pressurized with a backpressure of 2 bar (gauge). The fuel cell hardware was maintained at a temperature of 80 °C. Relative humidity (RH) values were achieved by adjusting the temperature of the humidification bottles. Moreover the backpressure of the system was corrected to account for the different water partial pressure and to

match the back pressure at 100% RH. Before any data collection it was ensured that the cell was stable at the respective current density, with a potential drift below 5 mV/hour. Polarization curves were performed utilizing an electronic load (Kikusui KFM2150). Gases were humidified via a humidification system from Fuel Cell Technologies, Inc.

### 3.5 References

- [1] Shao M., Chang Q., Dodelet J.P., Chenitz R. Recent Advances in Electrocatalysts for Oxygen Reduction Reaction. *Chemical Reviews*, 116(6), 3594–3657, March 2016. doi:10.1021/acs.chemrev.5b00462.
- [2] Elbaz L., Wu G., Zelenay P. Heat-Treated Non-precious-Metal-Based Catalysts for Oxygen Reduction. In M. Shao, editor, *Electrocatalysis in Fuel Cells*, number 9 in Lecture Notes in Energy, pages 213–246. Springer London, 2013. ISBN 978-1-4471-4910-1 978-1-4471-4911-8.
- [3] Jaouen F., Proietti E., Lefèvre M., Chenitz R., Dodelet J.P., et al. Recent advances in non-precious metal catalysis for oxygen-reduction reaction in polymer electrolyte fuel cells. *Energy Environ. Sci.*, 4, 114–130, December 2010. doi:10.1039/C0EE00011F.
- [4] Dodelet J.P. The Controversial Role of the Metal in Fe- or Co-Based Electrocatalysts for the Oxygen Reduction Reaction in Acid Medium. In M. Shao, editor, *Electrocatalysis in Fuel Cells*, number 9 in Lecture Notes in Energy, pages 271–338. Springer London, 2013. ISBN 978-1-4471-4910-1 978-1-4471-4911-8. doi:10.1007/978-1-4471-4911-8\_10.
- [5] Malko D. *The Oxygen Reduction Reaction (ORR) Catalyzed by Non Precious Metal/Nitrogen/Carbon Composites*. Master thesis, FAU Erlangen-Nürnberg/Imperial College London, 2013.
- [6] Malko D., Lopes T., Symianakis E., Kucernak A.R. The intriguing poison tolerance of non-precious metal oxygen reduction reaction (ORR) catalysts. *Journal of Materials Chemistry A*, November 2015. doi:10.1039/C5TA05794A.
- [7] Marinho B., Ghislandi M., Tkalya E., Koning C.E., de With G. Electrical conductivity of compacts of graphene, multi-wall carbon nanotubes, carbon black, and graphite

- powder. *Powder Technology*, 221, 351–358, May 2012. doi:10.1016/j.powtec.2012.01.024.
- [8] Alicılar A., Meriç G., Akkurt F., Şendil O. Air Oxidation of Ferrous Iron in Water. *J. Int. Environmental Application & Science*, 3(5), 409–414, 2008.
- [9] Gasteiger H.A., Kocha S.S., Sompalli B., Wagner F.T. Activity benchmarks and requirements for Pt, Pt-alloy, and non-Pt oxygen reduction catalysts for PEM-FCs. *Applied Catalysis B: Environmental*, 56(1–2), 9–35, March 2005. doi:10.1016/j.apcatb.2004.06.021.
- [10] Paulus U., Schmidt T., Gasteiger H., Behm R. Oxygen reduction on a high-surface area Pt/Vulcan carbon catalyst: A thin-film rotating ring-disk electrode study. *Journal of Electroanalytical Chemistry*, 495(2), 134–145, January 2001. doi:10.1016/S0022-0728(00)00407-1.
- [11] US DoE. Fuel Cell Measurements of Performance and Durability of Non-PGM ORR Electrocatalysts. [http://energy.gov/sites/prod/files/2015/08/f25/fcto\\_dwg\\_non-pgm\\_orr\\_catalyst\\_fc\\_testing\\_protocol.pdf](http://energy.gov/sites/prod/files/2015/08/f25/fcto_dwg_non-pgm_orr_catalyst_fc_testing_protocol.pdf). Accessed: 2016-09-27.
- [12] Masa J., Xia W., Muhler M., Schuhmann W. On the Role of Metals in Nitrogen-Doped Carbon Electrocatalysts for Oxygen Reduction. *Angewandte Chemie International Edition*, 54(35), 10,102–10,120, August 2015. doi:10.1002/anie.201500569.
- [13] De Soete D. *Neutron Activation Analysis*. Wiley Interscience, New York, 1972.
- [14] Biddinger E.J., von Deak D., Singh D., Marsh H., Tan B., et al. Examination of Catalyst Loading Effects on the Selectivity of CN<sub>x</sub> and Pt/VC ORR Catalysts Using RRDE. *Journal of The Electrochemical Society*, 158(4), B402–B409, January 2011. doi:10.1149/1.3552944.
- [15] Bonakdarpour A., Lefevre M., Yang R., Jaouen F., Dahn T., et al. Impact of Loading in RRDE Experiments on Fe–N–C Catalysts: Two- or Four-Electron Oxygen Reduction? *Electrochemical and Solid-State Letters*, 11(6), B105–B108, January 2008. doi:10.1149/1.2904768.
- [16] Muthukrishnan A., Nabae Y., Okajima T., Ohsaka T. Kinetic Approach to Investigate the Mechanistic Pathways of Oxygen Reduction Reaction on Fe-Containing

- N-Doped Carbon Catalysts. *ACS Catalysis*, 5(9), 5194–5202, September 2015. doi:10.1021/acscatal.5b00397.
- [17] Tylus U., Jia Q., Strickland K., Ramaswamy N., Serov A., et al. Elucidating Oxygen Reduction Active Sites in Pyrolyzed Metal–Nitrogen Coordinated Non-Precious-Metal Electrocatalyst Systems. *The Journal of Physical Chemistry C*, 118(17), 8999–9008, May 2014. doi:10.1021/jp500781v.
- [18] Jaouen F., Herranz J., Lefèvre M., Dodelet J.P., Kramm U.I., et al. Cross-Laboratory Experimental Study of Non-Noble-Metal Electrocatalysts for the Oxygen Reduction Reaction. *ACS Applied Materials & Interfaces*, 1(8), 1623–1639, August 2009. doi:10.1021/am900219g.
- [19] Masa J., Ozoemena K.I., Schuhmann W., Zagal J.H. Fundamental Studies on the Electrocatalytic Properties of Metal Macrocyclics and Other Complexes for the Electroreduction of O<sub>2</sub>. In M. Shao, editor, *Electrocatalysis in Fuel Cells*, number 9 in Lecture Notes in Energy, pages 157–212. Springer London, 2013. ISBN 978-1-4471-4910-1 978-1-4471-4911-8. doi:10.1007/978-1-4471-4911-8\_7.
- [20] Weast R., Astle M. *CRC Handbook of Chemistry and Physics: A Ready-Reference Book of Chemical and Physical Data*. The CRC Press, Boca Raton, Fla., 1982. ISBN 978-0-8493-0463-7.
- [21] Bard A.J., Faulkner L. *Electrochemical Methods: Fundamentals and Applications*. John Wiley & Sons, New York, 2nd edition, January 2001. ISBN 978-0-471-04372-0.
- [22] Pumera M., Miyahara Y. What amount of metallic impurities in carbon nanotubes is small enough not to dominate their redox properties? *Nanoscale*, 1(2), 260, 2009. doi:10.1039/b9nr00071b.
- [23] Kelemen S.R., George G.N., Gorbaty M.L. Direct determination and quantification of sulphur forms in heavy petroleum and coals. *Fuel*, 69(8), 939–944, August 1990. doi:10.1016/0016-2361(90)90001-7.
- [24] Wertz J.E., Bolton J.R. *Electron Spin Resonance: Elementary Theory and Practical Applications*. Chapman and Hall, 1986. ISBN 978-0-412-01161-0.

- [25] Malko D., Kucernak A.R., Lopes T. *In situ* electrochemical quantification of active sites in Fe-N/C non-precious metal catalysts. *Nature Communications*, 7, September 2016. doi:10.1038/ncomms13285.
- [26] Wang J., Wang G., Miao S., Jiang X., Li J., et al. Synthesis of Fe/Fe<sub>3</sub>C nanoparticles encapsulated in nitrogen-doped carbon with single-source molecular precursor for the oxygen reduction reaction. *Carbon*, 75, 381–389, August 2014. doi:10.1016/j.carbon.2014.04.017.
- [27] Deng D., Yu L., Chen X., Wang G., Jin L., et al. Iron Encapsulated within Pod-like Carbon Nanotubes for Oxygen Reduction Reaction. *Angewandte Chemie International Edition*, 52(1), 371–375, January 2013. doi:10.1002/anie.201204958.
- [28] Wu G., More K.L., Johnston C.M., Zelenay P. High-performance electrocatalysts for oxygen reduction derived from polyaniline, iron, and cobalt. *Science*, 332(6028), 443–447, April 2011. doi:10.1126/science.1200832.
- [29] Wu W., Zhu Z., Liu Z., Xie Y., Zhang J., et al. Preparation of carbon-encapsulated iron carbide nanoparticles by an explosion method. *Carbon*, 41(2), 317–321, February 2003. doi:10.1016/S0008-6223(02)00292-0.
- [30] Proietti E., Jaouen F., Lefèvre M., Larouche N., Tian J., et al. Iron-based cathode catalyst with enhanced power density in polymer electrolyte membrane fuel cells. *Nature Communications*, 2, 416, August 2011. doi:10.1038/ncomms1427.
- [31] Lefèvre M., Proietti E., Jaouen F., Dodelet J.P. Iron-based catalysts with improved oxygen reduction activity in polymer electrolyte fuel cells. *Science*, 324(5923), 71–74, April 2009. doi:10.1126/science.1170051.
- [32] Kramm U.I., Lefèvre M., Larouche N., Schmeisser D., Dodelet J.P. Correlations between Mass Activity and Physicochemical Properties of Fe/N/C Catalysts for the ORR in PEM Fuel Cell via <sup>57</sup>Fe Mössbauer Spectroscopy and Other Techniques. *Journal of the American Chemical Society*, 136(3), 978–985, January 2014. doi:10.1021/ja410076f.
- [33] Ferrandon M., Kropf A.J., Myers D.J., Artyushkova K., Kramm U., et al. Multitechnique Characterization of a Polyaniline–Iron–Carbon Oxygen Reduction Catalyst.



- The Journal of Physical Chemistry C*, 116(30), 16,001–16,013, August 2012. doi: 10.1021/jp302396g.
- [34] Kramm U.I., Herranz J., Larouche N., Arruda T.M., Lefèvre M., et al. Structure of the catalytic sites in Fe/N/C-catalysts for O<sub>2</sub>-reduction in PEM fuel cells. *Phys. Chem. Chem. Phys.*, 14(33), 11,673–11,688, August 2012. doi:10.1039/C2CP41957B.
- [35] Denaro T., Baglio V., Girolamo M., Antonucci V., Arico' A.S., et al. Investigation of low cost carbonaceous materials for application as counter electrode in dye-sensitized solar cells. *Journal of Applied Electrochemistry*, 39(11), 2173–2179, March 2009. doi: 10.1007/s10800-009-9841-2.
- [36] Slater J.C. Atomic Radii in Crystals. *The Journal of Chemical Physics*, 41(10), 3199–3204, November 1964. doi:10.1063/1.1725697.
- [37] Schmidt T.J., Gasteiger H.A., Stäb G.D., Urban P.M., Kolb D.M., et al. Characterization of High-Surface-Area Electrocatalysts Using a Rotating Disk Electrode Configuration. *Journal of The Electrochemical Society*, 145(7), 2354–2358, January 1998. doi:10.1149/1.1838642.
- [38] van der Vliet D., Strmcnik D.S., Wang C., Stamenkovic V.R., Markovic N.M., et al. On the importance of correcting for the uncompensated Ohmic resistance in model experiments of the Oxygen Reduction Reaction. *Journal of Electroanalytical Chemistry*, 647(1), 29–34, August 2010. doi:10.1016/j.jelechem.2010.05.016.
- [39] Paganin V.A., Ticianelli E.A., Gonzalez E.R. Development and electrochemical studies of gas diffusion electrodes for polymer electrolyte fuel cells. *Journal of Applied Electrochemistry*, 26(3), 297–304, July 1995. doi:10.1007/BF00242099.

*Information on the active site and the mechanism was gathered through subjecting the catalyst to various external conditions. Surprisingly, the ODAN catalyst is resistant to a wide range of environmental contaminants which makes it suitable for challenging applications. Catalyst deactivation of the Fe-N/C catalyst was achieved by NO and by chemical modification. Nitrogen cycle molecules will be used in the subsequent chapters to provide further insight. Gas sorption was conducted and suggests that the catalyst readily activates molecular oxygen as an oxidant and this will be exploited for organic epoxidation reactions later in this work. The energy of desorption for molecular oxygen has been determined to be  $77.89 \text{ kJ mol}^{-1}$ . In the range of pH 0 - 9 the mechanism does not seem to change and has most likely a proton coupled electron transfer as rate determining step. This is inferred from the pH dependence and is supported by a kinetic isotope effect of 3.4. The reaction becomes more facile under alkaline conditions with the changeover occurring at a pH >10 and a kinetic isotope effect of 2.5 at pH 14.*

## Chapter 4

# Experimental identification of the active site and mechanistic insight into its activity

### 4.1 Introduction

Although tremendous efforts have been invested, insight into the nature of the active site is limited. [1–3] This is mainly because of the lack of a probe for the active site, therefore making the study challenging. [1–3] Although extensive ex-situ investigations, such as

EXAFS and Mössbauer have been conducted, direct correlation to the active site could not be shown. [2, 4–6] This is because such techniques are not surface specific and will probe sites within the bulk of the material, which is inaccessible to reactants and hence cannot act as active site. [2] Additionally, knowledge on the reaction mechanism is limited. Information on the rate determining step could help to improve the activity.

In this chapter it is intended to probe the active sites by subjecting it to different environments. In the first part a probe will be identified in order to further generate information on the behaviour of the active site. It is tried to deactivate the activity by poisoning. Finding a useful probe can then be used to create experiments which yield further insight into the nature of the active site. The mechanism will be probed by varying the reaction pH and by investigating the kinetic isotope effect (KIE) on the ORR.

The first surprising finding was that the **ODAN** catalyst is almost immune to poisons that typically detrimentally affect Pt based catalysts. Various poisons were studied and the implications will be reported.

## 4.2 Results and Discussion

### 4.2.1 Poison tolerance and implications for practical devices<sup>1</sup>

For practical applications, an electrocatalyst should ideally be resilient to trace amount of compounds and species, which are abundant in the environment.

While Pt and also other metals show high activities, they are not selective towards the desired reaction and catalyse other unwanted side-reactions. They are therefore susceptible to poisons such as methanol, hydrocarbons, chlorine/chloride and hydrogen sulphide. [8–10] This limits the use of Pt and other catalysts for green technologies under demanding conditions, where the ORR could otherwise be applied. Surprisingly, the **ODAN** is tolerant to all of these substances. To assess the poison tolerance, RDE measurements were taken in pure electrolyte and in the presence of contaminants at different concentrations. As a measure of loss in activity, the decrease in current density for oxygen reduction at the half-wave potential (determined in the poison free environment) upon introduction

---

<sup>1</sup>This section is an excerpt of Ref. [7]. The results were produced in close collaboration with Dr. Thiago Lopes. Some RRDE poisoning experiments and all MEA poisoning experiments were carried out by Dr. Thiago Lopes.

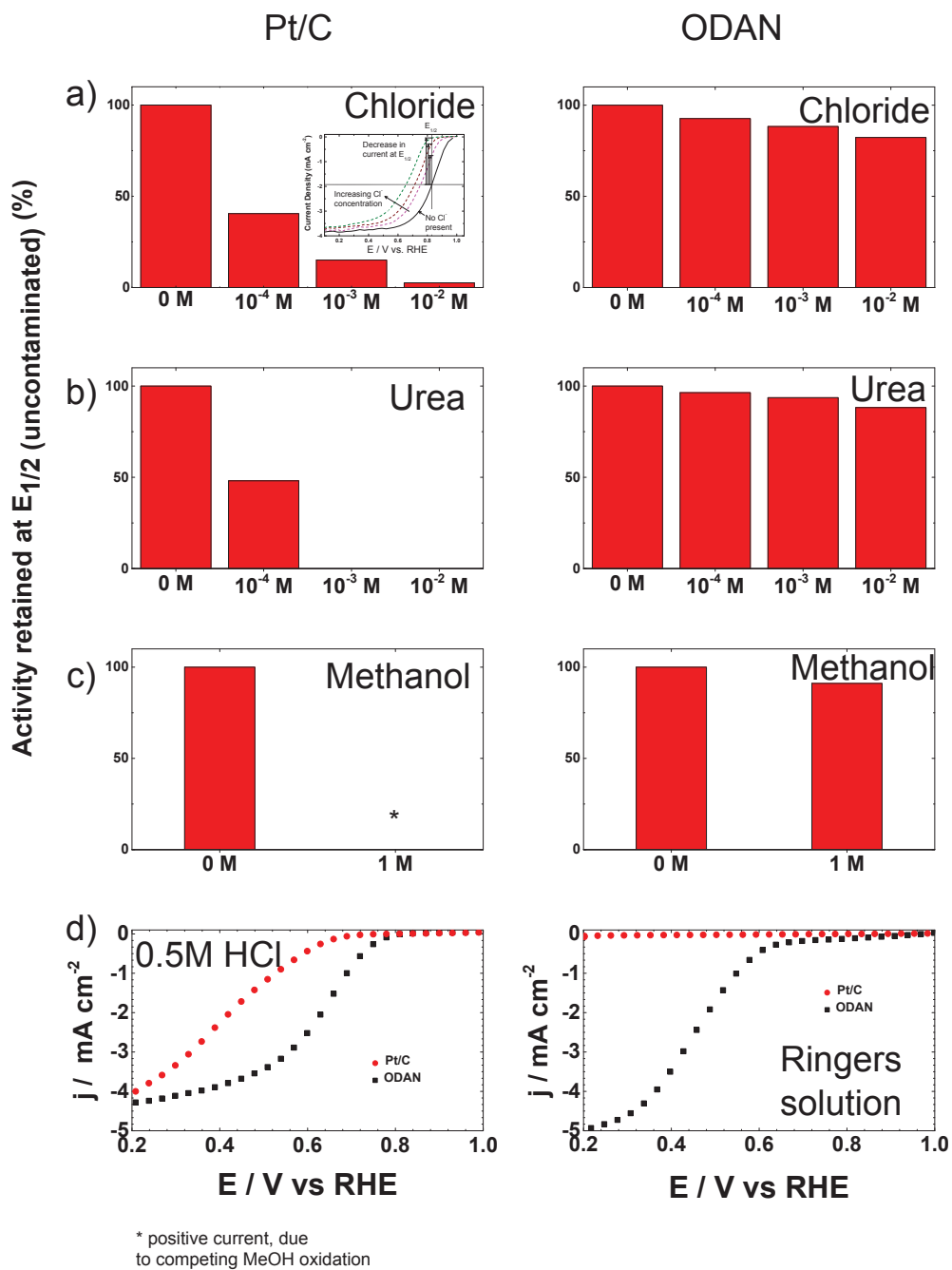


FIGURE 4.1: Bar plots showing the performance at the respective half wave potential of the RDE measurement, comparing a Pt/C catalyst to ODAN at a rotating speed of 1600 rpm, 30 s hold, 30 mV step potential, catalyst loading: ODAN: 750  $\mu\text{g cm}^{-2}$ , Pt/C: 30  $\text{mg}_{\text{Pt}} \text{cm}^{-2}$ , O<sub>2</sub>-saturated at 1 atm before and after adding (a) Cl<sup>-</sup> to 0.5 M H<sub>2</sub>SO<sub>4</sub>, (b) urea to 0.5 M H<sub>2</sub>SO<sub>4</sub> and (c) methanol to 0.1 M NaOH to obtain the respective concentrations. (d) RDE measurements, comparing the ORR activity of ODAN to Pt/C in (left) 0.5 M HCl and (right) Ringers solution (same conditions and parameters as (a) - (c)). [Taken with permission from Ref. [7]]

of the contaminant is taken (see inset in Figure 4.1 (a) (inset)). While the activity of the Pt catalyst is always reduced significantly, the **ODAN** is not or only slightly affected in its activity (Figure 4.1 (a) - (c)). Chloride was introduced into the electrochemical cell, because of the abundance of that element in the environment and as representative species for ions that will strongly adsorb to precious metal surfaces and decrease their activity. While the influence on the activity the **ODAN** catalyst is minute, the activity of the Pt/C catalyst is significantly reduced, as can be seen by the dramatic drop in performance at the half wave potential (Figure 4.1 (a)). Urea was added, because of its relative abundance. It is a common waste product of all mammals. [11] Moreover it is taken as representative for nitrogen rich molecules. A large impact on the Pt activity is observed. Even at a very low concentration of only  $10^{-4}$  M the performance at the half wave potential is halved and at  $10^{-3}$  M shut down completely, while the effect on the **ODAN** catalyst is minimal (Figure 4.1 (b)). Although Holze *et al.* showed the methanol tolerance of this type of catalyst already, it is also included in this study in order to show the generality of the poison resistance. [12] MeOH was added to 0.1M NaOH, because for Pt catalysts, the competing methanol oxidation lowers the activity. As is well known, this is a drawback of Pt catalysts for the use at the cathode in direct methanol fuel cells, where methanol crossover to the cathode can occur, thus lowering the overall fuel efficiency dramatically. [12] It is also detrimental where the oxygen reduction reaction is carried out in the presence of oxidisable organic molecules, such as in waste water treatment or as counter electrode for other electrochemical devices. Additionally to methanol, other alcohols are also oxidized at potentials that interfere with the ORR, which is another potential problem for traditional catalysts. [13] As expected, no effect of MeOH on the catalyst was observed, while the methanol oxidation completely shuts down the oxygen reduction on the Pt catalyst (Figure 4.1 (c)). To further show the broad applicability of our catalyst an RDE measurement was also taken in 0.5 M HCl (Figure 4.1 (d)), a highly corrosive environment, and it can be seen that the activity of the **ODAN** catalyst is far superior to the commercial catalyst. Another possible application of this catalyst is the application in medical implantable fuel cells that run on glucose on the anode side and on oxygen on the cathode side. Such devices have already been described. [14] Again the susceptibility of Pt to all kinds of poisons is a limiting factor here. To demonstrate the feasibility of the catalyst under physiological conditions, a Ringers solution was chosen as an electrolyte to probe the ORR activity against Pt (Figure 4.1 (e)). While **ODAN** still shows good ORR activity, the activity of Pt is completely shut down. It has to be

noted that the thick catalyst layer and therefore higher total surface area compared to Pt/C can introduce some benefits for the non-precious metal catalyst due to the filtering capability of carbon and the respective longer time of contaminants to diffuse through the carbon structure to the non-precious active site. A measurement of the transient of the contamination has been conducted to estimate if the polarisation time was long enough in order to allow the contaminants to reach the active site. The contamination of the Pt based catalyst takes place in less than 1 second. Assuming a BET surface area of  $250 \text{ m}^2 \text{ g}^{-1}$  and a  $40 \text{ } \mu\text{g cm}^{-2}$  carbon loading on the RDE tip for the Pt/C catalyst *versus* a surface area of  $614 \text{ m}^2 \text{ g}^{-1}$  and  $750 \text{ } \mu\text{g cm}^{-2}$  loading for **ODAN**. Therefore, the total carbon surface area is 46 times higher for the non-precious metal catalyst. This means, in the worst case, the contaminants would take 46 times longer or 46 seconds to reach the active sites. The measurements are performed under steady state and a 30-second hold with 30 mV step potential. By the time the measurement reaches the respective half-wave potential, several minutes have passed and access of the contaminant to the active site has been achieved.

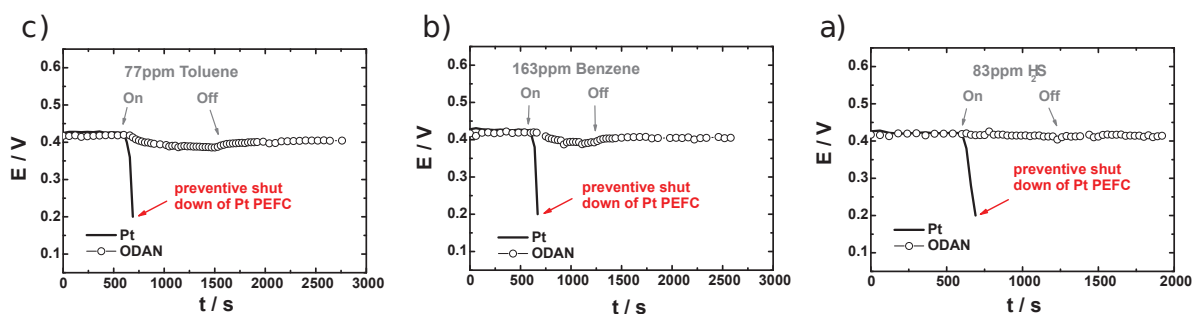


FIGURE 4.2: Cell voltage of MEA running on Pt or ODAN as cathode catalyst, before and after adding (b) 83 ppm  $\text{H}_2\text{S}$  (c) 77 ppm toluene and (d) 163 ppm benzene into the cathode gas stream. [Adapted with permission from Ref. [7]]

To further study the activity under real fuel cell operating a polymer electrolyte membrane (PEM) single cell was prepared and tested. The catalyst was paint brushed onto a Toray carbon paper containing a microporous layer, which was used as cathode and a commercial Pt electrode as anode. The loading of **ODAN** at the cathode was  $4 \text{ mg cm}^{-2}$ . It was compared to a state of the art commercial Pt cathode with a loading of  $0.4 \text{ mg}_{\text{Pt}} \text{ cm}^{-2}$ . The anode in both cases was a commercial Pt anode with a loading of  $0.4 \text{ mg}_{\text{Pt}} \text{ cm}^{-2}$ . The high anode Pt loading makes sure that the anode reaction is not the limiting factor. The impact of poisons on the operating fuel cell was studied. Different contaminants were fed into the gas stream and the potential was monitored. When as little as 83 ppm of  $\text{H}_2\text{S}$  was fed into the cathode gas stream, the cell utilising Pt cathode catalyst had

an almost instantaneous drop in potential, while the **ODAN** cell (Figure 4.2 (a)) was completely unaffected. It can be suspected that this behaviour could be extrapolated to longer chain organic sulphides as well. The same phenomenon was observed with 77 ppm toluene (Figure 4.2 (b)) and 163 ppm benzene (Figure 4.2 (c)), which can be taken as representatives for volatile organic compounds. The ratio in total carbon surface area within the fuel cell test is 60 times higher for the **ODAN** cell compared to the Pt cell. Indeed in the operating fuel cell, the effect of contamination takes place slower. The whole operation time of the **ODAN** cell after contamination shall therefore be normalised to the higher surface area *versus* Pt. For instance after contamination the measurement was continued for 2100 seconds in the **ODAN** cell contaminated with toluene. Therefore 2100 s were normalised to the 60 times higher surface area to match 35 s in the Pt cell. The potential drop at 35 s in the Pt cell is therefore compared to the potential drop in the **ODAN** cell after 2100 s (post contamination) and likewise in the other experiments. The values are 40 mV *versus* 14 mV for toluene, 33 mV *versus* 17 mV for benzene and 40 mV *versus* 5 mV for H<sub>2</sub>S for Pt *versus* **ODAN** respectively. Even if the contamination time scales linearly with total surface area, **ODAN** is still less affected than the Pt catalyst. However more complex processes are likely to be determining the contamination and ultimately failure time of the cell. This shows that the resistance to poisons shown in RDE studies can be transferred to device level.

**To summarise:** The **ODAN** catalyst is exceptionally poison-tolerant. While the reference Pt catalyst is always severely affected by a wide variety of substances, **ODAN** is mostly resistant, or at worst showing only a minor reduction in performance. The generality of this poison tolerance is curious, given that a metal centre is proposed as active site.

#### 4.2.2 Nitrogen cycle molecules as possible active site probes

Although the poison tolerance of the catalyst is useful for practical applications, the absence of a molecular active site probe makes it challenging to generate insight into this complex material. It is well known that nitrogen cycle molecules such as nitric oxide, nitrite and hydroxylamine interact with the iron complexes. [15, 16] Therefore the effect of NOBF<sub>4</sub> and NO on the **Fe-N/C** catalyst was investigated.

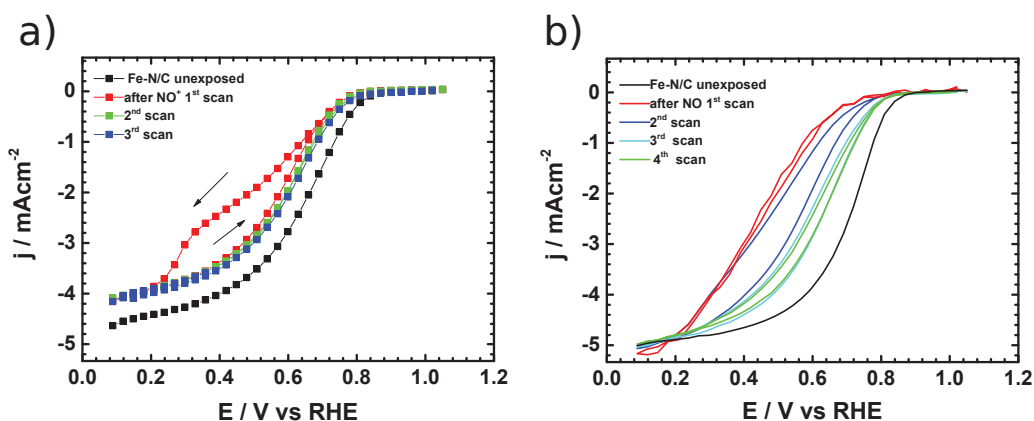


FIGURE 4.3: (a) Steady-state RDE measurements of Fe-N/C catalyst in 0.5 M  $\text{H}_2\text{SO}_4$ , before and after exposure to  $\text{NO}^+\text{BF}_4^-$ , catalyst loading:  $750 \mu\text{g cm}^{-2}$ , rotating speed: 1600 rpm, 30 s hold, 30 mV step potential,  $\text{O}_2$ -saturated at 1 atm. (b) RDE measurement of Fe-N/C catalyst in 0.5 M  $\text{H}_2\text{SO}_4$ , before and after exposure to NO gas, catalyst loading:  $750 \mu\text{g cm}^{-2}$ ,  $5 \text{ mV s}^{-1}$ , rotating speed: 1600 rpm,  $\text{O}_2$ -saturated at 1 atm.

Figure 4.3 (a) shows the ORR activity before and after exposing the electrode to a solution of 0.1 M  $\text{NO}^+\text{BF}_4^-$  in acetone. It can be seen that a clear poisoning effect is present. The first cycle shows a slight recovery of the activity. The remaining activity decrease seems to stable. Figure 4.3 (b) shows the ORR activity before and after exposing the electrode to NO saturated 0.5 M  $\text{H}_2\text{SO}_4$ . Again the activity is significantly decreased. This shows that NO can be a potential probe for the active site. Therefore, nitrogen cycle molecules were studied in more depth in Chapter 5 and it was possible to utilise nitrite as a probe to determine the active site density, which is detailed in Chapter 6.

### 4.2.3 Organic reactions to track the active site

It has been shown for model compounds, that the chemical environment of the macrocycle can lead to a significant increase in activity. Especially electronegative substituents increase the activity significantly. [17] Furthermore Ramaswamy et al reported that the electronic properties of the carbon support influence the catalytic activity by modulating the  $\text{Fe}^{2+}/\text{Fe}^{3+}$  transition. [18] Therefore it was intended to post-synthetically graft electron withdrawing groups onto the carbon support and probe the effect onto the ORR activity.

The first attempt was the acylation of the carbon support with the *Friedel-Crafts* reaction, by treating the catalyst with a acetyl chloride in the presence of  $\text{AlCl}_3$ . This reagent has been chosen, as it readily reacts with aromatic rings to attach an electron withdrawing



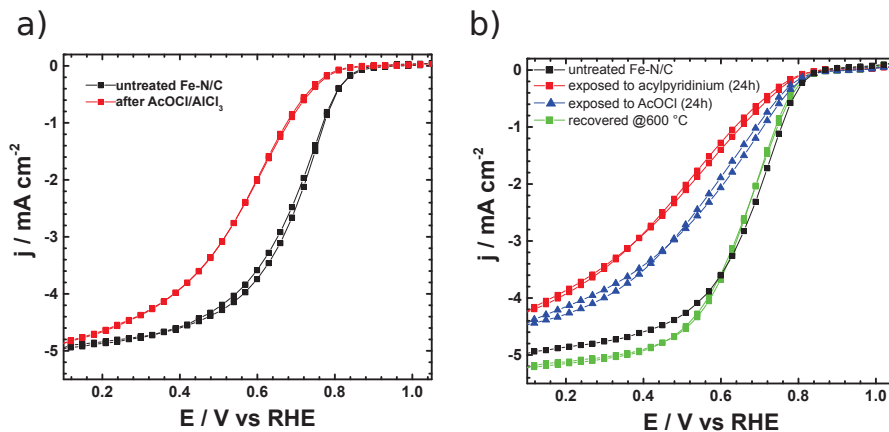


FIGURE 4.4: Steady-state RDE measurements of Fe-N/C catalyst in 0.5 M  $\text{H}_2\text{SO}_4$ , catalyst loading:  $750 \mu\text{g cm}^{-2}$ , rotating speed: 1600 rpm, 30 s hold, 30 mV step potential,  $\text{O}_2$ -saturated at 1 atm. Before and after (a) exposing to *Friedel-Crafts* conditions and (b) acylpyridinium, acyl chloride and recovery.

acyl group. [19] Figure 4.4 (a) shows the ORR activity before and after treatment. It can be seen that the activity is irreversibly decreased. Although it is not the sought for effect, an activity decrease means some sort of interaction with the active centre and could therefore potentially yield further information on the active site. As the mixture used (acetyl chloride with  $\text{AlCl}_3$ ) is aggressive and therefore unspecific, a more specific reagent, which is used to acylate nitrogen functionalities was used. The acyl-pyridinium method is typically used in organic synthesis to mildly acylate nitrogen functional groups. [20]

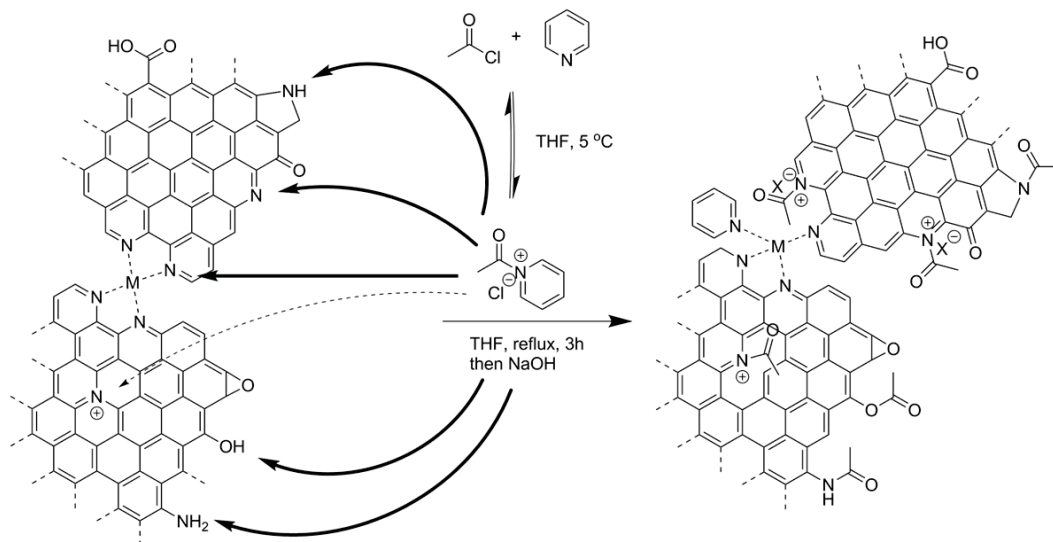


FIGURE 4.5: Scheme showing the possible reactions of the acylpyridinium species with the Fe-N/C catalyst.

Figure 4.5 shows a proposed scheme of how the acyl-pyridinium reagent could react with the different functional groups of the Fe-N/C catalyst. Figure 4.4 (b) shows the ORR

activity in 0.5 M  $\text{H}_2\text{SO}_4$  before and after treating the catalyst with the acylpyridinium method and with only acetyl chloride. It can be seen that both methods slightly decrease the activity, while the addition of pyridine increases the detrimental effect on the ORR activity. Electrochemically this activity decrease seems to be stable. However, heating the catalyst at 600 °C under nitrogen fully recovers the activity. The recovery temperature was chosen below the typically used 700 - 1000 °C, which is believed to be necessary to form new active sites. Hence the increase in activity is attributed to the recovery of already present active sites rather than the formation of new active sites. Further investigation, such as the analysis of released gas with temperature, other treatments and physical characterisation of the modified catalyst might yield further insight into this material.

**To summarise:** The acylation reaction has been successfully carried out on the **Fe-N/C** catalyst and decreases the ORR activity. Recovery is possible by heat treatment at temperatures below those used to form active sites. This shows the use of organic chemical reactions can be used to potentially probe the active site of the material. Further investigation seems worthwhile.

#### 4.2.4 Gas sorption of oxygen on Fe-N/C catalyst

The physical and chemical interaction of the **Fe-N/C** catalyst with oxygen was investigated with gas sorption experiments. The catalyst was subjected to a heat treatment regimen under inert atmosphere and the desorbed gas species have been tracked with a mass spectrometer.

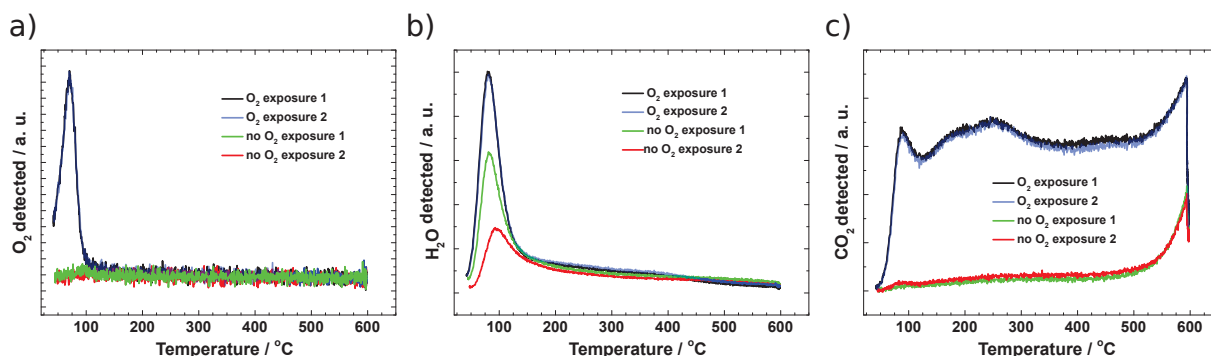


FIGURE 4.6: Gas desorption measurements, when heating the Fe-N/C catalyst at  $10 \text{ min}^{-1}$ , after exposure to  $\text{O}_2$  or Ar for 1h at room temperature. Species detected in the mass spectrometer (a)  $m/z=32$ , oxygen (b)  $m/z=17$ , water and (c)  $m/z=44$ , carbon dioxide.

In Figure 4.6 (a) the amount of O<sub>2</sub> released *versus* temperature is shown when the catalyst is pre-exposed to O<sub>2</sub> as compared to when it is not exposed to O<sub>2</sub>. The catalyst was heated to 600 °C under a constant flow of Ar prior to each cycle in order to remove any adsorbed species. The catalyst was then subjected to O<sub>2</sub> or Ar for 1 h at room temperature and then to Ar for 1 h at room temperature to remove any non-adsorbed O<sub>2</sub>. Two O<sub>2</sub> exposure cycles and two Ar exposures cycles were then recorded in sequence. There is a clear O<sub>2</sub> peak at ~70 °C in the samples pre-exposed to O<sub>2</sub> and no peak in the samples pre-exposed to Ar. This confirms that the desorbed oxygen is due to an adsorption process beforehand and not from decomposing species within the catalyst itself. The fact that the peak has the same height for both O<sub>2</sub> cycles suggests a reversible process. A water peak (Figure 4.6 (b)) can be observed in all cycles, whether the catalyst was exposed to O<sub>2</sub> or not. The source of the water peak could not be confirmed. It might be trace amounts present in the utilised gases which adsorb onto the dry catalyst, or water molecules condensed in the micro and mesopores of the carbon catalysts which are difficult to remove due to capillary condensation. The water peak is larger in the O<sub>2</sub> samples. Although definitive analysis is not possible from these results, they suggest a number of intriguing possibilities. Interestingly, only pre-exposure to O<sub>2</sub> results in the observation of CO<sub>2</sub>. It is striking that the CO<sub>2</sub> release already present at relatively low temperature (< 100 °C). At ~ 50 °C, the continuous release of CO<sub>2</sub> can be observed. This is an unusually low temperature for the oxidation of amorphous carbon and indicates that the catalysts is able to activate oxygen and create a powerful oxidant. [21] The absence of CO<sub>2</sub> production in the non-exposed cycle, suggests that the oxygen atoms within this released CO<sub>2</sub> stem from the preadsorbed O<sub>2</sub> molecules. This further implies that some O<sub>2</sub> will strongly chemisorb onto the catalyst and might even be subjected to O-O bond cleave, so that atomic oxygen species might be present at the surface of the catalyst. Therefore, this catalyst might be utilised as catalyst for the oxidation of organic compounds utilising molecular oxygen. The catalyst might be able to activate oxygen, in order to produce superoxide species, thus providing a good oxidant. (this topic is discussed in Chapter 7)

Figure 4.7 shows the O<sub>2</sub> (a) and H<sub>2</sub>O (b) desorption at various heating rates. From the variation of the temperature maximum  $T_{\max}$  with heating rate  $\beta$ , the energy of desorption was determined according to equation ( 2.30). For O<sub>2</sub> an energy of desorption  $E_{\text{des}} = 77.96$  kJ mol<sup>-1</sup> was determined. This lies well in the region of chemisorption and shows that the oxygen strongly interacts with the catalyst. [22] For H<sub>2</sub>O an  $E_{\text{ads}} = 98.08$  kJ mol<sup>-1</sup>

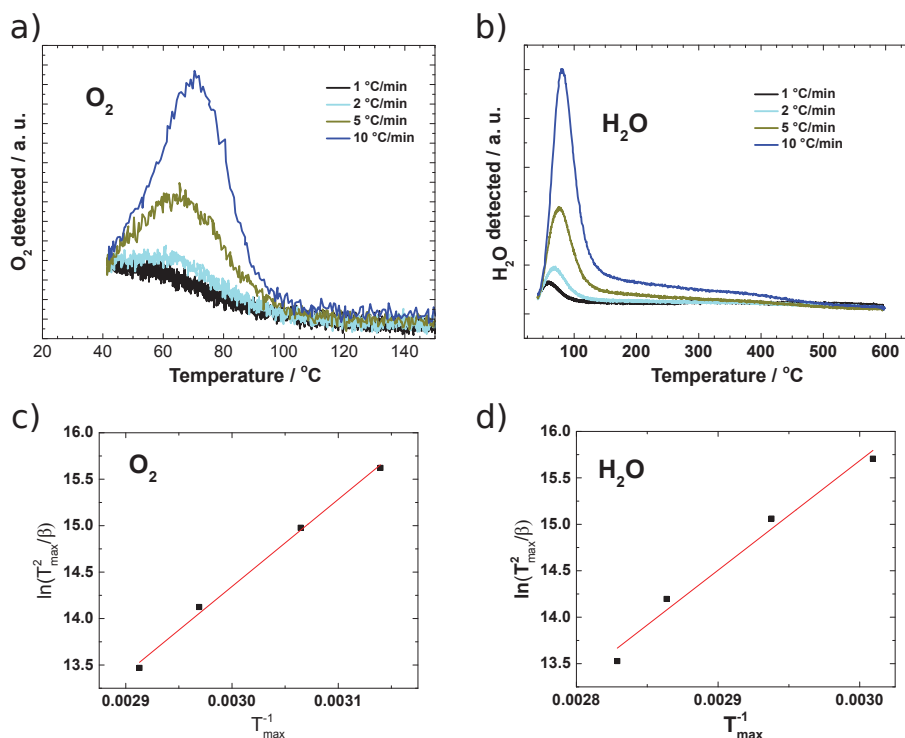


FIGURE 4.7: Temperature programmed desorption measurements at different heating rates, after exposing the Fe-N/C catalyst to O<sub>2</sub> for 1h at room temperature. Detection of species with a mass spectrometer (a)  $m/z=32$ , oxygen (b)  $m/z=17$ , water. (c) and (d) linearisation of  $T_{\max}$  and  $\beta$  relationship of measurements (a) and (b), respectively.

was determined. However, this value should be taken with care, as more investigation is necessary to confirm the source of the water peak. Nevertheless the successful extraction of  $E_{\text{des}}$  for O<sub>2</sub> might be useful to investigate this parameter as descriptor for the activity, when investigating a range of catalysts with different activities. This might yield further insight.

**To summarise:** O<sub>2</sub> could be successfully adsorbed onto the Fe-N/C catalyst and desorbed via heating. The desorbed species detected were O<sub>2</sub>, H<sub>2</sub>O and CO<sub>2</sub>. Especially the release of CO<sub>2</sub> at a relatively low temperature is striking and suggests that the catalyst is capable of creating a powerful oxidant from molecular O<sub>2</sub> at relatively low temperatures. The energy of desorption of O<sub>2</sub> was determined to be 77.96 kJ mol<sup>-1</sup> which suggests chemisorption rather than physisorption.

#### 4.2.5 Mechanistic investigation of Fe-N/C catalyst

In order to improve catalysis, detailed knowledge of the mechanism is necessary. Some insight can be gained by probing the role of protons in the ORR mechanism. This has

been done by varying the pH across the full scale from pH 0 to 14 and by measuring the kinetic isotope effect under acidic as well as alkaline conditions.

#### 4.2.5.1 pH dependence of the ORR

To investigate whether the underlying catalytic mechanism is liable to be the same at higher pH values compared to the technologically important acidic activity and what the influence of protons are within the reaction mechanism, the oxygen reduction reaction was studied at various pH values, which previously has only been investigated for low (0-2) and high (12-14) pH values. [23]

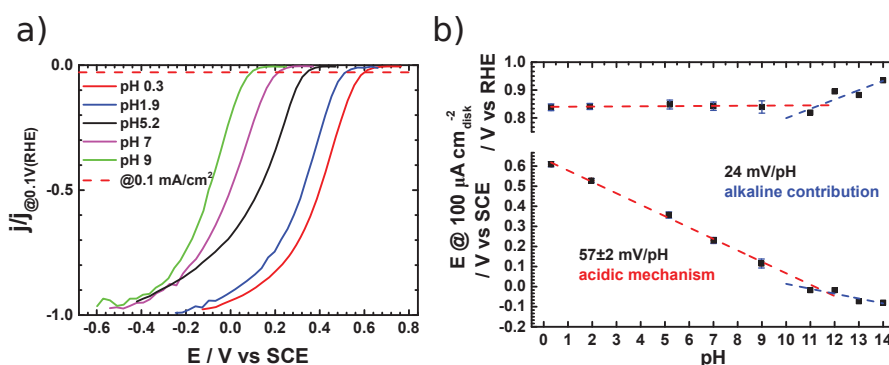


FIGURE 4.8: (a) Rotating disk electrode measurements of Fe-N/C catalyst at different pH values in O<sub>2</sub>-saturated 0.5 M electrolytes, 1600 rpm, 5 mV s<sup>-1</sup>; Loading 270 μg cm<sup>-2</sup>. Corrected for solution resistance, capacitive background and different oxygen solubility and diffusivity. b) Plot of the potential at a current density of 0.1 mA cm<sup>-2</sup> (iR-free) versus pH. (bottom) versus SCE; linear fit shows a slope of 57±2 mV pH<sup>-1</sup> in the pH range 0 - 9 (top) corrected to RHE scale. All values become the same within the error margin in the pH range 0 - 9.

Figure 4.8 (a) shows the, iR-free, background corrected RDE linear sweep voltammograms of the catalyst, which were normalised to the different oxygen solubility in the respective electrolytes, at 1600 rpm in oxygen saturated electrolyte. By plotting the current at 0.1 mA cm<sup>-2</sup> versus pH, a linear plot with a slope of close to 59 mV pH<sup>-1</sup> is obtained (Figure 4.8 (b)). This indicates a proton coupled electron transfer as rate determining step for the reduction of oxygen to water at high potentials. This is intriguing and might inspire approaches on how to accelerate the rate determining step. It can be seen that in the pH range between 0 9 the activity at high potentials (Figure 4.8 (b) top) is the same. It is known that the ORR is more facile in alkaline solution and a changeover in mechanism is likely at high pH. [18] Therefore the analysis of the ORR activity was extended until pH 14 and it can be observed that a significant deviation from 59 mV pH<sup>-1</sup> and the associated changeover in mechanism is only present above pH 9 (Figure 4.8 (b)).

It can clearly be seen that the pH dependence changes only at this high pH ( $>9$ ) and only then the rate enhancing effect of using alkaline conditions becomes measurable. This is also evident from the increase in activity above pH 10, when compared on the RHE scale (Figure 4.8 (b) top).

TABLE 4.1: Mean values and standard deviation for pH, apparent Tafel slopes and potentials at the respective pH, corresponding to measurements shown in Figure 4.8, from 3 independent runs for each data point. Independent here means that for each run a new catalytic layer from a different newly prepared ink was measured.

pH	Tafel slope [mV dec <sup>-1</sup> ]	$E_{j=0.1 \mu\text{A cm}^{-2}}$ [mV <i>vs</i> SCE]	$E_{j=0.1 \mu\text{A cm}^{-2}}$ [mV <i>vs</i> RHE]
$0.30 \pm 0.03$	$83 \pm 14$	$609 \pm 12$	$838 \pm 12$
$1.96 \pm 0.01$	$98 \pm 14$	$528 \pm 11$	$841 \pm 11$
$5.16 \pm 0.04$	$80 \pm 12$	$357 \pm 16$	$848 \pm 16$
$7.00 \pm 0.06$	$97 \pm 4.0$	$230 \pm 15$	$842 \pm 15$
$8.98 \pm 0.06$	$77 \pm 14$	$115 \pm 22$	$839 \pm 22$

Table 4.1 shows the respective potentials at  $0.1 \mu\text{A cm}^{-2}$  *versus* SCE and RHE and the apparent *Tafel*-slopes for a given pH in the range 0 - 9. It can be seen that within the error margin, the *Tafel*-slopes are the same in this range, supporting the presence of the same reaction mechanism.

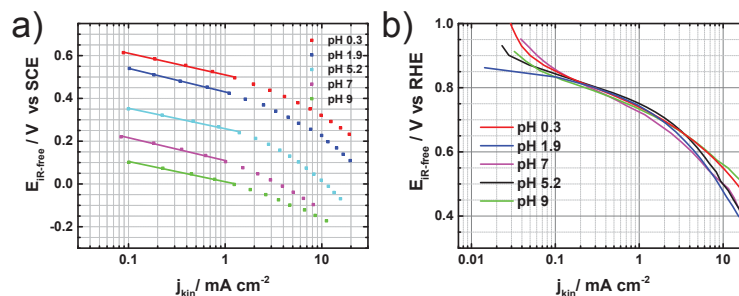


FIGURE 4.9: (a) *Tafel*-plots corresponding to measurements in Figure 4.8 (a) *versus* SCE scale, (b) *versus* RHE scale.

Figure 4.9 (a) shows that the *Tafel*-plots of the measurement in Figure 4.8 (a). When corrected to the RHE scale, and corrected to kinetic currents all collapse onto one curve (Figure 4.9 (b)). This strongly suggests that the underlying catalytic mechanism is likely to be the same in this pH range.

#### 4.2.5.2 Kinetic isotope effect of the ORR in alkaline and acid

Due to the relevance of the ORR in PEFCs, which operate in an acidic environment, the catalyst was subjected to the respective low pH and pD electrolytes, 0.45 M  $\text{H}_2\text{SO}_4$  and 0.45 M  $\text{D}_2\text{SO}_4$  respectively. Cyclic voltammetry was conducted in nitrogen saturated solution. In order to validate whether a significant kinetic isotope effect (KIE) would be discernible under the utilised experimental conditions, the hydrogen evolution reaction was used to estimate how a primary KIE could electrochemically manifest itself. The electrochemical isotope effect for the HER is well investigated due to its technological relevance. [24–27]

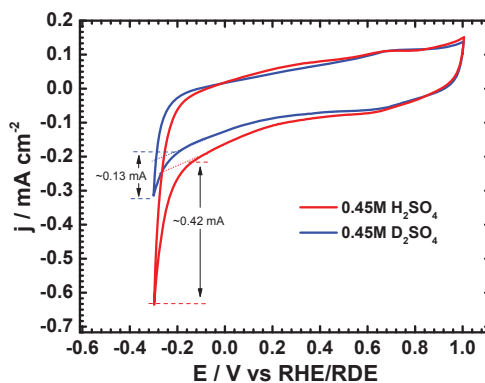


FIGURE 4.10: Rotating disk electrode (RDE) measurements of Fe-N/C catalyst in  $\text{N}_2$ -saturated electrolyte at 1 atm and 25°C. 1600 rpm, 5  $\text{mV s}^{-1}$ ; Loading: 270  $\mu\text{g cm}^{-2}$

Figure 4.10 shows the cyclic voltammetry of the **Fe-N/C** catalyst in nitrogen saturated solution. The onset of the hydrogen evolution reaction is clearly visible, starting at  $\sim -0.1\text{V vs RHE/RDE}$ . It can also be seen that the reaction is significantly more facile in the hydrogen containing electrolyte compared to the deuterated one. From the kinetic current, as indicated in Figure 4.10, the KIE was estimated to be  $\sim 3.4$  on the **Fe-N/C** catalyst. This shows, if present, a large KIE is detectable with the present set-up. Although it is not possible to be certain of the RDS in this reaction, it is inferred from this value that a primary KIE would at least show a value of 3. This is in agreement with values observed for the proton discharge being the RDS on metal electrodes (3-6). [26, 27] Since there are no data available on how a primary kinetic isotope effect would manifest itself for the ORR under these conditions, a value of 3 is taken as a reference.

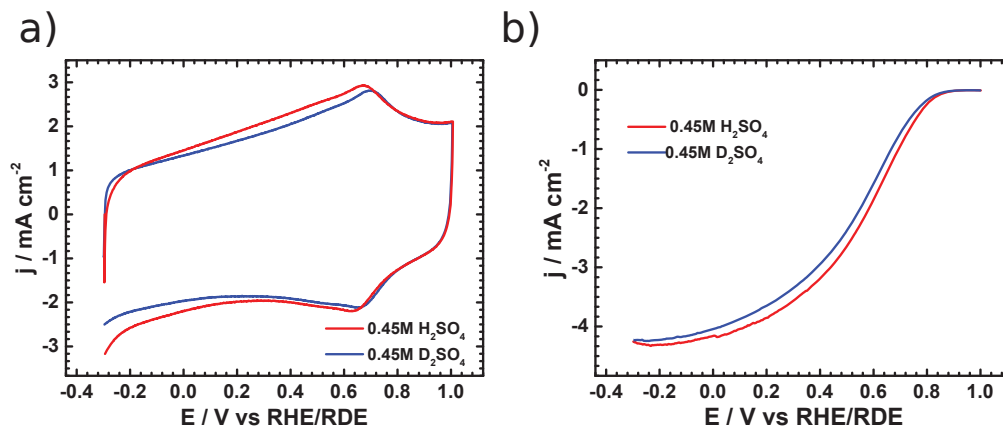


FIGURE 4.11: Rotating disk electrode (RDE) measurements of Fe-N/C catalyst, 1600 rpm, loading  $270 \mu\text{g cm}^{-2}$ . (a)  $50\text{mV s}^{-1}$ ,  $\text{N}_2$ -saturated electrolyte, (b) background corrected,  $5 \text{mV s}^{-1}$   $\text{O}_2$ -saturated electrolyte, at 1 atm and  $25^\circ\text{C}$ .

In order to confirm whether the accessible electrochemical surface area in the hydrogen and deuterium containing electrolytes are comparable, cyclic voltammetry was performed. It can be seen in Figure 4.11 (a), that while the deuterated solvent shows a slightly smaller capacitance, it is not significantly different as compared to the hydrogen equivalent. However a shift of  $\sim 40 \text{ mV}$  in the reversible peak at  $\sim 0.7 \text{ V vs RHE/RDE}$  is observed, indicating a process which involves the transfer of protons in agreement with a quinone/hydroquinone couple. The slightly smaller capacitance might be due to the larger size of the deuterium atoms or other changes in the double layer associated with the different properties, such as the dielectric constant. [28] This leads to less charged species being able to accumulate in the double layer and hence decreasing the specific capacitance of the system. [29] Nevertheless this indicates that the accessible electrochemical surface area and hence observed activity should be comparable. Figure 4.11 (a) shows the oxygen reduction activity of the **Fe-N/C** catalyst. A slight change in limiting current is undoubtedly caused by the variation in diffusion coefficient and solubility of oxygen in the deuterated solvent. [30]

Correction of the results to overpotentials taking into account the different thermodynamics in  $\text{D}_2\text{O}$  versus  $\text{H}_2\text{O}$  (see Experimental section 4.4.5) shows that the reaction in  $\text{H}_2\text{SO}_4$  is significantly faster than in  $\text{D}_2\text{SO}_4$  (Figure 4.12). It can then be seen that the ratio of the kinetic currents,  $j_{\text{kin}}(\text{H})/j_{\text{kin}}(\text{D})$  is  $\sim 3.4$ . The currents have been compared in the region of low overpotential ( $< 0.1 \text{ mA cm}^{-2}$ , *i.e.* less than 10% limiting current). This should eliminate mass transport effects, although as the results are performed on the same electrode, these should be very similar. It can be seen in Figure 4.12 (inset),



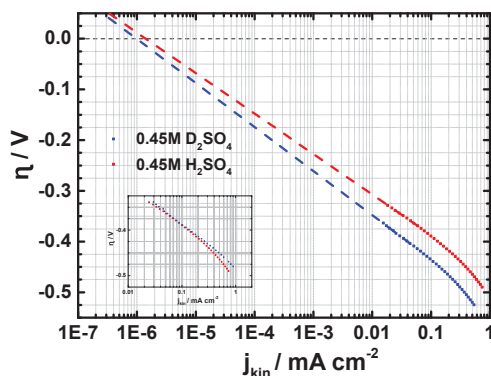


FIGURE 4.12: *Tafel*-plots, where the potentials have been converted to overpotential, corresponding to the measurements in Figure 4.11

if multiplied with 3.4, the kinetic current in  $D_2SO_4$  overlaps with the measurement in  $H_2SO_4$  validating the determined value. The Tafel slopes have been determined to be  $\sim 80 \text{ mV dec}^{-1}$  and  $\sim 85 \text{ mV dec}^{-1}$  for hydrogen and deuterium respectively, which shows no significant difference and indicates a constant KIE across a wide potential range. Although formally it would be more appropriate to compare the exchange current densities, doing so is associated with a large error, due to the extrapolation to zero overpotential being made over 4 orders of magnitude in current density. The value obtained by taking the ratios of the apparent exchange current densities is  $\sim 1.4$ , however with a very large error due to the significant uncertainty of the *Tafel*-slope. Therefore, it is deemed more representative to compare the determined kinetic currents in the area of the fit. A KIE of 3.4 would be indicative of a primary kinetic isotope effect. This suggests that a proton transfer is directly involved in the rate determining step (RDS). A slight decrease in activity could also be attributed to non-mechanistic sources such as due to the lower overall accessible electrochemical surface area. This contribution should be small however. This large KIE in acid is in agreement with mechanistic suggestions present in literature, which emphasise the importance of the proton transport capabilities of the active site. [31] This suggests that the RDS might be for example the reductive adsorption of oxygen to the active site with a concerted proton transfer. This is different to metal surfaces where the sole reductive adsorption is assumed to be the RDS. [32] The non-negligible KIE in the Fe-N/C catalyst however indicates that a proton in the vicinity of the active site might contribute to stabilising the transition state that leads to this intermediate as suggested by Herranz *et al.* [31]

It is known that in alkaline the ORR proceeds in a much more facile manner and several

M-N/C and N/C materials have been reported which have comparable activity to Pt. [33] The ORR in alkaline might be interesting for alkaline fuel cells and depolarised chlor-alkali electrolysis and a different mechanism is most likely present in alkaline solutions. Therefore the KIE investigation was extended to high pH and pD in 1M NaOH and 1M NaOD respectively.

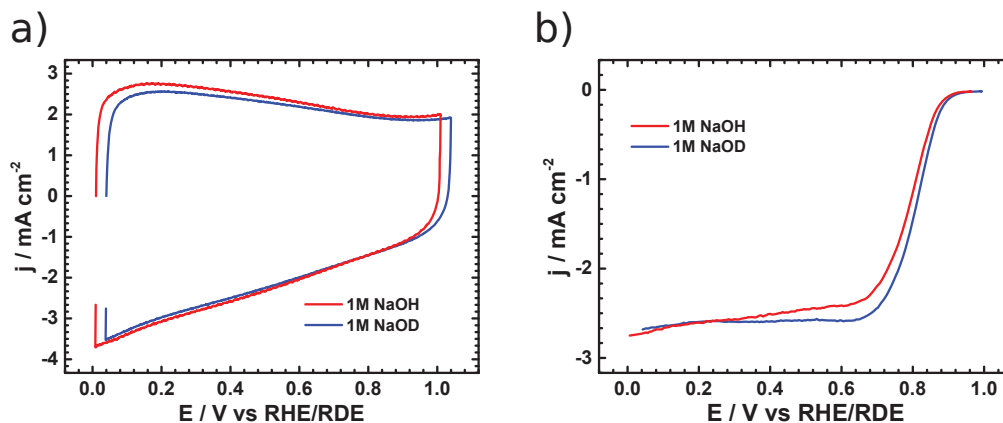


FIGURE 4.13: Rotating disk electrode (RDE) measurements of Fe-N/C catalyst, 1600 rpm, loading  $270 \mu\text{g cm}^{-2}$ . (a)  $50\text{mV s}^{-1}$ ,  $\text{N}_2$ -saturated electrolyte, (b) background corrected,  $5 \text{mV s}^{-1}$   $\text{O}_2$ -saturated electrolyte, at 1 atm and  $25^\circ\text{C}$ .

The cyclic voltammetry in  $\text{N}_2$ -saturated electrolyte (Figure 4.13 (a)) again reveals that the capacitance of the deuterated solvent is slightly lower. Figure 4.13 (b) shows the ORR curves recorded in the alkaline electrolytes

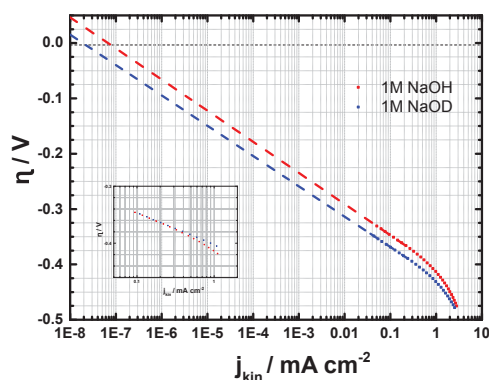


FIGURE 4.14: *Tafel*-plots, where the potentials have been converted to overpotential, corresponding to the measurements in Figure 4.13

and Figure 4.14 the kinetic analysis. This time the ratio  $j_{\text{kin}}(\text{H})/j_{\text{kin}}(\text{D})$  is  $\sim 2.5$ , which is smaller than under acidic conditions. The Tafel slopes are  $56 \text{mV dec}^{-1}$  and  $55 \text{mV dec}^{-1}$  in NaOH and NaOD respectively and a good overlap of the traces is again achieved when multiplying the kinetic current in the deuterium measurement with the KIE (Figure 4.14

(inset)). While a small variations can again stem from various sources, this decrease in KIE is significant. The smaller KIE in alkaline might indicate a significant contribution from a second pathway, which has a proton independent RDS, as suggested by Ramaswary *et al.* [33]

#### 4.2.5.3 Rate determining step proposal

The observed findings are used to suggest the RDS for both acid and alkaline. In acid the mechanism will most likely proceed with an inner sphere electron transfer.[29, 33] This means that the oxygen molecule has to adsorb onto the active site. The results suggest that the reductive adsorption might proceed concerted with a protonation of the adsorbed superoxide intermediate. The following mechanism for the RDS, where the transition state could be stabilised by a proton might be relevant for the first electron transfer:

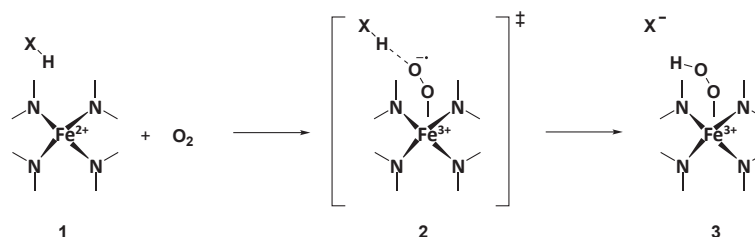


FIGURE 4.15: Proposed proton coupled electron transfer as rate determining step under acidic conditions.

X represents a species which can carry protons, such as solvating water molecules or functional groups in the vicinity of the active site, and a transition state as represented by species 2 might be present. In alkaline on the other hand a combination of inner-sphere and outer sphere electron transfer has been suggested. [33] This gives the possibility that additional to the mechanism shown in Figure 4.15 an outer sphere mechanism as follows is present:

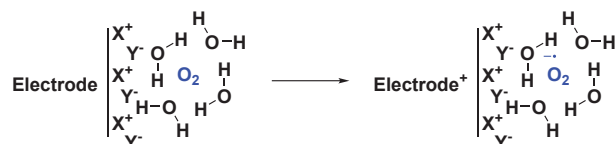


FIGURE 4.16: Possible outer sphere electron transfer in highly alkaline conditions.

This second mechanism yields a solvated superoxide molecule which might be proton independent and then continues to adsorb to the surface for the further reduction to water or peroxide. However detailed mechanistic considerations should be taken with caution,

as numerous factors can influence the KIE. Nevertheless the insight of a significant KIE in acid as well as alkaline is interesting and might have important implications for follow up studies.

### 4.3 Conclusion

When searching for an active site probe it was found that the **ODAN** catalyst is surprisingly resilient to many substances that typically affect Pt based material. While the reference Pt catalyst is always severely affected by a wide variety of substances, our catalyst is mostly resistant, or at worst showing only a minor reduction in performance. The catalyst operates well in the presence of chloride, urea, methanol, Ringers solution, HCl, H<sub>2</sub>S, benzene and toluene, these substances exemplify strongly adsorbing ions, amides/amines, alcohols, biological fluids, corrosive electrolytes, sulphur containing compounds and hydrocarbons respectively. The technological applications could be wide ranging and include fuel cells, that have to operate on gas streams in challenging conditions, oxygen sensing in different kinds of biological fluids, counter electrode catalysts, where the ORR is preferred over hydrogen evolution, such as in chlor-alkaline oxygen depolarized electrolysis, metal-air batteries and waste water treatment.

Nitrogen cycle molecules nitric oxide and NO<sup>+</sup> were identified as molecular probes for the **Fe-N/C** catalyst and will be used in the following chapters to gain further information on the active site.

It has been shown that organic reactions with the example of the acylation reaction can potentially be used to probe the active site.

Gas sorption has shown that the catalyst might be a good oxidation catalyst by activating molecular oxygen. This was inferred due to the low temperature CO<sub>2</sub> production from the carbonaceous structure, after exposure to O<sub>2</sub>. The O<sub>2</sub> energy of desorption from the **Fe-N/C** catalyst suggests that it chemisorbs onto the surface.

Mechanistic investigation has found that a proton coupled electron transfer might be the RDS in acid as well as in alkaline. It was further found that the mechanism and the active site is likely to stay the same across a wide pH range from 0 to 10, with a changeover to an alkaline mechanism, which is kinetically more facile. This information is useful, when

information on the active site obtained at intermediate pH are used to draw conclusions on the technologically important acidic activity.

The results obtained in this chapter have inspired in depth investigations in the following chapters.

## 4.4 Experimental Part

### 4.4.1 RDE poisoning experiments

RDE was conducted as described in 3.4.2. The experiments where the catalysts are exposed to poisons were carried out by quantitatively adding the desired substance into the electrolyte to reach the mentioned concentration levels. For the experiments where chloride anions are involved, a quantitative volume of HCl (HCl 37%, Sigma-Aldrich) was added to the main compartment of the electrochemical glass cell, which is the same condition for when methanol (ACS grade, VWR) was employed. In the experiments where urea was involved the respective amount of a 2.5 M Urea solution (from Urea 99%, Sigma-Aldrich) in 0.5M H<sub>2</sub>SO<sub>4</sub> was added. When NO<sup>+</sup>BF<sub>4</sub><sup>-</sup> was used, the RRDE tip was removed from the electrolyte and submerged into a 0.1M solution of NOBF<sub>4</sub> (99%, Sigma-Aldrich) in acetonitrile (AnalaR NORMAPUR<sup>®</sup>, VWR) at a rotation rate of 300 rpm for 5 minutes and subsequently washed thoroughly in H<sub>2</sub>O (MiliQ 18.2 MΩ cm) before returning to the electrolyte solution and measuring the contaminated performance. When NO was used, the RRDE tip was submerged into a 0.5 M H<sub>2</sub>SO<sub>4</sub> solution saturated with NO gas before washing and returning to the electrolyte. NO gas was generated in a *Kipp's* apparatus from NaNO<sub>2</sub> (99%, Sigma-Aldrich) and 2 M H<sub>2</sub>SO<sub>4</sub> (prepared from 95% H<sub>2</sub>SO<sub>4</sub> ACS grade, Sigma-Aldrich) and passed through 2 washing bottles with 3M KOH (from pellets, AnalaR NORMAPUR<sup>®</sup>, VWR) in order to remove residual NO<sub>2</sub>.

### 4.4.2 MEA poisoning experiments

The MEA was prepared and conditioned as described in 3.4.10. For the contamination experiments in the MEA, the contaminated gas stream was achieved by mixing pure air (from a compressor) with an N<sub>2</sub> or air stream containing the desired substance (*e.g.* H<sub>2</sub>S, benzene or toluene). The contaminated gas stream was directly passed into the main

gas stream (pure air), which was already humidified. For the experiment where H<sub>2</sub>S was employed, 50 ccm of 1000 ppm H<sub>2</sub>S in nitrogen (from Air Products) was mixed with 550 ccm of air, reaching a final flow rate of 600 ccm, containing 83 ppm of H<sub>2</sub>S. For when Benzene or Toluene was utilized, an air stream (50 ccm) was passed through a solution of either Benzene (AnalaR NORMAPUR<sup>®</sup>, VWR) or Toluene (99.8% from Sigma Aldrich) prior to mixing with 550 ccm of air. The concentration of toluene and benzene in the 50 ccm air stream was verified by the use of a bench-top UV-Vis spectrometer (Perkin Elmer Lambda 25). For this experiment 50 ccm of air was passed through either a pure benzene or toluene solution and fed into a quartz flow cell in the spectrometer, by recording the absorbance of the characteristic peaks for benzene and toluene the respective concentrations in the gas stream could be determined.

#### 4.4.3 Organic treatment of catalyst

**The *Friedel-Crafts* reaction** was conducted on the Fe-N/C catalyst by adding a solution of AlCl<sub>3</sub> (10 mg, 0.075 mmol, 98% Sigma-Aldrich) in acetyl chloride (20 mL, 22 g, 0.28 mol, 98% Sigma-Aldrich) to the Fe-N/C catalyst in a 50 mL round bottom flask and then stirring overnight. Subsequently the catalyst was filtered off and washed thoroughly with acetone (AnalaR NORMAPUR<sup>®</sup>, VWR) and water (MilliQ 18.2 MΩ cm) before drying at 60 °C overnight, to obtain the modified catalyst.

**For the acyl-pyridinium procedure**, the Fe-N/C catalyst (60 mg), in a 50 mL round bottom flask, was ultrasonically dispersed in THF (15 mL, AnalaR NORMAPUR<sup>®</sup>, VWR) and acetyl chloride (1.5 mL, 1.7 g, 21 mmol, 99% Sigma-Aldrich) was added. The mixture was cooled to 7 °C in a water/ice bath under constant stirring. Pyridine (1.7 mL, 1.7 g, 21 mmol, 99% Sigma-Aldrich) was dissolved in THF (15 mL, AnalaR NORMAPUR<sup>®</sup>, VWR) and added drop-wise over 15 min to the cooled mixture. The combined reaction mixture was allowed to heat to room temperature, stirred overnight and then refluxed for 3h. The catalyst was then filtered off, washed thoroughly first with THF (AnalaR NORMAPUR<sup>®</sup>, VWR) and then with acetone (AnalaR NORMAPUR<sup>®</sup>, VWR) and water (MilliQ 18.2 MΩ cm) and dried overnight at 60 °C before use to obtain the Fe-N/C-AC catalyst. The regenerated catalyst was obtained by heating the Fe-N/C-AC catalyst in a tube furnace under an inert atmosphere of N<sub>2</sub> (BOC N6.0 Grade), at a heating rate of 20 °C min<sup>-1</sup> to 600 °C and cooling down to room temperature immediately.

#### 4.4.4 Gas sorption and TPD

Gas sorption and TPD was carried out in a Micromeritics Autochem II 2920. The samples were heated under an inert atmosphere of Ar (BOC N5.5 Grade) at a flow rate of 20 mL min<sup>-1</sup> and a heating rate of 10 °C min<sup>-1</sup> to 600 °C and held there for 1h before each experiment, in order to ensure that the catalyst surface is clean. The exposure to oxygen (BOC N6.0 grade), was performed at room temperature for 1h at a flow rate of 20 mL min<sup>-1</sup>. The control experiments were conducted with Ar instead of oxygen. After exposure to oxygen the catalyst was purged with Ar (20 ml min<sup>-1</sup>), for 1h at room temperature before starting the heating ramp, in order to ensure that gas trapped in the porous structure was removed. The heating ramp was conducted under a continuous flow of Ar and the exhaust gas was passed to a mass spectrometer (MKS Cirrus II) for detection of the desired elements.

#### 4.4.5 pH study

RDE was conducted as described in 3.4.2. A catalyst loading of 0.27 mg cm<sup>-2</sup> was chosen to study the pH dependence of the ORR, as it was found to give a good uniform catalyst layer, as confirmed with a light microscope. Furthermore, it was a compromise between a relatively thin layer and a sufficient activity, to ensure adequate signal to noise ratio. For measurements in 0.5 M H<sub>2</sub>SO<sub>4</sub>, a RHE (GaskatelHydroFlex) was used. For measurements in the higher pH electrolytes a saturated calomel electrode SCE (VWR) was used and the potentials with respect to the RHE scale were determined by measuring the change from hydrogen evolution to hydrogen oxidation in the respective H<sub>2</sub>-saturated electrolyte on a platinized platinum wire. Electrolytes were prepared in ultrapure water (MilliQ 18.2 MΩ cm). 0.5 M H<sub>2</sub>SO<sub>4</sub> from 95% sulphuric acid (Aristar, VWR), 0.5 M phosphate buffer pH 2 from phosphoric acid (AnalaR NORMAPUR<sup>®</sup>, VWR) and NaH<sub>2</sub>PO<sub>4</sub> (AnalaR NORMAPUR<sup>®</sup>, VWR), 0.5 M acetate buffer pH 5.2 from sodium acetate (99%, Sigma-Aldrich) and glacial acetic acid (AnalaR NORMAPUR<sup>®</sup>, VWR), 0.5 M phosphate buffer pH 7 from NaH<sub>2</sub>PO<sub>4</sub> (AnalaR NORMAPUR<sup>®</sup>, VWR) and Na<sub>2</sub>HPO<sub>4</sub> (AnalaR NORMAPUR<sup>®</sup>, VWR) and 0.5 M borate buffer from boric acid (ACS reagent, 99.5%, Sigma-Aldrich) and NaOH (AnalaR NORMAPUR<sup>®</sup>, VWR). The pH was adjusted with 0.5 M NaOH and confirmed with a ROSS Ultra Glass pH Electrode (Orion 8102BNUWP). The normalised current density was corrected to account for the different

solubility and diffusivity of oxygen in the different electrolytes. The current at 0.1 V was used to determine a "normalised" current to which all the currents were ratioed. Therefore the normalised current density was obtained by:  $j_{norm} = \frac{j}{j_{(E=0.1V)}}$ , where  $j$  is the geometric current density and  $j_{norm}$  the normalised current density. The kinetic current density was estimated as follows;  $j_{kin} = \frac{j*j_{lim}}{j_{lim}-j}$ , where  $j_{lim}$  was taken as the current density achieved at 0.1 V *vs* RHE as the limiting current in the respective electrolyte. The error introduced due to the deviation from the theoretical limiting current in the respective electrolyte, which was caused by insufficient activity of the catalyst at this loading, was found to be small (<1.5%) at the potential of interest (0.8 V *vs* RHE).

#### 4.4.6 H/D experiments

RDE was conducted as described in 3.4.2 and 4.4.5. The utilised glass cell was jacketed and thermostated at 25 °C with a water recirculator (Huber MPC), in order to ensure that the measured kinetics were not subject to temperature effects. A leak free Ag|AgCl electrode (Warner Instruments) was used as reference electrode. This ensured independence of the potential from the protons/deuterons and the avoidance of contamination of the solution with the filling electrolyte of the electrode. Electrolytes containing hydrogen were prepared in ultrapure water (MilliQ 18.2 MΩ cm). For 0.45 M H<sub>2</sub>SO<sub>4</sub>, 95% sulphuric acid (Aristar, VWR) and for 1 M NaOH, NaOH pellets (VWR, ACS grade) were used to prepare the solutions. The deuterated electrolytes were prepared in D<sub>2</sub>O (Sigma-Aldrich, 99.9% atom % D). For 0.45 M D<sub>2</sub>SO<sub>4</sub>, 96% D<sub>2</sub>SO<sub>4</sub> (Sigma-Aldrich, 99.5 atom % D) and for 1 M NaOD, 30 wt% solution in D<sub>2</sub>O (Sigma-Aldrich, 99 atom % D) were used to prepare the solutions. Experiments under the respective acidic and alkaline conditions were conducted from the same catalyst layer, in order to prevent errors due to the variation of the amount of deposited catalyst. The electrode tip with the catalyst layer was immersed into ultrapure water or into D<sub>2</sub>O for 10 minutes under a rotation of 300 rpm prior to transferring it into the respective H or D containing solutions to avoid cross contamination and to ion exchange the Nafion binder. The potential of the Ag|AgCl reference electrode was determined *versus* self-made reversible hydrogen/deuterium electrodes (RHE/RDE) in the respective electrolytes. In order to be able to compare the kinetic currents of the hydrogen and deuterium measurements, the overpotential  $\eta$  was determined by  $\eta = E(\text{RHE/RDE}) - E_0(\text{H}_2\text{O}/\text{D}_2\text{O})$ , where  $E(\text{RHE/RDE})$  is the measured potential *versus* the reversible hydrogen electrode or the reversible deuterium electrode,



RHE or RDE respectively, and  $E_0$  is the thermodynamic equilibrium potential for the reduction of oxygen to water or deuterium oxide,  $H_2O$  or  $D_2O$ , respectively.  $E_0$  is for  $H_2O$  1.229 V and for  $D_2O$  1.262 V.

## 4.5 References

- [1] Shao M., Chang Q., Dodelet J.P., Chenitz R. Recent Advances in Electrocatalysts for Oxygen Reduction Reaction. *Chemical Reviews*, 116(6), 3594–3657, March 2016. doi:10.1021/acs.chemrev.5b00462.
- [2] Dodelet J.P. The Controversial Role of the Metal in Fe- or Co-Based Electrocatalysts for the Oxygen Reduction Reaction in Acid Medium. In M. Shao, editor, *Electrocatalysis in Fuel Cells*, number 9 in Lecture Notes in Energy, pages 271–338. Springer London, 2013. ISBN 978-1-4471-4910-1 978-1-4471-4911-8. doi: 10.1007/978-1-4471-4911-8\_10.
- [3] Jaouen F., Herranz J., Lefèvre M., Dodelet J.P., Kramm U.I., et al. Cross-Laboratory Experimental Study of Non-Noble-Metal Electrocatalysts for the Oxygen Reduction Reaction. *ACS Applied Materials & Interfaces*, 1(8), 1623–1639, August 2009. doi: 10.1021/am900219g.
- [4] Kramm U.I., Lefèvre M., Larouche N., Schmeisser D., Dodelet J.P. Correlations between Mass Activity and Physicochemical Properties of Fe/N/C Catalysts for the ORR in PEM Fuel Cell via  $^{57}Fe$  Mössbauer Spectroscopy and Other Techniques. *Journal of the American Chemical Society*, 136(3), 978–985, January 2014. doi: 10.1021/ja410076f.
- [5] Tylus U., Jia Q., Strickland K., Ramaswamy N., Serov A., et al. Elucidating Oxygen Reduction Active Sites in Pyrolyzed Metal–Nitrogen Coordinated Non-Precious-Metal Electrocatalyst Systems. *The Journal of Physical Chemistry C*, 118(17), 8999–9008, May 2014. doi:10.1021/jp500781v.
- [6] Kramm U.I., Herranz J., Larouche N., Arruda T.M., Lefèvre M., et al. Structure of the catalytic sites in Fe/N/C-catalysts for  $O_2$ -reduction in PEM fuel cells. *Phys. Chem. Chem. Phys.*, 14(33), 11,673–11,688, August 2012. doi:10.1039/C2CP41957B.

- [7] Malko D., Lopes T., Symianakis E., Kucernak A.R. The intriguing poison tolerance of non-precious metal oxygen reduction reaction (ORR) catalysts. *Journal of Materials Chemistry A*, November 2015. doi:10.1039/C5TA05794A.
- [8] Lopes T., Paganin V.A., Gonzalez E.R. The effects of hydrogen sulfide on the polymer electrolyte membrane fuel cell anode catalyst: H<sub>2</sub>S–Pt/C interaction products. *Journal of Power Sources*, 196(15), 6256–6263, August 2011. doi:10.1016/j.jpowsour.2011.04.017.
- [9] Cheng X., Shi Z., Glass N., Zhang L., Zhang J., et al. A review of PEM hydrogen fuel cell contamination: Impacts, mechanisms, and mitigation. *Journal of Power Sources*, 165(2), 739–756, March 2007. doi:10.1016/j.jpowsour.2006.12.012.
- [10] Schmidt T.J., Paulus U.A., Gasteiger H.A., Behm R.J. The oxygen reduction reaction on a Pt/carbon fuel cell catalyst in the presence of chloride anions. *Journal of Electroanalytical Chemistry*, 508(1–2), 41–47, July 2001. doi:10.1016/S0022-0728(01)00499-5.
- [11] Brown G.W., Cohen P.P. Comparative biochemistry of urea synthesis. I. Methods for the quantitative assay of urea cycle enzymes in liver. *The Journal of Biological Chemistry*, 234(7), 1769–1774, July 1959.
- [12] Holze R., Vogel I., Vielstich W. New oxygen cathodes for fuel cells with organic fuels. *Journal of Electroanalytical Chemistry and Interfacial Electrochemistry*, 210(2), 277–286, October 1986. doi:10.1016/0022-0728(86)80580-0.
- [13] Markiewicz M.E.P., Bergens S.H. Electro-oxidation of 2-propanol and acetone over platinum, platinum–ruthenium, and ruthenium nanoparticles in alkaline electrolytes. *Journal of Power Sources*, 185(1), 222–225, October 2008. doi:10.1016/j.jpowsour.2008.06.023.
- [14] Rapoport B.I., Kedzierski J.T., Sarpeshkar R. A Glucose Fuel Cell for Implantable Brain–Machine Interfaces. *PLOS ONE*, 7(6), e38,436, June 2012. doi:10.1371/journal.pone.0038436.
- [15] Rosca V., Duca M., de Groot M.T., Koper M.T.M. Nitrogen Cycle Electrocatalysis. *Chemical Reviews*, 109(6), 2209–2244, June 2009. doi:10.1021/cr8003696.

- [16] Einsle O., Messerschmidt A., Huber R., Kroneck P.M.H., Neese F. Mechanism of the Six-Electron Reduction of Nitrite to Ammonia by Cytochrome c Nitrite Reductase. *Journal of the American Chemical Society*, 124(39), 11,737–11,745, October 2002. doi:10.1021/ja0206487.
- [17] Elbaz L., Wu G., Zelenay P. Heat-Treated Non-precious-Metal-Based Catalysts for Oxygen Reduction. In M. Shao, editor, *Electrocatalysis in Fuel Cells*, number 9 in Lecture Notes in Energy, pages 213–246. Springer London, 2013. ISBN 978-1-4471-4910-1 978-1-4471-4911-8.
- [18] Ramaswamy N., Tylus U., Jia Q., Mukerjee S. Activity Descriptor Identification for Oxygen Reduction on Nonprecious Electrocatalysts: Linking Surface Science to Coordination Chemistry. *Journal of the American Chemical Society*, 135(41), 15,443–15,449, October 2013. doi:10.1021/ja405149m.
- [19] Smith M.B., March J. *March's Advanced Organic Chemistry: Reactions, Mechanisms, and Structure*. John Wiley & Sons, January 2007. ISBN 978-0-470-08494-6.
- [20] Dunetz J.R., Xiang Y., Baldwin A., Ringling J. General and Scalable Amide Bond Formation with Epimerization-Prone Substrates Using T3P and Pyridine. *Organic Letters*, 13(19), 5048–5051, October 2011. doi:10.1021/ol201875q.
- [21] Laine N.R., Vastola F.J., Walker P.L. THE IMPORTANCE OF ACTIVE SURFACE AREA IN THE CARBON-OXYGEN REACTION. *The Journal of Physical Chemistry*, 67(10), 2030–2034, October 1963. doi:10.1021/j100804a016.
- [22] Wetterer S.M., Lavrich D.J., Cummings T., Bernasek S.L., Scoles G. Energetics and Kinetics of the Physisorption of Hydrocarbons on Au(111). *The Journal of Physical Chemistry B*, 102(46), 9266–9275, November 1998. doi:10.1021/jp982338+.
- [23] Wan K., Yu Z.p., Li X.h., Liu M.y., Yang G., et al. pH Effect on Electrochemistry of Nitrogen-Doped Carbon Catalyst for Oxygen Reduction Reaction. *ACS Catalysis*, 5(7), 4325–4332, July 2015. doi:10.1021/acscatal.5b01089.
- [24] Shibuya S., Matsushima H., Ueda M. Study of Deuterium Isotope Separation by PEFC. *Journal of The Electrochemical Society*, 163(7), F704–F707, January 2016. doi:10.1149/2.1321607jes.

- [25] Bell R.P. Isotope effects and the nature of proton-transfer transition states. *Discussions of the Faraday Society*, 39(0), 16–24, January 1965. doi:10.1039/DF9653900016.
- [26] Conway B.E., Salomon M. Studies on the Hydrogen Evolution Reaction Down to  $-150^{\circ}\text{C}$  and the Role of Proton Tunneling. *Journal of Chemical Physics*, 41, 3169–3177, November 1964. doi:10.1063/1.1725692.
- [27] Conway B.E. The Electrolytic Hydrogen-Deuterium Separation Factor and Reaction Mechanism. *Proceedings of the Royal Society of London A: Mathematical, Physical and Engineering Sciences*, 247(1250), 400–419, September 1958. doi:10.1098/rspa.1958.0194.
- [28] Malmberg C. Dielectric constant of deuterium oxide. *Journal of Research of the National Bureau of Standards*, 60(6), 609, June 1958. doi:10.6028/jres.060.060.
- [29] Bard A.J., Faulkner L. *Electrochemical Methods: Fundamentals and Applications*. John Wiley & Sons, New York, 2nd edition, January 2001. ISBN 978-0-471-04372-0.
- [30] Han P., Bartels D.M. Temperature Dependence of Oxygen Diffusion in  $\text{H}_2\text{O}$  and  $\text{D}_2\text{O}$ . *The Journal of Physical Chemistry*, 100(13), 5597–5602, January 1996. doi:10.1021/jp952903y.
- [31] Herranz J., Jaouen F., Lefèvre M., Kramm U.I., Proietti E., et al. Unveiling N-Protonation and Anion-Binding Effects on Fe/N/C Catalysts for  $\text{O}_2$  Reduction in Proton-Exchange-Membrane Fuel Cells. *The Journal of Physical Chemistry C*, 115(32), 16,087–16,097, August 2011. doi:10.1021/jp2042526.
- [32] Koper M.T.M. Theory of multiple proton–electron transfer reactions and its implications for electrocatalysis. *Chemical Science*, 4(7), 2710–2723, June 2013. doi:10.1039/C3SC50205H.
- [33] Ramaswamy N., Mukerjee S. Influence of Inner- and Outer-Sphere Electron Transfer Mechanisms during Electrocatalysis of Oxygen Reduction in Alkaline Media. *The Journal of Physical Chemistry C*, 115(36), 18,015–18,026, September 2011. doi:10.1021/jp204680p.

*Within this chapter it is sought to provide insight into the chemical behaviour of the Fe–N<sub>x</sub> active site. Although major progress has recently been achieved through ex situ methods, there is still a lack of understanding as direct correlations are not possible. Utilising nitrite, nitric oxide and hydroxylamine as molecular probes it was found that the active site for the ORR is different under acidic and alkaline conditions. An in depth investigation revealed a behaviour which is similar to iron macrocyclic complexes and suggests a contribution of the metal centre in the catalytic cycle. It was also found that the Fe-N/C catalyst is highly active towards nitrite and nitric oxide electroreduction under various pH values with ammonia as a significant by-product. This study offers fundamental insight into the chemical behaviour of the active site and demonstrates a possible use of these materials for nitrite and nitric oxide sensing applications or environmental nitrite destruction.*

## Chapter 5

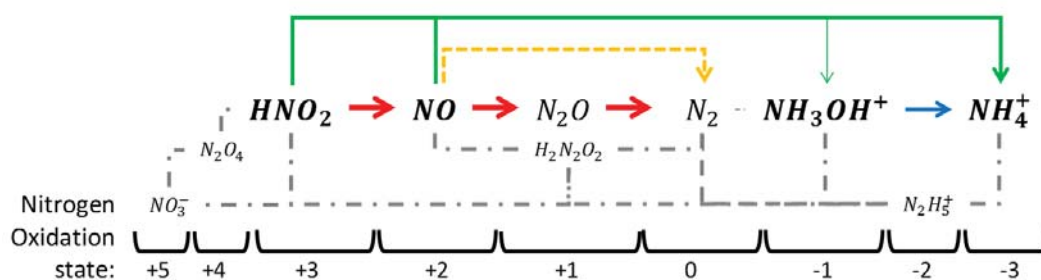
# Interaction of nitric oxide and nitrite with the Fe-N/C catalyst

### 5.1 Introduction

Recent studies on Fe-N/C catalysts obtained via different routes suggest that atomic iron centres, which are coordinated with nitrogen and embedded into the carbon lattice, might serve as one major type of active site. [1–7] These sites were found to be present in most of the materials with the highest activities under acidic conditions. [1–7] This implies that these sites should chemically behave similar to iron heme type systems or other iron macrocyclic complexes and interact with molecules such as CO, NO and H<sub>2</sub>S. [8] Other possible active sites are carbon encapsulated iron or iron carbide particles or metal free

nitrogen moieties in the carbon lattice which might not necessarily interact with these molecules. [9] Although significant progress has recently been made in establishing the active centre(s), most studies only provide indirect evidence for the active site as the material is characterised *ex situ* with sophisticated procedures and experiments that are open to interpretation, such as X-ray absorption and Mössbauer spectroscopy [1–3, 10] and hence establishing correlations is challenging. Electrochemically investigating the active site *in situ* is difficult and requires a probe that interacts strongly. There are some studies that investigate the effect of certain molecules on the activity of Fe-N/C catalysts (as discussed in Chapter 3, the term **N/C** is used to denote the iron-free nitrogen/carbon catalyst and **Fe-N/C** to denote the same catalyst with iron). Gupta *et al.* noted early on that cyanide in alkaline solution decreases the activity of iron macrocyclic compounds. [11] Thorum *et al.* investigated the effect of various small molecules on a pyrolyzed iron phthalocyanine catalyst under different conditions and also found that it is strongly inhibited upon cyanide treatment in alkaline solution. [12, 13] Singh *et al.* studied the effect of H<sub>2</sub>S on a pyrolyzed Fe-N/C catalyst and noted that *ex situ* treatment decreases the electrochemical activity. [14] They inferred an iron centred structure as active site. However, as discussed in Chapter 1, there are also studies that suggest that iron might not necessarily be the active site. [15, 16] The most prominent study that raised doubts on the active site was from the Dodelet group which did not find an electrochemical interaction of the catalyst with carbon monoxide an otherwise strong poison for iron. [17] In Chapter 4, the peculiar poison tolerance of this material to hydrogen sulphide, aromatic molecules (benzene, toluene), anions (chloride, phosphate) and methanol is also shown. [18] Although this insensitivity to poisons seems contradictory, it does not necessarily exclude a metallic active site. From metal complexes it is known that the structural and chemical environment significantly influences the affinity of the active site to certain substrates. [8] Another recent study investigates a broad spectrum of various small molecules such as anions, thiocyanide, CO and NO<sub>x</sub>. [19] It found a slight activity decrease with anions, a large effect of thiocyanate and no interaction with CO and NO<sub>x</sub>. An iron(III) centre was proposed as active site as CO would only interact with iron(II). However, NO should interact with an iron(III) centre. [20] Although these studies provided some information, no detailed study of the chemical and electrochemical behaviour was presented. Ideally, a molecular probe that interacts with the active site forms stable adducts which are electrochemically accessible and behave differently depending on the external conditions. Such information would allow correlation of *ex situ* and *in situ* measurements and elucidate

hitherto inaccessible trends, such as activities and densities of specific sites. This could lead to the structured synthesis of the site with the highest activity and the ability to overcome the currently insufficient performance. Molecules from the aqueous nitrogen cycle, such as nitric oxide or nitrite are an attractive option. This is due to the fact that the nitrogen molecule exhibits a rich electrochemical behaviour and can exist in 9 oxidation states. [21, 22] As nitric oxide and nitrite have a tremendous importance for biological systems and environmental chemistry, their interaction with iron macrocycles has been extensively investigated. [8, 23–29] The electrochemistry of nitrite and nitric oxide reduction is also well documented for precious metal based catalysts. [22, 28–34] The reduction of nitrite might be of environmental benefit through the destruction of this pollutant; sensing application are also of interest for biological systems. [22, 35–37]



SCHEME 5.1: Typical compounds of the different nitrogen oxidation states present in an acidic aqueous solution in descending order of oxidation state. The major pathways for nitrite and nitric oxide electroreduction are highlighted. Green and blue pathway: possible products and intermediates upon subsequent cleavage of N-O bonds without N-N bond formation. Red and yellow pathway: likely products and intermediates upon N-O cleavage with N-N bond formation. Grey dash-dot pathway: kinetically hindered route. [21, 22]

Scheme 5.1 shows the different oxidation states of nitrogen in aqueous solutions. [21] The compounds of interest for this study are highlighted. It can be seen that there are different pathways for the electroreduction of nitrite and nitric oxide. The green and blue pathway involve N-O bond cleavage without N-N bond formation, while the yellow and red pathways include N-N bond formation. [22] In this study, we present a series of experiments that investigate the interaction of an Fe-N/C catalyst or an N/C catalyst with nitrite, hydroxylamine and nitric oxide under various reaction conditions. It is found that the chemical and electrochemical behaviour observed can be explained using the chemistry of iron macrocycles. It is also found that the Fe-N/C catalyst is highly active towards the electroreduction of nitrite and nitric oxide. The difference in overpotential for the Fe-N/C catalyst compared to the N/C catalyst is similar to the difference when performing

the oxygen reduction reaction. Ammonia is a major product and hydroxylamine only a minor by-product. Besides introducing a new powerful substrate to study Fe-N/C catalysts, a highly active catalyst for the useful nitrite and nitric oxide reduction reaction, able to break both N-O bonds in the nitrite, which could be exploited in biological and environmental chemistry is demonstrated. [23, 37]

## 5.2 Results and Discussion

### 5.2.1 The interaction of the Fe-N/C catalyst with nitrogen containing poisons

The synthesis and characterisation of Fe-N/C and N/C catalyst was described in Chapter 3. Moreover, evidence has been provided that the active sites in the Fe-N/C material are likely atomic iron sites coordinated with nitrogen, [1, 2, 7] as opposed to encapsulated metallic or carbide phases which would have been visible in the microscopy images at this resolution (see Chapter 3). [38–40]

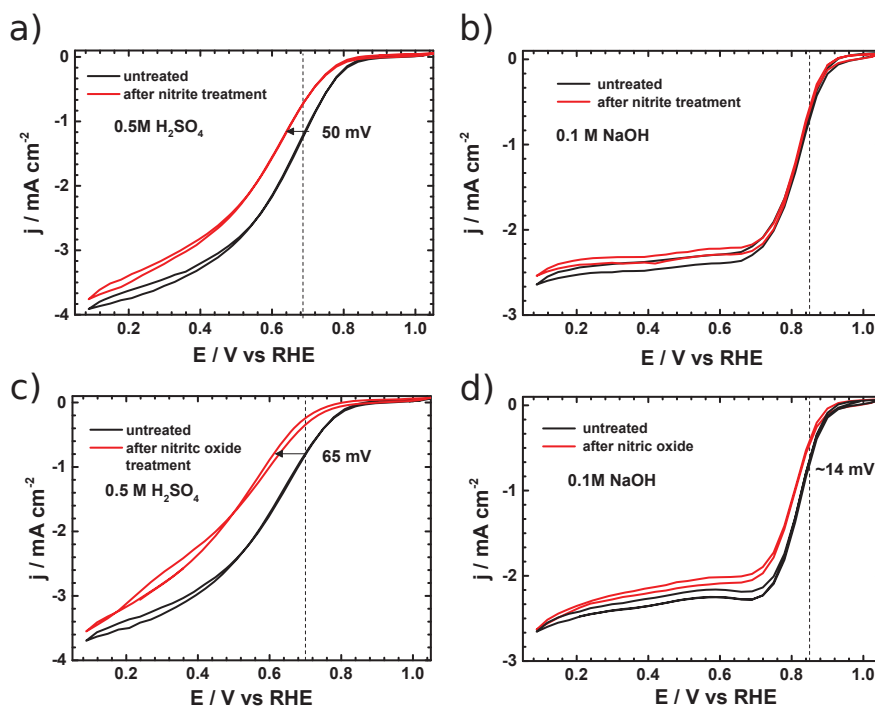


FIGURE 5.1: Rotating disk electrode (RDE) measurements of the ORR activity in acid (a,c) or base (b,d) of a Fe-N/C catalyst before (untreated) and after subjecting it to poisoning by a 0.125 M NaNO<sub>2</sub> solution at pH 7 (a,b); or nitric oxide saturated 0.5 M PO<sub>4</sub>-buffer at pH 7. RDE at 1600 rpm, catalyst loading at 270 μg cm<sup>-2</sup>, scan rate at 5 mV s<sup>-1</sup> and O<sub>2</sub>-saturated electrolytes. Electrodes washed with DI water before retuning to the electrolyte solutions, 0.5 M H<sub>2</sub>SO<sub>4</sub> or 1.0 M NaOH for the poisoned measurement.



In order to gain further information about the chemical behaviour of the active site, a set of experiments were performed with inspiration taken from metal macrocyclic complexes, which are known to interact with nitrite and nitric oxide. In order to understand the poisoning effect of these species on the active site, the **Fe-N/C** catalyst deposited onto a glassy carbon rotating disk electrode (RDE) disk was assessed for oxygen reduction reaction (ORR) activity in 0.5 M H<sub>2</sub>SO<sub>4</sub> or in 1 M NaOH both before and after treatment with the poisons under neutral pH conditions. In Figure 5.1 it can be seen that there is a significant poisoning on the activity of the catalyst under acidic conditions after treatment with NO<sub>2</sub><sup>-</sup> (a) and NO (c), whereas under alkaline conditions the effect is almost unnoticeable (b) and (d), respectively. Combined with the significant improvement in performance when moving to alkaline conditions, this suggests that the sites active under alkaline conditions do not contribute significantly to the performance under acid conditions. If the alkaline active site is not active or has only a low activity in acid and we assume a site which promotes an inner sphere electron transfer, it would be desirable to find ways to prevent the formation of this alkaline active site and promote the formation of the site which is highly active in acid if the catalyst is to be used in a proton exchange membrane fuel cell (PEFC) (and *vice versa* if it is to be used in an alkaline fuel cell). The presence of low activity sites will occupy space on the catalyst surface which could otherwise be occupied by highly active sites, suggested in recent literature via *ex situ* techniques to be atomic iron centres. [1–4, 7, 10] This dilution of highly active sites would make it difficult to reach the required active site density with the necessary turnover frequency suggested by Gasteiger *et al.* [41] Using the present probe in combination with physical characterisation methods might enable a differentiation of sites.

As one of the major possible uses for these catalysts is in PEFCs based on acidic membranes, and as the largest effect on the ORR on these catalysts are seen under acidic conditions, in the following, the rest of the experiments will predominantly be confined to consider the ORR over the **Fe-N/C** catalyst in acid.

### 5.2.2 The interaction of the Fe-N/C catalyst with nitrite

The interaction of the **Fe-N/C** catalyst with the nitrite anion was investigated in more depth.

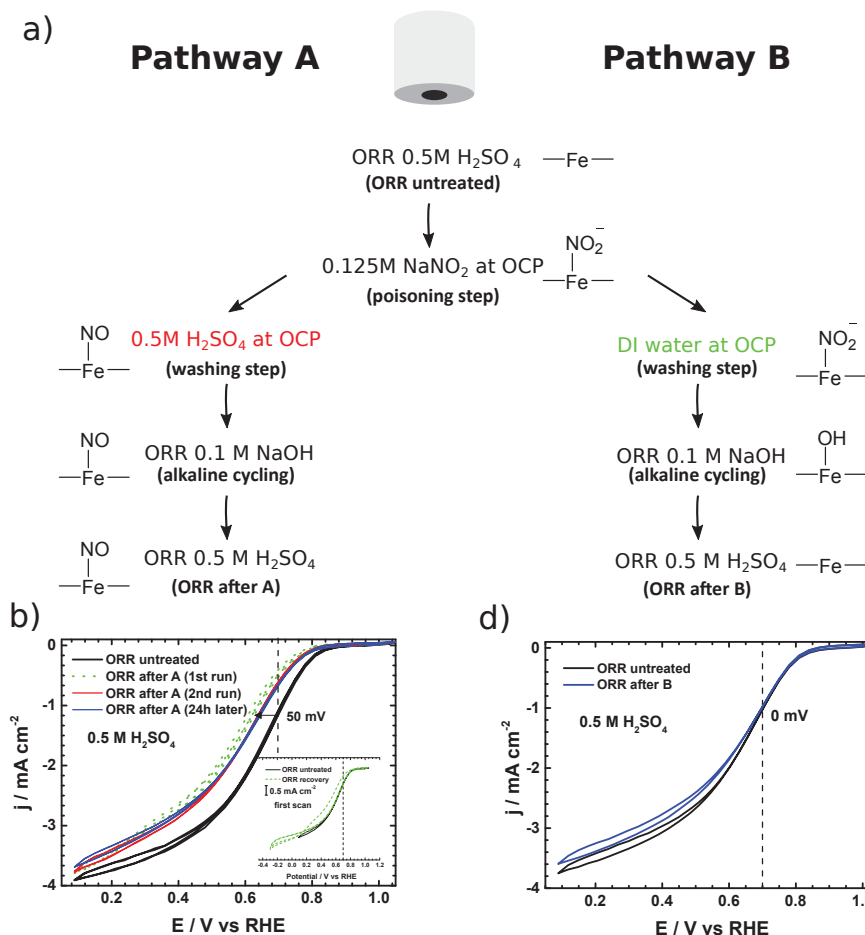
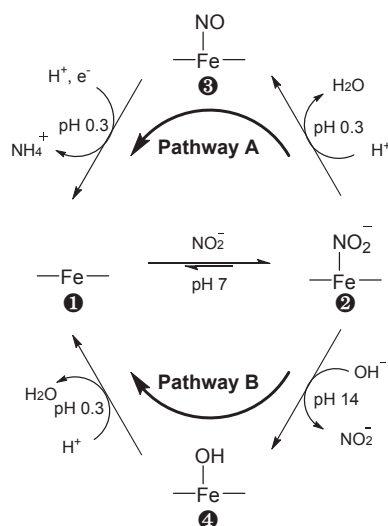


FIGURE 5.2: (a) Scheme showing the sequence of catalyst layer treatments, with the crucial difference is the washing step that was either performed in 0.5 M H<sub>2</sub>SO<sub>4</sub> (**Pathway A**) or DI water (**Pathway B**). The corresponding measurements are shown in (b) and (c): Rotating disk electrode (RDE) measurements in O<sub>2</sub>-saturated 0.5 M H<sub>2</sub>SO<sub>4</sub> of the ORR activity of a Fe-N/C catalyst before (untreated) and after poisoning by a 0.125 M NaNO<sub>2</sub> solution at pH 7. (b) Performance towards the ORR after acid wash following nitrite treatment and then cycling in 1 M NaOH alkaline solution before returning to acid solution to perform the ORR. Inset: Effect of shifting cathodic endpoint to -0.3 V; (c) Performance towards the ORR after DI water wash following the poisoning protocol and then cycling in 1 M NaOH alkaline solution before returning to acid solution to perform the ORR. 1600 rpm, catalyst loading at 270 μg cm<sup>-2</sup>, scan rate at 5 mV s<sup>-1</sup>.

In Figure 5.2, the stability of the poisoning species formed after exposure to nitrite and (i) variations of pH; (ii) potential cycling in the ORR region; (iii) extended periods at the OCV is considered. Figure 5.2 (a) shows the steps taken in two different pathways to poison the catalyst with the corresponding measurements shown in (b) and (c). The crucial difference in the treatment is the washing step. It is either performed at low or neutral pH (Figure 5.2 (a)). Figure 5.2 (b) shows that the poison forms when the electrode is immersed in the nitrite solution at pH 7 and then washed with an acid solution (**Pathway A**). Once the acid wash is performed, exposure of the electrode to alkaline solution (and even performing the ORR in alkaline solution) does not recover the

activity and there is still a 50 mV loss in performance upon returning to the ORR in the acidic solution (Figure 5.2 (b)). This performance loss is also stable to extended cycling under ORR conditions (between 1.05 V and 0.1 V *vs* RHE), and leaving the electrode in solution at its OCV for 24 hours. Thus the poisoning species, once formed, is quite stable. However, it can be removed by cycling the potential to -0.3 V at which potential the poisoning species is reductively desorbed and the ORR activity recovered (Figure 5.2 (b) inset). In contrast, if instead of washing the electrode in acid solution after exposure to nitrite, the electrode is washed with water instead of acid (**Pathway B**) and then exposed to alkaline solution, the ORR performance is immediately recovered on cycling in acid (Figure 5.2 (c)). This highlights the requirement for the adsorbed nitrite to be exposed to acid solution in order to form the stable adduct.



SCHEME 5.2: Proposed reaction steps of the Fe-N/C active site after treatment with a nitrite containing solution and subsequent treatment under different pH conditions.

The response in Figure 5.2 (b) and (c) are rationalised in Scheme 5.2. After treating the catalyst with nitrite solution and washing it with water, immersion of the nitrite complexed Fe-N/C catalyst **2** into an acidic solution (0.5 M H<sub>2</sub>SO<sub>4</sub>) forms a poisoned species **3** (see results in Figure 5.2 (b)). This species is stable in alkaline solution, as shown from the protocol used in Figure 5.2 (b) in which the poisoned electrode is cycled in alkaline solution before returning to acid solution to perform the ORR results displayed. These steps seem to be associated with the decomposition of the nitrite ligand, which is only weakly bound, to form a nitrosyl complex **3**, which is significantly stronger bound. The lower bond strength of a nitrite ( $\sim 13 - 17 \text{ kJ mol}^{-1}$ ) [42] compared to a nitrosyl ligand ( $\sim 17 - 126 \text{ kJ mol}^{-1}$ ) [43] is documented for iron heme based complexes and enzymes. Only

when the potential is sufficiently cathodic (Figure 5.2(b) inset), the nitrosyl complex is reductively desorbed from the surface and the original activity completely recovered. Interestingly, once formed, the poisoned complex ③ is also stable when extensively cycled in an oxygen saturated alkaline solution (0.1 M NaOH) and then transferred back into the acid solution to perform the ORR reaction. However, if complex ② is immersed in alkaline solution after washing with water and not exposed to acid, the ORR activity in acid is immediately regenerated (Figure 5.2 (c)). This confirms that upon treatment with acid, a different species is formed. It also suggests that the nitrite ligand is exchanged during the cycling in alkaline solution before a strong nitrosyl species is formed with the possibility that a hydroxo species ④ is formed. Immersion in acid then yields the unpoisoned active site ①. Iron interacts strongly with hydroxide, as can be seen from the formation of stable hydroxides. [44] For iron macrocyclic complexes, it has been shown that the nitrite ligand can be converted to nitrosyl upon reaction with protons and removal of water. [45] This parallelism points towards an iron centred active site in acidic electrolyte. While the nitrite ligand is only weakly bound to the active site and can be replaced by the relatively strong hydroxo ligand, the nitrosyl ligand, which forms upon acid treatment, is significantly stronger and will not be replaced (Figures 5.2 (a) and (b)). It also indicates that the iron centre is not accessible as active site in strongly alkaline solutions. This is supported by the fact that catalysts completely devoid of metal have been reported with high activities in alkaline electrolytes but not in acid. [46–48] It has to be pointed out that the metal free N/C catalyst was weakly affected by nitrite (see further below). This minor effect is likely due to the residual metal content (~60 ppm) which would be consistent with the hypothesis of a metal centred active site. As the active site adduct ③ can be reductively destroyed, it is possible to use this technique to "count" active metal centres. This will be done in Chapter 6. As will be shown below, the product of the electrochemical reduction of the nitrosyl adduct is ammonia.

### 5.2.3 The interaction of the Fe-N/C catalyst with nitric oxide

In order to confirm whether a strong nitrosyl compound is the poisoned species, the poisoning step in Figure 5.2 (a), where the catalyst coated electrode was subjected to a 125 mM NaNO<sub>2</sub> solution was replaced with a saturated solution of nitric oxide in a pH 7 phosphate buffer and the electrode immersed in that solution for 5 minutes at a rotation of 300 rpm. As with the previous experiments the stability of the adduct formed was studied

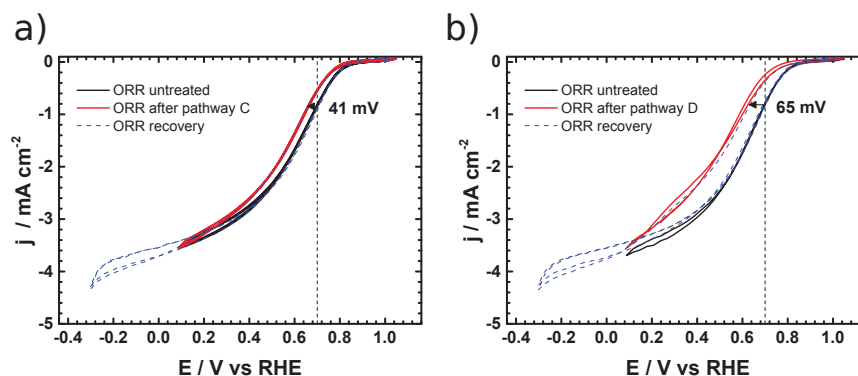
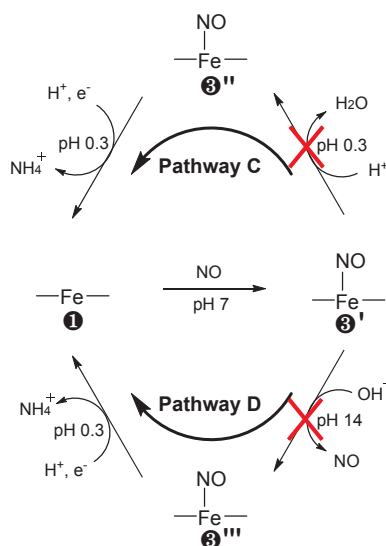


FIGURE 5.3: Rotating disk electrode (RDE) measurements in O<sub>2</sub>-saturated 0.5 M H<sub>2</sub>SO<sub>4</sub> of the ORR activity of a Fe-N/C catalyst before (untreated) and after poisoning in a NO-saturated 0.5 M PO<sub>4</sub>-buffer solution at pH 7. Performance towards the ORR after (a) acid wash following NO treatment and then cycling in 1 M NaOH alkaline solution before returning to acid solution to perform the ORR or (b) DI water wash following NO treatment and then cycling in 1 M NaOH alkaline solution before returning to acid solution to perform the ORR. In both cases the effect of extending the potential sweep to -0.3 V is also displayed. 1600 rpm, loading: 270 μg cm<sup>-2</sup>, 5 mV s<sup>-1</sup>, electrolyte: 0.5 M H<sub>2</sub>SO<sub>4</sub>, O<sub>2</sub>-saturated electrolyte.

as a function of i) immersion in acid solution; ii) cycling in alkaline solution and iii) cycling into a deeply reducing potential. Again, two different pathways (post-poisoning), an acid and an alkaline one have been followed, where **Pathway C** is analogous to **Pathway A**, *i.e.* replacing the poisoning step with NO instead of NO<sub>2</sub><sup>-</sup> while keeping all other steps the same, and **Pathway D** is analogous to **Pathway B**, respectively.



SCHEME 5.3: Proposed reaction steps of the Fe-N/C active site after treatment with nitric oxide at pH 7 and subsequent treatment under different pH conditions.

The results are shown in Figure 5.3 and interpreted in Scheme 5.3. In the acid **Pathway C** (Figure 5.3 (a)), the catalyst was subjected to acid, before cycling in alkaline and then performing the ORR in acid again. After this treatment, the ORR activity did not recover.

Interestingly the catalyst could be recovered in the same way as the nitrite treated adduct (Figure 5.2 (b) inset) by scanning to a lower potential and reductively stripping off the adduct. This suggests that the active site complex formed with nitrite in acid (③) and the stable intermediate formed with nitric oxide (③',③'') are the same and supports the hypothesis of the formation of a nitrosyl complex upon acid treatment. If the nitrosyl complex indeed is present and is the stable species, it should form without acid treatment and survive the cycling in alkaline electrolyte. Therefore, the same experiments were performed without acid treatment, Figure 5.3 (b). In this experiment, after subjected to nitric oxide in the pH 7 buffer and subsequent DI water wash, the catalyst was cycled in 1 M NaOH leading to ③. It was found that with nitric oxide, the stable complex ③'' forms without acid treatment, as can be seen from the decreased ORR performance (Figure 5.3 (b)). Again the performance can be recovered under low potential. This suggests that the same complex is formed upon nitric oxide treatment (③',③'', ③'') and nitrite/acid treatment (③). The interaction of the catalyst with nitric oxide was then investigated in more depth in order to assess whether interpretable differences could be found.

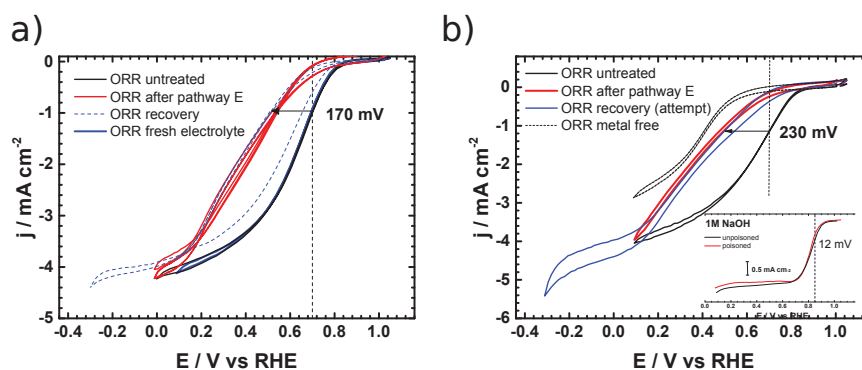
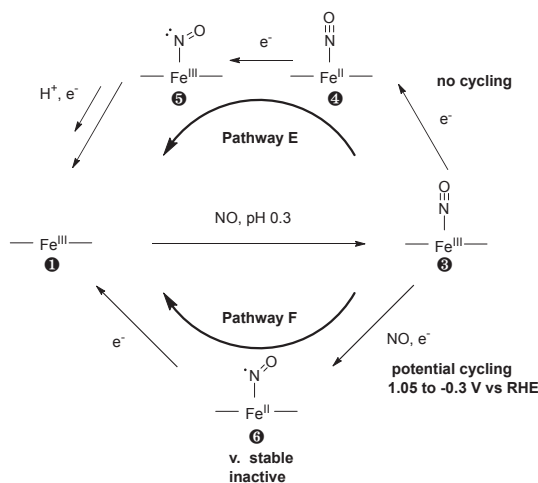


FIGURE 5.4: Rotating disk electrode (RDE) measurements in O<sub>2</sub>-saturated 0.5 M H<sub>2</sub>SO<sub>4</sub> of the ORR activity of a Fe-N/C catalyst before (untreated) and after poisoning in a saturated nitric oxide 0.5 M H<sub>2</sub>SO<sub>4</sub> solution. (a) effect of poisoning the electrode at OCV; (b) effect of poisoning the electrode by performing cyclic voltammetry (1.05 V to -0.3 V) in the NO-saturated 0.5 M H<sub>2</sub>SO<sub>4</sub> solution. Inset: ORR response of electrode in 1 M NaOH. In both cases the effect of extending the potential sweep to -0.3 V is also displayed. 1600 rpm, loading: 270 μg cm<sup>-2</sup>, 5 mV s<sup>-1</sup>, electrolyte: 0.5 M H<sub>2</sub>SO<sub>4</sub>, O<sub>2</sub>-saturated electrolyte.

This time, the catalyst (RDE) was poisoned by immersion in an acidified NO solution (instead of the pH 7 solution described above). Two different cases were considered. In the first the electrode was poisoned by immersion at OCV (shown as **Pathway E** in Scheme 5.4 with experiments in Figure 5.4 (a)), in the second it was poisoned by electrochemical cycling in the acidified NO solution (shown as **Pathway F** in Scheme 5.4 with experiments in Figure 5.4 (b)). When the electrode was poisoned at the open circuit

potential at 300 rpm for 10 minutes and subsequently washed in DI water, there is a clear poisoning effect which is significantly stronger ( $\sim 170$  mV compared to  $\sim 41$  -  $\sim 65$  mV) than previously observed when the catalyst was subjected to nitric oxide at pH 7 for 5 minutes (Figure 5.3).



SCHEME 5.4: Proposed reaction steps and active site species formed when subjecting the catalyst to an acidic NO solution, without electrochemical cycling (**Pathway E**) and with electrochemical cycling (**Pathway F**).

Possibly, this is due to the formation of other intermediates, **4** or **5** in Scheme 5.4, formed due to the change in open circuit potential caused by the pH shift (pH 7 compared to pH 0.3). Nevertheless, full recovery is still possible for these proposed poisoned species if the potential is reduced low enough to allow reductive stripping. However, the full recovery involves the change of electrolyte this time, which was not necessary before. It might be possible that a second set of active sites is poisoned during this protocol or the product that stripped off at low potentials contaminates the electrolyte due to a higher concentration, which might not have been the case before (*e.g.* ammonium trapped in the sulfonated groups of the Nafion<sup>™</sup> binder). When the electrode is cycled in the acidified NO containing electrolyte between 1.05 and -0.3 V *vs* RHE (Figure 5.4 (b)) no recovery was possible. Even extensive cycling to low potentials and the change of electrolyte could not recover the electrode. Interestingly, the activity decrease is even larger as compared to the OCP case (Figure 5.4(a)) ( $\sim 230$  mV *vs*  $\sim 170$  mV). Indeed, the poisoned catalyst approaches the activity of the nominally metal free N/C catalyst. This might indicate that almost all the metal induced active sites are poisoned (*e.g.* formation of **6**) or leached out. Interestingly, the alkaline activity of the strongly poisoned compared to the unpoisoned Fe-N/C catalyst is not significantly different (only a 12 mV shift in half-wave potential) as can be seen in the inset in Figure 5.4 (b). This again supports the hypothesis

of a non-metal centred active site in alkaline electrolyte, even if metal sites are present in the material. Ramaswamy *et al.* suggested an outer sphere electron transfer mechanism on this type of catalyst in alkaline electrolyte. [6] This means that even if the metal is covered by hydroxyl or nitrosyl, it still might be able to contribute to the activity. The irreversible poison effect observed in Figure 5.4 (b) could be interpreted as the formation of an even more stable nitrosyl species (⑥) which acts as a kinetic dead end. [4, 49, 50] For iron complexes, two different conformations of nitrosyl ligation are possible; the linear (④) and the bent form (⑥). [49, 51] However, further experiments would be necessary to confirm this hypothesis. Severe degradation of the active site might also be considered. The use of nitrite and nitrosyl in combination with *ex situ* characterisation methods such as X-ray absorption spectroscopy, Mössbauer spectroscopy and electron spin resonance might enable insight into the underlying phenomena and differentiation among metal centred active sites.

#### 5.2.4 The interaction of the Fe-N/C catalyst with hydroxylamine

As can be seen in Scheme 5.1, hydroxylamine is an intermediate in the nitrite/nitric oxide reduction pathway to ammonia,[22] analogous to peroxide being the intermediate for the ORR to water. It is known that hydroxylamine interacts with iron macrocyclic complexes and also that it decomposes upon contact with transition metal ions.[52] This is a similar behaviour as hydrogen peroxide.[53] The effect of hydroxylamine treatment on the catalyst was investigated to gain further information.

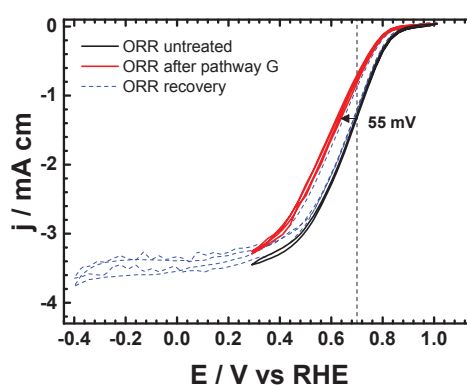
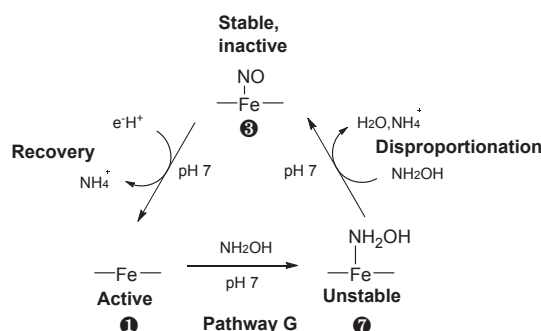


FIGURE 5.5: ORR performance before and after treatment in a 0.125 M hydroxylamine solution at pH 7. 1600 rpm, loading: 270  $\mu\text{g cm}^{-2}$ , 5  $\text{mV s}^{-1}$ , electrolyte: 0.5 M pH 7 PO<sub>4</sub>-buffer, O<sub>2</sub>-saturated.



After determining the original activity in a pH 7 phosphate buffer (in 4.2.5.1 it has been shown that mechanism and active site are likely to be the same in the pH region 0 - 9), the electrode was subjected to a neutral solution of hydroxylamine and then washed in DI water. In order to avoid the acidic decomposition, the ORR was then carried out at pH 7 in a phosphate buffer, so the electrode was never in contact with an acidic solution. Figure 5.5 shows that the same behaviour of poisoning and recovery is observed as for NO treatment in alkaline and acid (in the absence of potential cycling).



SCHEME 5.5: Proposed reaction steps of the active site upon contact with hydroxylamine and subsequent electrochemical recovery.

This same poisoning effect as seen for nitrite suggests the formation of the same nitrosyl complex (③, in Scheme 5.5). This can be explained by a spontaneous disproportionation of hydroxylamine to form NO and water which is reported for the contact of hydroxylamine with transition metals or heme complexes. [52, 54] It further supports the similarity of the active site to iron macrocyclic complexes or at least metallic centres.

### 5.2.5 Effect of poisons on metal free N/C catalyst

Figure 5.6 shows that the effect of nitrite, nitric oxide and hydroxylamine is negligible on the metal free N/C catalyst.<sup>1</sup> The slight effect is attributed to the residual metal content of 60 ppm (see 3.2.3).

<sup>1</sup>Poisoning with nitrite and nitric oxide was performed analogous to **Pathway A** and **C**, respectively, omitting the cycling step in alkaline. For hydroxylamine, the same steps have been taken as for the Fe-N/C catalyst.

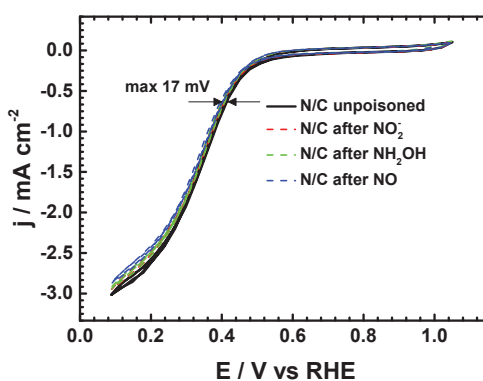


FIGURE 5.6: Rotating disk electrode measurements of the metal free N/C catalyst before and after subjecting it to nitrite, hydroxylamine and nitric oxide, 1600 rpm, loading: 270  $\mu\text{g cm}^{-2}$ , 5  $\text{mV s}^{-1}$ , 0.5M  $\text{H}_2\text{SO}_4$ ,  $\text{O}_2$ -saturated electrolyte.

### 5.2.6 Effect of the poison on the cyclic voltammetry of the Fe-N/C catalyst

When cyclic voltammetry is performed on this type of catalysts in the absence of oxygen, many iron containing catalysts exhibit a reversible redox peak at around 0.6 - 0.8 V *versus* RHE. [6, 55] As many metal free catalysts do not exhibit this peak, some publications associated it with the metal centred  $\text{Fe}^{2+}/\text{Fe}^{3+}$  redox peak of the active site. [6, 55] It has to be pointed out that this peak can also be associated with a quinone/hydroquinone couple on the carbon surface. [56] Nevertheless, it is peculiar that a catalyst devoid of metal and prepared in the same way does not exhibit this peak. Ramaswamy *et al.* reported a relationship with the position of the redox peak and the activity of the catalyst. [6] The charge associated with this peak was used to determine the number of active sites and hence the site density.

Comparing the **Fe-N/C** catalyst with the metal free catalyst **N/C** (Figure 5.7 (a)), it becomes apparent that the metal free catalyst does not exhibit this reversible redox peak, while the metal containing catalyst does. Therefore, the effect of the poison on this peak was investigated. De Groot *et al.* investigated iron heme compounds and iron containing enzymes, which were immobilised on electrodes, for their interaction with nitric oxide and its catalytic activity towards NO reduction. [28, 29] In that study, they also investigated the redox behaviour and the effect of the formation of a nitrosyl complex on the  $\text{Fe}^{2+}/\text{Fe}^{3+}$  redox peak and found that this peak is suppressed upon exposure to nitric oxide. If the redox peak was associated with the iron centre which serves as active site, there should

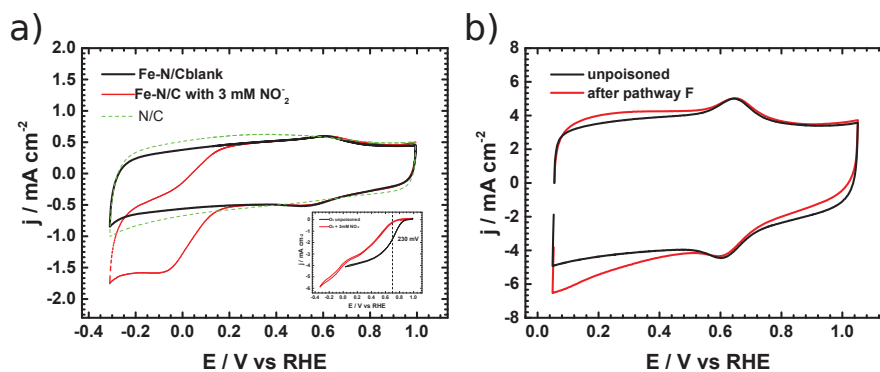


FIGURE 5.7: Cyclic voltammetry of the Fe-N/C catalyst in nitrogen saturated electrolyte, comparing the unpoisoned state to the strongly poisoned state. It can be seen that the redox peak at  $\sim 0.6$  V *vs* RHE is not significantly affected by the poison. (a)  $10 \text{ mV s}^{-1}$  in pH 5.2 acetate buffer without and with 3 mM NaNO<sub>2</sub>. The N/C catalyst does not show this redox peak. Inset: measurement in O<sub>2</sub>-saturated electrolyte with and without 3 mM NaNO<sub>2</sub>,  $5 \text{ mV s}^{-1}$  (b)  $100 \text{ mV s}^{-1}$  in 0.5 M H<sub>2</sub>SO<sub>4</sub> before and after subjecting it to cycling in NO saturated electrolyte. 1600 rpm, loading:  $270 \text{ } \mu\text{g cm}^{-2}$ , N<sub>2</sub>-saturated electrolyte.

be some effect on the position or magnitude of the peak. However, it can be seen that neither the Fe-N/C catalyst cycled in a 3 mM nitrite containing solution (Figure 5.7 (a)), which significantly affects the catalytic activity (210 mV potential shift see Figure 5.7 (a) inset), nor the irreversibly poisoned Fe-N/C catalyst, which almost lost its complete metal centered activity (230 mV potential shift see Figure 5.4 (b)), shows a significant effect on the alleged Fe<sup>2+</sup>/Fe<sup>3+</sup> peak (Figure 5.7 (b)). The slight change in capacitance of the catalyst after **Pathway F** (Figure 5.7 (b)) is likely due to oxidation of the carbon surface by nitric oxide. However, the redox peak is unaffected. There are different possibilities as to this behaviour;

- (i) The peak is not associated with the metal redox peak and/or the catalytic activity whatsoever, *e.g.* it might arise due to the quinone/hydroquinone couple. The addition of metal merely increases the concentration of this species;
- (ii) The peak is associated with metallic active sites that are significantly less active and do not interact with the poison. The highly active sites, however, strongly interact with nitrite and nitric oxide;
- (iii) The species associated with the peak is buried within the material and has no access to the surface and hence the poison. It might or might not influence the activity indirectly via long range effects.

A better understanding of this phenomenon might lead to better catalysts and should be investigated further.

### 5.2.7 Nitrite electroreduction to ammonia

As the Fe-N/C catalyst interacts strongly with nitrite, a question arose whether it would be active towards the electroreduction of the compound. This could on the one hand provide more information on the active site and on the other hand be useful in itself, as nitrite is an environmental pollutant and important biological messenger molecule. [22, 23]

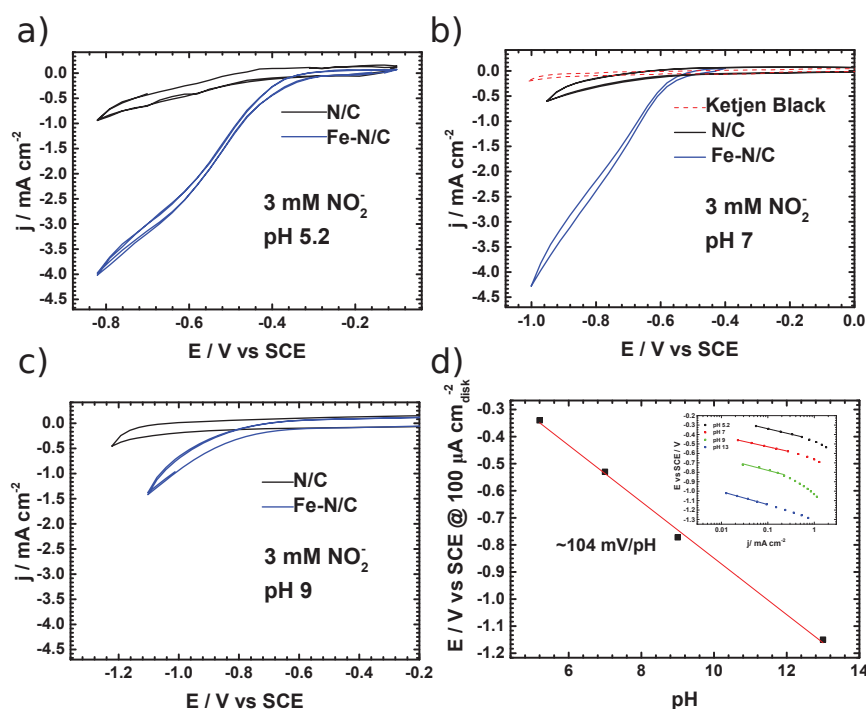


FIGURE 5.8: Rotating disk electrode measurements of a metal free catalyst N/C and an iron containing catalyst Fe-N/C towards nitrite reduction as a function of pH. 3 mM NaNO<sub>2</sub> containing N<sub>2</sub>-saturated electrolyte (a) pH 5.2 acetate buffer, (b) pH 7 phosphate buffer (c) pH 9 borate buffer. (d) pH dependence of the corrected potential at 0.1 mA cm<sup>-2</sup> towards nitrite reduction on the Fe-N/C catalyst Inset: corresponding *Tafel*-plots.

Therefore, the catalytic activity of the Fe-N/C and the N/C catalysts was compared at different pH values towards nitrite reduction. Figure 5.8 (a) - (c) shows rotating disk electrode measurements of the catalysts in 3 mM NaNO<sub>2</sub> containing buffer solutions at pH 5.2, 7 and 9 respectively. It can be clearly seen that the Fe-N/C catalyst is significantly more active towards the reduction of nitrite than N/C. The onset potentials are  $\sim -0.3$  V vs SCE ( $\sim -0.2$  V vs RHE),  $-0.5$  V vs SCE ( $0.1$  V vs RHE) and  $-0.8$  V vs SCE ( $-0.08$  V vs RHE), respectively. Interestingly, these overpotentials are significantly

lower than the ones reported by Duca *et al.* for hemin adsorbed on pyrolytic graphite. [57] Therefore, the pyrolysed catalyst might be more active than unpyrolysed iron heme centres. Although the pyrolyzed material might have more accessible active sites as compared to the unpyrolyzed material. However, an increase in activity would be analogous to the effect of heat treatment of heme based systems on the activity towards the oxygen reduction reaction. [58, 59] It can also be seen that the N/C catalyst while still showing some activity requires an extra overpotential over the Fe-N/C catalyst of -230, -295 and -355 mV, respectively. It is also evident that the nitrite reduction becomes more sluggish towards higher pH values. It shows a slope of  $\sim 104$  mV pH<sup>-1</sup> (Figure 5.8 (d)), somewhat different to the 59 mV pH<sup>-1</sup> unit expected for a simple proton coupled electron transfer. This indicates that a complicated multielectron and multiproton reduction is expected for this process. Duca *et al.* showed that for hemin adsorbed on pyrolytic graphite, the reduction of nitrite must occur via the decomposition of HNO<sub>2</sub> prior to electroreduction. [57] However, for the Fe-N/C catalyst shown here, this is not the case, as the concentration of HNO<sub>2</sub> is too low to be able to obtain the observed currents. This is even more obvious at pH 7 and higher, where the observed currents are orders of magnitudes higher than would be possible with the concentration of HNO<sub>2</sub>.<sup>2</sup> It is therefore inferred that the catalyst is capable of activating the unprotonated nitrite molecule.

A Koutecky-Levich analysis at pH 5.2 and 7 indicates a high electron transfer number of 5.2 and 4.8 respectively (Figure 5.9 (a) and (b)). In order to achieve a better idea of the product distribution of this complex reaction, the hydroxylamine content was monitored via the rotating ring disk electrode (RRDE) with a Pt ring (Figure 5.9). It was found to be negligible at pH 5.2 (Figure 5.9 (c)) and slightly higher ( $\sim 3\%$ ) at pH 7 (Figure 5.9 (d)). The high electron transfer number and the low hydroxylamine content suggest the production of ammonia. Therefore, a long term electrolysis experiment of 10 mM potassium nitrite in 50 mM potassium acetate buffer at pH 5.2 was performed and the ammonia and nitrite content was followed over time with ion chromatography.

Figure 5.10 shows the amount of ammonia produced and nitrite consumed *versus* the charge passed. It can be seen that at least 25% of the nitrite consumed is converted into ammonia. The other 75% might be nitrogen. It indicates that this complex reaction

<sup>2</sup>From the Levich equation by determining  $C(\text{HNO}_2)$  with the equilibrium constant  $K = 4 \cdot 10^{-4} \text{ M}^2$  for the  $\text{NO}_2 + \text{H}^+ \rightleftharpoons \text{HNO}_2$  couple at the respective pH and a  $\text{NO}_2^-$  concentration of 3 mM, a limiting current of  $3.9 \cdot 10^{-3} \text{ mA cm}^{-2}$  is calculated for pH 7 and  $3.9 \cdot 10^{-5} \text{ mA cm}^{-2}$  for pH 9, if HNO<sub>2</sub> was the species that was reduced. However,  $4.0 \text{ mA cm}^{-2}$  and  $1.5 \text{ mA cm}^{-2}$  were the measured maximum current densities in this work, respectively.  $D = 1.2 \cdot 10^{-5} \text{ cm}^2 \text{ s}^{-1}$  (from Ref [60]),  $v = 0.01 \text{ cm}^2 \text{ s}^{-1}$  (from Ref. [60]),  $n = 6$ .

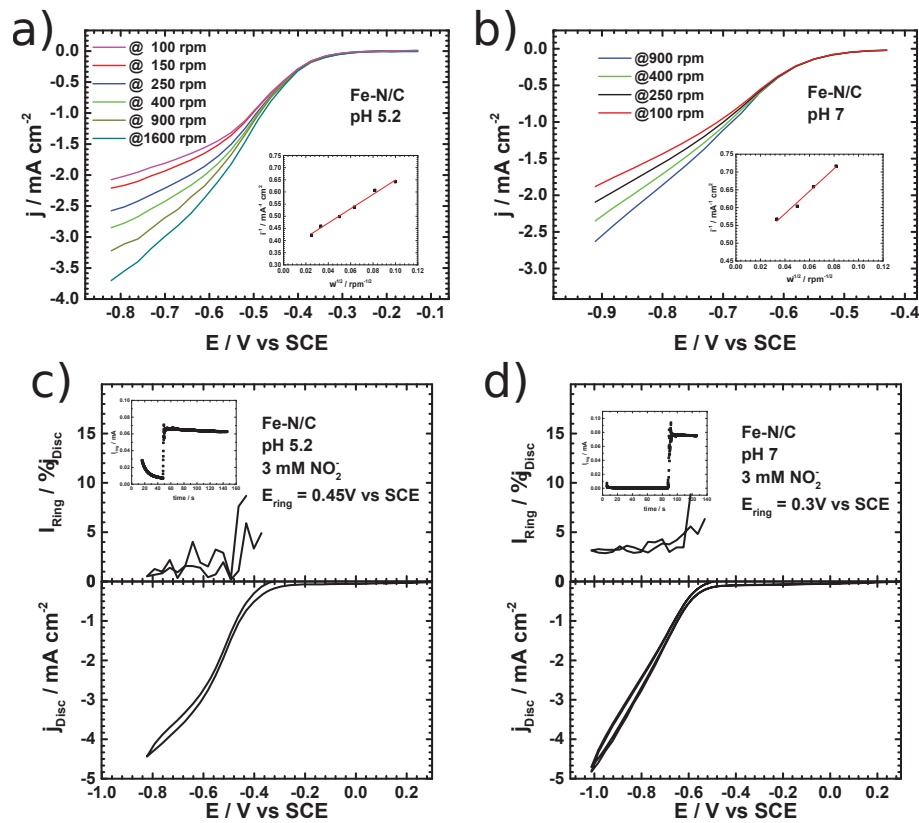


FIGURE 5.9: (a) and (b) Rotating disk electrode (RDE) *Koutecky-Levich* (K-L) analysis of the Fe-N/C towards nitrite reduction in (a) 0.5 M pH 5.2 acetate buffer, (b) 0.5 M pH 7 PO<sub>4</sub>-buffer. Insets: K-L plots to extract electron transfer number (c) and (d) Rotating ring disk electrode (RRDE) measurements, to determine the amount of hydroxylamine formed. (bottom) disk current (top) ring current in % disk current, when taking the collection efficiency of the ring into account. (c) Electrolyte: 0.5 M pH 5.2 acetate buffer; Ring potential: 0.45 V vs SCE (b) Electrolyte: 0.5 M pH 7 PO<sub>4</sub>-buffer; Ring potential: 0.3 V vs SCE. 1600 rpm, 270 μg cm<sup>-2</sup> catalyst loading, 5 mV s<sup>-1</sup>. (inset) chronoamperometry of the ring at the respective ring potential before and after adding 1 μM hydroxylamine to the solution. Current spike occurs when the solution is added.

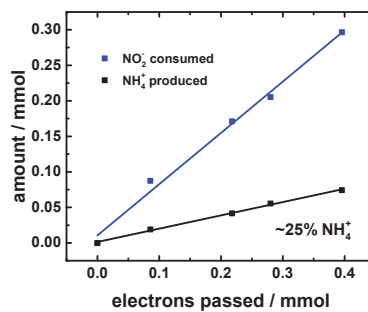


FIGURE 5.10: Ion chromatographic ammonia yield and nitrite consumed *versus* charge.

proceeds via different pathways (see Scheme 5.1). The low production of hydroxylamine and the high detected amount of ammonia is striking, as both N-O bonds are broken. This is not typical for simple iron-heme based catalysts, as they have been reported to produce close to 100% hydroxylamine and are not able to break the second N-O bond. [28] Either complex enzymes or precious metal based catalysts have been reported to produce ammonia depending on the conditions. [22]

### 5.2.8 Nitric oxide electroreduction

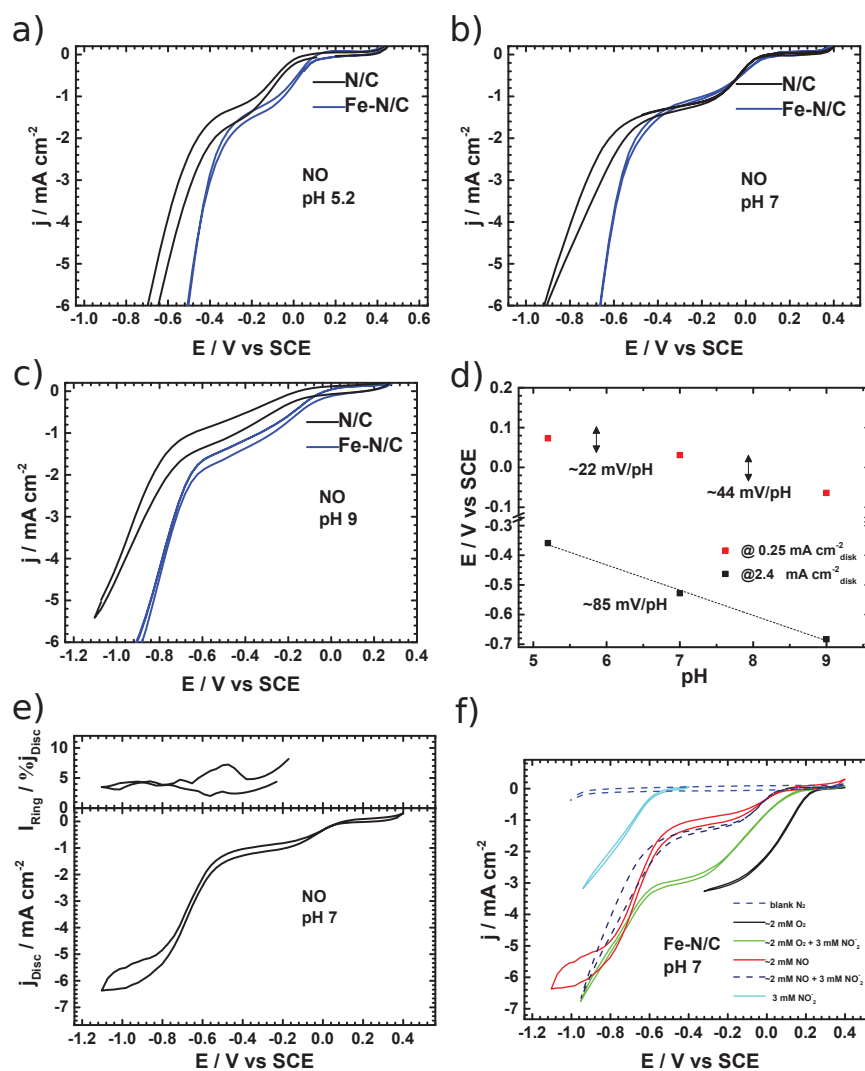


FIGURE 5.11: Rotating disk electrode (RDE) measurements in O<sub>2</sub>-saturated 0.5M H<sub>2</sub>SO<sub>4</sub> of the ORR activity of a Fe-N/C catalyst before (untreated) and after poisoning by a 0.125 M NaNO<sub>3</sub> solution at pH 7. a) Performance towards the ORR after acid wash following nitrite treatment and then cycling in 1M alkaline solution before returning to acid solution to perform the ORR. Inset: Effect of shifting cathodic endpoint to -0.3V; b) Performance towards the ORR after DI water wash following the poisoning protocol and then cycling in 1M alkaline solution before returning to acid solution to perform the ORR. RDE at 1600 rpm, catalyst loading at 270  $\mu\text{g cm}^{-2}$ , scan rate at 5  $\text{mV s}^{-1}$ .

The nitric oxide reduction reaction was examined as well in order to gain further information. Again, three pH values 5.2, 7 and 9 were evaluated (Figure 5.11 (a) - (c)). It can be seen that the onset potential is shifted upwards for both the **Fe-N/C** and **N/C** catalyst as compared to the nitrite reduction. Also striking is that the difference in overpotential between the two catalysts is significantly smaller than that for nitrite reduction. It is  $\sim 83$  mV,  $\sim 5$  mV and  $\sim 120$  mV for pH 5.2, pH 7 and pH 9, respectively. This indicates that the nitric oxide molecule is activated differently as compared to the nitrite molecule, presumably on the metal containing active site as well as on another metal free site or on the doped carbon surface via an outer sphere mechanism. It is also apparent that the reductive wave shows a plateau for both the **Fe-N/C** and the **N/C** catalyst. This behaviour was observed for the NO reduction on precious metal catalysts but not for iron heme based systems, as they only showed a single reduction wave at significantly lower potentials (higher overpotentials). [28] In the case of the **Fe-N/C** catalyst, a plateau with a current of  $\sim 1.5$  mA cm<sup>-2</sup> is visible (Figure 5.11 (a) - (c)) suggesting a one electron transfer, which would have a theoretical limiting current of 2.3 mA cm<sup>-2</sup>, and suggesting the reduction of NO to N<sub>2</sub>O (see Scheme 5.1). Interestingly, De Groot *et al.* observe a similar shape with a reductive pre-wave at a current of 1.63 mA cm<sup>-2</sup> and at similar potentials, but on a Pt disk, and argued that this would correspond to a one electron reduction. [28] This puzzling result could have interesting implications on the different modes of activation towards small molecules in this type of material. The carbon catalyst might exhibit an electrocatalytically active surface that might be modified by different dopants in addition to distinct active sites. It is also striking that the **N/C** catalyst performs **not** significantly worse than the **Fe-N/C** catalyst. Moreover, it shows a similar shape of a reductive pre-wave. This suggests indeed a different activation of NO as compared to nitrite. Investigating the effect of pH on the two reductive waves shows that the first wave exhibits a very low pH dependence ( $\sim 20$ - $40$  mV pH<sup>-1</sup>) of the potential at which a kinetic current of 0.25 mA cm<sup>-2</sup> is achieved (Figure 5.11). Such low values are significantly smaller than the expected 59 mV pH<sup>-1</sup> when a proton is involved in the rate determining step. This indicates a contribution from a pH independent pathway. The reduction to N<sub>2</sub>O would be such a reaction that could be pH independent. In contrast, the second wave shows a much larger pH dependence of  $\sim 85$  mV pH<sup>-1</sup>. The values for the **N/C** catalyst are  $\sim 18$  mV pH<sup>-1</sup> and  $\sim 100$  mV pH<sup>-1</sup>, respectively. The second wave

<sup>3</sup>Calculated from the Levich equation.  $D = 2.2 \times 10^{-5}$  cm<sup>2</sup> s<sup>-1</sup> (from Ref. [61]),  $v = 0.01$  cm<sup>2</sup> s<sup>-1</sup> (from Ref. [60]),  $C = 1.7$  mM (from Ref. [61])



however shows a slope of  $\sim 85$  mV pH<sup>-1</sup> for the **Fe-N/C** catalyst and  $\sim 100$  mV pH<sup>-1</sup> for the **N/C** catalyst, which suggest a strong pH dependence, similar to the nitrite reduction. It can also be seen that the difference in overpotential between **Fe-N/C** and **N/C** of the second wave is smaller when compared to the nitrite reduction. This also indicates that the second wave for the nitric oxide reduction has both a contribution from the metal free activity and the metal containing site. This makes NO in combination with nitrite and *ex situ* characterisation methods a powerful experimental approach to probe the different active sites. Further insight might be gained by investigating the product distribution in more detail, with studies such as differential electrochemical mass spectrometry (DEMS) as has been done for other catalysts. [32]

### 5.2.9 Possible use of Fe-N/C catalysts as diagnostic sensor materials

Sensors which can simultaneously determine nitric oxide, nitrite and oxygen would be desirable for biological systems, due to the importance of these molecules in regulating metabolic functions. [23, 35–37, 43, 62] The voltammetric response of the **Fe-N/C** catalyst to different combinations of substrates in the electrolyte is shown in Figure 5.11. The response of the catalyst towards the different substrates has been probed with the rotating disk electrode at 1600 rpm under physiological conditions in a pH 7 phosphate buffer. It can be clearly seen that there are significant differences. In the absence of any reactive substrate, under nitrogen, the catalyst does not show any current in a wide potential window. When the electrolyte is saturated with pure oxygen, it exhibits a clear wave with an onset potential of  $\sim 0.24$  V *vs* SCE. A solution of 3 mM nitrite in the absence of oxygen (nitrogen saturation) shows a reductive wave with an onset potential of  $-0.56$  V *vs* SCE. Importantly the reductive wave is significantly different to the response for pure nitric oxide, which shows a pre-wave at higher potential ( $0.08$  V *vs* SCE onset potential) and a limiting current at lower potential ( $\sim -1.0$  V *vs* SCE). The combination of nitrite and nitric oxide shows a similar response to pure nitric oxide but without a limiting current. This makes it possible to differentiate between nitrite and nitric oxide and even distinguish between pure nitric oxide and the combination of both. Finally, the combination of nitrite and oxygen shows again a different response with a first wave associated with oxygen reduction, an onset potential of  $\sim 0.16$  V *vs* SCE and a second wave associated with nitrite reduction starting at  $\sim -0.53$  V *vs* SCE. This specific behaviour could be exploited for sensors in biological systems.

## 5.3 Conclusions

Here, we demonstrated that a heat treated **Fe-N/C** catalyst interacts strongly with nitrite, nitric oxide and hydroxylamine. The catalyst was exposed to different treatments after the poisoning step allowing formation of either a weakly bound nitrite complex or a significantly stronger nitrosyl complex with, presumably, an iron centred active site. These species are stable towards electrochemical cycling and time, but can be recovered (removal of adsorbate) if cycled to low potentials. With nitric oxide, there is the possibility to form a species which cannot be recovered. This behaviour is an indication for a set of active sites with similar behaviour to iron heme based catalysts. However, a more in depth analysis is now possible by utilising this probe. The **Fe-N/C** catalyst is highly active towards reduction of nitrite, showing a large difference to the metal free **N/C** catalyst, which is significantly less active, as is also seen for the oxygen reduction reaction. In contrast to iron heme complexes, which predominantly form hydroxylamine, *i.e.* do not break the second N-O bond, the Fe-N/C catalyst forms ammonia as a major by-product and is able to break both N-O bonds. While iron heme complexes cannot activate unprotonated nitrite, the **Fe-N/C** catalyst does catalyse the reduction even at high pH values. This behaviour is similar to complex enzymes or precious metal surfaces. The nitric oxide reduction shows a different behaviour with two reductive waves similar to precious metal surfaces. This study offers insight into the chemical behaviour of the active site and a new probe for further investigation through *ex situ* methods. This might facilitate the identification of key features of highly active sites and the improvement of this type of catalyst. The significant difference in the response towards nitrite, nitric oxide and oxygen might inspire the development of new sensors for biochemical and environmental applications.

## 5.4 Experimental Part

### 5.4.1 Electrochemical Experiments

RRDE was conducted as described 3.4.2 and 4.4.5. And electrolytes were prepared as described in 4.4.5. When nitric oxide (from BOC >99%) was used, it was passed through 2 washing bottles filled with 3M KOH (AnalaR NORMAPUR<sup>®</sup>, VWR). This was necessary

in order to remove trace amounts of NO<sub>2</sub>. [28] Before passing NO into the electrochemical cell, the electrolyte was degassed with nitrogen and blanketed afterwards in order to avoid the reaction of NO with O<sub>2</sub>. [63] Electrolytes were prepared in ultrapure (DI) water (MilliQ 18.2 MΩ cm). The nitrite solution was prepared from NaNO<sub>2</sub> (ACS reagent, 99%, Sigma-Aldrich) and the hydroxylamine solution was prepared from NH<sub>2</sub>OH · HCl (ReagentPlus<sup>®</sup>, 99%, Sigma-Aldrich) in pH 7 phosphate buffer. For the long term electrolysis experiment a pH 5.2 0.05 M acetate buffer was prepared from potassium acetate (99%, Sigma-Aldrich) and glacial acetic acid (AnalaR NORMAPUR<sup>®</sup>, VWR) and the nitrite source was 0.01 M KNO<sub>2</sub> (VWR, 99%). The lower concentration and the use of potassium instead of sodium was necessary, as the low expected signal of ammonium would otherwise have been swamped by the large signal of sodium with a similar elution time. In a general procedure for the poisoning experiments, the rotating disk electrode disk with deposited catalyst was washed in DI water and then immersed into a pH 7 solution of the respective poison (125 mM NaNO<sub>2</sub>, NO saturated 0.5 M phosphate buffer, 125 mM hydroxylamine solution) at open circuit potential (OCP) for 5 minutes under a rotation of 300 rpm, and then washed for 5 minutes under a rotation of 300 rpm, before measuring the ORR performance post exposure.

### 5.4.2 Poisoning Protocols

Steps taken for each pathway. All experiments were carried out on the RRDE tip.

#### Pathway A:

1. Cyclic voltammetry in O<sub>2</sub>-saturated 0.5 M H<sub>2</sub>SO<sub>4</sub> at 5 mV s<sup>-1</sup> between 1.05 - 0.1 V *vs* RHE @ 1600 rpm (**ORR untreated**)
2. Immersion of the electrode into a 125 mM NaNO<sub>2</sub> solution at open circuit potential (OCP) for 5 minutes @ 300 rpm (**poisoning step**)
3. Immersion of the electrode into 0.5 M H<sub>2</sub>SO<sub>4</sub> at OCP for 1 minute @ 300 rpm
4. Cyclic voltammetry in O<sub>2</sub>-saturated 1 M NaOH at 5 mV s<sup>-1</sup> between 1.05 - 0.1 V *vs* RHE @ 1600 rpm
5. Cyclic voltammetry in O<sub>2</sub>-saturated 0.5 M H<sub>2</sub>SO<sub>4</sub> at 5 mV s<sup>-1</sup> between 1.05 - 0.1 V *vs* RHE @ 1600 rpm (**ORR after pathway 1**)

6. Cyclic voltammetry in O<sub>2</sub>-saturated 0.5 M H<sub>2</sub>SO<sub>4</sub> at 5 mV s<sup>-1</sup> between 1.05 - -0.3 V *vs* RHE @ 1600 rpm (**ORR recovery**)

**Pathway B:**

1. Cyclic voltammetry in O<sub>2</sub>-saturated 0.5 M H<sub>2</sub>SO<sub>4</sub> at 5 mV s<sup>-1</sup> between 1.05 - 0.1 V *vs* RHE @ 1600 rpm (**ORR untreated**)
2. Immersion of the electrode into a 125 mM NaNO<sub>2</sub> solution at OCP for 5 minutes @ 300 rpm (**poisoning step**)
3. Immersion of the electrode into DI water at OCP for 1 minute @ 300 rpm
4. Cyclic voltammetry in O<sub>2</sub>-saturated 1 M NaOH at 5 mV s<sup>-1</sup> between 1.05 - 0.1 V *vs* RHE @ 1600 rpm
5. Cyclic voltammetry in O<sub>2</sub>-saturated 0.5 M H<sub>2</sub>SO<sub>4</sub> at 5 mV s<sup>-1</sup> between 1.05 - 0.1 V *vs* RHE @ 1600 rpm (**ORR after pathway 2**)

**Pathway C:**

1. Cyclic voltammetry in O<sub>2</sub>-saturated 0.5 M H<sub>2</sub>SO<sub>4</sub> at 5 mV s<sup>-1</sup> between 1.05 - 0.1 V *vs* RHE @ 1600 rpm (**ORR untreated**)
2. Immersion of the electrode into a NO saturated 0.5 M phosphate buffer at pH 7 at OCP for 5 minutes @ 300 rpm (**poisoning step**)
3. Immersion of the electrode into 0.5 M H<sub>2</sub>SO<sub>4</sub> at OCP for 1 minute @ 300 rpm
4. Cyclic voltammetry in O<sub>2</sub>-saturated 1 M NaOH at 5 mV s<sup>-1</sup> between 1.05 - 0.1 V *vs* RHE @ 1600 rpm
5. Cyclic voltammetry in O<sub>2</sub>-saturated 0.5 M H<sub>2</sub>SO<sub>4</sub> at 5 mV s<sup>-1</sup> between 1.05 - 0.1 V *vs* RHE @ 1600 rpm (**ORR after pathway C**)
6. Cyclic voltammetry in O<sub>2</sub>-saturated 0.5 M H<sub>2</sub>SO<sub>4</sub> at 5 mV s<sup>-1</sup> between 1.05 - -0.3 V *vs* RHE @ 1600 rpm (**ORR recovery**)

**Pathway D:**

1. Cyclic voltammetry in O<sub>2</sub>-saturated 0.5 M H<sub>2</sub>SO<sub>4</sub> at 5 mV s<sup>b</sup> between 1.05 - 0.1 V *vs* RHE @ 1600 rpm (**ORR untreated**)

2. Immersion of the electrode into a NO saturated 0.5 M phosphate buffer at pH 7 at OCP for 5 minutes @ 300 rpm (**poisoning step**)
3. Immersion of the electrode into DI water at OCP for 1 minute @ 300 rpm
4. Cyclic voltammetry in O<sub>2</sub>-saturated 1 M NaOH at 5 mV s<sup>-1</sup> between 1.05 - 0.1 V *vs* RHE @ 1600 rpm
5. Cyclic voltammetry in O<sub>2</sub>-saturated 0.5 M H<sub>2</sub>SO<sub>4</sub> at 5 mV s<sup>-1</sup> between 1.05 - 0.1 V *vs* RHE @ 1600 rpm (**ORR after pathway D**)
6. Cyclic voltammetry in O<sub>2</sub>-saturated 0.5 M H<sub>2</sub>SO<sub>4</sub> at 5 mV s<sup>-1</sup> between 1.05 - -0.3 V *vs* RHE @ 1600 rpm (**ORR recovery**)

**Pathway E:**

1. Cyclic voltammetry in O<sub>2</sub>-saturated 0.5 M H<sub>2</sub>SO<sub>4</sub> at 5 mV s<sup>-1</sup> between 1.05 - 0.1 V *vs* RHE @ 1600 rpm (**ORR untreated**)
2. Immersion of the electrode into a NO saturated 0.5 M H<sub>2</sub>SO<sub>4</sub> solution at OCP for 10 minutes @ 300 rpm (**poisoning step**)
3. Immersion of the electrode into DI water at OCP for 1 minute @ 300 rpm
4. Cyclic voltammetry in O<sub>2</sub>-saturated 1 M NaOH at 5 mV s<sup>-1</sup> between 1.05 - 0.1 V *vs* RHE @ 1600 rpm
5. Cyclic voltammetry in O<sub>2</sub>-saturated 0.5 M H<sub>2</sub>SO<sub>4</sub> at 5 mV s<sup>-1</sup> between 1.05 - 0.1 V *vs* RHE @ 1600 rpm (**ORR after pathway E**)
6. Cyclic voltammetry in O<sub>2</sub>-saturated 0.5 M H<sub>2</sub>SO<sub>4</sub> at 5 mV s<sup>-1</sup> between 1.05 - -0.3 V *vs* RHE @ 1600 rpm (**ORR recovery**)
7. Change of 0.5 M H<sub>2</sub>SO<sub>4</sub> electrolyte
8. Cyclic voltammetry in O<sub>2</sub>-saturated 0.5 M H<sub>2</sub>SO<sub>4</sub> at 5 mV s<sup>-1</sup> between 1.05 - -0.3 V *vs* RHE @ 1600 rpm (**ORR recovered**)

**Pathway F:**

1. Cyclic voltammetry in O<sub>2</sub>-saturated 0.5 M H<sub>2</sub>SO<sub>4</sub> at 5 mV s<sup>-1</sup> between 1.05 - 0.1 V *vs* RHE @ 1600 rpm (**ORR untreated**)

2. Cyclic voltammetry in NO-saturated 0.5 M H<sub>2</sub>SO<sub>4</sub> at 5 mV s<sup>-1</sup> between 1.05 - -0.3 V *vs* RHE @ 1600 rpm (**poisoning step**)
3. Immersion of the electrode into DI water at OCP for 1 minute @ 300 rpm
4. Cyclic voltammetry in O<sub>2</sub>-saturated 1 M NaOH at 5 mV s<sup>-1</sup> between 1.05 - 0.1 V *vs* RHE @ 1600 rpm
5. Cyclic voltammetry in O<sub>2</sub>-saturated 0.5 M H<sub>2</sub>SO<sub>4</sub> at 5 mV s<sup>-1</sup> between 1.05 - 0.1 V *vs* RHE @ 1600 rpm 6.) Cyclic voltammetry in O<sub>2</sub>-saturated 0.5 M H<sub>2</sub>SO<sub>4</sub> at 5 mV s<sup>-1</sup> between 1.05 - -0.3 V *vs* RHE @ 1600 rpm (**ORR recovery**)
6. Cyclic voltammetry in O<sub>2</sub>-saturated 0.5 M H<sub>2</sub>SO<sub>4</sub> at 5 mV s<sup>b</sup> between 1.05 - 0.1 V *vs* RHE @ 1600 rpm (**ORR after pathway F**)

#### **Pathway G:**

1. Cyclic voltammetry in O<sub>2</sub>-saturated 0.5 M H<sub>2</sub>SO<sub>4</sub> at 5 mV s<sup>-1</sup> between 1.05 - 0.1 V *vs* RHE @ 1600 rpm (**ORR untreated**)
2. Immersion of the electrode into a 125 mM NH<sub>3</sub>OHCl solution in 0.5 M pH 7 phosphate buffer at OCP for 5 minutes @ 300 rpm (**poisoning step**)
3. Immersion of the electrode into a 0.5 M pH 7 phosphate buffer at OCP for 1 minute @ 300 rpm
4. Cyclic voltammetry in O<sub>2</sub>-saturated 0.5 M pH 7 phosphate buffer at 5 mV s<sup>-1</sup> between 1.05 - 0.1 V *vs* RHE @ 1600 rpm (**ORR after pathway G**)
5. Cyclic voltammetry in O<sub>2</sub>-saturated 0.5 M H<sub>2</sub>SO<sub>4</sub> at 5 mV s<sup>-1</sup> between 1.05 - -0.3 V *vs* RHE @ 1600 rpm (**ORR recovery**)

### **5.4.3 Ion Chromatography**

Ion chromatography was performed on a Metrohm 850 Professional ion chromatography system. The instrument was calibrated with 3 different concentrations prepared from a standard for nitrite (for IC TraceCERT<sup>®</sup>, 1000 mg L<sup>-1</sup> NO<sub>2</sub><sup>-</sup>, Sigma-Aldrich) and ammonium (TraceCERT<sup>®</sup>, 1000 mg L<sup>-1</sup> NH<sub>4</sub><sup>+</sup>, Sigma-Aldrich). An aliquot of 5 mL of the electrolyte was removed via a syringe after a respective amount of charge has been passed and diluted by a factor of 50 with the respective cation or anion eluent in order

to determine the concentration of nitrite and ammonium in the electrolyte. The columns used were Metrosep A sup 5 150/4.0 at a flow rate of 0.7 mL min<sup>-1</sup> for anions and Metrosep C4-150/4.0 at a flow rate of 0.9 ml min<sup>-1</sup> for cations. Eluents used were 3.2 mM H<sub>2</sub>CO<sub>3</sub> + 1.0 mM NaHCO<sub>3</sub> for anions and 1.7 mM nitric acid + 0.7 mM dipicolinic acid for cations, obtained by dilution of commercial concentrates Nitric Acid/Dipicolinic Acid 20x (Fluka) and Sodium bicarbonate/Sodium carbonate 20x (Fluka). Ultrapure water (MiliQ 18.2 MΩ cm) was used to prepare all dilutions and eluents.

## 5.5 References

- [1] Kramm U.I., Herranz J., Larouche N., Arruda T.M., Lefvre M., et al. Structure of the catalytic sites in Fe/N/C-catalysts for O<sub>2</sub>-reduction in PEM fuel cells. *Physical Chemistry Chemical Physics*, 14(33), 11,673–11,688, August 2012. doi: 10.1039/c2cp41957b.
- [2] Kramm U.I., Lefvre M., Larouche N., Schmeisser D., Dodelet J.P. Correlations between Mass Activity and Physicochemical Properties of Fe/N/C Catalysts for the ORR in PEM Fuel Cell via <sup>57</sup>Fe Mössbauer Spectroscopy and Other Techniques. *Journal of the American Chemical Society*, 136(3), 978–985, January 2014. doi: 10.1021/ja410076f.
- [3] Sahraie N.R., Kramm U.I., Steinberg J., Zhang Y., Thomas A., et al. Quantifying the density and utilization of active sites in non-precious metal oxygen electroreduction catalysts. *Nature Communications*, 6, 8618, October 2015. doi:10.1038/ncomms9618.
- [4] Herranz J., Jaouen F., Lefvre M., Kramm U.I., Proietti E., et al. Unveiling N-Protonation and Anion-Binding Effects on Fe/N/C Catalysts for O<sub>2</sub> Reduction in Proton-Exchange-Membrane Fuel Cells. *The Journal of Physical Chemistry C*, 115(32), 16,087–16,097, August 2011. doi:10.1021/jp2042526.
- [5] Tylus U., Jia Q., Strickland K., Ramaswamy N., Serov A., et al. Elucidating Oxygen Reduction Active Sites in Pyrolyzed MetalNitrogen Coordinated Non-Precious-Metal Electrocatalyst Systems. *The Journal of Physical Chemistry C*, 118(17), 8999–9008, May 2014. doi:10.1021/jp500781v.

- [6] Ramaswamy N., Tylus U., Jia Q., Mukerjee S. Activity Descriptor Identification for Oxygen Reduction on Nonprecious Electrocatalysts: Linking Surface Science to Coordination Chemistry. *Journal of the American Chemical Society*, 135(41), 15,443–15,449, October 2013. doi:10.1021/ja405149m.
- [7] Kramm U.I., Herrmann-Geppert I., Behrends J., Lips K., Fiechter S., et al. On an Easy Way To Prepare Metal-Nitrogen Doped Carbon with Exclusive Presence of MeN<sub>4</sub>-type Sites Active for the ORR. *Journal of the American Chemical Society*, 138(2), 635–640, December 2015. doi:10.1021/jacs.5b11015.
- [8] Cooper C.E., Brown G.C. The inhibition of mitochondrial cytochrome oxidase by the gases carbon monoxide, nitric oxide, hydrogen cyanide and hydrogen sulfide: chemical mechanism and physiological significance. *Journal of Bioenergetics and Biomembranes*, 40(5), 533–539, October 2008. doi:10.1007/s10863-008-9166-6.
- [9] Strickland K., Miner E., Jia Q., Tylus U., Ramaswamy N., et al. Highly active oxygen reduction non-platinum group metal electrocatalyst without direct metal-nitrogen coordination. *Nature Communications*, 6, 7343, June 2015. doi:10.1038/ncomms8343.
- [10] Ferrandon M., Kropf A.J., Myers D.J., Artyushkova K., Kramm U., et al. Multi-technique Characterization of a PolyanilineIronCarbon Oxygen Reduction Catalyst. *The Journal of Physical Chemistry C*, 116(30), 16,001–16,013, August 2012. doi:10.1021/jp302396g.
- [11] Gupta S., Fierro C., Yeager E. The effects of cyanide on the electrochemical properties of transition metal macrocycles for oxygen reduction in alkaline solutions. *Journal of Electroanalytical Chemistry and Interfacial Electrochemistry*, 306(1-2), 239–250, May 1991. doi:10.1016/0022-0728(91)85233-f.
- [12] Thorum M.S., Hankett J.M., Gewirth A.A. Poisoning the Oxygen Reduction Reaction on Carbon-Supported Fe and Cu Electrocatalysts: Evidence for Metal-Centered Activity. *The Journal of Physical Chemistry Letters*, 2(4), 295–298, February 2011. doi:10.1021/jz1016284.
- [13] Oberst J.L., Thorum M.S., Gewirth A.A. Effect of pH and Azide on the Oxygen Reduction Reaction with a Pyrolyzed Fe Phthalocyanine Catalyst. *The Journal of Physical Chemistry C*, 116(48), 25,257–25,261, December 2012. doi:10.1021/jp309707b.



- [14] Singh D., Mamtani K., Bruening C.R., Miller J.T., Ozkan U.S. Use of H<sub>2</sub>S to Probe the Active Sites in FeNC Catalysts for the Oxygen Reduction Reaction (ORR) in Acidic Media. *ACS Catalysis*, 4(10), 3454–3462, October 3, 2014 2014. doi:10.1021/cs500612k.
- [15] Wiesener K. N<sub>4</sub>-chelates as electrocatalyst for cathodic oxygen reduction. *Electrochimica Acta*, 31(8), 1073–1078, August 1986. doi:10.1016/0013-4686(86)80022-6.
- [16] Ozaki J.i., Anahara T., Kimura N., Oya A. Simultaneous doping of boron and nitrogen into a carbon to enhance its oxygen reduction activity in proton exchange membrane fuel cells. *Carbon*, 44(15), 3358–3361, December 2006. doi:10.1016/j.carbon.2006.08.022.
- [17] Birry L., Zagal J.H., Dodelet J.P. Does CO poison Fe-based catalysts for ORR? *Electrochemistry Communications*, 12(5), 628–631, May 2010. doi:10.1016/j.elecom.2010.02.016.
- [18] Malko D., Lopes T., Symianakis E., Kucernak A.R. The intriguing poison tolerance of non-precious metal oxygen reduction reaction (ORR) catalysts. *Journal of Materials Chemistry A*, 4(1), 142–152, December 2015. doi:10.1039/c5ta05794a.
- [19] Wang Q., Zhou Z.Y., Lai Y.J., You Y., Liu J.G., et al. Phenylendiamine-Based FeN<sub>x</sub>/C Catalyst with High Activity for Oxygen Reduction in Acid Medium and Its Active-Site Probing. *Journal of the American Chemical Society*, 136(31), 10,882–10,885, August 2014. doi:10.1021/ja505777v.
- [20] Wayland B.B., Olson L.W. Nitric oxide complexes of iron(II) and iron(III) porphyrins. *Journal of the Chemical Society, Chemical Communications*, 23, 897–898, January 1973. doi:10.1039/c39730000897.
- [21] Bard A.J., Parsons R., Jordan J. *Standard Potentials in Aqueous Solution*. CRC Press, August 1985. ISBN 978-0-8247-7291-8.
- [22] Rosca V., Duca M., de Groot M.T., Koper M.T.M. Nitrogen Cycle Electrocatalysis. *Chemical Reviews*, 109(6), 2209–2244, June 2009. doi:10.1021/cr8003696.
- [23] Pereira C., Ferreira N.R., Rocha B.S., Barbosa R.M., Laranjinha J.a. The redox interplay between nitrite and nitric oxide: From the gut to the brain. *Redox Biology*, 1(1), 276–284, 2013. doi:10.1016/j.redox.2013.04.004.

- [24] Silaghi-Dumitrescu R., Svistunenko D.A., Cioloboc D., Bischin C., Scurtu F., et al. Nitrite binding to globins: linkage isomerism, EPR silence and reductive chemistry. *Nitric Oxide*, 42, 32–39, November 2014. doi:10.1016/j.niox.2014.08.007.
- [25] Tsou C.C., Yang W.L., Liaw W.F. Nitrite Activation to Nitric Oxide via One-fold Protonation of Iron(II)-O,O-nitrito Complex: Relevance to the Nitrite Reductase Activity of Deoxyhemoglobin and Deoxyhemerythrin. *Journal of the American Chemical Society*, 135(50), 18,758–18,761, December 2013. doi:10.1021/ja4105864.
- [26] Silaghi-Dumitrescu R. Nitric Oxide Reduction by Heme-Thiolate Enzymes (P450nor): A Reevaluation of the Mechanism. *European Journal of Inorganic Chemistry*, 2003(6), 1048–1052, March 2003. doi:10.1002/ejic.200390136.
- [27] Lundberg J.O., Weitzberg E., Gladwin M.T. The nitratennitritenic oxide pathway in physiology and therapeutics. *Nature Reviews Drug Discovery*, 7(2), 156–167, February 2008. doi:10.1038/nrd2466.
- [28] de Groot M.T., Merckx M., Wonders A.H., Koper M.T.M. Electrochemical Reduction of NO by Hemin Adsorbed at Pyrolytic Graphite. *Journal of the American Chemical Society*, 127(20), 7579–7586, May 2005. doi:10.1021/ja051151a.
- [29] de Groot M.T., Merckx M., Koper M.T.M. Heme Release in Myoglobin/DDAB Films and Its Role in Electrochemical NO Reduction. *Journal of the American Chemical Society*, 127(46), 16,224–16,232, November 2005. doi:10.1021/ja0546572.
- [30] Duca M., Figueiredo M.C., Climent V., Rodriguez P., Feliu J.M., et al. Selective Catalytic Reduction at Quasi-Perfect Pt(100) Domains: A Universal Low-Temperature Pathway from Nitrite to N<sub>2</sub>. *Journal of the American Chemical Society*, 133(28), 10,928–10,939, July 2011. doi:10.1021/ja203234v.
- [31] Rosca V., Beltramo G.L., Koper M.T.M. Reduction of NO Adlayers on Pt(110) and Pt(111) in Acidic Media: Evidence for Adsorption Site-Specific Reduction. *Langmuir*, 21(4), 1448–1456, February 2005. doi:10.1021/la0475831.
- [32] de Vooy A.C.A., Koper M.T.M., van Santen R.A., van Veen J.A.R. Mechanistic study of the nitric oxide reduction on a polycrystalline platinum electrode. *Electrochimica Acta*, 46(6), 923–930, January 2001. doi:10.1016/s0013-4686(00)00678-2.

- [33] de Vooy A.C.A., Beltramo G.L., van Riet B., van Veen J.A.R., Koper M.T.M. Mechanisms of electrochemical reduction and oxidation of nitric oxide. *Electrochimica Acta*, 49(8), 1307–1314, March 2004. doi:10.1016/j.electacta.2003.07.020.
- [34] Koper M.T.M., van Santen R.A. Electric field effects on CO and NO adsorption at the Pt(111) surface. *Journal of Electroanalytical Chemistry*, 476(1), 64–70, October 1999. doi:10.1016/s0022-0728(99)00367-8.
- [35] Zen J.M., Kumar A.S., Wang H.F. A dual electrochemical sensor for nitrite and nitric oxide. *The Analyst*, 125(12), 2169–2172, December 2000. doi:10.1039/b008176k.
- [36] Boo Y.C., Mun G.I., Tressel S.L., Jo H. Detection of low levels of nitric oxide using an electrochemical sensor. *Methods in Molecular Biology*, 704, 81–89, nov 2011. doi:10.1007/978-1-61737-964-2\_7.
- [37] Hetrick E.M., Schoenfish M.H. Analytical Chemistry of Nitric Oxide. *Annual Review of Analytical Chemistry*, 2(1), 409–433, jul 2009. doi:10.1146/annurev-anchem-060908-155146.
- [38] Wu W., Zhu Z., Liu Z., Xie Y., Zhang J., et al. Preparation of carbon-encapsulated iron carbide nanoparticles by an explosion method. *Carbon*, 41(2), 317–321, February 2003. doi:10.1016/s0008-6223(02)00292-0.
- [39] Wu G., More K.L., Johnston C.M., Zelenay P. High-performance electrocatalysts for oxygen reduction derived from polyaniline, iron, and cobalt. *Science*, 332(6028), 443–447, 2011/04/22 2011. doi:10.1126/science.1200832.
- [40] Deng D., Yu L., Chen X., Wang G., Jin L., et al. Iron Encapsulated within Pod-like Carbon Nanotubes for Oxygen Reduction Reaction. *Angewandte Chemie International Edition*, 52(1), 371–375, January 2013. doi:10.1002/ange.201204958.
- [41] Gasteiger H.A., Kocha S.S., Sompalli B., Wagner F.T. Activity benchmarks and requirements for Pt, Pt-alloy, and non-Pt oxygen reduction catalysts for PEMFCs. *Applied Catalysis B: Environmental*, 56(1-2), 9–35, March 2005. doi:10.1016/j.apcatb.2004.06.021.
- [42] Fujii H., Yamaki D., Ogura T., Hada M. The functional role of the structure of the dioxo-isobacteriochlorin in the catalytic site of cytochrome cd1 for the reduction of nitrite. *Chemical Science*, 7(4), 2896–2906, March 2016. doi:10.1039/c5sc04825g.

- [43] Hunt A.P., Lehnert N. Heme-Nitrosyls: Electronic Structure Implications for Function in Biology. *Accounts of Chemical Research*, 48(7), 2117–2125, July 2015. doi:10.1021/acs.accounts.5b00167.
- [44] Brookins D.G. *Eh-pH Diagrams for Geochemistry*. Springer, softcover reprint of the original 1st ed. 1988 edition edition, December 2011. ISBN 978-3-642-73095-5.
- [45] Einsle O., Messerschmidt A., Huber R., Kroneck P.M.H., Neese F. Mechanism of the Six-Electron Reduction of Nitrite to Ammonia by Cytochrome c Nitrite Reductase. *Journal of the American Chemical Society*, 124(39), 11,737–11,745, October 2002. doi:10.1021/ja0206487.
- [46] Yang Z., Yao Z., Li G., Fang G., Nie H., et al. Sulfur-Doped Graphene as an Efficient Metal-free Cathode Catalyst for Oxygen Reduction. *ACS Nano*, 6(1), 205–211, January 2012. doi:10.1021/nn203393d.
- [47] Zheng Y., Jiao Y., Chen J., Liu J., Liang J., et al. Nanoporous Graphitic-C<sub>3</sub>N<sub>4</sub>@Carbon Metal-Free Electrocatalysts for Highly Efficient Oxygen Reduction. *Journal of the American Chemical Society*, 133(50), 20,116–20,119, December 2011. doi:10.1021/ja209206c.
- [48] Wang S., Zhang L., Xia Z., Roy A., Chang D.W., et al. BCN Graphene as Efficient Metal-Free Electrocatalyst for the Oxygen Reduction Reaction. *Angewandte Chemie International Edition*, 51(17), 4209–4212, April 2012. doi:10.1002/ange.201109257.
- [49] Blair E., Sulc F., Farmer P.J. Biomimetic NO<sub>x</sub> Reductions by Heme Models and Proteins. In J.H. Zagal, F. Bedioui, J.P. Dodelet, editors, *N<sub>4</sub>-Macrocyclic Metal Complexes*, pages 149–190. Springer New York, 2006. ISBN 978-0-387-28429-3 978-0-387-28430-9.
- [50] Matsumura H., Hayashi T., Chakraborty S., Lu Y., Monne-Loccoz P. The Production of Nitrous Oxide by the Heme/Nonheme Diiron Center of Engineered Myoglobins (FeBMbs) Proceeds through a trans-Iron-Nitrosyl Dimer. *Journal of the American Chemical Society*, 136(6), 2420–2431, February 2014. doi:10.1021/ja410542z.
- [51] Zagal J.H., Bedioui F., Dodelet J.P. *N<sub>4</sub>-Macrocyclic Metal Complexes*. Springer Science & Business Media, 2007-07-16 2007. ISBN 978-0-387-28430-9.

- [52] Bari S.E., Amorebieta V.T., Gutierrez M.M., Olabe J.A., Doctorovich F. Disproportionation of hydroxylamine by water-soluble iron(III) porphyrinate compounds. *Journal of Inorganic Biochemistry*, 104(1), 30–36, January 2010. doi:10.1016/j.jinorgbio.2009.09.024.
- [53] Kim S.J., Yoon B.H. Catalytic Decomposition of Hydrogen Peroxide by Transition Metal Ions. *Journal of Korea Technical Association of The Pulp and Paper Industry*, 38, 79–84, 2006.
- [54] Pacheco A.A., McGarry J., Kostera J., Corona A. Techniques for investigating hydroxylamine disproportionation by hydroxylamine oxidoreductases. *Methods in Enzymology*, 486, 447–463, 2011. doi:10.1016/b978-0-12-381294-0.00020-1.
- [55] Chlistunoff J. RRDE and Voltammetric Study of ORR on Pyrolyzed Fe/Polyaniline Catalyst. On the Origins of Variable Tafel Slopes. *The Journal of Physical Chemistry C*, 115(14), 6496–6507, April 2011. doi:10.1021/jp108350t.
- [56] Kinoshita K., Bett J.A.S. Potentiodynamic analysis of surface oxides on carbon blacks. *Carbon*, 11(4), 403–411, August 1973. doi:10.1016/0008-6223(73)90080-8.
- [57] Duca M., Khamseh S., Lai S.C.S., Koper M.T.M. The Influence of Solution-Phase HNO<sub>2</sub> Decomposition on the Electrocatalytic Nitrite Reduction at a Hemipyrrolic Graphite Electrode. *Langmuir*, 26(14), 12,418–12,424, July 2010. doi:10.1021/la101172f.
- [58] Yeager E. Electrocatalysts for O<sub>2</sub> reduction. *Electrochimica Acta*, 29(11), 1527–1537, November 1984. doi:10.1016/0013-4686(84)85006-9.
- [59] van Veen J.A., van Baar J.F., Kroese C.J., Coolegem J.G.F., De Wit N., et al. Oxygen reduction on transition-metal porphyrins in acid electrolyte i. activity. *Berichte der Bunsengesellschaft für physikalische Chemie*, 85(9), 693–700, September 1, 1981 1981. doi:10.1002/bbpc.19810850917.
- [60] Press C.R.C., Weast R.C., editors. *CRC Handbook of Chemistry and Physics: A Ready-Reference Book of Chemical and Physical Data*. CRC Press, Inc., 61st edition, 1981.

- [61] Zacharia I.G., Deen W.M. Diffusivity and Solubility of Nitric Oxide in Water and Saline. *Annals of Biomedical Engineering*, 33(2), 214–222, February 2005. doi:10.1007/s10439-005-8980-9.
- [62] Tsai A.L., Berka V., Martin E., Olson J.S. A Sliding Scale Rule for Selectivity among NO, CO, and O<sub>2</sub> by Heme Protein Sensors. *Biochemistry*, 51(1), 172–186, January 10, 2012 2012. doi:10.1021/bi2015629.
- [63] Lewis R.S., Deen W.M. Kinetics of the Reaction of Nitric Oxide with Oxygen in Aqueous Solutions. *Chemical Research in Toxicology*, 7(4), 568–574, July 1, 1994 1994. doi:10.1021/tx00040a013.

*In the previous chapter it was found that nitrite is a useful probe for Fe-N/C catalysts and reversibly deactivates certain active sites. Here a protocol is demonstrated that allows the quantification of these active centres which operate under acidic conditions by means of reductive nitrite stripping, with direct correlation to the catalytic activity. The poisoning protocol is reversible, but the poisoned catalyst is quite stable, allowing direct measurement of catalytic activity of the poisoned catalyst followed by regeneration to the original activity. The method is demonstrated for differently prepared materials. This indicates applicability to a wide range of Fe-N/C catalysts and will allow researchers to easily assess the active site density and mean turnover frequency of a specific type of highly active sites. It was further found that the catalyst contains two fundamental types of Fe active sites. One type (A) that reversibly binds nitrite to form a stable adduct and another type (B) which interacts with nitrite and is blocked only if the species is present in solution. Once moved to an uncontaminated electrolyte after poisoning, type A is still poisoned and needs to be reductively regenerated, while type B is regenerated immediately.*

## Chapter 6

# *In situ* electrochemical quantification of active sites in Fe-N/C catalysts

### 6.1 Introduction

As discussed in previous chapters, the exact nature of the active sites in Fe-N/C materials remains elusive. Recent spectroscopic studies provide evidence that one type of highly

active sites might be atomic iron centres, possibly coordinated with nitrogen. [1–3] These might chemically behave similarly to haem-like complexes. [1–3] *Ex situ* quantification of iron sites in these materials has recently been demonstrated. [4] However, techniques such as Mössbauer and X-ray absorption spectroscopy are not surface specific, do not allow the direct correlation to the oxygen reduction activity and are impractical. [5] The intrinsic catalytic activity of an electrocatalyst at a given potential is correlated with the current density by the following relationship:

$$i [\text{A g}^{-1}] = F [\text{A s mol}^{-1}] \times TOF [\text{electrons site}^{-1} \text{ s}^{-1}] \times MSD [\text{mol g}^{-1}] \quad (6.1)$$

where  $i$  is the gravimetric current density at a given potential,  $F$  is Faradays constant, TOF is the turnover frequency in electrons per site per second and MSD the gravimetric active site density. [6] There are two ways to improve the catalyst performance. Either the turnover frequency or the accessible site density has to be increased. [6] It is therefore necessary to accurately determine these values in order to develop a rational structure/activity relationship. To date there is no coherent and simple method to measure the intrinsic activity of Fe-N/C catalysts. These materials are usually prepared by high temperature heat treatment of a suitable precursor material that contains carbon, nitrogen and iron. [7–10] Recently, it has been shown that different routes lead to a similar set of presumably atomic iron sites. [5, 11, 12] A common probe to these iron sites would allow a consistent approach to evaluating their activity. Although extensive efforts have been employed, to date no true understanding could be established as how to increase the active site density or turnover frequency. Although changes to catalyst synthesis can lead to changes in electrocatalytic performance, the only clear trend identified to date within Fe-N/C catalysts is a correlation of iron content and activity, indicating that an increase in metallic centres increases the active site density while preserving the TOF. [13] However, for other changes such as different gas treatments, it is not clear whether the increase in activity is due to changes in the activity of the catalyst site (TOF), or the site density (MSD). The latter may occur by improving access to sites through morphological changes in the catalyst structure during treatment. We cannot simply count the amount of transition metal in our catalyst as a large proportion has been shown to be in inactive phases or buried within the structure. [4] Although cyanide, thiocyanide or hydrogen



sulphide do interact or poison Fe-N/C catalysts, these species could not be successfully utilized as electrochemical probes. [14–16]

In contrast, it is also shown in Chapter 5 that Fe-N/C catalysts strongly interact with the nitrite anion and form a stable poisoned catalyst adduct, while a metal free catalyst is unaffected. The stability of this adduct is remarkable and enables its use as an active site probe - once formed the adduct is not removed even after storing the electrode at OCP in electrolyte for 24 hours, or by performing an ORR scan across the potential region typically used. Such stability and ability to operate during the ORR is not commonly seen for such "reversible" poisons, *e.g.* CO adsorption on platinum. Moreover, under the right conditions, the catalytic activity can be completely recovered through reductive nitrite stripping at very low potentials. The stripping charge compared to the extent of the poisoning allows quantification of the number of active sites and direct correlation to the activity allows the determination of the mean TOF. Furthermore, it is found that there are two fundamental types of Fe sites, which are ORR active and interact with nitrite differently.

## 6.2 Results and Discussion

Although nitrite poisons the catalytic activity in acid electrolyte at a pH of 0.3 as it does at higher pH electrolytes, it was necessary to resort to higher pH values for the stripping experiments. This was done in order to improve quantification of the stripping peak and to remove interference caused by the formation of NO and NO<sub>2</sub> by acid decomposition of nitrite. The justification for using pH 5.2 and evidence for the applicability of the findings at pH 5.2 to the technologically important acidic pH is provided in 6.2.6.

### 6.2.1 Electrochemical stripping protocol

In order to determine the number of active sites, it is necessary to perform a series of experiments with the catalyst deposited on a rotating disk electrode (RDE) in a 3-electrode setup. [17] A 0.5 M acetate buffer at a pH of 5.2 was used as electrolyte in order to improve reproducibility. At this pH it was found that the nitrite reduction is sufficiently facile, while the nitrite anion is sufficiently stable (see also Chapter 6).

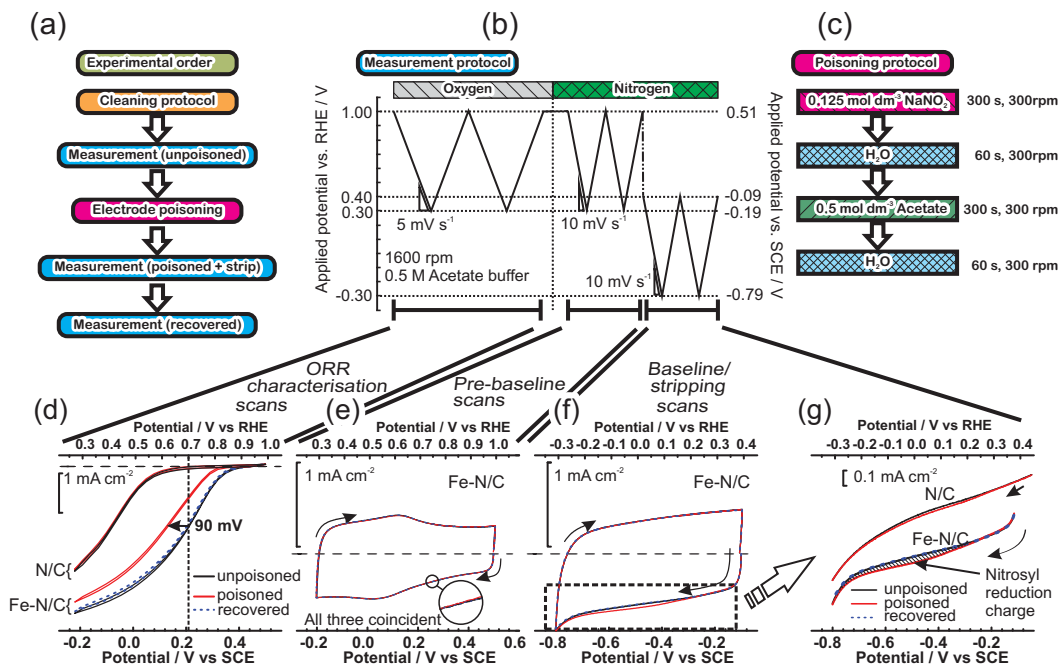


FIGURE 6.1: (a) flow diagram showing steps required to assess the performance of a catalyst and determine the catalyst site density; (b) Measurement protocol used to measure the electrochemical performance of the ORR and assess the charge associated with reductive stripping of the adsorbed nitrite; (c) protocol used to poison the electrode using a nitrite containing solution. (d) ORR performance of catalyst layer before, during and after nitrite adsorption; (e) wide range baseline scan (avoiding nitrite reduction area) for the catalyst layer before, during and after nitrite adsorption; (f) Narrow baseline scan in the nitrite reductive stripping region before, during and after nitrite adsorption (g) expansion of the region associated with nitrite stripping. All experiments were performed in a 0.5 M acetate buffer at pH 5.2 for Fe-N/C catalyst using a rotating disk electrode (RDE) setup, loading 270  $\mu\text{g cm}^{-2}$ . [Taken with permission from Ref. [18]]

This enables the correlation of the stripping onset potential to the nitrite reduction onset potential (Figure 6.2 (b)) and also shows that the metal free catalyst does not appreciably reduce solution phase nitrite. A saturated calomel electrode (SCE) was used as reference electrode and the potentials were converted to the reversible hydrogen electrode (RHE) scale (as described in 4.4.5). Figure 6.1 (a) depicts the order of experimental steps. After the electrode has undergone a cleaning protocol, a background scan is performed utilising the steps shown in Figure 6.1 (b). These steps not only measure the performance of the catalyst towards the ORR, but also measure the voltammetry in an oxygen free environment over both, a wide potential range, avoiding the nitrite reduction area, and a narrow potential range, in a more reductive region within which nitrite reduction occurs. Following these preliminary scans, the electrode is poisoned following the protocol shown in Figure 6.1 (c) utilising a nitrite concentration of 0.125 mol dm<sup>-3</sup>. The protocol shown in 6.1 (b) is then repeated to measure the performance of the catalyst in its poisoned state. The last sets of scans performed in the narrow, more reductive region lead to the

reductive desorption of the nitrite. Finally the protocol shown in 6.1 (b) is again repeated to see if the electrode has been recovered and returned to its initial state. Figures 6.1 (d) - (g) collect the respective voltammograms from each of the respective phases of the measurements. Figure 6.1 (d) shows the ORR performance of the catalyst as a function of poisoning. The catalyst performance is significantly reduced by the presence of an adsorbed nitrite intermediate, leading to a 90 mV shift in performance at 0.7 V (RHE). Thus, activity of the catalyst is reduced to less than 20% of its unpoisoned state. Following the stripping process, the ORR performance is totally recovered. Figure 6.1 (e) shows that there is no discernible difference to the electrode voltammetry over a wide potential range which avoids the nitrite reductive stripping region - all sweeps overlap each other. In contrast, when the potential is swept to a lower potential, Figure 6.1 (f), there is an excess in cathodic charge only when the electrode has been pre-exposed to nitrite. Furthermore, this excess charge disappears on subsequent scans, and the scans are perfectly coincident with those taken before exposure to nitrite. This region is shown in greater detail in Figure 6.1 (g), and the excess charge is perfectly correlated with the electrode being pre-exposed to nitrite during the poisoning protocol. As the catalytic activity is completely recovered after the stripping CV is performed (Figure 6.1 (d)), the amount of stripped charge is directly correlated to the decrease and recovery of the catalyst performance. Moreover, the same experiments performed on a metal free **N/C** catalyst ( $\sim 60$  ppm Fe) do not show a significant poison effect or a significant stripping charge (see 6.2.5), nor homogeneous nitrite reduction (see also Chapter 6). This indicates that nitrite interacts with the metal centre of the **Fe-N/C** catalyst. Therefore, the determination of the intrinsic catalytic activity induced by the metal is possible.

Figure 6.2 shows the difference in current between the stripping peak and background (*i.e.* difference in curves shown in Figure 6.1(g)) for both the **Fe-N/C** and **N/C** catalyst. It can be seen that there is some stripping charge for the **N/C** catalyst, and it assigned to residual iron in the sample ( 3.2.3 and 6.2.5). Also shown in Figure 6.2 is the homogeneous reduction of nitrite on the same catalyst when nitrite is present in the acetate buffer at a concentration of 3 mM together with the stripping voltammetry. It can be seen that there is a clear coincidence between the stripping peak and the beginning of nitrite reduction, strongly suggesting that they are the same process.

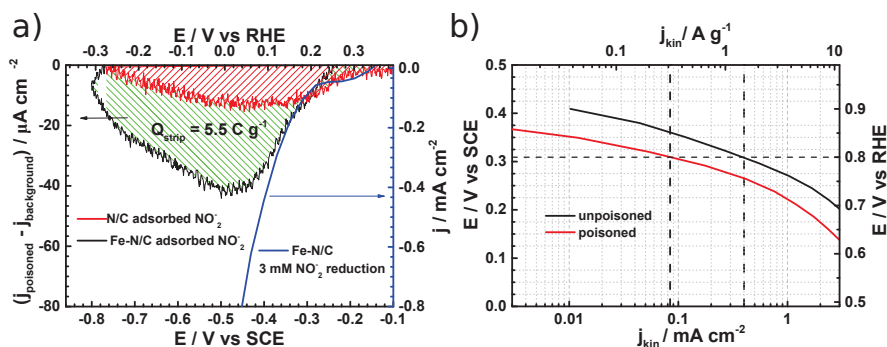


FIGURE 6.2: (a) comparison between homogeneous reduction of aqueous nitrite ( $3 \text{ mM NaNO}_2$  in acetate buffer), and excess current associated with reductive stripping of intermediate on  $\text{Fe-N/C}$  or  $\text{N/C}$  catalyst. The reductive stripping curve is produced by subtracting the unpoisoned from poisoned curve in Figure 3(g) (b) Kinetic current density of  $\text{Fe-N/C}$  catalyst before and after the poisoning step.  $\text{O}_2$ -saturated electrolyte,  $5 \text{ mV s}^{-1}$  background and  $iR$ -corrected RDE experiments at  $1600 \text{ rpm}$ , electrolyte:  $0.5 \text{ M}$  acetate buffer, loading:  $0.27 \text{ mg cm}^{-2}$ . [Adapted with permission from Ref. [18]]

## 6.2.2 Alternative coulometric stripping protocol

The stripping charge can alternatively be determined by stripping chronocoulometry.

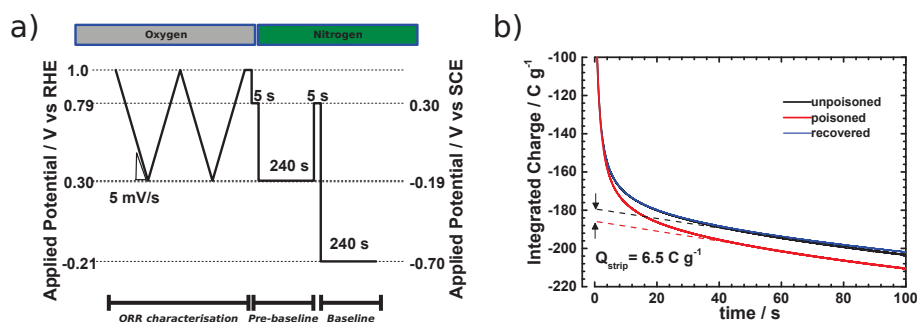
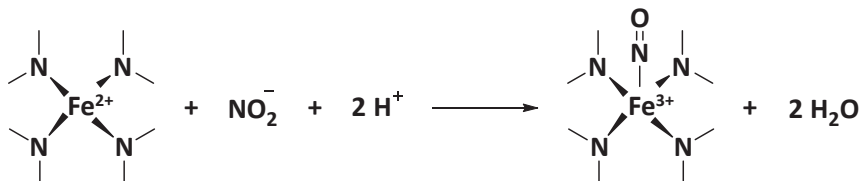


FIGURE 6.3: (a) Potential time protocol for the chronocoulometric stripping protocol (analogous to Figure 6.1) (b) Chronoamperometric transients for determination of the reductive stripping charge for the  $\text{Fe-N/C}$  catalyst. [Adapted with permission from Ref. [18]]

The protocol is shown in Figure 6.3 (a) and a typical coulometric measurement Figure 6.3 (b). After preparing the electrode in the same manner as described in Figure 6.1, the electrode potential is stepped from  $0.79 \text{ V}$  to  $0.21 \text{ V}$  versus RHE and the charge is recorded.

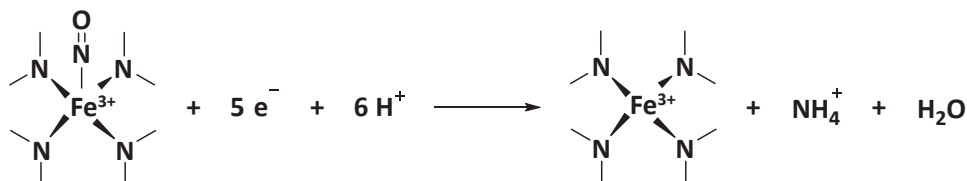
## 6.2.3 Active site density and turnover frequency

In Chapter 6 it is shown that ammonia is a major product and if only adsorbed nitrite is present (*i.e.* no nitrite in solution for the N-N bond formation) the only possible product. Hence, it is assumed that the nitrite ligand is transformed to a nitrosyl ligand upon cycling with a net reaction as shown in Scheme 6.1. [19, 20]



SCHEME 6.1: Formation of a nitrosyl complex.

It is further assumed that the stripping product is ammonia and therefore a transfer of 5 electrons per stripped molecule is tentatively used here as shown in Scheme 6.2. [19, 20]



SCHEME 6.2: Reduction of nitrosyl complex to ammonia.

A detailed analysis of the nitrite reduction and electron transfer number is shown in Chapter 6. The number of active sites is then equal to the number of stripped molecules. The areal site density (SD) is the number of active sites normalised to the surface area. The external surface area is used here, as the micropores might not be electrochemically accessible. [21]

$$SD \text{ [sites nm}^{-2}\text{]} = \frac{Q_{\text{strip}} \text{ [C g}^{-1}\text{]} \times N_{\text{A}} \text{ [mol}^{-1}\text{]}}{n_{\text{strip}} \times F \text{ [C mol}^{-1}\text{]} \times SA \text{ [nm}^2 \text{ g}^{-1}\text{]}} \quad (6.2)$$

Where  $Q_{\text{strip}}$  is the excess coulometric charge associated with the stripping peak (Figure 6.2 (a) and (b)),  $n_{\text{strip}}$  is the number of electrons associated with the reduction of one adsorbed nitrosyl per site, and SA is the surface area of the material. Likewise, the gravimetric site density (MSD), which is the amount of active sites normalised to the mass, is calculated from:

$$MSD \text{ [mol sites g}^{-1}\text{]} = \frac{Q_{\text{strip}} \text{ [C g}^{-1}\text{]}}{n_{\text{strip}} \times F \text{ [C mol}^{-1}\text{]}} \quad (6.3)$$

Figure 4(c) shows the difference of the kinetic current between the poisoned and the unpoisoned state of the Fe-N/C catalyst. By extracting the difference in kinetic current  $\Delta j_{\text{kin}}$  at 0.8 V vs RHE, the mean TOF of all different nitrite sensitive active sites with respect to electrons can be obtained via:

$$TOF(@0.8V \text{ vs RHE}) [\text{electrons site}^{-1} \text{ s}^{-1}] = \frac{\Delta j_{kin} [\text{A g}^{-1}]}{F [\text{As mol}^{-1}] \times MSD [\text{mol g}^{-1}]} \quad (6.4)$$

For our Fe-N/C catalyst we arrive at an MSD of  $12 \pm 2 \mu\text{mol g}^{-1}$  ( $7.2 \cdot 10^{18}$  sites  $\text{g}^{-1}$ ).<sup>1</sup> Interestingly, if iron is assumed as the active site, the utilisation compared to the total iron content (as determined by TXRF) is only  $\sim 4.5\%$ , which suggests that strategies could be implemented to increase the activity by making more iron sites accessible. The residual unutilised or undetected iron might be present as either Fe-N<sub>x</sub> sites which are buried within the structure, thus inaccessible or inactive and/or buried iron or iron based nanoparticulate phases (although such phases have not been detected in the present system). It has been shown that this type of material can contain up to 5 different types of Fe-N<sub>x</sub> sites and different TOFs have been assigned to those. [2, 5, 22] Due to the chemical similarity, it is likely that several of these different sites interact with nitrite. Therefore, this method will yield an average TOF for all different sites combined. Nevertheless, it is now possible to track whether a higher mean TOF is possible by enriching the catalyst with a certain type of site, as suggested by Mössbauer measurements. [5] The SD in the Fe-N/C catalyst is  $0.07 \pm 0.01 \text{ nm}^{-2}$  ( $0.02 \pm 0.002 \text{ nm}^{-2}$  with respect to the total surface area).<sup>1</sup> The mean TOF at 0.8 V vs RHE is  $1.6 \pm 0.2 \text{ electrons site}^{-1} \text{ s}^{-1}$ ,<sup>1</sup> which is in excellent agreement with the TOF for these types of active sites as reported by Sahraie et al., [4] which was determined to be  $\sim 1.5 \text{ electrons site}^{-1} \text{ s}^{-1}$  by a combined Mössbauer/chemisorption study and supports the validity of the here presented method. The activity decrease at 0.8 V vs RHE is  $\sim 80\%$ . The source of the residual activity is discussed in 6.2.9 and a second metal based active site which interacts with nitrite differently seems to be present.

## 6.2.4 Comparison to Pt based catalysts

In order to put the obtained results into perspective, a comparison of site density and turnover frequency to Pt is useful. The mass transport free specific activity of Pt based catalysts at 0.8 V vs RHE is too high to be extracted from RDE data. Therefore, the

<sup>1</sup>The mean and standard deviation are calculated from data obtained from 6 independent measurements, 3 of which were obtained via voltammetric stripping as described in 6.2.1 and 3 from the coulometric method as described in 6.2.2. Independent here means that each measurement was conducted from a separately prepared catalyst layer.

kinetic currents were extracted from work conducted by Zalitis *et al.* on the floating electrode, which eliminates mass transport effects at this potential. [23] A specific current density  $j_s$  of 4.03 mA cm<sup>-2</sup> is extracted from Fig. 8 inset in Ref. [23] The TOF can then be obtained by:

$$TOF(@0.8V \text{ vs RHE}) [\text{electrons site}^{-1} \text{ s}^{-1}] = \frac{j_s [\text{A cm}^{-2}] \times N_A [\text{mol}^{-1}]}{F [\text{As mol}^{-1}] \times SSD[\text{site cm}^{-2}]} \quad (6.5)$$

where  $j_s$  is the Pt specific current density at 0.8 V *vs* RHE,  $N_A$  Avogadro's constant and  $SSD$  the surface site density of Pt. Assuming for a Pt(111) surface  $1.5 \cdot 10^{15}$  atoms of Pt cm<sup>-2</sup> and further assuming that 2 atoms are necessary to form an active site for the ORR, one arrives at  $0.75 \cdot 10^{15}$  for the  $SSD$ . [24, 25] Using these values, a TOF of  $\approx 32$  is achieved by Pt. This is more than one order of magnitude higher than seen for the iron site. However, one has to consider that the conditions within this study were highly beneficial for Pt, as a non-adsorbing electrolyte was used and the data were extracted at the forward sweep from a high scan rate (20 mV s<sup>-1</sup>), hence the operational TOF should be lower, as it is known that the increasing oxygen coverage at high potential will decrease the activity at these potentials. [6] In fuel cell operation the TOF for Pt has been estimated to be  $\approx 11.4$  electrons site<sup>-1</sup> s<sup>-1</sup> at 0.8 V *vs* RHE. [25] In terms of active site density, the Fe-N/C catalyst with its  $7 \cdot 10^{12}$  sites cm<sup>-2</sup> exhibits more than one order of magnitude lower site density. It might be possible to increase the site density by one order of magnitude. However, in order to create a Fe-N/C catalyst with the same mass activity of Pt seems infeasible, as both active site density and TOF would have to be increased by more than one order of magnitude. Nevertheless, the aim of 1/10 the volumetric activity, as suggested by Gasteiger *et al.* might be feasible, considering the obtained values. [6] (see also 1.5) Further research and correlation with fuel cell activities might reveal the limitations of Fe-N/C materials.

### 6.2.5 Stripping charge on the metal free N/C catalyst and systematic error

While the effect on the metal free catalyst is small, it is still significant. From the extrapolation of the *Tafel*-plot to 0.8 V *vs* RHE (Figure 6.4) it can be seen that upon nitrite

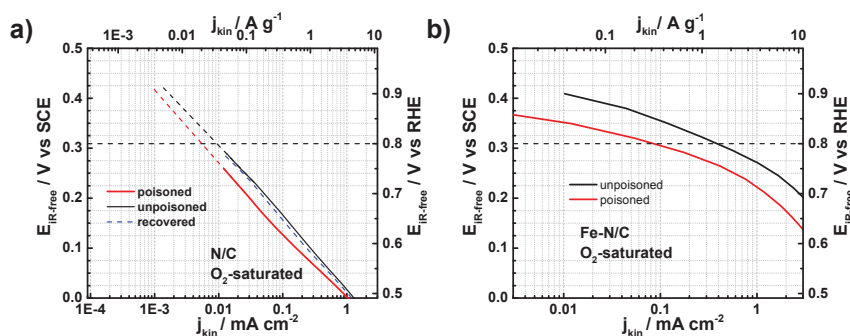


FIGURE 6.4: *Tafel*-plots of the **N/C** and **Fe-N/C** catalyst in the unpoisoned and poisoned state. Corresponding to measurements on the respective catalysts shown in Figure 6.1

exposure the **N/C** catalyst shows an activity decrease of  $43 \pm 4.0\%$  as compared to  $80 \pm 1.5\%$  for the **Fe-N/C** catalyst.<sup>1</sup> This is most likely due to the low but still finite residual metal content of  $\sim 60$  ppm. It can also be seen that the poisoning effect is only present at higher potentials. Nitrite treatment might therefore also reveal metal contributions in presumably metal free catalysts.

Ideally the quasi metal free catalyst should exhibit a zero stripping charge. However, even on the metal free **N/C** catalyst, a significant excess charge of  $1.9 \pm 0.4 \text{ C g}^{-1}$  as compared to  $6.0 \pm 1.0 \text{ C g}^{-1}$  for the **Fe-N/C** material is measured upon nitrite stripping.<sup>1</sup> This is 32% of the metal associated charge. This means in the worst case the calculated turnover frequency is underestimated by  $\sim 30\%$ . Therefore, the determined TOF of 1.60 electrons  $\text{site}^{-1} \text{ s}^{-1}$  might be as high as 2.35 electrons  $\text{site}^{-1} \text{ s}^{-1}$ . Nevertheless, this fact does not reduce the significance of the here demonstrated method, as activity trends can be followed and the here presented direct correlation can be used to unravel activity descriptors.

The stripping charge seem on the **N/C** catalyst might be attributed to different sources:

1. The residual metal content will be covered by nitrite and hence contribute to the stripping charge on the **N/C** catalyst. However this amount should be rather small. If all the metal (60 ppm) in the catalyst was on the surface and would contribute to the stripping charge, the maximum charge to be obtained would be  $\sim 0.53 \text{ C g}^{-1}$ . Therefore, only a fraction of the observed charge is to be attributed to the residual metal.
2. Other metal free active sites might also interact with nitrite, however much weaker.



3. Even though care was taken to wash off unspecifically adsorbed nitrite molecules, there might still be a residual amount that might be electrochemically reduced.
4. A chemical reaction between the nitrite containing solution and the carbon surface of the catalyst increases slightly the capacitance and therefore the baseline in the potential region of interest is slightly shifted.
5. A general uncertainty in the capacitance due to the transfer of the catalyst layer between solutions can contribute to a parasitic charge, which might lead to a systematic error.
6. A systematic error caused by other unknown sources.

## 6.2.6 Justification for using pH 5.2

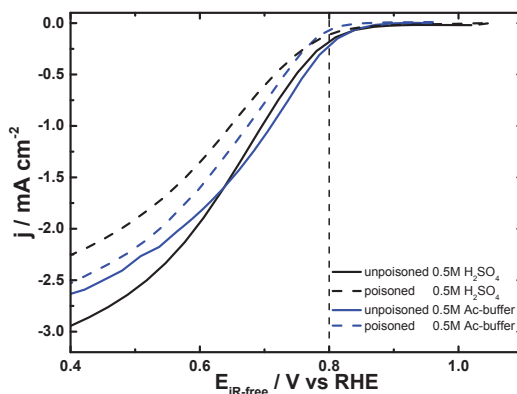


FIGURE 6.5: RDE measurement of Fe-N/C catalyst before and after poisoning with 0.125 M nitrite. Comparing 0.5 M acetate buffer (pH 5.2) to 0.5 M H<sub>2</sub>SO<sub>4</sub>. Loading: 0.27 mg cm<sup>-2</sup>, 1600 rpm, 5 mV s<sup>-1</sup>, background corrected, normalised to the same limiting current and iR-corrected. Note that there are different limiting current densities in the two electrolytes due to the difference in solubility and diffusion coefficient of oxygen in the two electrolytes, and (to a much lesser extent) the difference of viscosity of the two electrolytes. [Taken with permission from Ref. [18]]

In Figure 6.5 it can be seen that nitrite treatment poisons the activity at pH 5.2 as it does at pH 0.3, the effect of poisoning and the obtained current densities @0.8 V *vs* RHE are sufficiently similar to each other.

In 4.2.5.1 it has already been shown that mechanism and active site of the **Fe-N/C** catalyst should be the same in the pH region between 0 -9. An accelerating effect on the ORR is only present at pH values above 10. Hence at pH 5.2 the proton concentration is

sufficiently high to prevent this changeover in mechanism. Therefore, values for TOF and SD obtained at pH 5.2 should be transferable to acidic conditions. In acid, adsorption and subsequent stripping of nitrite is complicated due to the disproportionation of the nitrous acid formed in acidic conditions ( $pK_a = 3.4$ ) into NO and  $NO_2$ .



These species act as interferents and make quantification less accurate, this also means that care must be taken in selecting the appropriate concentration of nitrite.

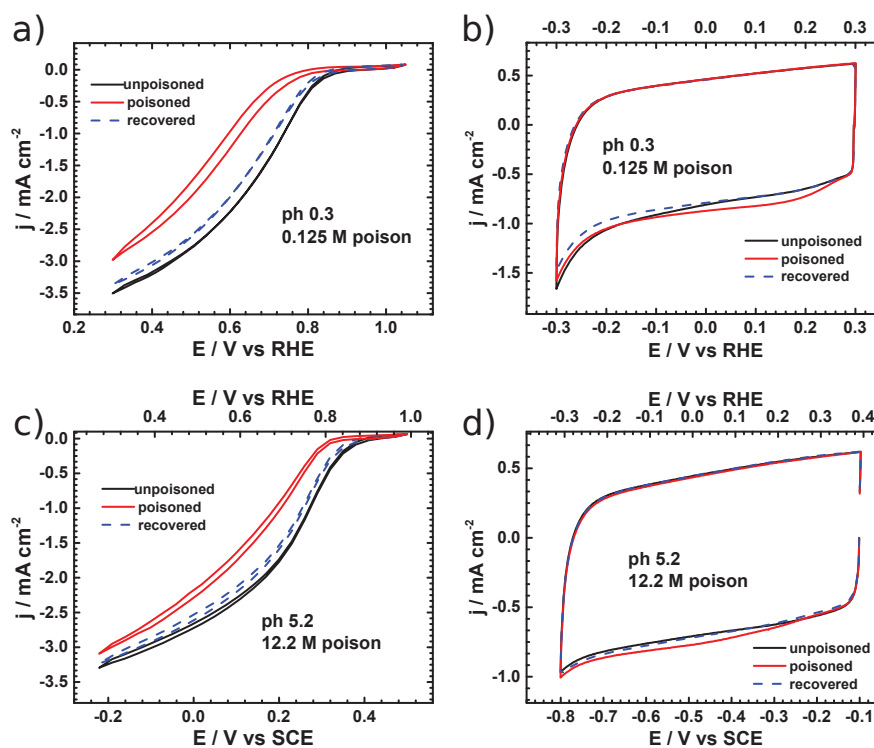


FIGURE 6.6: RDE measurement of Fe-N/C catalyst before and after poisoning and recovery. Loading:  $0.27 \text{ mg cm}^{-2}$ , 1600 rpm (a and c)  $O_2$ -saturated electrolyte,  $5 \text{ mV s}^{-1}$ . (b and d) Stripping voltammetry,  $N_2$ -saturated electrolyte,  $10 \text{ mV s}^{-1}$ . Comparing the behaviour in  $0.5 \text{ M H}_2\text{SO}_4$  when  $0.125 \text{ M}$  nitrite was used as poison (top) to  $0.5 \text{ M}$  acetate buffer when  $12.2 \text{ M}$  nitrite was used as poison (bottom). [Taken with permission from Ref. [18]]

In Figure 6.6 (a) and (b) it can be seen that when the method was conducted where ORR and stripping were performed in an acidic pH of 0.3, the general pattern of activity decrease, stripping peak and recovery stayed the same as at pH 5.2. However, a full recovery was not achieved. In order to confirm that this slight change in pattern was indeed

due to possible NO and NO<sub>2</sub> interferences, the method was conducted at pH 5.2, however the poisoning nitrite solution at a concentration of 12.2 M, while all other parameters were kept constant. At pH 5.2, the equilibrium concentration of HNO<sub>2</sub> in a 0.125 M nitrite solution is 2 mM (*i.e.* 1.5% exists as nitrous acid). At pH 0.3, 99.96% of the nitrite exists as nitrous acid, and the rate of the disproportionation reaction is fast. At 12.2 M nitrite and pH 5.2, the concentration of HNO<sub>2</sub> is similar to the HNO<sub>2</sub> concentration at 0.125 M nitrite and pH 0.3. This means the concentration of NO and NO<sub>2</sub> are comparable.<sup>2</sup> In Figure 6.6 (c) and (d) it can be seen that the pattern matches the pattern of when the method is conducted on the catalyst in acidic electrolyte. This confirms that the mechanism is the same at both pH values and also suggests that the concentration of nitrite solution needs to be chosen with care. This was investigated in 6.2.9.

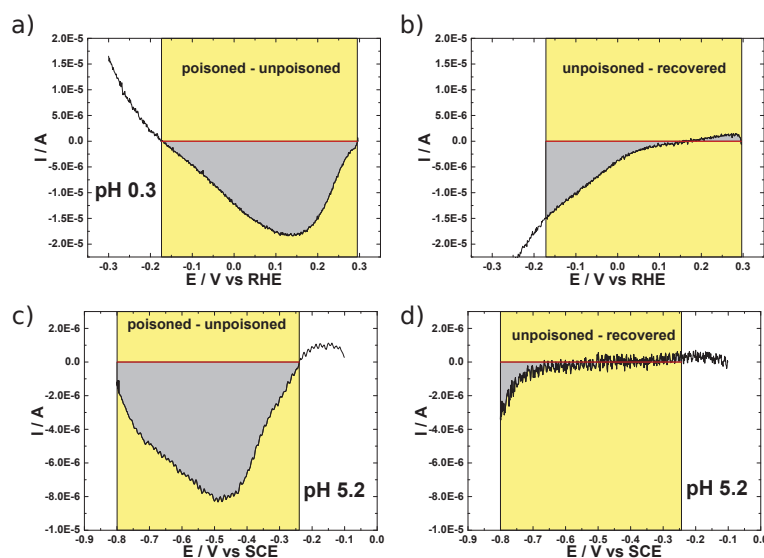


FIGURE 6.7: Difference between capacitive traces as measured for the respective wide scan at pH 0.3 (a and b) and pH 5.2 (c and d) in the stripping region. The charge difference between the poisoned and unpoisoned trace has been used to extract the stripping charge (a and c), while the difference between unpoisoned and recovered trace has been used to estimate the uncertainty due to varying capacitance. [Taken with permission from Ref. [18]]

In order to estimate the uncertainty due to changes in the baseline upon poisoning, the excess charge of the poisoned to the unpoisoned trace in the region of interest  $\Delta Q_{\text{pu}}$  (Figure 6.7 (a) and (c)) has been compared to the excess charge in the same region between unpoisoned and recovered trace  $\Delta Q_{\text{ur}}$  (Figure 6.7 (b) and (d)). The uncertainty

<sup>2</sup>Determining the concentration of HNO<sub>2</sub> with the equilibrium constant  $K = 3.98 \cdot 10^{-4} \text{ M}^2$  ( $\text{p}K_{\text{a}}=3.4$ ) for the  $\text{NO}_2^- + \text{H}^+ \rightleftharpoons \text{HNO}_2$  couple at the respective pH and the respective  $\text{NO}_2^-$  concentration. The rate of HNO<sub>2</sub> decomposition is approximated as  $k[\text{HNO}_2]^2$ , as can be seen in Eq 6.2.6. Hence it is significantly faster at higher concentrations, producing a higher concentration of NO and NO<sub>2</sub> interferences.

in determining the charge due to baseline inaccuracy  $\Delta Q_{\text{ur}}/\Delta Q_{\text{pu}}$  is at pH 0.3 35% and at pH 5.2 only 5%. Therefore, pH 5.2 was chosen in this study.

### 6.2.7 Application of the stripping technique to other Fe-N/C catalysts

The method has been conducted on a standard catalyst in this field in order to test the wide applicability to Fe-N/C materials. [9]

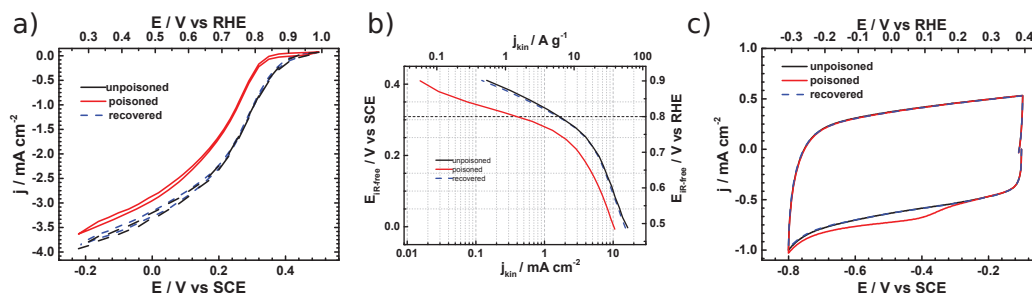


FIGURE 6.8: (a) RDE measurement of standard Fe-N/C catalyst,  $5\text{ mV s}^{-1}$ ,  $\text{O}_2$ -saturated electrolyte. (b) *Tafel*-plot. (c) Stripping voltammetry  $10\text{ mV s}^{-1}$ ,  $\text{N}_2$ -saturated electrolyte. Loading:  $0.27\text{ mg cm}^{-2}$ ,  $1600\text{ rpm}$ ,  $0.5\text{ M}$  acetate-buffer, pH 5.2

In Figure 6.8 (a) - (c) it can be seen that the method works excellently on this typical Fe-N/C catalyst.<sup>3</sup> A TOF of  $\sim 2.1$  electrons site<sup>-1</sup> s<sup>-1</sup> was found.

### 6.2.8 Application of the stripping technique to a FeCo-N/C catalysts

In order to further confirm the broad applicability of the method, it has also been conducted on a bimetallic FeCo catalyst reported in literature. [26] The synthesis procedures lie on the 2 different extremes in preparation conditions described in literature. These are for the **FeCo-N/C** and **Fe-N/C** catalyst,

- (i) carbon support *vs* self-supporting;
- (ii) molecular N-source *vs* aromatic N-source;
- (iii) bimetallic *vs* monometallic;
- (iv) no 2<sup>nd</sup> heat treatment *vs* 2<sup>nd</sup> heat treatment, respectively.

<sup>3</sup>The catalyst was provided by Dr. Anna Schuppert (University of Montpellier) for another collaboration and has been tested with this methodology to confirm the wide applicability. The catalyst was synthesised via decomposition of Fe phenanthroline over MOF as described in Ref. [9]

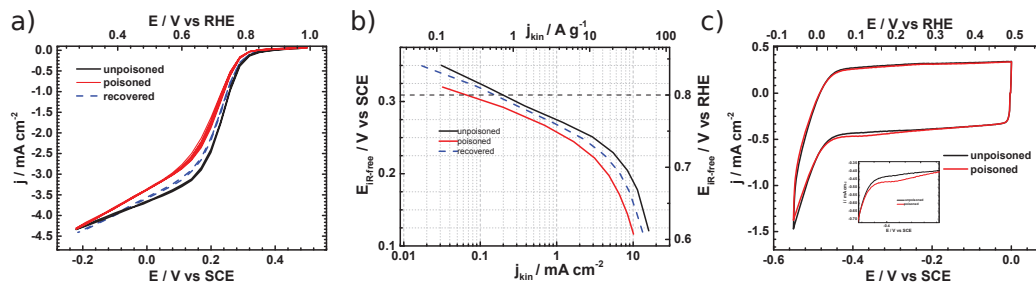


FIGURE 6.9: (a) RDE measurement of bimetallic FeCo catalyst,  $5 \text{ mV s}^{-1}$ ,  $\text{O}_2$ -saturated electrolyte. (b) *Tafel*-plot. (c) Stripping voltammetry  $10 \text{ mV s}^{-1}$ ,  $\text{N}_2$ -saturated electrolyte. Loading:  $0.27 \text{ mg cm}^{-2}$ ,  $1600 \text{ rpm}$ ,  $0.5 \text{ M}$  acetate-buffer,  $\text{pH } 5.2$ . [Adapted with permission from Ref. [18]]

Figure 6.9 (a) shows the ORR activities obtained, following the described procedure in the main text. It can be seen that a similar behaviour can be observed. Figure 6.9 (b) shows the respective kinetic current densities and (c) the associated stripping peak following the procedure described in 6.2.1.

It can be seen that the difficulty in evaluating the Co containing catalyst **6**FeCo-N/C is that it exhibits a significant hydrogen evolution activity (Figure 6.9 (c)). This will mask the stripping peak and make the use of this method challenging. Nevertheless, a stripping peak with associated recovered activity can be identified and analysed. It shows a TOF of  $\sim 0.43 \text{ electrons site}^{-1} \text{ s}^{-1}$  and an activity decrease of  $\sim 63\%$ . The hydrogen evolution activity is presumably caused by the Co content, as there are several reports in literature for cobalt containing hydrogen evolution catalysts, either atomic or as chalcogen. [7, 27] However, there is no report of highly active iron-only hydrogen evolution catalysts with similar structure to the Fe-N<sub>x</sub> type catalyst investigated here. It is therefore inferred that the stripping method should work excellently for most Fe-N/C iron-only catalysts with Fe-N<sub>x</sub> sites and can give useful information for other non-precious metal catalysts. Interestingly, the activity decrease of the catalyst FeCo is relatively lower (17% difference) than the Fe-N/C catalyst. This suggests that while a similar set of active sites is present in both catalysts, the catalyst FeCo might also contain a second set of active sites which is not affected by nitrite. This could possibly be attributed particulate phases or the cobalt content of the FeCo catalyst.

### 6.2.9 Concentration of nitrite - evidence for 2 types of Fe active sites

More information was gained by conducting the ORR in the presence of nitrite in solution and comparing the extent of poisoning to the metal free activity.

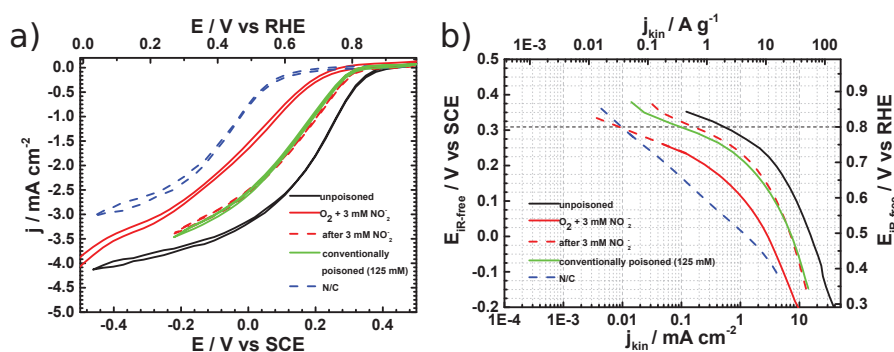


FIGURE 6.10: (a) RDE measurements of the Fe-N/C catalyst under different conditions compared to the N/C catalyst. (b) kinetic currents. Loading:  $0.27 \text{ mg cm}^{-2}$ , 1600 rpm,  $\text{O}_2$ -saturated electrolyte, 0.5 M acetate-buffer, pH 5.2,  $5 \text{ mV s}^{-1}$ . [taken with permission from Ref. [18]]

It can be clearly seen in Figure 6.10 that in the presence of nitrite in solution, the ORR is clearly inhibited to almost metal free level, while when removing the nitrite from the solution the poisoning is the same (within the accuracy of the measurement) for the 3 mM solution as for conventional poisoning in a 125 mM solution. This indicates that there are 2 fundamental types of active sites correlated to the iron centre. One which interacts with nitrite to bind it and form a stable adduct (Type A). This needs to be reductively removed in order to be recovered. The second type (Type B) however can easily be recovered by washing, but is blocked when nitrite is in solution. Type A accounts for  $\sim 80\%$  of the Fe induced activity while Type B is responsible for the remaining  $\sim 20\%$ . It is however not possible from the obtained data to make a statement on the TOF and SD of site Type B. It is either possible that

1. there are few sites with a significantly higher activity than Type A; in this case it would be desirable to identify and preferably synthesise this site.
2. SD and TOF are comparable for both sites;
3. the vast majority of iron is responsible for type B sites and those sites have hence a low TOF; in this case, it would be desirable to prevent the formation of Type B sites in order to allow more space for the higher activity Type A sites.

However, regardless of the nature of Type B sites, if all the iron in a 1.5 wt% Fe material could be utilised for the Type A sites, rather than the presently utilised 4.5%, a catalyst would result with 20x higher mass activity. This is intriguing and might lead to performances comparable to PGM catalysts.

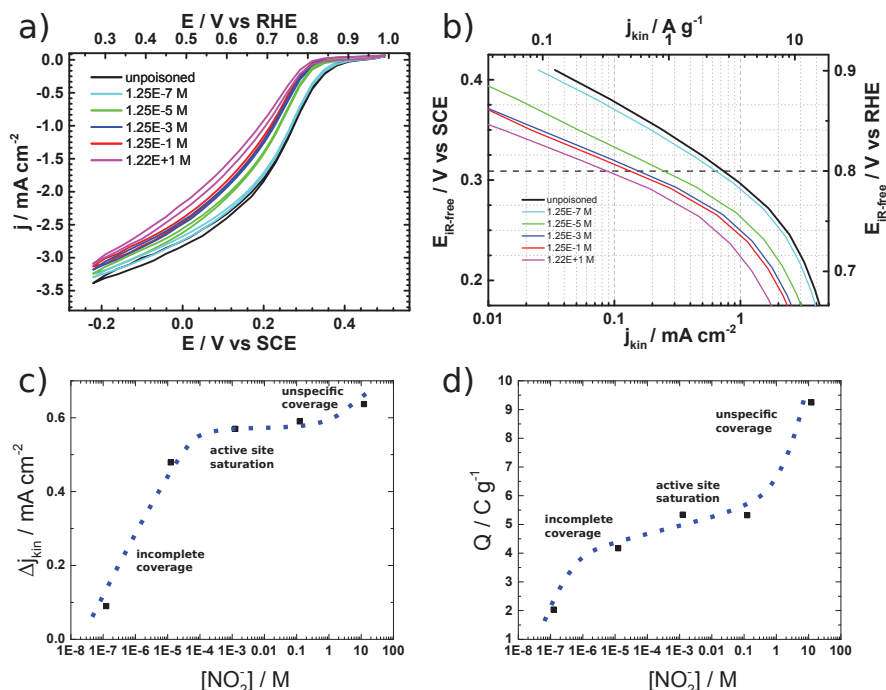


FIGURE 6.11: (a) RDE measurements of the Fe-N/C catalyst after subjecting it to the poisoning/stripping protocol at different concentrations of nitrite solution. (b) Kinetic currents. Loading: 0.27 mg cm<sup>-2</sup>, 1600 rpm, O<sub>2</sub>-saturated electrolyte, 0.5 M acetate-buffer, pH 5.2, 5 mV s<sup>-1</sup>. (c) effect of nitrite concentration on the magnitude of activity decrease (d) effect of nitrite concentration on the magnitude of stripping charge. The included blue dotted lines shall aid interpretation and do not represent a mathematical fit.[taken with permission from Ref. [18]]

In order to improve the understanding of the nitrite interaction with the different types of active sites, the concentration of the nitrite containing poisoning solution was varied, while all other parameters were kept constant. Figure 6.11 (a) shows the ORR performance before and after subjecting the catalyst layer to these different concentrations. Figure 6.11 (b) shows the respective kinetic currents. The nitrite concentration has been varied over 8 orders of magnitude, in order to cover a wide spectrum of interactions. Figure 6.11 (c) shows the decrease in activity plotted *versus* the logarithm of nitrite concentration. It can be clearly seen that at very low concentrations, the decrease in kinetic current is dependent on the concentration of nitrite. This effect persists to approximately millimolar level. Going to higher concentrations, a plateau is reached which extends over at least 2 orders of magnitude in concentration. When increasing the concentration further (*i.e.* to

a saturated solution), there is again a slight further decrease in activity. The associated correlation of stripping charge with the nitrite concentration is shown in Figure 6.11 (d). It can be seen that the same behaviour is observed and a plateau is reached which extends over 2 orders of magnitude in nitrite concentration. After exposing the catalyst to the saturated nitrite solution, there is a significant increase in stripping charge.

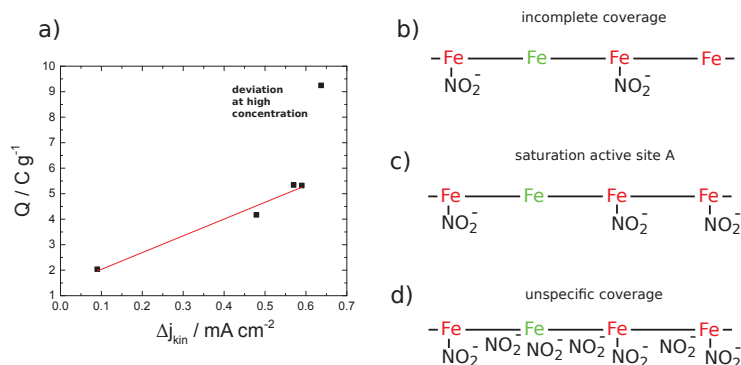


FIGURE 6.12: (a) Correlation of stripping charge to decrease in activity. (b) - (d) scheme to aid interpretation of the observed correlations of poison concentration, charge and activity decrease. 2 general metal based active sites are proposed. Strongly with nitrite interacting type A (red) and weakly interacting type B (green).[taken with permission from Ref. [18]]

Figure 6.12 (a) shows the correlation of stripping charge with activity decrease. It can be seen that over a wide range (6 orders of magnitude in poison concentration) there is a good correlation of activity decrease with stripping charge. Only when exposed to the saturated solution, the charge deviates from this direct correlation. This might possibly be reasoned in terms of a behaviour that is analogous to an isothermal adsorption of a species with a saturation process and a second mode of adsorption thereafter *e.g.* BET adsorption. In Figure 6.12 (b) - (d) an analysis utilising the presence of two hypothetical sites (as discussed above) is attempted. It is assumed that there are two types of sites: The strongly interacting Type A and the weaker interacting Type B. At low concentrations not all active sites of Type A are covered (Figure 6.12 (a)) *i.e.* from 125 nM to 12.5 M. Only at sufficiently high poisoning concentration, all active sites of type A are covered (Figure 6.12 (b)). This is where the plateau is reached and hence where the concentration of nitrite used in this study was situated. Increasing the concentration further results in the unspecific adsorption of nitrite onto the catalyst surface (Figure 6.12 (c)). The further decrease in activity could either be due to blocking of the active site or other undefined effects. This is also where a significant increase in stripping charge is observed. Nevertheless, these results clearly show that the activity decrease is correlated with the stripping charge, making our methodology suitable to determine catalyst parameters. It



furthermore confirms that the concentration used to poison the catalyst in this study is chosen appropriately, as it lies in the region where only specific adsorption to active sites is likely.

This second type of active site (type B) can either be in the form of nanophases or specific types of Fe–N<sub>x</sub> sites with a higher affinity to oxygen as compared to nitrite. The steric effects on the relative affinity of different substrates on iron centres is documented for enzymes. [28, 29] Interestingly, Lefevre *et al.* found that the abundance of less active ORR sites amounts to 20%, where the remaining 80% was assigned to a more active (and more desirable) ORR site. [30, 31] This coincides with the 80% decrease in ORR activity at 0.8 V *vs* RHE observed in the present work upon poisoning the Fe catalyst with nitrite, while the remaining 20 % metal centred activity are attributed to the second type B. Follow-up studies using *ex situ* techniques in combination with the nitrite probe might identify which site-type is more active and hence more desirable to pursue.

### 6.3 Conclusions

A method to determine the intrinsic activity of Fe-N/C catalysts has been developed. Nitrite was used as a probe. It has been shown that the charge of reductive nitrite stripping is directly correlated to the ORR activity. Using this methodology the density and mean TOF of a certain type of active sites, which are responsible for 80 % of the activity @0.8V *vs* RHE, could be determined. It was found that the method works best at pH 5.2. Evidence was provided that the results obtained can be translated to the technologically important acidic electrolyte. It was shown that the reason for the difficulties at lower pH are interferences caused by the decomposition of nitrite, *i.e.* NO and NO<sub>2</sub>. The methodology has also been successfully tested on a literature Fe-N/C and FeCo-N/C catalyst. This suggests general applicability to a wide range of Fe-N/C catalysts. Interestingly, there seems to be 2 different modes of poisoning. When the ORR is conducted in the presence of nitrite in solution, the activity of the **Fe-N/C** catalyst is reduced to the "metal free" **N/C** activity. When returning the catalyst into a solution without nitrite, about 20 % of the activity is instantly recovered, while the remaining 80 % need to be reductively recovered. It is suggested that 2 fundamental types of metal induced active sites are present. The dependence of the activity decrease on the concentration of the poison was investigated and the activity decrease reaches a plateau

over a wide concentration range and increases further at very high poison concentrations. This is reasoned with saturation of active site type A (the strongly interacting type) and only at high poison concentrations type B (the weakly interacting site) will be affected as well.

To summarize, an easy methodology to obtain crucial catalyst properties, namely mean TOF and active site density, is presented. The method is easy to conduct and requires no special equipment on top of the standard electrochemical characterisation tools. Poisoned sites are stable over the long term, so the catalyst can be prepared for *ex situ* measurements, and then recovered through an electrochemical treatment. This might be very useful in pinpointing the sites of relevance to the production of the majority of current which could be probed through the use of Mössbauer and EXAFS spectroscopy. Then one could track different catalysts and analyse which ones show variations in MSD and which variations in TOF. Because the adduct formed with nitrite is stable under oxidative systems, it is possible to measure the performance of the poisoned catalyst during the ORR, something which is not possible during, for instance, the CO-dependent poisoning of platinum. This approach will allow researchers to identify hitherto inaccessible trends and will significantly speed up the improvement of Fe-N/C catalysts. For instance, one could use this technique to assess what ammonia treatment does - does it increase TOF or MSD or both?

## 6.4 Experimental Part

### 6.4.1 Electrochemical stripping experiments

The RDE procedure, electrolytes and normalisations were as described in 3.4.2 and 4.4.5. A loading of  $0.27 \text{ mg cm}^{-2}$  was chosen as loading in all experiments, as it was found to give a good catalyst layer. Furthermore, it was a compromise between a relatively thin layer and a sufficient activity, to ensure adequate signal to noise ratio.

### 6.4.2 Electrochemical cleaning protocol

In order to obtain a non-changing oxygen reduction performance and non-changing cyclic voltammograms under nitrogen for the duration of the experiment, the catalyst layer

has to be conditioned. Therefore extensive cycling was performed in order to remove entrapped gas bubbles within the catalyst layer, making the layer hydrophilic and allow a complete wetting. The procedure consisted of extensive cycling, alternating between N<sub>2</sub>-saturated electrolyte at 100 mV s<sup>-1</sup> (20 cycles) and 10 mV s<sup>-1</sup> (10 cycles) and O<sub>2</sub>-saturated electrolyte at 5 mV s<sup>-1</sup> (6 cycles), in the potential window 1.05 - -0.4 V *vs* RHE. This was repeated until stable non changing oxygen reduction performance and cyclic voltammograms under nitrogen were achieved (ca. 3 - 4 times).

### 6.4.3 Stripping protocol using cyclic voltammetry

After the typical break-in procedure and background scan:

- (a) Record the unpoisoned ORR performance in O<sub>2</sub>-saturated electrolyte, 1.0 - 0.3 V *vs* RHE, 5 mV s<sup>-1</sup>
- (b) Record a pre-baseline cyclic voltammogram (CV) in N<sub>2</sub>-saturated electrolyte 1.0 - 0.3 V *vs* RHE, 10 mV s<sup>-1</sup>. This is necessary, in order to remove any residual dissolved oxygen which might falsify the results. It was furthermore found that this step increases the accuracy of the baseline during the stripping scan in the region of interest.
- (c) Record a baseline CV in N<sub>2</sub>-saturated electrolyte 0.4 - -0.3 V *vs* RHE, 10 mV s<sup>-1</sup>.
- (d) Dip RDE into 125 mM NaNO<sub>2</sub> solution for 5 minutes at open circuit potential (OCP), 300 rpm.
- (e) Wash electrode in DI water for 1 minute at OCP, 300 rpm.
- (f) Wash electrode in electrolyte solution for 5 minutes at OCP, 300 rpm.
- (g) Wash electrode in DI water for 1 minute at OCP, 300 rpm; the washing steps were found to be necessary in order to remove unspecifically adsorbed nitrite and to avoid nitrite contamination of the electrolyte.
- (h) Record ORR of poisoned electrode in O<sub>2</sub>-saturated electrolyte, 1.0 - 0.3 V *vs* RHE, 5 mV s<sup>-1</sup>.
- (i) Record pre-baseline CV of poisoned electrode in N<sub>2</sub>-saturated electrolyte, 1.0 - 0.3 V *vs* RHE, 10 mV s<sup>-1</sup>.

- (j) Record stripping CV in N<sub>2</sub>-saturated electrolyte, 0.4 - -0.3 V *vs* RHE, 10 mV s<sup>-1</sup>.
- (k) Repeat steps (h)-(j) to confirm recovery of ORR performance and baseline CV.

#### 6.4.4 Stripping protocol using chronocoulometry

When chronocoulometry is used instead of stripping voltammetry, the ORR steps remain the same. The pre-baseline CV is replaced with 240 s of chronoamperometry @0.3 V *vs* RHE (stepped from 0.79 V *vs* RHE 5 s) in N<sub>2</sub>-saturated electrolyte at a rotation of 1600 rpm, in order to remove any dissolved oxygen or unspecifically adsorbed nitrite. Then the baseline step of the unpoisoned catalyst and stripping voltammetry step of the poisoned catalyst are replaced with a chronocoulometry step under nitrogen at a rotation rate of 1600 rpm. The chronocoulometry step was performed by first equilibrating the surface @0.79 V *vs* RHE for 5 s and then stepping to -0.29 V *vs* RHE to record the charge passed *versus* time for 240 s (Figure 6.3). In order to control potential and measure charge an Autolab PGSTAT 20 potentiostat equipped with an integrator module was used. The stripping charge can then be extracted by plotting the integrated charge *versus* time and extrapolating the linear region to  $t = 0$ . The difference in the intercept of the unpoisoned to the poisoned catalyst is the charge associated with nitrite stripping. The small steady increase in charge in the linear region is due to the non-zero constant current associated with hydrogen evolution at this potential (-0.1 V *vs* RHE) and rotation rate (1600 rpm).

#### 6.4.5 Synthesis of FeCo catalyst:

The catalyst denoted FeCo was synthesized following a published method that was slightly modified. [26] In a typical route, 0.5 g of carbon black (Ketjenblack<sup>®</sup> EC-600JD) was refluxed in 200 mL of a 1.0 mol dm<sup>3</sup> HCl solution at 80 °C for 8 h to remove trace metals from the carbon black. Subsequently, this was vacuum filtrated, washed with plenty of ultrapure water (18.2 MΩ cm) and dried at 80 °C for 10 h. 200 mg of this pre-treated carbon black was weighted and dispersed in approximately 70 mL of absolute ethanol in an ultrasonication bath. A separate beaker was used to dissolve, in 30 mL of absolute ethanol (VWR), 0.0058 g of FeCl<sub>3</sub> (Sigma-Aldrich), 0.0063 g of Co(NO<sub>3</sub>)<sub>2</sub> (Sigma-Aldrich) along with 2 mL of N-ethylamine (Sigma Aldrich). This solution was added to the carbon black suspension and let to reflux for 8 h at 80 °C in a water bath. Subsequently, the

resulting solids were filtered and washed with ultrapure water and dried in an oven at 100 °C for 8 h. The dried powders were heat-treated in a tubular oven at 900 °C under nitrogen atmosphere for 1 h after ramping the temperature from room temperature at 20 °C min<sup>-1</sup>. Finally, the catalyst was refluxed in 100 mL of 0.5 mol dm<sup>3</sup> H<sub>2</sub>SO<sub>4</sub> at 80 °C for 24 h to remove soluble metal phases. This suspension was vacuum filtrated and washed with excess ultrapure water and dried at 80 °C for 10 h.

## 6.5 References

- [1] Zitolo A., Goellner V., Armel V., Sougrati M.T., Mineva T., et al. Identification of catalytic sites for oxygen reduction in iron- and nitrogen-doped graphene materials. *Nature Materials*, 14(9), 937–942, September 2015. doi:10.1038/nmat4367.
- [2] Kramm U.I., Herranz J., Larouche N., Arruda T.M., Lefvre M., et al. Structure of the catalytic sites in Fe/N/C-catalysts for O<sub>2</sub>-reduction in PEM fuel cells. *Physical Chemistry Chemical Physics*, 14(33), 11,673–11,688, August 2012. doi:10.1039/c2cp41957b.
- [3] Ramaswamy N., Tylus U., Jia Q., Mukerjee S. Activity Descriptor Identification for Oxygen Reduction on Nonprecious Electrocatalysts: Linking Surface Science to Coordination Chemistry. *Journal of the American Chemical Society*, 135(41), 15,443–15,449, October 2013. doi:10.1021/ja405149m.
- [4] Sahraie N.R., Kramm U.I., Steinberg J., Zhang Y., Thomas A., et al. Quantifying the density and utilization of active sites in non-precious metal oxygen electroreduction catalysts. *Nature Communications*, 6, 8618, October 2015. doi:10.1038/ncomms9618.
- [5] Kramm U.I., Lefvre M., Larouche N., Schmeisser D., Dodelet J.P. Correlations between Mass Activity and Physicochemical Properties of Fe/N/C Catalysts for the ORR in PEM Fuel Cell via <sup>57</sup>Fe Mössbauer Spectroscopy and Other Techniques. *Journal of the American Chemical Society*, 136(3), 978–985, January 2014. doi:10.1021/ja410076f.
- [6] Gasteiger H.A., Kocha S.S., Sompalli B., Wagner F.T. Activity benchmarks and requirements for Pt, Pt-alloy, and non-Pt oxygen reduction catalysts for PEMFCs. *Applied Catalysis B: Environmental*, 56(1-2), 9–35, March 2005. doi:10.1016/j.apcatb.

2004.06.021.

- [7] Jaouen F., Proietti E., Lefèvre M., Chenitz R., Dodelet J.P., et al. Recent advances in non-precious metal catalysis for oxygen-reduction reaction in polymer electrolyte fuel cells. *Energy & Environmental Science*, 4(1), 114–130, December 2010. doi:10.1039/c0ee00011f.
- [8] Wu G., More K.L., Johnston C.M., Zelenay P. High-Performance Electrocatalysts for Oxygen Reduction Derived from Polyaniline, Iron, and Cobalt. *Science*, 332(6028), 443–447, April 2011. doi:10.1126/science.1200832.
- [9] Proietti E., Jaouen F., Lefèvre M., Larouche N., Tian J., et al. Iron-based cathode catalyst with enhanced power density in polymer electrolyte membrane fuel cells. *Nature Communications*, 2, 416, August 2011. doi:10.1038/ncomms1427.
- [10] Malko D., Lopes T., Symianakis E., Kucernak A.R. The intriguing poison tolerance of non-precious metal oxygen reduction reaction (ORR) catalysts. *Journal of Materials Chemistry A*, 4(1), 142–152, December 2015. doi:10.1039/c5ta05794a.
- [11] Ferrandon M., Kropf A.J., Myers D.J., Artyushkova K., Kramm U., et al. Multi-technique Characterization of a PolyanilineIronCarbon Oxygen Reduction Catalyst. *The Journal of Physical Chemistry C*, 116(30), 16,001–16,013, August 2012. doi:10.1021/jp302396g.
- [12] Kramm U.I., Herrmann-Geppert I., Behrends J., Lips K., Fiechter S., et al. On an Easy Way To Prepare Metal–Nitrogen Doped Carbon with Exclusive Presence of MeN<sub>4</sub> -type Sites Active for the ORR. *Journal of the American Chemical Society*, 138(2), 635–640, January 2016. doi:10.1021/jacs.5b11015.
- [13] Jaouen F., Dodelet J.P. Average turn-over frequency of O<sub>2</sub> Electro-Reduction for Fe/N/C and Co/N/C catalysts in PEFCs. *Electrochimica Acta*, 52(19), 5975–5984, May 2007. doi:10.1016/j.electacta.2007.03.045.
- [14] Singh D., Mamtani K., Bruening C.R., Miller J.T., Ozkan U.S. Use of H<sub>2</sub>S to Probe the Active Sites in Fe-N/C Catalysts for the Oxygen Reduction Reaction (ORR) in Acidic Media. *ACS Catalysis*, 4(10), 3454–3462, October 2014. doi:10.1021/cs500612k.

- [15] Wang Q., Zhou Z.Y., Lai Y.J., You Y., Liu J.G., et al. Phenylenediamine-Based FeN<sub>x</sub>/C Catalyst with High Activity for Oxygen Reduction in Acid Medium and Its Active-Site Probing. *Journal of the American Chemical Society*, 136(31), 10,882–10,885, August 2014. doi:10.1021/ja505777v.
- [16] Gupta S., Fierro C., Yeager E. The effects of cyanide on the electrochemical properties of transition metal macrocycles for oxygen reduction in alkaline solutions. *Journal of Electroanalytical Chemistry and Interfacial Electrochemistry*, 306(1-2), 239–250, May 1991. doi:10.1016/0022-0728(91)85233-f.
- [17] Paulus U.A., Schmidt T.J., Gasteiger H.A., Behm R.J. Oxygen reduction on a high-surface area Pt/Vulcan carbon catalyst: a thin-film rotating ring-disk electrode study. *Journal of Electroanalytical Chemistry*, 495(2), 134–145, January 2001. doi:10.1016/s0022-0728(00)00407-1.
- [18] Malko D., Kucernak A.R., Lopes T. *In situ* electrochemical quantification of active sites in Fe-N/C non-precious metal catalysts. *Nature Communications*, 7, September 2016. doi:10.1038/ncomms13285.
- [19] Einsle O., Messerschmidt A., Huber R., Kroneck P.M.H., Neese F. Mechanism of the Six-Electron Reduction of Nitrite to Ammonia by Cytochrome c Nitrite Reductase. *Journal of the American Chemical Society*, 124(39), 11,737–11,745, October 2002. doi:10.1021/ja0206487.
- [20] Rosca V., Duca M., de Groot M.T., Koper M.T.M. Nitrogen Cycle Electrocatalysis. *Chemical Reviews*, 109(6), 2209–2244, June 2009. doi:10.1021/cr8003696.
- [21] Yamada H., Nakamura H., Nakahara F., Moriguchi I., Kudo T. Electrochemical Study of High Electrochemical Double Layer Capacitance of Ordered Porous Carbons with Both Meso/Macropores and Micropores. *The Journal of Physical Chemistry C*, 111(1), 227–233, January 2007. doi:10.1021/jp063902g.
- [22] Lefèvre M., Proietti E., Jaouen F., Dodelet J.P. Iron-Based Catalysts with Improved Oxygen Reduction Activity in Polymer Electrolyte Fuel Cells. *Science*, 324(5923), 71–74, April 2009. doi:10.1126/science.1170051.

- [23] Zalitis C.M., Kramer D., Kucernak A.R. Electrocatalytic performance of fuel cell reactions at low catalyst loading and high mass transport. *Physical Chemistry Chemical Physics*, 15(12), 4329–4340, February 2013. doi:10.1039/C3CP44431G.
- [24] Jaramillo T.F., Jørgensen K.P., Bonde J., Nielsen J.H., Horch S., et al. Identification of Active Edge Sites for Electrochemical H<sub>2</sub> Evolution from MoS<sub>2</sub> Nanocatalysts. *Science*, 317(5834), 100–102, July 2007. doi:10.1126/science.1141483.
- [25] Lopes T., Kucernak A., Malko D., Ticianelli E.A. Mechanistic Insights into the Oxygen Reduction Reaction on Metal–N–C Electrocatalysts under Fuel Cell Conditions. *ChemElectroChem*, 3(10), 1580–1590, October 2016. doi:10.1002/celec.201600354.
- [26] Choi J.Y., Hsu R.S., Chen Z. Highly Active Porous Carbon-Supported Nonprecious MetalN Electrocatalyst for Oxygen Reduction Reaction in PEM Fuel Cells. *The Journal of Physical Chemistry C*, 114(17), 8048–8053, May 2010. doi:10.1021/jp910138x.
- [27] Fei H., Dong J., Arellano-Jimnez M.J., Ye G., Dong Kim N., et al. Atomic cobalt on nitrogen-doped graphene for hydrogen generation. *Nature Communications*, 6, 8668, October 2015. doi:10.1038/ncomms9668.
- [28] Hashimoto T., Baldwin J.E., Basolo F., Dyer R.L., Crossley M.J. Ligand, Oxygen, and Carbon Monoxide Affinities of iron(II) Modified "capped" porphyrins. *Journal of the American Chemical Society*, 104(8), 2101–2109, April 1982. doi:10.1021/ja00372a003.
- [29] Hayashi T., Dejima H., Matsuo T., Sato H., Murata D., et al. Blue Myoglobin Reconstituted with an Iron Porphycene Shows Extremely High Oxygen Affinity. *Journal of the American Chemical Society*, 124(38), 11,226–11,227, September 2002. doi:10.1021/ja0265052.
- [30] Lefèvre M., Dodelet J.P., Bertrand P. O<sub>2</sub> Reduction in PEM Fuel Cells: Activity and Active Site Structural Information for Catalysts Obtained by the Pyrolysis at High Temperature of Fe Precursors. *The Journal of Physical Chemistry B*, 104(47), 11,238–11,247, November 2000. doi:10.1021/jp002444n.
- [31] Lefèvre M., Dodelet J.P., Bertrand P. Molecular Oxygen Reduction in PEM Fuel Cells: Evidence for the Simultaneous Presence of Two Active Sites in Fe-Based Catalysts. *The Journal of Physical Chemistry B*, 106(34), 8705–8713, August 2002.



doi:10.1021/jp020267f.

*The epoxidation reaction of alkenes catalysed by M-N/C materials was investigated in order to gain further insight into the active site. It was found that the Fe-N/C catalyst is capable of epoxidising even difficult alkenes such as 1-hexene, utilising molecular oxygen and a coreductant under ambient conditions. The reaction conditions are similar to those found for metal macrocyclic complexes and the catalyst performs significantly better than free Fe ions. This is an indication of a metal centred active site, where the activity is increased by the chemical environment. The oxygen uptake and the potential of the reaction mixture were measured and both values are correlated. The TON and TOF are exceptionally high. A further study of this system might enable fundamental insight into the catalytic activity and provide a robust heterogeneous catalyst for the industrially important mild epoxidation of alkenes with molecular oxygen. A new kind of "heteroelectrochemical" mechanism involving electron transfer between active sites is proposed.*

## Chapter 7

# M-N/C materials as catalysts for alkene epoxidation

### 7.1 Introduction

In 4.2.3 it has been shown that the active site of the **Fe-N/C** catalyst can be addressed via organic chemical reactions. It has also been shown via gas sorption and TPD ( 4.4.4) that the catalyst apparently activates molecular oxygen to provide a strong oxidant. This was inferred from the observed self-oxidation of the carbon structure to CO<sub>2</sub> at relatively low temperatures (<90 °C), subsequent to O<sub>2</sub> exposure. Furthermore in chapters 5 and 6

it has been shown that one type of active sites within the **Fe-N/C** material interact with nitrite and nitric oxide in a similar pattern as iron macrocyclic complexes.

Based on these previous observations the approach in this chapter is to provide further evidence for metal centred activity by using M-N/C materials as catalysts for organic reactions.

The epoxidation reaction of alkenes has been chosen, for the following reasons:

- (i) It can be achieved through reaction with molecular oxygen, if a suitable catalyst is present.
- (ii) It has a sophisticated mechanism, which could help to gather further information on the active site by varying the reaction conditions and understanding the mechanism.
- (iii) It can be catalysed by transition metal macrocyclic complexes and iron containing enzymes.
- (iv) The mechanism of epoxidation with macrocyclic complexes has been well studied.
- (v) The epoxidation is an important industrial reaction.

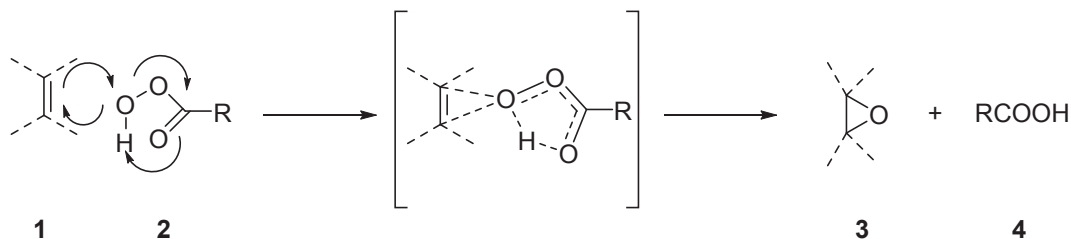
Therefore a robust catalyst which enables the replacement of harsh reaction conditions and oxidants with the use of oxygen under mild conditions would be highly desirable. [1]

### 7.1.1 Epoxidation reactions

*An extensive review of the epoxidation reaction is outside the scope of this work and the reader is referred to the respective literature instead.*

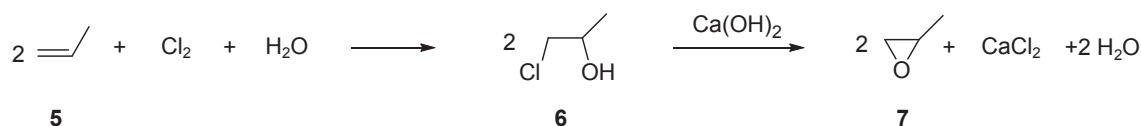
Epoxides are important chemical intermediates for bulk chemical synthesis as well as fine chemicals and pharmaceuticals. This is because the epoxy group is a reactive moiety that makes a wide range of functionalities accessible upon reaction with various nucleophiles or through rearrangements. [1] The largest quantity bulk chemicals produced through olefin epoxidation are ethylene oxide (~15 million t/year) and propylene oxide (~7.5 million t/year). [2, 3]

Traditional routes to epoxides involve the reaction of alkenes with an oxidising agent, capable of transferring one oxygen atom to the olefin. [1] The *Prilezhaev* reaction shown in Scheme 7.1 is the most widely used method. [1] It involves the reaction of an alkene

SCHEME 7.1: Accepted mechanism for *Prilezhaev* reaction to form an epoxide. [1]

(1) with a peracid (2), to give the epoxide (3) and the carboxylic acid (4). Reaction conditions such as solvent, electronic effects of the alkene and the peracid and acid content of the reaction mixture play an important role in determining the yield and selectivity of the reaction. [1] This epoxidation is stereospecific, meaning *cis* and *trans* olefins give *cis* and *trans* epoxides, respectively. [1] Another prominent oxidant for epoxidations are hydroperoxides, *e.g.* *tert*-butyl hydroperoxide. [1]

On an industrial scale the use of an expensive oxidant is not viable because of high costs and poor atom economy. [1, 4] Traditionally, for the large scale production of ethylene oxide, oxygen is reacted with ethylene over a silver catalyst. However, the reaction requires elevated temperature and pressure (*i.e.* 250 °C and 1.5 MPa) with significant over-oxidation reactions, depressing the yield. [2]



SCHEME 7.2: General reactions in the chlorohydrin process. [4]

An alternative approach is shown in Scheme 7.2, for the production of propylene-oxide via the chlorohydrin process was developed, where the alkene (5) is reacted with chlorine and water in a complex reaction setup to give the chlorohydrin (6), which is then reacted with a base to obtain the epoxide (7). [3, 4] It can easily be seen that this process involves the stoichiometric use of chlorine which significantly increases costs and the environmental footprint. [4] In practice a 9:1 mixture of  $\alpha$ - and  $\beta$ -chlorohydrin will be produced, which both give the same propylene-oxide. [4]

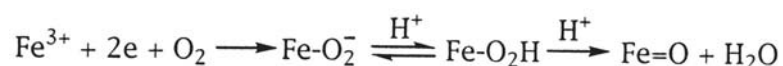
Recently the HPPO process was developed for the production of propylene-oxide via oxidation of propylene with hydrogen peroxide. A titanium silicalite-1 (TS-1) catalyst is utilised and allows the use of mild conditions (*e.g.* 40 °C and 1 atm). [4] Although cheaper and environmentally more benign, hydrogen peroxide as oxidant is still necessary and has

to be synthesised, adding to the cost of the process. The large scale implementation of this process underlines the interest into sustainable methods to generate epoxides.

The use of molecular oxygen under mild conditions with high selectivity would be the ideal case. However, this is challenging, as the O<sub>2</sub> molecule has to be activated to selectively produce the epoxide. To achieve this biomimetic catalysts could be used.

### 7.1.2 Epoxidations with transition metal macrocycles

For enzymatic systems, such as cytochromes, it is known that those possess impressive oxygen activation capabilities. [5, 6]



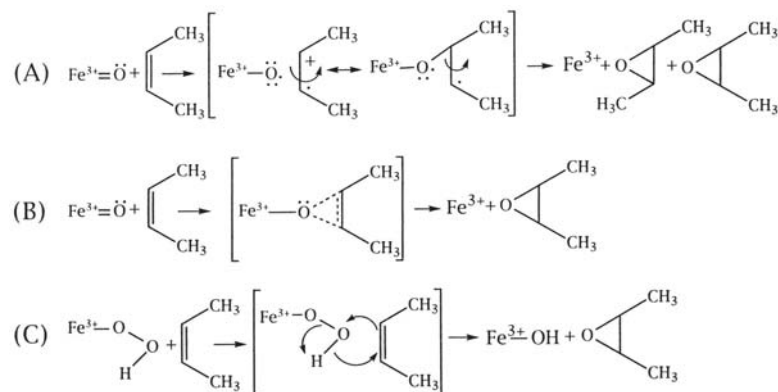
SCHEME 7.3: Scheme showing steps in oxygen activation by P450 involving electron and proton uptake, where Fe represents the heme iron atom. [Taken with permission from Ref. [6]]

As discussed in Chapter 1 and shown in Scheme 7.3 cytochrome is capable of activating oxygen to produce a Fe=O species which can be a strong oxidant. [5, 6] For epoxidation reactions, the selectivity of the catalyst is crucial as well. It has been shown that cytochromes are capable of selectively catalysing the epoxidation reaction. [6]

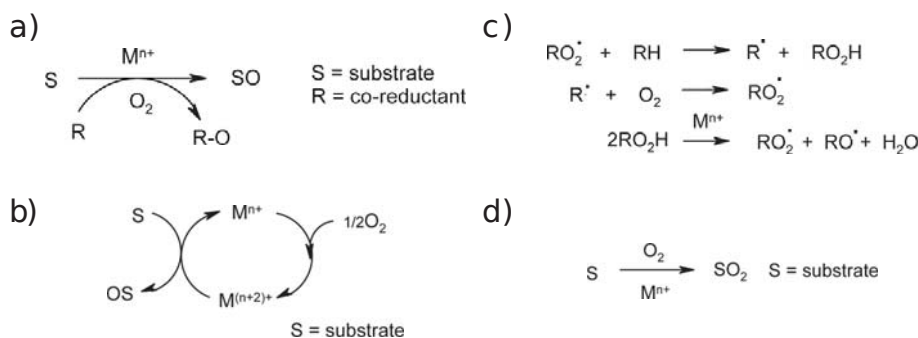
As can be seen in Figure 7.4 various mechanisms of oxygen transfer have been proposed. [6] The drawback of enzymatic systems is their lack of stability and their dependence on narrow reaction conditions. This makes their production expensive and infeasible for practical applications. Nevertheless, those studies are not only useful to gain insight into fundamental mechanisms of enzyme functions, but can potentially provide clues on how a metal center would behave if it was the active site in Fe-N/C catalysts.

Metal macrocyclic complexes, such as iron manganese and cobalt porphyrins, have also been reported to activate O<sub>2</sub> for oxidation and epoxidation reactions. [7]

The general mechanisms found for the oxidation via transition metal catalysts are shown in Figure 7.5. [7] The mechanism mimicking monooxygenase enzymes (to which the cytochromes belong) relies on a coreductant, where one oxygen atom is transferred to the

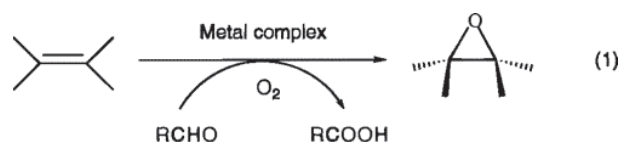


SCHEME 7.4: Mechanisms of olefin epoxidation (A) by oxenoid-iron involving a charge-transfer complex and leading to epimerization, (B) by oxenoid-iron leading to a concerted insertion of oxygen, and (C) by hydroperoxo-iron in a concerted reaction. [Taken with permission from Ref. [6]]



SCHEME 7.5: (a) Oxidation based on the model of monooxygenase. (b) Free radical oxidation. (c) Oxidation of a coordinated substrate by a metal ion. (d) Oxidation mimicking dioxygenase. [Adapted with permission from Ref. [7]. Copyright 2005 American Chemical Society.]

substrate while the second is transferred to the coreductant to regenerate the catalyst (Figure 7.5 (a)) or reduced to water with a concurrent electron and proton transfer. [8] The reaction may be radical in nature. [7] The contribution of the metal center might be at different points within the mechanism and is discussed in more detail later (see 7.2.8). [7, 9, 10] The free radical mechanism involves the formation of some sort of radical chain reaction, where various scenarios of metal contribution can be possible (Figure 7.5 (b)). [7] The main contribution of the metal centre is the formation of free radicals. The oxidation can also proceed via a coordinated substrate (Figure 7.5 (c)) or via transfer of both oxygen atoms to the substrate by mimicking dioxygenase enzymes (Figure 7.5 (d)). [7]



SCHEME 7.6: Reaction of alkene with oxygen to give an epoxide with concomitant oxidation of isobutyraldehyde as coreductant. A transition metal complex is added as catalyst. [Reprinted with permission from Ref. [9]. Copyright 1996 American Chemical Society.]

For the epoxidation reaction in this work, the coreductant method mimicking the monooxygenase model has been studied. This was inspired by the capability of transition metal macrocyclic complexes to promote the epoxidation, utilising oxygen at room temperature and pressure, with the addition of an aldehyde as coreductant. [6, 9–17] In a typical reaction, as depicted in Scheme 7.6, the metal complex is dissolved in an aprotic solvent (*e.g.* acetonitrile or dichloromethane) and oxygen is supplied, either through bubbling or via a reservoir, blanketing the reaction mixture. [6, 9–17] The alkene and the coreductant (*e.g.* isobutyraldehyde) are added and the mixture is stirred at room temperature for a certain amount of time. [6, 9–17] Usually an excess of aldehyde is added which is oxidised to the carboxylic acid during the course of the reaction. [6, 9–17] Remarkably, in the presence of a metal complexes, such as iron porphyrins derivatives, the reaction proceeds with high selectivity towards the epoxide at room temperature and pressure. [6, 9–17]

The benefit of using the here developed M-N/C materials for the reaction instead of the typically used metal complexes would be,

- (i) lower cost, as the ligands need costly synthesis procedures;
- (ii) higher stability;
- (iii) easy recyclability, due to the heterogeneous nature.

Although this reaction system might seem attractive, it is not so feasible for large scale production at the moment, as it consumes an excess of coreductant. However, investigation of this system might lead to the discovery of either reversible coreductants or the cogeneration of valuable products from a suitable coreductant thus making the material more attractive for these reactions.

### 7.1.3 Information to be gained for the active site

Additionally to the potentially useful nature as a heterogeneous oxidation catalyst, the main focus within the scope of this work is to gather evidence on the behaviour of the active site. Finding a complex reaction system which interacts with the catalyst might enable this insight. The notion within this chapter is to find interpretable trends and to develop a methodology which might be useful for the study of M-N/C materials via organic reactions. Although reports exist of the use of M-N/C materials as oxidation catalysts, such as alcohol oxidation and dehydrogenation, no attempts were made to utilise these reaction in order to provide further insight into the active centre. [18–20]

It has been found that the M-N/C catalysts developed here catalyse the coreductant dependent epoxidation reaction in the same way as metal macrocyclic complexes do. The reaction proceeds with high recyclability of the catalyst, high turnover number (TON), apparent turnover frequency (TOF), yield and selectivity. This might be further evidence for a metal centred activity. Various substrates have been analysed and a method was developed to track the apparent rate of reaction. The potential of the reaction mixture was tracked and coincides with the rate of oxygen uptake. A mechanistic proposal is given. The here developed method might be a useful starting point to investigate a hitherto unexplored field with potentially fundamental insight and practical use in heterogeneous catalysis.

## 7.2 Results and Discussion

### 7.2.1 M-N/C catalyst for ORR and epoxidation of cyclohexene

The materials **Fe-N/C**, **Co-N/C** and **N/C** were investigated as catalysts for the epoxidation reaction. The synthesis and characterisation of the materials is described in Chapter 3.

In order to allow for a possible correlation of oxygen reduction to epoxidation capability of the materials, the RDE measurements in oxygen saturated 0.5 M H<sub>2</sub>SO<sub>4</sub> are shown in Figure 7.1 (a). The order of activity is **Fe-N/C** > **Co-N/C** > **N/C**. The epoxidation reaction was conducted in order to determine if the catalyst may chemically behave in the haem-like manner hypothesised and for which evidence was provided in chapters 5 and 6.



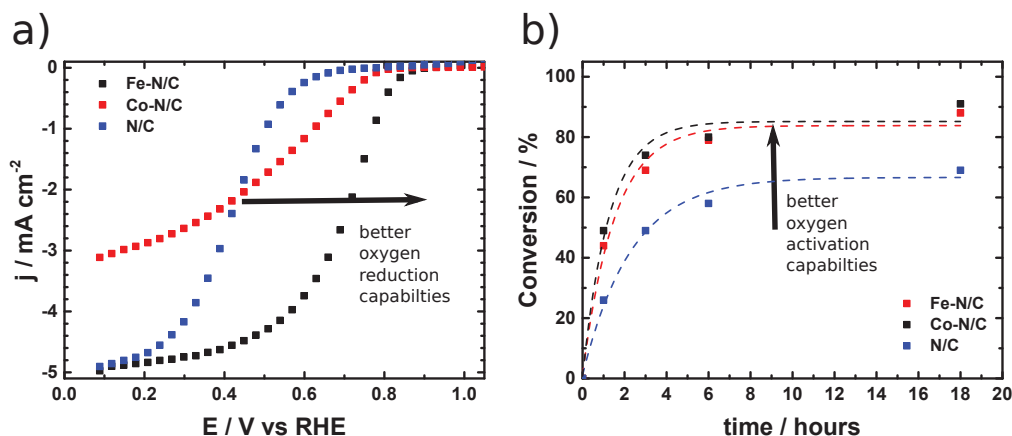
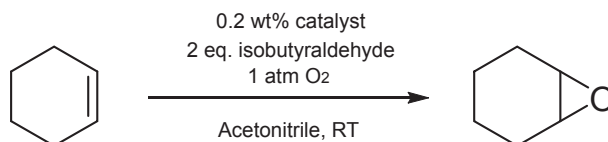


FIGURE 7.1: (a) Steady-state RDE measurements in 0.5 M H<sub>2</sub>SO<sub>4</sub>, rotating speed: 1600 rpm, 30 s hold, 30 mV step potential, catalyst loading: 750 μg cm<sup>-2</sup>, O<sub>2</sub>-saturated at 1 atm. (b) Conversion of cyclohexene in epoxidation reaction with different M-N/C catalyst over time, as determined by GC. 2 eq of isobutyraldehyde and 0.2 wt% catalyst to cyclohexene, 1 atm O<sub>2</sub>.



SCHEME 7.7: Epoxidation of cyclohexene to cyclohexene-oxide.

The reaction conditions were chosen as those reported to work for metal macrocyclic complexes. The reaction as shown in Scheme 7.7 was carried out in acetonitrile, where the respective amount of catalyst was ultrasonically dispersed before addition of a 2:1 molar ratio of isobutyraldehyde as the coreductant and cyclohexene as the substrate. Oxygen was then administered through a septum by a syringe to which a balloon was attached. The progress of the reaction was analysed after various time periods, by removal of an aliquot from the reaction mixture and analysis via gas chromatography (GC). The conversion of cyclohexene, the yield of cyclohexene-oxide and selectivity of the reaction towards the epoxide were determined. Figure 7.1 (b) shows the conversion of cyclohexene within the reaction mixture over time. It can be seen that a higher conversion is achieved for the metal containing catalysts. The trend is **Fe-N/C**  $\approx$  **Co-N/C**  $\gg$  **N/C**.

Table 7.1 shows the conversion, yield and selectivity of the different catalysts, together with control experiments where i) the aldehyde ii) the catalyst or iii) oxygen were excluded, after 6 h, analogous to the conditions described above. It can be seen that in the absence of catalyst there is still a small amount of product, however with a poor selectivity. This demonstrates that the addition of a catalyst indeed has an accelerating effect on the reaction while also increasing the selectivity towards the epoxide. When the aldehyde

TABLE 7.1: Epoxidation of cyclohexene with different metal centres and metal free catalyst. 2 eq of isobutyraldehyde and 0.2 wt% catalyst to cyclohexene, 1 atm O<sub>2</sub>. Values after 6 h at room temperature as determined by GC.

Entry	Catalyst	Conversion [%]	Yield [%]	Selectivity [%]
1	Fe-N/C	80	70	87
2	Co-N/C	79	59	74
3	N/C	58	40	69
4	no catalyst	16	4.8	30
5	no aldehyde*	0	0	0
6	no oxygen*	0	0	0

\* Fe-N/C catalyst.

was omitted, there is was reaction. This is the exact same pattern as seen for iron porphyrins. [9] When the reaction was blanketed with nitrogen, no reaction took place. This confirms that oxygen is indeed the terminal oxidant. It can further be seen that the yield and selectivity towards the epoxide follows the trend **Fe-N/C** > **Co-N/C** > **N/C**  $\gg$  **no catalyst**. The residual activity of the **N/C** catalyst might either stem from the residual metal content of (60 ppm) or from the metal free active sites. The metric for performance in the epoxidation is a higher yield with a higher selectivity in a shorter time. The metric for performance for the electrocatalytic ORR is a higher current at higher potential. Therefore a correlation between electrochemical and chemical activity might be present.

The TON would be at least 50000 for the **Fe-N/C** catalyst, if the majority of iron as determined by TXRF present in this catalyst serves as the active site.<sup>1</sup> However, as shown in Chapter 6, only 4.5% of the 1.5 wt% iron detected by TXRF is actually present in one type of ORR active site. This means the TON could be as high as 1000000. This is speculative however, as it is not clear if the metal centre actually is the active site, since the catalyst with a significantly lower metal content still exhibits a relatively high apparent TOF, therefore assumptions in this chapter are put at 1 wt% active iron in the catalyst. If the iron centre was the active site, the **N/C** catalyst would have a TON with respect to the catalyst of around 5000000. Metal free active sites, *e.g.* nitrogen embedded into the carbon framework, might be contributing to the epoxidation activity. It is accepted

<sup>1</sup>The value was determined by calculating the amount of Fe in the reaction flask, assuming 1 wt% active iron in the catalyst. The molar ratio of converted cyclohexene to Fe is the the TON. Note: In this study 1 wt% iron was assumed to be active, assuming some of the 1.5 wt% iron detected by TXRF, is buried within the structure and thus inactive. Although in Chapter 6 it has been found that only 4.5% of the iron in the sample contributes to the majority of the ORR activity, *i.e.*  $\sim 0.07$  wt%, it is not known how strongly these active sites are correlated. The higher assumption made here shall prevent overestimation of the TON and TOF.



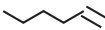
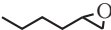
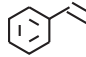
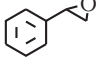
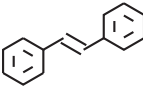
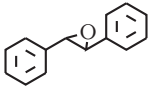
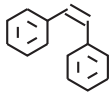
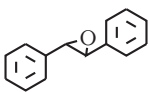
that metal free nitrogen doped carbon is active towards electrochemical oxygen reduction in alkaline medium. Therefore an oxygen activation through the "alkaline" mechanism might be possible (see 4.2.5.1 for details on the different mechanisms). In fact, the reaction conditions, *i.e.* low proton concentration, might favour this route.

Although the reaction conditions are different to the acidic electrolyte used for the ORR, *e.g.* nonprotic *versus* protic, the initial results encouraged further analysis of this system, due to the importance of the epoxidation reaction.

## 7.2.2 Epoxidation of different substrates with the Fe-N/C catalyst

It is known that cyclohexene undergoes a more facile epoxidation reaction than other alkenes. [1] To test whether the catalyst is also active towards other olefins that are harder to epoxidise, the **Fe-N/C** catalyst was used with other substrates. [1] The amount of catalyst was increased for these experiments.

TABLE 7.2: Epoxidation of different alkenes with Fe-N/C catalyst. Substrate:Fe molar ratio 3000:1, assuming 1 wt% active Fe in the Fe-N/C catalyst. 2 eq of isobutyraldehyde to alkene, 1atm O<sub>2</sub>, room temperature. Values as determined by GC.

Entry	Alkene	Epoxide	Conversion [%]	Yield [%]	Selectivity [%]	time [h]
1			99	91	91	6
2			72	27	38	7
3			70	12	17	7
4			78	52	67	17
5			79	76*	96	17

\* of which *trans*-stilbene:*cis*-stilbene ~9:1.

Table 7.2 shows the respective substrates with conversion, yield and selectivity. It can be seen that for cyclohexene excellent values are achieved under these conditions. The values for the conversion of the other alkenes was significant as well. The poor yield of styrene at the high conversion rate points to some kind of side reaction occurring. Possibly the polymerisation to polystyrene, which is a facile reaction and the reason for

the addition of inhibitors to the product. No other significant product was observed in the gas chromatogram that could explain the consumption of styrene. Therefore, a side-product such as polystyrene, might be precipitated. Due to the presence of the catalyst it was not possible to determine whether a precipitate actually formed. The same applies for the discrepancy of 1-hexene conversion and yield. It has to be pointed out that linear alkenes are notoriously difficult to epoxidise and the fact that even 1-hexene-oxide was obtained under these mild conditions is remarkable. [1] Interestingly, comparing the reaction of *cis*-stilbene to *trans*-stilbene shows an intriguing difference. While *cis*-stilbene is converted to its epoxide with excellent selectivity and conversion, the *trans*-stereomere has a significantly lower yield and selectivity. The *cis*-stilbene is predominately converted to the *trans*-epoxide, while the *trans*-stilbene is also converted to the *trans*-epoxide. This stereospecificity is the same as observed for iron porphyrins and a radical mechanism was suggested. [9] In any case, a concerted oxygen transfer process is excluded by this conformation.

### 7.2.3 Recyclability of Fe-N/C catalyst

One possible mechanism would be that Fe ions were leached out of the catalyst into the solution, where they act as homogeneous catalysts and that the material itself is not a heterogeneous catalyst. Recycling experiments, where the catalyst was recovered after each reaction and then reused where conducted. A Substrate:Fe ratio of 3000:1 as in 7.2.2 with the cyclohexene epoxidation was used.

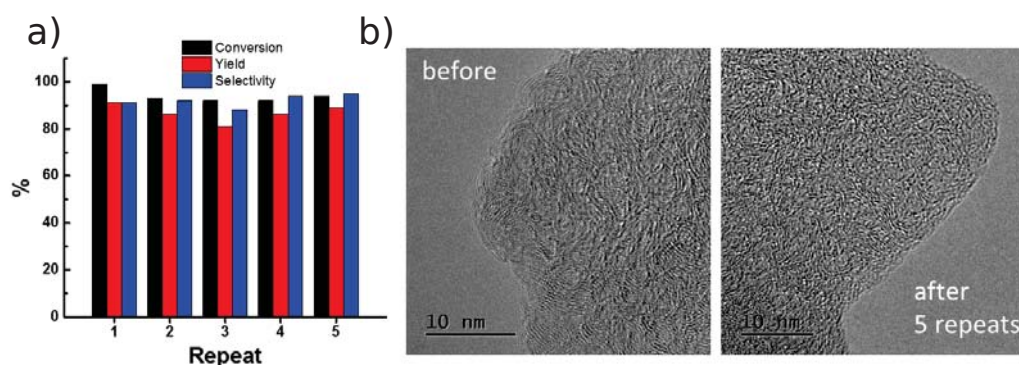


FIGURE 7.2: (a) Conversion, yield and selectivity of the Fe-N/C catalyst towards cyclohexene epoxidation, when reusing the catalyst multiple times. (b) TEM image of unused Fe-N/C catalyst and after 5 repeats.

In Figure 7.2 (a) it can be seen that conversion, yield and selectivity are constant when recycling the Fe-N/C catalyst for 5 times. This indicates that the material is stable for

reuse and does not lose its activity after the initial reaction. Figure 7.2 (b) shows that no structural change is discernible in the TEM images.

#### 7.2.4 Oxygen uptake measurements - estimation of reaction rate

In order to estimate the TOF, an oxygen uptake measurement was performed.

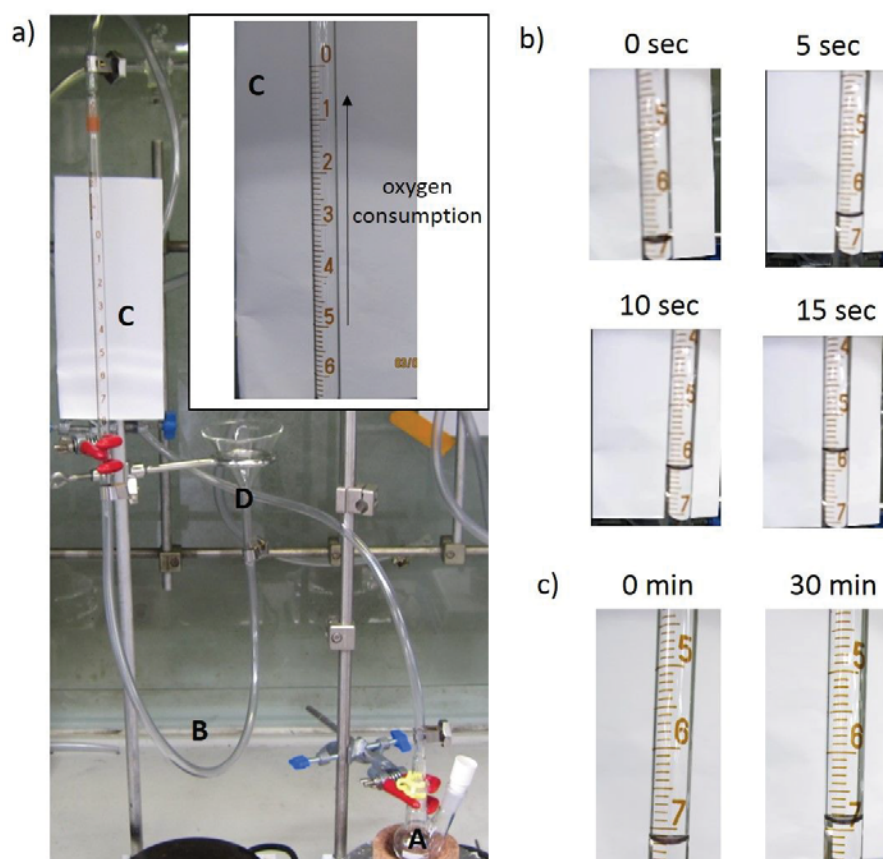


FIGURE 7.3: (a) Set-up used to measure oxygen uptake. (b) oxygen uptake measurement for the Fe-N/C catalyst and (c) without catalyst during the epoxidation reaction. Stirring rate: 1400 rpm, 30 mg catalyst, 1 mL cyclohexene and 1 mL isobutyraldehyde in 25 mL acetonitrile.

The set-up is shown in Figure 7.3 (a). The reaction flask (A), containing the Fe-N/C catalyst and acetonitrile solvent was sealed and connected via tubing to a pipette (C), which served as a measuring device. The pipette was then connected via a second tubing (B) to a funnel (D), such that the level of the funnel approximately matched the bottom of the pipette. The funnel was filled with water until the water level penetrated into the pipette. The head-space and the reaction mixture were saturated with oxygen. Then a 1:1 volume mixture of aldehyde and olefin was injected via a syringe through the septum at the reaction flask. Due to the set-up of the device, once oxygen consumption starts,

the water level in the pipette rises, therefore allowing determination of the oxygen uptake. After an initiation time of approximately 5 minutes, following injection of substrate and reductant, the system started rapid oxygen uptake. The rate was dependent on the stirring speed. This indicates some kind of diffusion control during the reaction. Figure 7.3 (b) shows the level of water progressing at different times, from which the reaction rate could be roughly determined. The rate of oxygen uptake was surprisingly rapid. When no catalyst was added, no significant oxygen uptake was observed as shown in Figure 7.3 (c). This clearly demonstrates the significant catalytic activity of the catalyst. The TOF was estimated to be  $\sim 10$  per Fe site per second at a stirring rate of 1400 rpm, when 1 wt% Fe was assumed as active.<sup>2</sup> This is unusually high in terms of heterogeneous catalysis, where typical TOFs of  $1 \text{ site}^{-1} \text{ s}^{-1}$  are considered high. [21] The underlying catalytic mechanism might therefore be different to one active site where the complete reaction cycle takes place.

### 7.2.5 Measuring the potential of the reaction mixture

In order to gain further insight, the potential of the reaction mixture was measured, before and after addition of the reactants.

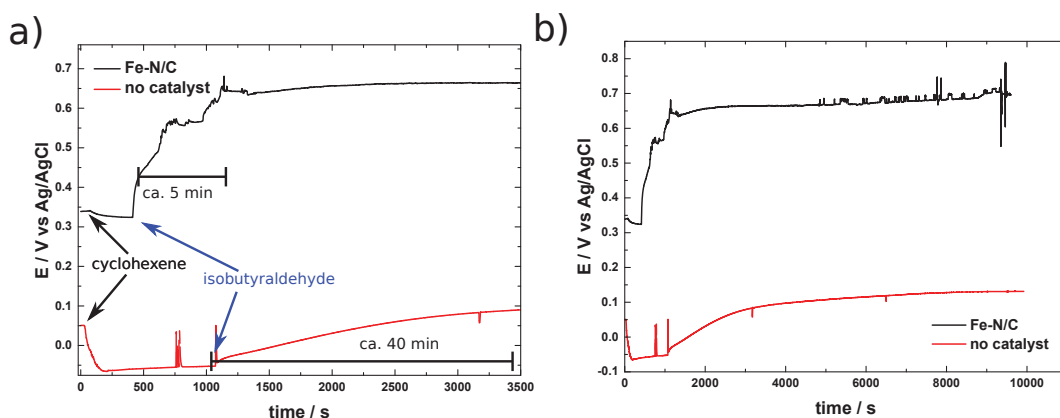


FIGURE 7.4: Potential of reaction mixture measured over time before and after addition of reactants cyclohexene and isobutyraldehyde to the solvent containing either the **Fe-N/C** catalyst or no catalyst. (a) Starting period. (b) Full time scale. Solvent: Acetonitrile +  $0.1 \text{ mM } (t\text{-Bu})_4\text{NBF}_4$

The reaction flask was filled with the acetonitrile solvent and the catalyst with the addition of  $0.1 \text{ mM } (t\text{-Bu})_4\text{NBF}_4$  to provide the necessary conductivity. The potential of carbon

<sup>2</sup>The TOF was estimated, by estimating the number of oxygen molecules reacting per iron site per second. Standard conditions for the molar volume were used to convert the volume of oxygen consumed to molecules.

fibres, as working electrode in the solution *versus* a leak free Ag/AgCl reference electrode was monitored over time as shown in Figure 7.4. First cyclohexene was added and it can be seen that the potential slightly decreased (Figure 7.4 (a)). Then, after the potential stabilised, isobutyraldehyde was added. Surprisingly, the potential began to slowly rise significantly. It can be seen in Figure 7.4 (b) that the potential steadily rises over the course of approximately 5 minutes by  $\sim 300$  mV, and then flattens off and stays constant for over 2 h. The experiment was also repeated without the catalyst. It can be seen that the potential is significantly lower (50 mV *vs.* 340 mV with catalyst). The potential also drops to a lower level when adding cyclohexene (-70 mV *vs.* 320 mV with catalyst) and the potential rises to a significantly lower level after addition of isobutyraldehyde (125 mV *vs.* 680 mV with catalyst). Curiously, the initiation time of  $\sim 5$  minutes found before oxygen uptake started, coincided with the time it took for the potential to rise to its plateau level. It can also be seen that the potential rise is slower in the measurement without the catalyst (5 min. *vs.* 40 min.). The clear effect of the catalyst on the potential of the reaction mixture and the timing of oxygen uptake and potential rise indicate a correlation of potential and rate of reaction. To investigate this further, more sophisticated set-up was constructed with the help of a Masters student to measure potential and oxygen uptake simultaneously. [22] Some results which support this study shall be summarised in the following.

### 7.2.6 Correlating the potential with oxygen consumption

In order to measure the oxygen flow rate more accurately a mass flow meter was used and the potential was monitored in the same set-up as the oxygen uptake. The set-up is shown in Figure 7.5. More details can be found in Ref. [22].

Figure 7.6 shows the potential of the reaction together with the oxygen consumption. This experiment and further experiments conducted with different substrates show a correlation of oxygen uptake and potential of the reaction mixture. [22]

### 7.2.7 Comparison of Fe-N/C catalyst to free Fe ions

Schröder *et al.* [23] reported the epoxidation of stilbene, styrene and derivatives with a system of iron chloride, imidazole ligands, and ethyl 2-oxocyclohexanecarboxylate as

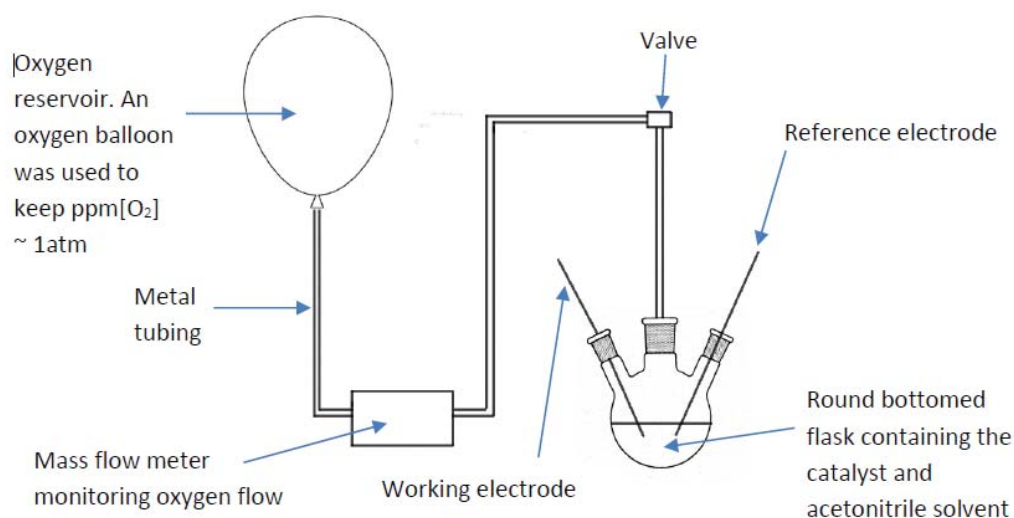


FIGURE 7.5: Set-up used to study the rate of oxygen uptake at the same time as the electrochemical potential. [Taken from Ref. [22]]

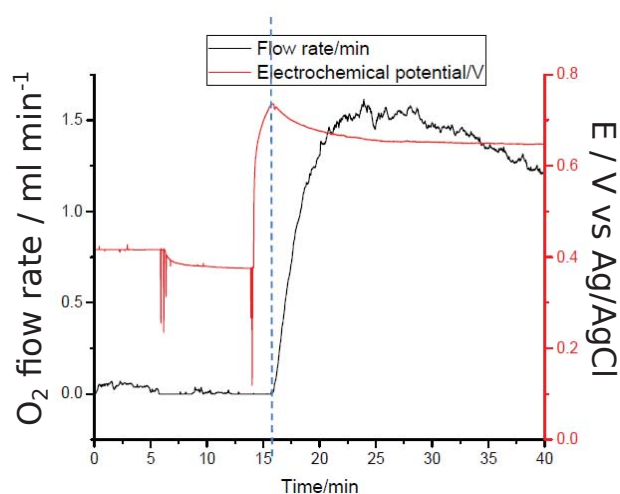


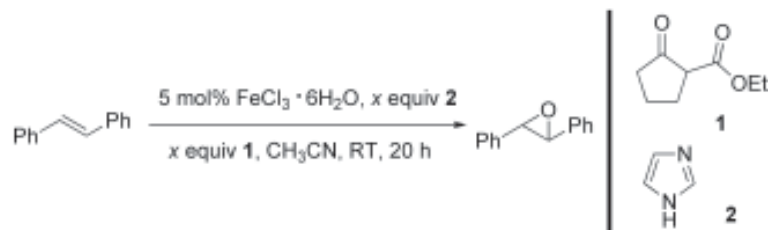
FIGURE 7.6: Correlation of oxygen flow rate to the electrochemical potential during the epoxidation reaction. Addition of cyclohexene at 6 minutes and isobutyraldehyde at 14 minutes. [Taken from Ref. [22]]

shown in Scheme 7.8.

As proposed by the authors the complexation of iron with the imidazole and carboxylate additives might be an important factor in creating an active catalyst. [23]

In order to exclude that the **Fe-N/C** catalyst is merely a source of free iron(III), an experiment was conducted where the epoxidation as described in 7.2.2 was performed with  $\text{FeCl}_3 \cdot \text{H}_2\text{O}$  instead of the **Fe-N/C** material. Air was used as the oxidant rather than oxygen and the amount of catalysts was chosen to contain the same amount of iron, where 1 wt% active iron was assumed for the **Fe-N/C** catalyst. [22]





SCHEME 7.8: Iron-catalyzed epoxidation of stilbene with air. [Taken with permission from Ref. [23]]

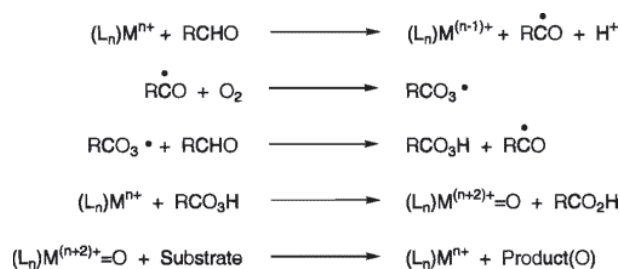
TABLE 7.3: Epoxidation of cyclohexene comparing Fe-N/C catalyst to  $\text{FeCl}_3 \cdot 6\text{H}_2\text{O}$ . 2 eq of isobutyraldehyde and 5 mol% Fe to cyclohexene, 1 atm air. Values after 24 h at room temperature as determined by GC. [data taken from Ref. [22]]

Entry	Catalyst	Conversion [%]	Yield [%]	Selectivity [%]
1	Fe-N/C	23	18	77
2	$\text{FeCl}_3 \cdot 6\text{H}_2\text{O}$	50	0	0

The results are shown in Table 7.3. It can be seen that due to using air rather than oxygen, the conversion with the **Fe-N/C** catalyst was lower compared to when pure oxygen was used with this catalyst (see Table 7.2). However, the selectivity was still high. For  $\text{FeCl}_3 \cdot 6\text{H}_2\text{O}$  there was alkene consumption, but no epoxide was formed. This indicates that free Fe ions are not capable of catalysing the epoxidation in this system and some sort of ligation of the central metal ion is needed to create an active catalyst. It further suggests that if iron is the active site in this reaction, the chemical environment is an important factor in governing its activity. This is an indication of direct involvement of an active site within the **Fe-N/C** catalyst in the cycle.

### 7.2.8 Mechanistic considerations

Due to the complex mixture of reagents, a complicated mechanism seems to be present. Even for well-defined iron complexes it is not clear what the metal contribution is.



SCHEME 7.9: Mechanism proposed in Ref. [9] for the epoxidation of alkene with  $\text{O}_2$  and aldehyde, catalysed by metal complexes. [Reprinted with permission from Ref. [9].

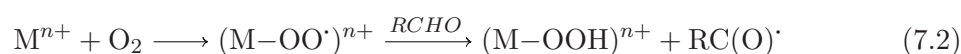
Copyright 1996 American Chemical Society.]

Figure 7.9 shows a mechanism which was often proposed for this type of reaction with transition metal complexes. [9] Within this mechanism the metal centre serves two roles; i) it oxidises the aldehyde to produce a radical species and a proton. ii) it reacts with the peroxy-radical which is formed by the reaction of the aldehyde-radical with oxygen. The resulting metal-oxo species can then epoxidise the olefin to regenerate the metal. [9] However, Nam *et al.* came to the conclusion that a metal-oxo species is not a prerequisite to form an epoxide, as it has been found that the acyl-peroxy radical is capable of epoxidising the olefin on its own, be it with lower overall efficiency. [9] A further possible active species which was proposed is a complex of the acyl-peroxy compound with the metal. This was inferred as it is known that peroxy compounds such as metaliodosylbenzene complex, metalhydroperoxide, metalalkylperoxide, and metalperoxyacid can react to form epoxides. [9] Interestingly, the investigation of *cis*-stilbene resulted in the same preference for the *trans*-epoxide as found with the **Fe-N/C** catalyst presented here (see 7.2.2).

As for the generation of the acyl radical, two possible scenarios were suggested; i) the metal ion itself catalyses the oxidation of the aldehyde to form the radical as shown in Equation 7.1. [9]

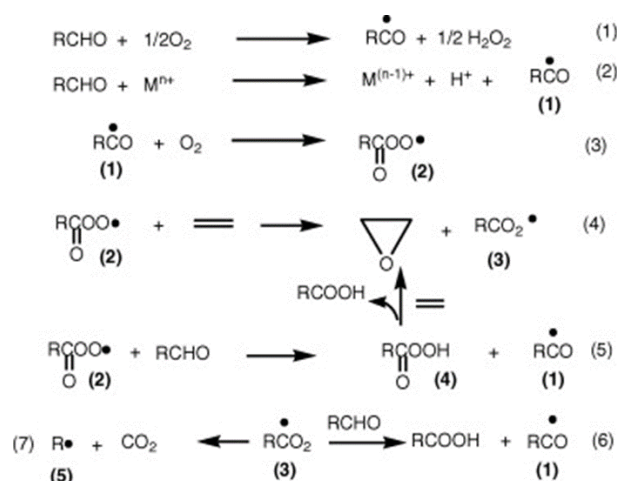


or ii) the metal reacts with oxygen to form a superoxide radical, which then abstracts a hydrogen atom from the aldehyde to form the peroxy species as shown in Equation 7.2. [9]



Another model put forward by Serra *et al.* proposes that the metal centre is not involved at all in the oxygen transfer. [10] The mechanism is shown in Figure 7.10. [10] The study concludes due to the observation that simple metal salts, such as  $Mn(OAc)_2$  can catalyse the reaction as well. [10] It was proposed that the main oxidising species are percarboxylic acid and acyl-peroxy radical. Once the initiation of the radical chain reaction starts, it will be propagated by various steps in the mechanism. [10]

However, although the addition of a metal salt was capable of forming the epoxide in this study, an induction time of several hours was observed. [10] This is in stark contrast



SCHEME 7.10: Mechanism proposed for the epoxidation of alkene with  $\text{O}_2$  and aldehyde, catalysed by metal salts. [Taken with permission from Ref. [10]]

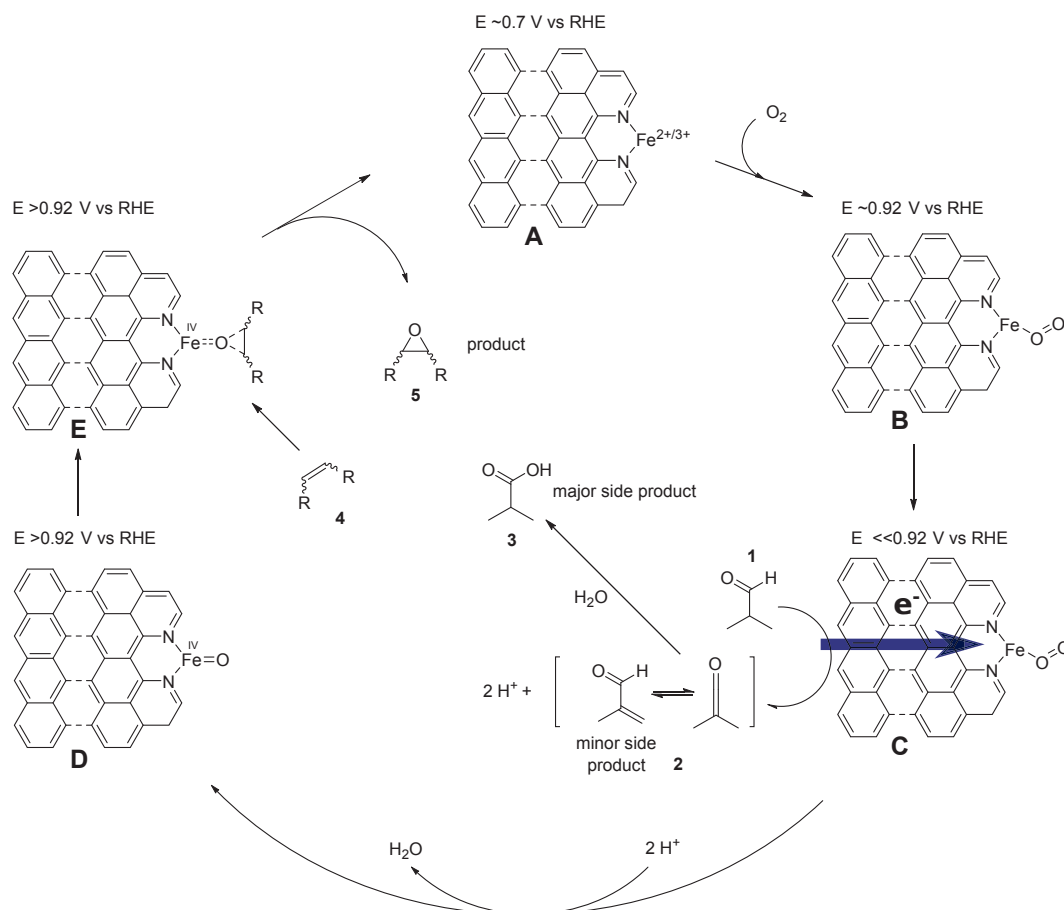
with the induction time found with the **Fe-N/C** catalyst which was between 5 - 10 minutes. This suggests that either the heterogeneous catalyst is significantly more efficient in forming the radical species than the metal salt or a different mechanism is present.

A combination of all the proposed mechanisms is possible as well. In Ref. [22] it was found that the aldehyde alone will react with a high rate to the carboxylic acid without the addition of the alkene. Therefore, this radical oxidation of the aldehyde is a major side reaction. The observed increase in potential might arise due to the formation of a large amount of peroxy species.

Nevertheless, a direct metal involvement in the mechanism is plausible. The presence of an induction time is curious. The fact that the **Fe-N/C** catalyst behaves exactly the same as metal porphyrins under these conditions is intriguing and points to a similar mechanism. This high apparent TOF for a heterogeneous material and a correlation of the reaction with the potential is striking.

Unlike metal salts or complexes, the heterogeneous nature together with the conductivity of the material gives the possibility for a different "*heteroelectrochemical*" mechanism. It might be possible that various reactions take place on the surface of the catalyst at different sites and electrons are transferred across the conductive material where they are consumed.

Scheme 7.11 shows one possible manifestation of such a mechanism. At the start the uncoordinated catalyst (**A**) has some resting potential, which is defined by the redox potential of the species within the material, e.g.  $\text{Fe}^{2+}/\text{Fe}^{3+}$ . After oxygen coordination



SCHEME 7.11: Possible mechanism for the epoxidation of alkene with  $\text{O}_2$  and aldehyde, catalysed by Fe-N/C catalyst.

to the active iron site, the open circuit potential of the system (**B**) will rise. The higher potential of the catalyst surface will allow for the oxidation of the aldehyde (**1**). This results in the release of protons and the formation of methacrolein<sup>3</sup> (**2**) as minor side product and isobutyric acid (**3**) as major side product. The reaction can occur on any other site on the catalyst surface and the released electrons can be transferred to the active site. The electron and proton transfer then leads to the formation of the Fe-oxo species which has a significantly higher open circuit potential (**D**). This species (**E**) can then react with the olefin (**4**) to form the epoxide (**5**).

Another plausible alternative would be the release of superoxide formed by species **C** upon electron transfer, thereby facilitating radical formation as shown in Equation 7.2 ("*superoxide mechanism*").

<sup>3</sup>Small amounts of methacrolein were found in the GC spectra of all reactions.

### 7.2.9 Further possible experiments

The findings in this chapter can be the basis for further fundamental insight. A range of experiments can now be carried out in order to support or rule out the hypotheses and mechanistic proposals provided in this chapter:

- (i) Is the active site of the electrochemical ORR and the epoxidation the same? - This could be tested by determining the effect of nitrite on the rate of epoxidation with the set-up developed here. A significant effect on the epoxidation reaction would strongly suggest a correlation.
- (ii) Is there the possibility of a novel "*heteroelectrochemical*" reaction mechanism? - The effect of the concentration of various compounds, which participate in the proposal in Scheme 7.11, on the reaction rate and product distribution might give more insight. The effect of water could be investigated and the reaction mixture could be analysed for product water.
- (iii) Further evidence for the "*heteroelectrochemical*" mechanism could be sought by separating the alkene and coreductant into 2 flasks with solvent and catalyst. Connecting these flasks ionically and electronically and tracking the potential and oxygen consumption of these half cells might verify this mechanism. If the epoxidation reaction takes place when the cells are connected, while it does not otherwise, an electron transfer between active sites would be highly likely.
- (iv) The "*superoxide mechanism*" on the other hand could be verified by adding a superoxide probe to the reaction mixture to verify the presence of significant amounts of superoxide.

## 7.3 Conclusions

In order to gain further information on the chemical behaviour of the active site, a new concept of using organic chemical reactions as "probe" for the activity was introduced. The epoxidation reaction of alkenes with molecular oxygen and the co-oxidation of isobutyraldehyde was studied. Usually this reaction is carried out with metal macrocyclic complexes. Different M-N/C catalysts were used instead of metal complexes. It was found that those act as catalysts towards the epoxidation reaction in the same manner as

the metal complex. The TON was exceptionally high and could be as high as 1 000 000 on per active site basis. It seems a better ORR catalyst is a better epoxidation catalyst. Encouraged by this apparent correlation, the most active **Fe-N/C** catalyst was investigated in more depth. It was found that even notoriously difficult alkenes can be epoxidised by this system. The stereoselectivity of *cis*-stilbene to *trans*-stilbene-oxide indicates a radical mechanism. The rate of oxygen uptake was measured and an apparent TOF of  $\sim 10$  per iron site has been estimated, which is exceptionally high for heterogeneous catalysis. It was found that an initiation time of  $\sim 5$  minutes precedes oxygen uptake. The potential in the reaction mixture was monitored. Upon addition of the coreductant isobutyraldehyde, the potential rose during  $\sim 5$  minutes by  $\sim 300$  mV. A correlation of oxygen uptake and potential of the reaction mixture was found. It was found that the **Fe-N/C** catalyst performs significantly better than free iron ions in the form of added  $\text{FeCl}_3 \cdot 6 \text{H}_2\text{O}$ . Mechanistic proposals in literature were discussed and parallels of the behaviour of the **Fe-N/C** catalyst to Fe porphyrin complexes were found. It seems plausible that the metal centre takes part in the catalytic cycle, which consists of some kind of radical chain reaction. A new "*heteroelectrochemical*" reaction mechanism is also possible. Due to the conductive nature of the catalyst, electron transfer between active sites is possible. A further study of this system might have several benefits; i) it might lead to fundamental insight into the behaviour of the active site and lead to improvements for the ORR in fuel cells. ii) it might lead to the development of a robust heterogeneous catalytic system, which uses oxygen under mild conditions and might become an important industrial process. iii) if this newly proposed mechanism is present it could inspire new synthetic approaches for chemical compounds.

## 7.4 Experimental Part

### 7.4.1 Epoxidation reactions

In a round bottomed flask, the catalyst (25 mg) was sonicated in acetonitrile (25 mL, LC-MS Grade from Fluka) in order to finely disperse the catalyst. Cyclohexene (6.70 mmol,  $\geq 99.0\%$  Sigma-Aldrich) and coreductant isobutyraldehyde (7.32 mmol,  $\geq 99.0\%$  Sigma-Aldrich) were added to the flask. A balloon containing approx. 5 litres oxygen (Research Grade, BOC) was attached via a needle and allowed to bubble in order to saturate the

solution with oxygen. Then the system was closed and left stirring. Aliquot were removed and subjected to GC analysis after the respective periods. When other ratios were used those are specified in the text.

#### 7.4.2 GC analysis of reaction mixture

For GC analysis, an aliquot (approx. 1 mL) was removed from the flask with a syringe. The catalyst was removed from the aliquot with a syringe filter (0.2  $\mu\text{m}$  PTFE, Merck Millex<sup>®</sup>). For calibration, the relative response factor of each quantified compound was determined against mesitylene as internal standard with at least 3 measurements per compound (see 2.2.11). GC vials were prepared with 50 mg mesitylene ( $\geq 98\%$ , Sigma-Aldrich) and approx. 0.8 mL of crude filtered reaction mixture and run through the GC (Agilent 6890 Series gas chromatograph, equipped with a FID and a BPX5 capillary column: 30 m, I.D. 0.32 mm. Helium was used as a carrier gas). The exact amount of standard and aliquot was determined gravimetrically on an analytical fine balance (Ohaus Discovery, 10  $\mu\text{g}$  resolution), in order to minimise errors.

#### 7.4.3 Oxygen uptake measurements

The set-up used to study the oxygen uptake is described in 7.2.4.

#### 7.4.4 Potential measurements

A three-necked round bottom flask was used as reaction medium. A leak free Ag/AgCl reference electrode (Warner Instruments) and carbon fibre/gold working electrode were inserted into the reaction solution via two different openings and care was taken to prevent short circuit. By using rubber septa (Sigma-Aldrich) the system was sealed. A Gamry 3000 Potentiostat/Galvanostat was used to track the open circuit potential between both electrodes. The oxygen was supplied as described above via the third opening. The reaction mixture was as described above with the addition of 0.1 mM of  $(t\text{-Bu})_4\text{NBF}_4$  to introduce the necessary conductivity for the electrochemical measurement.

## 7.5 References

- [1] Sienel G., Rieth R., Rowbottom K.T. Epoxides. In *Ullmann's Encyclopedia of Industrial Chemistry*. Wiley-VCH Verlag GmbH & Co. KGaA, 2000. ISBN 978-3-527-30673-2.
- [2] Rebsdats S., Mayer D. Ethylene Oxide. In *Ullmann's Encyclopedia of Industrial Chemistry*. Wiley-VCH Verlag GmbH & Co. KGaA, 2000. ISBN 978-3-527-30673-2.
- [3] Kahlich D., Wiechern U., Lindner J. Propylene Oxide. In *Ullmann's Encyclopedia of Industrial Chemistry*. Wiley-VCH Verlag GmbH & Co. KGaA, 2000. ISBN 978-3-527-30673-2.
- [4] Russo V., Tesser R., Santacesaria E., Di Serio M. Chemical and Technical Aspects of Propene Oxide Production via Hydrogen Peroxide (HPPO Process). *Industrial & Engineering Chemistry Research*, 52(3), 1168–1178, January 2013. doi:10.1021/ie3023862.
- [5] Meunier B., de Visser S.P., Shaik S. Mechanism of Oxidation Reactions Catalyzed by Cytochrome P450 Enzymes. *Chemical Reviews*, 104(9), 3947–3980, September 2004. doi:10.1021/cr020443g.
- [6] Vaz A.D.N., McGinnity D.F., Coon M.J. Epoxidation of olefins by cytochrome P450: Evidence from site-specific mutagenesis for hydroperoxo-iron as an electrophilic oxidant. *Proceedings of the National Academy of Sciences*, 95(7), 3555–3560, March 1998.
- [7] Punniyamurthy T., Velusamy S., Iqbal J. Recent Advances in Transition Metal Catalyzed Oxidation of Organic Substrates with Molecular Oxygen. *Chemical Reviews*, 105(6), 2329–2364, June 2005. doi:10.1021/cr050523v.
- [8] Coon M.J. CYTOCHROME P450: Nature's Most Versatile Biological Catalyst. *Annual Review of Pharmacology and Toxicology*, 45(1), 1–25, 2005. doi:10.1146/annurev.pharmtox.45.120403.100030.
- [9] Nam W., Kim H.J., Kim S.H., Ho R.Y.N., Valentine J.S. Metal Complex-Catalyzed Epoxidation of Olefins by Dioxygen with Co-Oxidation of Aldehydes. A Mechanistic Study. *Inorganic Chemistry*, 35(4), 1045–1049, January 1996. doi:10.1021/ic950782a.



- [10] Serra A.C., d'A. Rocha Gonsalves A.M. Mild oxygen activation with isobutyraldehyde promoted by simple salts. *Tetrahedron Letters*, 52(27), 3489–3491, July 2011. doi:10.1016/j.tetlet.2011.04.120.
- [11] Zhang A., Li L., Li J., Zhang Y., Gao S. Epoxidation of olefins with O<sub>2</sub> and isobutyraldehyde catalyzed by cobalt (II)-containing zeolitic imidazolate framework material. *Catalysis Communications*, 12(13), 1183–1187, July 2011. doi:10.1016/j.catcom.2011.04.013.
- [12] Köckritz A., Blumenstein M., Martin A. Epoxidation of methyl oleate with molecular oxygen in the presence of aldehydes. *European Journal of Lipid Science and Technology*, 110(6), 581–586, June 2008. doi:10.1002/ejlt.200700279.
- [13] Farokhi A., Hosseini-Monfared H. A recyclable Mn–porphyrin catalyst for enantioselective epoxidation of unfunctionalized olefins using molecular dioxygen. *New Journal of Chemistry*, April 2016. doi:10.1039/C6NJ00808A.
- [14] Jarboe S.G., Beak P. Mechanism of Oxygen Transfer in the Epoxidation of an Olefin by Molecular Oxygen in the Presence of an Aldehyde. *Organic Letters*, 2(3), 357–360, February 2000. doi:10.1021/ol991304x.
- [15] Farzaneh F., Tayebi L., Ghandi M. Epoxidation of alkenes with molecular oxygen and isobutyraldehyde catalyzed by immobilized vitamin B12 within Al-MCM-41. *Reaction Kinetics and Catalysis Letters*, 91(2), 333–340, August 2007. doi:10.1007/s11144-007-5101-9.
- [16] Li Y., Zhou X., Chen S., Luo R., Jiang J., et al. Direct aerobic liquid phase epoxidation of propylene catalyzed by Mn(III) porphyrin under mild conditions: Evidence for the existence of both peroxide and Mn(IV)-oxo species from in situ characterizations. *RSC Advances*, 5(38), 30,014–30,020, March 2015. doi:10.1039/C4RA15601C.
- [17] Lan H.Y., Zhou X.T., Ji H.B. Remarkable differences between benzaldehyde and isobutyraldehyde as coreductant in the performance toward the iron(III) porphyrin-catalyzed aerobic Baeyer–Villiger oxidation of cyclohexanone, kinetic and mechanistic features. *Tetrahedron*, 69(21), 4241–4246, May 2013. doi:10.1016/j.tet.2013.03.088.

- [18] Banerjee D., Jagadeesh R.V., Junge K., Pohl M.M., Radnik J., et al. Convenient and Mild Epoxidation of Alkenes Using Heterogeneous Cobalt Oxide Catalysts. *Angewandte Chemie International Edition*, 53(17), 4359–4363, April 2014. doi:10.1002/anie.201310420.
- [19] Cui X., Li Y., Bachmann S., Scalone M., Surkus A.E., et al. Synthesis and Characterization of Iron–Nitrogen-Doped Graphene/Core–Shell Catalysts: Efficient Oxidative Dehydrogenation of N-Heterocycles. *Journal of the American Chemical Society*, 137(33), 10,652–10,658, August 2015. doi:10.1021/jacs.5b05674.
- [20] Jagadeesh R.V., Junge H., Beller M. “Nanorust”-catalyzed Benign Oxidation of Amines for Selective Synthesis of Nitriles. *ChemSusChem*, 8(1), 92–96, January 2015. doi:10.1002/cssc.201402613.
- [21] Ross J.R.H. *Heterogeneous Catalysis: Fundamentals and Applications*. Elsevier, Amsterdam, 1 edition edition, November 2011. ISBN 978-0-444-53363-0.
- [22] Jones P. *Towards a mechanistic understanding of olefin epoxidation with a novel Fe-N/C catalyst*. Master thesis, Imperial College London, 2016.
- [23] Schröder K., Join B., Amali A.J., Junge K., Ribas X., et al. A Biomimetic Iron Catalyst for the Epoxidation of Olefins with Molecular Oxygen at Room Temperature. *Angewandte Chemie International Edition*, 50(6), 1425–1429, February 2011. doi:10.1002/anie.201004623.

*The effect of ionomer to carbon (I/C) ratio on the performance of PEMFC MEAs was investigated for three different M-N/C catalysts at the cathode with Pt/C-based anodes. It was found that the ideal ionomer content is a key factor for improving the performance of the catalyst. Non-optimal ionomer loading leads to two different features in the impedance spectrum: deviation of the slope in the high frequency region of the Nyquist-representation from a 45° line and a deviation from a 90° line in the low frequency region. An electrode morphology based on the presence of inhomogeneous resistance distribution within the porous structure is suggested to explain the observed phenomena. It is shown how impedance spectroscopy can be used to quickly assess whether the optimal, a too high or a too low ionomer content is present in the catalyst layer. A simple flowchart to aid fuel cell optimisation is provided. This study can therefore help to speed up the optimisation of PEM single cells operated on M-N/C cathode catalysts.*

## Chapter 8

# M-N/C catalysts in PEM single cells - catalyst layer optimisation utilising impedance spectroscopy

### 8.1 Introduction

Commercialisation of low temperature fuel cells requires significant cost reductions. [1] Replacing expensive platinum at the cathode with non-precious metal based catalysts (NPMCs) is a promising option. [2] Although these materials show remarkable activity under fuel cell operating conditions, their intrinsic catalytic activity is still lower than

that of Pt. [2, 3] Due to the lower price, a higher loading is conceivable to compensate for this drawback. However, there is limited benefit in increasing the thickness of the catalyst layer (CL) in the membrane electrode assembly (MEA) beyond a certain value. This is partly because proton resistance ( $H^+$ ), electronic resistance of the CL ( $\rho_{el\_cath}$ ) and mass transport resistance ( $\rho_{mt}$ ) become limiting factors as the thickness is increased. This will eventually outweigh the benefit of more catalyst. Therefore the US department of energy (DoE) defined targets (2020) for the volumetric activity of non-precious metal catalysts of  $>300 A cm^{-3}$  at 0.8 V cell voltage. [4] It has been shown that the ionomer to carbon (I/C) ratio is a significant performance determining factor, both for Pt based catalysts and for non-precious metal catalysts. [5, 6] Moreover, for Pt on carbon it has been shown that the optimal ionomer content depends strongly on the microstructure of the carbon support and the influence of the ionomer content on the proton conductivity has also been well investigated. [6, 7] These studies helped to understand the behaviour of the catalyst layer and provided information that led to significant performance increase in cathodes operated with platinum based catalysts. However, these results cannot be easily translated to cathodes operated on NPMCs. This is firstly because the microstructure and composition of newly developed NPMCs varies widely. [3] Secondly, while the activity of precious metal catalysts is localized on micro- and/or nanoparticles that are attached to the carbon support, the activity in non-precious metal catalysts is believed to be highly dispersed within the carbon structure itself or situated on the opening of micropores. [8] This has tremendous impact on the requirements for proton and gas transport within the catalyst layer.

Much work has been devoted to tune the ionomer content and electrode preparation process for precious metal catalysts in order to facilitate efficient proton and gas transport to the reaction site and water away from the reaction site. [4, 9–20] While a homogeneous ionomer coverage is on one hand desired for effective proton transport it is on the other hand detrimental for the gaseous reactant transport as it creates a barrier for the reactant to access the active site, resulting in mass transport resistance. Numerous NPMCs have already been reported in active fuel cells. However to date there is no study that investigates the phenomena present within such catalyst layers.

## 8.2 Electrochemical Impedance Spectroscopy for fuel cell analysis

The general concept of impedance was discussed in 2.1.2. Electrochemical impedance spectroscopy (EIS) on single cells operating on H<sub>2</sub>/O<sub>2</sub> can be used to extract the high frequency resistance, which is associated with the electronic resistances of the current leads and cell assembly as well as of the membrane. The high frequency resistance corrected cell potential values are better suited to compare catalyst performance, since unrelated performance losses are compensated for. This high frequency corrected cell potential is given by:

$$E_{\text{HFR-free}} = E_{\text{cell}} + j * \text{HFR} \quad (8.1)$$

where  $E_{\text{HFR-free}}$  is the high frequency corrected cell potential in V,  $E_{\text{cell}}$  is the measured uncorrected cell potential in V,  $j$  is the current density at the respective cell potential in A cm<sup>-2</sup> and HFR is the high frequency area specific resistance, as extracted from the real value of the impedance at 0 degree phase angle in Ω cm<sup>2</sup>.

Further insights into the fuel cell cathode performance can be gained from electrochemical impedance spectroscopy measurements in the absence of a faradaic reaction. Although simple, the transmission line model is suitable to examine H<sub>2</sub>/Argon PEMFC single cell properties. [6, 13, 14]

Figure 8.1 (a) shows the equivalent circuit of the transmission line without a faradaic reaction. The contributions within the catalyst layer consist of protonic resistance ( $R_p$ ) and double layer capacitance ( $C_{DL}$ ). In the presence of a faradaic reaction (Figure 8.1 (a)) the charge transfer resistance of the reaction ( $R_{CT}$ ) contributes as well. The impedance derived from this transmission line model in the absence of a faradaic reaction (Figure 8.1 (a)) is given by: [22]

$$Z(i\omega) = \sqrt{\frac{R_D}{i\omega C_D}} \coth(i\omega R_D C_D) \quad (8.2)$$

where  $R_D$  is the total distributed resistance in Ω and  $C_D$  the total distributed capacitance in F. Applying asymptotic approximations one arrives at a 45° line at high frequency

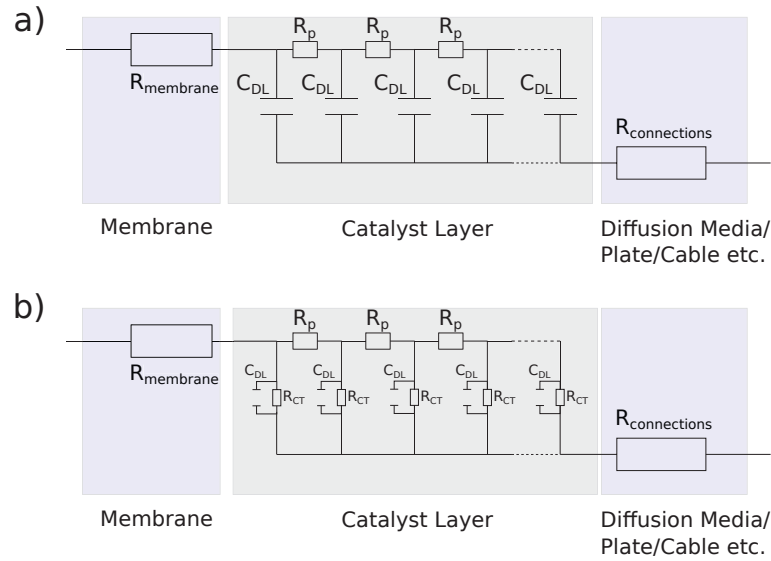


FIGURE 8.1: (a) Transmission line equivalent circuit of the catalyst layer (grey) between the membrane (ionic) and electronic resistive elements in the absence of a faradaic reaction, with the protonic resistance  $R_{\text{p}}$  and the double layer capacitance  $C_{\text{DL}}$ . (b) Transmission line equivalent circuit in the presence of a faradaic reaction represented by the addition of the charge transfer resistance  $R_{\text{CT}}$ . [Adapted from Ref. [21]]

and a vertical line towards low frequency in the *Nyquist*-plot. [22] From this feature the proton resistances in catalyst layers have been extracted for Pt based catalysts. [6, 7, 13] Furthermore one can extract the frequency dispersion in these electrodes which gives rise to the constant phase element (CPE) and is defined as: [23]

$$Z_{\text{CPE}} = \frac{1}{Q(i\omega)^\phi} \quad (8.3)$$

where,  $Q$  is the parameter related to the electrode capacitance ( $\text{F s}^{\phi-1} \text{cm}^{-2}$ ), and  $\phi$  is the dimensionless constant phase exponent and related to the deviation from the pure capacitive line of  $90^\circ$  towards an angle of  $90^\circ \cdot \phi$  in the *Nyquist*-plot at low frequencies or a deviation of the limiting phase angle below  $90^\circ$  in the *Bode* phase angle plot. [23] The origin of this CPE can be attributed to adsorption/diffusion processes at the catalyst surface. [23] A CPE behaviour in a fuel cell electrode could therefore originate from inhomogeneous proton diffusion towards the gas diffusion electrode, where the proton mobility is restricted due to low or inhomogeneous ionomer coverage. Hence a higher frequency dispersion might be detrimental for cell performance.

### 8.3 Information on catalyst layer structure

In this chapter impedance spectroscopy in combination with a varying ionomer content on three different NPMCs with different activity and microstructure is employed in order to investigate the impact of the I/C ratio on their performance. Experiments were made in the presence and absence of reactant in order to gain deeper insight into the operation of the fuel cell and to determine whether the ionomer content is too high or too low by EIS. This analysis opens the way for understanding of the behaviour of non-precious metal catalyst layers, which is fundamental for the further development of alternative oxygen reduction reaction catalysts. Furthermore, it helps to develop a simple strategy for the estimation of the optimal I/C ratio for a newly prepared carbon based catalyst thus accelerating developments in this field.

## 8.4 Results and Discussions<sup>1</sup>

### 8.4.1 Microstructure and RDE performance of 3 different catalysts

To highlight the structural differences of the catalysts, the BET surface area as determined by nitrogen adsorption analysis in Chapter 3 is shown here. The BET surface areas of the catalyst powders are 789 m<sup>2</sup> g<sup>-1</sup> for **FeCo-N/C**, 478 m<sup>2</sup> g<sup>-1</sup> for **Fe-N/C** and 1249 m<sup>2</sup> g<sup>-1</sup> for **MgO\_APS\_2**.

The *Barrett-Joyner-Halenda* (BJH) pore size distribution as shown in Figure 8.2 is also qualitatively different for each sample.

The performance of the differently prepared catalysts was initially determined by the rotating disk electrode method in 0.5 M H<sub>2</sub>SO<sub>4</sub> acid at a loading of 750 μg cm<sup>-1</sup> (Figure 8.3). This allows comparison of the activity of the catalysts. It is seen that the activity of the **FeCo-N/C** catalyst (0.077 A g<sup>-1</sup> @ 0.8 V *vs* RHE or 0.192 A cm<sup>-32</sup>) is significantly lower than **Fe-N/C** (0.77 A g<sup>-1</sup> or 1.93 A cm<sup>-3</sup>) and **MgO\_APS\_2** (1.36 A g<sup>-1</sup> or 3.4 A cm<sup>-3</sup>)

<sup>1</sup>The experiments for this chapter were conducted in collaboration with Dr. Thiago Lopes during an Imperial College Global Engagement Project at the University of Sao Carlos, hosted by Prof. Edson A. Ticianelli.

<sup>2</sup>Assuming a catalyst layer density of 0.4 g cm<sup>-2</sup> [1]

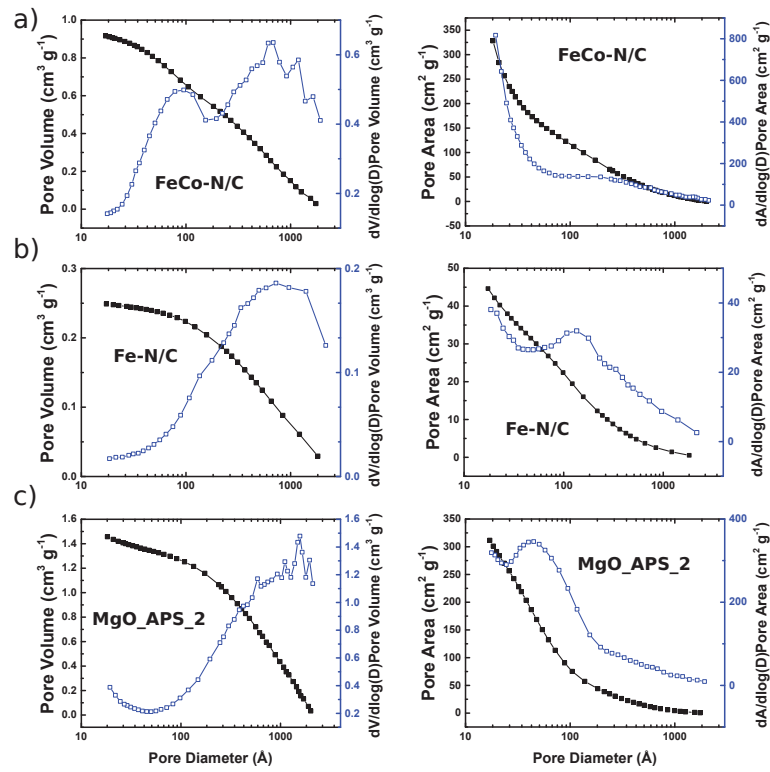


FIGURE 8.2: Pore size distribution, as determined by the BJH method from the desorption branch of the respective isotherm for (a) FeCo-N/C catalyst (b) Fe-N/C catalyst and (c) MgO\_APS\_2 catalyst. [Adapted from Ref. [21]]

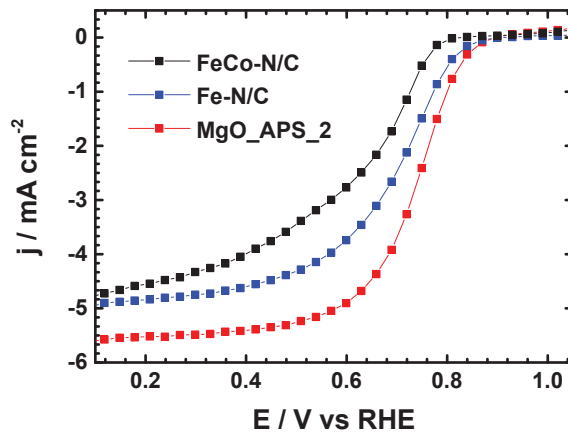


FIGURE 8.3: Steady-state Rotating Disk Electrode (RDE) measurements of utilized catalysts. Catalyst loading:  $750 \mu\text{g cm}^{-2}$ , rotation rate: 1600 rpm,  $\text{O}_2$ -saturated 0.5 M  $\text{H}_2\text{SO}_4$ , 30 s hold 30 mV step potential. [Adapted from Ref. [21]]



at the same potential.<sup>3</sup> These results demonstrate the differences in the surface area and microstructure, as well as in the activity of the different catalysts.

#### 8.4.2 Structure and thickness of the catalyst layer

These materials were fabricated into membrane electrode assemblies (MEA) for single cell performance testing. The cathode catalyst loading used in this study was  $4 \text{ mg cm}^{-2}$ , while the anode loading was  $0.4 \text{ mg}_{\text{Pt}} \text{ cm}^{-2}$  (Alfa Aesar, Johnson Matthey Hydrogen Reformate/Cathode). A relatively high Pt anode loading was chosen in order to ensure that no limiting effects of the anode reaction, which could interfere with the results, were experienced.

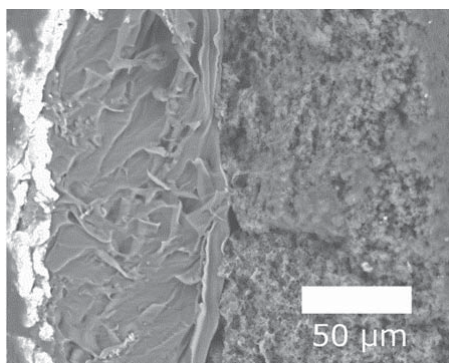


FIGURE 8.4: Representative scanning electron micrograph showing the freeze fractured cross section of a membrane electrode assembly, with the anode catalyst layer/membrane/cathode catalyst layer from left to right. [Adapted from Ref. [21]]

Figure 8.4 shows a representative scanning electron micrograph of the cross section of such a MEA. It can be clearly seen that the non-precious metal catalyst layer on the right hand side is significantly thicker ( $\sim 100 \mu\text{m}$ ) compared to the anode catalyst layer on the left hand side ( $\sim 10 \mu\text{m}$ ). Such thin catalyst layers as seen in the anode are representative of those seen on the cathode when platinum is used as electrocatalyst. This illustrates the large difference between Pt based and NPMC catalyst layers. This large thickness has a significant impact on properties such as proton and mass transport.

High resolution SEM images of the catalyst layers of different ionomer content are shown in Figure 8.5. It can be clearly seen that ionomer agglomerations are increasingly present for increasing ionomer loading in the sample.

<sup>3</sup>Implications on the activity interpretation caused by the differing limiting currents are discussed in Chapter 3.2.4. The purpose of the RDE plot here is to show that these material possess different properties. This shall verify that the phenomena found are not dependent on the catalyst.

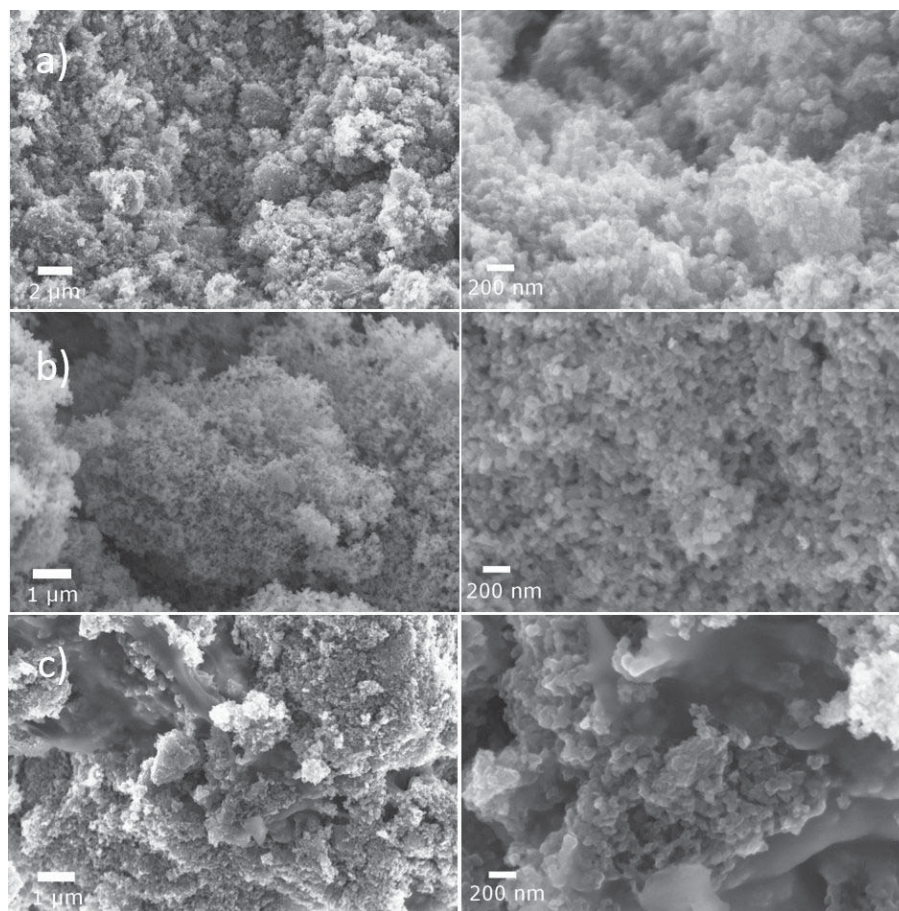


FIGURE 8.5: High resolution SEM images at low magnification (**left**) and high magnification (**right**) of catalyst layer cross section for the cathode with catalyst FeCo-N/C (a) I/C 0.5 (b) I/C 1 (c) I/C 2. [Taken with permission from Ref. [21]]

It also visualises the structural difference of the 3 investigated catalysts, additional to the difference in BET surface area and BJH pore size distribution.

### 8.4.3 Performance of catalysts with different ionomer loadings

Figure 8.6 shows plots of the  $iR$ -free cell potentials *versus* current density for the different electrodes, operated with the respective catalysts at different ionomer loadings.

Ionomer to catalyst ratios between 0.5 and 3 have been chosen in this study as the optimum value always falls within this range. A wide range of optimal ionomer loadings is not surprising, given the difference in activity and microstructure. However, it is time consuming to determine the optimum ionomer ratio for a specific catalyst. While for the catalysts **FeCo-N/C** and **MgO\_APS\_2** an I/C ratio of 1 has been identified as the optimum, for catalyst **Fe-N/C** it is 1.5. The current density at 2 different  $iR$ -corrected

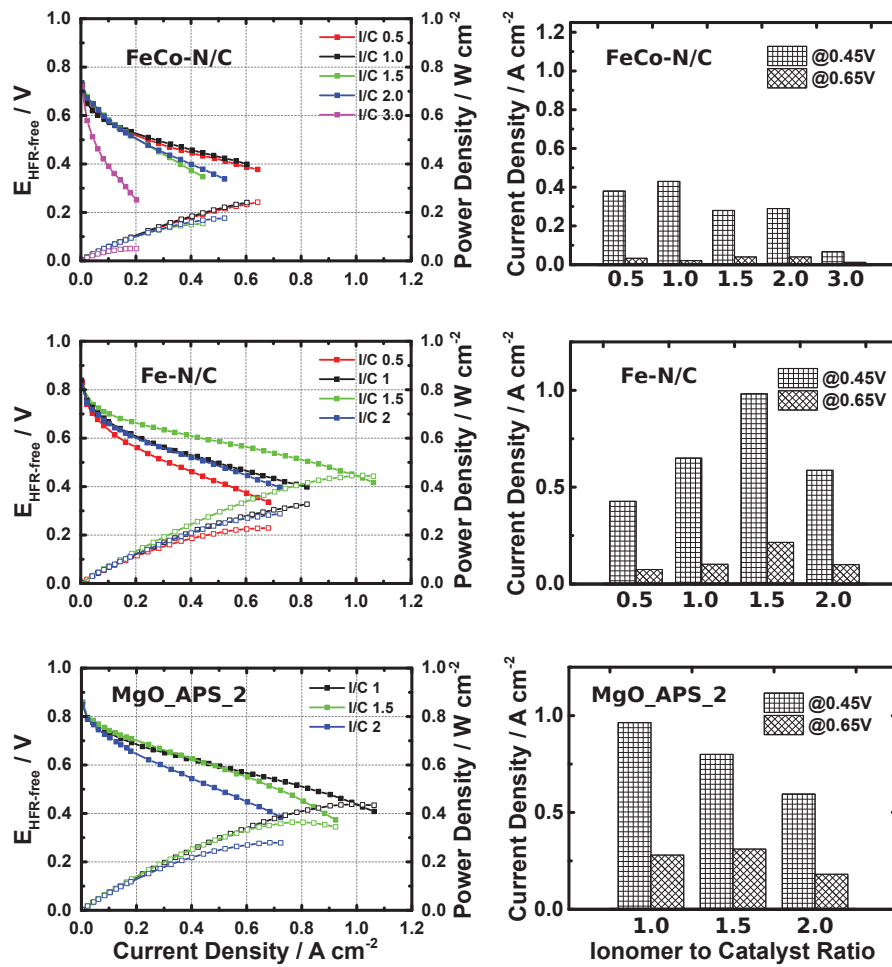


FIGURE 8.6: **Left:** Galvanostatic polarisation curves for single cells with different ionomer loadings at the cathode, Anode:  $\text{H}_2$ , 160 sccm, 2 bar back pressure (gauge), 100% RH, Johnson Matthey Hydrogen reformate electrode  $0.4 \text{ mg}_{\text{Pt}} \text{ cm}^{-2}$ , Cathode:  $\text{O}_2$ , 550 sccm, 2 bar back pressure (gauge), 100% RH,  $4 \text{ mg}_{\text{catalyst}} \text{ cm}^{-2}$ ; Cell Temperature:  $80^\circ \text{C}$ . **Right:** Bar plot depicting the respective current density at 2 different cell potentials. a) FeCo-N/C b) Fe-N/C c) MgO\_APS\_2. Cell voltages are  $iR$ -corrected using the resistance determined from the high frequency intercept with the real axis in the *Nyquist*-plot. [Taken with permission from Ref. [21]]

cell potentials are depicted in Figure 4 on the right hand side. It can be seen that at low current densities, *i.e.* high cell potential, the trend is not the same for the catalysts **FeCo-N/C** and **MgO\_APS\_2** which operate better with a low ionomer content at high current densities. For the catalyst **MgO\_APS\_2**, at low current density, a higher ionomer content is indeed beneficial. The reason might be that with a higher ionomer content more active sites might be accessible. However this benefit might be lost at high current densities, where proton and mass transport become more important.

### 8.4.4 Impedance in the absence of a faradaic reaction

Figure 8.7 shows the *Nyquist* (left, and in expanded view on the right) and *Bode* phase angle (centre) plots for the cells with the cathode under an inert environment at 0.1 V with the three different cathode catalysts.

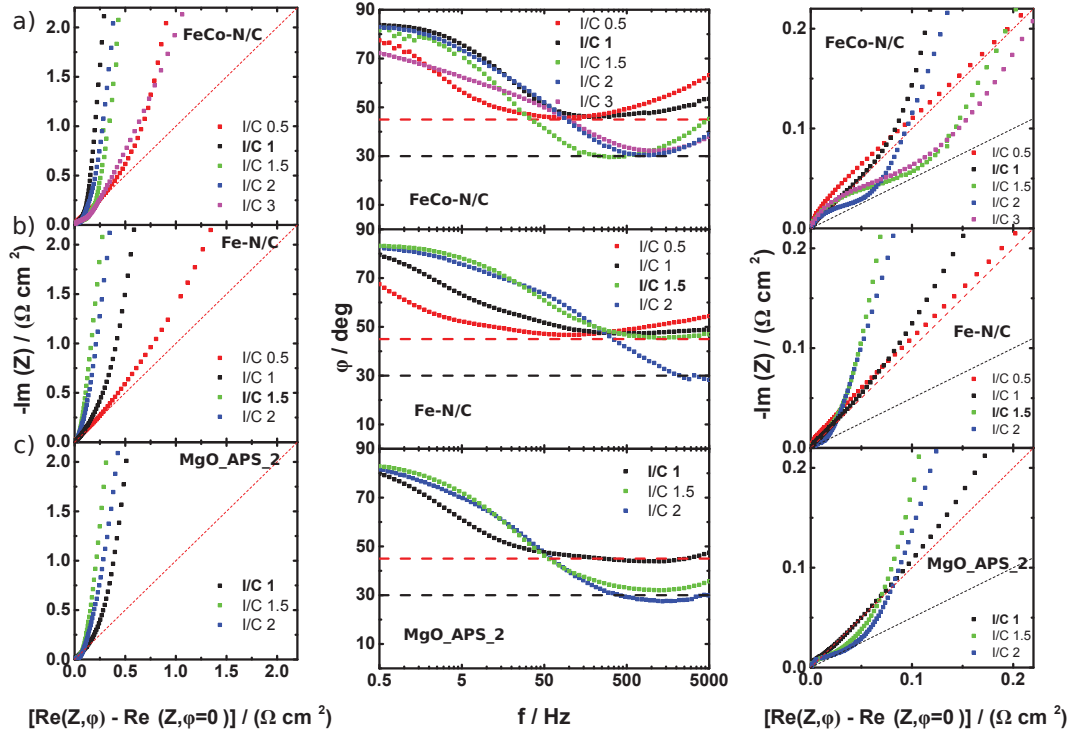


FIGURE 8.7: **Left:** *Nyquist*-plots, **centre:** *Bode* phase angle plots, **right:** Magnified *Nyquist*-plots, recorded for the cells operating on (a) FeCo-N/C (b) Fe-N/C (c) MgO\_APS.2 at the cathode at 0.1 V cell potential, anode: 20 sccm hydrogen, cathode: 550 sccm argon. Dashed red line corresponds to 45° in *Nyquist*-plot. Dashed black line corresponds to 30°. [Taken with permission from Ref. [21]]

*Nyquist* and *Bode*-plots are corrected for the uncompensated high frequency resistance, as described in the experimental part. Corresponding results for H<sub>2</sub>/O<sub>2</sub> single cells under operation are shown in Figures 8.8 and 8.9 for cell potentials of 0.60 V and 0.27 V, respectively.

The results for operation in H<sub>2</sub>/Argon (Figure 8.7) show that there is a consistent predictor across all three catalysts for the best performing ionomer/carbon ratios (highlighted bold in the figure legend). The predictor is based on the phase angle response at low and high frequencies. The best performing systems meet the following criteria:

- (a) At high frequencies they show phase angles close to 45° (*cf.* Equation 8.2)

- (b) At low frequencies, they maintain phase angle shifts close to  $90^\circ$  up to the highest possible frequency (*cf.* Equation 8.3)

Moreover, there are two aspects of the phase angle shift which can be used to ascertain whether a catalyst layer has too much or too little ionomer in it:

- (a) Catalyst layers with too much ionomer show phase shifts below  $45^\circ$ , and tend to approach shifts of  $30^\circ$  (*i.e.* I/C 1.5, 2 and 3 for catalyst **FeCo-N/C**, I/C 2 for **Fe-N/C** and I/C 1.5 and 2 for **MgO-APS.2** all show phase angle minima of  $30^\circ$  and contain more ionomer than the optimum value).
- (b) Catalyst layers with too little ionomer deviate from the low frequency  $90^\circ$  plateau at much lower frequencies than catalyst layers with excess ionomer (*i.e.* I/C 0.5 for **FeCo-N/C**, I/C 0.5 and 1 for **Fe-N/C**).

Hence cells with the highest performance are those which remain close to the  $45^\circ$  phase shift at the highest frequency (red dashed lines in plots) and which show an extended plateau region of ca.  $90^\circ$  in the low frequency *Bode* phase angle plot.

The criteria are rationalised in the following way:

If the electrode is fully flooded with ionomer then the entire porous structure is accessible with the lowest possible pore resistance, and so the system shows an extended low frequency region in which the response is dominated by the electrode capacitance. In our case all electrodes seem to asymptotically approach a limiting phase angle of  $85^\circ$  at low frequency suggesting the constant phase exponent,  $\phi$ , is close to one. As the ionomer content is decreased, this gives rise to an increasing pore resistance and decreasing coverage of the ionomer on the carbon shifting the phase angle response from  $\sim 85^\circ$  to lower values at a given frequency (*i.e.* the pole in the frequency response shifts down in frequency). Increasing the ionomer content above the minimum required to suitably access the entire surface area of the catalyst will result in extra transport losses to no benefit of the catalyst performance. The response at high frequency is rationalised on the basis of Equation 8.2 [22], which predicts a  $45^\circ$  angle line in the phase plot at high frequency [13]. It is interesting that the poorly performing electrodes (*e.g.* those with too much ionomer) show high frequency phase angles which fall below this value and seem to approach a characteristic value of  $30^\circ$ .

### 8.4.5 Impedance under operation

This anomalous effect in the *Nyquist*-plot can also be seen in the fuel cells operating with oxygen on the cathode (Figure 8.8, left), especially for the **FeCo-N/C** catalyst. Interestingly, this behaviour seems to be correlated with the performance of the *iR*-corrected results, especially at higher current densities, depicted in Figure 8.6 (a).

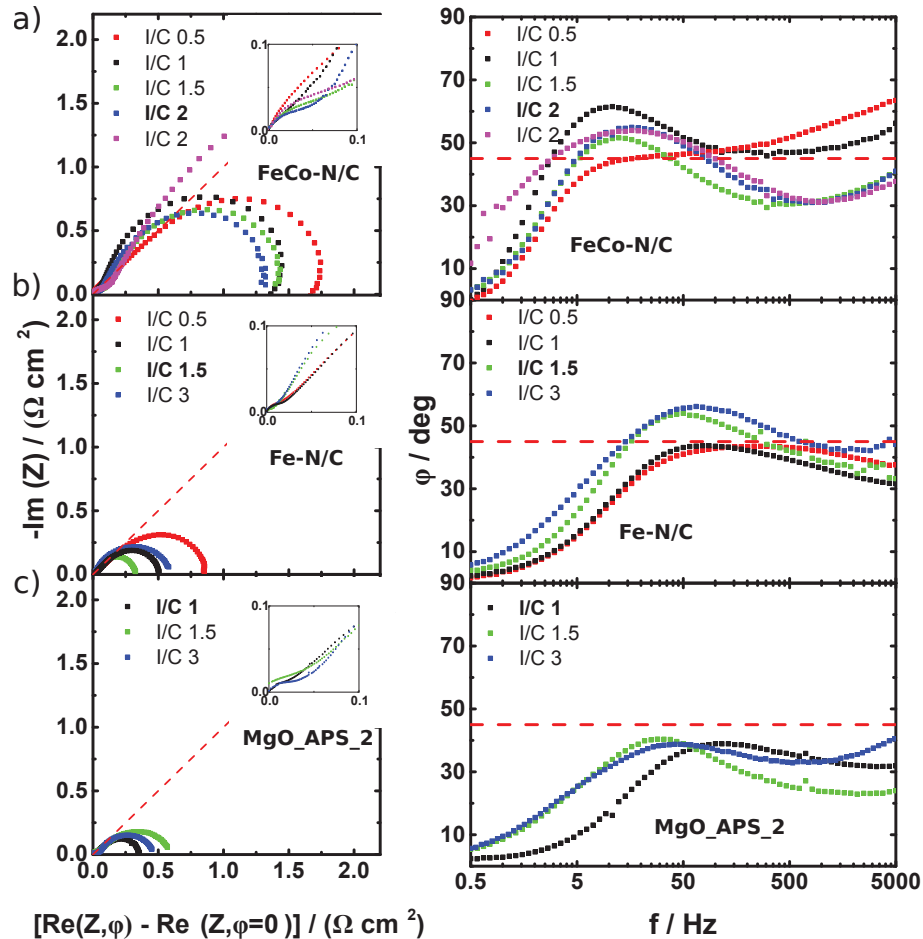


FIGURE 8.8: **Left:** *Nyquist*-plots, *inset:* magnification of high frequency region, **right:** *Bode* phase angle plots, recorded for the cells operating on (a) FeCo-N/C (b) Fe-N/C (c) MgO\_APS\_2 at the cathode at 0.6 V cell potential, Anode: 160 sccm hydrogen, Cathode: 550 sccm oxygen. Dashed red line corresponds to  $45^\circ$  in *Nyquist*-plot. [Taken with permission from Ref. [21]]

Another interesting finding is that at high current densities, a significant Warburg impedance is visible in the impedance spectrum (Figure 8.9), for the MEAs operating with the better performing catalysts **Fe-N/C** and **MgO\_APS\_2**.

This is deduced because of the clearly visible  $45^\circ$  line or indication of a second arc at low frequencies (Figure 7 8.9 (b) and (c) left). Especially for catalyst **Fe-N/C** at its optimal I/C ratio of 1.5 and the catalyst **MgO\_APS\_2** at its optimal I/C ratio of 1.

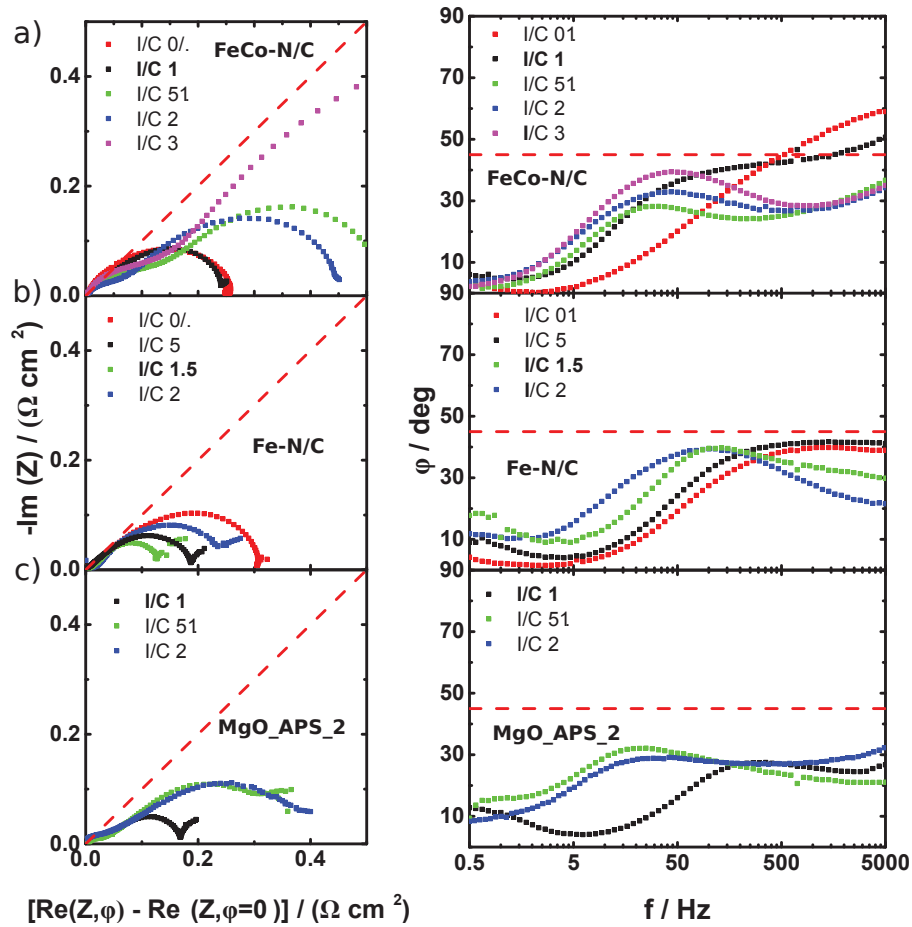


FIGURE 8.9: **Left:** Nyquist-plots, **right:** Bode phase angle plots, recorded for the cells operating on (a) FeCo-N/C (b) Fe-N/C (c) MgO\_APS\_2 at the cathode at 0.6 V cell potential, Anode: 160 sccm hydrogen, Cathode: 550 sccm oxygen. Dashed red line corresponds to 45° in Nyquist-plot. [Taken with permission from Ref. [21]]

This means that a significant mass transport resistance is present even at a relatively low current density of  $1.2 \text{ A cm}^{-2}$ . Usually single cells with a similar active area working with Pt based cathode catalyst under pure oxygen can reach current densities that are up to 3-5 times higher before experiencing mass transport limitations. [24] This indicates that not only proton conductivity and catalytic activity have to be optimised, but also the gas transport properties of the catalyst layer have to be taken into account, in order to eventually reach performances similar to Pt based cathodes. Furthermore it can be seen that the maximum in the phase angle (Figure 8.8 and 8.8 right) of the Bode phase plots in the cells operating under  $\text{H}_2/\text{O}_2$  shifts to lower frequencies at a higher ionomer loading. This is more pronounced under higher current densities. This might indicate that the dispersion of time constants of individual  $R - S$  elements within the catalyst layer is increasing. [23] In all cases the compositions with the maximum performance

(highlighted in bold in the figure legends) are those with the smallest absolute magnitude at low frequencies.

#### 8.4.6 Effect of CL thickness, relative humidity and backpressure on the EIS spectrum

To confirm whether the deviation from the 45° slope, as seen in Figure 8.8, can be solely attributed to the ionomer content and is not related to catalyst layer thickness, electrodes with a different loading and hence different thickness were prepared, while using the optimal ionomer content as determined before.

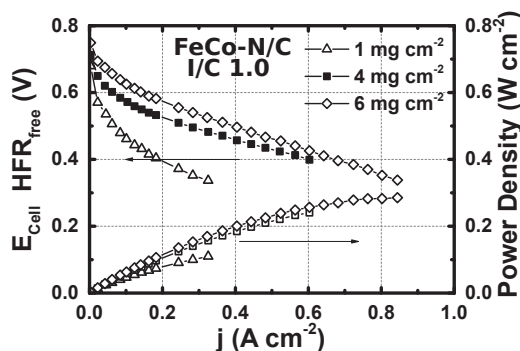


FIGURE 8.10: Galvanostatic polarisation curves for single cells with different catalyst loadings at the cathode, anode: H<sub>2</sub>, 160 sccm, 2 bar back pressure (gage), 100% RH, Johnson Matthey Hydrogen reformate electrode 0.4 mg<sub>Pt</sub> cm<sup>-2</sup>, cathode: O<sub>2</sub>, 550 sccm, 2 bar back pressure (gage), 100% RH, 4mg<sub>catalyst</sub> cm<sup>-2</sup>; Cell temperature: 80 °C. [Taken with permission from Ref. [21]]

Figure 8.10 shows the iR-corrected polarisation curves of single cells with different catalyst loadings. Not surprisingly, a higher catalyst loading provides a higher performance. However, in an additional study it was shown that significant mass transport losses are present when increasing the catalyst layer thickness, placing limitations on the maximum amount of catalyst feasible. [25]

Figure 8.11 shows the corresponding H<sub>2</sub>/Argon single cell *Nyquist* impedance plot. It can be seen that the slope at high frequency follows the 45° slope without any dependence on the thickness.

To rule out any effect of the back pressure, spectra with and without backpressure were recorded (Figure 8.12), and these did not evidence a significant effect. These results clearly show that this phenomenon can be solely attributed to processes related to the



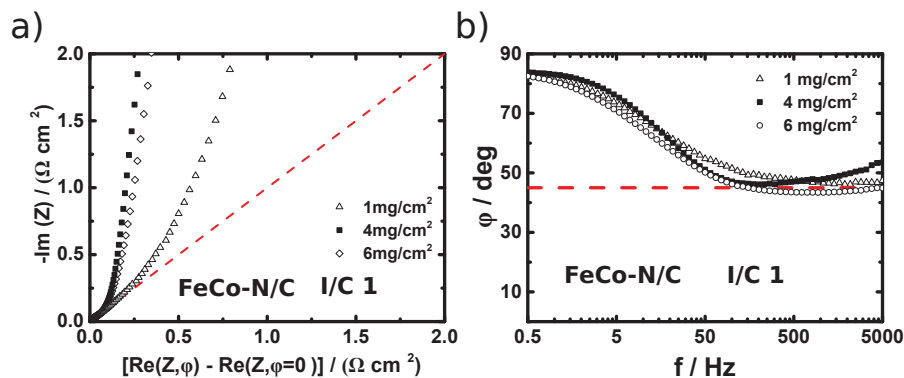


FIGURE 8.11: *Nyquist*-plots (**left**) and *Bode* phase plot (**right**) for the cells operating on catalyst FeCo-N/C at the cathode at 0.1 V cell potential with different loadings, anode: 160 sccm hydrogen, cathode: 550 sccm argon. Dashed red line corresponds to 45° angle. [Taken with permission from Ref. [21]]

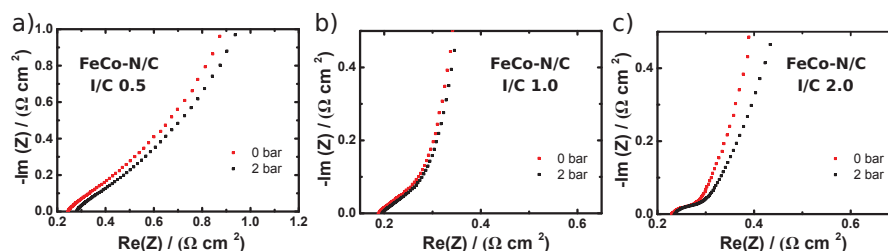


FIGURE 8.12: H<sub>2</sub>/Ar *Nyquist*-plots for catalyst FeCo-N/C with and without backpressure at I/C ratio (a) 0.5 (b) 1.0 (c) 2.0. [Taken with permission from Ref. [21]]

ionomer. Furthermore, the fact that this effect is present in the absence of a faradaic reaction means that it is likely correlated with the proton conductivity.

To investigate whether this is a structural feature of the electrode or dependent on the operating conditions, the relative humidity and thus the proton conductivity was varied (Figure 8.13). For a lower RH value, as expected the proton resistance increases. However for the system with the optimum I/C ratio (Figure 8.13 (a)), the 45° slope was retained at all humidities. This indicates that the operating conditions do not exhibit an influence that affects this high frequency feature at the optimal ionomer loading. However, a more profound effect is seen for a non-optimised I/C ratio, as seen in Figure 8.13 (b). In this case there is a significant variation in the high frequency response with a range of different limiting phase angles seen in the *Bode*-plot.

#### 8.4.7 Interpretation of observed results

The impedance study of porous electrodes is a well-developed topic, as it has tremendous practical importance. [20, 22, 23, 26–36] The deviation from 45° at high frequency observed

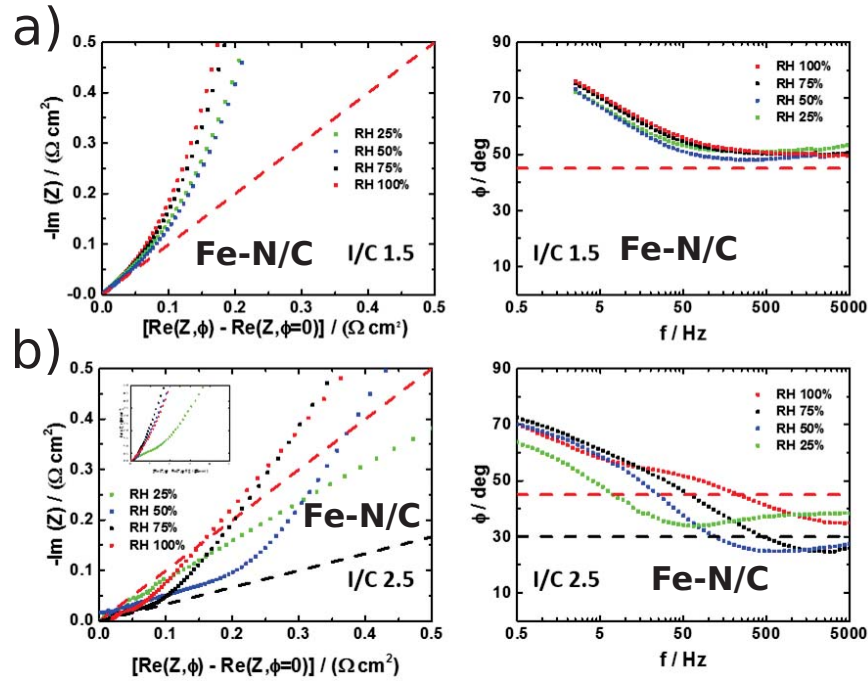


FIGURE 8.13: *Nyquist*-plots for the cell operating on catalyst Fe-N/C for an optimum I/C ratio (a), and a non-ideal ratio (b). 0.1 V cell potential at different relative humidity levels, anode: 160 sccm Hydrogen, cathode: 550 sccm Argon. Dashed red line corresponds to 45° angle and dashed black line to 30°. [Taken with permission from Ref. [21]]

here has been ascribed to different effects. For example, Keiser *et al.* modelled the impedance response for pores with different shapes. [30] The model is based on a recursive method where the disc is divided into segments with fixed height and radius. Each pore has its own electrolyte resistance and double layer capacitance. The electrolyte resistance down the pore varies according to the respective cross section in this segment. Therefore pores of different shapes can be constructed. The standardized pore impedance is then obtained by a recursion formula. More details can be found in Ref. [30]. The resistance of the pore changes with the pore radius. This means that for the pore with a narrow neck and wide body, the resistance decreases, as the A/C current penetrates deeper into the pore and the cross section has a larger radius. The situation is different for the narrowing pore, which has an increasing resistance. In summary, it is found that pore shapes which significantly deviate from a cylindrical geometry lead to a behaviour in the *Nyquist*-plot which is intriguingly similar to that observed in our spectra. This model predicts that when a pore has a narrow mouth and a wide body, the slope drops significantly below the typical 45°, while having a wide pore mouth and narrowing down towards the end of the pore provides a line that stays above 45° as observed for our spectra with low ionomer content. The slope calculated for the perfect cylindrical pore yields the 45° high frequency

slope.

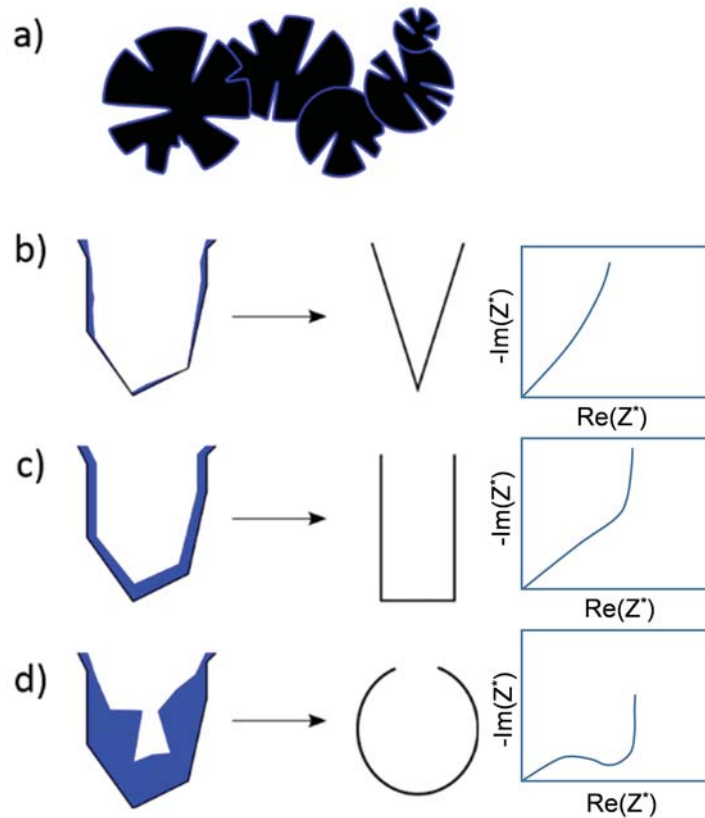


FIGURE 8.14: (a) Schematic describing porous carbon covered with a layer of ionomer (b) - (d) showing how the ionomer coverage corresponds to electrolyte filled pores. (b) incomplete coverage (c) homogeneous coverage (d) high loading with inhomogeneously filled pore. On the right hand side are representative Nyquist plots associated with the characteristic pore shapes as described in Ref. [30]. [Taken with permission from Ref. [21]]

These findings have been used to suggest an explanation for the behaviour observed in the spectra. Figure 8.14 (a) depicts a model of the carbon particles covered with ionomer. Figure 8.14 (b) shows how a narrowing down pore would translate into an ionomer coverage that does not completely penetrate to the bottom of the pore (low ionomer loading). This is analogous to a pore which narrows along its length. A homogeneous coverage depicted in Figure 8.14 (c) will lead to homogeneous layer thickness and will hence show a uniform resistance down the pore, which is analogous to a cylindrical pore. A high ionomer loading as depicted in Figure 8.14 (d) will fill up the pore and will lead to a lower resistance further inside the pore and would translate into a pore with a narrow mouth and wide body. Although this might be an oversimplified model it can explain the anomalous effects observed here.

A non-optimal ionomer loading will inevitably lead to an inhomogeneous resistance within the catalyst layer, consistent with the anomalous impedance behaviour observed for the H<sub>2</sub>/Argon single cells at high frequencies and the Warburg impedance seen at high current densities for the H<sub>2</sub>/O<sub>2</sub> cells. The method proposed here can easily identify the presence of such inhomogeneities and hence significantly aid in strategies for the optimization of the electrode catalyst layer structures.

#### 8.4.8 Optimisation protocol

In Figure 8.15 a simple flow diagram shows how an optimisation process for these electrodes would be implemented is provided.

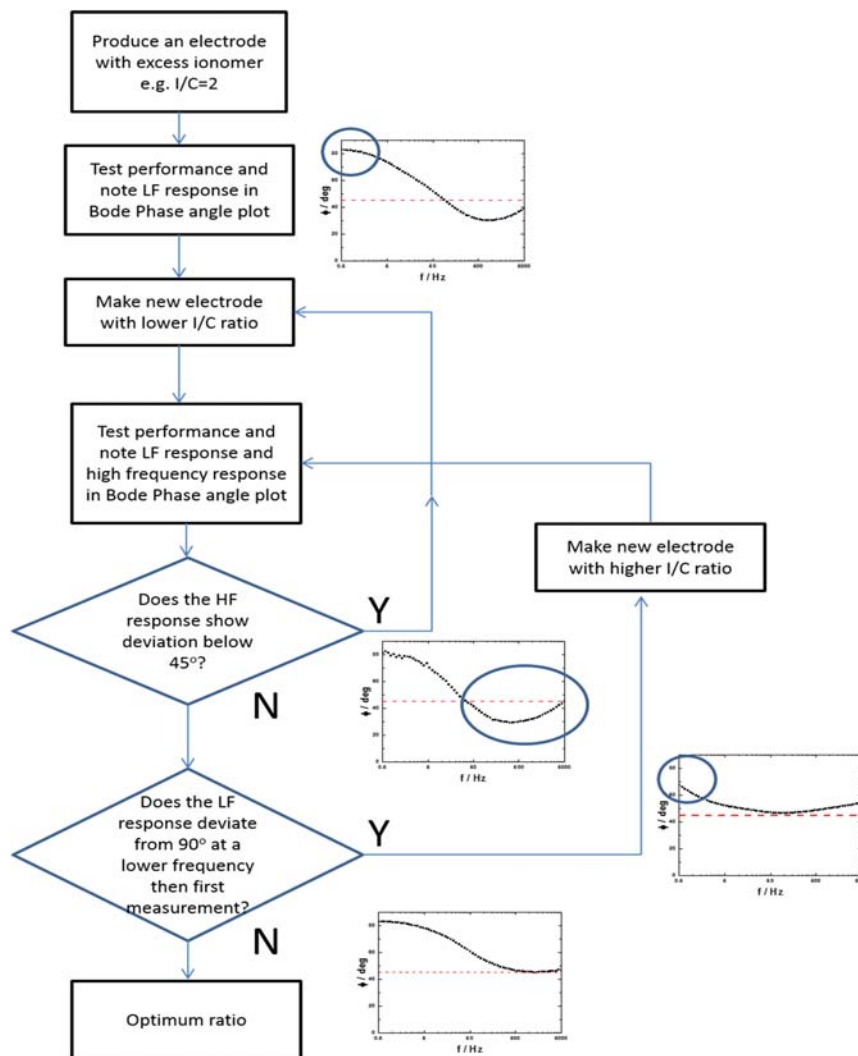


FIGURE 8.15: Flow chart illustrating the optimisation strategy to obtain the best performing catalyst layer. [Taken with permission from Ref. [21]]

The approach involves making a succession of electrodes and determining their EIS performance in a fuel cell configuration running on H<sub>2</sub>/Argon. Utilising this approach the optimum configuration would be determined for all the presented catalyst systems in a minimum number of steps.

## 8.5 Conclusions

By performing an extensive electrochemical impedance spectroscopy (EIS) investigation of three different non-precious metal catalysts with different ionomer content in PEM single cells, it was found that impedance spectroscopy can be used as a diagnostic tool to find an optimised ionomer loading for a given new catalyst. An ionomer coverage which is too high will lead to a deviation from the high frequency 45° line in the *Nyquist*-plot with a tendency to follow a 30° line when the cell is operated in the absence of a faradaic reaction. At low frequencies a phase angle closer to 90° is beneficial. These features are independent of catalyst layer thickness or operating conditions such as relative humidity or back pressure. This strongly suggests a structural origin. An inhomogeneous current distribution, caused by over- or undersaturation of the porous structure with ionomer, is suggested as source of this phenomenon. Although the suggestion relies on an oversimplified model it may give an idea of what impact an inhomogeneous resistance within pores can exhibit. A flow chart illustrates the steps needed to optimise the catalyst layer and determine the optimum ionomer content. This study will help to speed up the time consuming optimisation of MEAs operated on newly developed catalysts.

## 8.6 Experimental Part

### 8.6.1 Electrochemical testing

RDE and MEA testing were performed as described in 3.4.2 and 3.4.10, respectively.

### 8.6.2 AC Impedance Measurements

Electrochemical Impedance spectroscopy (EIS) experiments were carried out from 100 kHz to 0.1 Hz and at 10 points per decade using a potentiostat/galvanostat, Autolab model

302N. Measurements were carried out in the H<sub>2</sub>/O<sub>2</sub> PEMFC working under galvanostatic mode, with the AC current modulation (peak-to-peak) being 5% of the DC current when oxygen was present at the cathode. For measurements in the absence of oxygen, the cathode was purged with argon for 30 minutes prior to EIS measurement under flowing Ar (550 sccm). For these measurement EIS was conducted potentiostatically at 0.1 V with an AC excitation of 5 mV<sub>p-p</sub> (*i.e.* 5% of polarisation). It was ensured that no faradaic current was detected prior to data collection. Linearity of the current/potential response was verified for every measurement. Cells were conditioned at the desired DC current or the desired potential for 60 s prior to EIS experiments. Care was taken to minimize the inductance of the collection leads and cell. Moreover, to ensure a good signal to noise ratio, every data point was collected over 5 integration cycles with an integration time of 0.125 s per cycle. To further ensure validity of the collected data, collection was made from high to low frequency, as well as from low to high frequency for selected cells with several hours of operation in between. No significant deviation was detected. All data were checked for Kramers-Kronig conformity according to an improved method developed by Schoenleber *et al.* [37–39] No drift in the spectra was detected. The correction of the Impedance spectra for high frequency resistance was performed in order to allow a better cross comparison of the catalysts. The correction also reveals the important 45 degree feature in the *Bode* phase plot. Correction was performed by subtracting the high frequency resistance extracted from the high frequency zero intercept on the real axis of the *Nyquist*-plot, where the phase angle is zero. The phase angle and modulus were then recalculated according to equation 2.13 with the corrected real part of the impedance and plotted accordingly.

### 8.6.3 SEM

The SEM samples were prepared by freeze fracturing at liquid nitrogen temperature in order to ensure a clean cut. A Hitachi TM3030 operated in secondary electron mode was used for recording the images of the MEA cross section at low magnification. For the high resolution catalyst layer images, a high resolution field emission gun scanning electron microscope (LEO Gemini 1525 FEGSEM) was used.

### 8.6.4 BET

The isotherms were collected as described in 3.4.4

## 8.7 References

- [1] Gasteiger H.A., Kocha S.S., Sompalli B., Wagner F.T. Activity benchmarks and requirements for Pt, Pt-alloy, and non-Pt oxygen reduction catalysts for PEMFCs. *Applied Catalysis B: Environmental*, 56(1-2), 9–35, March 2005. doi:10.1016/j.apcatb.2004.06.021.
- [2] Jaouen F. Heat-Treated Transition Metal-N<sub>x</sub>C<sub>y</sub> Electrocatalysts for the O<sub>2</sub> Reduction Reaction in Acid PEM Fuel Cells. In Z. Chen, J.P. Dodelet, J.Z. Dodelet, editors, *Non-Noble Metal Fuel Cell Catalysts*, pages 29–118. Wiley-VCH Verlag GmbH & Co. KGaA, 2014. ISBN 978-3-527-66490-0.
- [3] Jaouen F., Proietti E., Lefèvre M., Chenitz R., Dodelet J.P., et al. Recent Advances in Non-Precious Metal Catalysis for Oxygen-Reduction Reaction in Polymer Electrolyte Fuel Cells. *Energy Environ. Sci.*, 4(1), 114–130, December 2010. doi: 10.1039/C0EE00011F.
- [4] US Department of Energy. US DRIVE Fuel Cell Technical Team Roadmap. <http://energy.gov/eere/vehicles/downloads/us-drive-fuel-cell-technical-team-roadmap>. Accessed: 2016-06-03.
- [5] Jaouen F., Goellner V., Lefvre M., Herranz J., Proietti E., et al. Oxygen reduction activities compared in rotating-disk electrode and proton exchange membrane fuel cells for highly active Fe-N/C catalysts. *Electrochimica Acta*, 87, 619–628, January 2013. doi:10.1016/j.electacta.2012.09.057.
- [6] Liu Y., Ji C., Gu W., Baker D.R., Jorne J., et al. Proton Conduction in PEM Fuel Cell Cathodes: Effects of Electrode Thickness and Ionomer Equivalent Weight. *Journal of The Electrochemical Society*, 157(8), B1154–B1162, January 2010. doi: 10.1149/1.3435323.

- [7] Neyerlin K.C., Gu W., Jorne J., Gasteiger H.A. Determination of Catalyst Unique Parameters for the Oxygen Reduction Reaction in a PEMFC. *Journal of The Electrochemical Society*, 153(10), A1955–A1963, January 2006. doi:10.1149/1.2266294.
- [8] Dodelet J.P. The Controversial Role of the Metal in Fe- or Co-Based Electrocatalysts for the Oxygen Reduction Reaction in Acid Medium. In M. Shao, editor, *Electrocatalysis in Fuel Cells*, number 9 in Lecture Notes in Energy, pages 271–338. Springer London, 2013. ISBN 978-1-4471-4910-1 978-1-4471-4911-8. doi:10.1007/978-1-4471-4911-8\_10.
- [9] Eikerling M., Kornyshev A.A. Modelling the performance of the cathode catalyst layer of polymer electrolyte fuel cells. *Journal of Electroanalytical Chemistry*, 453(1-2), 89–106, August 1998. doi:10.1016/s0022-0728(98)00214-9.
- [10] Eikerling M., Kornyshev A.A. Electrochemical impedance of the cathode catalyst layer in polymer electrolyte fuel cells. *Journal of Electroanalytical Chemistry*, 475(2), 107–123, October 1999. doi:10.1016/s0022-0728(99)00335-6.
- [11] Iden H., Sato K., Ohma A., Shinohara K. Relationship among Microstructure, Ionomer Property and Proton Transport in Pseudo Catalyst Layers. *Journal of The Electrochemical Society*, 158(8), B987–B994, January 2011. doi:10.1149/1.3598141.
- [12] Lefebvre M.C., Martin R.B., Pickup P.G. Characterization of Ionic Conductivity Profiles within Proton Exchange Membrane Fuel Cell Gas Diffusion Electrodes by Impedance Spectroscopy. *Electrochemical and Solid-State Letters*, 2(6), 259–261, January 1999. doi:10.1149/1.1390804.
- [13] Liu Y., Murphy M., Baker D., Gu W., Ji C., et al. Determination of Electrode Sheet Resistance in Cathode Catalyst Layer by AC Impedance. *ECS Transactions*, 11, 473–484, September 2007. doi:10.1149/1.2780961.
- [14] Makharia R., Mathias M.F., Baker D.R. Measurement of Catalyst Layer Electrolyte Resistance in PEFCs Using Electrochemical Impedance Spectroscopy. *Journal of The Electrochemical Society*, 152(5), A970–A977, January 2005. doi:10.1149/1.1888367.
- [15] Malevich D., Jayasankar B.R., Halliop E., Pharoah J.G., Peppley B.A., et al. On the Determination of PEM Fuel Cell Catalyst Layer Resistance from Impedance



- Measurement in H<sub>2</sub>/N<sub>2</sub> Cells. *Journal of The Electrochemical Society*, 159, F888–F895, January 2012. doi:10.1149/1.3635606.
- [16] Morris D.R.P., Liu S.P., Villegas Gonzalez D., Gostick J.T. Effect of Water Sorption on the Electronic Conductivity of Porous Polymer Electrolyte Membrane Fuel Cell Catalyst Layers. *ACS Applied Materials & Interfaces*, 6(21), 18,609–18,618, November 2014. doi:10.1021/am503509j.
- [17] Passalacqua E., Lufrano F., Squadrito G., Patti A., Giorgi L. Nafion content in the catalyst layer of polymer electrolyte fuel cells: effects on structure and performance. *Electrochimica Acta*, 46(6), 799–805, January 2001. doi:10.1016/s0013-4686(00)00679-4.
- [18] Roshandel R., Ahmadi F. Effects of catalyst loading gradient in catalyst layers on performance of polymer electrolyte membrane fuel cells. *Renewable Energy*, 50, 921–931, February 2013. doi:10.1016/j.renene.2012.08.040.
- [19] Saab A.P., Garzon F.H., Zawodzinski T.A. Determination of Ionic and Electronic Resistivities in Carbon/Polyelectrolyte Fuel-Cell Composite Electrodes. *Journal of The Electrochemical Society*, 149(12), A1541–A1546, January 2002. doi:10.1149/1.1516771.
- [20] Yi J.S., Song T.w. Performance Characterization of PEM Fuel Cells Using AC Impedance Spectroscopy I. Model-Based Analysis. *Journal of The Electrochemical Society*, 160(2), F141–F152, January 2013. doi:10.1149/2.053302jes.
- [21] Malko D., Lopes T., Ticianelli E.A., Kucernak A. A Catalyst Layer Optimisation Approach Using Electrochemical Impedance Spectroscopy for PEM Fuel Cells Operated with Pyrolysed Transition Metal-N-C Catalysts. *Journal of Power Sources*, 323, 189–200, August 2016. doi:10.1016/j.jpowsour.2016.05.035.
- [22] Raistrick I.D. Impedance studies of porous electrodes. *Electrochimica Acta*, 35(10), 1579–1586, October 1990. doi:10.1016/0013-4686(90)80013-e.
- [23] Lasia A. *Electrochemical Impedance Spectroscopy and its Applications*. Springer, New York, NY, 2014 edition, July 2014. ISBN 978-1-4614-8932-0.

- [24] Springer T.E., Zawodzinski T.A., Wilson M.S., Gottesfeld S. Characterization of Polymer Electrolyte Fuel Cells Using AC Impedance Spectroscopy. *Journal of The Electrochemical Society*, 143(2), 587–599, January 1996. doi:10.1149/1.1836485.
- [25] Lopes T., Kucernak A., Malko D., Ticianelli E.A. Mechanistic Insights into the Oxygen Reduction Reaction on Metal–N–C Electrocatalysts under Fuel Cell Conditions. *ChemElectroChem*, 3(10), 15801590, September 2016. doi:10.1002/celec.201600354.
- [26] Bisquert J., Garcia-Belmonte G., Fabregat-Santiago F., Compte A. Anomalous transport effects in the impedance of porous film electrodes. *Electrochemistry Communications*, 1(9), 429–435, September 1999. doi:10.1016/s1388-2481(99)00084-3.
- [27] Eloot K., Debuyck F., Moors M., Peteghem A.P.V. Calculation of the impedance of noncylindrical pores Part I: Introduction of a matrix calculation method. *Journal of Applied Electrochemistry*, 25(4), 326–333, April 1995. doi:10.1007/bf00249650.
- [28] Hernandez R.d.P.B., Aoki I.V., Tribollet B., de Melo H.G. Electrochemical impedance spectroscopy investigation of the electrochemical behaviour of copper coated with artificial patina layers and submitted to wet and dry cycles. *Electrochimica Acta*, 56(7), 2801–2814, February 2011. doi:10.1016/j.electacta.2010.12.059.
- [29] Hitz C., Lasia A. Experimental study and modeling of impedance of the her on porous Ni electrodes. *Journal of Electroanalytical Chemistry*, 500(1-2), 213–222, March 2001. doi:10.1016/s0022-0728(00)00317-x.
- [30] Keiser H., Beccu K.D., Gutjahr M.A. Abschätzung der porenstruktur poröser elektroden aus impedanzmessungen. *Electrochimica Acta*, 21(8), 539–543, August 1976. doi:10.1016/0013-4686(76)85147-x.
- [31] Lasia A. Nature of the two semi-circles observed on the complex plane plots on porous electrodes in the presence of a concentration gradient. *Journal of Electroanalytical Chemistry*, 500(1-2), 30–35, March 2001. doi:10.1016/s0022-0728(00)00361-2.
- [32] Musiani M., Orazem M., Tribollet B., Vivier V. Impedance of blocking electrodes having parallel cylindrical pores with distributed radii. *Electrochimica Acta*, 56(23), 8014–8022, September 2011. doi:10.1016/j.electacta.2010.12.004.

- [33] Paasch G., Micka K., Gersdorf P. Theory of the electrochemical impedance of macro-homogeneous porous electrodes. *Electrochimica Acta*, 38(18), 2653–2662, December 1993. doi:10.1016/0013-4686(93)85083-b.
- [34] Park J.R., Macdonald D.D. Impedance Studies of the Growth of Porous Magnetite Films on Carbon Steel in High Temperature Aqueous Systems. *Corrosion Science*, 23(4), 295–315, January 1983. doi:10.1016/0010-938X(83)90063-X.
- [35] Song H.K., Hwang H.Y., Lee K.H., Dao L.H. The effect of pore size distribution on the frequency dispersion of porous electrodes. *Electrochimica Acta*, 45(14), 2241–2257, March 2000. doi:10.1016/s0013-4686(99)00436-3.
- [36] Barsoukov E., Macdonald J.R. *Impedance Spectroscopy: Theory, Experiment, and Applications*. John Wiley & Sons, Hoboken, N.J, 2nd edition, April 2005. ISBN 978-0-471-64749-2.
- [37] Schönleber M., Klotz D., Ivers-Tiffée E. A Method for Improving the Robustness of linear Kramers-Kronig Validity Tests. *Electrochimica Acta*, 131, 20–27, June 2014. doi:10.1016/j.electacta.2014.01.034.
- [38] Schönleber M., Ivers-Tiffée E. Approximability of impedance spectra by RC elements and implications for impedance analysis. *Electrochemistry Communications*, 58, 15–19, September 2015. doi:10.1016/j.elecom.2015.05.018.
- [39] Boukamp B.A. A Linear Kronig-Kramers Transform Test for Immittance Data Validation. *Journal of The Electrochemical Society*, 142(6), 1885–1894, January 1995. doi:10.1149/1.2044210.

## Chapter 9

# Concluding remarks

### 9.1 Final Conclusions

As discussed in Chapter 1, the further optimisation of M-N/C materials for the replacement of Pt as ORR catalysts in PEMFCs has recently slowed down. This comes after promising initial results with significant successive improvements. Yet activity and stability are still too low for practical applications. Fundamental understanding of the active site and other catalyst properties is expected to allow for further advancements, eventually bridging the remaining gap.

However, current knowledge is unsatisfactory for the following reasons:

- (a) The complex structure of the material. The material predominantly consists of strongly light absorbing high surface area carbon and contains a low amount of transition metal, which is believed to serve as active site. This makes the use of spectroscopic techniques and other physical characterisation techniques challenging
- (b) A lack of a suitable probe that interacts with the active site in order to draw meaningful conclusions. A stable probe would allow to correlate *ex-situ* characterisations with the catalytic activity.
- (c) No possibility to determine the intrinsic catalytic activity, *i.e.* active site density and TOF, of a given material. This makes it challenging to establish trends.
- (d) Little understanding as to how ubiquitous the catalyst is and whether it can be used to address other important catalytic reactions, such as seen for platinum.

- (e) Poor understanding of the catalyst behaviour in working single cells. Few studies systematically investigated non-precious metal catalysts in MEAs. The thicker catalyst layer, caused by the higher loading, is expected to pose challenges in mass transport, water management and ion conductivity.
- (f) The laborious determination of an optimal single cell configuration when preparing a new MEA. This makes it time consuming to perform large studies.

This work achieved advancement in the above mentioned shortcomings by investigating the active site of a suitable model material with various different approaches and experimental techniques, which are described in Chapter 2.

A model catalyst was synthesised and characterised in Chapter 3, addressing some of the issues raised in (a) above:

- It was found that the polymerisation and subsequent pyrolysis of 1,5-diaminonaphthalene provides a catalytically active material. The fact that this catalyst is self supporting, **i.e.** the use of carbon black or a sacrificial support was not necessary, allowed for the establishment of trends.
- Different metal centres and the effect of surface area was investigated. It was found that Fe is the most active amongst the 3d metals and that the activity seems to be correlated with the microporous surface area rather than the total BET surface area.
- Various physical characterisations have been carried out. Using BET, XPS, TXRF, EPR and high resolution electron microscopy, it was found that this material most likely resembles the key properties of other highly active catalysts reported in literature, *i.e.* amorphous nitrogen doped carbon with atomic metal centres. Therefore it was deemed suitable as a model system to further investigate active sites within the material.

In Chapter 4, an attempt was made to address point (b) above and the catalyst was subjected to varying conditions in order to investigate the effect of the chemical environment on the active site:

- It was found that the catalyst is surprisingly poison tolerant and operates well in the presence of chloride, urea, methanol, H<sub>2</sub>S and volatile organic compounds. The

reference Pt catalyst was always severely affected. This is interesting for applications, where the catalyst has to operate under challenging conditions, such as in waste water treatment.

- Nitrogen cycle molecules and treatment with organic chemicals, *i.e.* *Friedel-Crafts*-conditions have been found to decrease the activity and this has been utilised to probe the active site later in the work.
- Gas sorption has determined the energy of desorption for molecular oxygen to be 79.09 kJ mol<sup>-1</sup> on the **Fe-N/C** catalyst.
- pH dependence and the kinetic isotope effect strongly suggest a proton coupled electron transfer as rate determining step.

The fact that nitrite and nitric oxide interact with the **Fe-N/C** catalyst has been used to generate further insight into the active site, addressing points (b) and (c), as described in Chapter 5:

- It could be shown that the active site in alkaline and in acid seem to be different.
- The interaction with nitrite shows the formation of either a strong or a weak adduct depending on treatment conditions.
- It was found that the nitrite and nitric oxide interact with the Fe-N/C material but not with the N/C material, suggesting a metal centre as active site
- It was found that the Fe-N/C catalyst is active towards NO and NO<sub>2</sub><sup>-</sup> reduction with ammonia as major product. This can be useful for environmental nitrite destruction of sensor applications.

A method has been developed to determine the intrinsic activity of Fe-N/C catalysts in Chapter 6, addressing point (c):

- It was found that nitrite could be reductively stripped from the catalyst surface
- The stripping peak could be directly correlated with the activity. This allowed the determination of the number of active sites and the TOF of those.
- It was found that 2 types of active sites seem to be present within the material. Type A which is responsible for 80% of the activity and forms a stable bond with

nitrite which can then be stripped and Type B, which is only affected when nitrite is present in solution

In Chapter 7, it was decided to see how ubiquitous this catalyst is, addressing point (d), and it was shown that the catalyst efficiently promotes the epoxidation of alkenes:

- It was found that the reaction proceeds under the same conditions as for metal macrocyclic complexes, suggesting analogies in the chemical behaviour.
- The reaction works under ambient conditions, *i.e.* room temperature and pressure. This could inspire the development of new catalytic systems, capable of promoting a range of oxidation reactions under mild conditions.
- A system has been developed which allows the simultaneous tracking of oxygen consumption and electrochemical potential. It is expected that further investigations utilising this set-up lead to new insight into the catalytic behaviour, useful for both the ORR and the epoxidation.

Finally, in Chapter 8, the catalyst was investigated in a MEA single cell, addressing points (e) and (f):

- A parametric study was performed, where the ionomer content of 3 different M-N/C catalysts was varied and impedance spectroscopy was performed in the presence and absence of a faradaic reaction
- It was found that the impedance spectrum can be used as a diagnostic tool to determine whether the assembled MEA contains the ideal ionomer content or not. This will significantly speed up the time consuming investigation of MEAs operated with newly developed catalysts.

Although in this work no catalyst was developed that surpassed the highest reported activities, significant insight into the behaviour of the catalytic site could be generated. Tools have been provided to advance the further development in the field. The work has opened new avenues for experiments which can provide more insight and optimised catalysts with higher activities.

## 9.2 Future work

Catalyst development:

- The fact that the catalyst developed in this work is self supporting and the pore structure can be tuned with a nanoparticulate support, might enable the tuning of the pore structure for efficient reactant support. Specifically, a mixture of nanoparticles with a range of different sizes could be used as template, in order to optimise the porosity of the catalyst.
- Heat treatment with ammonia gas could improve the catalytic activity as for similar catalysts

Poison tolerance:

- The poison tolerance of the catalyst could be exploited to use it under challenging conditions. This could be as ORR catalyst for waste water treatment or sensing applications in biological fluids.

Active site modifications:

- The *Friedel-Crafts* reaction was only one example of post synthetic treatments of the catalyst. Other reactions could be attempted in order to graft functional groups to the catalyst surface, making it more electronegative or electropositive, thereby possibly influencing the activity beneficially.

Nitrite, nitric oxide electrochemistry in combination with *ex-situ* characterisations:

- Based on the specific interaction of the catalyst with nitric oxide and nitrite, various different treatments could be performed on the catalyst as described in chapters 5 and 6. The treated catalyst could then be analysed with Mössbauer, EXAFS and EPR, in order to find which moiety exactly is deactivated upon treatment with those compounds. This might unambiguously determine the active site within Fe-N/C catalysts. Once these sites were identified, a bottom up synthesis could be developed.
- The stripping methodology in conjunction with a study, where different catalysts are analysed could determine which treatment increases TOF and which active site



density. With this knowledge new strategies could be implemented on how to develop a synthesis procedure which promotes the formation of the highest proportion, high TOF sites, thereby producing a catalyst with a higher activity.

Oxidation catalysis:

- Other reactions, which are usually catalysed by transition metal complexes could be investigated with the Fe-N/C catalyst. It might be possible to develop a new heterogeneous catalyst platform for the heterogeneous activation of small molecules in industrial catalysis, harnessing the powerful catalytic properties of metal macrocyclic compounds, while being more robust, lower cost and easily recyclable.
- The developed set-up for simultaneously tracking oxygen consumption and potential can now be used to study the reaction mechanism of the catalyst, by varying the concentration of reactants and the alkene, as described in Chapter 7. This will provide further insight.

Mechanism of oxygen reduction on these catalysts:

- Further mechanistic insight might be available by studying the ORR over a wide range of oxygen partial pressure and temperature in combination with mechanistic modelling.

Fuel cell operation:

- Further parametric studies, varying the oxygen partial pressure in combination with performance testing and impedance spectroscopy can provide more insight into the source of mass transport losses.
- Further studies into the degradation mechanism are necessary in order to better understand the stability of the material and be able to develop mitigation strategies, in order to improve longevity.
- Using the data sets obtained, computational models might be established and verified, providing further understanding on the behaviour of thick catalyst layers. This might lead to catalyst layer design strategies, which might then lead to higher a performance for a given catalyst.

---

At the moment it is not possible to foresee, whether M-N/C catalyst ever become feasible for transportation applications in terms of activity, selectivity and stability. However, this work offers significant insight into the active site and provides tools that might enable the improvements of the materials and to gather further insight. It also provides the alternative applications for these materials.

THE END